UNIVERSITÁ DEGLI STUDI DI MILANO

Department of Chemistry

Ph.D. Course in Industrial Chemistry

Cycle XXX

DESIGN AND CHARACTERIZATION OF Cu_2O PHOTOCATHODES FOR PHOTOELECTROCHEMICAL WATER SPLITTING.

Tutor: **Prof. Sandra Rondinini.**

Co-tutor: **Prof. Alberto Vertova, Prof. Alessandro Minguzzi.**

Ph.D. Thesis of:

Alberto Visibile

Academic Year 2016/2017

List of Contents

Extended Abstract

The exploitation of renewable energy sources is one of the most addressed aspects for the sustainable development of human activities. Molecular hydrogen can be considered one of the most interesting energy vectors to fulfill humankind's needs. In this context, photoelectrochemical water splitting (PEC-WS) using solar energy to produce H_2 at semiconducting materials is considered one of the most interesting technologies. In the present study, Cu_2O was selected as cathode material for its correct band position for hydrogen evolution, together with non–toxic and low-cost starting material.

The research activity was devoted to the development of photocathodes for the PEC-WS and their characterization under working conditions with different techniques. The work was divided in:

I) The role of the underlayer in Cu_2O photocathodes for PEC-WS;

II) Characterization of copper oxide based materials under PEC-WS by X-Ray Absorption Spectroscopy (XAS)

III) Characterization of Photoactive Semiconductor Materials by Cavity Micro-Electrodes (C_ME) & Scanning ElectroChemical Microscopy (SECM)

IV) Development of new protective layers for the PEC_WS systems: FeOOH and CuO/Cu_2O core-shell systems

V) Application of the Density Function Theory (DFT) to study doping materials and vacancy formation in Cu_2O

1) The complete electrode scheme is constituted by (i) a transparent conductive support (usually FTO), (ii) a conductive underlayer of electrodeposited Cu, that is assumed to enhance the electron-hole separation (iii) the semiconductor, (iv) a thin transparent protective overlayer of about 80 nanometers. In the present study, the underlayer of Cu replaces the expensive and toxic Cr/Au underlayer. Therefore, a specific protocol for the preparation of the Cu_2O photoconverter was developed and validated, obtaining good results in terms of generated photocurrent (Figure 1). Appropriate modifications of underlayer deposition conditions also lead to large increase in the Cu_2O photocurrents, thus denoting that the underlayer has a marked influence on the system performances.

In the final deposition protocol, several parameters were defined and controlled: deposition potential and the relevant current intensity; temperature, pH and stirring conditions; loading (C/cm^2) of Cu(0) underlayer and Cu_2O active layer. In particular, the thickness of the Cu underlayer was controlled in order to obtain a transparent layer while maintaining high electric conductivity. Transparency of the entire support is an important feature, allowing the use of the electrode in both front and back illumination configurations. Moreover, a complete study of the copper lactate bath was performed with electrochemical methods and X-ray Absorption Spectroscopy (XAS).

The experiments show that the best fit is obtained by a model where four lactate ions act as monodentate ligands, 1:4 (Cu:L), in a distorted tetrahedral geometry.

Notwithstanding the good results in photocurrent, the actual Cu_2O photoconverter is able to work at the highest potential only for a few minutes and for this reason the development of a protective overlayer was mandatory as explained later.

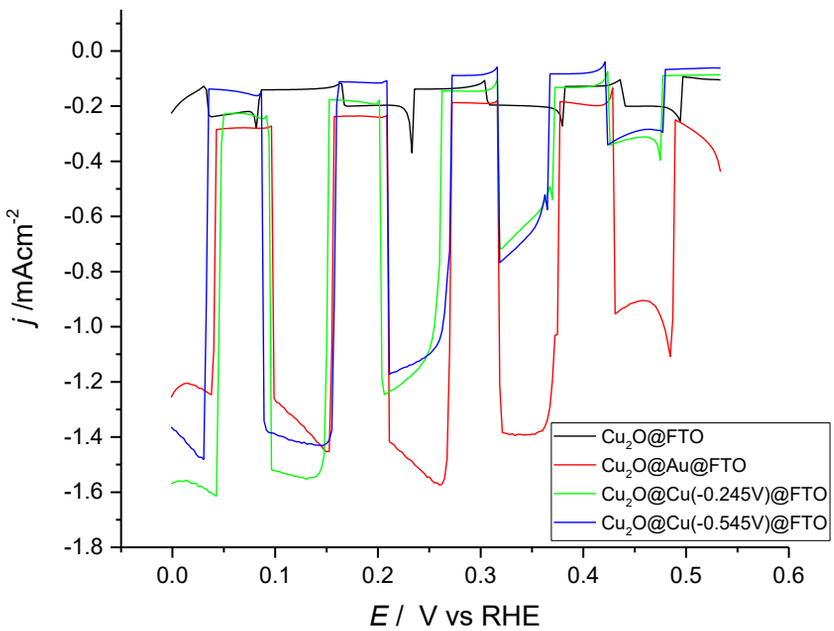

Figure 1. *Comparison between photocurrents obtained with bare FTO (black line), Au (red line), Cu(0) (green and blue line) and as underlayers for Cu_2O semiconductor under pulsed light in pH 11 buffer electrolyte.*

2) The short life of Cu_2O photoconverter is due to photodegradation. In order to investigate this phenomenon, XAS measurements at Cu-K edge were performed to define photodegradation products, individuate stability potential window and elucidate the possible combined effects of light and potential.

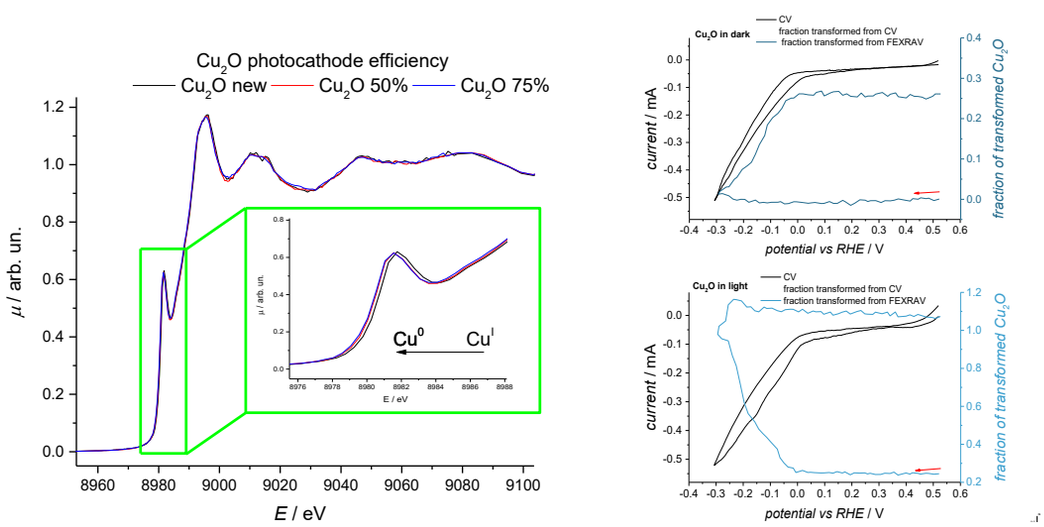

Figure 2*. A) XANES spectra of Cu_2O electrode: new, at 50%, and 75% reduction of the initial photocurrent. B) FEXRAV under dark and light conditions of Cu_2O@Au@FTO electrode.*

In-situ and *operando* techniques like X-Ray Absorption Near Edge Structure (XANES), Extended X-Ray Absorption Fine Structure (EXAFS) and Fixed Energy X-Ray Absorption Voltammetry (FEXRAV) allow us to better understand material behavior. Changes in copper oxidation states upon light and/or applied potential were observed and with XANES was possible to evaluate the amount of photo-generated Cu(0) responsible of the loss of activity (Figure 2A). FEXRAV measurements allow following the material (photo)degradation and defining the stability windows (Figure 2B). With difference light and dark XANES spectra the local changes in electronic structure upon spectro-electrochemical conditions were also investigated.

3) The photodegradation reaction showed by Cu_2O, is common to many other materials for HER and OER (Oxygen Evolution Reaction,). This instability occurs when the redox potential of the material lies between valence band and conduction band. This implies that the photocurrents recorded in normal pulsed experiments are composed by the sum of water splitting and photodegradation. The novel method here presented allows the evaluation of the intensity of the photo-degradation processes, giving at the same time a rapid screening tool for differently prepared materials. Moreover, this method allows to evaluate the activity of a semiconductor without any influence of the supporting material. In addition, low experimental times and low amount of photo-produced material are required if compared to actual methods (GC and volume displacement). Scanning ElectroChemical Microcopy (SECM), here used in Tip Generation/ Substrate Collection mode (TG/SC), allows to discriminate between water splitting and photo-degradation. The system is so composed:

- Tip (working electrode 1) is a micro cavity electrode filled with the semiconducting powder. The electrode potential is varied in the potential window of interest under light steps.
- Substrate is a Pt foil (working electrode 2) with potential fixed at the H_2 (or O_2) oxidation (reduction) value, working as a "probe" for the species of interest.

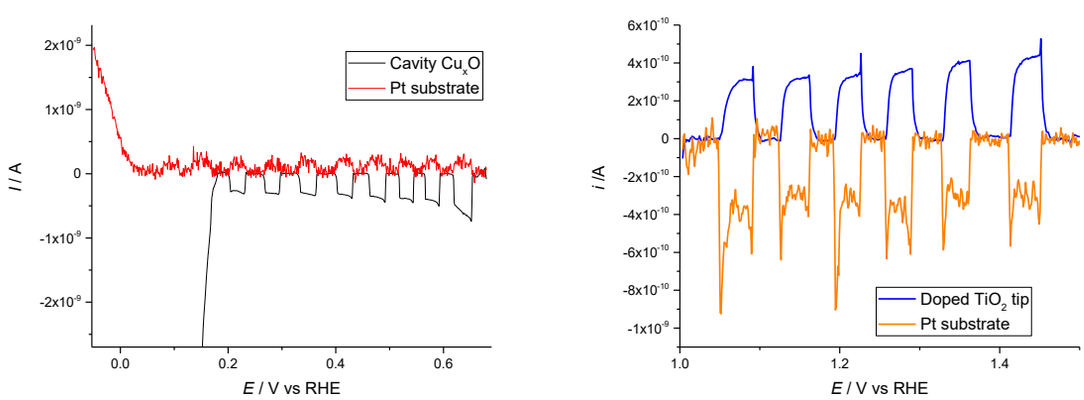

***Figure 3**. Linear sweep voltammetry of Cu_XO powder recorded in TG-SC mode on SECM in pH 7 buffer electrolyte under pulsed light. B) Linear sweep voltammetry of TiO_2 powder in NaOH 0.1M under pulsed light.*

Several materials were studied with good results: Cu_XO, CuI, NiO and TiO_2. Influence of cavity depth and light intensity were tested too. From data analysis we can demonstrate different photocurrent efficiencies for the studied materials.

Obviously TiO_2 is near to 100% (Figure 3B) as expected from its very high stability while other materials, as CuI, in spite the high photocurrents, shows very low amount of photogenerated H_2.

Material	**Cu_XO**	**NiO**	**CuI**	**TiO_2**
% of photoefficeincy	68-92%	28-53%	12-35%	75-100%

4) Previously, we have seen how Cu_2O photodegradation is due to the combination of light and potential. The phenomenon occurs because the photogenerated electrons have enough energy to reduce water but also to reduce the material itself. For this reason, the development of a protective layer that can avoid the photodegradation is of paramount importance. Different materials were considered, and the final choice falls on the two phases of iron oxyhydroxide, α-FeOOH and γ-FeOOH, non-toxic and low-cost materials, deeply studied because they are corrosion products of chlorate process cathodes. These materials were here studied by electrochemical and XAS techniques to gain information about their oxidation state during HER and its reversibility. Then the final interaction of FeOOH and Cu_2O was studied to explore the possibility of protecting the Cu(I) oxide by 80 nm of a transparent FeOOH layer.

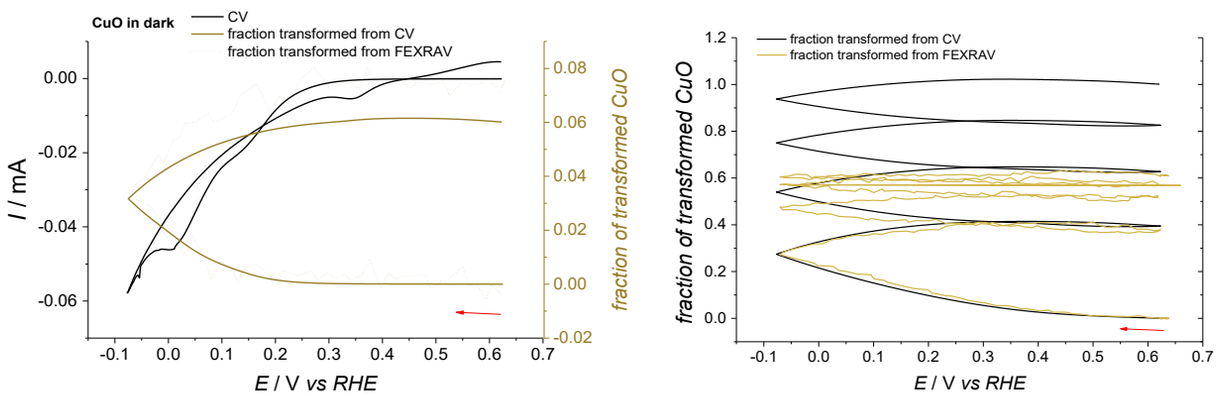

Figure 4. *Fraction of reduced CuO and current intensity as a function of the applied potential during a FEXRAV experiment of a Cu_XO electrode at 8981 eV in the dark (A) and under LED 400 nm illumination (B).*

A different approach was then adopted with the preparation of a CuO/Cu_2O core-shell material (denoted as Cu_XO). Cu_XO is composed by a CuO core and an external shell of Cu_2O with the proportion determined via FEXRAV. Cu_2O is grown on CuO by cycling the potential as in Figure 4, and eventually a stable and active material for HER is obtained. We were also able to assess that CuO is not an active species for HER, but also that the electrochemically generated Cu_2O (the true active material for HER) is protected from photo-degradation by the CuO core.

Our explanation for this protective action lies in the relative band position of CuO and Cu_2O. CuO has a smaller band gap (1.5eV) that lies inside the larger band gap of Cu_2O. FEXRAV (Figure 4B) supports this explanation, since the signal becomes constant in time, to indicate that the material transformation is stopped and that the only reaction occurring at the electrode is hydrogen evolution.

These results are in agreement with the high photoefficiency of the Cu_XO powder determined with SECM.

5) According to literature the p-type character of Cu_2O is strictly related to the formation of copper vacancies in its lattice. Doping can enhance the formation of vacancies, improving the number of majority carriers (holes) and their mobility, and modifying the band gap by shifting the Cu_2O states or by introducing an intermediate band within the band gap (Figure 5B). On the basis of the electrochemical results obtained with different underlayers, this work firstly aims to study a large array of potentially effective metal underlayers.

The role of Density Functional Theory (DFT) is here to rank the underlayers' aptitude in modifying the properties of Cu_2O, and, in particular, the formation of copper or oxygen vacancies in the semiconductor.

Then, the doping of the material is studied for a selected number of transition metals. For each material, the valence and conduction band positions were computed as well as the number of vacancies and their formation energies.

Eventually the influence of lattice strain on material band gap and energy levels is studied both with expansion and reduction of the Cu_2O lattice after the deposition onto different substrates. The use of the alkaline metals as well as atomic hydrogen as dopants allowed to evaluate the influence of the dopant size on the doped material.

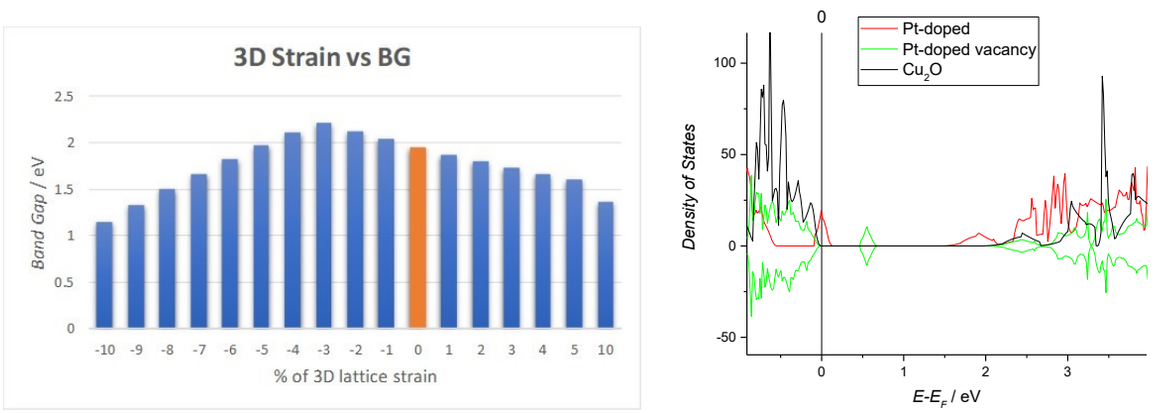

Figure 5. *A) Influence of lattice strain on Cu_2O band gap. B) Density of states of Pd-doped Cu_2O compared to pure material.*

1. Introduction

1.1 Hydrogen Economy

This chapter synthetically discusses the main aspects that are at the basis of the so-called "hydrogen economy", starting with a brief summary of the world energy production trends, with specific focus on the technologies for the H_2 production, storage and delivery already available on the market or under development. A short market analysis is included aimed at estimating the future possibilities for these technologies. After this general review, the reader will enter more in the topic of the work with a discussion about the developing of PEC-WS system and the characteristic of the chosen material, Cu_2O. Eventually, the different techniques used in this work will be briefly presented in order to make the reader more familiar with them in view of the successive discussion of the obtained results.

1.1.1 Energy Trends

According to the 2016 IEA report on "Key World Energy Trends", the 2014 world energy production was 13800 Mtoe with an increase of 1.1 % compared to the previous year. This trend is quite expected due to the higher and higher energy demanding life of every day in OECD countries together an even higher contribute of countries like China, India and Brazil due to their extremely fast economical and industrial development. On a worldwide scale fossil fuels still play the main role in the energy supply (Figure 1A). Despite this, in the last 40 years but even more nowadays, a larger increase in the interest devoted in renewable sources (Figure 1B) is noticeable [1].

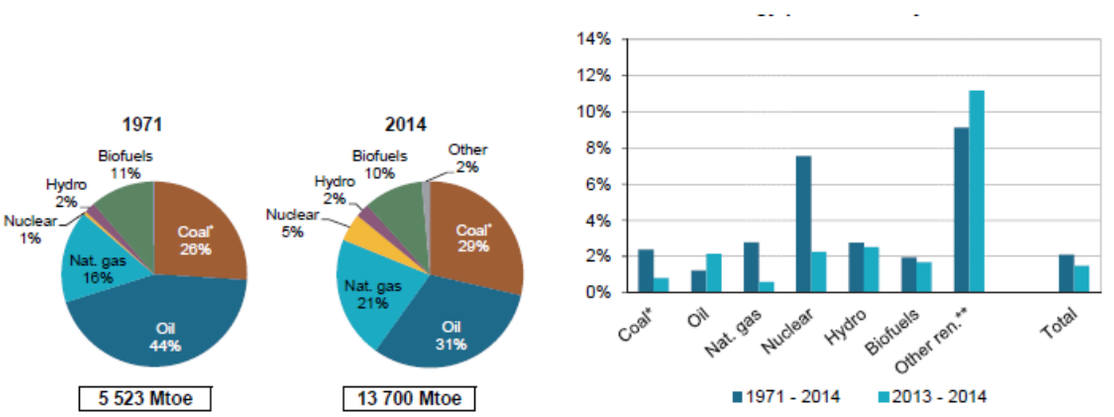

***Figure 1**. A) Total primary energy supplied by fuels in 1971 and 2014. Image from "Key World Energy Trends, IEA 2016". B) Global annual change in energy production. In dark-blue is reported the long-term change, in light-blue the short one related to 2013-2014. Image from "Key World Energy Trends, IEA 2016"* [1].

This trend is even more evident looking at the 105 TWh decrease in fossil fuels consumption for electricity generation, followed by an 11% increase in renewable sources to compensate this decrease (Figure 2A). Looking at the sources, coal is still the most used with 29% of the total produced Mtoe but is interesting how the percentage of renewable sources is increasing. Between the latter is possible to notice how, while hydro have more or less reached its maximum capacity, other sources like solar, wind, bio and geothermal are the main actors in the fossil fuel-free alternatives growth. Their contribute was big in the last decades and they will be the majority of the estimated generation sources in the next 20 years (Figure 2B) [2].

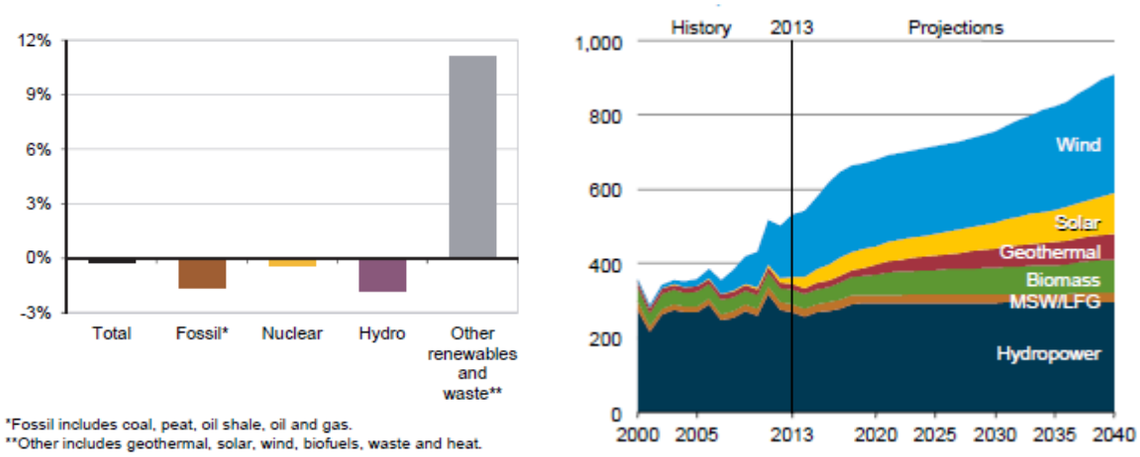

***Figure 2**. A) OECD electricity generation 2014-2015 changes. Image from "Key World Energy Trends, IEA 2016". B) OECD renewable electricity generation 2000-2040 in billions of KWh. Image from "Key World Energy Trends, IEA 2016"* [1].

Of Course, this are general trend, looking in more detail in the single countries some differences could be evident according to different economically and politically related energetic plans. In Figure 3 is reported the estimated trend for U.S until 2040 with respect to the political agreements before 2017.

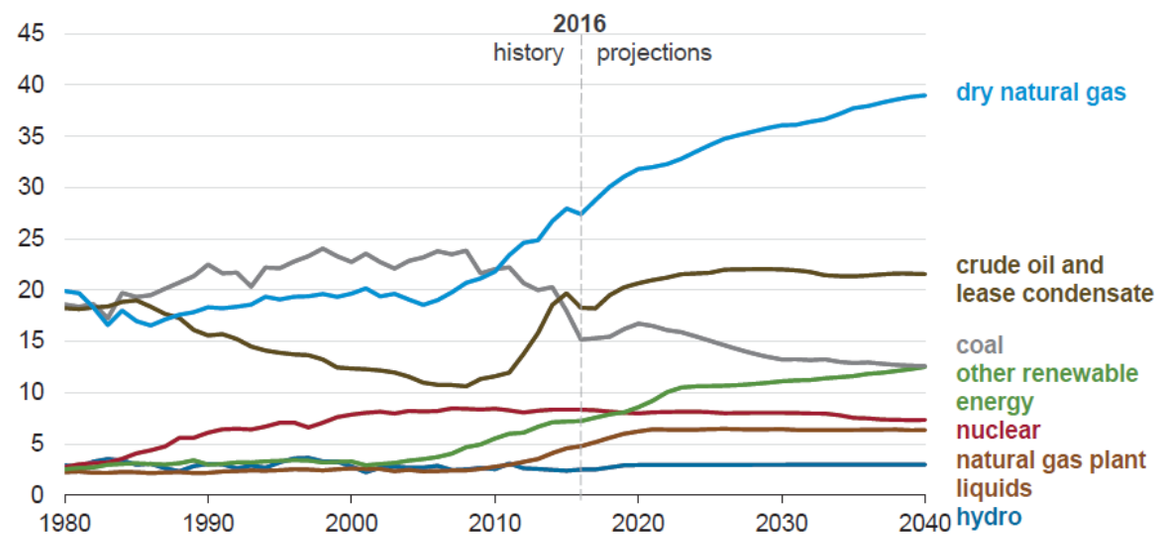

***Figure 3.** U.S energy production at 2016 and projection to 2040. Image from IEA Annual Energy Report 2017* [3].

This large increase in renewable sources market is mostly due to the need to face the last century climate changes, together with a significative decrease in these technologies price and increase in efficiency. Wind and solar photovoltaics (PV) are the sources with the fastest growth mainly because the great effort of researchers who sustain their technological progress and also thanks to the subsidies and financing condition performed by several governments. We can easily see how the cost of wind and solar generated electricity decreased of 80 and 35% respectively between 2008 and 2015 (Figure 4) making these technologies almost ready to be competitive, mature and economically affordable 4–6. Figure 5 shows in detail the price reduction in Italy occurred in those years.

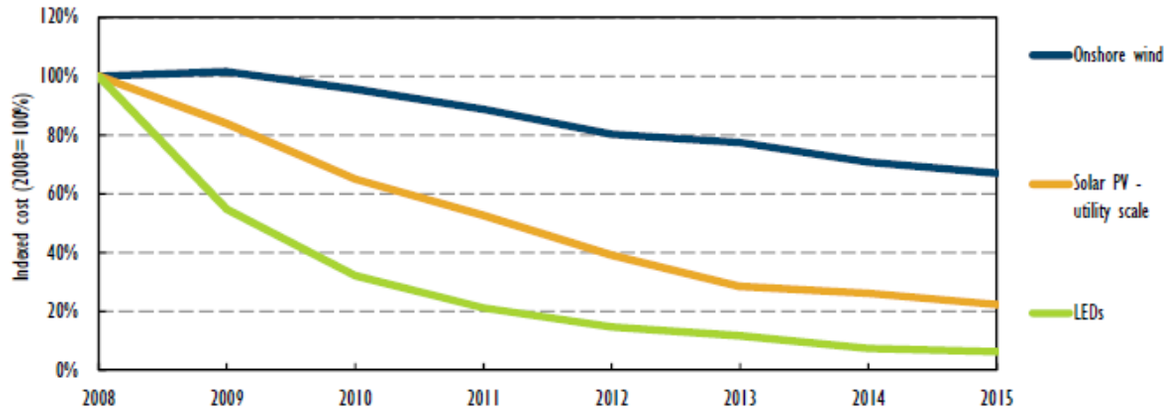

Note: LED = light-emitting diode; numbers report non-subsidised cost of energy.
Source: Adapted from IEA (2015a), *Medium-Term Renewable Energy Market Report 2015*.

Figure 4. *Indexed cost of onshore wind, utility-scale PV and LED lighting, 2008-2015. Image from "Next Generation Wind and Solar Power. From cost to value by IEA 2016"* [4].

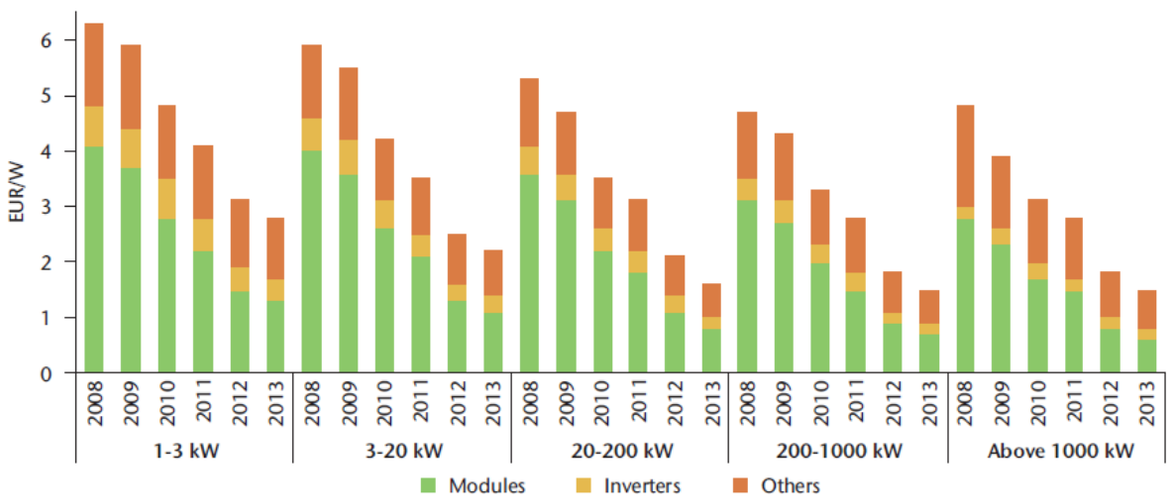

Source: Gestore dei Servizi energetici (GSE) (2014), *PV in Italy: Generation Costs and Value Chain*, May, Rome.

Figure 5. *System prices in Italy 2008-2013. Image from Technology Roadmap, Solar Photovoltaic Energy, IEA, 2014*[6].

1.1.2 Smart Grids

Simultaneously to their growth, the renewable sources based system, need the development of a smart grid in the near future or the development of a sustainable and efficient storage system[7,8]. With renewable sources indeed, the total input in the power grid is floatable and strongly related to the availability of the source (wind, sun etc..).

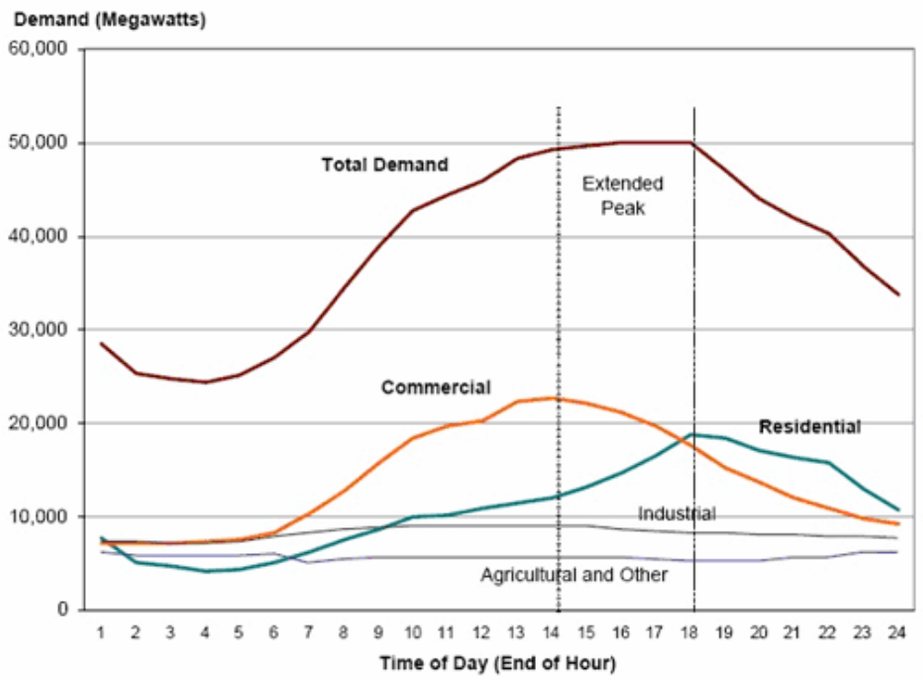

Figure 6. *Average electricity demand (in MW) during the day recorded in the U.S. Image from Lawrence Berkeley National Laboratory. The same trend can be assumed for all the developed countries.*

Moreover, the total load connected to the power grid can significantly vary over time depending on season and time of the day (Figure 6). Traditionally, to respond to a rapid increase in power consumption, generators never work at the maximum load. Transmission and distribution infrastructures allow bidirectional energy flows with small (on domestic scale) and distributed renewable inputs coming. A large implementation, far away better than the actual, will be not easy and the presence of an efficient energy storage system will be mandatory. Batteries cannot fulfill this aim due to their low energy density (Figure 7 and Figure 16) and high cost mostly for large scale applications[9]. Ragone plots provide the available energy of an energy storage devices (ESD) for constant active power request. The qualitative form of Ragone plots strongly depends on the type of storage (battery, capacitor, SMES, flywheel, etc.). We can see how the specific energy density for lithium ion batteries (and batteries in general) is 1-2 order of magnitude lower respect to fuel cell based systems. The specific power of the formers is higher but for large application the cost will be prohibitive[8,10].

In this view, hydrogen seems to be one of the most promising energy vectors both on the large and the small scale. Indeed, H_2 can be easily produced from large facilities (windmill fields) but also from small solar applications. Solar production pathways are also promising because their higher production is during the time of the day with the higher demand.

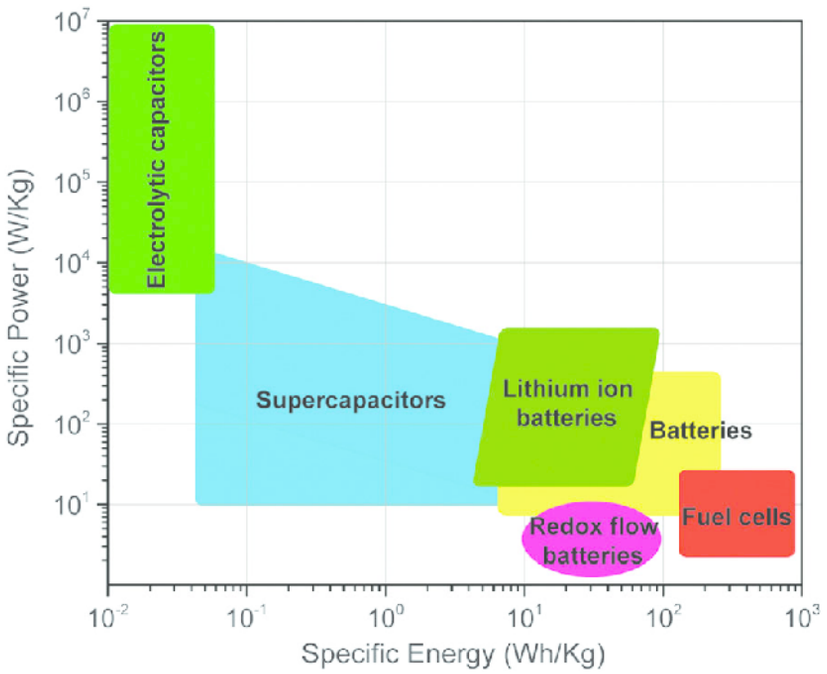

Figure 7. *Ragone plot comparing the performance of various systems. Figure from T. B Schon, The rise of organic electrode materials for energy storage, Chemical Society Reviews 45(22), 2016* [11].

Figure 8 shows a schematic representation of a smart grid composed by the central distribution with large-scale facilities surrounded by several small distributed producers based on renewable energies. Different storage systems based on energy vectors like hydrogen have to be implemented in order to keep the energy demand/production constant despite the possible fluctuation of customer demand and renewable sources production[12].

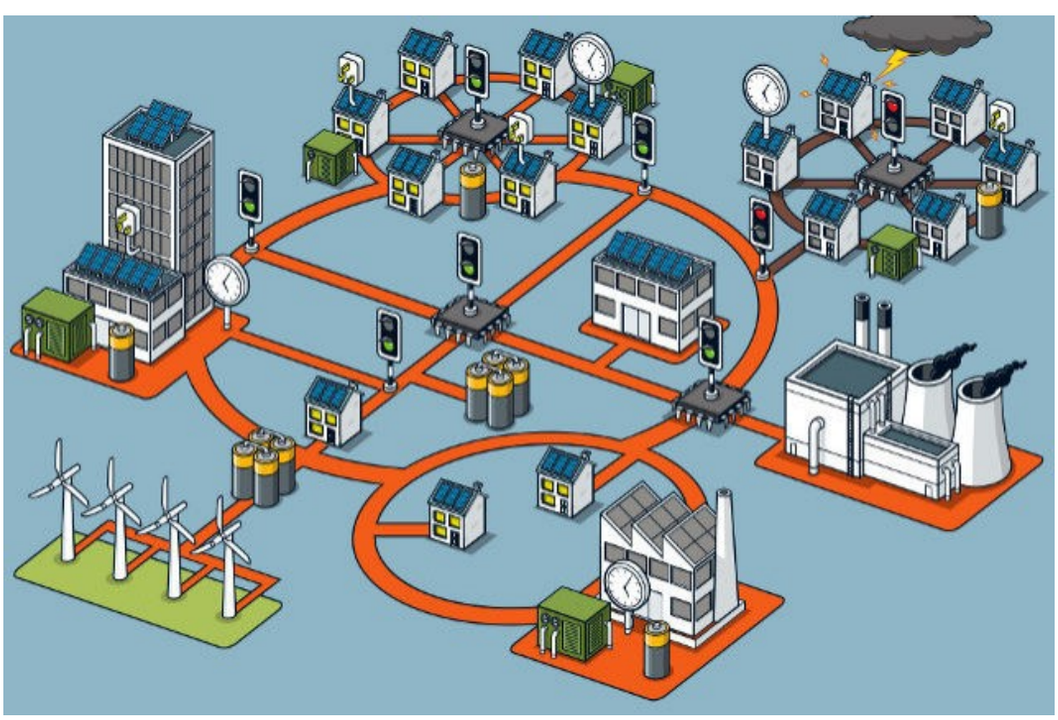

Figure 8*.Smart distribution grids at the heart of a power system. Image from "Next Generation Wind and Solar Power. From cost to value by IEA 2016"* [4].

1.1.3 Hydrogen as Energy Vector

Hydrogen gas is the simplest molecule on earth and is one of the most promising energy vectors for a clean and sustainable energetic future of humankind. Molecular hydrogen is not an energy source because it has to be produced, but is a carrier. Fossil fuels are both a source and a carrier because an energy vector is a substance or a system containing energy that can be later converted to other forms such as mechanical work or heat or to operate chemical or physical processes. Such carriers include springs, electrical batteries, capacitors, pressurized air, dammed water, hydrogen, petroleum, coal, wood, and natural gas.

Once produced hydrogen, apart from its use as chemical that is its main actual destination, can be consumed in fuel cells to generate power thanks to the conversion of chemical energy into electricity through an electrochemical reaction with oxygen or another oxidizing agent. Fuel cells are different from batteries in requiring a continuous source of fuel and oxygen (usually from air) to sustain the chemical reaction, whereas in a battery, the chemical energy comes from chemicals already present in the battery. Fuel cells can produce electricity continuously for as long as fuel and oxygen are supplied and as additional advantage they produce only heat and water as by-products. In this view, hydrogen can be used from small applications to bigger ones (portable powers, houses, cars, and even satellites and space capsules). According to IEA hydrogen-based technologies are best suited to large-scale electricity storage applications (from wind and PV) at the 10-1000 megawatt scale (Figure 9)[13].

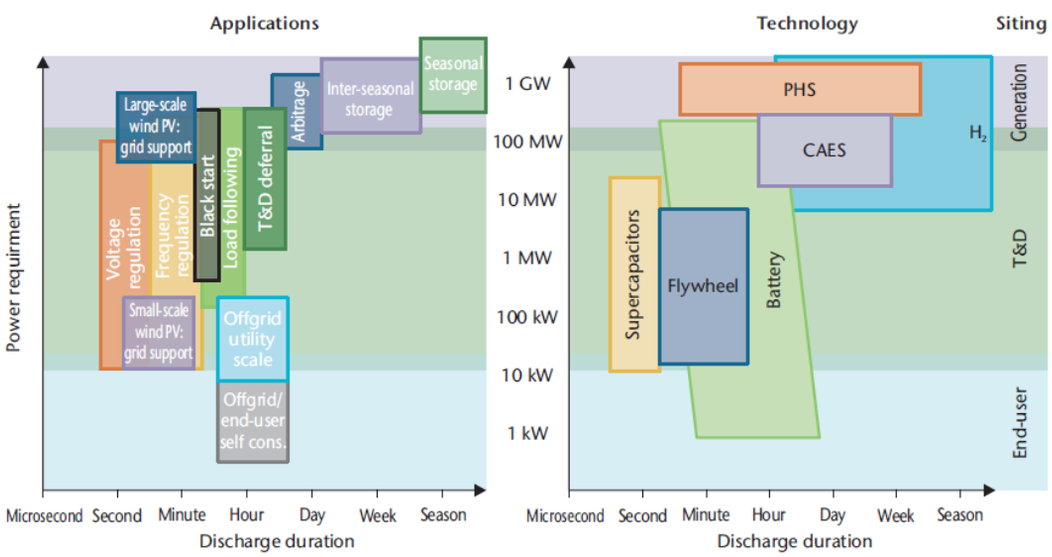

Figure 9*. Electricity storage applications and technologies. Image from "Technology Roadmap Hydrogen and Fuel Cells by IEA, 2015"* [13]*.*

However, H_2 is not to be restricted as an electricity storage system only. It could integrate surplus from variable renewable energies (VRE) electricity, but also be used as an energy source for end-user fuel cell electric vehicles (FCEVs), transformed in synthetic methane (with a reduction of dispersed CO_2 in the environment) or used as a feedstock, e.g. in the reefing industry.

Of course, all the hydrogen-based VRE final destinations needs different transformation steps that reduce the final efficiency as shown by Figure 10. Higher are the number of steps required higher are the losses in the overall process.

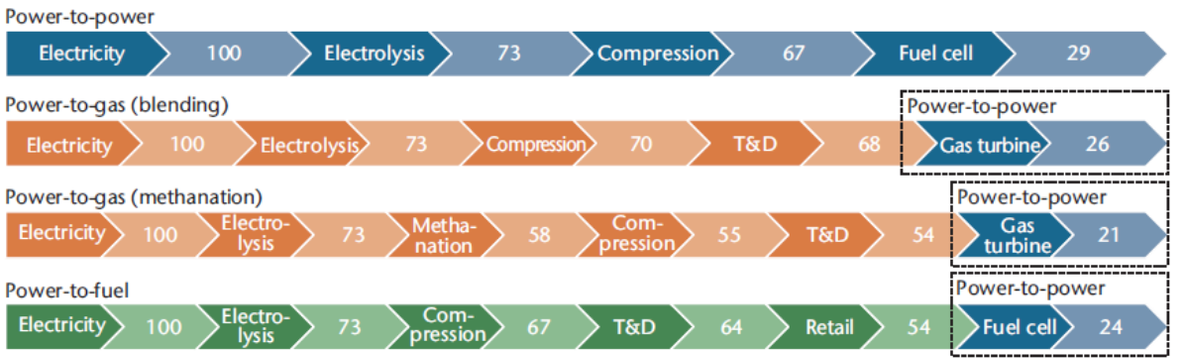

Figure 10. *Current conversion efficiencies of various hydrogen-based VRE integration pathways. The more the steps the less is the final efficiency. Image from "Technology Roadmap Hydrogen and Fuel Cells by IEA, 2015."*

1.1.4 Hydrogen Production

There are different sources for hydrogen production. Some of them are well-established technologies, while other are still under research but enclose large and interesting possibilities for further developments.

- Fossil fuels and natural gas: this is the most employed source nowadays for H_2 production. The reforming of fossil fuels to obtain hydrogen from hydrocarbons is an advanced and mature technique that, by the way, will not make our society independent from fossil fuels consumption and abuse. Another used technology from fossil fuels is coal gasification but the same drawbacks of reforming are here present.
- Nuclear energy: able to work on large scale processes it can generate greenhouse gasses free H_2 from water by electrolysis, thermochemical, and hybrid processes. Due to recent events, this technology is going to be dismissed in several countries.
- Renewable sources: as biomass, wind, solar, geothermal, and hydroelectric power. Any of these clean processes can be split in different sub-categories:
    - Solar; use an abundant and unlimited source. Processes related to sunlight are Solar Thermochemical Hydrogen (STCH), Photoelectrochemical (PEC), Electrolysis, and Photobiological ones. A solar based system, the photoelectrochemical water splitting (PEC-WS) will be the main topic of this work.
    - Biomass; is another abundant and renewable source. Easily produced domestically it can be converted in H_2 as well as in many other useful byproducts. An additional advantage of biomass-based processes is their ability of removing CO_2 from atmosphere. The main processes are: Biomass gasification, biomass-derived liquid reforming and microbial biomass conversion.
    - Wind; is an abundant but variable resource for the generation of electricity. Its proper use needs the development of a smart grid with a hydrogen based storage system able to generate H_2 from water electrolysis.

Apart from natural gas reforming, all H_2 production technologies require significant improvements before their commercial applicability. While some sustainable technologies are further from commercial readiness than others, all these production pathways have the potential to improve hydrogen availability and affordability while helping our society in moving away from fossil fuels dependence. Some technologies will be cost-competitive for the transition period, while others are considered longer-term technologies (Figure 11) [14].

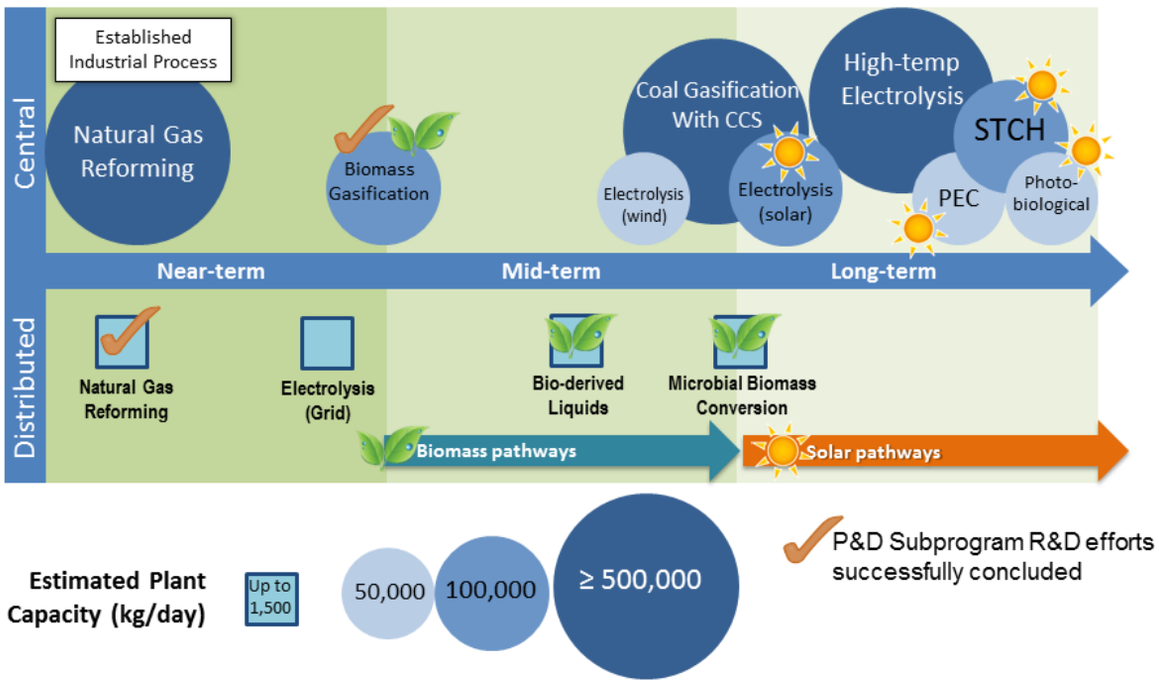

Figure 11. *Scheme of H_2 production in near, mid, and long term with different sources in which these technologies are expected to move into commercial production. Image from US Drive, Hydrogen Production Technical Team Roadmap 2013*[14].

According to the International Energy Agency (IEA) to fulfil the goals of the 2DS scenario, where there is at least a 50% chance of limiting the average global temperature rise of 2°C, a large increase (63%) of renewable power is needed within 2050[15]. In order to reduce the amount of greenhouse gasses, fossil fuels consumption have to be reduced as well. We can see from the prediction that the leader technologies to afford this big change are expected to be wind and solar (Figure 12). As stated before, the growth of these technologies is strongly related to the development of an efficient hydrogen-based power storage system.

As we can see from the prediction suggested by IEA, the main changes are addressed to wind and solar technologies that are supposed to fulfil a large portion of the future power production.

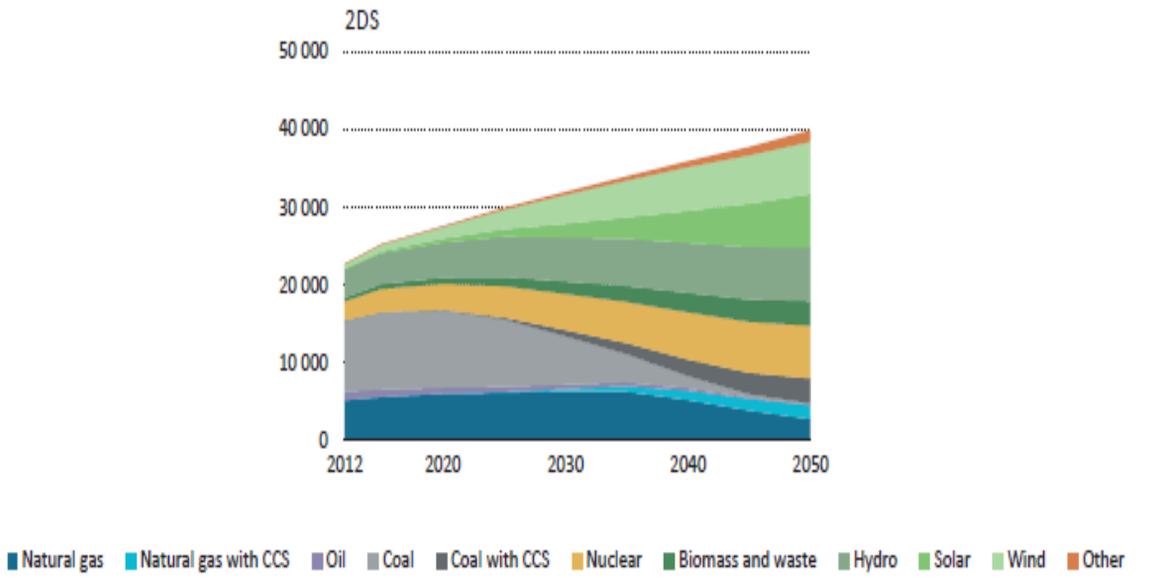

***Figure 12**. Prediction of global power sources change needed to fulfil the 2DS scenario. From Technology Roadmap Hydrogen and Fuel Cell 2015 (IEA)*[13].

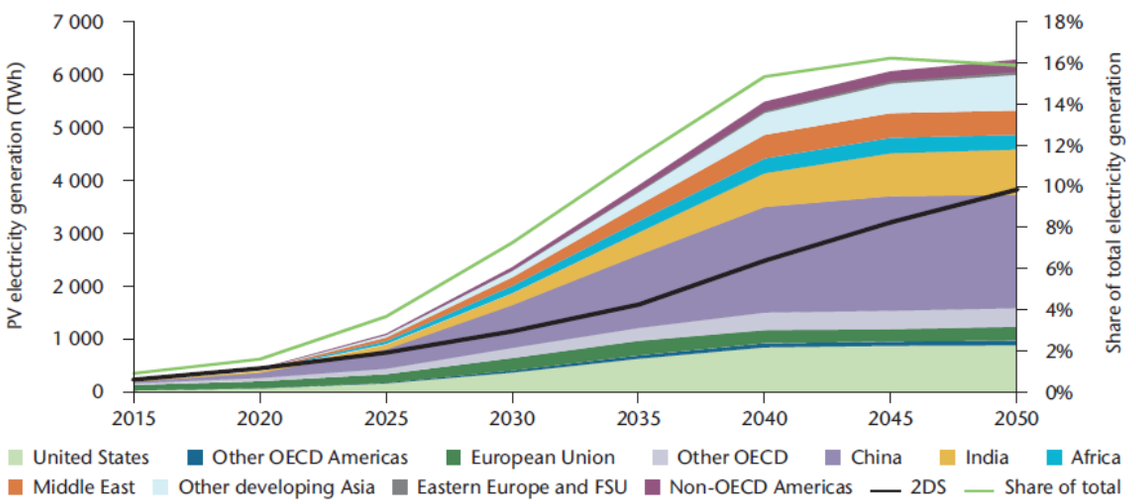

***Figure 13.** PV global electricity generation prediction in TWh until 2050. Image from Technology Roadmap, Solar Photovoltaic Energy, IEA, 2014* [6].

In the Scenario PV will provide 16% of global electricity by 2050 with China having a 35% share on the total production followed by US and India.

1.1.5 Hydrogen Production Facilities

Actually, there are 3 different possible sizes for hydrogen production facilities: central, semi-central and distributed[16]. The different resources and processes used in the hydrogen production are strongly related to the scale of the plant.

Distributed Production: This is the most interesting approach for viable distribution of hydrogen in the near-term due to the initial small demand of hydrogen. H_2 is produced in small units located where they are needed (e.g. vehicles refueling stations). The starting resources for such facilities could be ethanol and bio-oil or small-scale water (photo) electrolysis. Of course, the production cost in such small plants will be higher, but will allow to reduce transport and storage costs.

Centralized Production: It includes facilities able to produce up to 750000 Kg/d of H_2. Is the most interesting one for the storage of renewable energies due to the reduced cost of economies of scale. Off course, it will require more capital investments and efficient hydrogen transport and delivery infrastructures.

Semi-Central Production: This is the most interesting for the long-term use of hydrogen thanks to its quite high hydrogen production (5000-50000 Kg/d) and its location in close proximity of the consumption sites (25-100 miles). This size is able to combine the reduced cost of scale economy together with minimized hydrogen transport costs [17].

1.1.6 Hydrogen Delivery

Hydrogen delivery is quite complicate despite some delivery technologies and infrastructures are currently available. Together with the limited spreading of hydrogen consumption from consumers, this is one of the main reasons why hydrogen actually is made in big facilities and used in-loco (e.g. near petroleum refineries H_2 is produced for oil processing and chemical preparations like NH_3). Indeed, H_2 is the smaller and lightest molecule on earth (10 liter of H_2 have a mass of 0.00198 Kg) and it have to be pressurized to be delivered as compressed gas or liquefied. This means that is very important where H_2 is produced and consumes due to the large volumes required to obtain the same amount of energy obtained from oil (e.g. 1kg of gasoline is equivalent to 1 Kg of H_2 but the required volume is more than 3000 times higher).

There are different methods for hydrogen transportation:

Hydrogen Pipelines: The same pipelines for natural gas could be used for gaseous hydrogen. Some of them are operative but the high costs and the problems related to leakages and embrittlement, have limited this technology to large plants production such as petroleum refineries and chemical plants.

Hydrogen Tube Trailers: H_2 is compressed to the pressure of 180 bar in long and heavy cylinders stacked on trucks or on trains. This method is currently uncommon and typically not cheap unless the hydrogen is in its liquid form.

Liquefaction: Hydrogen is most commonly transported and delivered as liquid. Gaseous hydrogen is liquefied by cooling it to below −253°C and then stored in large insulated tanks. The liquefaction is expensive and consumes more than 30% of the H_2 energy content.

Moreover, some stored hydrogen is lost due to evaporation or boil-off. This method is cheaper for longer distances but still challenging due to boil-off issues.

Novel Hydrogen Carriers: Hydrogen is stored in a different chemical state rather than as free molecules. Hydrogen is bonded to other chemical compounds in the production plant and then released on consumption site. Potential carriers include metal hydrides, metal organic frameworks (MOF), carbon or other nanostructures, reversible hydrocarbons, or other liquids. It is a technology still under research and not ready for the market.

Most of these technologies, are currently available but they are not sufficient for a widespread use of hydrogen unrelated with large scale industrial plants. Costs, risks and energetic losses are the most important reasons blocking this energy vector to be largely available for consumers[18].

	Capacity	*Transport distance*	*Energy loss*	*Fixed costs*	*Variable costs*	*Deployment phase*
Gaseous tube trailers	Low	Low	Low	Low	High	Near term
Liquefied truck trailers	Medium	High	High	Medium	Medium	Medium to long term
Hydrogen pipelines	High	High	Low	High	Low	Medium to long term

***Figure 14**. Hydrogen transport and delivery technologies with the respective performances in transport distances, energy losses, technological developments and costs. Image from Technology Roadmap Hydrogen and fuel cell 2015, IEA*[13].

Figure 15 gives an outline of the recommended systems and their expected actualization time.

This roadmap recommends the following actions		*Time frame*
Underground hydrogen storage	Establish national inventories of underground caverns suitable for hydrogen storage. Develop demonstration projects for hydrogen storage in salt caverns and prove feasibility to reduce investment costs for storage to USD 1 per kWh. Prove the feasibility of hydrogen storage in depleted oil and gas fields as well as aquifers.	Complete by 2025-35
Pressurised tanks	Reduce material costs for high-pressure tanks on board FCEVs to at least USD 15 per kWh.	Complete by 2025
Cryogenic storage and liquefaction of hydrogen	Improve the efficiency of the liquefaction process to reduce energy losses to below 30%. Reduce boil-off through improved insulation of the vessel as well as increased pressure levels.	Complete by 2030-35
Metal hydrides and carbon nano-structures	Ensure continued R&D funding to further explore the potential application of solid hydrogen storage options.	2015 onwards

***Figure 15.** Roadmap for hydrogen delivery system predicted by Technology Roadmap Hydrogen and fuel cell 2015, IEA*[13].

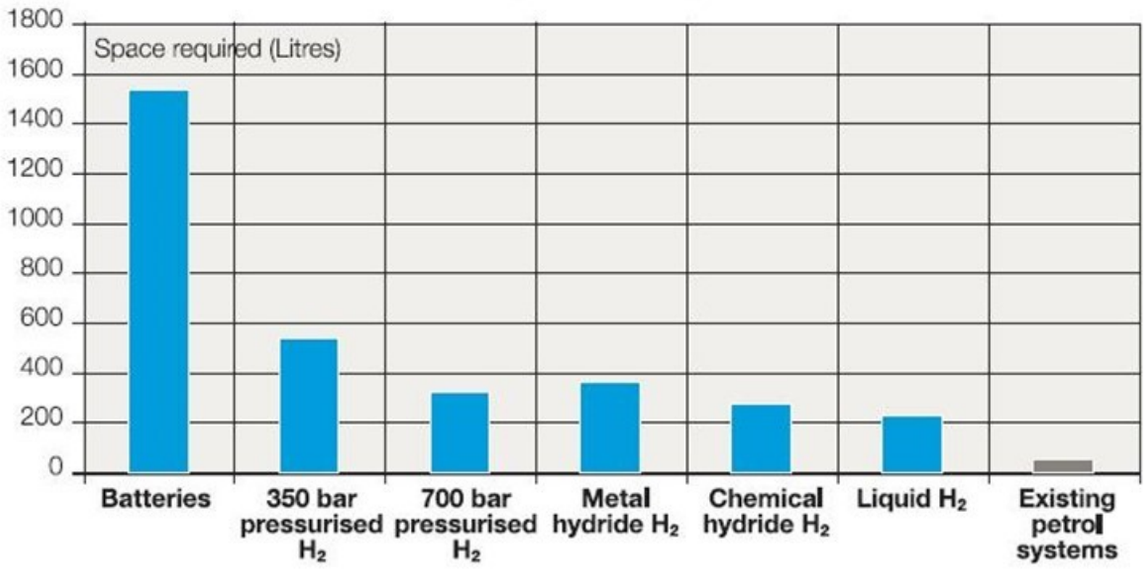

Figure 16. *Space required by different energy storage systems in litres. Image from Istitut fur Kraftfahrzeuge, Road2Hy.com*

From Figure 16 we can see how hydrogen is an interesting energy vector, apart from all its safety requirements if compared to batteries which are off course suitable only for smaller applications. If compared to the oil system, H_2 requires higher volumes for the same amount of energy transported.

1.1.7 Actual Use of Hydrogen

The hydrogen production is nowadays quite low and mostly focused on chemicals production and oil refining. This is mainly due to the poor maturity of hydrogen based storage system. An improvement in this direction will surely come from the need of changing our energy supply system in the near-term due the lack of fossil fuels together with the need to stop climate changes[19].

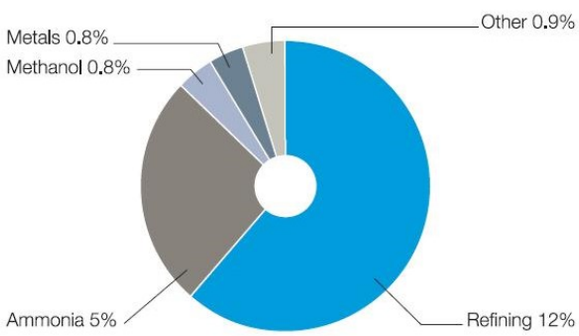

Figure 17. *Hydrogen consumption in Western Union (2013 data). Image from Istitut fur Kraftfahrzeuge, Road2Hy.com*

The total production is 19 million tonnes of oil equivalent per year. In energy terms, this is almost equivalent to 0.5% of the world's annual oil consumption and is possible to notice how the energetic use is absolutely not contemplated (Figure 17).

1.1.8 The Hydrogen Cost

The high production cost is the main challenge for H_2 production. Find a fossil-fuels free production, with a cost-competitive transport and storage system compared to conventional fuels and technologies is the goal that hydrogen must reach to be largely implemented in our lifes. Moreover, increase hydrogen energy efficiency, achieve high hydrogen purity, and minimize leakages from storages are additional tasks that must be fulfilled.

The goal is to reduce the price for hydrogen production to less than 4$/Kg delivered and dispensed (this goal is actually achieved only by natural gas reforming) from environmental friendly route. The cost at which hydrogen fuel cells electric vehicles will be competitive is estimated to be $2-$4/gge (gasoline gallon equivalents). The following table from DOE (U.S Department of Energy) lists the technical targets, the costs and the performance parameters that different renewable systems should fulfill to be competitive[20].

Reduce the Cost of Hydrogen to <$2.00 Produced and Untaxed.
This Goal Is Independent of the Technology Pathway.

By 2015	$5.90/gge	Distributed production of hydrogen from bio-derived renewable liquids
	$3.90/gge	Distributed production of hydrogen from water electrolysis
	$3.00/gge	Central production of hydrogen from water electrolysis using green electricity
	$2.10/gge	Central production of hydrogen from biomass gasification
	$14.80/gge	Central production of hydrogen from solar-driven high-temperature thermochemical water splitting
	$17.30/gge	Central production of hydrogen from solar-driven low-temperature photoelectrochemical water splitting
By 2020	$2.30/gge	Distributed production of hydrogen from bio-derived renewable liquids
	$2.30/gge	Distributed production of hydrogen from water electrolysis
	$2.00/gge	Central production of hydrogen from water electrolysis using green electricity
	$2.00/gge	Central production of hydrogen from biomass gasification
	$3.70/gge	Central production of hydrogen from solar-driven high-temperature thermochemical water splitting
	$5.70/gge	Central production of hydrogen from solar-driven low-temperature photoelectrochemical water splitting
	$9.20/gge	Central photolytic biological production of hydrogen

Figure 18. *DOE Hydrogen production cost reduction goals. Image from Hydrogen Production Technical Team Roadmap 2013, DOE*[14].

To achieve these results some technological barriers should be overcome[21,22].

- Hydrogen quality: this is one of the major issues for H_2 destined to fuel cells due to the possible poisoning of Pt catalysts in these systems. Therefore, hydrogen technologies must produce directly high-purity hydrogen or incorporate low-cost purification systems downstream.
- Control and safety: Working with a high-combustible molecule requires strict safety requirements with remote monitoring and maintenance schedules.
- Capital and operating costs: nowadays, the cost is still too high to be competitive and for this reason the development of better materials and larger-scale manufacturing are the main routes to follow to reduce capital costs.
- Community acceptance barriers: regulations, codes, education.

Each source has its R&D priorities:

Production Technologies	R&D Priorities
Distributed Natural Gas Reforming	Pre-competitive technical and cost challenges have been sufficiently addressed for steam methane reforming so that industry may complete technical development without additional DOE resources
Bio-derived Liquids Reforming	Catalyst development, capital cost reduction, and affordable feedstocks
Coal and Biomass Gasification	Capital cost reduction, carbon capture and storage, and greater flexibility for use of renewable biomass feedstock
Water Electrolysis	Capital cost reduction, higher efficiency, and materials development
Thermochemical Hydrogen	Chemical cycle selection and materials development for improved kinetics and durability, reactor design and development for high solar to hydrogen efficiency
Photoelectrochemical	Identification and development of optimal materials, integrated devices, and reactor configurations
Biological	Biological candidate identification and genetic engineering to increase hydrogen production efficiency

Figure 19. *R&D priorities for the most developed H_2 production technologies. Image from Hydrogen Production Technical Team Roadmap 2013[14].*

In Table 1 are reported the actual and the predicted costs for hydrogen production in $/Kg.

Technology	Cost 2011	Cost 2015	Cost 2020	Final target
Photoelectrochemical water splitting	N.A	17.30	5.70	2.10
Biomass gasification/pyrolysis	2.20	2.10	2.00	
High-temperature Thermochemical H_2 production	NA	14.80	3.70	2.00
Photolytic Biological H_2 production	NA	NA	9.20	2.00
Photosynthetic bacterial H_2 production	NA	3.00	4.50	
Dark fermentative H_2 production and Microbial Electrolysis Cells	13.50	10.00	8.00	
Water electrolysis (distributed)	6.60	5.60	4.00	
Water electrolysis (centralized)	4.10	3.00	2.00	
High-Temperature Ethanol reforming	9.10	7.70	4.00	

Table 1*. Different H_2 production technologies and their predicted costs in the next years.*

Is possible to notice how only the biomass gasification is actually able to fulfil the DOE threshold for H_2 cost sustainability. This is indeed the most mature technology, but it still presents some big drawbacks. The main ones are the need of highly-localized structures close to the feedstock production, the high dependence from the feedstock type and the limited flexibility.

Emissions (primarily coal)	GHG emissions, specifically carbon dioxide, result from the use of coal. Technologies to capture and store these emissions effectively are not economically viable.
Feedstock Issues (primarily biomass)	Sources and supplies of feedstock are not consistent or reliable with respect to composition and quality. Feedstock preparation, storage and handling systems, and transportation are all costly and underdeveloped. In addition, competition for biomass may limit its availability in some geographic areas.
Capital Costs	Current gasification systems are capital-intensive because of non-standardized plant designs and inefficient, multi-step processes. Hydrogen quality requirements for PEM fuel cells also result in significant capital costs.
Operations and Maintenance	O&M costs need to be reduced. BOP equipment needs to be made more efficient and durable than that which is currently available. Feedstock on-site storage, handling, and preparation need to be improved. Hydrogen monitoring also increases O&M costs. Additional data and demonstration of the numerous combinations of coal and biomass types and concentrations that can be co-fed into high-pressure gasifiers would be useful.
Control and Safety	Improved sensors and controls that enable feed-flexible operation would reduce costs.

***Figure 20**. Main drawbacks of biomass/coal gasification for H_2 production. Image from Hydrogen Production section of the Fuel Cell Technologies Office's Multi-Year Research, Development, and Demonstration Plan" of U.S. Department of Energy*[22].

Due to the large amount of risks and costs related to the H_2 transportation and storage is suggestion of this work to move to semi-central or distributed production with the use of renewable sources like sun and wind. Compared to biological processes these systems are indeed more efficient and are not limited by the availability of the proper biomass. Sun-driven systems, like PEC-WS are a promising route to directly obtain hydrogen from the solar light without the additional step of electrolysis required as example by the wind-generated H_2 production systems. The main advantage of PEC-WS is its ability to generate chemical energy from light as hydrogen. An additional advantage is the high purity of the so produced hydrogen that can be used as reagent for fuel cells without undergoing to further purification steps.

Moreover, in the last years, people attention to solar-based systems is largely increased and domestic installations increased up to 400%. Is of paramount importance that public opinion and market moves toward this direction in order to improve the spreading of these new technologies.

Figure 21 shows the wide acceptance of solar technologies all over the world with its exponential growth in the last years.

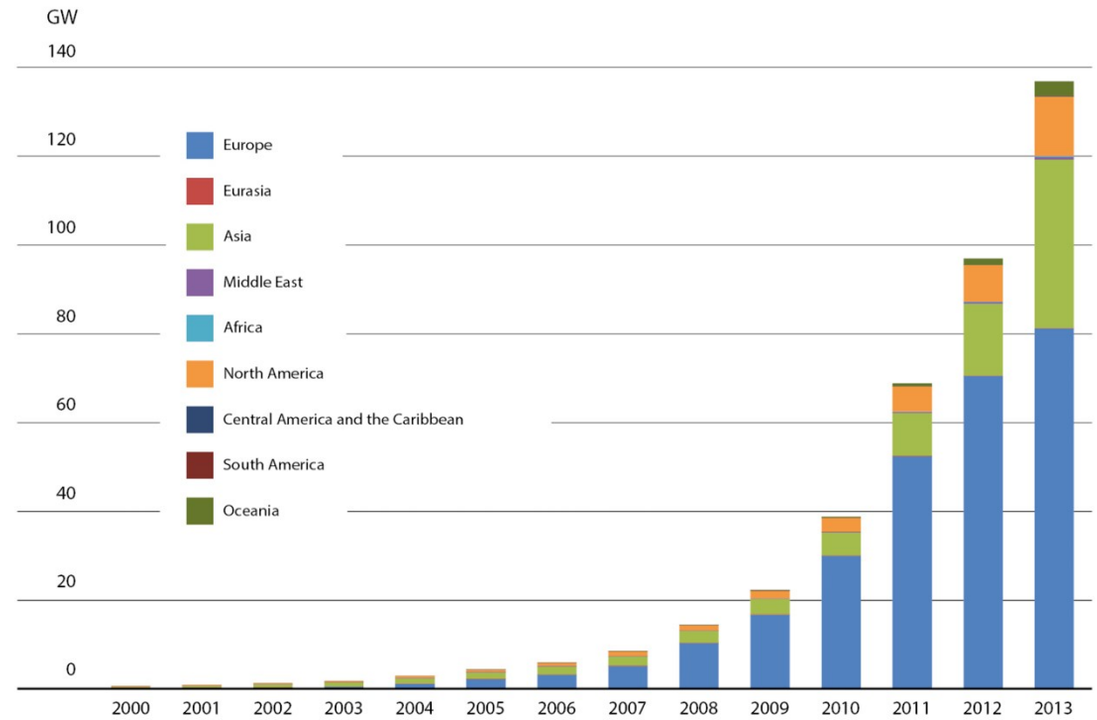

Figure 21. *Increase in the global installed capacity of residential-scale solar PV (2010-2014) in the world. Image from International Renewable Energy Agency (IRENA)*[23].

Between all the suggested routes for H_2 production, photoelectrochemical water splitting, the main topic of this work, has in addition some further advantages.

- It is a technology that can be used both for large central applications and for semi-distributed facilities like fuel stations for new fleets of hydrogen vehicles without any additional distribution cost.
- No need of any supply of feedstock, it only needs sunlight and water.
- Higher production during the time of the day with higher users demand.
- High purity product with less purification steps required (compared for example with biomass H_2) being more suitable for fuel cells usage without any poisoning of the Pt catalysts.
- Well-developed knowledge on the materials thanks to consolidated PV technology.
- According to the projections the cost of photoelectrochemical hydrogen is on the way to be competitive.

1.1.8.1 Photoelectrochemical Hydrogen Production Cost:

Characteristics	Units	2011 Status	2015 Target	2020 Target	Ultimate Target
Photoelectrochemical hydrogen cost[a]	$/kg	NA	17.30	5.70	2.10
Capital cost of concentrator and PEC receiver (non-installed, no electrode)	$/m^2	NA	200	124	63
Annual electrode cost per TPD H_2[b]	$/yr-TPD H_2	NA	2.0M	255K	14K
Solar to hydrogen (STH) energy conversion ratio [c,d]	%	4 to 12	15	20	25
1-sun hydrogen production rate[e]	kg/s per m^2	3.3x10^{-7}	1.2x10^{-6}	1.6x10^{-6}	2.0x10^{-6}

[a] Hydrogen cost represents the complete system hydrogen production cost for purified, 20bar compressed gas. System level losses and expenses due to solar collection/concentration, window transmittance/refraction, replacement parts, operation, and maintenance are included in the cost calculations

[b] Annual electrode cost refers to the annual replacement cost of the PEC photoelectrode panel normalized by the design capacity of the system (in metric tons H_2 per day). Electrode cost includes both the material and manufacturing cost of the PEC electrode used within the reactor.

[c] STH energy conversion ratio is defined as the energy of the net hydrogen produced (LHV) divided by full-spectrum solar energy consumed. For systems utilizing solar energy input only, the consumed energy is calculated based on the incident irradiance over the total area of the solar collector. For hybrid systems, all additional non-solar energy sources (e.g., electricity) must be included as equivalent solar energy inputs added to the denominator of the ratio

[d] The Status of STH ratio is in the range of 4% and 12% for different semiconductor material systems exhibiting different levels of operational durability. Thin film material systems have been demonstrated with STH >4% for hundreds of hours

[e] The hydrogen production rate in kg/s per total area of solar collection under full-spectrum 1-sun incident irradiance (1,000 W/m^2). Under ideal conditions, STH can be related to this rate as follows: STH = H_2 Production Rate (kg/s per m^2) * 1.23x10^8 (J/kg) / 1.00x10^3 (W/m^2). Measurements of the 1-sun hydrogen production rate can provide an invaluable diagnostic tool in the evaluation of loss mechanisms contributing to the STH ratio.

Example Parameter Values to Meet Cost Targets for PEC-WS H_2 Production

Characteristics	Units	2011 Status	2015	2020	Ultimate
Solar to hydrogen (STH) energy conversion ratio	%	NA	15	20	25
PEC electrode cost[a]	$/m^2	NA	300	200	100
Electrode cost per TPD H_2[b]	$/TPD	NA	1.0M	510K	135K
Electrode replacement life-time[c]	Years	NA	0.5	2	10
Balance of plant cost per TPD H_2[d]	$/TPD	NA	420K	380K	310K

[a] PEC photoelectrode cost refers to the material and manufacturing cost of the PEC electrode. Area is based on the actual area of the electrode itself.
[b] This parameter is the PEC photoelectrode cost (as defined above) normalized by the metric tons per day of hydrogen design capacity of the electrode.
[c] Electrode replacement lifetime denotes the projected total duration of the electrode being immersed in electrolyte and under cyclic solar illumination until process energy efficiency drops to 80% of its original values. Thus, a 10-year electrode replacement lifetime refers to 10 years of operation under diurnal cycles and approximately 5 years of actual hydrogen production.
[d] This parameter denotes non-electrode, non-concentrator/PEC receiver, non-installation balance of plant costs normalized by the metric tons per day of hydrogen design capacity of the electrode.

Note: all the previous data are taken from “Hydrogen Production section of the Fuel Cell Technologies Office's Multi-Year Research, Development, and Demonstration Plan” of U.S. Department of Energy. For full details about technical targets and process conditions the reader is invited to look at the original data.

Of course, PEC-WS cannot be the only method for hydrogen production but will surely be one of the available alternatives in the near-future portfolio for clean and sustainable semi-central and central hydrogen production. Is indeed not suggested to focus the whole world energy economy on a single route as we have done until now with fossil fuels.

1.2 Photoelectrochemical Water Splitting (PEC-WS)

1.2.1 Semiconductor Materials

Semiconductors are materials characterized by a full valence band (VB) and an empty conduction band (CB). The band gap, compared to those of insulating materials, is quite small, in the range of 1-2.5 eV. Thanks to this small forbitten energy band, a small number of electrons can move from the VB to the empty CB just because of thermal energy. The number of electrons that can jump from VB to CB because of thermal energy is given by:

$$n = n_0 T^{3/2} \cdot e^{\left(\frac{-E_g}{2kT}\right)}$$

Where n is the number of electrons, n_0 is a constant specific for the semiconductor, T is the absolute temperature and E_g is the value of the band gap. From a basic analysis of the dependence of n from T is possible to notice how semiconductors present a positive thermal conductivity coefficient. Indeed, growing the T, the number of electrons leaving the VB increase. Photons of the proper wavelength can also induce the same behavior.

Once an electron leaves the VB, an empty level is generated inside the VB in place of the moved electron. This empty level, formally positive, is called hole. Usually, in a semiconductor, a hole and a free electron tend to recombine with the restoration of the previous bond. The recombination time is in the range between micro and milliseconds.

1.2.2 Doping

By defining the Fermi level as the energy at which half of the electronic levels are occupied, it is easy to understand how in a pure semiconductor it lies in the middle between CB and VB[24,25].

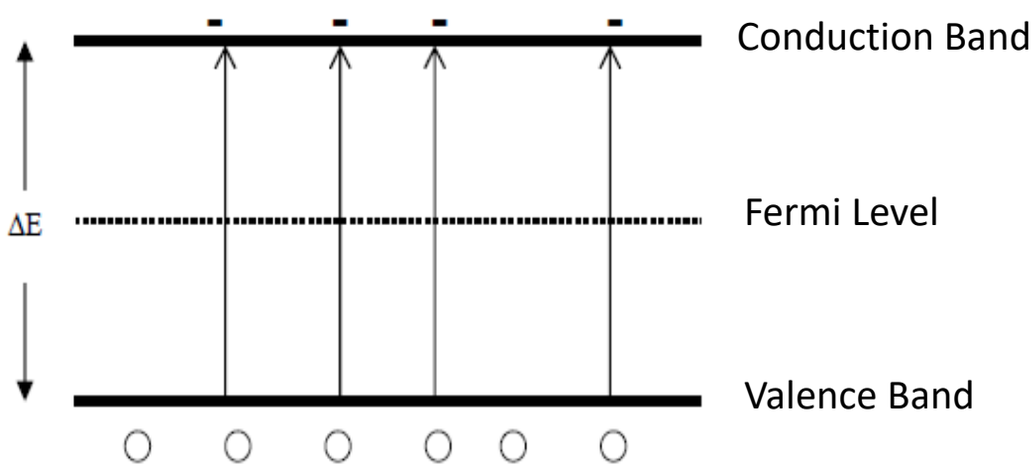

***Figure 22**. Bands disposition in a pure semiconductor. The Fermi level characterizes the hypothetical energy level of an electron and lies between VB and CB. Scheme adapted from Chapter II, Bruno Scrosati, Celle fotovoltaiche[25].*

In a pure semiconductor, the number of holes and free electrons is the same. The semiconductor is then called intrinsic. The addition of different atoms in the lattice (dopants) can modify this situation giving to a doped semiconductor with extrinsic properties (Figure 23).

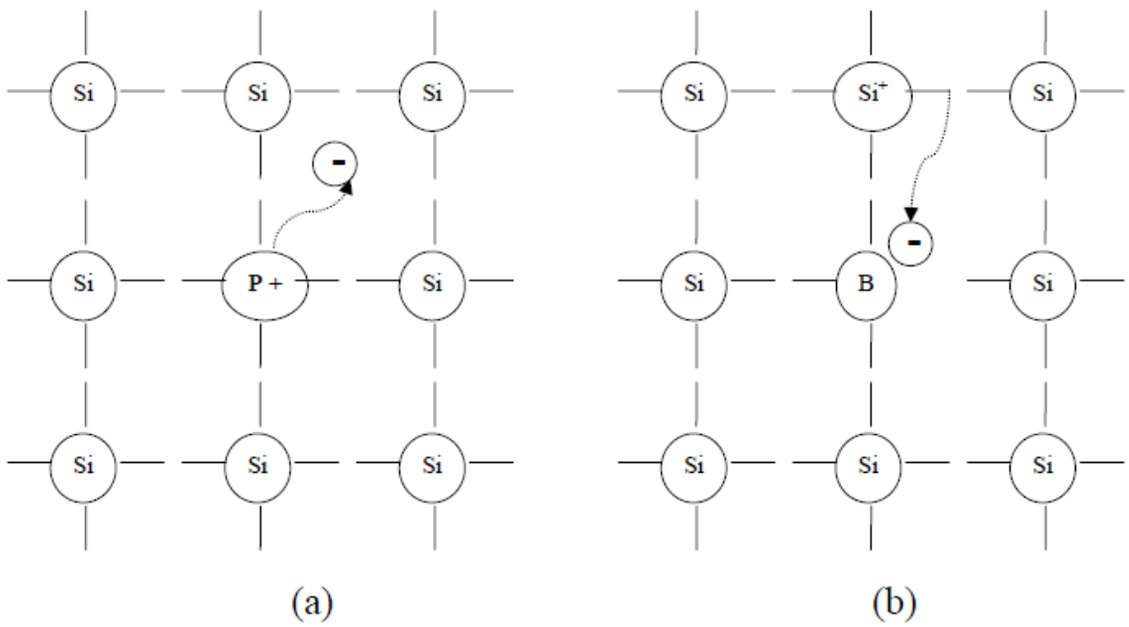

Figure 23. *a) n-type semiconductor with a dopant having an additional electron with respect to Si; b) p-type semiconductor with a dopant having one electron less with respect to Si. Image from Chapter II, Bruno Scrosati, Celle fotovoltaiche*[25]*.*

If a V group dopant is added to a silicon crystal, the structure will present a weakly bonded additional electron is its lattice. Is then very easy, also with small energies, make this electron free. In this way, a n-type semiconductor is generated, and the formal charge of the system is negative. The added atom is called donor because add an electron to the system. On the other side if in pure Si crystal is added a III group impurity the semiconductor is formally positive (one electron is missing) and the atom is called acceptor. This type of semiconductor is called p-type extrinsic semiconductor. The formation of a p-type or n-type semiconductor can shift the position of the Fermi level because of the presence the acceptor and donor level respectively[26].

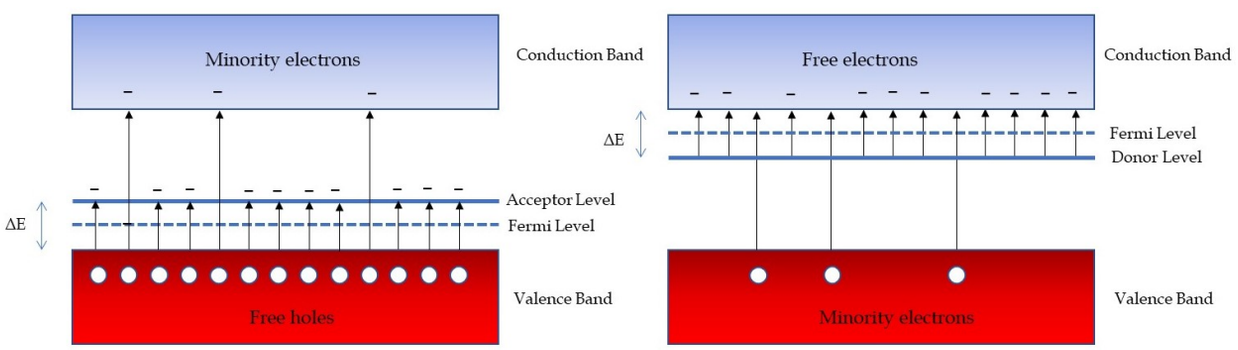

Figure 24. *Band diagrams for an extrinsic semiconductor of p-type and n-type.*

In a n-type semiconductor, electrons are the majority carriers (holes are called minority carriers), so once an electric field is applied, the current is mainly transported by electrons. Opposite situation for a p-type semiconductor where holes supply the conductivity.

1.2.2.1 The Energy Scale

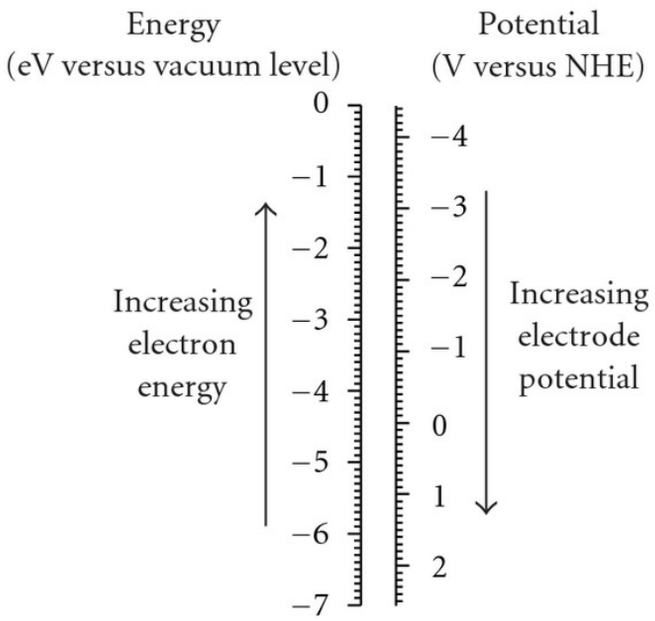

Figure 25. *Schematic representation for the conversion between the absolute energy scale (on the left) and the electrochemical one (on the right). Advances in Physical Chemistry Volume 2011 (2011), Article ID 786759, 20.*[27]

First of all, is important to define the absolute energy scale and correlate it with the electrochemical one. In the first one, mostly used by physics, the zero value is the energy of electrons in the vacuum, in the second on, is the standard redox potential of hydrogen electrode. The conversion factor is -4.5 eV.

1.2.3 Photoelectrochemical Water Splitting

Photoelectrochemical water splitting is one of the promising routes for the renewable hydrogen generation in a future hydrogen economy. The process occurs thanks to semiconductor materials with the appropriate band gap and bands alignment respect to hydrogen evolution reaction (HER) and oxygen evolution reaction (OER) for a photocathode and a photoanode respectively. The semiconductor is immersed in a water-based electrolyte while the sunlight is the driving force for the water splitting reaction. The advantages of PEC-WS system are that it involves a relative simple process (compared to other H_2 production routes) and that it can work in wide range of temperatures (basically no upper limit and lower limit higher than 0°C) and the absence of a warm-up step (if the temperature is above 0°C).

In a photoelectrochemical cell, the semiconductor is in direct contact with a redox couple. Once the electrolyte-semiconductor interface is created semiconductor and solution electrochemical potentials tend to equilibrate themselves to the same value. In the semiconductor, the electrochemical potential is given by the Fermi energy, in the solution is given by the Nernst potential of the redox couple.

If the Fermi level of a p-type semiconductor is lower than the one of the electrolyte, once immersed, holes will move from the semiconductor to the electrolyte. This will create an electrons-rich area with respect to the bulk of semiconductor. Therefore, a band bending with a potential barrier able to stop any further transfer from the semiconductor to the electrolyte is formed.

Under light, photons with higher energy than the band gap are absorbed by the material creating electrons-holes couples' due to excitation of electrons present in the VB. The so generated electrons and holes move in opposite directions under the influence of the applied electric field. In a p-type material, electrons go to the solution while holes move toward the bulk semiconductor and then to the counter electrode. The use of an external bias, can be useful to overcome eventual overpotentials and to improves the band bending giving an efficient charges separation [28,29].

There are some requirements for a PEC-WS system to work properly.

- An efficient absorption of solar light to induce excited states inside the semiconductor.
- A good charges separation to avoid recombination between the excited electrons and the holes. This will ensure a high light-to-chemicals conversion.
- The proper bands position to fulfill the desired reactions from the thermodynamically and kinetic points of view.
- High stability to photodegradation processes.

Is not easy to accomplish all these points mainly because semiconductors able to perform the desired reaction without undergoing to photodegradation show a wide band gap that reduce the portion of solar spectra available for the absorption (e.g. TiO_2 with a 3eV band gap can absorb only in the UV) [30].

Anyway, if these requirements are satisfied at a photoanode will take place the following reaction:

$$H_2O \rightarrow \frac{1}{2}O_2 + 2H^+ + 2e^-$$

While at a photocathode will take place the water reduction thanks to the high energy electron excited in the CB.

$$2H_2O + 2e^- \rightarrow 2H_2 + 2OH^-$$

1.2.3.1 Side Reactions

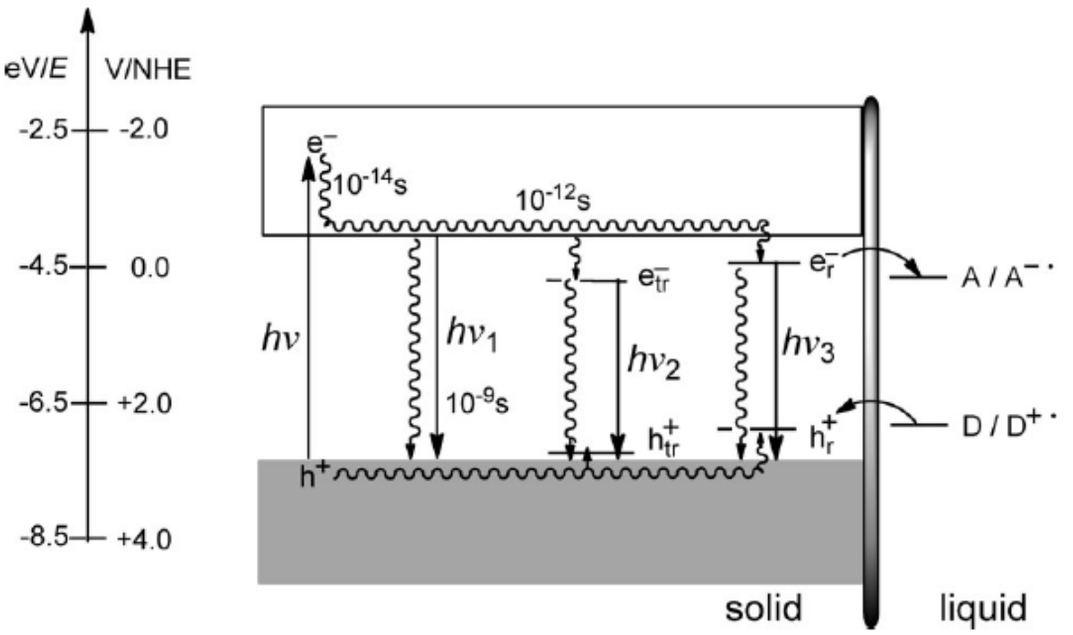

Figure 26. *Schematic representation of the possible pathways that electrons and holes can follow after the irradiation of the semiconductor. Image from Angew. Chem. Int. Ed. 2013, 52, 812 – 847*[31].

The desired electrons transfer is not the only available route for holes and electrons. Figure 26 summarizes the different processes occurring after the absorption of a photon in a semiconductor material immersed in an electrolyte with a donor D and an acceptor A. Once light-excited electrons and holes are located close to the corresponding edges of energy bands they can undergo nonradiative and radiative recombination and trapping (reactive and non-reactive) on surface sites. These undesired paths for the electron-hole couples reduce the conversion efficiency of sunlight to H_2 (and O_2).

The main cause of material degradation is the electron-transfer reaction to the material itself with consequent loss of activity, but this reaction is not included in the scheme. Such process does not occur on any semiconductor, e.g. TiO_2 is a stable from this point of view, but ZnS, CdS or Cu_2O tend to be reduced to the corresponding metals (see Figure 31). This photo-degradation reaction is even stronger for very pure materials suggesting the importance of doping [31].

1.2.3.2 Stability of the Semiconductor

Of all the undesired processes occurring after electron-hole excitation the worst one is photodegradation that reduce material activity with time. Indeed, the main problem of semiconductors for photoelectrochemical water splitting is their poor stability to photodegradation processes.

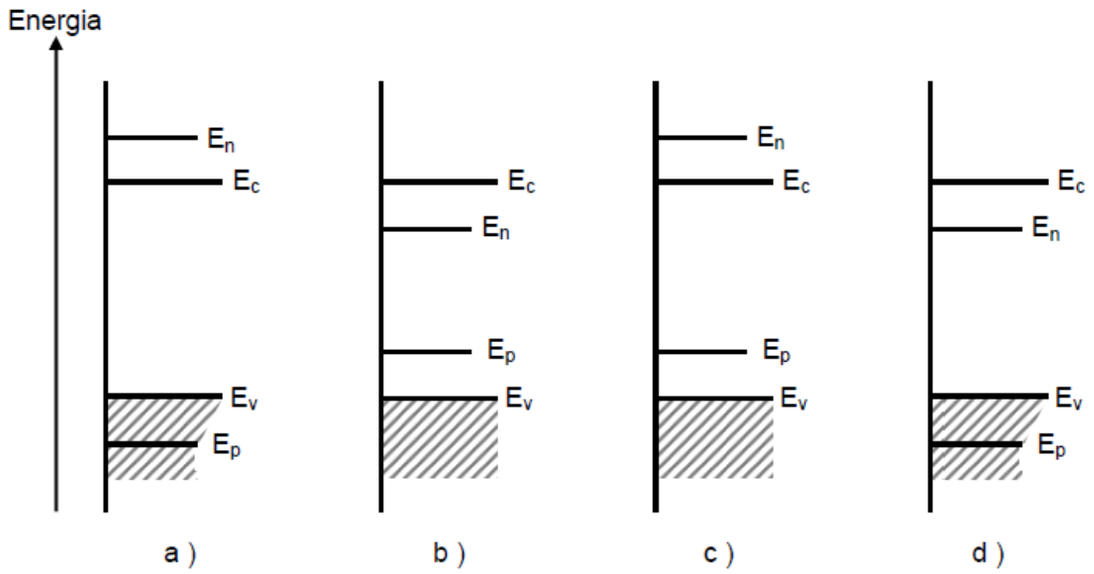

***Figure 27**. Models of thermodynamic stability. a) thermodynamic stability, b) possible anodic and cathodic photodegradations, c) possible anodic degradation, d) possible cathodic degradation. Image from Chapter II, Bruno Scrosati, Celle fotovoltaiche.*

The comparison of VB and CB levels with respect to the redox potentials of semiconductor decomposition reactions gives an idea of the stability. There are 4 different situations:

- Thermodynamic stability: the redox potentials of anodic and cathodic decomposition reactions are respectively more negative and more positive then the VB and CB.
- Anodic and cathodic degradations: both redox potentials for degradation lie inside the BG. The material can then be affected by both electrons reduction and holes oxidation.
- Anodic degradation: the semiconductor is stable from cathodic degradation because CB is more negative than that redox potential. The material is moreover still affected by anodic corrosion performed by holes.
- Cathodic degradation: the material is safe from the possible holes degradation but is subdued to the cathodic one performed by the high energy electrons excited in the CB under light.

The photodegradation process is in competition with the desired one of surface electrons transfer. The reaction with less work required is the favored one but also the kinetics is important and for this reason it is not always easy to predict the final behavior of the material[32]. Other important parameters affecting the stability are electrolyte concentration and pH, temperature, impurity levels and other parameters (e.g. stirring that can affect the rate of electrode processes).

1.2.3.3 PEC Photocell Cost Factors

A key factor in cost-effectiveness of PEC photocells is the PV components cost, which has been a significant barrier to low-cost solar cells and low-cost PEC systems in the past. For the photocell, pathways to reduced costs are:

• Minimizing thickness of individual PV layers.

• Use of low cost printing techniques for materials deposition.

• Use of lower cost PV materials.

• Low cost conductive coatings to protect against corrosion.

Year	Production Scale		Cost/gge (produced)
2015 Target	Central	• Photoelectrode system • Photo-particle system	$ 17.30 $28.60
2020 Target	Central	• Photoelectrode system • Photo-particle system	$5.70 $4.60

Table 2. *Prediction of H_2 total cost/gge produced. Table from Technoeconomic Analysis of photoelectrochemical (PEC) Hydrogen Production, DOE* [33]*.*

1.2.3.4 The PEC-WS Challenges

The main challenges that have to be overcome in this system are:

- Long lifetime for photoelectrodic materials (mainly due to (photo)corrosion processes).
- Proper thermodynamic bands edge alignment for the redox reactions.
- Fast kinetics for HER/OER.
- High photons efficiencies with suitable optical band gap for optimal light absorption.
- Good charges transport in the bulk semiconductor.
- Reduced internal resistance losses.
- Reduced undesired paths for excited electrons and holes (trapping, recombination etc. See Figure 26).
- Reduced plant capital costs.
- Low-cost materials with wide availability.

Between all the renewable available technologies is our opinion that PEC-WS will be a valuable alternative for the storage of energy in the near future. It is a technology almost ready and mature for electrode reactors. Despite the higher cost of the predicted H_2 production in these systems, continuous improvements in this field are promising for the future scalability of this technology.

The aim of this work is to develop a stable, low-cost and efficient photocathode for the photoelectrodes system to make the produced H_2 price for these systems more affordable. Different approaches were considered:

- First of all, to improve the material is important to have a full knowledge of the interfacial processes occurring under working conditions. The research was mainly devoted on new methods for the evaluation of photodegradation processes using innovative techniques like X-ray Absorption Spectroscopy (XAS) and Scanning Electrochemical Microscopy (SECM).
- Then was important to select a cheap material with high performance. Cu_2O was found to be the best candidate. Moreover, in order to reduce the price of the whole electrode setup and improve its stability, studies on the nature and role of underlayer were performed in order to avoid the use of expensive materials like Au (see Result and Discussion section). Eventually the study of a cheap protective overlayers was taken in account.
- To achieve better material performances the proper modifications of the band gap were considered. Improving the absorption will increase the number of photons than can be used to produce H_2 (and then the STH efficiency). The possibility of tuning the BG with doping or strain effect was performed by the use of Density Functional Theory (DFT).

1.3 Cu_2O General Review

In this section is given a brief review of the most relevant properties of Cu_2O.

1.3.1 Crystalline Structure

Cu_2O crystallizes in the so-called cuprite structure, a simple cubic Bravais lattice with the symmetry of the 224th space group (*O*4h, Pn3m). Few other compounds have the same structure as Ag_2O, Pb_2O, $Cd(CN)_2$ and $Zn(CN)_2$. Inside the unit cell the oxygen ions are located on a bcc sub-lattice, while copper ions on a fcc sub-lattice. Inside the cell the copper ions are on the vertices of an oxygen tetrahedron and they are twofold coordinated with the oxygen ions (D_{3d} site symmetry), whereas the oxygen ions are fourfold coordinated with copper (T_d site symmetry)[34,35].

The lattice is composed by two interpenetrating sub-lattices in which each oxygen is surrounded by 4 copper atoms and each copper is directly connected with 2 oxygen atoms by linear bonds[36]. Conduction arises from the spontaneous formation of Cu vacancies inside the lattice that creates holes in the valence band (VB). The top of the VB is composed by Cu *3d* states while the conduction band by a mixture of Cu *4s* and O *2p*. In Figure 28 is reported the 2x2x2 supercell with the two interpenetrating sub-lattices marked in two different colors.

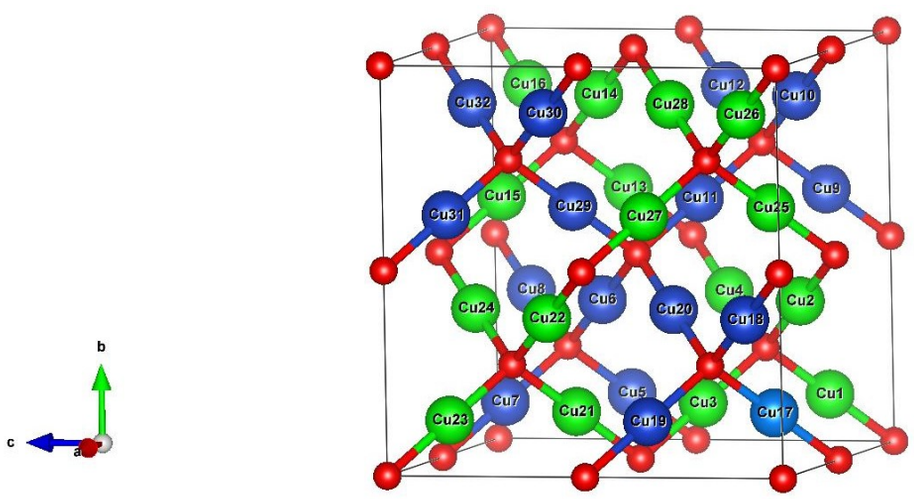

Figure 28. *VESTA representation of a $Cu_{32}O_{16}$ supercell. Oxygen atoms are in red while the Cu atoms of the two interpenetrating sub-lattices are showed in green and blue.*

Lattice constants and crystal structure have been usually measured by X–ray powder diffraction (XRD) using Cu-K radiation (Table 3). Cu_2O transforms from the cuprite to a hexagonal structure at a pressure of 10 GPa (a = 4.18Å). This hexagonal form changes in the pressure range from 13 to 18 GPa into another hexagonal form, with $CdCl_2$ type structure. Up to 24 GPa, the highest pressure generated, no decomposition of Cu_2O into Cu and CuO was observed. Despite this, the only structure considered in this work is the one stable at atmospheric pressure.

It is important to note that the given values are almost independent of the temperature, because Cu_2O has a very small expansion coefficient (the lattice constants change less than 0.5% from 0 to 600K). However, a very interesting behaviour of the Cu_2O is its negative thermal expansion below 300K[37].

Lattice Parameters	Values	Units
Lattice constant “a”	4.27	Å
Cu-O bond length	1.85	Å
O-O bond length	3.68	Å
Cu-Cu bond length	3.02	Å

***Table 3**. Tabulated lattice parameters for Cu_2O obtained by XRD. Data from Werner, A. and Hochheimer, H. D. High–pressure X–ray study of Cu_2O and Ag_2O. Physical Review B, 25 (1982), 5929*[38].

1.3.2 Cu_2O General Properties

In the following table are reported some parameters of interest in the study of Cu_2O.

Parameters	Values	Units
Density	6.10	gcm^{-3}
Molar mass	143.092	$gmol^{-1}$
Molar volume	23.46	cm^3mol^{-1}
Appearance	Reddish-brown	
Solubility (in water)	insoluble	
Melting point	1232	°C
Boiling point	1800	°C
Band gap	2.17	eV
R-phrases	R22, R50/53	
S-phrases	(S2), S22, S60, S61	
Thermal conductivity[39]	4.5	$WK^{-1}m^{-1}$
Specific heat capacity[39]	70	$JK^{-1}mol^{-1}$
Thermal diffusivity[39]	0.015	cm^2s^{-1}

***Table 4.** General physicochemical properties of Cu_2O. Data from Safety Data Sheet of Cu_2O.*

Figure 29 is the Poubarix diagram of copper obtained from Medusa®. It maps out possible stable (equilibrium) phases of an aqueous electrochemical system. Predominant ion boundaries are represented by continuous lines while water stability range is defined by the dotted lines at 0 and 1.23 V at pH 0. The concentration of Cu^{2+} considered, was the one present in the deposition bath of Cu_2O (as will be presented in the Result and Discussion section) used in this work.

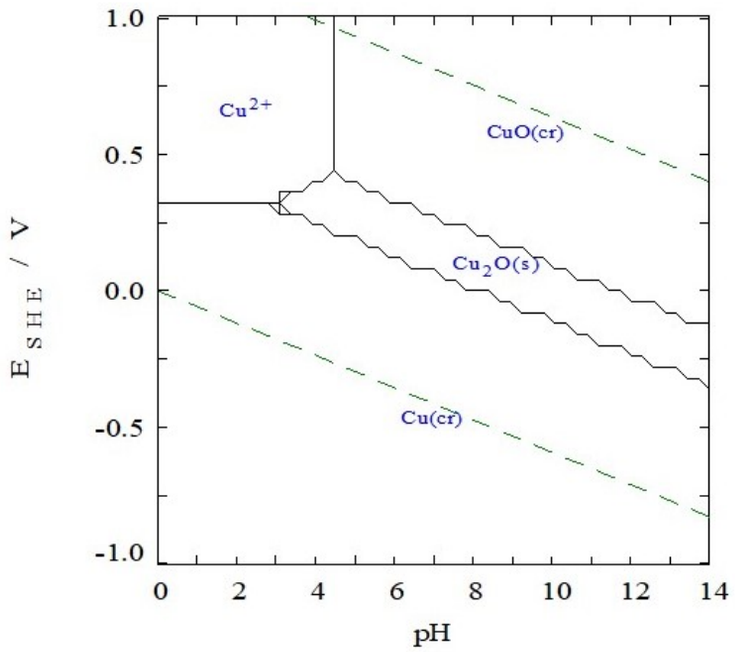

Figure 29. *Poubarix diagram of Cu for Cu^{2+} 70mM at 25°C from Medusa® software.*

In the absence of any complexing agent the formation of Cu(I) is forbidden because of the precipitation of the insoluble $Cu(OH)_2$ at pH > 8. Cu_2O is unstable in air at room temperature. Nonetheless, the kinetics of the transformation in CuO is so slow at room temperature that Cu_2O can be considered stable for all applications[40].

1.3.3 Optical Properties

Cu_2O has a direct forbidden band gap as stated before. Figure 30 shows the absorption spectrum which evidences how Cu_2O starts to absorb the light only above about 2.4 eV. This energy is related to the dipole allowed transition between the higher valence band and the second lower conduction band[41].

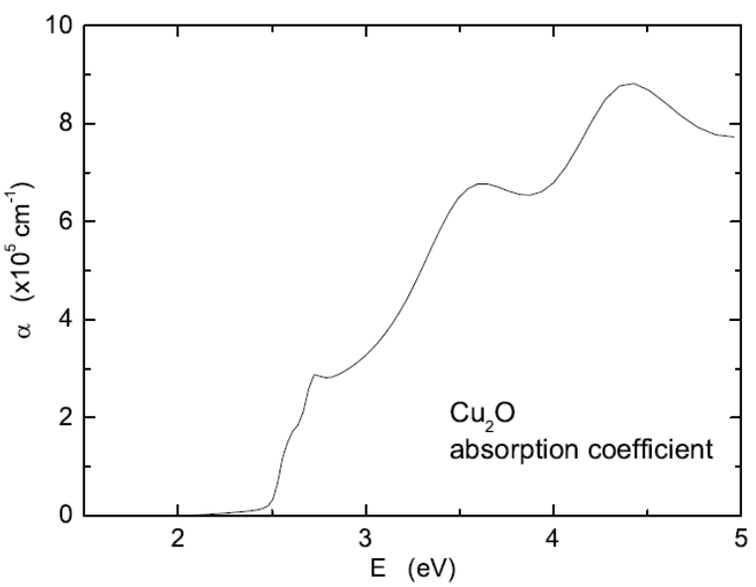

Figure 30*. Absorption coefficient of Cu_2O at room temperature obtained combining data from references [42,43].*

1.3.4 Preparation Methods:

Different preparation methods can be used to obtain an effective Cu_2O for photo-application. Here the main ones will be briefly discussed.

1.3.4.1 Thermal Oxidation

This is the most widely used method for the synthesis of several high-quality oxides. The procedure usually involves the oxidation of a high purity copper foil for few minutes or several hours depending on the desired thickness of the Cu_2O layer required. The operative temperatures are in the range between 1000-1500°C under pure oxygen atmosphere or in a mixed gas atmosphere (like Ar + O_2)[44]. The result is a polycrystalline Cu_2O with different grains structures according to the used experimental conditions. Two possible reactions can occur during the thermal process:

$$4Cu+O_2 \longrightarrow 2Cu_2O$$

$$2Cu_2O+O_2 \longrightarrow 4CuO$$

In was noticed by different authors that because the possible formation of a mixture of two major oxides products, such as, CuO and Cu_2O, the percentage of oxygen present during the annealing must be strictly controlled. It has been reported that the formation of Cu_2O occurs first and only after longer oxidation time CuO appears[45].

An alternative method transforms a Cu foil in $Cu(OH)_2$ by the use of 0.125 M $(NH_4)_2S_2O_8$ and then by thermal reduction obtain nanocorals of Cu_2O[46] or nanosized Cu_2O if an oxidation is performed in KOH and then a dehydration step is performed[47].

1.3.4.2 Electrodeposition

Electrodeposition is an extremely attractive method because of its low cost, the simplicity for the deposition on different substrates and the possibility of tuning the material properties and morphology with parameters like: the applied potential, the current, the temperature, and the pH of the bath.[48] The first electrochemical synthesis of Cu_2O was developed by Stareck[49] in the mid-thirties. Later many other authors present different synthetic procedures involving different copper precursors electrolytes and electrochemical techniques[50–52].

For example, Mao et al. used a solution of 0.01 M $Cu(NO_3)_2$ + 0.1 M NH_4NO_3 with a current density of 0.5 $mAcm^{-2}$ for 60 min at 313 K. The so-obtained photocurrent by the way are very low. [53]. Wan et al. started from 0.02M $Cu(Ac)_2$ and 0.1M sodium acetate aqueous solution with 1.5mM KCl, being able to control the shape of the grains with pH modulation, but the conductivity of the so obtained material was n-type. Zhao et al. electrochemically oxidized a Cu foil in a solution of 280 gL^{-1} NaCl and 0.1 gL^{-1} $Na_2Cr_2O_7$, with pH adjusted to value 12 by 1.0 M NaOH[54].

To the best of our knowledge, the best results in terms of photocurrent were achieved by using a $CuSO_4$ solution with lactic acid and the pH shifted to basic value (usually 12)[55]. The original recipe derived from Golden et al.[56] and was successively developed by the Graetzel group.[57–59] Not all the authors using this solution obtained the same high photocurrents. For example Nian et al. [60] obtain a maximum photocurrent of -0.025$mAcm^{-2}$ on FTO.

Despite this, usually the performances of PEC_WS systems fabricated with this method are nowadays one of the most efficient and with higher photocurrents. This method allows also to have high uniformity of the layer and the possibility of controlling the morphology and the size of the particles together with their properties[61,62] by simply varying some bath conditions like potential, temperature and pH.

In view of the electrochemical synthesis, we can consider also all the preparation methods consisting in the controlled oxidation of a copper foil in different solutions[63,64]. This method was tested but due to the poor performance was discarded and not reported in the thesis.

1.3.4.3 Other Synthetic Procedures

Other synthetic procedures includes reduction of copper-amine complex solution with glucose under microwaves irradiation[65], the use of different surfactants [66–71] and micelles[72] mostly to control the morphology of the particles. By these methods Cu_2O nanocrystals and nanowires[73] with cubic[74–76], cuboctahedral, truncated octahedral, octahedral[77], and multipod structures[78] have been prepared[79]. To avoid interference from these surfactants some authors developed also surfactant free synthesis[80–82]. Sol-gel [83]and solvothermal methods[84,85] are also used. Wet chemical routes[86,87], thermal evaporation[88,89], chemical vapour deposition[90],sonochemical synthesis[91], hydrothermal[92–94] and electroless[95] methods are only few of the other alternatives methods for the synthesis of this semiconductor. Sputtering is an interesting technique for the preparation of thin films with high homogeneity, low cost and easy synthesis[96].

1.3.5 Cu_2O Advantages for PEC-WS System

The choice of using electrodeposited Cu_2O is due to the following reasons:

- Cu_2O presents a 2.17 eV band gap. This value is high enough to have the proper energy for HER but still allows the material to absorb in visible range of light. This is a great advantage if compared to material like TiO_2 able to absorb only in the UV due to their large BG (~3 eV).
- Cu_2O presents a proper bands position for both hydrogen evolution reaction (HER) and oxygen evolution reaction (OER). In this work the material was studied as a photocathode (Cu_2O CB lies at -0.46V vs NHE).
- Cu_2O is an abundant and economic material.
- Cu_2O is non-toxic. This is an advantage if compared to other semiconductors for PEC-WS containing As, Cd and other toxic metals.
- The use of electrodeposition allows to have a large control over synthetic procedures with the selection of the best parameters to obtain high-performance electrodes.
- Electrodeposition is a cheap and easy method for the preparation of a large number of electrodes. In addition, there are high possibilities of scaling up the technology.

Looking in detail at the band position of Cu_2O, in the next figure we can notice that is one of the few materials with a small band gap but still able to perform both HER and OER (CB more negative than H_2/H_2O redox potential and VB more positive than O_2/H_2O redox potential).

The same figure shows the main disadvantage of this material. Indeed, the redox potentials for material reduction/oxidation lie inside the band gap.

This means that Cu_2O can undergoes to the previously explained photodegradation process. In particular, for this material both holes and electrons can interact with the material leading to its oxidation or reduction respectively.

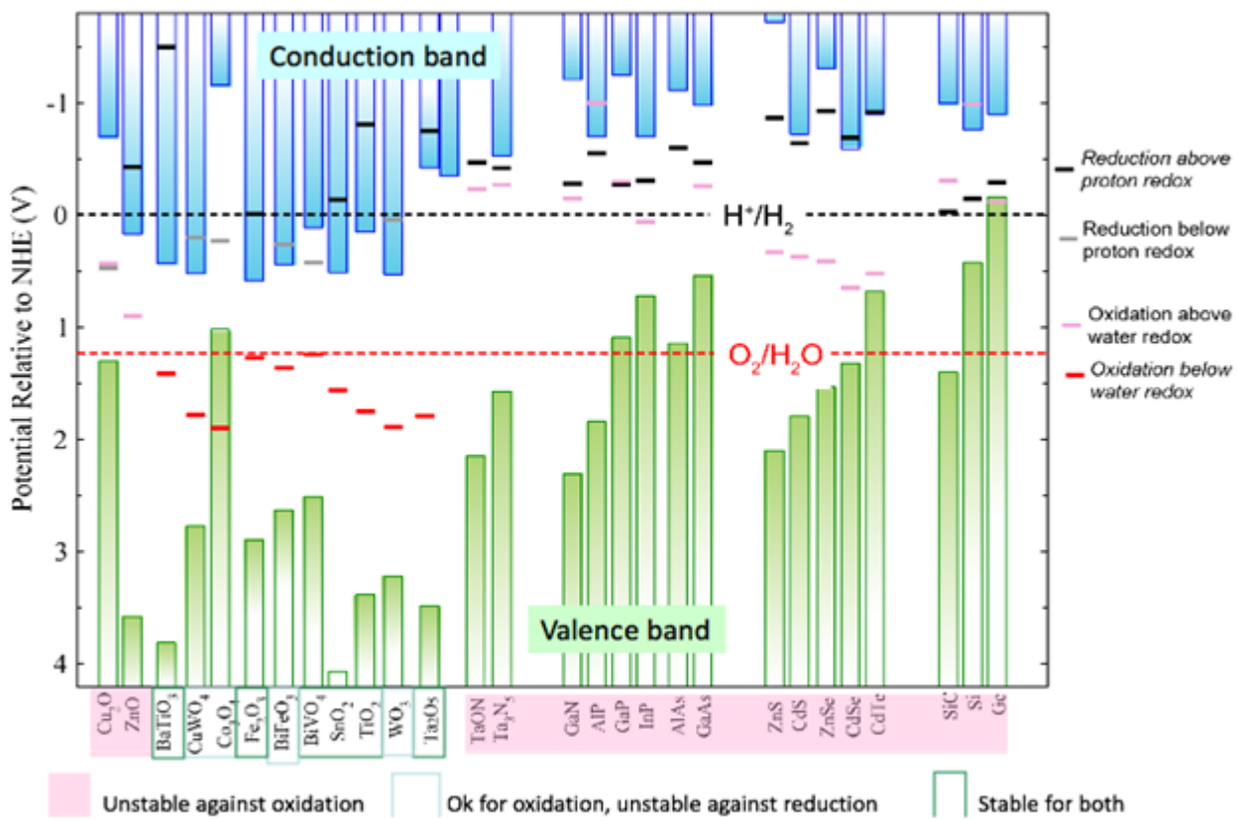

Figure 31. *Comparison of band gap, bands energies and redox potentials for different semiconductors for PEC-WS. From Chen, S.; Wang, L-W Chem. Mater. 24 (2012) 3659*[32]*.*

Two different approaches can be chosen to improve material performances: doping and protecting with an overlayer.

The former consists in the addition of impurities in the material lattice to modify band gap and bands position. This will allow to further increase the fraction of light that can be absorbed by the semiconductor together with carriers number and mobility.

The latter will allow to quickly take electrons from the Cu_2O thanks to the redox cascade principle so that they cannot react with the material itself. In this way, the life-time of the material can be improved. These two approaches will be better explained in the relevant chapters.

To have a full-knowledge of the phenomena occurring on Cu_2O is of paramount importance for the development of a high-performance, low-cost and with long life-time photocathodes. Stability is the main problem of the material and in order to characterize the degradation processes occurring under light different innovative techniques were used in this work. The next two chapters will introduce the reader in the details of the techniques to give a better compression of the further results.

1.4 XAS

X-rays Absorption Spectroscopy (XAS) refers to the absorption of X-rays by an atom at energies near and above its core-level binding energies.

XAS spectra particularly useful for the evaluation of:

- The oxidation states.
- The chemical surroundings: coordination number, bond distance and nature of neighbour atoms.

For all these advantages, XAS is a powerful tool to obtain information about chemical state and local atomic structure for the atomic species of interest. Nowadays XAS is applied to several chemical systems and in different experimental conditions (extreme temperature and pressure, light, solutions, NPs, etc..). For this reason, it is become an extremely powerful technique in different scientific fields, including biology, environmental science, catalysts research, and material science.

Additional advantages of XAS are:

- It can be used for every element.
- Crystallinity is not required for XAS measurements. Is one of the few structural probes available for non-crystalline and highly disordered materials, including solutions.
- Because X-rays energy are highly penetrating, it gives information on the whole material and not simply of the surface. If the interest is in surface phenomena, the use of nanostructures will help giving a material with a high surface/volume ratio.
- In many cases, XAS measurements can be made on elements of minority and even trace abundance, giving a unique and direct measurement of chemical and physical state of dilute species in several systems (e.g. dopants).
- XAS allows *ex-situ*, *in-situ*, and *operando* measurements. The latter is particularly useful to follow electrochemical reactions within or without the presence of light.
- It is element sensitive. Since every atom has core-level electrons with well-defined binding energies, we can select the element to analyse by tuning the X-ray energy at an appropriate absorption edge.

1.4.1 XAS Spectroscopy

A XAS spectrum reports the absorption coefficient as a function of incident X-rays energy close to absorption edge (from -20eV up to 1000 eV after the edge). In the full spectrum two main regions can be identified[97]:

- The XANES (X-ray Absorption Near Edge Structure) region; is the energy region closer to the edge.

- The EXAFS (Extended X-ray Absorption Fine Structure) region, at higher energies

Both regions give several information on the studied material. XANES gives information about the oxidation state of the selected element and coordination geometry (e.g., octahedral, tetrahedral coordination) of the absorbing atom.

Moreover, being a probe for empty orbitals, it provides additional information about those orbitals lying over the Fermi energy level. EXAFS is useful to evaluate the neighbour atoms respect to the absorption centre. It gives information about interatomic distances and coordination number of neighbour atoms.

1.4.2 The Synchrotron Light

X-rays are the portion of electromagnetic radiation with a wavelength between 25 and 0.025 Å. X-rays can be produced in the laboratory scale using a Coolidge tube whose characteristic spectrum is reported in Figure 33A. The so generated X-rays are continuous in their emission with a quite low intensity and with some characteristic emission lines due to the material forming the anticathode. To have a continuous radiation but with high intensity a synchrotron facility is needed. In a synchrotron, electrons are generated by thermionic effect from a W wire and then linearly accelerated until the booster ring. Here they are accelerated (in the so-called LINAC) with radiofrequency generator until a critical speed is reached (close to light speed) where an electromagnetic radiation is emitted in the range of X-rays.

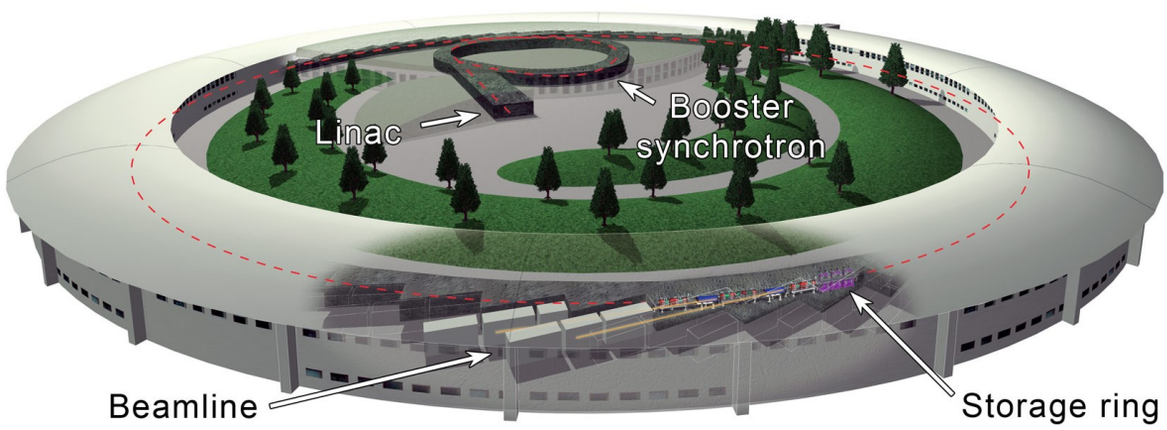

Figure 32. *ESRF schematic view. Is possible to notice the linear accelerator (LINAC) the booster synchrotron and all the beamline tangent to the main storage ring. Image from esrf.eu*

Then electrons enter in the main ring called storage ring. The storage ring is composed by linear sections and curved sections where the electron trajectory is bended thanks to bending magnets. The magnetic field, create a centripetal acceleration that force the electrons (a charged particle) to emit electromagnetic radiations tangentially to the ring. If this energy is higher than 1GeV then the electron emits X-rays with the emission spectrum showed in Figure 33B. The synchrotron intensity is very high, usually 10 orders of magnitude higher respect to the one of the Coolidge tube. In addition, the use of specific magnets (undulator) who force the sinusoid motion of the electrons, force the constructive interactions of emitted radiations leading to even higher intensities.

The maximum radiation energy, called cut-off, is strongly related to the length of the ring. Usually this intensity is reported as brilliance that is defined as follow:

$$B = \frac{I}{\phi \cdot A}$$

Where *I* is the intensity of the produced radiation, *Φ* is the angular aperture and *A* is the surface.

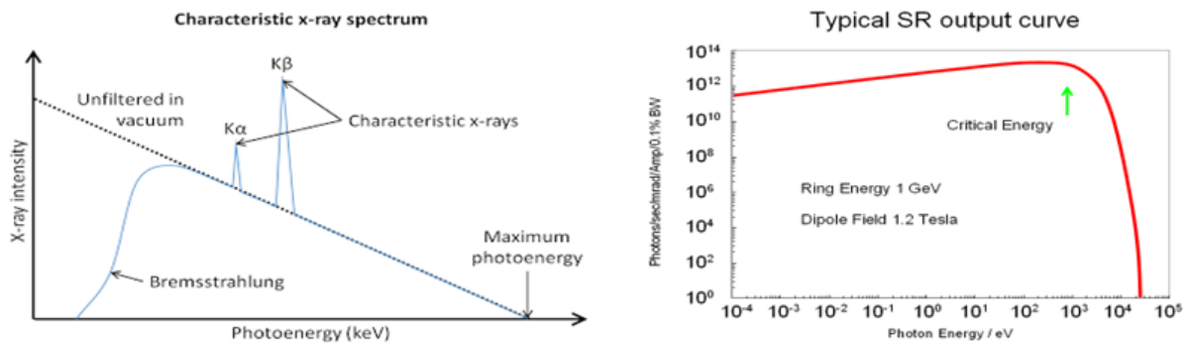

Figure 33. *Emission spectrum of a Coolidge tube (left) with the characteristic peaks and one of a synchrotron radiation source. Image from ISA centre for storage ring facilities, Aarhus University.*

X-rays absorption and the relaxation phenomena

X-rays are extremely energetic, so when interact with matter they are absorbed by core electrons.

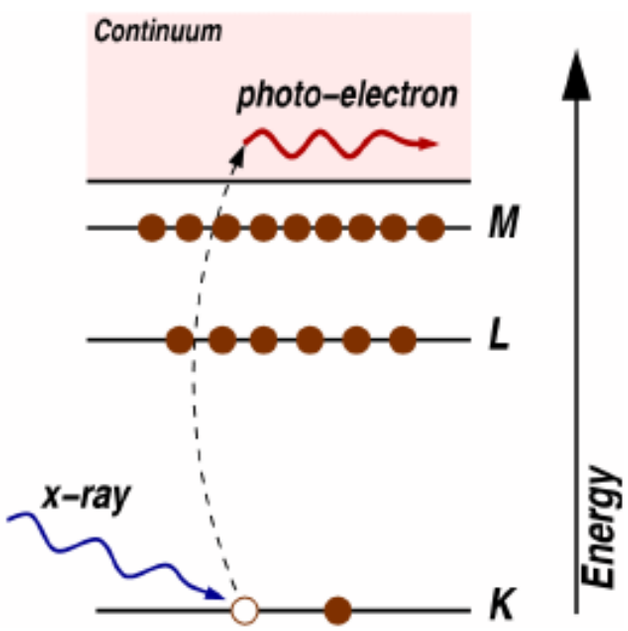

Figure 34. *Scheme of the photoelectric effect, in which an X-ray is absorbed, and a core level electron is promoted out of the atom. Image from Fundamentals of XAS, Matthew Newville, Consortium for Advanced Radiation Sources University of Chicago, Chicago, IL.*

This causes a depletion of the incident beam I_0 and the transmitted radiation intensity is given by the Lambert-Beer equation:

$$I = I_0 \cdot e^{-\mu \cdot x}$$

where μ is the linear absorption coefficient, a measure of the absorption phenomena probability, and *x* is the thickness of the sample.

The absorption coefficient slowly decreases with the increase of energy while is strongly related to the atomic number of the specie of interest according to the relation[98]:

$$\mu \sim \frac{\rho \cdot Z^4}{A \cdot E^3}$$

where ρ is the sample density, Z is the atomic number, A is the atomic mass and E is the energy. Due to the Z^4 dependence, it is quite easy to distinguish between different elements and the absorption levels for each element are far from each other allowing the technique to be element sensitive.

A XAS spectrum presents on the y-axes the absorption coefficient while the energy of incident radiation in on the x-axes. The shape of a typical XAS spectrum is reported in figure:

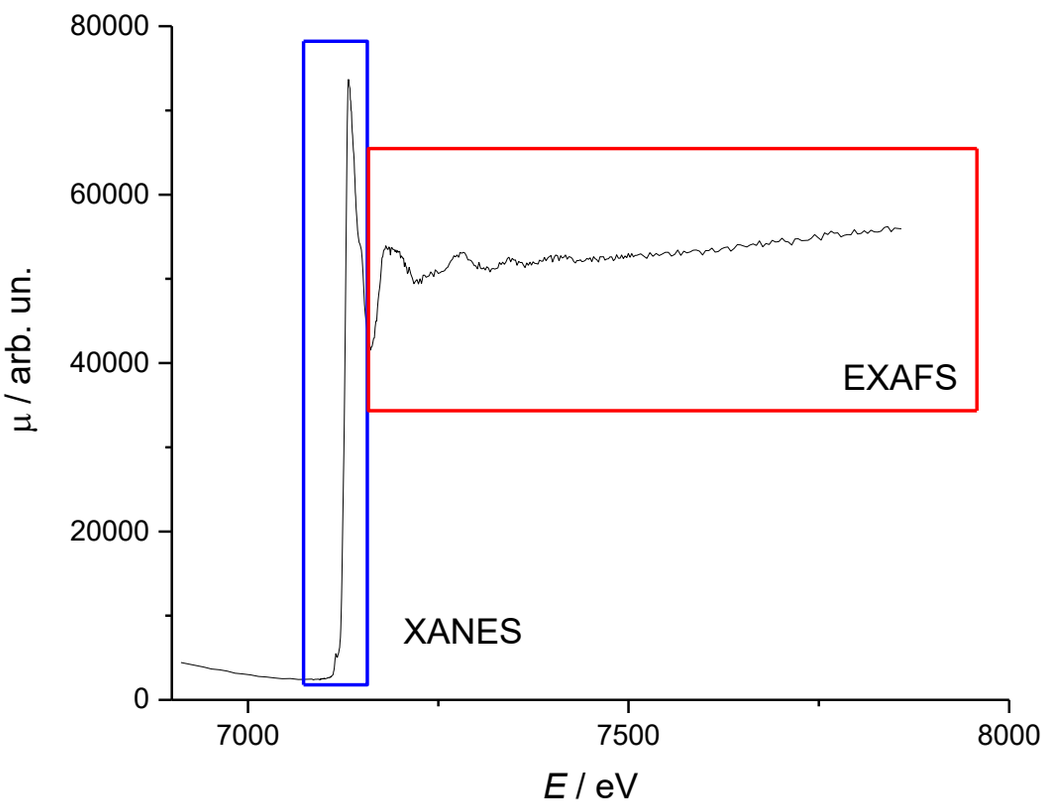

Figure 35. *XAS spectrum showing the 2 different regions of XANES (close to the edge in blue) and EXAFS, the portion of spectrum at high energy (in red). Spectra of alpha FeOOH on Ti.*

Before the edge, the absorption coefficient is zero, once this value is crossed instead the absorption coefficient rapidly increases giving the absorption edge. Indeed, after the edge point the energy of X-rays is enough to have photoionization, the excitation of an electron from core levels to continuum (Figure 35).

There are different edges according to the energy level originally occupied by the electron. According to Sommerfeld, if the electron comes from 1s level (n=1) we call it K-edge. If the quantum number is 2 then it comes from L-edges.

Three states are possible in this case: L_1 if the electron comes from 2s orbital, L_2 or L_3 if it comes from 2p orbitals according to the spin-orbital coupling (J = 1/2 e J = 3/2 respectively). The same explanation can be done for M-edges, but they have very small importance in XAS spectroscopy and will be no treated.

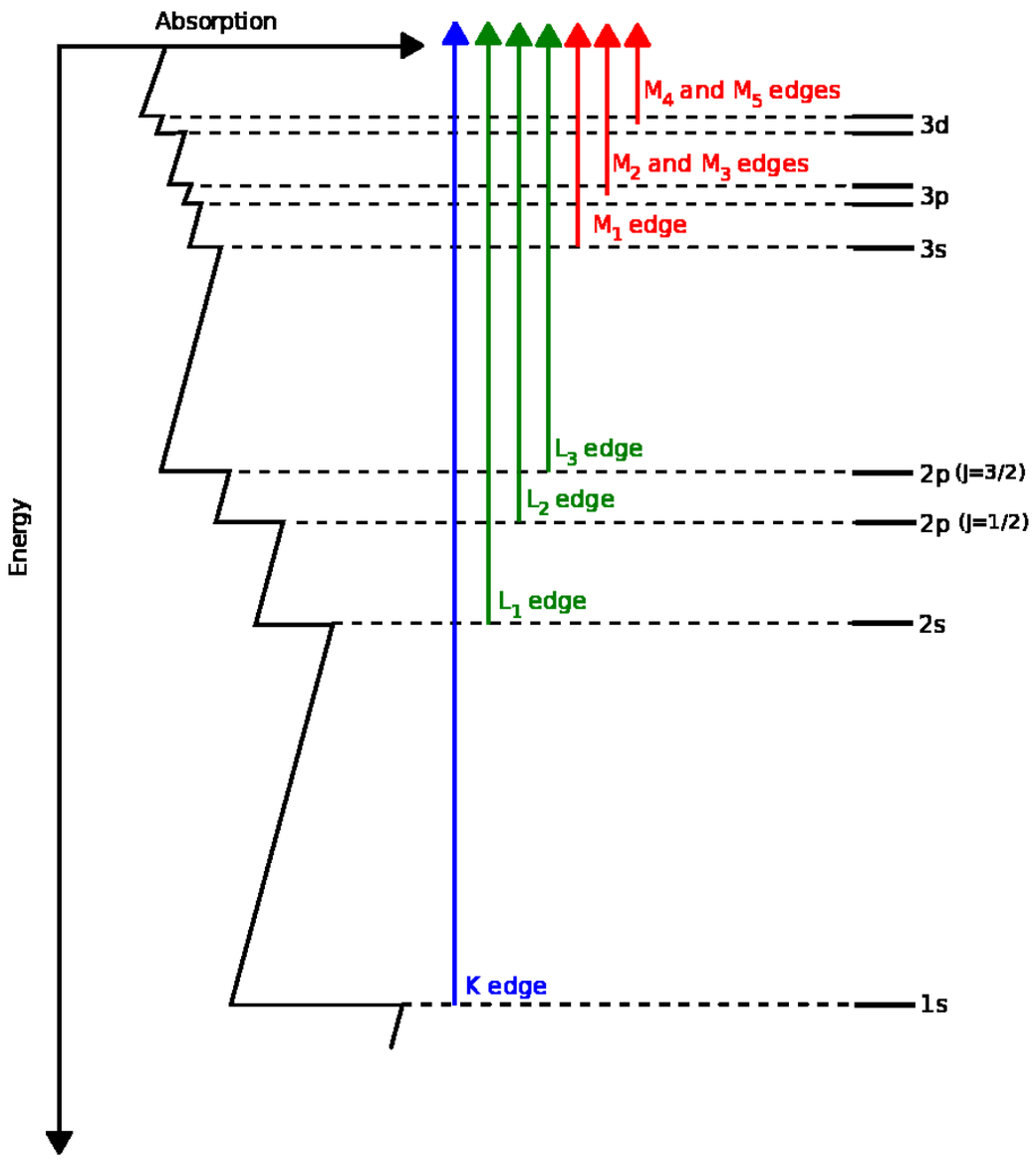

Figure 36. *Scheme of electronic transition according to Sommerfeld. Image from Wikipedia.*

The electron promoted in the continuum level leaves a hole behind in the starting orbital.

The original state can be restored with two different relaxation processes, each in competition with the other: Auger effect and fluorescence.

- **Auger effect:** is the preferential effect in lighter atoms and involves 2 electrons. The first one relaxes and fills the hole left in the starting level, while the second one is emitted because of the energy surplus.

- **Fluorescence**: is more common in heavier elements and consist in the emission of radiations once the hole is filled by an electron coming from external (shell) levels.

In both cases, the probability of emission (X-ray or electron) is directly proportional to the absorption probability.

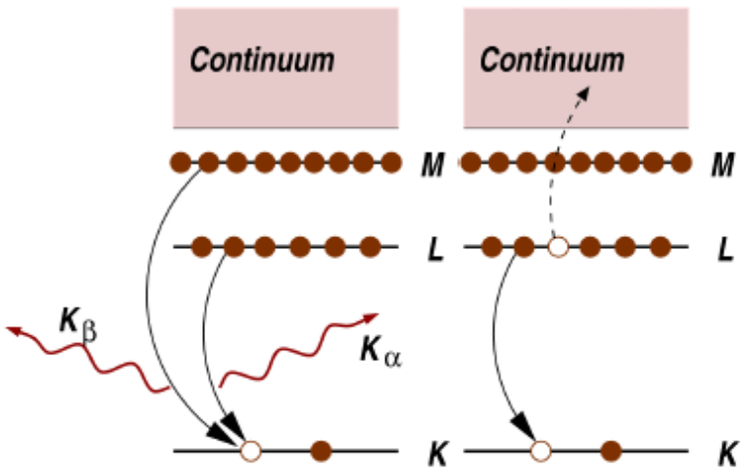

Figure 37. *Decay of the excited state: X-ray fluorescence (left) and the Auger effect (right). Image from Fundamentals of XAS, Matthew Newville, Consortium for Advanced Radiation Sources University of Chicago, Chicago, IL.*

A XAS spectrum can be measured both in transmittance and in fluorescence[99]. In the former case, the reduction of the beam intensity due to the sample is measured. The absorption coefficient is obtained from the Lambert-Beer equation:

$$\mu = ln\frac{I_0}{I}$$

If the amount of sample is very small the differences between incident beam and transmitted beam are very small and fluorescence mode is to be preferred. In this setup, the electrons detector is normal to the incident radiation in order to acquire only the emitted beam from the sample. In fluorescence mode, the absorption coefficient is given by:

$$\mu \propto \frac{I_f}{I_0}$$

Where I_f is the fluorescence intensity and I_o is the incident beam. In the fluorescence mode, traces of the element under study can be collected.

1.4.3 XANES Spectra

The XANES region is the part of the spectrum closer to the edge energy, usually in the window between -20eV and +50 eV respect to the edge. From XANES measurements is possible to obtain information about oxidation states. As example, Figure 38 reports the comparison between the XANES spectra of 3 different copper species, metallic copper (in blue), Cu_2O (in green) and CuO (in red). Is possible to notice how higher is the oxidation number, more is the shift to higher energies. The explanation for this phenomenon is that decreasing the number of electrons (increasing the nuclear charge), the electronic cloud is more compressed because of the higher coulombic interaction between nucleus and electrons.

Therefore, the energy for photoionization increases with a shift of the edge to higher energy together with the oxidation state.

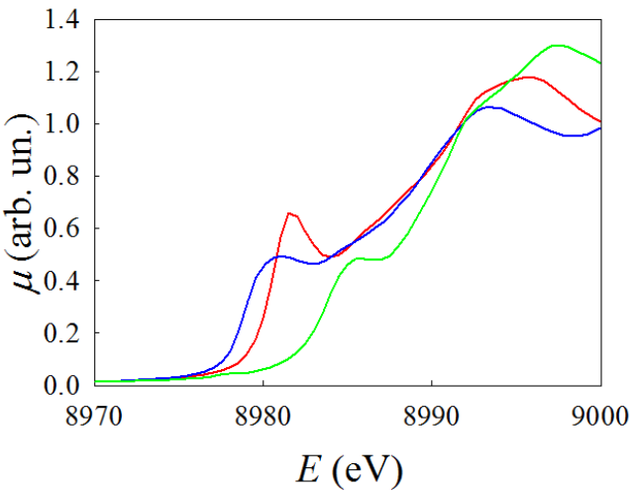

Figure 38. *Comparison between XANES standard spectra (acquired at copper K-edge) of metallic copper (blue line), Cu_2O (green line) and CuO (red line). Data acquired at GILDA beamline, ESRF, France.*

Before the edge, the X-ray radiation have not enough energy for photoelectric effect.

Because in the XANES region the energy supplied to the electron is barely enough for photoionization, the kinetic energy of the electron is very low. This leads to a very complicate sequence of interactions with neighbour atoms and is very difficult to mathematical describe this region of the spectrum.

Usually the XANES region is analysed on the base of its "fingerprinting" properties. Indeed, considering a single element, the shape of the spectrum can have huge variation according to the oxidation state, the chemical surrounding, and the coordination geometry. Moreover, not only edge energy variation occurs but the shape is also strongly dependant on ligands position and their nature. Looking at the K-edge spectra of Cr(VI) with tetrahedral environment (blue) and the one of Cu(III) with octahedral one is possible to notice dramatic differences in the shape due both to the change in oxidation state and the different geometry.

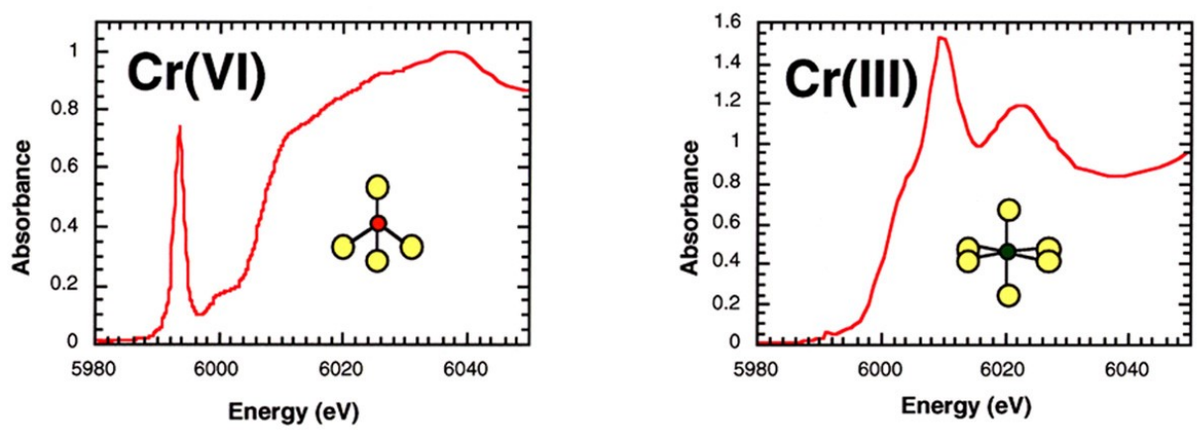

Figure 39. *Comparison between the XANES spectra of Cr(VI) and Cr(III) respectively blue and red lines, recorded at the Cr K-edge. The differences are related both to the oxidation state and to the coordination geometry, octahedral for Cr(III) and tetrahedral for Cr(VI).*

1.4.4 EXAFS Spectra

EXAFS is relevant to energies that leads to the photoemission of electrons.

When an atom is surrounded by other atoms, these behave like back scattering centres. According to the wave-particle dualism, the photoelectron and the retro-diffused one can be considered as waves. These waves can lead to constructive or disruptive interference phenomena. The results are the absorption coefficient oscillations recorded in the EXAFS spectra.

Then from the variation of the absorption coefficient is subtracted the value of the isolated atoms and the obtained value is divided by the number of photoabsorber. The obtained function χ(E), is strictly related to the chemical surrounding and is referred to a single absorber.

$$\chi(E) = \frac{\mu(E) - \mu_0(E)}{\Delta\mu_0}$$

The EXAFS signal is represented by χ as a function of the wave vector k, that is related to the energy by the equation:

$$k = \sqrt{\frac{2m(E - E_0)}{\hbar^2}}$$

The probability of retro-diffusion is related to the nature of the closer atoms surrounding the photoabsorber, to their number and to the energy of the incident photon.

1.4.5 FEXRAV

FEXRAV (Fixed Energy X-ray Absorption Voltammetry) is a recently invented technique highly useful for the evaluation of electrochemical systems because allows to follow simultaneously the variation of the absorption coefficient and the electrochemical signal (current or potential) during the course of a conventional electrochemical experiment[100–102]. FEXRAV is therefore an *operando* technique and consists in the evaluation of the absorption coefficient at a fixed energy value while the potential applied on the electrode (or a photoelectrode) is varied. The energy chosen for this technique is the one at which the difference in absorption coefficient between the oxidation states likely involved in the reaction is the highest.

In Figure 40, the electrode is composed by Cu_2O (red line). If we want to follow the reduction to metallic copper (blue line) the selected energy must be the one in which the difference between their absorption coefficient is the highest in their standard spectra. As reported by the black line, the chosen energy is 8979 eV where the Cu(0) coefficient is higher than the one of Cu_2O. Therefore, during the FEXRAV (Figure 40 on the right) an increase in the value of the absorption coefficient is related to a reduction of the material to metallic copper. From FEXRAV, knowing the amount of material on the electrode, is also possible to have an estimation of the transformed material to be compared with the variation in charge recorded by electrochemistry.

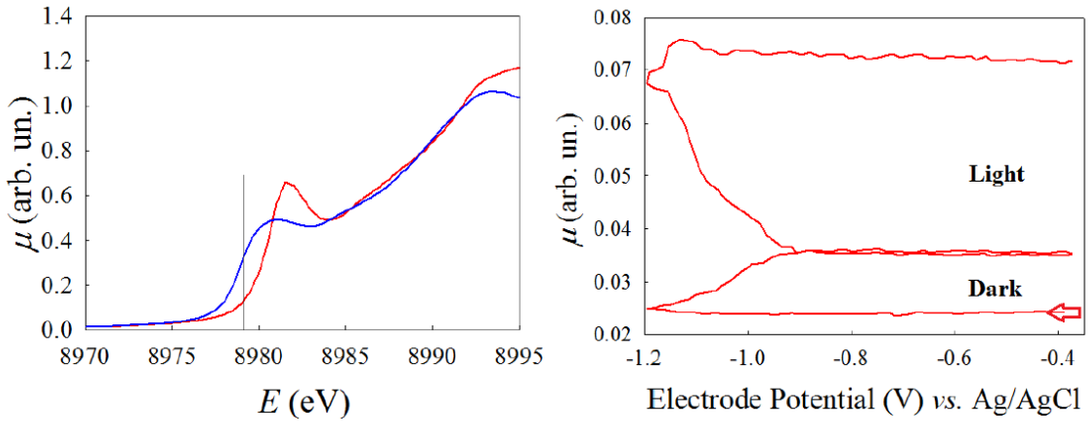

Figure 40. *On the left, comparison between XANES standard spectra of metallic copper (blue line) and Cu_2O (red line) with energy at which the variation of the absorption coefficient is higher (black line). On the right, an example of FEXRAV performed during 2 cycles (first in dark and second in light) of cyclic voltammetry on a Cu_2O electrode. An increase in the absorption coefficient intensity is related to the formation of metallic copper.*

Therefore, the FEXRAV and the electrochemical signals are complementary and synergistic in the study of electrochemical (and photoelectrochemical) phenomena, particularly when two or more phenomena occur in parallel and need to be decoupled. For example, once a strong gas evolution reaction occurs (HER or OER), the current recorded in a CV is quite high and able to cover any process occurring at the material itself (e.g. an oxidation state change).

Thanks to FEXRAV, we can define the active oxidation state of an oxygen evolution catalyst like IrO_x under OER condition or define the contribute of the material photodegradation under HER condition for a photocathodic material like Cu_2O[57]. FEXRAV is particularly useful for studying light-activated system like semiconductors for photoelectrochemical water splitting. The absorption coefficient is measured at fixed energy and at fixed potential in dark and in light: the absorption coefficient is thus related to the effect of light on the sample. Another advantage of FEXRAV is its low acquisition time, making this technique an interesting candidate for obtaining useful preliminary information and find the best operative conditions for further experiments. FEXRAV is, by definition, a real-time technique. In addition, it is very sensitive, and allows to detect minor changes in the absorption coefficients (such as those related to adsorption phenomena (see Appendix 2)) otherwise hardly visible from full spectra evaluations. Small effects might in fact easily erased in spectra post-analysis, including spectra normalization.

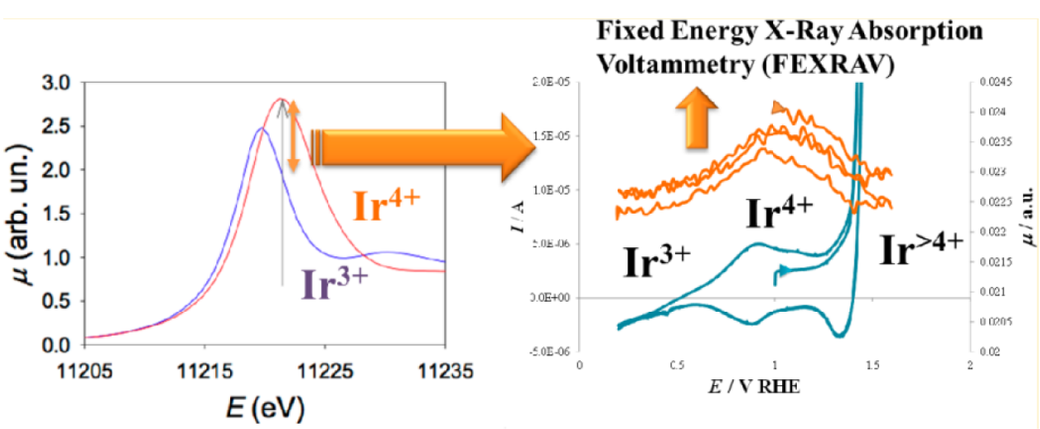

Figure 41. *A) Energy selection for FEXRAV and B) FEXRAV of iridium oxide on carbon screen printed electrode until oxygen evolution*[103].

1.4.6 Light-dark Difference Spectra

The difference spectra recorded under light and dark conditions gives us information about fast changes in the material under irradiation. In order to have an accurate comparison between spectra, experimental errors must be reduced. For this reason, the spectra are acquired with a stepping mode. For every value of energy, two values of the μ are recorded, one in dark and one in light. Only once the two values are recorded, the monochromator shift to the next energy. This workaround allows to avoid shift problems in the energy scale: the two values of μ can be directly subtracted. The resulting difference "light-dark" spectra give information about light induced reversible changes in the material.

1.4.7 Dispersive XAS

This particular application of XAS allows time resolved studies of dynamical processes. The beamline used during this work was ID24 at ESRF, the synchrotron in Grenoble (FR). Instead of selecting a single energy, all the wavelengths go thought a "polychromator" able to split the different energy components at different angles. These components are collimated on a focal plane that coincides with the sample. The transmitted beam hits a position sensitive detector, that records the intensities relevant to small intervals of wavelengths.

This allows the acquisition of a full spectrum in few milliseconds (instead of minutes or hours) and records fast sequences of full spectra in few minutes following any change in the sample with the changes of the spectra[104]. Of course, the energy resolution is lower than in a conventional XAS beamline.

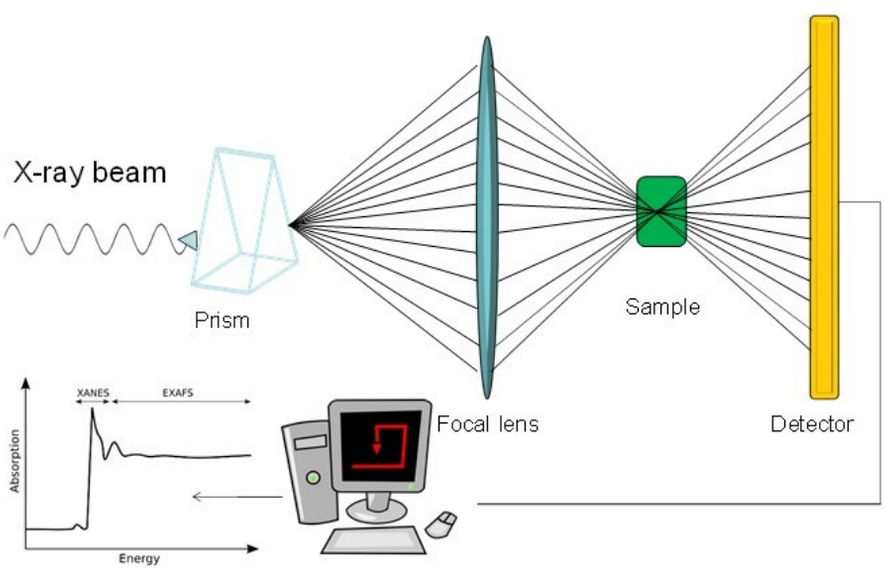

Figure 42. *Scheme of dispersive XAS setup.*

1.5 SECM

1.5.1 Scanning Electrochemical Microscopy (SECM)

SECM involves the measurement of the current at an ultramicroelectrode (UME, i.e. the so-called tip) (an electrode with a radius in the order of a few nm to 50 µm) than can be held or moved in 3D either in a solution or in the proximity of a "substrate" thanks to piezoelectric or stepper motors. Substrates can be of different types of solids(e.g., glass, metal, polymer, biological material[105]) or liquids (e.g., mercury, immiscible oil) that, in particular conditions, perturb the electrochemical response of the tip and this perturbation provides information about the nature and properties of the substrate[106]. The substrate is often a second electrode, and therefore SECM include typically a bipotentiostat. The development of SECM followed previous works on Ultra Microelectrodes (UMEs) in electrochemistry and the application of piezoelectric elements, as in scanning tunnelling microscopy (STM)[107], for the movement in the nano-micrometre scale.

1.5.1.1 Uses

SECM is an extremely powerful tool with a huge variety of applications: Record morphologic images, rapidly evaluate the activity of catalysts libraries, evaluate heterogeneous and homogeneous reactions kinetics[108,109]. The small dimension of tips allows the study of biological systems by means of cells imaging or the evaluation of enzymatic reactions or nanoparticles bio-effects screening[110]. Eventually the study of liquid-liquid interfaces, membranes and thin films can be performed, as well as the evaluation of surface reaction rates[111,112]. In this work, an innovative SECM mode for the study of semiconductors powders is described and applied to the evaluation of photodegradation processes.

1.5.1.2 Technique Setup

The SECM setup includes a 4 electrodes cell. Two working electrodes are present, the tip is usually the working 1 while the substrate is the working 2. Obviously, a simpler 3-electrodes configuration can be adopted by the use of an insulating plane instead of working 2. The tip and the substrate can be biased at the same time using only one counter and one reference electrode, thanks to the use of a bipotentiostatic circuit.

The core of the system is the piezoelectric/stepper motor able to change the relative position of the two working electrodes in the three dimensions (x, y and z) and also to move it with the desired scan rate. In this work, only the stepper motor is used.

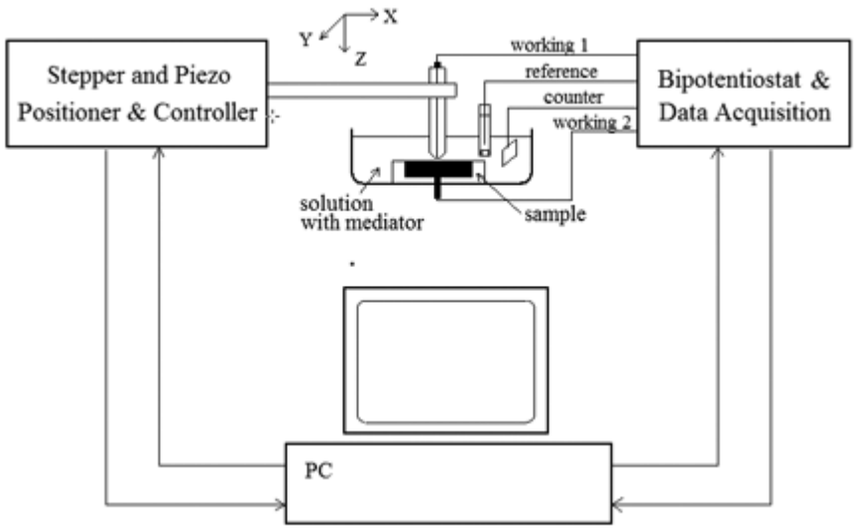

Figure 43. *Illustration of the SECM instrumentation. Image from Bard, A.J.; Mirkin, M.V. Scanning Electrochemical Microscopy, (2001) Marcel Dekker*[107]*.*

1.5.1.3 The Feedback Mode

One of the most commonly used way to operate with SECM is the feedback mode. The only requirement is the presence of an appropriate redox active specie in a solution of the supporting electrolyte. The role of the latter is to reduce the solution resistance and ensure that the transport of the redox specie to the tip occurs only by diffusion.

If the tip is kept at a potential at which the redox active specie (O) is reduced to R according to the reaction:

$$O + ne^- \rightarrow R$$

When the tip is far away from the substrate (in the bulk solution) the current flowing is related only to the hemispherical diffusion of the specie from the bulk to the electrode (Figure 44A). In this region, the steady state current (i_{tip}^{∞}) is reached according to the equation:

$$i_{tip}^{\infty} = 4nFDC_b a$$

When the tip is approached towards a substrate, down to a distance comparable to the radius of the tip, a higher or lower feedback current is measured depending on the nature of the used substrate. In the presence of a conductive substrate (with the proper E_0), the tip-produced R specie is oxidized again to O on the substrate. The O species produced at the substrate can then diffuse to the tip increasing the total amount of O reaching the tip (O from the bulk + re-oxidized O from the substrate). In this case an increase of tip current is recorded ($i_{tip} > i_{tip}^{\infty}$) and this is called positive feedback (Figure 44B)[113].

On the contrary, if the substrate is an insulating material or has not enough potential to re-oxidize R, it hinders the flux of O to the tip. The depleted amount of O species reaching the tip lead to a reduced tip current in the proximity of the substrate ($i_{tip} < i_{tip}^{\infty}$). This is called negative feedback (Figure 44C).

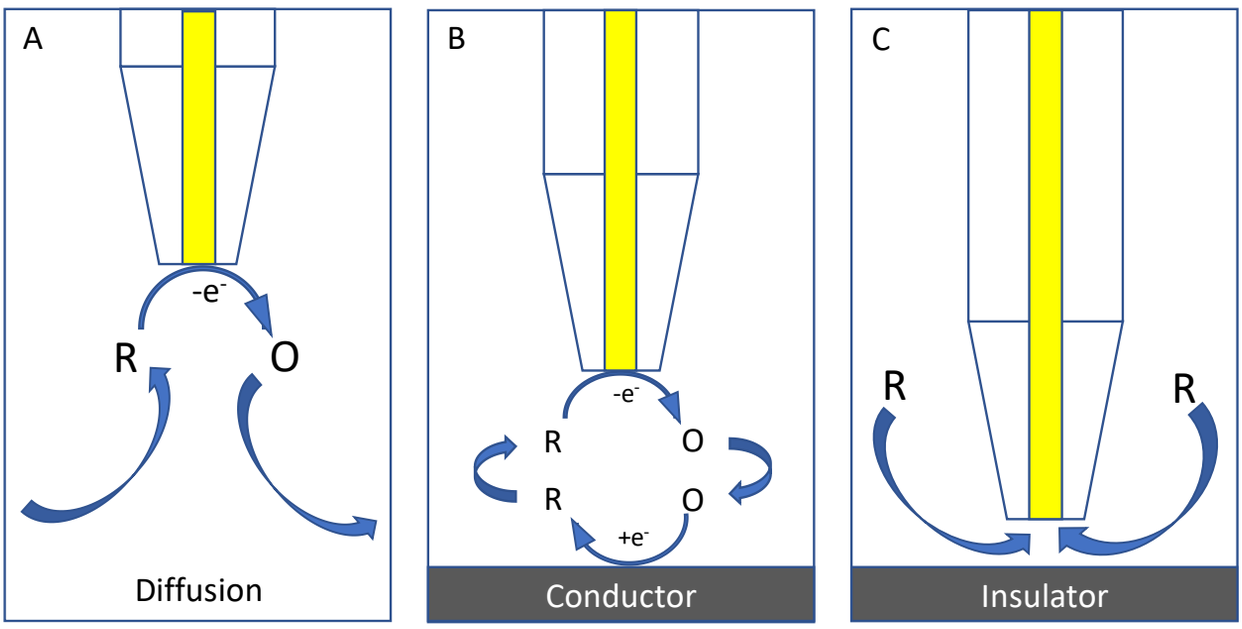

Figure 44. *The 3 different conditions of feedback mode: A) the tip is far from the substrate and the diffusion allows it to achieve the steady state; B) Positive feedback. The specie is regenerated at the substrate; C) Negative feedback. The specie in the bulk is prevented from reaching the tip by the insulating surface. Image adapted from P. Bertoncello, Energy Environ. Sci., 2010,3, 1620-1633*[113]

During a SECM experiment it is extremely important to know the relative distance between tip and substrate. This distance is indeed related with the performance of SECM in working as a good probe for the species of interest[114].

Negative feedback and positive feedback can be used to obtain this information. In a negative feedback approach, the shorter the tip-substrate distance the lower the i_{tip}/i_{tip}^{∞} current. In principle, when the tip touches the substrate, I tip=0 In the same way, with a conductive substrate, the contact between the two electrodes can be evaluated with the increase of the current as the tip approaches the substrate.

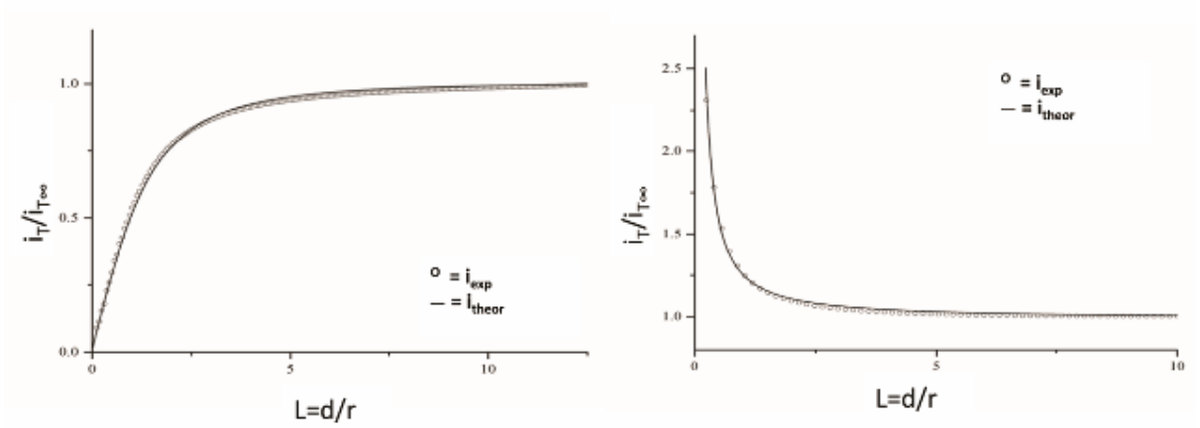

Figure 45*. Two examples of negative (on the left) and positive (on the right) feedback. As the tip approach to the substrate surface the tip current decrease and increase respectively. Image from Darren A. Walsh, Chem. Soc. Rev., 2010,39, 4185-4194*[114]

i_T / i_T^{∞} and L = d / a, are used to make the approach curves independent on the concentration and on the diffusion coefficient of the species R and on the electrode radius.

1.5.1.4 Working Mode

Due to the extremely sensitivity of the feedback mode to the intrinsic activity of a material it can be used only if the concentration of the reagent produced by the tip is low enough to maintain the reaction under diffusive control (e.g. in this work the couple O_2/H_2O naturally present in water is used to evaluate the tip distance from the substrate). Furthermore, this method is strictly dependent on the distance between tip and substrate.

These two conditions are quite often non-fulfilled and so Generation-Collection (GC) mode have to be applied. Two main GC modes can be used with SECM depending on the aim of the research and material properties, TG/SC (tip generation/substrate collection) and SG/TC (substrate generation/tip collection).

In SG/TC the substrate is biased at the potential required for the reaction of interest, while the tip work as a probe for the substrate-produced specie while being under diffusive control. In this mode, the tip current is obviously proportional to the amount of the specie produced at the substrate according to the previously introduced equation:

$$i_{tip}^{\infty} = 4nFDC_b a$$

In this way, the tip can be a probe for the substrate activity towards the reaction. Indeed, higher is the activity, higher is the production rate and higher is the current recorded at the tip. Even if the current changes with time if the substrate is small enough the steady state condition can be easily reached. This mode is useful to evaluate areas of different activity on the substrate like the study of large arrays of different electrocatalysts.

In the TG/SC, the tip is biased to a potential suitable to generate a reagent while substrate is biased at the proper potential to consumes it. Is then possible to measure the substrate current, which is strictly related to the activity of the tip. Indeed, higher is the activity of the tip, higher is the amount of specie produced and eventually higher the substrate consumption current. The advantage of this mode is that if, as usually occurs, the substrate area is much larger than the tip one, the collection efficiency, given by the ration $i_{substrate}/i_{tip}$ can be consider equal to 1. The collection efficiency parameter value decreases if in the space between the tip and the substrate, the tip-produced specie reacts or decompose. Moreover, the distance between the two electrode is also important to avoid the specie produced at the tip to be lost in the bulk before reacting with the substrate[115].

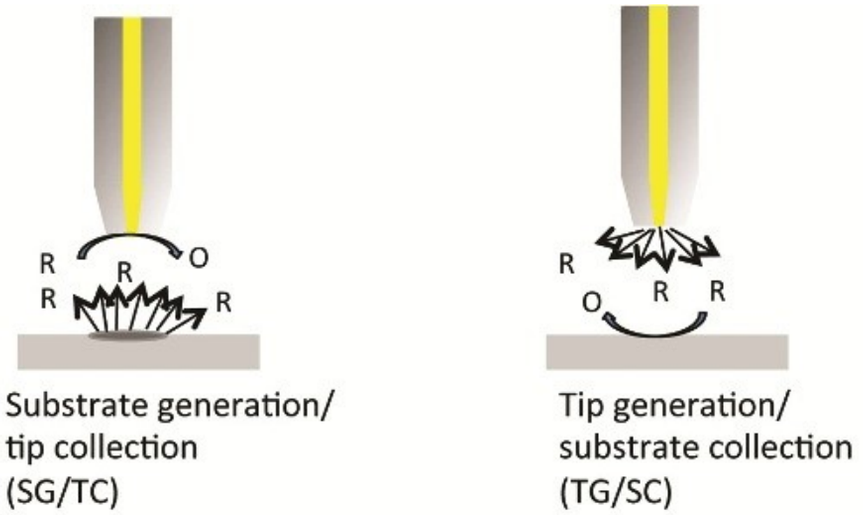

***Figure 46**. Generation collection mode. Left: Substrate generation/tip collection mode. Right: Tip generation/substrate collection mode. Image from AzoNano, Combining Atomic Force Microscopy with Scanning Electrochemical Microscopy, 2016*

1.5.1.5 Imaging

Another very important feature in SECM is the possibility of recording images, representation of the dependence of tip (or substrate) current as a function of the tip x-y position. Two parameters affect the current, substrate geometry and electrochemical properties.

Surface topography affects the tip current because of the changes in distance between the two electrodes. If the distance changes (in the range of tip dimensions), as explained for the feedback mode, the current is modified. A colour map of the surface can be obtained with useful information on topography. On the other hand, imaging can be used to evaluate difference in composition on the substrate. If the surface is not homogeneous with insulating (or less active) and conductive region, the tip current changes in relation with the amount of species produced by the different regions of the substrate. Is not easy to obtain clean result due to the diffusion of the produced species over the active spot of the substrate but if some expedients (shielded tips) are taken in account then the image can be a clear representation of the electrochemical properties of the different regions of the substrate[116–118].

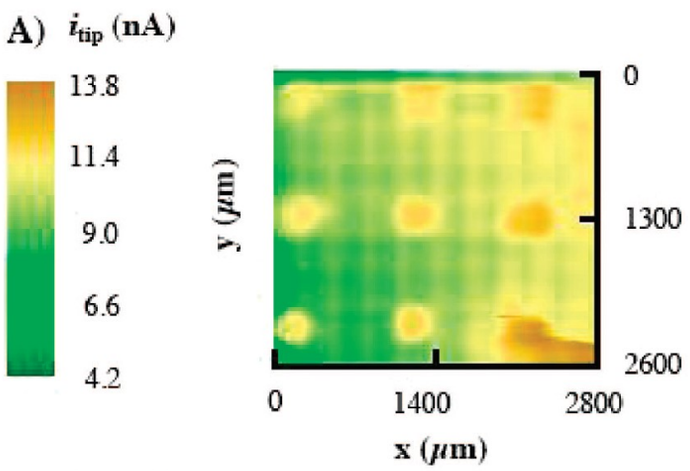

***Figure 47.** Examples of imaging. SECM images of an array of IrO_2 particles for oxygen evolution[119].*

1.5.2 Ultramicro Electrode (UME)

An ultramicroelectrode (UME) is an electrode whose radius ranges between few nm to 50 µm. In the case of disk UMEs to be used as SECM tips, the bottom end of the electrode has to be thin to allow the tip-substrate distance to be as small as possible. A key parameter to take in account is thus the so-called RG, defined as r_g/a where r_g is the radius of the tip considering both the insulating glass covering the metal wire and the metal wire itself (i.e. the entire tip radius), while "*a*" is the metallic disc radius.

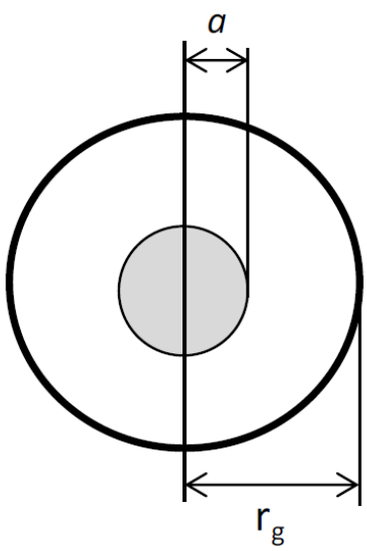

***Figure 48**. Schematic representation of a UME disc electrode with characteristic parameters: a = radius of the electroactive area; r_g = a + radius of the insulating shell.*

RG largely affects the collection efficiency and the performance of the microelectrode. If RG is high, the collection efficiency (when the tip is used as a probe) is higher, but it makes more difficult to reach short tip-substrate distances (the tip surface and the substrate are hardly perfectly parallel). For this reason, the RG value is often between 2 and 10. The desired value is obtained by manually sharpening the sealing glass on emery paper.

The small size of the tip allows to record currents in the range of nanoampere (or even smaller) largely reducing the relevant ohmic drops. Moreover, the cylindrical diffusion profile of the UME allows the system to reach a steady state condition in a very short time (in the order of milliseconds).

1.5.2.1 Cavity Microelectrodes (C-ME)

A cavity microelectrode (C-ME) is an innovative tool for the study of finely dispersed electrode materials[120,121]. C-ME are obtained from UME and consists in a cylindrical cavity, with micrometric dimensions, having a metal base and glass walls. The use of nanometre-sized tips was also recently introduced [122]. The powders under investigations can be entrapped inside the cavity and tested, using the metal base as the current collector.

Different advantages come from the use of a cavity microelectrodes respect to the use of a more classical powder support[123,124]:

- Minimized ohmic drop effects thanks to the micrometric size and therefore to the low associated current intensities.
- Very low amount of material needed, in the order of nanograms.
- No-gluing agents are needed, avoiding their interference in the electrochemical response;
- Extremely reduced contributions from the current collector (the microdisk at the bottom of the cavity, see Result and Discussion for C-ME preparation procedure) because its surface area is negligible in comparison to the powder one. This is of huge importance because once small amount of material is used, the influence of the support is usually very intense.
- Easy to load and clean with almost any powder electrode material.
- High reproducibility of the loading.
- Since the diameter and the depth of the cavity are known, it is possible to evaluate the amount of powder used, thus obtaining analysis that could be considered quantitative[125].

For what regards the last advantage, it should be taken in account that, because of possible irregularities in the cavity bottom, an inaccurate quantification of the amount of powder under study can make the quantitative analysis sometimes difficult. To avoid this, the preparation of the C-ME should be carefully carried out.

The use of a cavity microelectrode as working tip for SECM adds an additional advantage. In this case, a C-ME outer glass has to be sharpened as the one of a conventional tip. The preparation of an SECM tip is a long and complex procedure that cannot be performed with all the materials. In addition, only a few materials are available as wires of micrometre section to be used for preparing SECM tips. Cavity micro electrode compensate this lack, allowing to obtain tips made of any desired material. In addition, once the powder is obtained, is indeed extremely easy to fill the cavity with it and use it as a normal tip for SECM[126]. In this work C-MEs were used for the evaluation of different metal oxides semiconductor powders for which the preparation of a microelectrode would be impossible[127].

1.6 Heterojunction

1.6.1 Types of Heterojunction

To date, charge separation strategies have primarily centred on the use of semiconductor/electrolyte interfaces under the application of an external potential. When a semiconductor electrode is immersed in an electrolyte solution, electrons transfer takes place between the semiconductor and the electrolyte solution which results in equilibration of the Fermi level (E_F) to that of the redox potential of the electrolyte and thus is the basis of the semiconductor–liquid junction (SCLJ)[128]. Electrons transfer processes at the interface of the semiconductor/electrolyte causes band-bending and the bands positions are pinned. This bands bending is more pronounced for interfaces in close, intimate contact but less when the space charge layer width is greater than the particles size, in the case of nanoparticles.

Semiconductor–liquid interfaces are the most commonly employed type of junction for charge separation in water splitting and nanostructuring of the SCLJ has proven to be an effective approach to shorten the diffusion length of charge carriers[129]. Electrons transfer can occur between the semiconductor and electrolyte when the Fermi level of the semiconductor is in the appropriate position (more positive/ negative) than the potential of the electrolyte to then either accept/donate electrons. The space-charge layer contributes to the formation of an electric field; in n-type materials (photoanodes), photoexcited holes accumulate on the surface of the semiconductor are consumed in oxidation reactions, while electrons are transferred to a counter electrode via the back contact and an external circuit, where they are used in reduction reactions, such as proton reduction to H_2[130]. One of the main disadvantages in the use of this type of semiconducting system is the fast charge carriers recombination and photodegradation. Both the processes are related to light-excited electrons and holes that do not follow the desired path of water reduction and oxidation respectively. These junctions allow for efficient separation of electrons from holes, mimicking the pathway in natural photosynthesis. This is a key way to improved solar energy harvesting and high solar-to-hydrogen conversion efficiency.

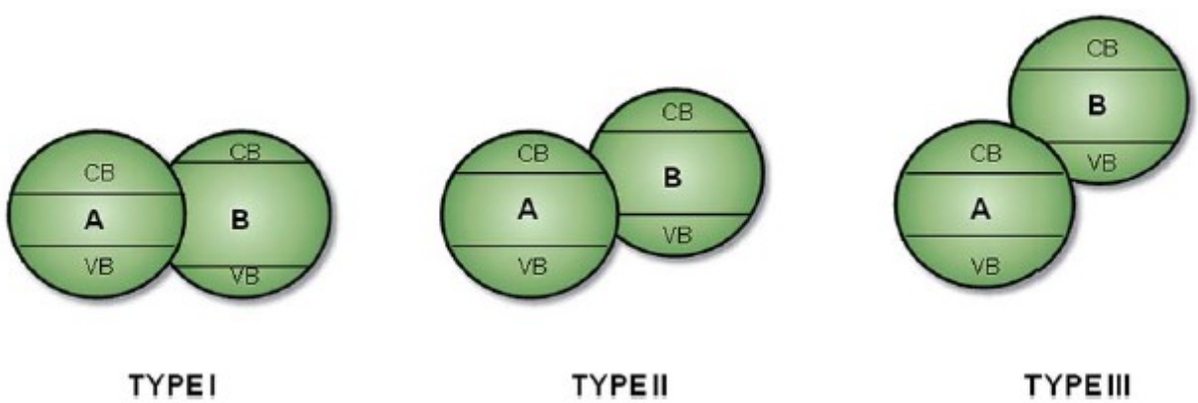

Figure 49. *Bands alignment in Type I, II and III heterojunctions. Image from Visible-Light Driven Heterojunction Photocatalysts for Water Splitting – A Critical Review, Jungwang Tang et al. Energy Environ. Sci., 8, 731*[131].

There are three main types of heterojunction architectures presented by Tang et al.[131] (Figure 49) where A corresponds to one semiconductor/component, and B corresponds to another semiconductor/component (if they are semiconductors, they can be either n-type or p-type). A Type I heterojunction is composed by (two) semiconductors where the CB of component B is higher than that of A and the VB of B is lower than that of A, so that both the bands of A lies inside the band gap of B. With this configuration holes and electrons will transfer and accumulate on component A because of the bands energy position. In Type II junction the CB of A is at energies less negative than the one of B, allowing the electrons to flow from B to A. Holes can travel in the opposite direction from the more positive VB of A to B, leading to all-round efficient charges separation and enhanced photocatalytic activity. The third type, is identical to Type II but the energy difference between the CBs and VB of the two materials is much higher giving higher driving force for charges transfer[132].

In the view of the creation of a protective overlayer for a photocathode, type II and III seems the most interesting allowing a good charges separation and a fast electrons flow to the more external semiconductor, the one in close contact with the electrolyte solution. Once selected the type of heterojunction is possible to select the different materials composing the system.

There are 3 main categories of heterojunction depending on the nature of the protective layer:

- Semiconductor-semiconductor (S-S) heterojunction: is the most employed architecture and usually composed by a p-type and a n-type semiconductor in close contact. Because of the contact, the formation of a space-charge region at the interface and an electric field occur due to the diffusion of charge carriers. This leads electrons to flow from the CB of the p-type material to the CB of the n-type (Figure 50a) and holes to flow from the VB of the n-type to the VB of the p-type material. In this way, a more efficient separation of charges with a longer charge carriers life-time and higher reaction rates are achieved. One example also tried in this work use CuS as external protective layer[133].
- Semiconductor-metal (S-M) heterojunction: when the two materials are in contact a Schottky barrier is formed (Figure 50b) due to the flow of electrons from the material with the higher Fermi level to the other one because of Fermi level alignment (e.g. Pt/TiO_2). In these systems, the metal acts like an electrons collector from the semiconductor. In this way, excited electrons are separated from the holes, reducing recombination because electrons cannot flow in the opposite direction[134].
- Semiconductor-carbon (S-C) heterojunction: different types of carbon are used like carbon nanotubes (CNTs), graphene[135,136] etc. They are used because of their high metal-like conductivity, high electrons mobility and high surface area. The basic principle is the same of S-M heterojunction allowing an easy flow of electrons from the excited semiconductor[137].

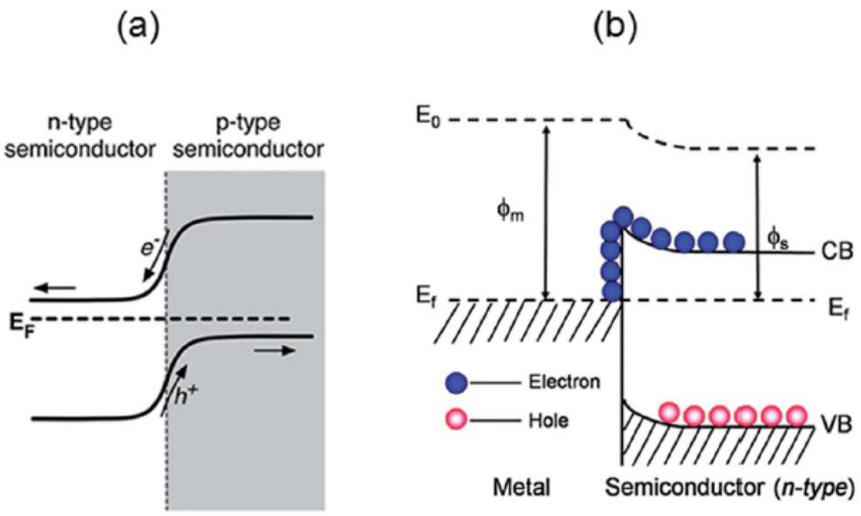

Figure 50. *Bands bending in (a) S-S and (b) S-M (or S-C) junction. In both cases photo-generated charges are driven in opposite directions due to favourable differences in bands energies and the formation of an electric field. Images from A. J. Cowan and J. R. Durrant, Chem. Soc. Rev., 2013, 42,2281–2293 and from H. Wang, L. Zhang, Z. Chen, J. Hu, S. Li, Z. Wang, J. Liu and X. Wang, Chem. Soc. Rev., 2014, 43, 5234–5244*[137,138]*.*

As stated before, an ideal semiconductor first of all should present a band gap wide enough to perform the hydrogen evolution reaction but also as narrow as possible in order to have an optimal absorption of the solar light[139].

These band gap requirements rule out the use of most known oxides semiconductors ($SrTiO_3$ and TiO_2, for example) while interesting candidates become the oxides of Group IV, III–V, II–VI, and chalcopyrite semiconductors. However, these materials usually are unstable in working conditions and undergoes either to dissolution or to the development of an insulating oxide coating. Two different paths can be used to overcome this problem: I) develop methods for the protection of those otherwise unstable semiconductors and II) discover new, low-cost and efficient semiconductors that are inherently stable under water splitting conditions and with band gaps in the desired range of energy and with the proper bands position. Our choice was to protect the Cu_2O from photodegradation.

The use of protective thin films to improve the electrochemical stability under HER (or OER) conditions for photocathodic materials (or photoanodic) is indeed one of the best options available to improve their life-time. Several examples are present in literature of Cu_2O-TiO_2[140–144] or Cu_2O-WO_3[145] junction for photovoltaic devices.

Corrosion of semiconductors is quite complicate due to the availability of electrons or holes at the surface that can participate in electrochemical processes under illumination. Different parameters like external potential, surface/bulk electronic properties, and the solution composition and pH can affect the rate of these processes.

Three different routes of degradation are available for semiconductor materials: photoelectrochemical, electrochemical, and chemical. The former two corrosions both require a charge transfer between the photoelectrode and the electrolyte; however, photoelectrochemical reactions involve photoexcited minority carriers (excited under light conditions), whereas electrochemical reactions involve majority carriers. As seen before photoelectrochemical degradation occurs when the redox potential of the material lies inside the band gap allowing the excited electrons or holes to perform the material reduction (from CB high-energy electrons) or oxidation (from VB high-energy holes). Chemical corrosion instead occurs without the charge transfer across the solid-electrolyte interface.

Surface functionalization with covalently bonded organic moieties has been tested for stabilization and manipulation of the interfacial energetics and kinetics of semiconductor electrodes in aqueous electrolytes to enhance the stability of semiconductor electrodes[146]. One of the most studied systems in this regard is the methyl-terminated Si(111) surface because nearly 100% of Si surface sites can be functionalized with a methyl group[147]. This type of functionalization is better for photocathodes than for photoanodes because of the lack of a reductive degradation mechanism due to oxidation of the organic moieties. Anyway, the use of organic compound is always limited by their poor stability in time that lead to some types of degradation. In our opinion, the use of inorganic materials will allow to achieve longer life-time.

The selected protective film should then[148,149]:

- Be electrically conductive in order to improve charge transfer processes. The addition of a further layer on the electrode should do not reduce the electrochemical performances. Moreover, the presence of a fast charge carrier system will allow to quickly separate holes and electrons avoiding recombination phenomena.
- Be electrochemically stable, to ensure long life-time for the electrode. A low cost and long-lasting electrode is one of the most important parameter to consider in the view of an industrial scale production.
- Be optically transparent. Indeed, the light-active part of the photoelectrode is still the semiconductor. Lower is the absorption from the protective layer, higher will be the light-to chemical yield of the photoelectrodes.
- Should prevent the semiconductor surface from directly contacting the electrolyte. Ideally, such a layer would also possess favourable optical and electronic properties (e.g., large barrier for transfer of majority carriers; small interface trap state density).

Clearly, not all coatings will fulfil these requirements. For example, too thick (i.e., more than a few nanometres) metal films will not be antireflective or optically transparent.

In addition, catalysts or co-catalysts can also be added to the outer surface or incorporated as an additional component in the protective layer. The composition of the protective film, the deposition technique, and the structure at the interface can play significant roles in the final behaviour.

1.6.2 Techniques for the Creation of Protective Layers

Different techniques can be used for the preparation of protective overlayers onto semiconductor surfaces. Of course, the technique will influence uniformity, stoichiometry, interfacial characteristics, and other structural and electronic properties of the film and hence may critically impact the stability and performances of the resulting composite photoelectrodes.

Physical-Vapor Deposition (PVD) techniques, such as thermal or electron-beam evaporation, magnetron sputtering, and pulsed-laser deposition, allow for precise control over the composition and thickness of the protective film. The main drawback of PVD techniques the possible inhomogeneous deposition on structured semiconductor surfaces that sometimes can be avoided by tuning the deposition conditions (e.g., chamber pressure and deposition geometry). Between PVD methods spattering is one of the most used ones but sometimes leads to surface damage due to the impact of high-energy ions[150]. Moreover, PVD techniques show a lack of chemical control at the interface between the semiconductor and the deposited film.

Chemical vapor deposition (CVD) techniques have also been used for forming corrosion protection coatings. These techniques are limited by the precursor volatility, stability, and deposition chemistry. Atomic-layer deposition (ALD) uses sequential, self-limiting surface reactions and is particularly suitable for uniform deposition on high aspect-ratio or porous materials[151]. Further, ALD exhibits a high degree of thickness control relative to traditional CVD and PVD techniques. Due to these advantages, a large number of recent studies on the protection of photoelectrodes have used ALD[57].

Electrodeposition is another well-studied technique that can coat high aspect-ratio materials and generally deposits materials where a conductive path and precursor species are simultaneously present. It allows to follow in detail the deposition and control the amount of material used. This technique is limited by the deposition conditions (e.g., near room temperature, liquid environment) and generally results in porous coatings[152]. Sol–gel, chemical bath, and spray deposition of materials are also of interest due to their low cost of implementation, but like electrodeposition, these techniques often result in porous films that can even remain somewhat porous after post-deposition annealing/ densification steps[153,154].

1.6.3 Cu_2O-based Junctions

One of the main limiting factors in the use of Cu_2O and indeed several protective layers were proposed in literature: Graetzel et al. reported a $Cu_2O/ZnO/Al_2O_3/TiO_2$/Pt electrode (Figure 51) able to reach photocurrents as high as -7.6 mA cm^{-2} at 0 V vs. RHE with high stability thanks to the protective nature of TiO_2 and high conductivity of ZnO/Al_2O_3 (AZO)[57]. Moreover, RuO_2 appears to have a longer lifetime as an HER catalyst in this system, and a subsequent work has reported half-cell efficiencies of up to 6% with 96 h of continuous operation using a p-Cu_2O/AZO/TiO_2/RuO_x structure[155].

Very recently the coupling of a surface-protected Cu_2O with a MoS_2 HER catalyst and a Ni–Mo catalyst layer resulted in the highest reported photocurrents for a Cu_2O-based photocathode without noble metals, with -6.3 mA cm^{-2} at 0 V vs RHE in 1 M KOH electrolyte[156].

This appears to be the first report of the stability of MoS_2 in highly basic conditions, as a cost-effective HER catalyst instead of Pt. Another group reported a Cu_2O/n-AZO/TiO_2/MoS_{2+x} heterojunction photocathode that exhibited improved stability in harsh acidic environments, with slightly lower photocurrents of -5.7 mA cm^{-2} at 0 V vs. RHE at pH 1[157].

According to some authors the presence of an HER co-catalyst is not necessary and stable and active photocathodes can be obtained. Siripala et al. presented a Cu_2O/TiO_2 heterojunction structure, with electrodeposited Cu_2O and TiO_2 overlayer made by electron-beam evaporation[158]. Cu_2O nanowires have also been protected by Lin et al. thanks to the deposition of spin-coated NiO[159].

Coupling of Cu_2O to n-type WO_3 is a strategy utilised to increase the stability; for example, a Cu_2O nanowire photocathode modified with a thin film of NiO_x coupled to a WO_3 nanosheet photoanode exhibited a photocurrent density of -4.98 mA cm^{-2} at -0.33 V vs. NHE and good stability over 20 min illumination time,[59] while a WO_3/Cu_2O NW also exhibited improved photocurrents for water reduction[160]. Similarly, a Cu/Cu_2O/CuO composite electrode also exhibited improved activity[161] as well as Cu_2O/CuO heterojunction where CuO is the layer in contact with the solution[162,163].

Other authors have tried the coupling of Cu_2O to RGO with an increases Cu_2O activity for CO_2 photoreduction and the photocurrent of this junction is nearly double than that of the bare Cu_2O photocathode. The improved activity together with the enhanced stability of Cu_2O was attributed to the efficient charges separation and transfer to RGO as well as the protection function of RGO[164,165].

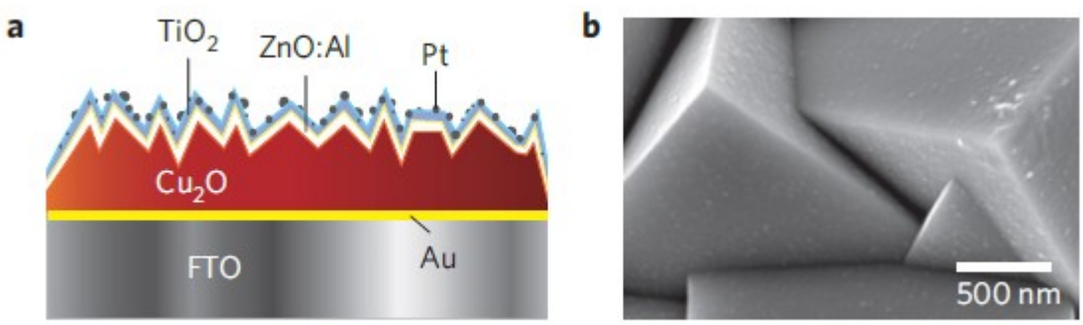

Figure 51. *Schematic representation of the Paracchino's Cu_2O electrodes structure and an SEM image of it. Figures from Adriana Paracchino et al. Highly active oxide photocathode for photoelectrochemical water reduction, Nature Materials, 2011, 10, 456-463* [57].

In this work were tested two possibilities for the protection of Cu_2O with the creation of heterojunction: an overlayer made of FeOOH and a CuO/Cu_2O core-shell system.

1.6.4 FeOOH

The chemistry of iron is extremely complex and wide, with 16 different compounds between oxides, hydroxides and oxide-hydroxides[166,167]. Iron oxides are widespread compounds in nature occurring in lithosphere, biosphere, and hydrosphere, but they can also easily be synthetized in laboratory. Nowadays they are used as pigments[168], catalysts for various reaction like oxygen evolution reaction (OER)[169–172], and also adsorbants[173] in the ecosphere. Moreover, they are steel corrosion products, and this makes these compounds largely study. In this work, we will focus our attention in the iron oxides coming from the use of steel as cathode for industrial electrochemical processes, FeOOH.

One example is the use of steel as cathode for the $NaClO_3$ production, the precursor of ClO_2, a bleaching agent with a huge worldwide market. The use of chlorine free (ECF) is one of the most used reaction for the bleaching of pulp. This process is environmental friendly and economically feasible. The active bleaching agent in the ECF bleaching, chlorine dioxide, is a very active specie and for practical and safety reasons its storage must be limited. Consequently, ClO_2 must be produced *in-situ* from its precursor, sodium chlorate ($NaClO_3$), that has no safety issue, by reduction with H_2O_2 or methanol under acid conditions[174].

The complete steps of $NaClO_3$ formation are here reported:

The main electrochemical reactions taking place in the cell are chloride oxidation to chlorine (1) and water reduction to hydrogen and hydroxide (2).

Anodic chloride oxidation:

$$2Cl^- \rightarrow Cl_2 + 2e^- \quad (1)$$

Cathodic water reduction:

$$2H_2O + 2e^- \rightarrow H_2 + 2OH^- \quad (2)$$

The formation of OH- from reaction 2 ensure the neutrality of the reaction.

Chlorine formed at a DSA anode is instantaneously dissolved and according to reaction 3, hydrolyzed to hypochlorous acid. In the bulk electrolyte acid base equilibrium reactions (4) and disproportionation reactions (5) between two hypochlorous acid molecules and one hypochlorite ion takes place.

$$Cl_2 + 2H_2O \rightleftharpoons HClO + H_3O^+ + Cl^- \quad (3)$$

$$HClO + H_2O \rightleftharpoons ClO^- + H_3O + \quad (4)$$

$$2HClO + ClO^- + 2H_2O \rightarrow ClO_3^- + 2H_3O^+ + 2Cl^- \quad (5)$$

The overall reaction for the formation of sodium chlorate is then:

$$NaCl + 3H_2O \longrightarrow NaClO_3 + 3H_2 \quad (6)$$

The electrochemical route here showed is a highly power demanding process and many efforts have been done in order to improve the feasibility of the process, mainly focusing on reduction of cathode overpotential. The worldwide used material for commercial cathodes is mild steel such as EN 10277-2-2008, which is a low alloyed steel with low amount of carbon. A good balance between low cost and current efficiency is provided by this material. Nevertheless, its main drawback is high corrosion rates that lead, in some circumstances, to lower current efficiency.

According to previous work XRD analysis on cathodes from different plants the formation of a thin layer of goethite (α-FeOOH) or lepidocrocite (γ-FeOOH) was noticed. The current efficiencies of these oxyhydroxides for water reduction is the same of mild steel once the reduced site is obtained on both the surfaces. In literature, the formation of $Fe(OH)_2$ was assumed as the main corrosion product of goethite and lepidocrocite under strong cathodic polarization mainly under alkaline condition[175]. Moreover, for most the authors this is just an assumption because of the difficulties in the characterization of the phase with techniques like Mossbauer spectroscopy, FTIR and other. All the authors confirm anyway the formation of an Fe(II)-specie that was not fully understand[176,177]. The use of *in-situ* techniques seems to be the best option to evaluate the reduced phase. Previous study using *in-situ* XAS and XRD were performed on lepidocrocite by Monnier et al. [178] at two different pH, 7.5 and 9. The authors claims the formation of two different main products, magnetite and $Fe(OH)_2$ respectively. A strong dependence on pH is then expected for this reaction.

These materials were here studied by electrochemical and XAS techniques to gain information about their oxidation state during HER and its reversibility. Both corrosion products were prepared by electrochemical method and tested in a well-established cell together from their open circuit potential (OCP) until strong hydrogen evolution reaction (HER) was recorded. A proof of the electrochemical specie involved during hydrogen evolution was so given while the reversibility of the system was studied too. In addition, the electrochromic properties of such material together with the self-conversion of α-FeOOH in γ-FeOOH were observed. Then the final interaction of FeOOH and Cu_2O was studied to explore the possibility of protecting the Cu(I) oxide by 80 nm of a transparent FeOOH layer.

1.6.4.1 FeOOH Brief Review

FeOOH has two main phases that occur widely in nature, goethite (the alpha phase) and lepidocrocite (the gamma phase). Different structures like beta and delta FeOOH were also found but their occurrence and stability in nature is much less evident.

Goethite: alpha-FeOOH is one of the most widespread iron oxides in natural environments. It has orthorhombic crystal system with space group *Pbnm.* Its *c*olor varies from yellowish to reddish, to dark brown or black. The lattice structure is here reported.

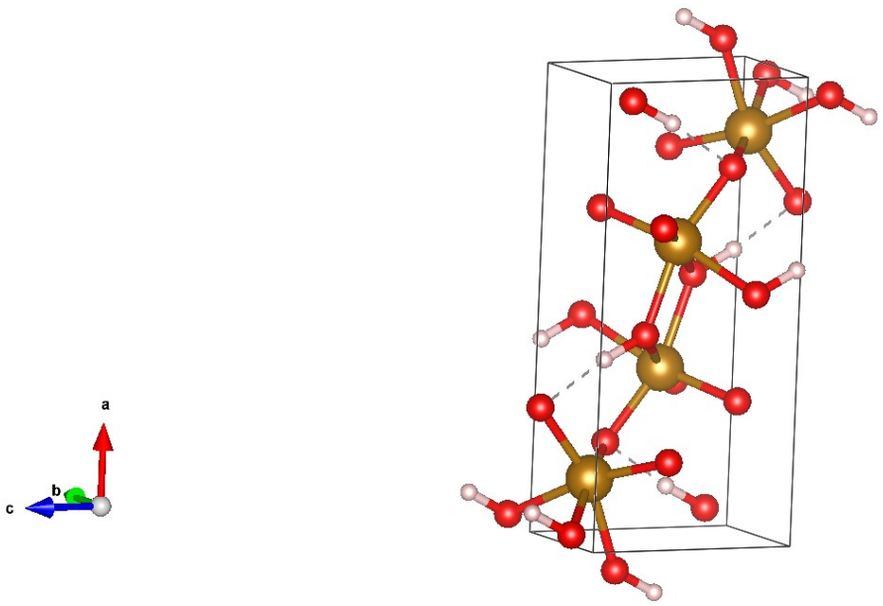

***Figure 52**. Goethite structure obtained with VESTA from Gualtieri A, Venturelli P, American Mineralogist 84 (1999) 895-904*[179]

Lepidocrocite (gamma-FeOOH), also called esmeraldite or hydrohematite, has an orthorhombic crystal structure with space group *Cmcm*. It is red to reddish-brown and it forms when iron-containing species undergoes oxidation underwater. Lepidocrocite is commonly found in the weathering of primary iron minerals and in iron ore deposits.

The structure of lepidocrocite is similar to the boehmite structure found in bauxite and consists of layered iron(III) oxide octahedra bonded by hydrogen bonding via hydroxide layers as is possible to notice in the computed structure below.

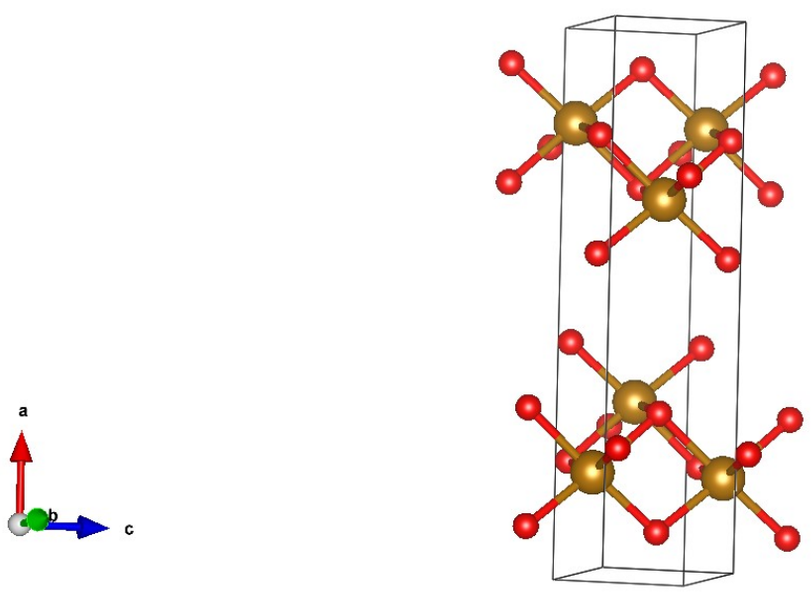

***Figure 53.** Lepidocrocite structure obtained with VESTA from Wyckoff R. W. G. Crystal Structures 1 (1963) 290-295 Second edition. Interscience Publishers, New York*[180].

1.7 DFT Calculation on Cu_2O

1.7.1 The Schrödinger Equation

Theoretical and computational chemistry are a subfield of chemistry dealing with mathematical methods and fundamental laws of physic combined together with the focus on solving chemically related problems with calculations. The base of those calculations is the Schrödinger' equation[181].

In quantum mechanics, the Schrödinger's equation is able to describe the temporal evolution of a system like a particle, an atom or a molecule. The equation is a differential equation known as a wave-equation. The unknow variable is ψ, the wave function. This is in accordance with the De Broglie hypothesis in which all the particles constituting the matter can be associated with a wave (wave-particle dualism). According to Copenhagen interpretation the square of the wave gives the probability of finding the particle in a specific region of space[182,183].

The time dependent Schrödinger equation, which gives a description of system evolving in time, is given by:

$$i\hbar\frac{\partial}{\partial t}\psi(r,t) = \hat{\mathrm{H}}\psi(r,t)$$

Where $\hbar$ is the Plank constant ($6.62607004 \times 10^{-34}$ m^2 kg s^{-1}) divided by 2π, ψ is the work function and $\hat{H}$ is the Hamiltonian operator, which is an energy operator with all the relevant energy operation for the system. In a molecular system, it contains the repulsive interaction between nuclei ($V_{n\text{-}n}$), the repulsive interaction between electrons ($V_{e\text{-}e}$), the attractive interaction between nuclei and electron ($V_{n\text{-}e}$) and the kinetic operator of electrons and nuclei, T_e and T_n respectively.

$$\hat{\mathrm{H}} = \hat{V}_{n-n} + \hat{V}_{e-e} + \hat{V}_{n-e} + \hat{T}_e + \hat{T}_n$$

Repulsive and attractive interactions are so described with i≠j for the repulsive contributes:

$$\hat{V}_{n-n} = \frac{1}{2}\sum_{i=1}^{N}\sum_{j=1}^{N}\left\{\frac{e^2}{4\pi\varepsilon_0}\right\}\frac{Z_i Z_j}{R_{ij}} \quad Nucleous - Nucleous\ repulsive\ interaction$$

$$\hat{V}_{e-n} = -\sum_{i=1}^{N}\sum_{j=1}^{n}\left\{\frac{e^2}{4\pi\varepsilon_0}\right\}\frac{Z_i}{|R_i - r_j|} \quad Electron - Nucleous\ attractive\ interaction$$

$$\hat{V}_{e-e} = \frac{1}{2}\sum_{i=1}^{n}\sum_{j=1}^{n}\left\{\frac{e^2}{4\pi\varepsilon_0}\right\}\frac{1}{r_{ij}} \quad Electron - Electron\ reulsive\ interaction$$

The definition of the kinetics operators comes from classical mechanic and is given by:

$$\hat{T} = \sum_i \frac{p_i^2}{2m_i}$$

Where m is the mass of the particle and p is the momentum defined as $p = i\hbar\nabla$, so that the kinetic contributes for electrons and nuclei are given respectively by:

$$\hat{T}_e = -\sum_{i=1}^{n}\left\{\frac{\hbar^2}{m_e}\right\}\frac{1}{2}\frac{\delta^2}{\delta r_i^2} \quad Kinetic\ energy\ of\ the\ electrons$$

$$\hat{T}_n = -\sum_{i=1}^{N}\{\hbar^2\}\frac{1}{2M_i}\frac{\delta^2}{\delta R_i^2} \quad Kinetic\ energy\ of\ the\ nuclei$$

Where:

$$\frac{\delta^2}{\delta R^2} = \frac{\delta^2}{\delta x^2} + \frac{\delta^2}{\delta y^2} + \frac{\delta^2}{\delta z^2}$$

And m_e is the electron mass = 9.1094x10^{-31} Kg, e is the elementary charge = 1.6022x10^{-19} and ε_0 is the vacuum permittivity = 8.8542x10^{-12} AsV^{-1}m^{-1}.

But usually, for quantum chemical calculation, is mostly used a time independent version of this equation where t=0. This simplified version is given by:

$$\hat{\mathrm{H}}\psi = E\psi$$

Where E is the energy eigenvalue.

With Schrödinger equation in principle is possible to find the exact solution of any quantum problem once the appropriate Hamiltonian is used. Unfortunately, in reality is possible to find the exact solution just for a very simple system like the H atom [181–184] or the H_2^+ ones[184]. Then electron-electron interaction makes the evaluation too complex. For all the other system are indeed required at least two approximations, the Born-Oppenheimer and the single particle approximation.

1.7.2 The Born-Oppenheimer Approximation

The Born-Oppenheimer approximation[183–187] assumes that the motion of atomic nuclei and electrons (vibrational and rotational) in a molecule can be separated. In this way, the computation of wavefunction and energy of a molecules is largely simplified. This separation is possible because the mass of electrons is much smaller than the one of nuclei (10^4 to 10^5 times lower) and that means that nuclei can be consider static if compared to the electrons movement. In this way nuclei can be considered as classical point charges that sit at well-defined positions and the Hamiltonian starts to depend on the R_i as parameter.

With this approximation, the term $\hat{T}_n$ vanishes and the term $\hat{V}_{n-n}$ becomes a constant that can be calculated.

Accordingly, the wavefunctions can be split into electronic and nucleus contributions:

$$\psi_{tot} = \psi_e\psi_n$$

1.7.3 The Hartree-Fock Equation

While the Born-Oppenheimer approximation is used to reduce the complexity of the Hamiltonian, the Hatree-Fock equation allows to solve a many body wave function[188–192]. Indeed, Schrödinger equation can be solved analytically only for 1 electron system due to the complication introduced by the electron-electron interaction. To solve this problem a multi-electrons system is decoupled in several 1-electron ones that can be solved with some approximation. Hartree-Fock equations are one of the available methods and they are used in all of modern quantum chemical methods. They introduce the exchange term and the Slater determinant of the wave function.

A Slater determinant is a linear combination of the product of independent electron wave functions ({φi(xi)}) (also known as spin orbitals) with all possible combinations of the permutations of their coordinates. Also, the Slater determinant satisfies the antisymmetric property of the electronic wave function, which is essential because electrons are fermions and obey Pauli's exclusion principle. For an N-electron system the HF wave function looks like:

$$\Psi(\{x_i\}) \approx \Psi^{HF}(\{x_i\}) = \frac{1}{\sqrt{N!}} \begin{vmatrix} \phi_i(x_i) & \phi_j(x_i) & \cdots & \phi_N(x_i) \\ \phi_i(x_j) & \phi_j(x_j) & \cdots & \phi_N(x_j) \\ \vdots & \vdots & \ddots & \vdots \\ \phi_i(x_N) & \phi_j(x_N) & \cdots & \phi_N(x_N) \end{vmatrix}$$

In the Hartree-Fock the electronic part of the atomic Hamiltonian, is used to solve the electronic Schrödinger equation. Thus, the Hamiltonian consists of the kinetic energy of the electrons $\hat{T}_e$, the electrostatic interactions between electrons and nuclei, which define the external potential ($v_{ext}(r)$) the electrons are moving in, and the Hartree potential $v_{Hartree}(r)$, which describes the interactions between the electrons. In this way, instead of using the exact position of the electrons is possible to use the effective potential of the surrounding electrons.

Then, to consider the Pauli principle and to remove the interaction of an electron with itself, an exchange terms and a Slater determinant were introduced giving the Hatree-Fock equation:

$$\left\{ \underbrace{-\frac{\hbar^2}{2m}\nabla^2}_{T_{el}} + \underbrace{-\sum_I \frac{Z_I e^2}{|r-R_I|}}_{v_{ext}(r)=v_{nucl-el}(r)} + \underbrace{\sum_j \int d^3r' \frac{e^2}{|r-r'|}|\Psi_j(r')|^2}_{v_{Hartree}(r)=v_{el-el}(r)} \right\} \Psi_i(r) - \underbrace{\sum_j \int d^3r' \frac{e^2}{|r-r'|} \Psi_j^*(r')\,\Psi_i(r')\Psi_j(r)\delta_{\sigma_i\sigma_j}}_{E_x} = \varepsilon_i \Psi_i(r)$$

In this equation, the physical situation is described by the kinetic energy and by the electrostatic contributions while the exchange part E_x is required to subtract the electrons self-interaction and the electrons interaction with other electrons with the same spin in the same spatial region introduced by the Hartree potential.

Then once all the 1-electron Hartree-Fock equations are solved the total energy of the system can be obtained by:

$$E_{tot} = \sum_i E_i - v_{Hartree} - E_x + v_{n-n}$$

Note that the Hartree potential is subtracted to avoid double counting.

Even though the Hamiltonian used to calculate the total energy is in principle exact for a non-relativistic system within the Born-Oppenheimer approximation, the energies obtained with the Hartree-Fock equation are generally poor compared to the exact total energy[193]. This deviation, which is generally negative, i.e. the Hartree-Fock energy is always larger than the exact energy, is called correlation energy[186]. The correlation effects can be attributed to inaccuracies resulting from the erroneous description of the correlated electrons movement, which results in a too weak repulsion of electrons in the effective potential used in Hartree-Fock (dynamic correlation). A second contribution to the correlation energy is the static correlation. Static correlation concerns the fact that only a single determinant is used to describe the wave function in the Hartree-Fock method. Although this approximation is valid in many cases it may not be sufficient for the ground state of all structures. The latter effect is especially problematic in systems were the ground state consists of several near-degenerate states as it can often be found in transition metal chemistry[194]. In ab initio quantum chemistry, a rich set of tools was developed to deal with both dynamic and static correlation effects[195]. These methods would in principle allow for very accurate results by systematic improvements of the basis set and methodology. A major drawback however results from the very high computational costs rendering these methods inapplicable for larger systems.

1.7.4 Density Functional Theory (DFT)

The basis of DFT[196] is the proof of Hoheberg and Kohn that the ground state electronic energy is completely determined by the electron density ρ[197]. The electron density is given by the square of the wave function integrated over N-1 electron coordinates. It only depends on 3 coordinates (four if spin is included) independently of the number of electrons. So, if increasing the system size will increase the wave function complexity, it will not affect the number of variables needed by the electron density. In the end, the goal of DFT is to find the functional connecting the electron density with the energy[198–201]. Is important to note that a function is a prescription able to generate a number from a variable while a functional is prescription for obtaining a number from a function which of course depends on variables. Wavefunction and electron density are function, while the energy, depending on those function is a functional.

The Hoheberg and Kohn theorem connects the external potential and the electron density considering that exist a unique external potential $v_{ext}(r)$ for any ground state electron density. This means that if the electron density is known is possible to define the interaction occurring between electrons and nuclei and then the Hamiltonian for the system.

This is not applicable for practical problem and so the Kohn-Sham equation[202] is introduced:

$$\left\{-\frac{\hbar^2}{2m}\nabla^2 + \underbrace{v_{ext}(r) + v_{Hartree}(r) + v_{xc}(r)}_{v_{eff}(r)}\right\}\Psi_i(r) = \varepsilon_i\Psi_i(r)$$

Where electron density ρ(r) is

$$\rho\,(r) = \sum_{i=1}^{N}|\psi_i(r)|^2$$

And there the addition of the exchange correlation functional $v_{xc}(r)$ which contains the non-classical part of the electrons kinetic energy and the correlation effect. The eigenvalue and eigenfunction obtained from Kohn-Sham equation are the correct one-particle energies that then can be used to calculate the whole energy of the system with the following expression:

$$E_{tot} = \sum_i \int |\phi_i(r)|\frac{\hbar^2}{2m}\nabla^2 dr + \sum_i\sum_j \int\int |\phi_i(r)|^2 \frac{e^2}{|r-r'|}\left|\phi_j(r')\right|^2 drdr' + E_{xc}[\rho(r)] - \sum_i \int \sum_A \frac{Z_A e^2}{|r-R_A|}|\phi_i(r)|^2\,dr$$

Unfortunately, the exact exchange-correlation functional is not known and it can only be approximated with the different functional developed over the years[203,204]. Any of these functionals is composed by an exchange and a correlation part. The former removes the interaction of the electron with itself and is known exactly from Hartree-Fock. Nevertheless, approximated exchange functional also allows to reduce the errors related to the non-exact correlation functional[194,201].

There are different approximations for an exchange correlation functional with several levels of complexity and accuracy. Perdew categorize all these functional in the so called “Jacob’s ladder” reported in Figure 54.

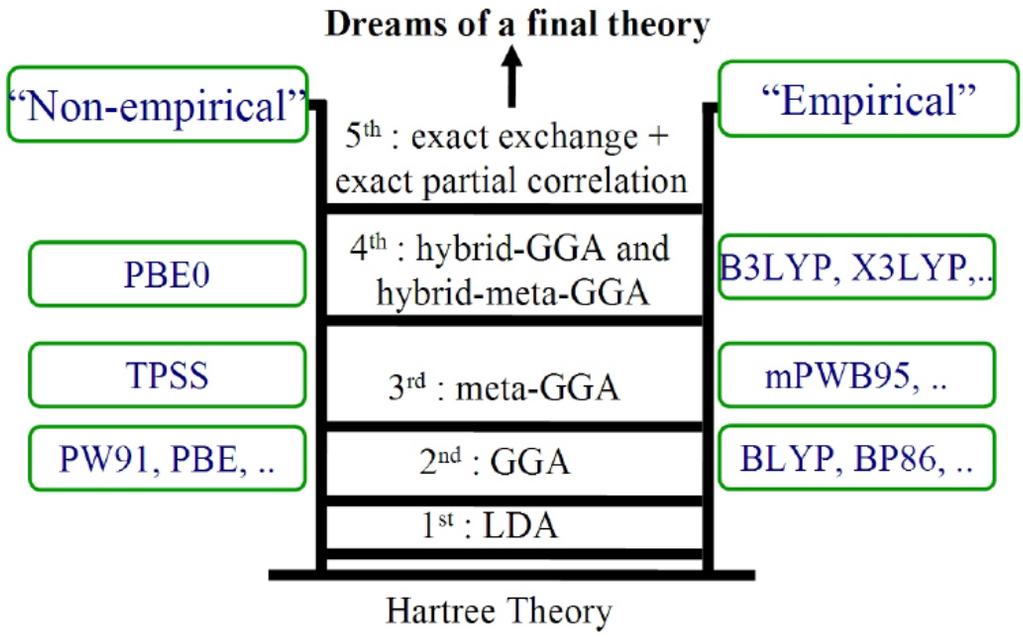

Figure 54. *Schematic view of "Jacob's ladder" of exchange-correlation functionals proposed by J. P. Perdew* [205].

Functional can be divided in empirical (formulated on the base of previous results on molecular properties) and non-empirical (formulated only according to physical laws). Some of them will be briefly presented together with the ones used in this thesis to give an idea of the differences.

LDA: Local-Density Approximation

This is the simplest and least time-expensive method. It assumes the local density constant as a uniform electron gas, or that the variation of the density is an extremely slowly varying function[199,202,206]. The functional is known with high accuracy but this approximation is acceptable only for strongly delocalized system like metals.

GGA: Generalized Gradient Approximation

This functional improve the previous one considering the variation of the electron density at least in the close proximity[207]. GGA can improve the quality of the result respect to LDA functional in many properties of the system like geometries and ground state energy of molecules and solids[208–210]. Especially, for covalent bond this functional is far better than LDA. Nevertheless, GGA is still pretty bad for very localized system such as molecules and it cannot capture Van Der Waals interaction or H-bonding at all. In this work a specific GGA functional was used for the calculation of all the ground state energies of the structure taken in account, the Perdew-Burke-Ernzerhof (PBE)[210–214].

Meta-GGA

It's the third generation of functionals and it uses the second derivative of the density and/or kinetic energy densities as additional degree of freedom. Is better than LDAs and GGAs functionals but of course it needs higher level resources and extended time.

Hybrid Functional

Hybrid functional are indeed particularly efficient in band gap calculation, where usually most of the other method suffer from underestimation of the real value[215]. They incorporate a portion of exact exchange from Hartree–Fock theory with exchange and correlation from other sources (ab initio or empirical). It remedies self-interaction error some extent and gives much better band gaps and reaction barrier heights than LDA and GGAs. Description of metals are worse than GGAs[216]. This kind of functional is the most requiring one in terms of computational resources. In this thesis HSE06 (Heyd-Scuseria-Ernzerhof [217]) was used for the calculation of high accuracy DOS.

1.7.5 Major Limits of DFT

The use of approximate functional introduces two main errors: the self-interaction error [199,218–220]and errors resulting from static correlation. The first one is because the electrons in DFT have repulsive interaction not only with other electrons but also with themselves. This leads to a forced delocalization and metallic behaviour (e.g. NiO appears to be metallic while from experiments it is found to be an insulating antiferromagnetic structure). Another drawback, of major importance in this work is the tendency of GGA DFT calculation in underestimate the band gap[221,222]. For this reason, hybrid, functional where used for the calculation of DOS, that largely improve the performances giving high reliable value[223]. Another solution is the use of GGA + U where U is a semi-empirical parameter used for the matching of the experimental energy value with the computational ones[224].

1.7.6 Cluster Computer

These calculations, especially hybrid methods, are extremely expensive in terms of time and computational resources needed. For this reason, all the calculations required the use of a computer cluster, or simply cluster, being able to overcome in performance a single computer. A cluster is a set of tightly connected computers working together in a way that they can be considered as a single system. The components of a cluster are usually connected through fast local area network.

For the cluster to be efficiently used it is equipped with a "batch processing system". The basic idea is that all computational tasks are packed and specified in advance, and then submitted as a "job" to the job scheduler of the batch processing system. The job scheduler will then put the job in its "job queue" and when the requested of computer resources are available it will execute the job on a partition of all the compute nodes of the cluster.

The result of this approach is a more efficient use of all the compute nodes of the cluster as jobs are scheduled and executed automatically without any required user intervention. Thus, the cluster is working day and night, weekends, and holidays as long as there are jobs in the queue.

To give an idea of the performance of those systems compared to PC, are here reported the hardware characteristics of the “Hebbe” cluster used for this work.

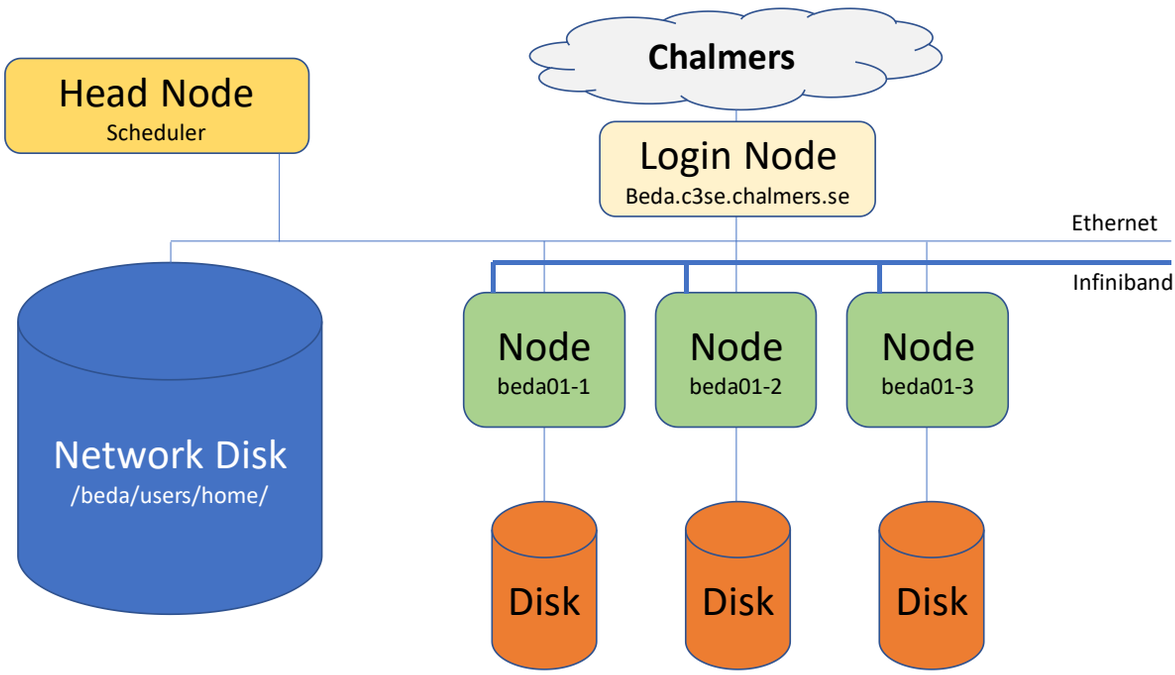

Figure 55. *Scheme of a Hebbe cluster computer architecture. Figure adapted from C3SE.se*

The Hebbe cluster is built on Intel 2650v3 (code-named "Haswell") CPU's. The system consists of in total 315 compute nodes (total of 6300 cores) with 26 TiB of RAM and 6 GPUs. More specific:

- 260 compute nodes with 20 cores and 64 GB of RAM (249 of these available for SNIC users).
- 38 compute nodes with 20 cores and 128 GB of RAM (30 of these available for SNIC users).
- 7 compute nodes with 20 cores and 256 GB of RAM (not available for SNIC users).
- 3 compute nodes with 20 cores and 512 GB of RAM (1 of these available for SNIC users).
- 1 compute node with 20 cores and 1024 GB of RAM.
- 4 compute nodes with 20 cores, 64 GB of RAM and 1 NVIDIA Tesla K40 GPU (2 of these available for SNIC users).
- 2 compute nodes with 20 cores, 256 GB of RAM and NVIDIA k4200 for remote graphics.

There are also 3 system servers used for accessing and managing the cluster.

There's a 10 Gigabit Ethernet network used for logins, and a dedicated management network with Infiniband high-speed/low-latency network for parallel computations and filesystem access. The nodes are equipped with Mellanox ConnectX-3 FDR Infiniband 56Gbps HCA's.

The server and computer node hardware were built by HP and delivered by GoVirtual.

The simulations were performed on resources at Chalmers Centre for Computational Science and Engineering (C3SE) provided by the Swedish National Infrastructure for Computing (SNIC).

1.8 Doping and Vacancies on Cu_2O

The Cu^+ ion external electronic structure is $3d^{10}4s^0$, with the 4s orbitals only slightly higher in energy than the *3d* levels. The Cu *3d* levels form the valence band of Cu_2O and the empty Cu *4s* levels form the conduction band[225,226]. This contrasts with the majority of metal oxides, which have O *2p* states at the top of the VB. From DOS analysis was demonstrated that Cu_2O is a semiconductor with a direct gap at the centre of the Brillouin zone (Γ point)[227].

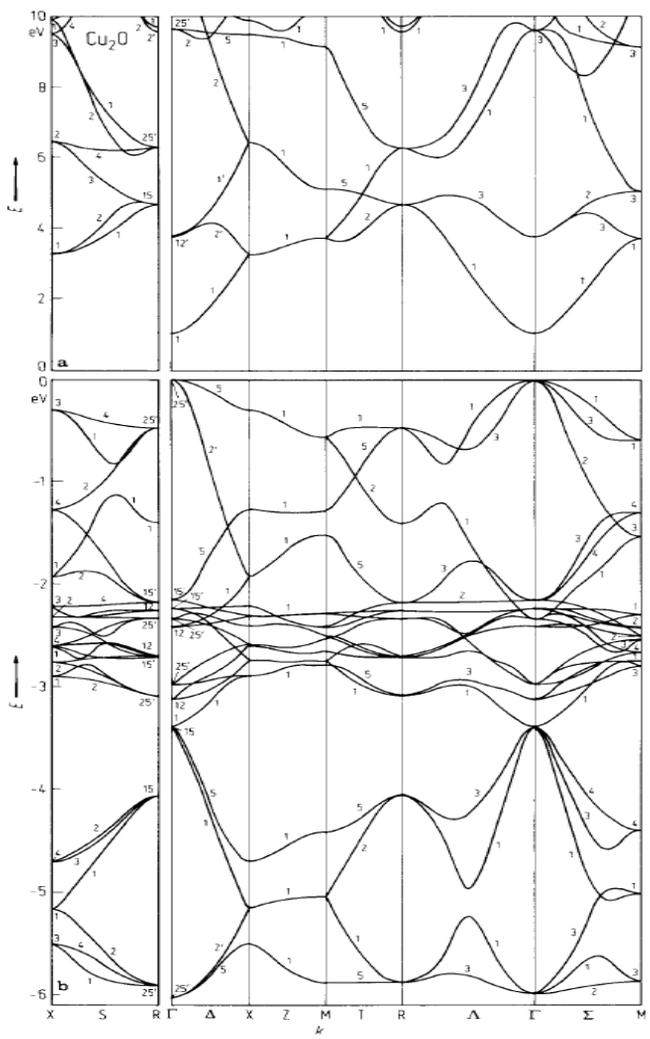

Figure 56. *Cu_2O bands structure plot calculated with LDA self-consistent method. A) Conduction band, B) Valence band. From Kleinman, L. and Mednick, K. Self-consistent energy bands of Cu_2O. Phisical Review B, 21 (1980), 1549*[228].

In the DOS from literature of Figure 56 is possible to notice the typical underestimated BG of LDA methods. Figure 57 instead calculated with hybrid functional shows a value closer to the real one and the different contribute of d-orbitals in the VB and CB.

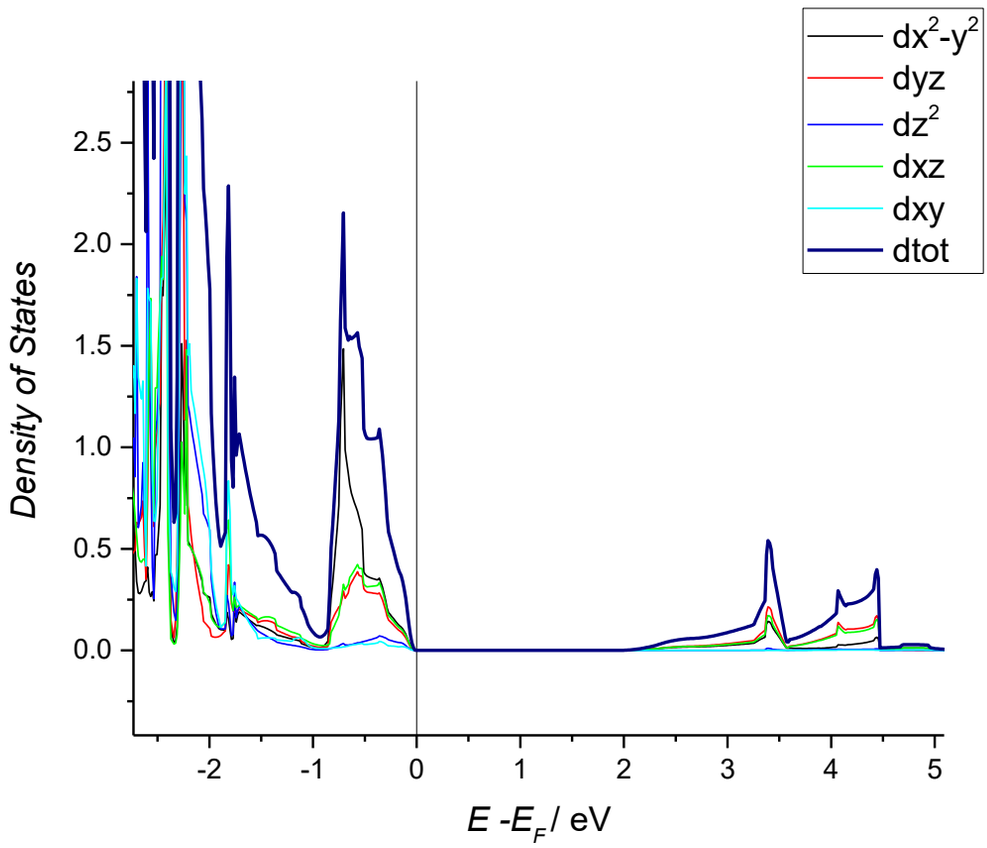

Figure 57. *Split Density of States (DOS) of Cu_2O obtained with VASP and HSE06 method. All the energies are reported to the Fermi level one.*

The measured energy gap is E_g = 2.1720 eV at 4.2K, obtained as the limit of the yellow exciton series and it decreases with temperature. Our computational value is of 1.95 eV.

One of the key parameters for photoelectrochemical water splitting semiconductors is their bands position with respect to the water oxidation and reduction potentials. Thermodynamically water reduction and oxidation potentials must lie between the valence band maximum (VB_{Max}) and conduction band minimum (CB_{Min}). The closer the CB_{Min} energy to the vacuum level, the stronger is the reducing power. On the other hand, the oxidizing power is measured by the VB_{Max} energy, lower it is, higher is the oxidizing power. The bands alignment of Cu_2O satisfy the above mentioned requirements with a CB_{Min} (-1.4 eV) far above the hydrogen production level (-0.65 eV) and VBM (+0.77 eV) slightly below the water oxidation level (+0.57 eV) at pH = 7[229,230].

The Cu_2O conductivity has been proved to come from copper vacancies creating acceptor states within the band gap at energy values of 0.3−0.5 eV above the top of the VB. Copper vacancies (V_{Cu}'s) can reach concentration up to 10^{20} cm^{-3}, but the concentration of free holes at room temperature is usually only about 10^{18} cm^{-3} since not all the vacancies are ionized. Calculated formation enthalpies of the defects suggest that processing conditions including O_2 partial pressure, temperature, and Fermi-level position can control their concentration effectively. Annealing temperature can increase the minority carrier lifetime of one order of magnitude[231–233].

1.8.1 Vacancies Formation

As showed in literature, Cu_2O shows a spontaneous p-type conductivity and moreover it is a compensated material where both intrinsic acceptors and, in smaller number, donors are present. The compensation ratio N_A/N_D, (the acceptor concentration over the donor concentration), in most cases is just slightly larger than 1 and in any case lower than 10. A possible explanation, often invoked to explain similar problems in other semiconductors, can be the self-compensation mechanism[234]: the more donor impurities are inserted, the more the energy of formation of acceptors is lowered; in this way, donors are always less than acceptors. The nature of the compensating donor is still controversial (simple candidates could be oxygen vacancies) and also their identification as intrinsic defects is not assessed. According to various author, the n-type doping seems to be impossible and this is probably attributable to the mechanism of self-compensation, while other claim to be able to obtain an n-type behaviour for example with Cl-doping[235–238].

Excitons are usually classified in two categories, Frenkel and Mott–Wannier excitons, which correspond to the limit cases of the ratio between the excitonic radius and the lattice constant. Frenkel excitons have a radius of the order of the lattice constant or smaller, whereas Mott–Wannier excitons have a much larger radius than the lattice constant. The excitons of Cu_2O are Mott-Wannier excitons[239].

Defect	ΔH_f (kJ/mol)	ΔH_f (eV/defect)	ΔS_f (J/(K mol))	ΔS_f (eV/defect)
V_{Cu}^0	74	0.77	−10	−0.10
V_O^0	294	3.06		
V_{Cu}^-	174	1.81	0.9	0.009
O_i^{2-}	300	3.12	1.4	0.014
$(V_O^0 - 2V_{Cu}^0)$	440	4.58		

Table 5. *Experimental enthalpies and entropies of neutral and charged defects taken from Aggarwal et al.*[240] *and Porat et al.*[241]

The formation energy for neutral Cu and O vacancies is computed as follows for a 2x2x2 Cu_2O supercell:

$$E_{Cu}^{vac} = [E(Cu_{31}O_{16}) + E^{ref}(Cu) - E(Cu_{32}O_{16})\ Copper\ vacancy\ formation$$

$$E_{O}^{vac} = [E(Cu_{32}O_{15}) + E^{ref}(O) - E(Cu_{32}O_{16})\ Oxygen\ vacancy\ formation$$

A negative formation energy is related to a spontaneous vacancy formation.

The computed energy for a Cu vacancy from literature[225] is 0.38 eV, a quite low value if compared to similar systems, so that their formation occurs easily and spontaneously. Once more than one vacancy is present, the formation energy change according to the reciprocal position of the vacancies and it was found that the most favourable position is on a different Cu_2O network.

Configuration	Electronic state	E^{vac}/eV per Cu	E_g/ eV	m^*/m_e
Clustered same network	Triplet	0.66	0.58	−1.44, −1.38
Clustered different network	Triplet	0.24	0.62	−1.26, −18.20
Clustered same network	Singlet	0.62	0.59	−1.60, −0.51
Clustered different network	Singlet	0.38	0.57	−1.34, −4.55
Isolated same network	Triplet	0.43	0.65	−0.45, −1.15
Isolated different network	Triplet	0.42	0.58	−0.45, −0.45
Isolated same network	Singlet	0.38	0.62	−0.54, −0.50
Isolated different network	Singlet	0.37	0.58	−0.46, −0.45

***Table 6**. Cu vacancy formation energy and effective hole masses for configuration with 2 Cu vacancies. Table from "Defects in Cu_2O, $CuAlO_2$ and $SrCu_2O_2$ transparent conducting oxides" by M. Nolan[225].*

The most stable configuration for dopant and Cu vacancy is the one in where the Cu vacancies are clustered, i.e., separated by the internetwork Cu-Cu nearest neighbour distance, with one vacancy on the same Cu_2O network as the dopant and the second vacancy on the other Cu_2O network. For three Cu vacancies, two of the three Cu vacancies are in the same Cu_2O network. For four Cu vacancies, three of the four Cu vacancies are found in the same Cu_2O network.

The presence of a neutral oxygen vacancy, able to add electrons to the system can compensate the holes but removing a single neutral oxygen atom tetrahedrally coordinated to a Cu atom costs 3.08 eV much more respect to a neutral Cu vacancy. Other distributions of Cu and oxygen vacancies show even larger formation energies. This means that the Cu vacancies compensation by formation of oxygen vacancies is not favoured and the process is not expected. Moreover, other study suggest that Cu vacancy formation will not produce hole traps, which would impact negatively on the conductivity[242].

The vacancy formation, number and position will affect the number of charge carrier, their mobility and so the conductivity of the whole material.

1.8.2 Doping

Doping Cu_2O with cations from different elements is one of the most promising strategies to modify the BG, the acceptor states, and the valence band (VB) population in Cu_2O. Doping can strongly affect the formation of defects such as vacancies and hence affect the electrical characteristics of the system, as well as impacting on the light absorption ability.

Effects of cation doping are related to changes in the material crystal structure composed by two interpenetrated Cu–O networks held together by non-bonding Cu–Cu interactions. Interesting the band gap of Cu_2O can be both increased or decreased using the appropriate dopant as the variation in the BG arises from the effect of three different mechanisms:

(i) The size of the dopant cation can influence the Cu–Cu interactions in the Cu_2O host lattice (e.g., Sn^{2+} widens the BG because of its large ionic radius by increasing the Cu–Cu distances reducing the metal character of the semiconductor). Dopants with ionic radii larger than Cu^+ (Ba^{2+}, Sn^{2+}, Cd^{2+}, In^{3+}, La^{3+}, Ce^{4+} etc..) produce strong structural distortions around the dopant site. Dopants with ionic radii smaller than Cu^+, such as Al^{3+}, Ga^{3+}, Ti^{4+}, and Cr^{4+}, show no structural distortions.

(ii) The alignment of the dopant electronic states with those in the VB or CB of Cu_2O with or without structural distortions (e.g., dopants such as In^{3+} (larger than Cu^+) or Al^{3+} (smaller than Cu^+) cause a reduction in the BG due to the presence of unoccupied *3s* states with much lower energies than the Cu *4s* orbitals).

(iii) The introduction of dopant ion states within the gap with the formation of an intermediate band.

An example that illustrates the need to fulfil all these requirements is provided by the isovalent doping of Cu_2O using Ag^+ or Au^+. In this case, doping produces little structural distortions into the Cu_2O lattice, and thus, E_g is not affected. Only small changes in the hole mobility occur because the d^{10} levels of Au^+ and Ag^+ are too low in energy to interact significantly with the d^{10} levels of Cu^+[243].

About structural distortions introduced by cations doping in Cu_2O, d^{10}-d^{10} interactions between copper atoms are essential in determining both the band gap and the width of the valence band. When the d^{10}-d^{10} interactions are suppressed the band gap is increased. This conclusion is related not only to 2D interactions but shows that the physical properties depend not only on local features of the crystal structure but also on its global spatial arrangement. So Cu—Cu 3D interactions must be improved in order to reduce the band gap[244].

The doping of cuprous oxide with larger cations than Cu^+ increases the band gap, while maintaining the cubic structure because it will distort the crystallographic lattice and consequently diminish 3D Cu–Cu interactions, leading in the end to a band gap increase. In addition, the distortion induced in the Cu_2O lattice to accommodate the dopant will, in general, depend on the size of the dopant. In the case of early TMs, the TM-Cu bond length (d_{N-N}) is shorter than the Cu-Cu bonds in the pure Cu_2O host.

This has been noted in other studies, where the proposed explanation is that the deviation from the d^{10} configuration results in stronger TM-Cu bonds. Indeed by many authors was found the great influence of Cu-Cu interaction on the band gap[244,245].

Cu^+ in Cu_2O behaves as a typical soft Lewis acid, with metallic Cu-Cu interactions producing high lying valence band states and low-lying conduction band states, and resulting in a higher conductivity and lower transparency than the oxides of harder Lewis acids (e.g., Na_2O). A further suggestion from literature[243] in the tuning of Cu_2O BG, is the use of cations from hard Lewis acid to increase the band gap, while cations from soft Lewis acid if the aim is the BG reduction. In Cu_2O, aliovalent dopants compensation is achieved by forming Cu vacancies. For a dopant of oxidation state n^+, (n - 1) Cu vacancies are requested to compensate, the subsequent, n^{th}, Cu vacancy is used to dope the system p-type. In this way the use of aliovalent cation would be a useful tool to increase the number of vacancies.

Dopant	Ionic radius (Å)	Experimental E_g (eV)	E_{n-1}^{vac}(eV)	E_n^{vac}(eV)	Computed E_g (eV)
Cu_2O	0.93	2.17	0.36	0.24	0.52
Sn^{2+}	0.93	3.05	-0.95	0.15	0.63
Zn^{2+}	0.40	3.30	-0.78	0.22	0.49
Mg^{2+}	0.49	7.80	-0.46	0.26	0.56
Ca^{2+}	1.00	7.03	-0.62	0.23	0.63
Sr^{2+}	1.16	5.90	-0.65	0.14	0.65
Ba^{2+}	1.36	4.10	-0.66	-0.12	0.62
Cd^{2+}	0.84	2.35	-0.28	0.18	0.45
Hg^{2+}	0.96	2.20	0.06	0.13	0.30
Al^{3+}	0.39	8.80	-0.30	0.36	0.36
Ga^{3+}	0.47	4.95	-0.08	0.14	0.11
In^{3+}	0.79	3.57	0.16	0.29	0.13
La^{3+}	1.06	5.40-5.80	-0.76	-0.57	0.67
Ti^{4+}	0.61	3.05	0.12	0.42	0.27
Cr^{4+}	0.44	3.25	0.22	0.34	0.04
V^{4+}	0.36	0.70	-0.02	0.15	0.04
Ce^{4+}	0.80	2.40	-1.26	0.51	0.05

***Figure 58**. Ionic radius and Cu vacancy formation energy (E^{vac}) and band gaps (E_g) for cation-doped Cu_2O from "Tuning the transparency of Cu2O with substitutional cation doping" by Nolan et al.* [243].

In the column headed E_{n-1}^{vac}, is presented the Cu vacancy formation energy for the first compensating Cu vacancy for dopant with oxidation state M^{n+}; in the column headed E_n^{vac}, is presented the Cu vacancy formation energy for the p-type Cu vacancy for dopant with oxidation state M^{n+};

Transition metals	Ti	V	Cr	Zn	Zr	Nb	Mo	Hf	Ta	W	Au
d_{NN} (Å)	1.94	1.92	1.96	1.93	2.07	2.00	1.96	2.00	1.94	1.90	2.02
Δd_{NN} (%)	3.8	2.5	4.9	3.4	10.5	6.9	4.8	7.2	4.0	1.4	8.3
d_{2NN} (Å)	3.02	3.02	3.05	3.07	3.04	3.00	2.94	3.00	2.94	2.92	3.08
Δd_{2NN} (%)	−1.2	−1.1	−0.10	0.56	−0.39	−1.7	−3.7	−1.8	−3.6	−4.4	0.75
E_{sub} (eV)	−0.608	0.364	0.118	0.198	−2.000	1.185	2.620	−0.181	1.562	3.268	0.903

***Table 7**. Geometrical relaxations around the dopant site. d_{N-N} is the distance between the dopant and the nearest O atom. d_{2N-N} is the distance between the dopant and its second nearest Cu atoms. E_{sub} is the substitution enthalpies for the different dopant from "Early transition metal dopants in cuprous oxide: to spin or not to spin" by Soon et al.* [246]

Cationic substitution of one Cu atom per supercell (32 Cu and 16 O) with a dopant, will give a dopant concentration of 3.13% (in agreement with experimental regime), while replacing and oxygen atom gives an a 6.25% anionic concentration[246].

These concentrations are reported by many authors to be enough for simulate the material behaviour and are consistent with the loading in experimental work[247]. For this reason, in this thesis the cell dimension was kept of this size.

The energy for the doping is calculated according to the following equations:

$$E_{Cu_{32}O_{16}} + \frac{1}{32}E_{M_{32}} \rightarrow E_{Cu_{31}MO_{16}} + \frac{1}{32}E_{cu_{32}} \quad (1)$$

$$E_{Cu_{32}O_{16}} + E_{M_{32}} \rightarrow E_{Cu_{31}MO_{16}} + E_{M_{31}Cu} \quad (2)$$

where equation 1 was used in the case of a simple substitution of a transition metal inside the Cu_2O lattice while the second one is for a double exchange with the formation of a metal-copper alloy in the underlayer. According to experimental results performed by Palacios et al.[248] doping is possible until the substitution require less than 2eV. Even if this value was obtained for slightly different chalcopyrite system we can consider this as a threshold value for doping substitution and we will see how in this work most of the substituted materials require far less energy.

Is to be noted that for the purpose of this thesis a doped material with reduced band gap is to be preferred. Moreover, an increased BG is of interest in the preparation of transparent and highly conductive oxides (TCO) to be used as transparent electrodes in flat panel displays and in solar conversion devices. An example of TCO are Indium Tin Oxide (ITO), ZnO or the FTO itself. For their preparation the synthesis of a semiconductor with large band gap and still high conductivity is mandatory[244]. Nowadays all TCO are n-type semiconductors, and the development of a hole conducting material (p-type) like Sr:Cu_2O[249] could generate new applications for this kind of materials like functional windows able to transmit visible light but at the same time to generate current due to the absorption of UV photons. Following is presented a list of the dopant material tested in literature and their results:

H and passivation: Using an exposure time of 30 minutes, pH_2 = 1mTorr and T_{sub} = 300 °C the authors[250] succeeded to reduce the carriers concentration from 1.7×10^{16} cm^{-3} to 2×10^{15} cm^{-3} and to increase the mobility from 5.3 to 28.9 $cm^2/(V\ s)$. Therefore, it seems that hydrogen can effectively passivate the acceptors. The authors explained this mobility increase by the lower effect of ionic impurity scattering due to the lower carrier concentration and then by the fact that the dangling bonds at the grain boundaries are passivated by the hydrogen reducing the barrier height. Passivation of nonradiative recombination centres can be also obtained by cyanide treatment with an increased holes density[251].

Alkaline Metals: The main effects of the alkaline doping on the optical properties were a reduction in the direct band gap and an approach of the acceptor level edge to the maximum of the valence band. Moreover, AFM showed an increase of the carrier density and electrical conductivity, and a reduction in the photocurrent with the dopant ion size.

The main effect of the alkaline substitution of copper atoms consists of polarizing O states, with a reduction in the insulating gap and splitting of the density of states just below the Fermi level[252].

Sodium: With Na loading the resistivity of the sample largely decrease from $1.2x10^6$ to 330 Ωcm and the carrier concentration arise from $5.1x10^{14}$ to $1.7x10^{18}$.

Small reduction of the band gap (from 2.19 to 2.04) due to the creation of an impurity acceptor level above the valence band were recorded[253–255].

Chlorine: Results on this material shows a conductivity about one order of magnitude greater than the undoped material. The measurements of the carriers concentration (holes) as a function of temperature suggest that chlorine acts both as a donor, substituting the oxygen, and as an acceptor, sitting in an interstitial position[238].

Nitrogen: N-doping slightly widens the band gap of Cu_2O, and form an intermediate band in the gap located at about 0.9 eV from the VB. This intermediate band is predominantly formed by hybridization between the N-*2p* states and the Cu-*3d* states. N-doped Cu_2O can absorb from the near infrared region to the ultraviolet region. Here N substitute O atoms acting as a p-type dopant[256] but other paper disagree considering too difficult to substitute O with N because of the larger radius of N[257]. In all the studied case there are improvements in the absorption coefficient spectra when the material is N-doped[258,259] as will be explained in the next paragraph.

Zinc and Indium: According to different authors the Zn-doping reduce the lattice constant of Cu_2O giving an increase of the BG when Zn act as a donor impurity[260,261]. Depending from the paper Zn-doped Cu_2O shows a larger resistivity than the undoped sample[262] while other authors found an improved carrier concentration and charge transfer, giving anyway extremely low photocurrent[263]. Another author[264], noticed a shape evolution of the Zn-doped Cu_2O microcrystals. Increasing relative concentrations of the Zn precursor followed an order in decreasing numbers of facets. Small increase in the band gap was recorded with the increase in Zn concentration. In-doped Cu_2O increases the lattice constant and increases the band gap. In some case can lead to the formation of the n-doped Cu_2O. Indium acts as a donor impurity in Cu_2O[262].

Silicon: The lowest resistivity obtained was 12 Ωcm and this sample showed a Hall mobility of about 10 $cm^2/(V\ s)$. Si should be coordinated by 4 oxygen atoms instead of 2 like the copper. Therefore, Si acts probably not a substitutional impurity but an element that produces SiO_2 inclusions[265].

Silver: Ag-doping generates minimal changes in the band gap and band gap energies. Ag-doped samples exhibit improved conductivity and fourfold increase in photocurrent density with respect to undoped samples[266]. This happens because Ag in Cu_2O is a supposed to disrupt O–Cu–O network and reduce Cu–Cu interactions, increasing the conductivity of the Cu_2O leading to more charge carrier generation, and therefore providing a greater photoresponse than the undoped Cu_2O. With higher concentration of dopant the performances are reduced because of recombination centres that inhibit the increased charge separation efficiency[266].

Iron: Fe-doping shows a reduced experimental BG (2.5→ 2.21eV) with enhanced photocurrent with just 2% doping compared to the undoped semiconductor. Higher concentrations are proved to generate more defect acting as recombination centre inhibiting the increased charge separation. The recorded improved conductivity could be moreover due to the appearance of Fe *3d* states in the doped sample[267,268].

Gold: Just a small (1.6% of the undoped value) optical absorption edge decrease was recorded with Au-doping. Moreover, it can improve the transmissions of photoelectron and vacancy, and reduce recombination of electron-hole pairs because of the formation of an impurity level, which can enhance the visible absorption, and reduce the absorption efficiency of ultraviolet (UV) light[269].

Magnesium: Mg-doped Cu_2O is an example of the advantage of doping on the conductivity. The fabricated doped thin films reached up to 17% of magnesium, resulting in morphology changes. Electrical resistivity largely decreases from 202 Ωcm was reduced to 6.6 Ωcm, due to the increase of charge-carrier density. The band gap has a little bit increased (2.4eV) compared to intrinsic cuprous oxide. On the other hand, the increase of the charge carrier density is clearly visible, ranging from $4.5x10^{15}cm^{-3}$ up to $8.1x10^{17}cm^{-3}$ for an increasing in Mg content from 0% to 17% thanks to the enhanced creation of copper vacancies. The two combined properties lead to a general decrease of resistivity[270]. Other authors claim that the similar ionic radius of Mg respect to copper together with its d^5 configuration should help Cu_2O to be less likely to form trap states. An improvement in electrical properties of Cu_2O thin films is observed upon doping with just 0.5 at %[271].

Strontium: It was found that strontium doping induces a significant improvement of the electrical properties with Sr:Cu_2O thin films resistivity down to 1.2 Ωcm at room temperature with a strontium content of 5-7%. However, at higher strontium content, the resistivity is deteriorated even after annealing. The room temperature free hole densities lies in the range of 1.2×10^{15} to 2.8×10^{17} cm^{-3}, depending on the strontium content and on the postdeposition annealing[272].

Other authors find that an increase in Sr content decreases resistivity from 10^6 to 10^2 Ωcm for film with 5-6% of Sr. Unlike Nolan's calculation[225] no increase of the band gap was recorded in the experiments while morphology is affected by Sr content indeed[273].

Manganese and Nickel: Sometimes doping does not improve the properties of the material as happens with Mn-doping. In this case the only result is an increased resistivity at room temperature for the doped sample[274]. In other case, the resistivity of the doped samples was lowered by a factor of 2 with respect to the undoped ones[275]. Undesired results were found also for Ni-doped Cu_2O where the Ni atoms enter the interstitial sites in Ni-doped Cu_2O film producing scattering centres of the neutral impurity, resulting in low mobility. The mobility in Ni-doped films monotonically increased with increasing deposition temperature while the mobility in undoped films decreased[276]. The most important conclusion is that the Ni impurities do not affect the carrier concentration but only the mobility.

1.8.3 Co-doping

Until now single cationic doping was discussed with the generation of acceptor states in the ban gap. These states could behave like recombination centre reducing the efficiency of the photocatalyst. Instead of mono-doping, anionic and cationic co-doping could improve the final performance of the material. Moreover, in case of poor dopant solubility, a feasible solution is to simultaneously incorporate certain amounts of p-type and n-type dopants, for lowering their formation energy, which is also the fundamental principle of compensated co-doping[277].

Indeed, the calculated defect formation energy shows that the co-doping is energetically more favourable than mono-doping due to the Coulomb interactions and charge compensation effects. Recent results were reported with TiO_2[278], ZnS, Bi_2WO_6[279,280] and of course on Cu_2O[230] with DFT calculations. On the latter the best combination found by the authors was composed by an Sn + B doping with reduction of the forbitten band-gap and an increased optical absorption. Due to the lack of computational time any co-doping was tested during this work, but their use could be helpful to improve the performance obtained with mono-doping and increasing the number of possible dopants.

1.8.4 Intermediate Band Doped System

As previously seen, the presence of a dopant can increase or reduce the band gap according to size, electronic structure, and capability of vacancies formation. Another interesting property of doped system is the introduction of an intermediate band inside the band gap of the semiconductor thanks to the energetic level of the dopant. These systems called intermediate band solar cell (IBSC) were firstly proposed by Luque[281,282] in 1997 and they are gaining more and more attention[283–285]. The intermediate band (IB) acts as a stepping stone for electrons coming from VB. In this way, electron can be excited not only by photons with an energy higher than the forbitten band, but also by those having at least the energy between IB-CB and IB-VB. With this trick the total carriers generation increase and the light absorption is expanded significantly[286–288].

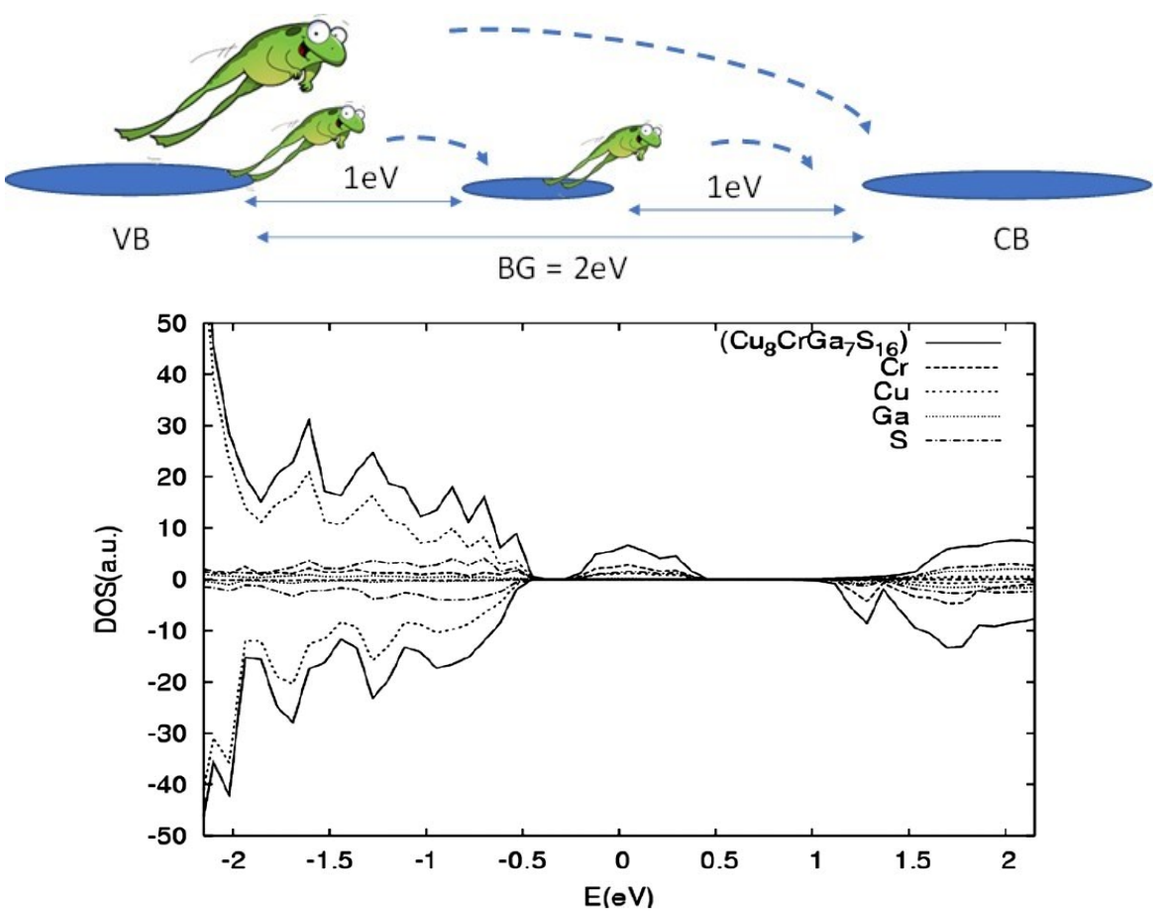

Figure 59. *A) Schematic representation of the IBSC system. B) DOS of a chalcopyrite doped system with intermediate band gap from reference*[248].

Actually on Cu_2O interesting results were obtained by Malerba et al.[289] and other authors[256,258,290] with N-doped Cu_2O both from computational and experimental point of view.

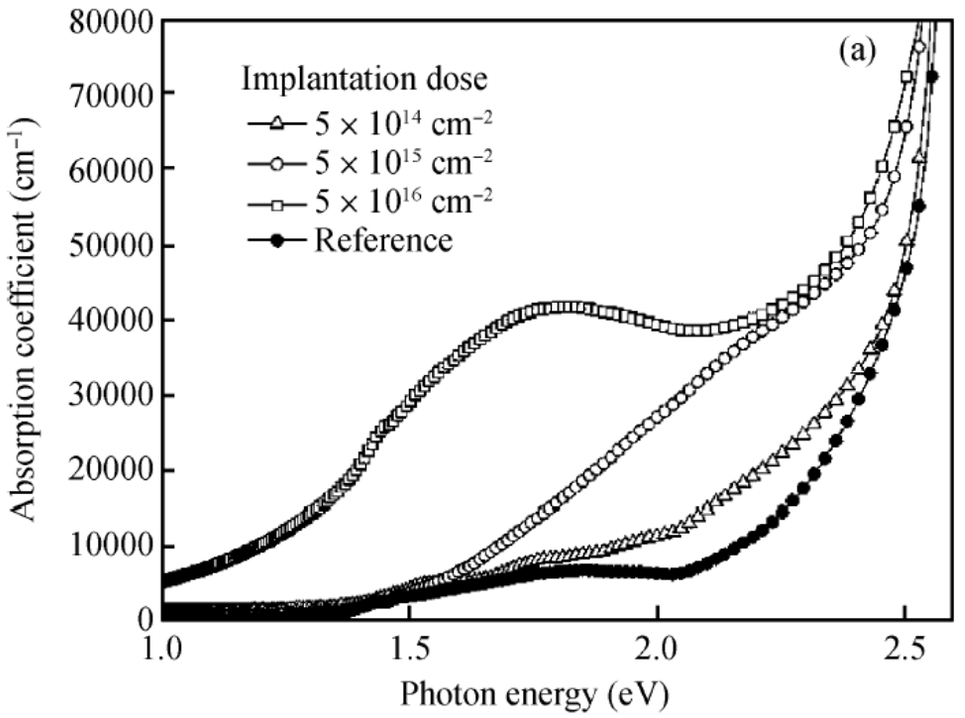

Figure 60. *Adsorption spectra of different doses N-doped Cu_2O and undoped films obtained from experimental results in "A combined experimental-computational study on nitrogen doped Cu_2O" by Ping et al.* [258]

From the results obtained by the authors[258], we can clearly see a new absorption peak below the BG with a red-shift of the absorption band edge. If more photons can be used for the electron-hole pair generation, this will improve the performance of the material.

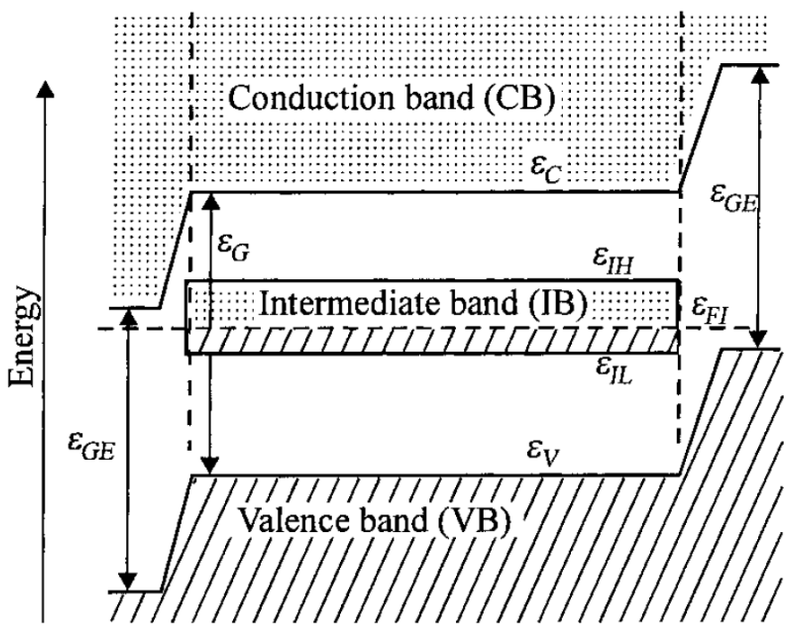

Figure 61*. Sketch of an intermediate band (IB) energy band diagram in thermal equilibrium showing the energy band extremes. Dashed and dotted regions correspond to electron-filled and empty bands respectively (at 0 K). Figure from "A metallic Intermediate Band High Efficiency Solar Cell' by A. Luque et al.* [291]

To obtain an efficient IB some requirements have to be fulfilled[281,291–294]

- It must be half-filled and lie on the Fermi level. This is necessary to have strong light absorption for transition to and from IB[248].
- Must be clearly separated both from VB and CB.
- Split the original BG in two sub-bandgaps of approximatively the same width.
- Don't being a centre for non-radiative recombination.
- It must have small dispersion and must not be a discrete level.

According to literature, on Cu_2O only nitrogen seems to be the effective material for the generation of the proper IB enhancing the light-catching performance of Cu_2O.

1.9 Additional Physicochemical Techniques

1.9.1 Scanning Electron Microscopy (SEM)

SEM is a powerful tool for solids morphology analysis. It allows to study shape, size, and structure of materials with high resolution (it can analyse samples in the nanometres scale). This microscope uses a focused electrons beam that interacts with the surface of the sample. The primary electrons beam scans the surface point by point on a small area of the sample under vacuum because air will stop the beam. The interaction of the primary beam with the matter generates secondary electrons. The latter are collected by a detector placed on the top of the sample with a given angle respect to the incident beam. The signal is then transformed in black and white images with extremely high resolution.

Since only the sample's surface is the source of secondary electrons, this technique can give only an image of the outer layers of the material.

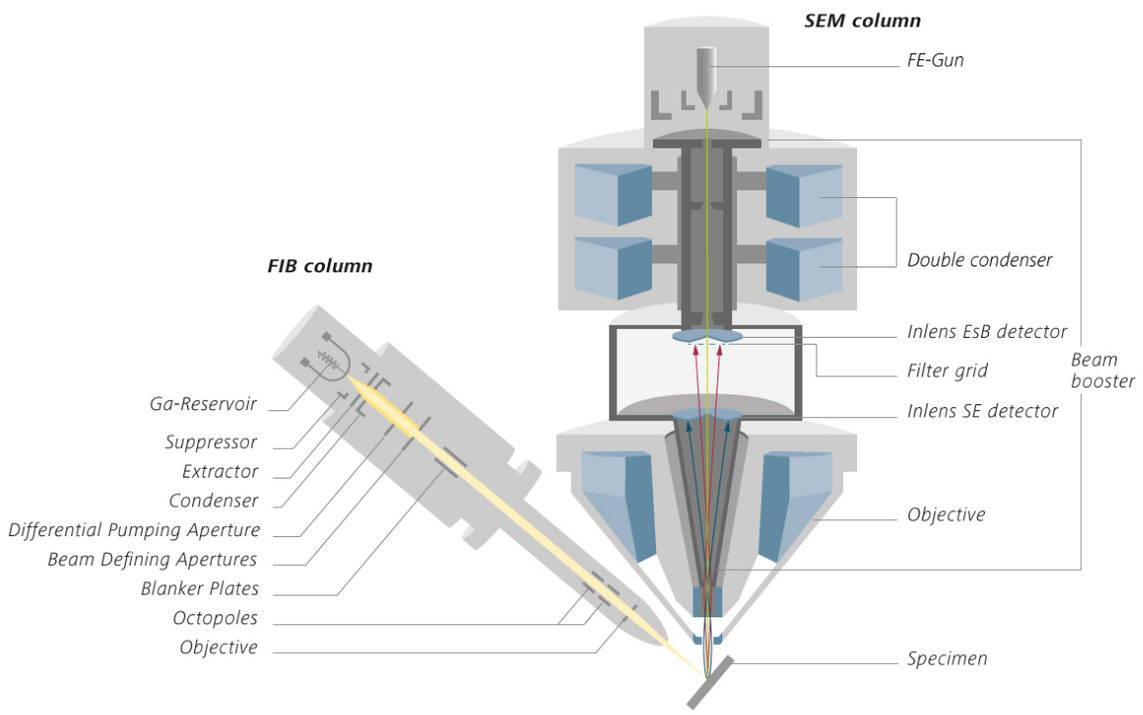

Figure 62. *Schematic view of a Scanning Electron Microscopy. Image from Zeiss SEM Electron Optics: https://www.zeiss.com/microscopy/int/products/fib-sem-instruments/crossbeam/crossbeam-technology.html*

1.9.2 Physical Vapor Deposition (PVD)

Physical Vapor Deposition, is a quite common method for the deposition of thin films under vacuum widely used in the production of electronic devices. The material of interest is heated and evaporated under vacuum as atoms or molecules, then, as a vapour, it condenses on the substrate. This technique can create thin layers in the order of few tens of nanometres over almost any surface. Obviously, adherence properties and homogeneity of the applied overlayer are strictly related to the substrate material and operative conditions.

Different systems are available on the market for the creation of the vapour. In this work the instrument was provided with a thermal evaporator based on Joule effect where a high current cross the crucible with the metal reservoir (Au) creating the gold cloud over the substrate[295].

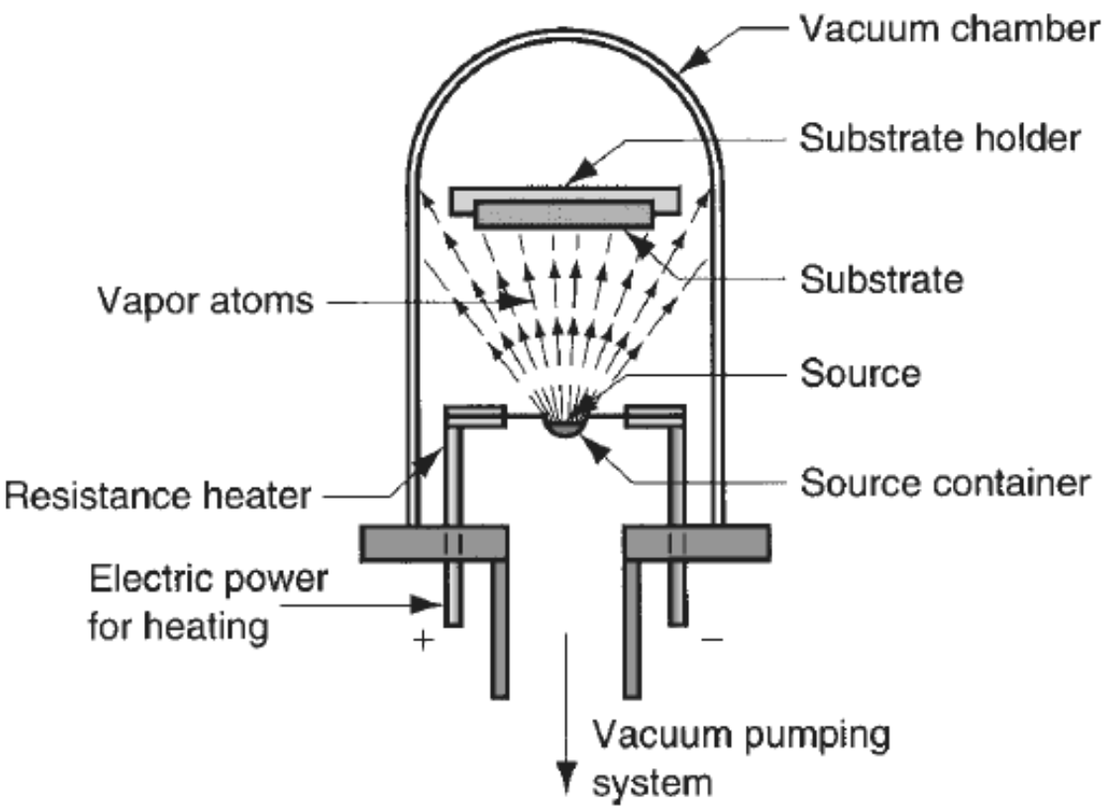

***Figure 63**. Schematic view of a Physical Vapour Deposition system.*

1.9.3 X-Ray Diffraction (XRD)

It's a non-destructive technique able to provide information about the crystal structure, the chemical composition and the physical properties of powder materials or thin film.

X-ray diffraction is based on constructive interference of monochromatic X-rays and a crystalline sample. These incident X-rays, generated by a cathode ray tube, interact with the sample producing a constructive interference (and a diffracted ray) when conditions satisfy Bragg's Law ($n\lambda=2d \sin \theta$). This law relates the wavelength of electromagnetic radiation to the diffraction angle and the lattice spacing in a crystalline sample. By scanning the sample through a range of 2θ angles, all possible diffraction directions of the lattice should be attained due to the random orientation of the powdered material. Conversion of the diffraction peaks to d-spacings allows to identify the material because each mineral has a specific pattern of d-spacings. The comparison with standard material spectra then allows the identification of the sample.

The instrument used in this work allows to modify the X-rays source angle in order to focus the beam mostly on the electrodeposited thin film than on the substrate.

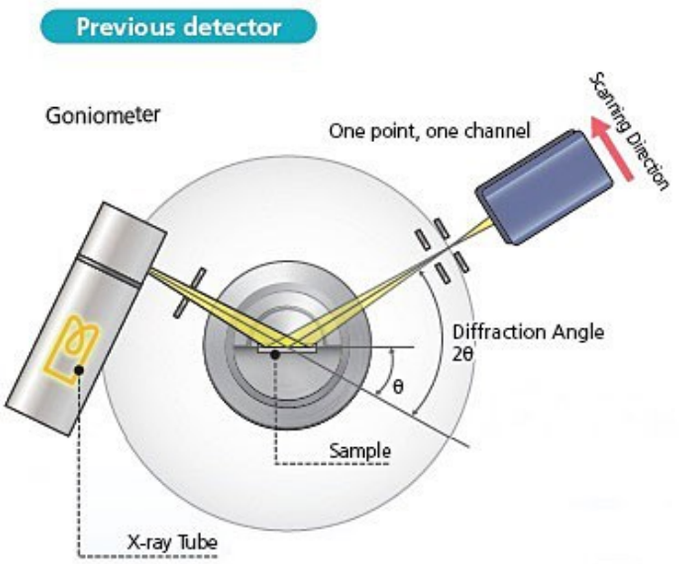

Figure 64. *XRD schematic view. The used instrument allows to modify both the detector and the source angle. Image from http://www.shimadzu.com/an/elemental/xrd/onesight.html*

1.9.4 Solar Simulator (SS)

A solar simulator is a light source with a spectrum as close as possible to the sun one so that it would be possible to perform indoor experiment for PV materials with controlled conditions that resemble the natural ones. The sun spectrum is very close to the one of a black body but the intensity reaching the Earth surface is different. The intensity of the solar simulator light is then defined by the air mass coefficient (AM). It is a measure of the direct optical path length trough the atmosphere at the zenith used as a standardize condition. Briefly is a measure of the attenuation of the sunlight induced by the presence of the atmosphere that can scatter and absorb the sunlight. In this work, a value of 1.5AM was used as in most of the solar panel characterization.

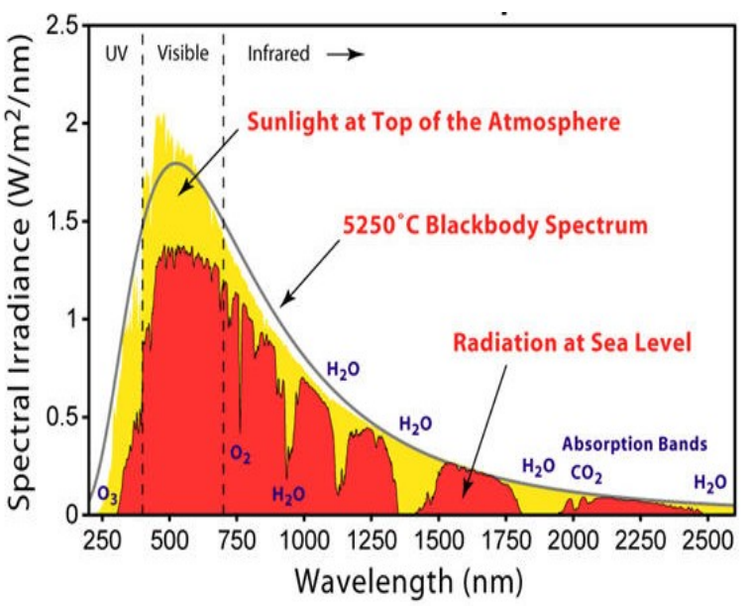

Figure 65*. Solar (yellow), black body (black line) and AM1.5 (red) spectra comparison. Figure from American Society for Testing and Materials (ASTM) (http://www.astm.org/)*

1.9.5 Electrochemical Impedance Spectroscopy (EIS)

Electrochemical Impedance Spectroscopy implies the application of small amplitude (5-10 mV) a.c. signals of selected frequencies. By varying the frequency of the signal, a selective perturbation of different physico-chemical phenomena can be performed, thus allowing the identification of their separate contributions. In this work EIS was used to obtain a Mott-Schottky plot of the semiconductor. This plot describes the reciprocal of the square of capacitance versus the potential difference between bulk semiconductor and bulk electrolyte. In many theories, and in many experimental measurements, the plot is linear. The use of Mott-Schottky plots to determine system properties such as flatband potential, doping density or Helmholtz capacitance. The equation used in the Mott-Schottky plot is:

$$\frac{1}{C^2} = -\frac{2}{e\varepsilon\varepsilon_0 N_A A^2}\left(E - E_{fb} + \frac{kt}{e}\right) \; for\ a\ p-type\ semiconductor$$

$$\frac{1}{C^2} = \frac{2}{e\varepsilon\varepsilon_0 N_D A^2}\left(E - E_{fb} - \frac{kt}{e}\right) \; for\ a\ n-type\ semiconductor$$

Where C is the capacitance, ε is the dielectric constant of the semiconductor, ε_0 is the permittivity of the free space, A is the working area and N_D and N_A are the donors and acceptors concentration respectively. E is the applied potential and E_{fb} is the flat band potential, the potential drop associated with the space charge in the semiconductor once in contact with a solution. The value of the capacitance can be obtained from the imaginary part of impedance measurements:

$$Z_{imm} = \frac{1}{2\pi f C}$$

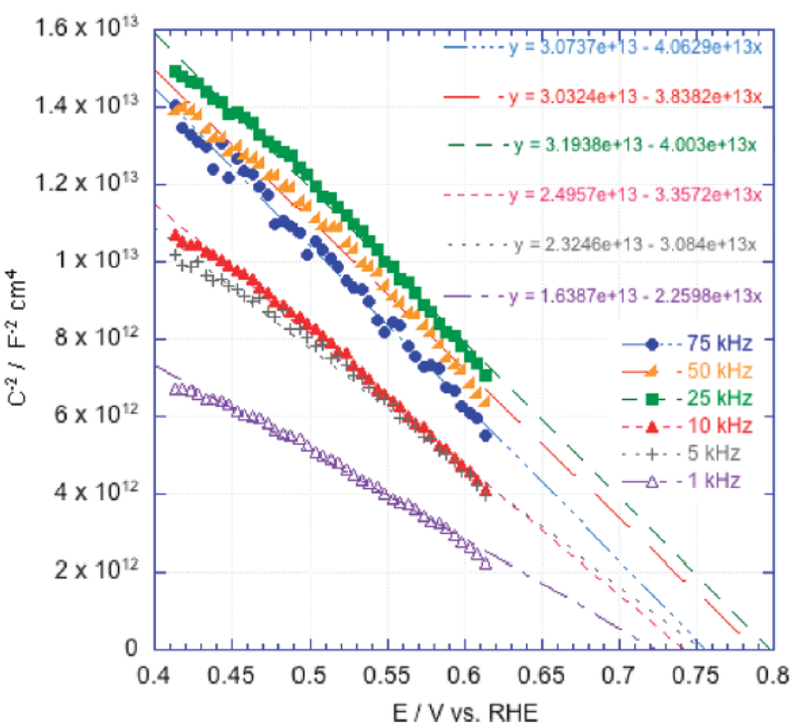

***Figure 66**. Mott-Schottky plot of Cu_2O from EIS analysis in 0.1M sodium acetate (pH7.85) in water in the dark. Figure from Paracchino A. et al., | J. Phys. Chem. C 2012, 116, 7341−7350.*

In the Figure 66 is reported an example of a p-type semiconductor Cu_2O at different frequencies. As reported a p-type semiconductor will show a negative slope in the $1/C^2$ vs E plot. Different information can be obtained from this type of plot:

- The value of the slope gives the number of carriers in the semiconductor.
- The intercept with the x-axes gives the flat band potential of the semiconductor.

2. Results and Discussion

This section is articulated in different chapters according to the different topics. Each chapter includes the experimental procedures for the preparation and characterization of electrodes and materials and the relevant experimental results.

In all the preparations MilliQ® water (Millipore system k=18.2MΩ) is used and all the measurements were carried out at atmospheric pressure.

2.1 Cu_2O Photoelectrodes

The first chapter is devoted to the preparation of Cu_2O photoelectrodes and their electrochemical characterization with classical techniques. The procedures involved in the deposition of the electrodes are the same for the XAS and FeOOH overlayer chapters if not declared differently.

2.1.1 Cu_2O Electrochemical Deposition

In the introduction, different methods for the preparation of Cu_2O were presented. Here, the electrochemical method was selected due to its large tunability and scalability allowing also preparing several electrodes in a reduced time. Moreover, to the best of our knowledge the so-prepared semiconducting material shows high photocurrents, high degree of homogeneity and offers a large matrix of parameters that can be modulated in order to achieve better performances.

The deposition occurs from the an aqueous solution of 0.2M $CuSO_4$, 0.5M K_2HPO_4 and 3M lactic acid, to which 2M aqueous KOH is slowly added until pH 12 is reached. The color of the solution changes from blue to turquoise (the formation of a foam-like precipitate will start at around pH 9) and finally to deep dark blue without any solid particle. Further information and analysis on this deposition bath will be given during the Result and Discussion chapter. This electrodeposition bath for Cu_2O was firstly reported by Golden[56], and lately used by Paracchino[57–59] and many other author[255,296,297] and allows to easily obtain Cu_2O. The high pH is mandatory for preparing the p-type Cu_2O[298,299]. According to different authors[58,300], working at low pHs the n-type is obtained, but the reason behind this outcome is still under discussion[236]. To avoid the precipitation of copper hydroxide at pH 12, the presence of lactic acid is mandatory. It is important to notice that $CuSO_4$ is the only "hazardous material" in this synthesis, making this procedure as eco-friendly as possible. As presented in the introduction the use of this bath together with the use of electrochemical methods allows a wide control over the shape and morphology of the Cu_2O. According to the original recipe, higher photocurrents are obtained under intensiostatic condition[296,301] and at $T \approx 30°C$[302]. However, we obtained better results under potentiostatic conditions and at $T \approx 60°C$. In particular, the potential control allows to determine the grain size, shape and composition[297,303,304] , while the higher temperature allows faster deposition and higher final performances[305].

The so prepared bath is then used at 60°C in a sealed thermostatic cell. Sealing the cell is extremely important to avoid solution evaporation and changes in bath concentration during the deposition.

Cu_2O were electrodeposited in the unstirred bath at 0.55V vs RHE in a typical 3-electrode cell configuration. A Pt foil 1x2cm was used as counter electrode in front to the working one and at almost 1 cm.

This ensures the formation of a homogeneous layer of Cu_2O due to the good current distribution. A Saturated Calomel Electrode (SCE) was used as reference (E = +0.248 mV VS NHE) in a KNO_3 0.5M double bridge configuration. The use of the double bridge avoids Cl^- contamination in the deposition bath, thus avoiding Cl- doping of the material (leading to a possible n-type conductivity), and at the same time preserves the life of the SCE in the strong basic environment. All the potentials are anyway here referred to RHE electrode ($E_{RHE} = E_{SCE} + 0.059 \cdot pH + 0.248V$).

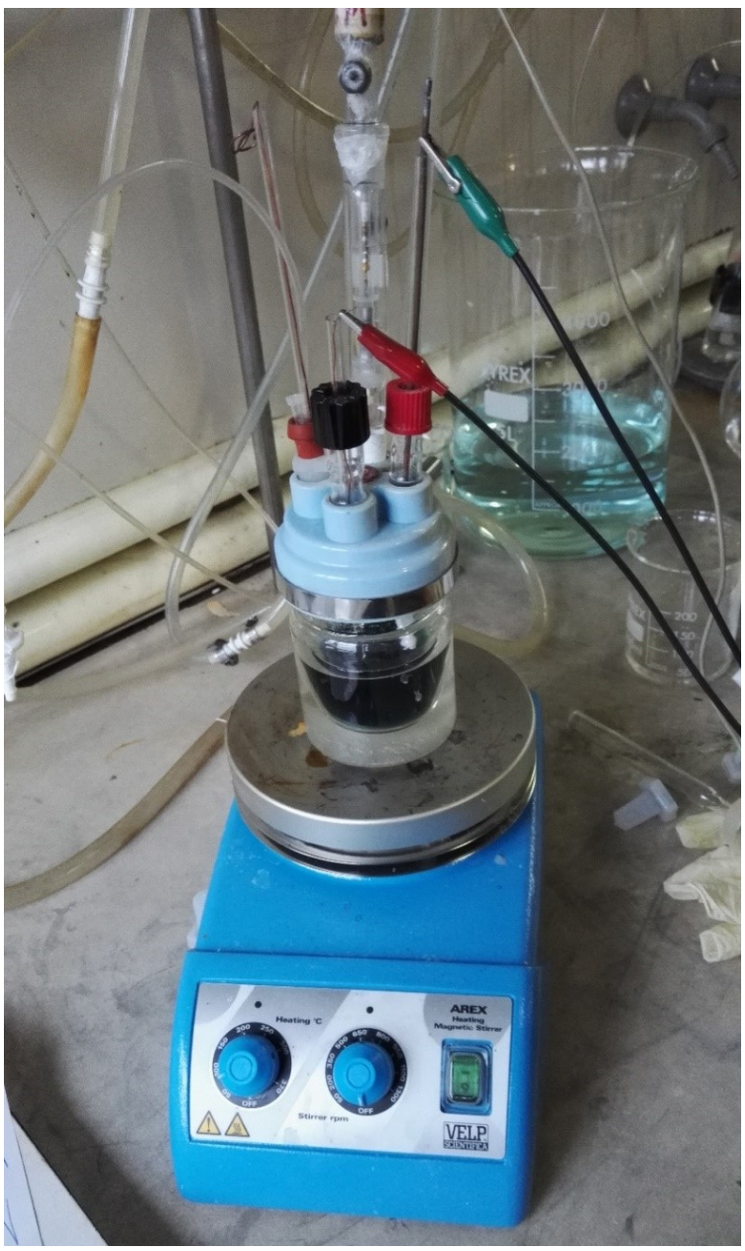

Figure 67. *Electrochemical setup for the Cu_2O (and Cu) deposition. A 3-electrode cell with thermostatic bath and magnetic stirring.*

Other methods, like thermal oxidation of Cu substrate treated in 0.125M $(NH_4)_2S_2O_8$ as chemical oxidant to obtain $Cu(OH)_2$[46] and different electrochemical synthesis where also tested but, due to the low photocurrents, and inhomogeneities of the samples, were abandoned and not reported.

2.1.1.1 Deposition Bath

To individuate the potential window for the electrodeposition, a series of CV experiments were performed at 10mVs^{-1} between 0.95 V vs RHE (close to the Cu2O Open Circuit Potential (OCP)) and hydrogen evolution reaction. In the first cycle, a first shoulder is observed at ≈0.4V vs RHE and two well defined peaks at -0.1 and -0.55 V vs RHE. According to the literature, the shoulder is to be referred to Cu_2O deposition[306] from free Cu^{2+} (according to the complexation equilibrium with lactate), while the two more negative peaks are related to the deposition of metallic copper.

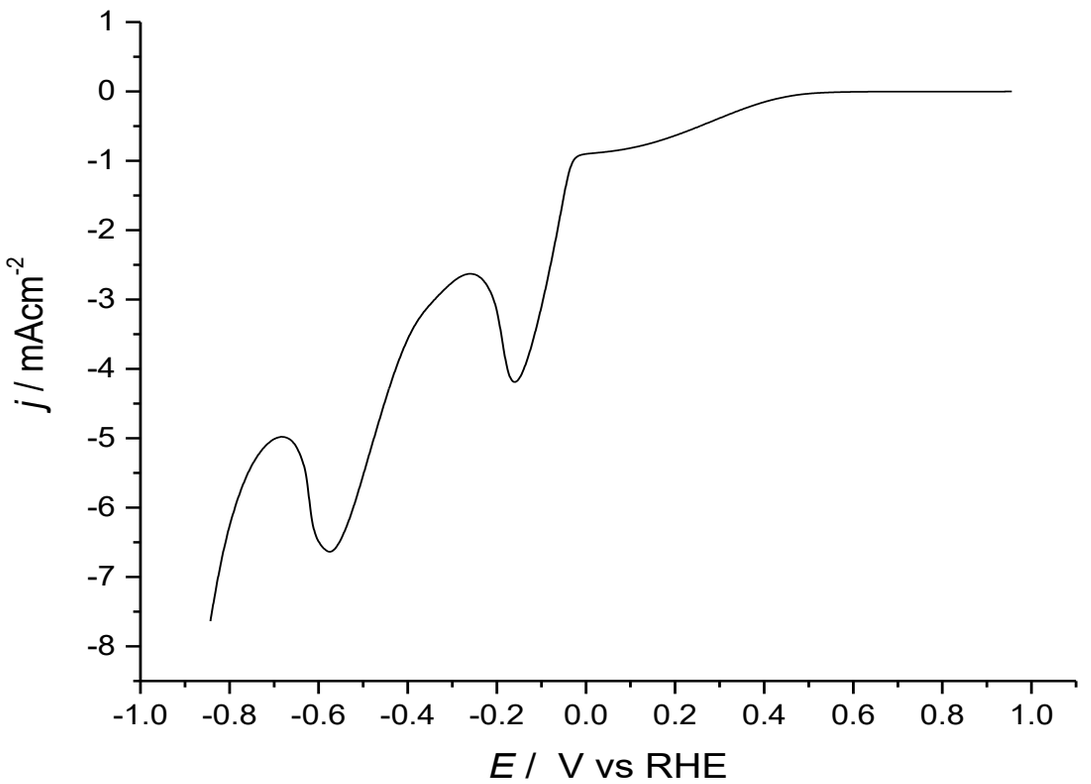

***Figure 68**. CV at a bare FTO working electrode in 0.2M $CuSO_4$ + 0.5M K_2HPO_4 + 3M lactic acid at pH 12. Scan rate 10mVs^{-1}, Pt counter electrode, at 60° C.*

The peaks were assigned by comparing a series of experiments at different bath compositions:

I. KOH pH 12
II. K_2HPO_4 + KOH pH12
III. K_2HPO4 + KOH + lactic acid pH 12
IV. K_2HPO_4 + KOH + lactic acid + $CuSO_4$ pH 12

This approach allowed also to test the potential stability window of the bath in the cathodic direction.

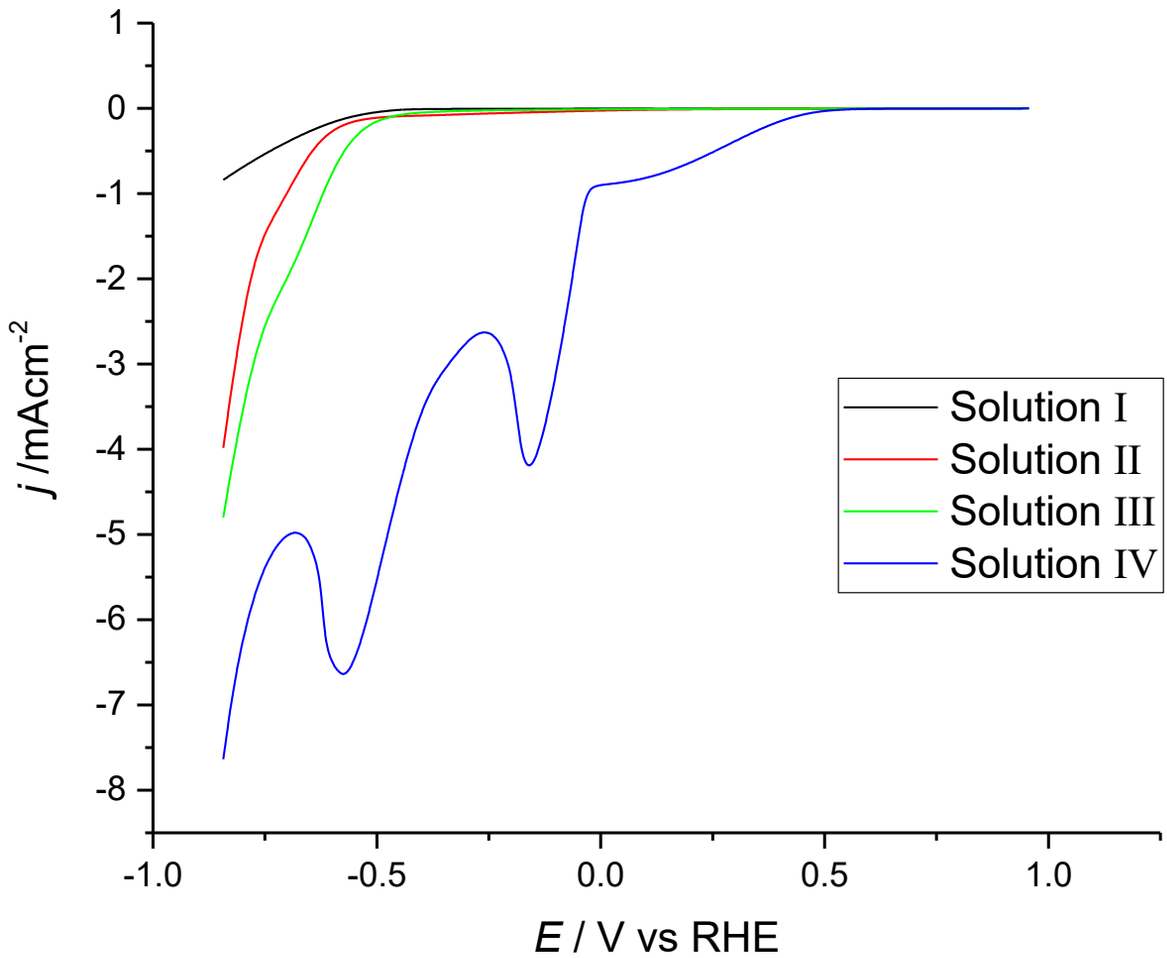

Figure 69. *CV at a bare FTO in: I) KOH pH 12, II) 0.5M K_2HPO_4 + KOH pH12, III) 0.5M K_2HPO_4 + KOH + 3M lactic acid pH 12 and IV) 0.2M $CuSO_4$ + 0.5M K_2HPO_4 + 3M lactic acid at pH 12 (addition of 2M KOH). Scan rate 10mVs^{-1}, Pt counter electrode.*

The CV's clearly show that in the absence of $CuSO_4$, no peak is recorded. This also excludes the reduction of lattic acid within this potential window.. The small shoulder just before HER in the presence of K_2HPO_4(II) and then lactic acid (III) is probably due to oxygen reduction and cannot be related to the much higher peak, recorded in presence of copper ions. In the presence of copper sulphate, the two large peaks are assigned to Cu deposition, by two different processes, which correspond to different possible phenomena:

i) The deposition from free Cu^{2+} ions (0.00025M) and from the copper-lactate complex.

ii) Two different nucleation mechanisms.

iii) Less likekly, the reduction of the already deposited Cu_2O[307], a possibility that is not supported by the peak charge integration.

In summary, this solution is stable enough to be used for the depostion of several electrodes (10 Cu_2O + 10 Cu),with the same good reproducibility. Indeed, the depostion of such an amount of material slightly modify the copper concentration in the bath.

On subsequent CV cycles, the potential of Cu(0) deposition peaks does not change while the Cu_2O occurs at more positive potentials. This behaviour can be explained by considering that at bare FTO surface an induction potential is needed for the formation of the first grains of Cu_2O. Once a first cycle is performed, this induction potential is not necessary because on the electrode are present some Cu_2O and Cu deposited in the first cycle at more cathodic potential.

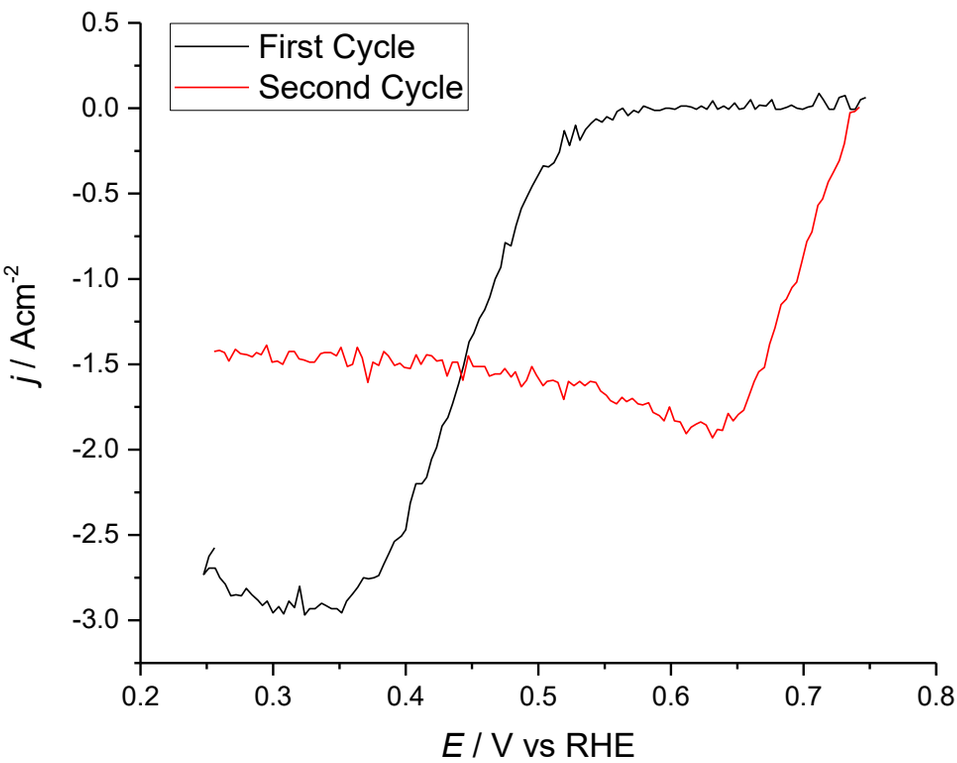

***Figure 70**. Linear Sweep Voltammetry (LSV) comparison between Cu_2O deposition peak on a FTO free surface (in black) and on a surface with some copper metal on it (red line). Is possible to notice the shift due to the higher energy required for grain formation. Scan rate 10mVs^{-1}, Pt counter electrode.*

A preliminary material characterization was performed by Scanning Electron Microscopy (SEM) coupled with Energy Dispersive X-ray (EDX) analysis and X-ray diffraction of the prepared sample. To confirm the p-type conductivity of the material Electrochemical Impedance Spectroscopy (EIS) was used.

2.1.2 Cu_2O Characterization

2.1.2.1 SEM Analysis

A sample of Cu_2O was analysed to have structural and chemical information about the deposited material. SEM analysis and EDX analysis were performed with a Carl Zeiss Gemini Ultra 55. EDX analysis confirm the presence of Cu_2O (Cu:O ratio equal to 2:1), while the SEM images are here reported at different magnification ratios. A clear crystalline structure is not found, and the obtained grains seems to have different sizes and shapes. The grain size varies between 50-200 nm, showing a size much smaller than the one reported in the literature for the same type of electrode(i.e.1000-2000 nm[57,308]). Only Bijani et al.[309] show a similar size. This is an interesting result because it suggests a larger real surface area for this material and thus a larger surface that can be light-activated. Moreover, a reduced size of the particles increases their stability[310] and their photocatalytic efficiency by changing the light scattering properties[311]. In addition, was possible to obtain this results within the use of surfactants or organic solvent likewise reported in different synthesis[312]. Moreover, despite the absence of a specific shape the electrodes performances are highly reproducible suggesting the low importance of this parameter in the final behaviour for HER.

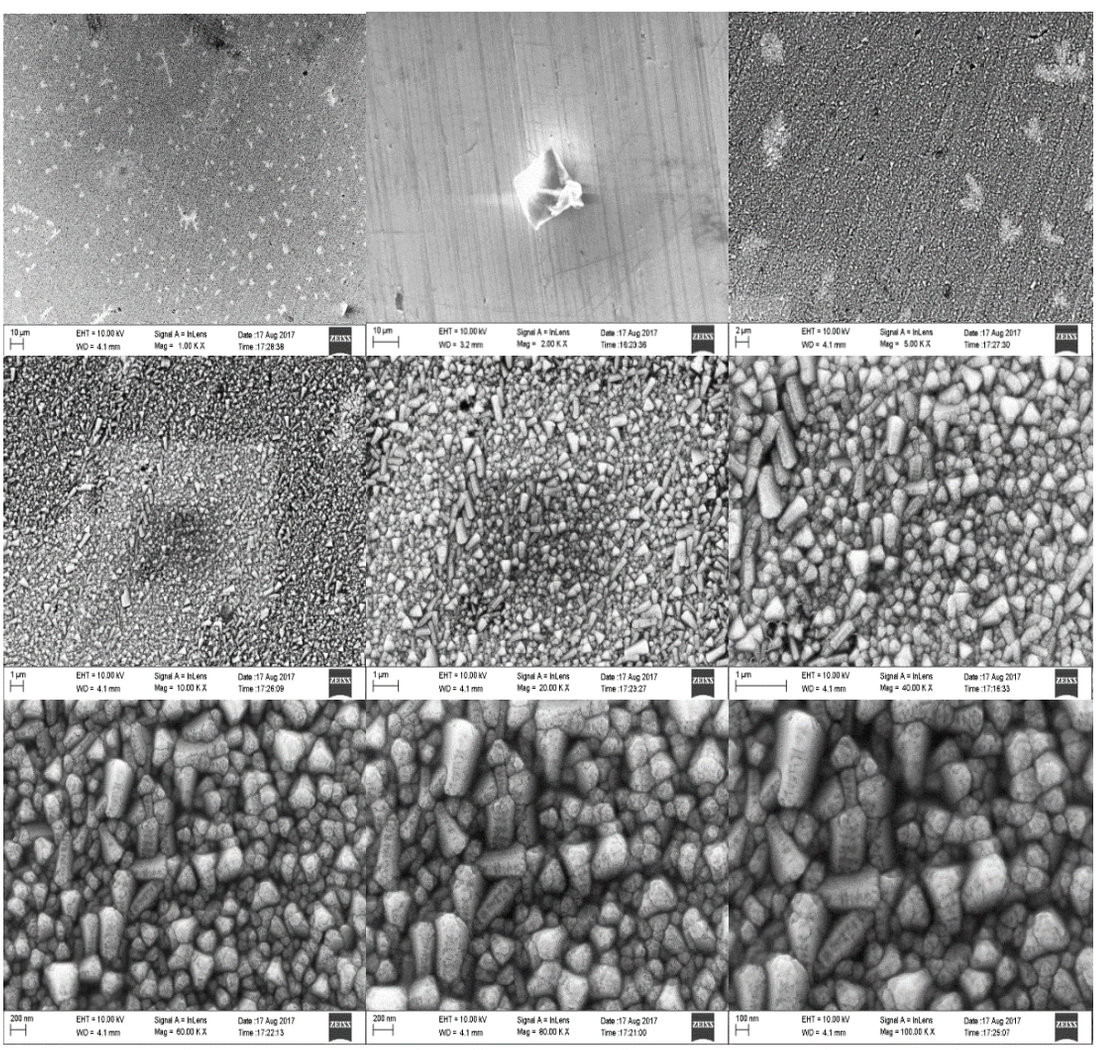

***Figure 71**. SEM images of a p-type Cu_2O sample. Different magnifications were used: a) 1000x, b)2000x, c)5000x, d)10000x, e) 20000x, f)40000x, g) 80000x and h) 100000x.*

The EDX analysis is reported below:

Element	Weight %	Atomic %
O	12.69	36.60
Cu	63.40	63.40

The EDX analysis shows the formation of pure Cu_2O. Is possible to notice how the amount of Cu is slightly less than the double amount of O. This can be explained by the formation of Cu vacancies, considered the main actor in the p-type conductivity of this material. Indeed, the formation of metallic copper at the deposition potential have to be excluded.

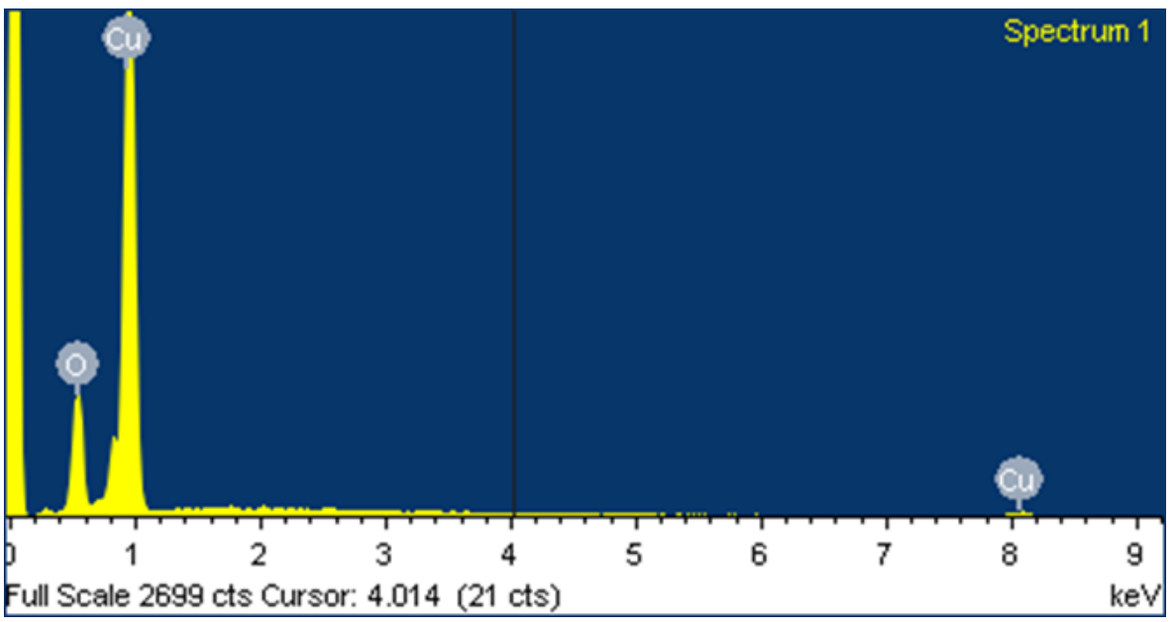

***Figure 72**. EDX analysis of a Cu_2O @Au sample deposited at 0.55V vs RHE from the copper lactate bath (pH12). The only available peaks are the one of Cu and O.*

2.1.2.2 EIS Analysis: Mott-Schottky Plot

Electrochemical impedance spectroscopy (EIS) was here used to have a direct confirmation of the p-type behaviour of the so deposited material. On an Au RDE electrode tip Cu_2O was deposited according to the previous procedure. Then a safe potential window in dark was identified between +0.56 and +0.16 V vs RHE. In this window, no faradic reaction occurs in a de-aerated solution of NaH_2PO_4 0.5M + NaOH 0.5M (pH 11). Then at the OCP, a frequency scan between 0.1HZ and 100KHz was performed and five different frequencies were chosen for the analysis: 1Hz, 10Hz, 220Hz, 1KHz and 6KHz. The OCP is the best potential for this evaluation because the only contributes here present will be the solution resistance and the capacitance of the electrode. Each measurement was performed in the same electrolyte used for the test of the electrode performance but for clarity is here reported only the one acquired at 220Hz.

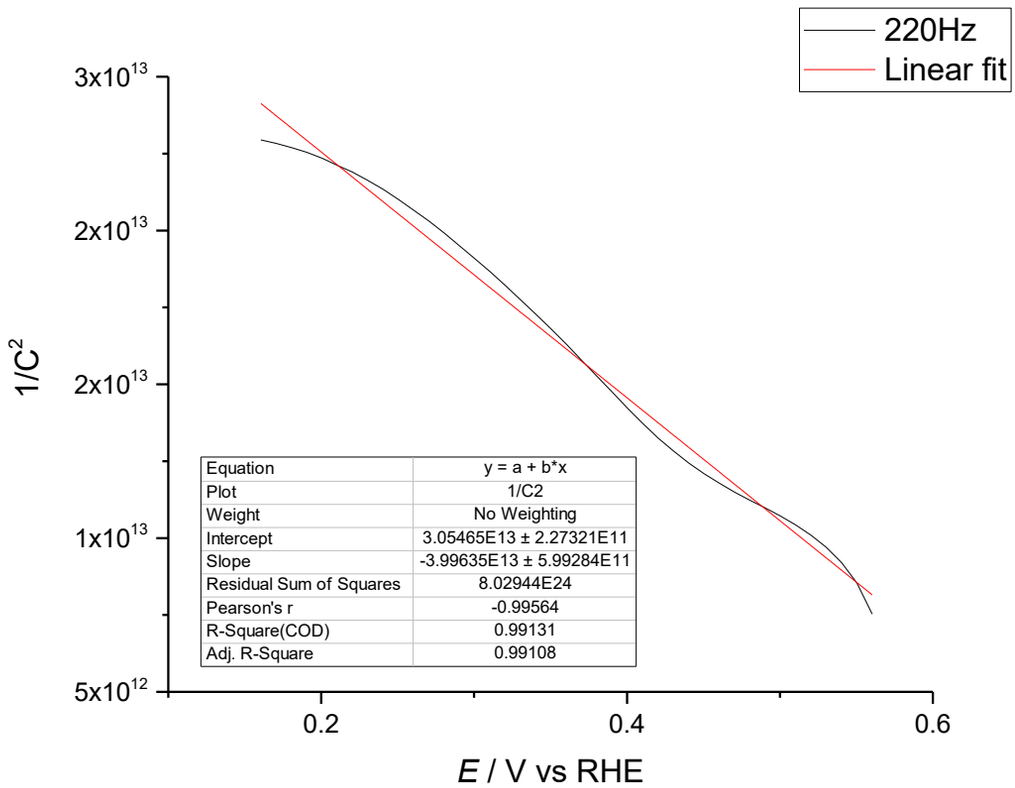

Figure 73. *Mott-Schottky plot at 220Hz of a Cu_2O@Au electrode in Na_2HPO_4 0.5M + NaOH 0.5M (pH 11) in a stability potential windows.*

At each of these frequencies the Mott-Schottky analysis was performed obtaining in all the cases a negative slope, as expected from a p-type semiconductor. Using the following parameters, the carrier concentration and the flat band potential were calculated.

Parameter	Value	
Area (A)	0.07	Cm^2
Elemental charge (e)	$1.602x10^{-19}$	Coulomb
Dielectric constant (ε)	6.6	
Permittivity in the vacuum ($ε_0$)	$8.85x10^{-12}$	$F{\cdot}m^{-1}$
Boltzmann constant (k)	$1.38x10^{-23}$	$m^2{\cdot}Kg{\cdot}s^{-2}{\cdot}K^{-1}$
Temperature (T)	298.15	K

Table 8. *Used parameters for the calculation of the flat band potential and carrier concentration for the Cu_2O@Au electrode.*

Using the following parameter for Cu_2O a carrier concentration (N_A) of $1.09x10^{18}$ cm^{-3} and a flat band potential of 0.79 V vs RHE were found. These results are in good agreement with the one found in literature for Cu_2O ($N_A = 5x10^{17}cm^{-3}$ and E_{fb} = 0.75 vs RHE).

2.1.2.3 XRD Analysis

XRD was performed on a Cu_2O@Au electrode. The results clearly show that the material deposited is the one of interest with no additional peaks due to lower or higher oxidation states in the material. The peaks intensity suggests the predominant formation of the [111][313] face (2ϑ = 37)[314] as expected working at pH 12[300,315] that is also the most active face for this application as showed by Paracchino et al[316].

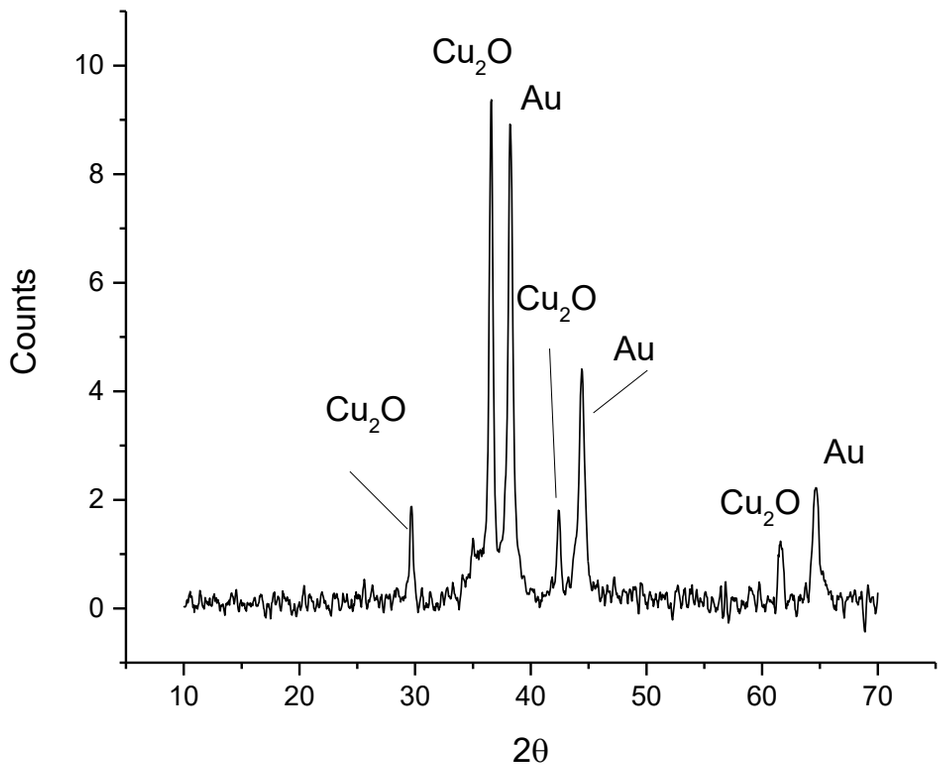

***Figure 74**. 4 degrees XRD of Cu_2O@Au sample.*

2.1.3 Influence of the Underlayer

According to the results obtained with one or more CV cycles was noticed a shift of the Cu_2O deposition peak to less negative energies. As stated before this can be related to the difficulties in grain formation on the bare FTO until a layer of metallic copper is formed at more negative potential. From these preliminary measurements was clear the importance of having an underlayer on the FTO electrode to improve the deposition.

In literature, a chromium/gold underlayer was used. The role of the underlayer is to increase the conductivity of the electrode, improve charge separation[149] and reduce electron-hole recombination. Moreover, it was noticed that different underlayers can lead to different grains size, shape and exposed faces with obviously different activity[317]. As we have seen in the introduction one of the main drawbacks of PEC-WS is the actual cost that prevent this technology to be competitive for a valuable H_2-economy. In our opinion, the use of an expensive layer of gold deposited by ALD together with Cr is unacceptable. Moreover, UE is going to ban chromium from all industrial processes and developing a technology using this material is unsatisfactory.

The first aim of this work was indeed to find a valuable, cheap, easy-to-prepare and efficient substitute for the Cr/Au underlayer. Based on the shape of the CV, metallic copper was chosen. The use of this metallic underlayer can add several advantages:

- Copper can be easily deposited from the same deposition bath of the semiconductor simply changing some deposition parameters. No need of different solution, washing steps or complex procedures.
- No need of expensive techniques, copper can be easily deposited by electrochemical method obtaining flat and homogeneous surfaces.
- Copper is a non-toxic and extremely cheap material.
- Copper and gold have quite similar (1.59 and 2.44×10^{-8} Ωm respectively) resistivity so no additional resistance would be added to the electrode[318].

From the voltammetric analysis of the bath two different peaks of Cu(0) deposition were found. Their differences were studied with different approach:

1. UPD measurements.
2. UV-vis spectrophotometer.
3. Electrochemical measurements.
4. XAS.

2.1.3.1 Under Potential Deposition

Under Potential Deposition (UPD) is an electrodeposition phenomenon, where a metal cation is reduced to solid metal on the surface of another metal at a potential less negative than the Nernst one. This means that the electrodeposition of the metal onto another metal is easier than the deposition on itself (that is the value of the equilibrium potential for a metal).

This occurs because the interaction between the electrodeposited metal M with the metallic substrate S is stronger than the M-M interaction. This stronger interaction is due to favourable lattice coupling between M and S respect to M-M. This is even clear if we consider that usually UPD occurs only up to a monolayer of M. The new electrodeposition potential for M on S is the underpotential deposition and is strongly related to the nature of S. The use of UPD is specifically indicated to obtain information about:

- The active area of an electrode; The active area can be evaluated from the charge passed in the electrode during the deposition, or from the charge recorded during the stripping of the monolayer. A specific value of $C \cdot cm^{-2}$ is tabulated for every M-S couple so that is easy possible obtain information on the active area of the electrode.
- Exposed crystal facets: Indeed, UPD peaks are much sharper on monocrystal than on polycrystalline materials. The UPD peaks position is different for every facet and on a policrystalline system and can be easily identified by a comparison with the UPD recorded on different monocrystals. Different facets indeed will show different UPD potential[319].

UPD on copper is performed using the lead electroreduction[320].

2.1.3.2 Preparation of Pb UPD on Cu

The solution required for the UPD measurement is composed by $Pb(OAc)_2$ 0.01, $NaClO_4$ 0.5M and $HClO_4$ 0.001M at pH 5.5[321,322]. The copper electrodes were synthetized from the copper lactate solution bath at -0.145, -0.245, -0.545 and -0.845 V vs RHE respectively with a total charge passed on the electrode of 0.47 Ccm^{-2} on the bare FTO. During the Cu deposition the bath was stirred and kept at the constant temperature of 30°C with the use of a thermostatic bath. This temperature was chosen to reduce as much as possible to formation on Cu_2O.

First, the copper electrode is immersed in the solution without Pb^{2+} ion to obtain a background CV from 0.422 to 0.122 V vs RHE of the electrode and be sure that no faradic reactions occur in absence of the redox specie. This potential window was selected to have the deposition of the single monolayer and avoid bulk deposition of Pb. The background will be subtracted from the UPD measurement in order to be able to relate the recorded current only to the faradic deposition of the lead monolayer without any capacitive contribute from the electrode.

Then the proper amount of lead is added to the solution (previously purged with N_2) and one CV cycle in the same potential windows of the background was recorded at 25°C with stirring. Is important to test the electrode for UPD as soon as possible after deposition and background or the surface of the electrode will reconstruct giving unreliable results.

UPD was used to study the surface of copper deposited at different potential: -0.545 and -0.245 V (III and II Potential) are the ones related to the different peak recorded in the LSV of the bath. In addition, were tested also -0.845V (IV Potential) (to evaluate the influence of strong hydrogen evolution during the deposition) and -0.145 V (I Potential) to see if any difference is present working at lower current respect to the -0.245 V peak.

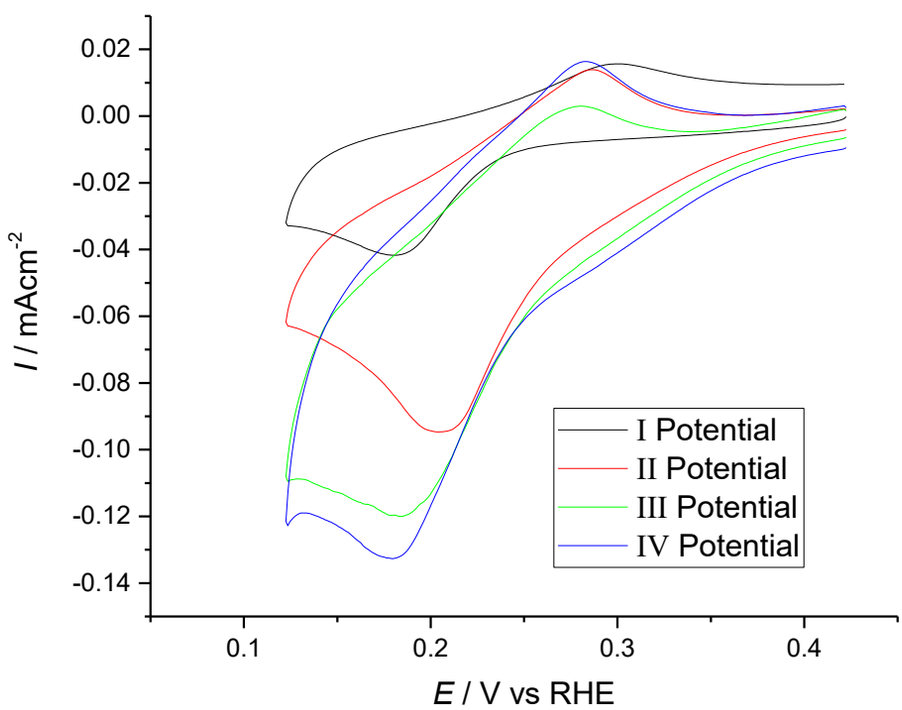

***Figure 75**. UPD measurements on Cu@FTO deposited at different potentials. I) -0.145V vs RHE, II) -0.245V vs RHE, III) -0.545V vs RHE and IV) -0.845V vs RHE. UPD bath: $Pb(OAc)_2$ 0.01, $NaClO_4$ 0.5M and $HClO_4$ 0.001M at pH 5.5. Scan rate 5mVs^{-1}, counter Pt.*

The exposed face, related to the UPD peak potential, and the amount of charge were almost the same for III and IV deposition potential while I potential have the same orientation but much smaller charge (smaller surface area available). The only one with strong differences in orientation and charge was the II Potential. Was our opinion that having an underlayer with higher surface area would have helped the performance of the final electrode with Cu_2O, allowing to have a wider surface that can be reached by the light and for this reason this potential was no further tested. The potential IV is extremely similar to the 3rd one but was not considered for further measurements because of the strong hydrogen evolution occurring on the electrode that can lead to material detachment during the deposition itself. Potential II and III were indeed considered the best compromise between high surface area (probably also ensured by the formation of small hydrogen bubbles during the deposition) and the possibility of studying two different orientations. Indeed, from literature[321,323] the UPD peak are expected to be at the following potentials according to different exposed facets:

Exposed Facet	Peak	E /mV vs RHE
[111]	E peak	188
[100]	E peak 1	150
	E peak 2	178
[110]	E peak 1	178
	E peak 2	193

***Table 9**. Exposed facets and their UPD potentials on monocrystals. Data obtained from "Phase Formation in the Underpotential Deposition of Metals by A. Bewick, J. Jovicevic and B. Thomas". Data converted from Pb reference to RHE.*

Looking at the obtained data it seems that the main exposed face is the 111 but the peak is too broad to be sure. The peak shift is clearly related to different exposed facet on the surface, but the peak is still too broad (different facets exposed at the same time) to have a clear information about the main one.

For these reasons, UPD analysis were performed on a series of pure Cu(0)@(-0.245)V electrode and Cu(0)@(-0.545V). We can clearly notice how the Pb UPD peak is largely shifted for the two measurements while the area (related to the amount of available surface area is more or less the same, as showed by Table 10.

Table 10 The areas are calculated with the use of Origin 2016® considering only the first half cycle. Indeed, the surface area is calculated based on the charge recorded during the reduction peak of the first monolayer. In some specific UPD, like the one of Au with Cu, is possible to obtain the same information from the oxidation (see. Appendix 3) of the previously deposited monolayer. Then a baseline is draw starting from the first point of the CV where a pure capacitive behaviour is recorded on the electrode. The area under the curve gives the total charge passed for the deposition of the monolayer.

Then using the specify charge (310 $\mu C \cdot cm^{-2}$ for a complete coverage of the surface[323]) and considering the scan rate ($5mVs^{-1}$ for all the measurements) is possible to obtain the surface area in cm^2.

The used equation is:

$$Area = \frac{Q_{Pb}}{Q_S}$$

Where Q_{Pb} is the charge passed only during the deposition peak of Pb^{2+} in C while Q_S is the specific charge for the reaction.

The Area under the curve is calculated as follow from the CV first cycle.

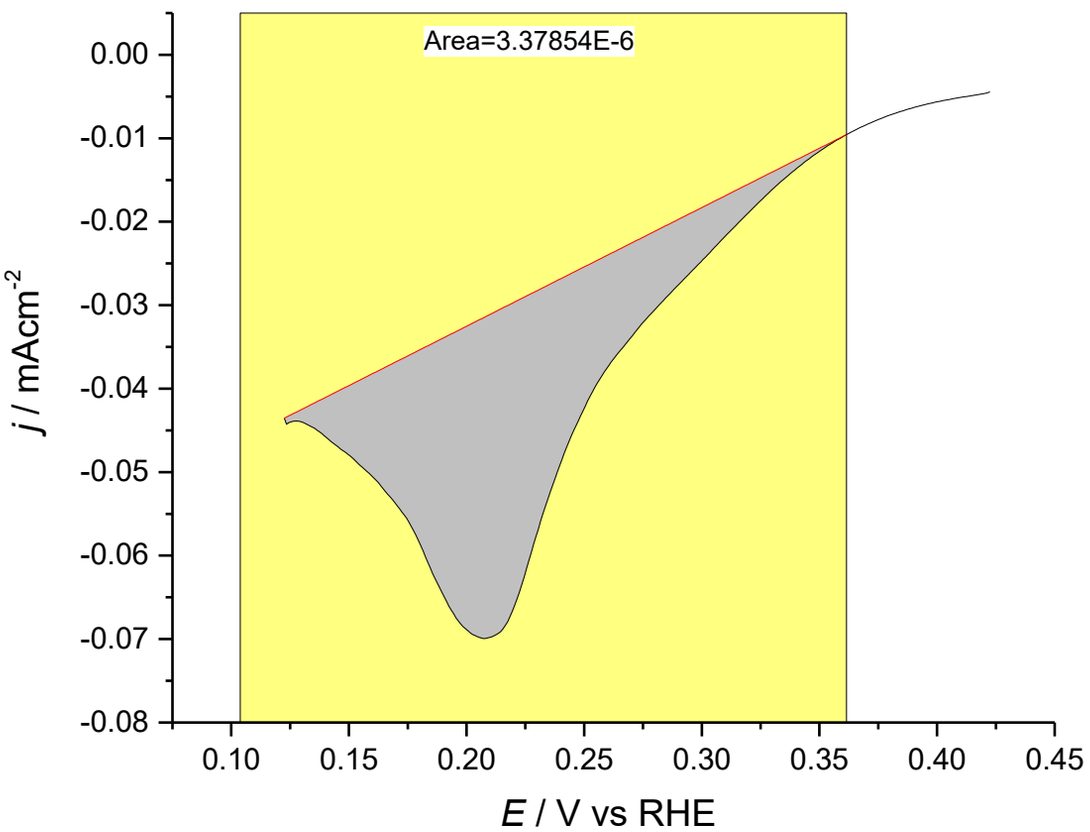

Figure 76. *Example of area evaluation from an UPD cathodic half-cycle. The baseline is constructed in the same way for all the reported electrodes. UPD bath: $Pb(OAc)_2$ 0.01, $NaClO_4$ 0.5M and $HClO_4$ 0.001M at pH 5.5. Scan rate 5mVs^{-1}, counter Pt.*

The obtained values are reported in the following table.

Electrode #	Deposition potential	Charge (C)	Area (cm^2)
18	-0.245	$4.09x10^{-6}$	0.0132
19	-0.245	$3.79x10^{-6}$	0.0122
25	-0.245	$3.28x10^{-6}$	0.0101
20	-0.545	$2.55x10^{-6}$	0.0082
21	-0.545	$3.06x10^{-6}$	0.0099
26	-0.545	$2.98x10^{-6}$	0.0096

Table 10*. Summary of area recorded for -0.245 and -0.545 V deposited Cu on FTO.*

All the Cu(0) electrodes deposited at -0.245 V vs RHE show the same peak position and surface area proving the high reproducibility of the results. Same for the one deposited at -0.545V vs RHE.

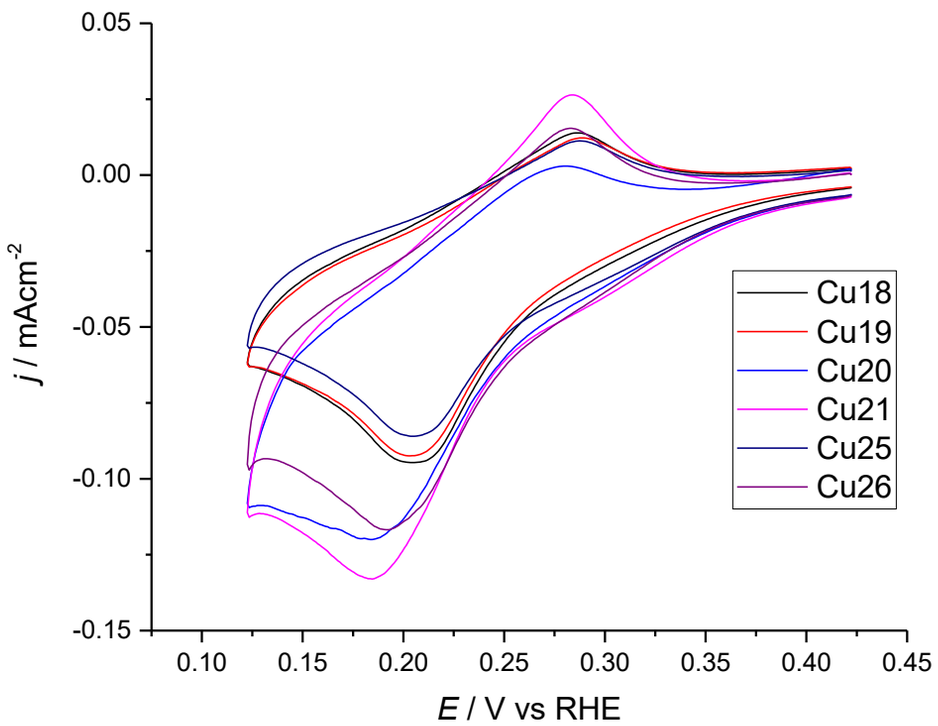

***Figure 77**. UPD cyclic voltammetries of 3 Cu electrodes deposited on FTO at -0.245V vs RHE (Cu18, 19 and 25) and 3 Cu deposited at -0.545V vs RHE (Cu 20, 21 and 26). The plot shows the good reproducibility between measurements and the different peaks positions. UPD bath: $Pb(OAc)_2$ 0.01, $NaClO_4$ 0.5M and $HClO_4$ 0.001M at pH 5.5. Scan rate 5mVs^{-1}, counter Pt.*

2.1.3.3 Spectrophotometer Measurements

To evaluate the differences between the two Cu(0) deposition potentials spectrophotometer measurements were performed. Indeed, with a simple visual analysis is immediately possible to notice how the electrodes with the same type and amount of Cu_2O showed different colours if deposited on Cu@-0.545V, Cu@-0.245 or on the bare FTO. The colour is important in photochemistry because is related to the absorption coefficient of the material.

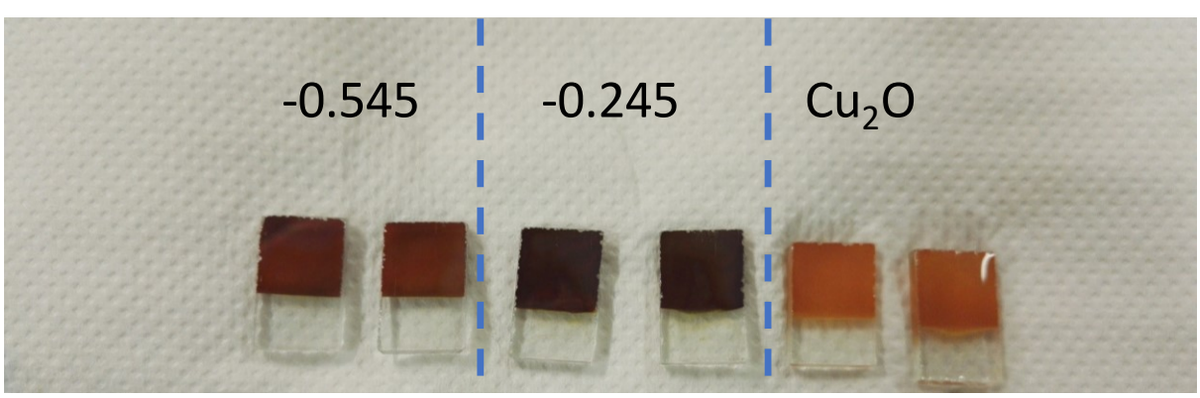

***Figure 78**. Photo of two Cu_2O@Cu@FTO electrodes deposited at -0.545V vs RHE (on the left) and at -0.245V vs RHE (in the middle) and Cu_2O on bare FTO (on the right). The different colour is a proof of a different absorption or of a different particles size.*

For this reason, an absorption spectrum of a Cu_2O@Cu(-0.245V)@FTO electrode, of a Cu_2O@Cu(-0.545V)@FTO and of a simple Cu_2O@FTO were measured using a spectrophotometer with integral sphere. The use of integral sphere was mandatory to study the reflection of a solid sample. The results are reported below with a previous smoothing of the original data.

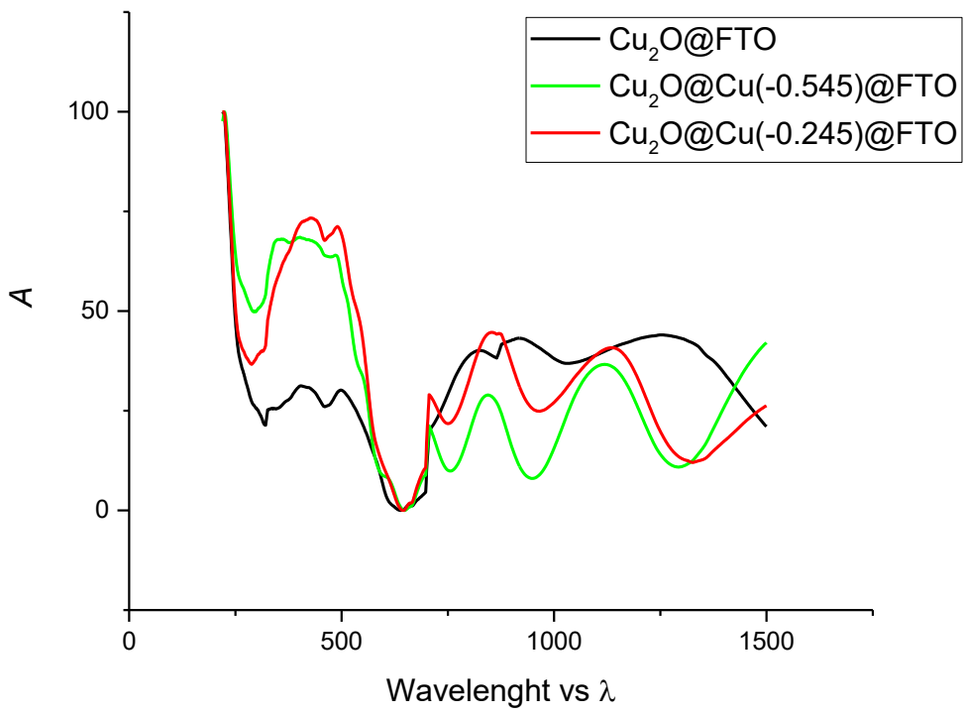

Figure 79. *Absorption spectra of 3 different supported Cu_2O electrodes; Cu_2O@Cu(-0.245)@FTO (red), Cu_2O@Cu(-0.545)@FTO (green) and Cu_2O@FTO (black) recorded with integral sphere.*

The absorption spectra recorded were unfortunately not fully understandable probably due to multilayered structure and because of the impossibility in having a proper background sample (differences in colour are present even in the Cu underlayer if deposition occurs at different potentials). Despite this, is possible to clearly see the absorption peak around 500nm as expected for a red sample and a higher absorption in presence of a metallic underlayers. This measure tells us that the absorption is higher not if the absorbed light can be used for the electron excitation inside the material.

2.1.3.4 Electrochemical Characterization in Dark

Linear sweep voltammetries of Cu_2O@FTO and Cu_2O electrodeposited on Cu@-0.545V and Cu@-0.245V were performed in dark. It was found that there are quite different onsets for the reduction of the material to metallic copper. From this point of view seems that the most stable electrode is the one deposited on an underlayer of Cu(0) deposited at -0.545V vs RHE. Then comes the electrode deposited at -0.245V vs RHE and finally the less stable material is the Cu_2O deposited on the bare FTO. A higher window of activity for the material, before Cu_2O→ Cu reaction, allows to work at higher potential without transform the electrode (although from photoactivated reactions).

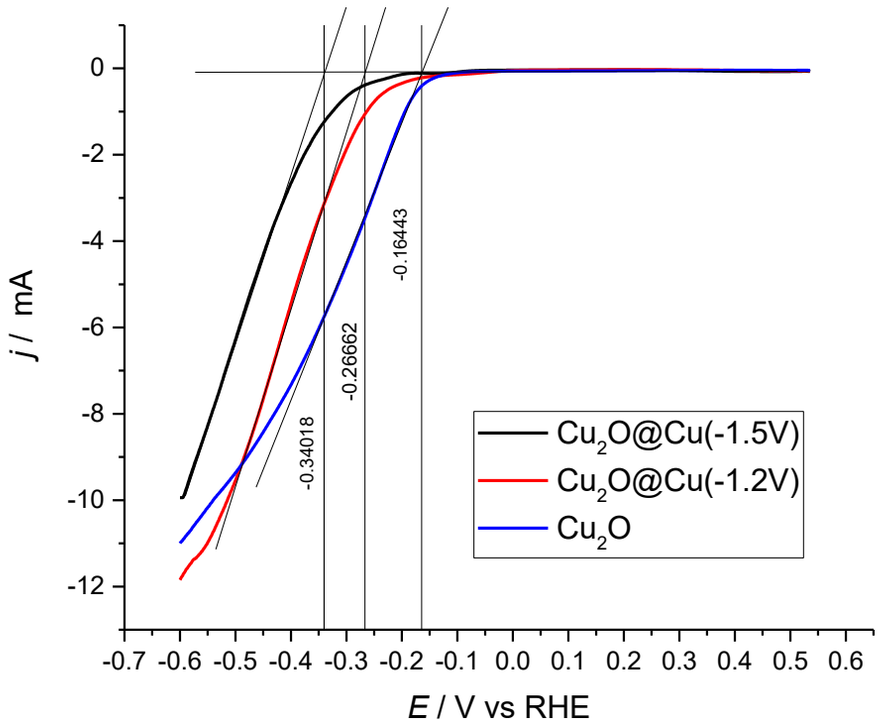

Figure 80. *Electrochemical reduction in dark of Cu_2O@Cu(-0.545V)@FTO (in black), Cu_2O@Cu(-0.245V)@FTO (in red) , Cu_2O@ FTO (in blue). Linear Sweep Voltammetries performed in Na_2SO_4 0.5M + NaOH 0.5M at 10mVs^{-1}.*

2.1.3.5 XAS Study of the Different Underlayers

The role of the underlayer was evaluated from the structural point of view with the use of XAS. Three Cu_2O electrodes were prepared on different substrates: FTO, Au@FTO (as a reference of the literature) and Cu@FTO. An EXAFS spectrum was recorded outside the solution for each kind of electrode and then compared with the Cu_2O standard pellet.

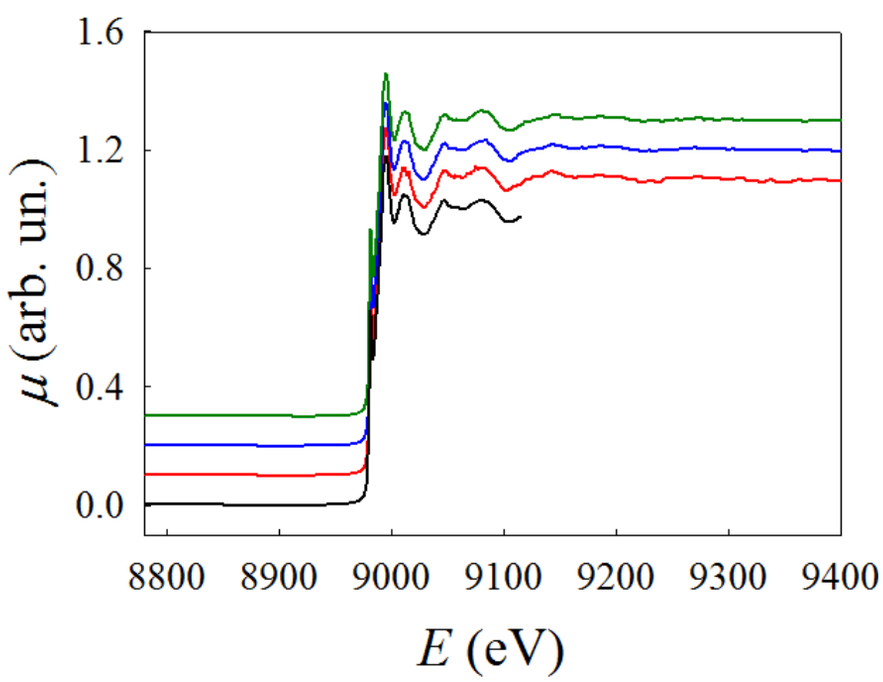

Figure 81*. XAS spectra recorded at the Cu-K edge: Cu_2O standard (black), Cu_2O@Au(PVD)@FTO (blue), Cu_2O@Cu(-0.545)@FTO (red), Cu_2O@FTO (green). The spectra are shifted on the y-axes for the sake of clarity.*

The spectra were recorded at the Cu-K edge at ESRF, the synchrotron facility in Grenoble (France) in the Italian beamline LISA. Spectra are shifted on the y-axes for the sake of clarity or they will completely overlap. The XANES region confirm the oxidation state +1 because the absorption edge of the standard and of the different electrodes falls exactly at the same energy. To evaluate any possible differences in the chemical surrounding the EXAFS signal were elaborated.

Cu_2O@Cu@FTO

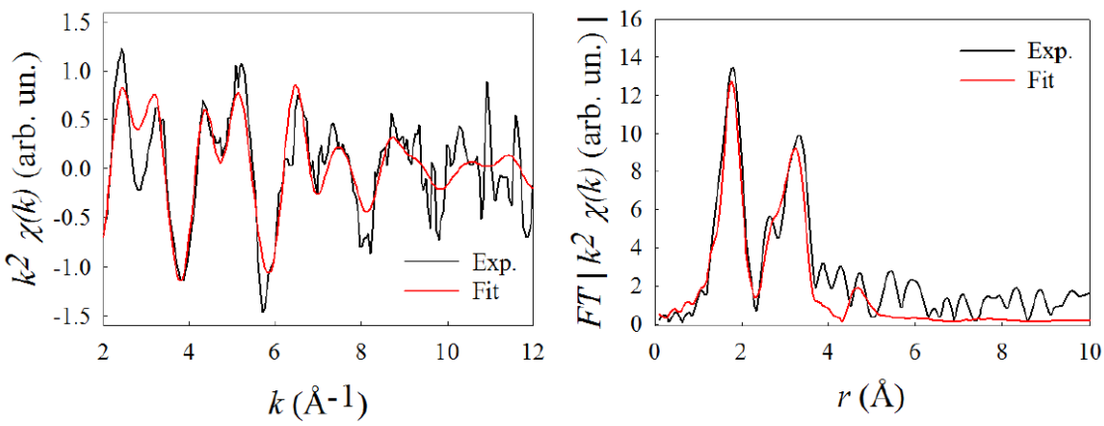

***Figure 82**. EXAFS spectra (on the left) and FT (on the right) for the Cu_2O@Cu(-0.545)@FTO electrode. The black line is the experimental data while the red one is the theoretical one after the fit.*

Shell	N	Atom	r (Å)	σ^2 (Å^2)	r_0 (Å)*
1	2	O	1.90(2)	0.007(3)	1.849
2	6	Cu	2.94(2)	0.010(2)	3.019
3	6	Cu	3.10(2)	0.010(2)	3.019

***Table 11.** Fitting parameters for the local surrounding of Cu in the Cu_2O@Cu(-0.545)@FTO electrode*

Cu_2O@Au@FTO

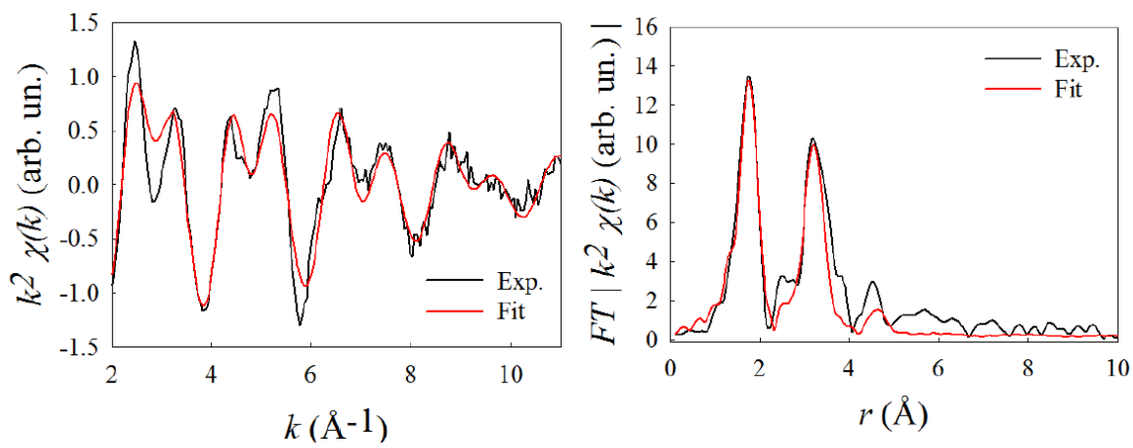

***Figure 83.** EXAFS spectra (on the left) and FT (on the right) for the Cu_2O@Au@FTO electrode. The black line is the experimental data while the red one is the theoretical one after the fit.*

Shell	N	Atom	r (Å)	σ^2 (Å^2)	r_0 (Å)*
1	2	O	1.89(2)	0.009(2)	1.849
2	6	Cu	2.89(3)	0.020(6)	3.019
3	6	Cu	3.04(2)	0.012(2)	3.019

Table 12. *Fitting parameters for the local surrounding of Cu in the Cu_2O@Au@FTO electrode*

Cu_2O@FTO

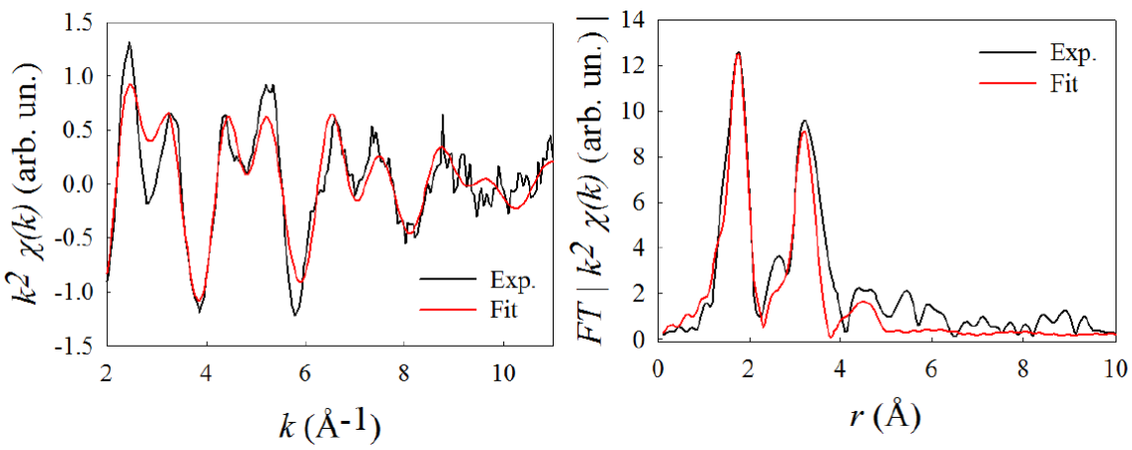

Figure 84. *EXAFS spectra (on the left) and FT (on the right) for the Cu_2O@FTO electrode. The black line is the experimental data while the red one is the theoretical one after the fit.*

Shell	N	Atom	r (Å)	σ^2 (Å^2)	r_0 (Å)*
1	2	O	1.89(2)	0.010(2)	1.849
2	6	Cu	2.90(4)	0.021(8)	3.019
3	6	Cu	3.04(2)	0.014(3)	3.019

Table 13. *Fitting parameters for the local surrounding of Cu in the Cu_2O@FTO electrode*

Looking at the structural parameters obtained of the EXAFS spectra is possible to notice how there are no significative differences because all the variances (coordination distances and Debye-Waller parameter) are within the error.

From this we can conclude that the presence of an underlayer does not change the local chemical surrounding of Cu in the three electrodes. All the differences in the final performances so must be related to some changes in the electrode that is not possible to identify with the use of XAS.

2.1.3.6 Results with Different Underlayers

The Cu_2O photoelectrodes on different substrates were then tested under irradiation to evaluate their performances. Two light sources were used in this work: a solar simulator and a green LED light. The solar simulator settled at 1.5AM is the closer one to the natural light that every day reach our planets in terms of intensity and wavelength range. The second source is a high intensity LED (LEDENGINE LZ1-00G102) with a single wavelength of 523nm. The green light is indeed the one mostly active for a reddish material like Cu_2O. Off course this light cannot be compared to the sun one but is used to obtain high excitation of the material and obtain relatives comparison between the different electrodes prepared.

The electrodes were tested in an optical glass cell with a flat window. The use of this material ensures to reduce to the minimum the amount of UV light absorbed by the glass itself. Tests were carried out in $NaHPO_4$ 0.5M + NaOH 0.5M purged with nitrogen for 30 minutes. During tests, the counter electrode was a platinum foil and the reference is an SCE in a double bridge. Two different types of measurements were performed on each electrode, a Linear Sweep Voltammetry (LSV) and a potentiostatic measurement. The former was carried out under pulsed light at the scan rate of $10mVs^{-1}$ from 0.523V to 0.13 V vs RHE. The latter was done working under pulsed light at 0.175 mV. The measures were performed in a closed metal box able to prevent ambient light from reaching the electrode and working as a Faraday cage as well.

As showed below under light the material generates a cathodic current of water reduction to H_2 before the thermodynamic potential of HER is reached. The light is indeed able to generate the electron-hole couple responsible for the reaction.

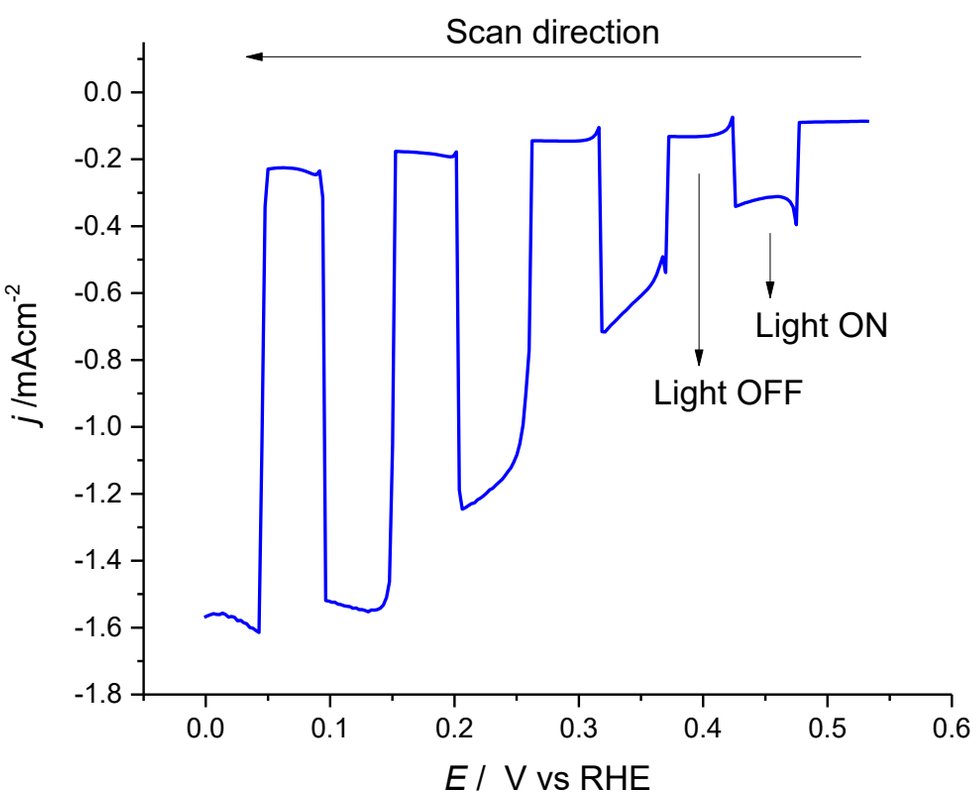

Figure 85. *Example LSV under pulsed light of a Cu_2O@Cu(-0.545V)@FTO sample. Under light is possible to recognize a cathodic current of water reduction not present in dark condition.*

The working electrode was always a Fluorine Tin doped Oxide glass (FTO), a special glass with a nanometric layer (20nm) of a conductive transparent oxide deposited on one of the sides of the glass, within or without selected metallic underlayers on the top of it. The studied underlayer material were:

1. Bare FTO electrode. So prepared electrodes were marked as Cu_2O@FTO. The FTO was previously washed in an ultrasound bath for 30 minutes in acetone, 30 minutes in ethanol and 30 minutes with water. This long procedure allows to remove any trace of skin grease and dust, who have a very strong influence in decreasing the final performances of the material under irradiation. The electrodes were then dried under N_2 flux before being used, otherwise they were kept in distilled water to avoid any type of contamination. To increase the first nucleation of Cu_2O grain the potentiostatic deposition of Cu_2O is preceded by a short potentiodynamic measurement (at $10mVs^{-1}$) until 0.25 V vs RHE (see Figure 70). Then, without removing the electrode from the solution the potential is moved to 0.55 V and the deposition was performed until the desired amount of charge was reached. During Cu_2O deposition no stirring is applied, and the temperature is kept constant at 60°C.
2. Au electrode. The so prepared electrodes were labelled as Cu_2O@Au@FTO. A thin layer (about 200nm) of gold is deposited on the bare a previously cleaned FTO (see procedure from point 1) using physical Vapour Deposition (PVD). Cu_2O is deposited directly at the potential of 0.55 V vs RHE because, as seen previously, once a metallic underlayer is applied the deposition occurs earlier. This underlayer was tested as term of comparison between our results and literature. In some specific measurements (XAS study of material degradation) it has been preferred in order to avoid interference from the Cu underlayer in the signal from the Cu_2O.
3. Cu electrode. The so prepared electrodes were labelled as Cu_2O@Cu@FTO. On a previously cleaned FTO, metallic copper is electrodeposited from the same deposition bath of the semiconductor. The only difference is that the bath is kept highly stirred, at 30°C and with a potential of -0.545 or -0.245V vs RHE. The potentials were chosen to be just slightly negative respect to the reduction peaks position recorded in the CV. The temperature during both metallic copper deposition was kept constant at 30°C with the use of a thermostatic bath. This temperature indeed preferentially forces the formation of metallic copper with respect to Cu_2O. The amount of metallic copper was controlled with the charge passed within the electrode. Different values of these parameters were tested as explained later.

Some differences were recorded during the potentiostatic deposition of Cu at the two different potentials. As is possible to see from Figure 86 the currents are largely different, and this can affect grains size, shape and orientation giving the differences showed before.

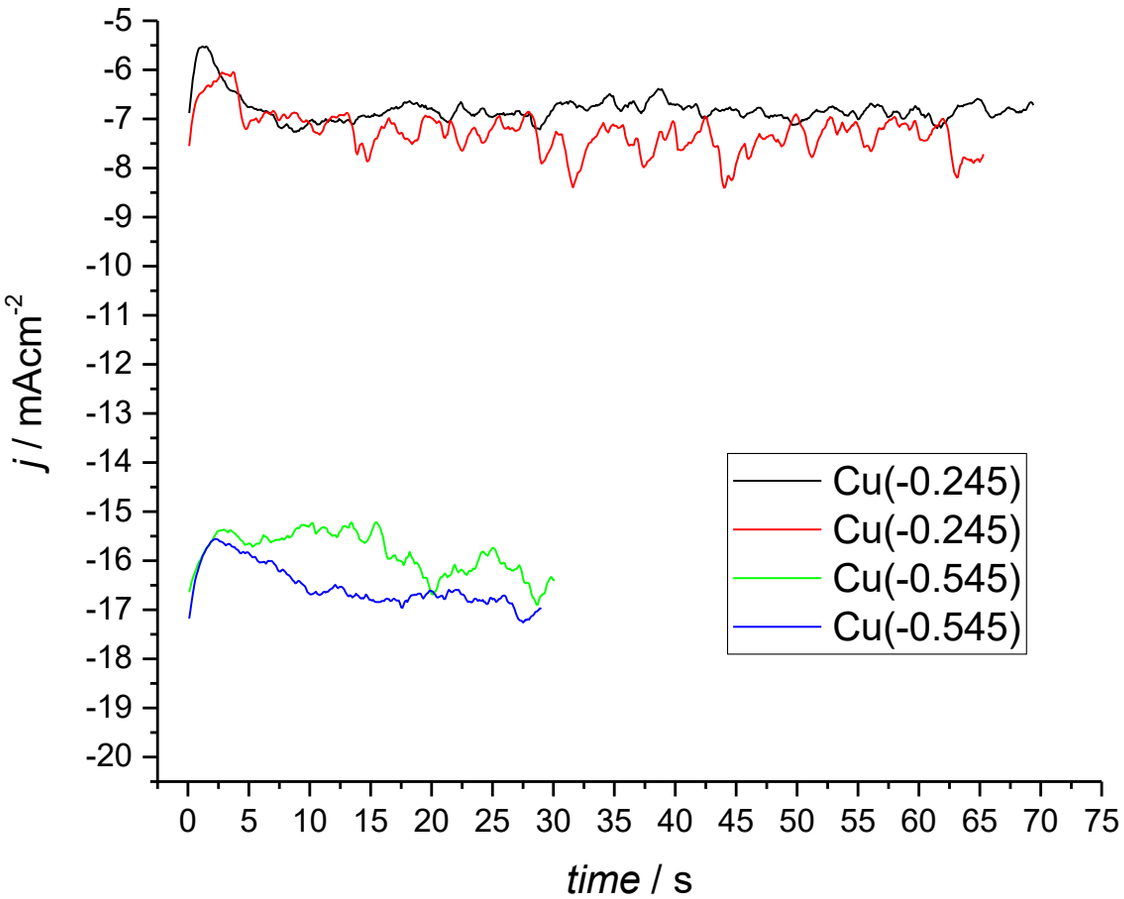

Figure 86. *Deposition currents recorded during Cu(0) deposition at -0.245V vs RHE (black and red) and at -0.545V vs RHE (green and blue).*

We can see how working at -0.545V vs RHE currents are more than 2 times higher. Being the amount of charge constant obviously the deposition times are reduced. Measurements are quite noisy due to the magnetic stirring performed during the deposition at both the potential.

All the depositions were carried out in a thermostatic 3-electrodes cell inside a Faraday cage. The used cell was accurately sealed to avoid evaporation of the solution during Cu_2O deposition. A platinum foil (2x1 cm) was used as counter electrode and the reference was a Saturated Calomel Electrode (SCE) in a double bridge filled with KNO_3 0.5M to avoid Cl^- interferences.

The electrode was then sealed with a Teflon® stripes to be sure that the available are is $1cm^{-2}$. The Cu_2O deposition then occurs until the required amount of charge is reached (usually 0.47 $C \cdot cm^{-2}$) then the electrodes were rinsed with water and immediately tested.

Looking at the deposition current for Cu_2O (Figure 87) we can see how the deposition currents are extremely similar while a slight difference is present on the deposition on gold. A particular behaviour was found for a certain amount of Cu_2O@FTO electrode where the currents have a double inversion in direction.

This was previously noticed by other authors[309] who claim Cu_2O follows in its deposition on FTO a 2D instantaneous nucleation mechanism (IN-2D) where nuclei are formed at the beginning of the electric pulse.

The first layer is then the one controlling shape and morphology of the next ones. This complex shape is related to the existence of different processes. Once the potential is applied, current sharply decrease (in absolute value) then start increasing again going for a plateau. The peak corresponds to the charge of the double layer and the beginning of the reduction process. According to Bijani the peak is mostly related to the adsorption of Cu(I) lactate species onto the clean substrate. While on gold and Cu the formed Cu_2O is immediately oriented leading the current to a plateau, on FTO an initial decrease due to an initial difficult grain formation is encountered, then the grown increase stabilizing to lower value of current as time goes on because of the low conductivity of Cu_2O.

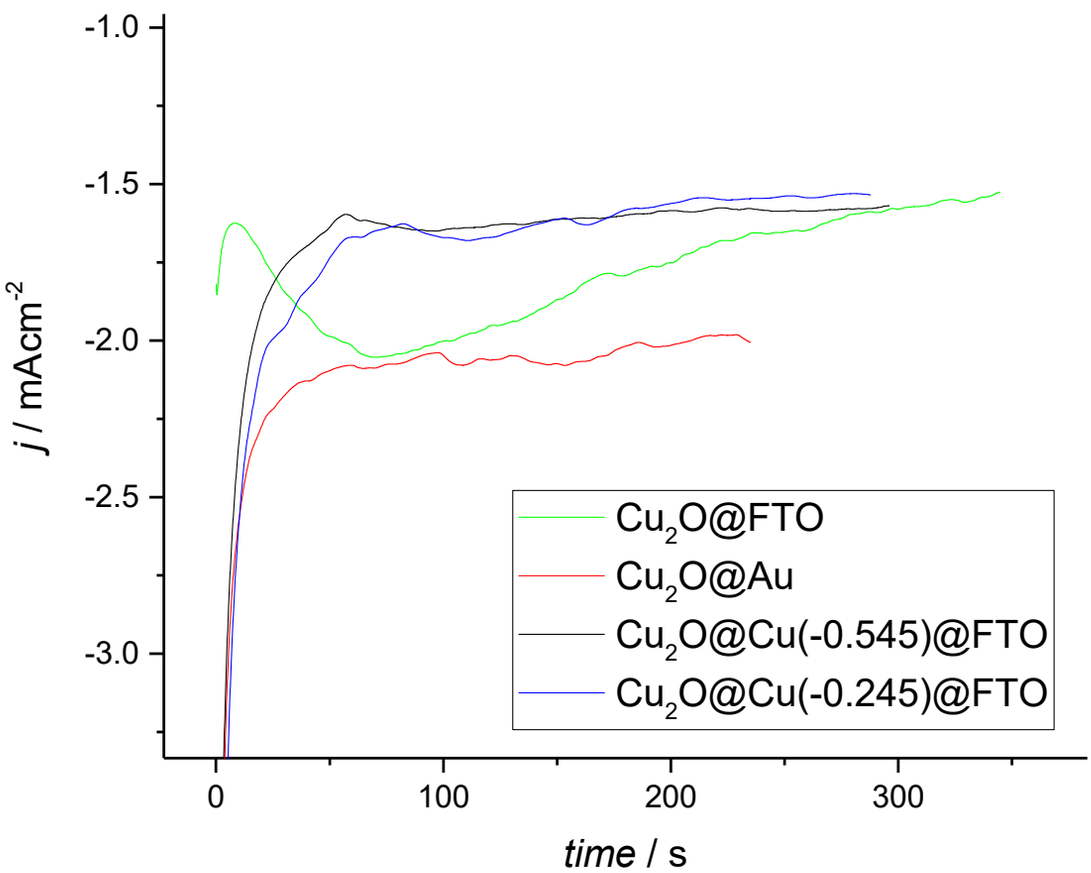

Figure 87. *Deposition currents recorded at -0.4V vs SCE during Cu_2O deposition on different substrates; FTO (green), gold (red), Cu deposited at -0.545V vs RHE (black) and Cu deposited at -0.245 V vs RHE.*

The following measurements show the different performances of the so prepared electrodes under working conditions. Every type of electrodes was performed several times obtaining high reproducibility.

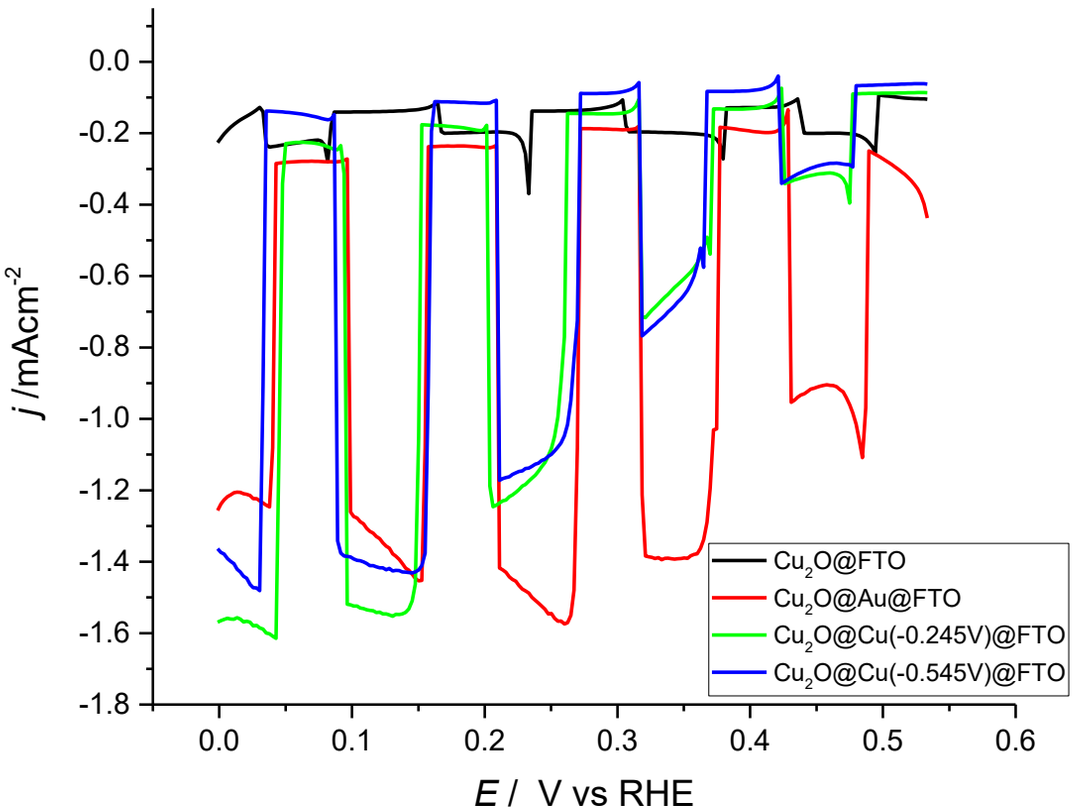

Figure 88. *Linear Sweep Voltammetries at 10mVs^{-1} performed in $NaSO_4$ 0.5M +0.5M NaOH on differently supported electrodes. Cu_2O@Au(PVD)@FTO (red), Cu_2O@Cu(-0.245)@FTO (green), Cu_2O@FTO (black) and Cu_2O@Cu(-0.545)@FTO (blue). Measurements taken under pulsed solar simulator light (1.5AM) in N_2-purged solution. Counter Pt.*

From Figure 88 we can notice the great importance of the underlayer. The black line is the Cu_2O deposited on the bare FTO, thus without any underlayer. Photocurrents are one order of magnitude lower than the other electrodes. This was a first proof of the great importance of the presence of an underlayer. The presence of a metallic underlayer strongly affect the amount of hydrogen produced by this material. Even in a comparison between Au and Cu underlayer we can see how the currents are high in both the case, but gold is able to generate high current at lower (less negative) potential, while with a copper underlayer, the photocurrents are higher, but a more negative potential are needed. Despite this, Cu(0) is still an interesting alternative to the use of gold (as suggested by literature) because of its lower cost and easier applicability. Indeed, it can simply be deposited from the same deposition bath of the semiconductor changing potential, temperature and stirring condition.

Despite the recorded differences in the analysis of the two possible types of Cu(0) once we move to a pulsed light measurement any differences between the two layers disappears and the obtained photocurrents are the same at all the potentials. Some differences are obviously present, but they will not affect the photocurrents that is the main parameter we are interested in. Different categories of Cu_2O@Cu@FTO electrode were then prepared. In particular, was evaluated the influence of the amount of material in the underlayer, the amount of Cu_2O, and the pH of the electrolyte for the electrodes testing.

2.1.4 Influence of Underlayer Loading

The influence of the underlayer was studied only on the Cu(0) underlayer because is the one that can be easily controlled in thickness and homogeneity with the amount of charge that passed into the electrode. Even if part of this charge can be related to the hydrogen evolution, occurring especially at -0.545V vs RHE, the absence of bubble on the electrode, together with some check at the analytical balance of the amount of material deposited allow us to consider Cu(0) the main species deposited at these potential (-0.545 and -0.245V vs RHE).

The following amount of charge were considered together with the theoretical thickness of the layer considering 100% cathodic efficiency for the deposition process.

Electrode number	Total charge (C)	Thickness (cm)
El 78 - 79 - 80	2.5	9.19 x10^{-5}
El 84 - 86 - 88	1	3.5 x10^{-5}
El 81 – 82 -83	0.47	1.73 x10^{-5}
El 65 -66 -67- 68	0.25	9.19 x10^{-6}
El 85 - 87	0.13	4.78 x10^{-6}

Table 14. *Summary of the electrodes tested with different underlayer loadings reported as charge passed through the electrode.*

Please consider that in the table for clearance is reported only one value of the calculated thickness. This value is calculated using the following equation:

$$Thickness = \frac{Charge * MM}{n * 96485} * \frac{1}{d} * \frac{1}{A}$$

Where "*Charge*" is the integrated charge passed into the electrode obtained by the instrument (in Coulomb), *MM* is the molecular mass (in g·mol^{-1}), *n* is the number of electrons, *F* is the faraday constant (96485 C/eq), *d* is the Cu density (in g·cm^{-3}) and *A* is the area of the electrode (usually 1cm^2, but any results refers to a calculated geometrical area of the surface).

In Figure 89 are reported Cu_2O@Cu(-0.545)@FTO electrodes with no differences in the Cu_2O layer that is the active part of the electrode. The only difference is in the amount and thickness of Cu(0) layer that is increased from 0.13C to up to 20 times (2.5C). The result clearly shows an increase in the recorded photocurrent densities (in absolute value) with the loading of the underlayer until a plateau is reached. This can be explained considering that increasing the thickness of the underlayer it increases the conductivity of the layer. Once the higher value is reached and the layer is homogeneous enough the photocurrents reach a plateau and no further improvements can be achieved. To balance performances with substrate transparency the value of 0.47C was chosen for further deposition. In this way, the electrode is still transparent enough to be able to work in a back configuration in the tandem cell but has the higher value of photocurrent obtainable. These data were obtained with the use of the green LED light.

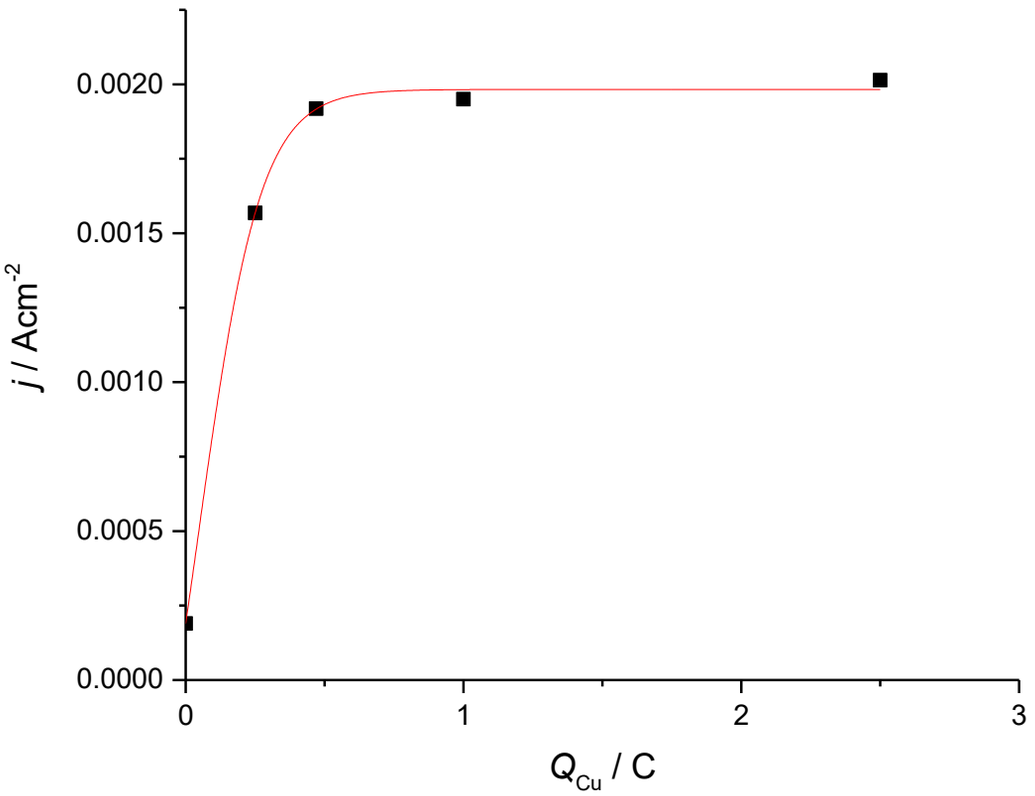

Figure 89. *Photocurrent densities recorded on Cu_2O@Cu(-0.545)@FTO with different amount of Cu. Photocurrent densities are reported in absolute value for sake of clarity.*

2.1.5 Influence of Semiconductor Loading

On the other side, was tested the influence of the loading of the semiconductor. Here we can be completely sure that the only possible reaction is Cu_2O deposition because we are quite far from any other faradic peak. The thickness of the semiconductor layer was again tested for the Cu_2O@Cu(-0.545)@FTO electrode and evaluated on the base of the charge using the equation showed in the previous paragraph.

The following table report the values tested and their calculated thickness.

Electrode number	Charge (C)	Thickness (cm)
El 63 – 64	0.25	$6.18x10^{-5}$
El 59 - 60	0.5	$1.24x10^{-4}$
El 58 – 65	1	$2.47x10^{-4}$
El 67 – 68	2	$4.94x10^{-4}$
El 61 - 62	4	$9.89x10^{-4}$

Table 15*. Summary of the electrodes tested with different semiconductor loadings reported as charge passed through the electrode.*

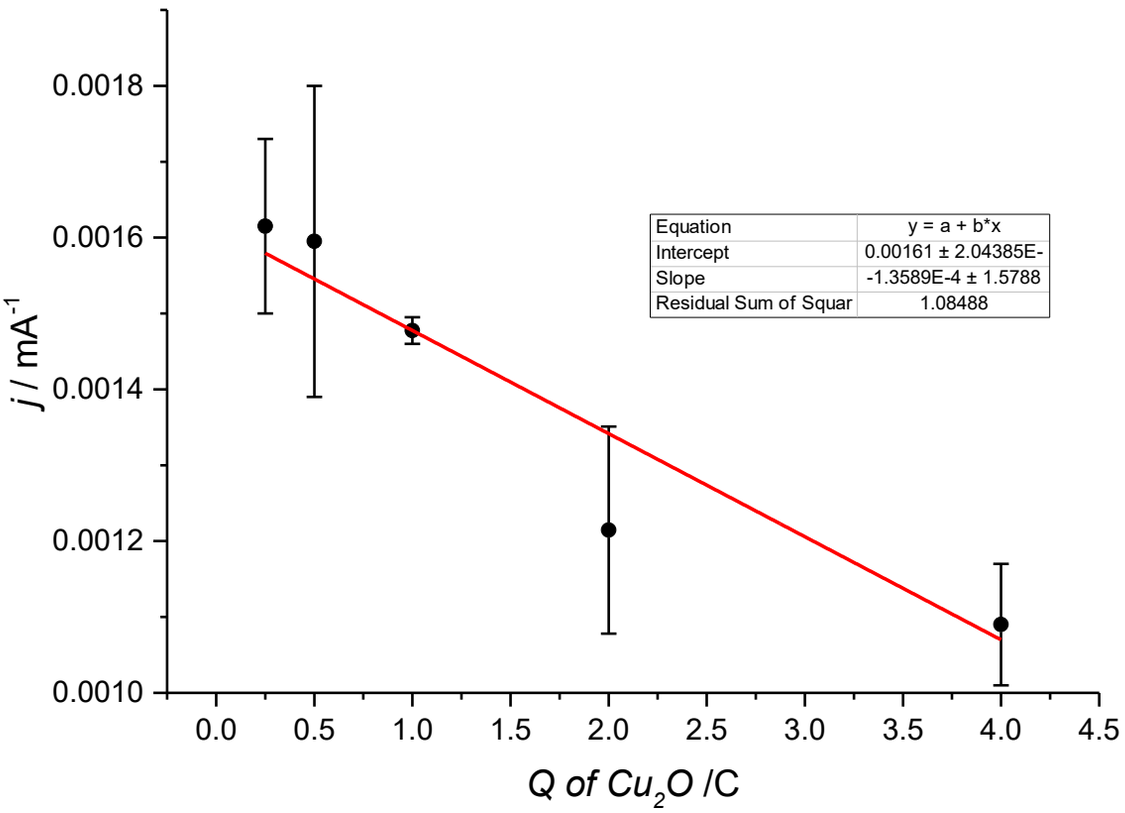

Figure 90. *Photocurrent densities recorded on Cu_2O@Cu(-0.545)@FTO with different amount of Cu_2O. Photocurrent densities are reported in absolute value for sake of clarity.*

From the comparison plot of Cu_2O@Cu(-0.545)@FTO electrodes with the same amount of Cu (0.47C) but different loading of Cu_2O is clear how increasing the amount of semiconductor the performance quickly decreases. This can be explained considering that only the upper layer of the material can be reached by light and so be active toward the reaction:

$$Cu_2O + 2h\nu + 2H^+ \rightarrow Cu_2O + H_2$$

In this way any additional layer can be consider as an increase in the sample resistance due to the poor conductivity of Cu_2O and moreover can enhance the possibility of electron-hole recombination. With these measurements was possible to evaluate the best amount of semiconductor to have high current and still a good homogeneity.

Thinner thicknesses were not considered to avoid inhomogeneity (with 0.08C of Cu_2O a decrease in photocurrent was recorded but the layer was not homogeneous so that data are here not considered) of the layer and wider ones were avoided because the drop of photocurrent was just too high with 4C Cu_2O.Those data were obtained with the use of the green LED light. In conclusion, the selected value was 0.5C as a balance between performances and layer homogeneity.

2.1.6 The pH Influence

Eventually, a series of different pH buffer electrolytes were tested to see the influence of ionic strength and pH on the photocurrents. In particular, the following buffers were used[324–326]:

- Na_2SO_4 1M +K_2HPO_4 0.1 M: pH 5
- Na_2HPO_4 0.5M + KH_2PO_4 0.5M: pH 7
- $Na_2B4O_7x10H_2O$ 0.1M: pH 9
- NaH_2PO_4 0.5M + NaOH 0.5M: pH 11
- Saturated $Ca(OH)_2$: pH 13

Buffer pH 5 is the one used by literature. Is supposed to be the best one because still in the stability range of Cu_2O (See Poubarix diagram in Introduction) but also because acid pH should favour the hydrogen evolution reaction.

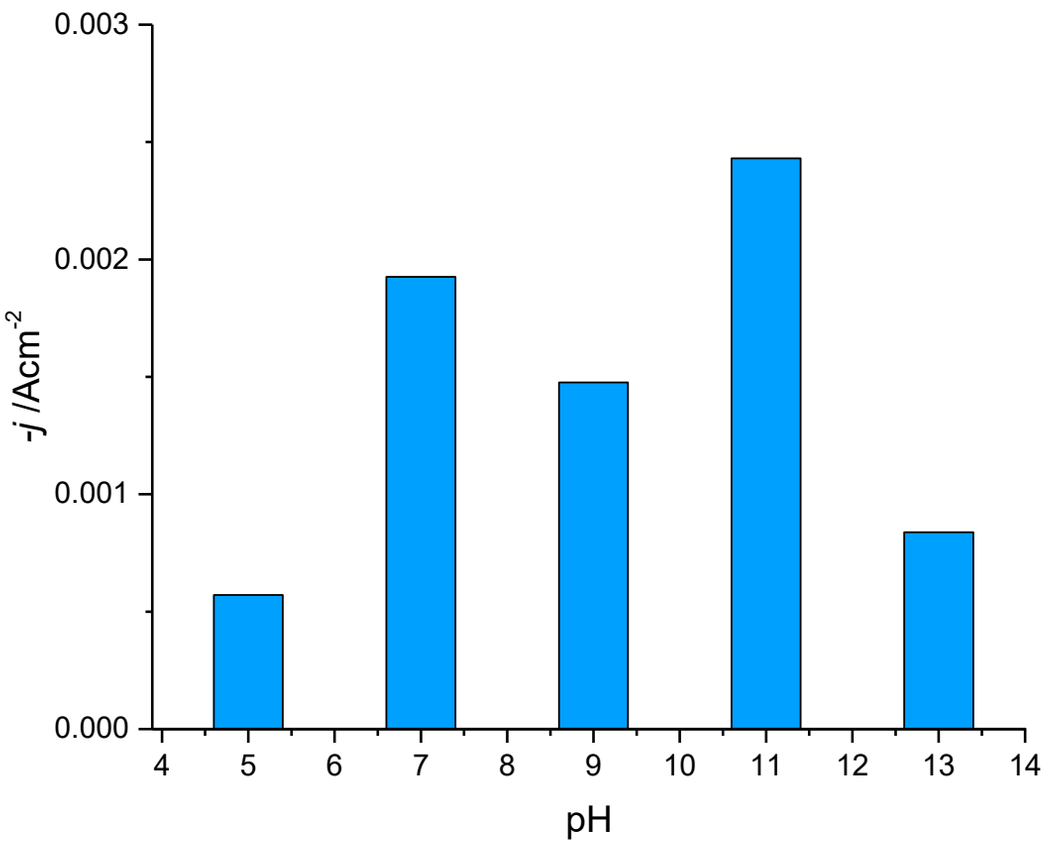

Figure 91. *Photocurrent density recorded on Cu_2O@Cu(-0.545)@FTO electrodes in different pH buffered solution. Photocurrent density are here reported in absolute value for the sake of clarity.*

From these measurements in standard buffered electrolytes it was possible to identify the best pH for the performance evaluation of the Cu_2O@Cu(-0.545)@FTO. It was found that pH 11 was surprising the best one while the electrolyte taken from literature seems to be able to give only less than 25% of pH 11 photocurrent densities. These data were obtained with the use of the green LED light.

2.1.7 Conclusions

In this first section were pointed out some parameters useful to increase the performances of the Cu_2O photoelectrode. First, was noticed the extremely high influence of the presence of a metallic underlayer in Cu_2O PEC-WS system with one order of magnitude increase in recorded photocurrent. Thus, the study of the electrochemical bath allows to determine the possibility of metallic copper deposition from the same solution for the Cu_2O. This have a series of advantages; first allows to avoid the use of expensive materials like Au and toxic ones like Cr but moreover allows to have a simple synthesis that do not need to use complex procedures and expensive techniques. Is indeed enough to change the temperature, the stirring condition and of course the potential to obtain a metallic underlayer with high homogeneity and that allows Cu_2O to have performances comparable to those of Au. From an industrial point of view these are enormous advantages because a simple and cheap synthesis will largely support the spreading of PEC-WS system as energy storage solutions. The choice between the two different potentials for Cu deposition in the end have given no substantial differences meaning that is mostly the nature of the underlayer respect to its orientation that affect the final performances.

Eventually was evaluated the influence of the loading of both semiconductor and metallic underlayer. It was found that increasing the underlayer loading improve the performance while the opposite trend was recorded for the semiconductor. In particular, the amount of both Cu and Cu_2O is selected to be as small as possible in order to have reduced cost for the material and a good transparency of the layer with the possible implementation of this kind of photocathode in a tandem cell.

2.2 DFT Study of Cu_2O

2.2.1 Introduction

According to the experimental results previously reported, different metallic underlayers gives extremely different performances in the photocurrent recorded on the material. To give an explanation to this phenomenon Density Functional Theory (DFT) was used to study different possible explanations: lattice strain in Cu_2O, the vacancies formation and the possible doping of the semiconductor with dopants from the underlayer.

The role of Density Functional Theory (DFT) is here to rank the underlayers' aptitude in modifying the properties of Cu_2O.

Initially, the influence of lattice strain on material band gap and energy levels is studied both with expansion and reduction of the Cu_2O lattice after the deposition onto different substrates. The lattice mismatch between Cu_2O lattice and the metallic underlayer ones indeed can induce some strain. As example it was found that a Au/Cu_2O core-shell system presents a lattice strain of around 4.3%[327]. The effect of distortion and strain on semiconductor properties like band gap was proved for materials within the perovskite family (ABO_3) and MoO_3 [328,329]. In this work, the possible influence of this effect was tested for Cu_2O.

Moreover, according to literature the p-type character of Cu_2O is indeed strictly related to the formation of copper vacancies in its lattice and this can affect the conductivity. Doping, instead, can enhance the formation of vacancies, improving the number of majority carriers (holes) and their mobility, and modifying the band gap by shifting the Cu_2O states or by introducing an intermediate band within the band gap[281,282,287,292,294]. Based on the electrochemical results obtained with different underlayers, this work firstly aims to study a large array of potentially effective metallic underlayers. The doping of the material is then studied for a selected number of transition metals. For each material, the valence and conduction band positions were computed as well as the number of vacancies and their formation energies.

Eventually, the use of the alkaline metals allowed to evaluate the influence of the dopant size on the doped material decoupling it from the electronic effect induced by the dopant.

DFT calculates the energy of molecules using the electron density, in particular the one of valence electrons, while pseudopotentials[195] are used to approximate the core electrons. The preliminary part of a calculation is the choice of a reasonable starting structure from X-ray databases literature (http://rruff.geo.arizona.edu/AMS/amcsd.php). Once selected the proper parameters for the calculation (required accuracy, spin polarization, energy cut-off, used method etc..) the system provides a final energy for the structure. The quality of the final structure should be checked in comparison with experimental results. With DFT systems with up to 200 atoms can be studied using cheap GGA class functionals. However, to reliably calculate band gaps more accurate methods correcting for the self-interaction error are required. Here either a GGA+U or hybrid functionals are required.

While the latter are more cost intensive they can be considered more reliable as they rely on a large test set when derived. This restricts the computations to significantly smaller systems. Thus, it is necessary to separate the highly complex interface between Cu_2O and the underlayer. The single structure energy itself, if taken alone, is meaningless. Once the energy of all the single specific structures involved in the reaction of interest is obtained is instead finally possible to calculate the energy for the whole reaction thanks to the equation:

$$E_{reaction} = \sum E_{products} - \sum E_{reagents}$$

A negative value corresponds to a spontaneous reaction. Moreover, considering that DFT work at 0°K, all the energies are composed only by the enthalpy contribute. This means that in a real situation, also materials with low positive $E_{reaction}$ could undergo to spontaneous reaction due to the entropic contribute that always work in our favor. Indeed, the vacancy formation in the pure material was computed to be 0.37eV and still this the formation occurs spontaneously. This value will be used as a threshold for the spontaneous vacancy formation.

Of course, all these results were obtained for an idealized model. It is therefore not the aim of these calculations to state absolute numbers but instead to obtain trends and possible explanations for the experimentally observed behavior. As example DFT is well known to underestimate band gaps[221,222]. Despite this, a comparison between the BG of different doped systems can give an idea of which materials increases or reduces the BG respect to the calculated undoped sample.

The use of structures of different sizes allows to be as close as possible to the real system. Generally wider structure gives more reliable results in terms of dopant concentrations (usually 1-3%). In our case was seen that a 2x2x2 supercell composed by 32 Cu atoms and 16 O atoms was enough because the results were very similar to the larger and resources-requiring 3x3x3 supercells[245,246]. In some cases, like for the study of the strain influence, the 1x1x1 supercell was sufficient since lattice variations are not affected by supercell size.

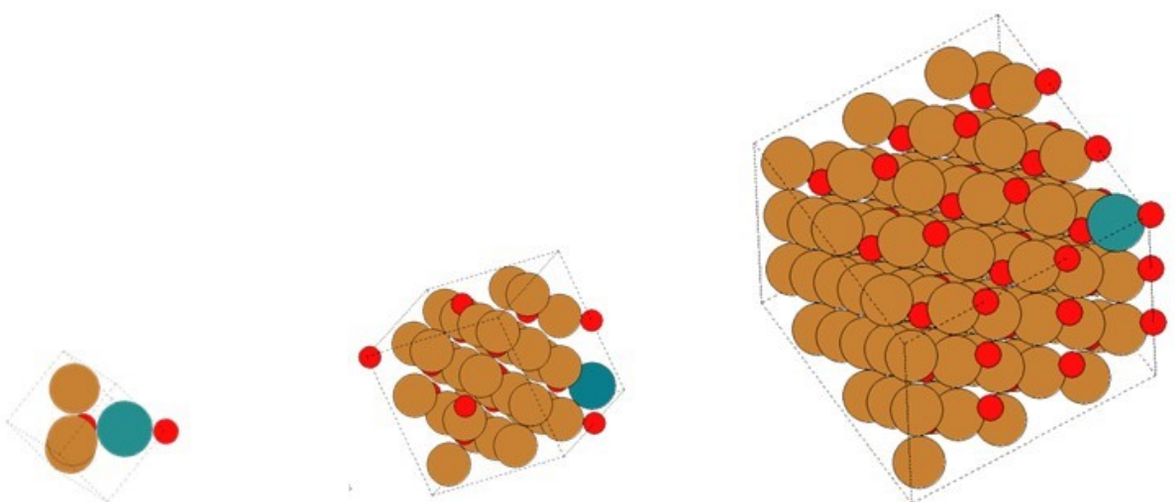

Figure 92. *Cu_4O_2 (1x1x1 supercell), $Cu_{32}O_{16}$ (2x2x2 supercell) and $Cu_{108}O_{54}$ (3x3x3 supercell) studied in this work. Colour code: O – red; blue – dopant; brown – Cu.*

2.2.2 Computational Details

The Vienna Ab-initio Simulation Package (VASP)[330–333] was used to compute an approximate solution of the many-bodies Schrodinger equation which use planes waves to describe the valence electronic states. Version 5.4.1 was used in all the calculations.

2.2.2.1 PBE Calculations

The GGA PBE functional[213,334,335] was used for different purposes during this work because able to provide qualitative information about metal ground state energies and due to the low computational costs associated with a GGA. PBE was used to obtain:

- Metallic underlayers ground state energy (M_4 and M_{32} structures).
- Cu_2O ground state energy with 3 cell dimensions (4, 32 and 108 Cu atoms).
- $MCu_{31}O_{16}$ ground state energy where M is one of the metallic underlayer used.
- $M_{31}Cu$ and $Cu_{31}O_{16}$ ground state energy.
- A converged structure for hybrid functional calculations.
- The most energetic favorable vacancy position in all the doped systems.

All calculations used a 450eV plane wave cutoff in combination with a 5x5x5 (1x1x1 supercell), 3x3x3 (2x2x2 supercell) or 1x1x1 (3x3x3 supercell) k-point sampling for Cu_2O. The metallic structures instead use or 5x5x5 for the 2x2x2 metal supercell or 9x9x9 k-point set for the smaller 1x1x1 one. Both k-point set and plane wave cutoff values were preliminary determined with different calculations for the same Cu_2O supercell. The chosen value is the one in where the total energy is no longer changing to a significant extend.

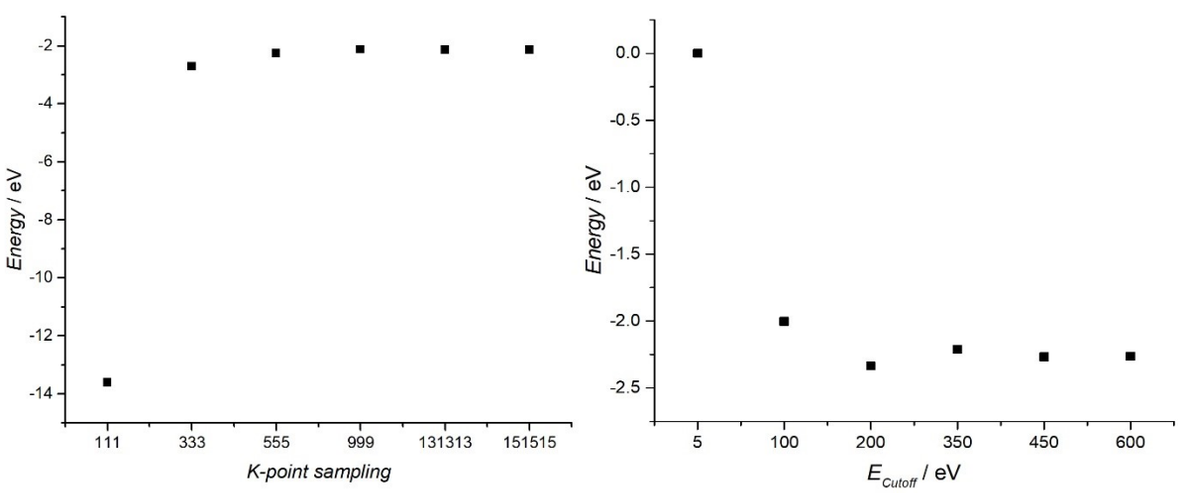

Figure 93. *K-point sampling and $C_{ut\text{-}off}$ value determination on Cu_2O 1x1x1 supercell.*

Core electrons were approximated by Projector Augmented Wavefunctions (PAW)[336]. To improve the convergence of the wavefunction, 0.1 eV smearing were added during the PBE calculations and 0.01 eV for the HSE06 calculations. For spin polarized systems, spin was allowed to converge to the ground state during the calculations of system with one or more vacancies. Metals from *3d* row were computed with fixed spin according to Table 16 while all the other systems were computed close-shell.

Convergence of the electronic structure was assumed for an energy difference of 10^{-10} eV. Geometries were converged using the conjugate gradient algorithm implemented into VASP. Convergence of the structure was assumed for the largest force being below -0.05 eV/Å.

Dopant	Electronic Configuration	Number of free e^-	Tested spin	Chosen spin
Ti^+	$4s^2\ 3d^1$	3	Quadruplet, duplet	Duplet
Cr^+	$4s^2\ 3d^3$	5	Sextuplet, quadruplet, duplet	Sextuplet
Mn^+	$4s^2\ 3d^4$	6	Septuplet, quintuplet, triplet, close-shell	Quintuplet
Fe^+	$4s^2\ 3d^5$	7	Quadruplet, duplet	Quadruplet
Co^+	$4s^2\ 3d^6$	8	Triplet, close-shell	Triplet
Ni^+	$4s^2\ 3d^7$	9	Duplet	Duplet

Table 16. *3d shell dopants with the tested possible spin and the most energetic favourable one in the $MCu_{31}O_{16}$ system.*

2.2.2.2 HSE Calculations

The range separated HSE06 hybrid functional[337], able to consider the electron self-interaction, is a much more computationally expensive method for the evaluation of semiconductor properties but in comparison to PBE is able to give results in BG and DOS that are far closer to the real ones. It was then used on PBE-converged structures of doped, undoped and strained systems to obtain the DOS and the DORI.

During HSE calculations the convergence of the electronic structure was assumed for an energy difference of 10^{-10} eV for the doped system without vacancies, 10^{-6} for system with one vacancy and 10^{-4} if two or more vacancies were present. Indeed, for these last systems no differences were recorded in the DOS shape recorded with higher value.

2.2.2.3 Construction of the Model System

The Cu_2O model system was constructed from the experimental crystal structure given by Hafner[338] according to other authors[34,35,38]. Doping was studied for models containing 1x1x1, 2x2x2 unit cells with 4 and 32 Cu atoms respectively. Doping was studied replacing one copper atom in the lattice with the selected dopant. The vacancies formation was studied on 1x1x1, 2x2x2 and 3x3x3 supercells with up to 108 Cu atoms. The recorded trend is the same for all the supercell sizes. For the vacancy creation was enough to delete one copper line in the lattice vectors according to the position more energetically favorable founded with previous calculations. Strain was studied on smaller cell (1x1x1) by applying -10% to +10% variations of the scaling factor. The evaluation of strained CB and VB occurs respect to core level state because it should not vary to much when straining the cell.

2.2.3 Strain Effect

This effect raises from the lattice mismatch between two different lattice structures, the substrate and the Cu_2O one. This possibility was studied to obtain information on the different behavior recorded with Au and copper underlayers respect to the semiconductor deposited on the bare FTO as well as obtaining a trend that can be useful for the discovery of the best underlayer.

The pure and unstrained Cu_2O shows a computed lattice constant of 4.296 Å that is in good agreement with the experimental one of 4.270 Å[38] or with previous computed ones (4.289 Å, Nolan et al.[243]). The Cu-Cu distances within the closer copper atom are 3.038 Å and they were strained within the reliable range of ± 10% of the original value. The results obtained with different strains comes from on a 1x1x1 cell with 4 copper atoms and 2 oxygens.

According to literature, where a limited number of dopant atoms and their geometric effect were studied, a stronger Cu-Cu interaction will lead to a reduced band gap[242,243,252]. However, previous works were more interested in the doping of the material so, as to bring forward in the introduction, they show a combined effect of lattice modifications and electronic effects. With this work, we have split the two contributes.

The results in Figure 95 show the BG variation with a 3D lattice strain. The trend in band gap have a bell shape in which the unstrained cell did not represent the maximum value. The computed value for the BG, calculate with the HSE method, is 1.95 eV for the unstrained system (in orange). We can see that a reduction of the Cu-Cu distance until 3% of the initial value lead to an increase of the computed band gap. Moreover, after that value, BG starts to deeply decrease due to the reduction of Cu-Cu distances. Interesting is how the same reduction, with a lower slope, was found also for an increase in the lattice strain.

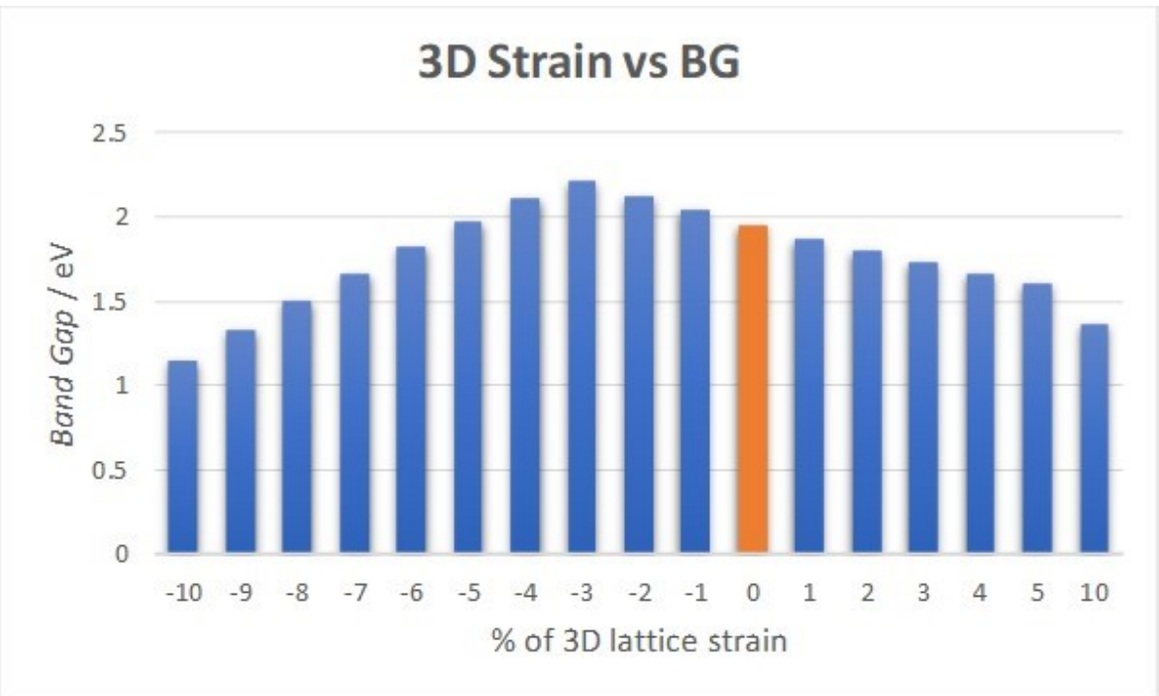

***Figure 94**. Computed BG (HSE06 level) of a 1x1x1 supercell of Cu_2O with 3D strain of the lattice.*

Similar results were confirmed applying a bi-dimensional and mono-dimensional strain which is more relevant when considering the strain induced by a lattice mismatch between Cu_2O and the underlayer. The recorded values of BG are different, but the trend recorded is the same. Only in the 1D case seems that the variations of BG were less pronounced.

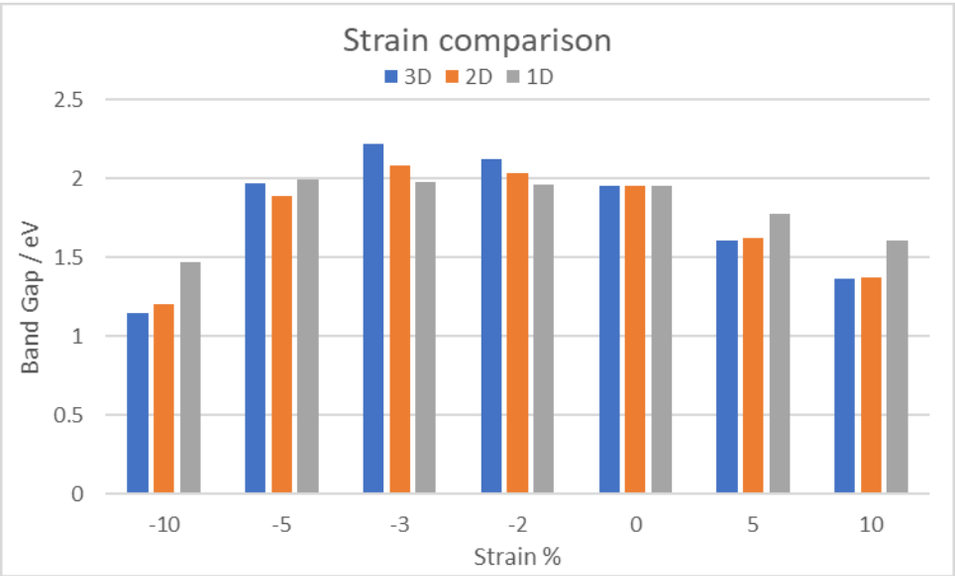

Figure 95. *Comparison of computed BG (HSE06 level) of a 1x1x1 supercell of Cu_2O with 3D, 2D and 1D strain of the lattice.*

2.2.3.1 Dori Evaluation

From a qualitative analysis of the DORI (Density Overlap Region Indicator)[339] we were able to identify the degree of covalent, ionic or metallic character in our O-Cu-O bond with respect to the strain. DORI was originally used to distinguish between covalent and non-covalent inter-molecular interactions. Bonding in solids is comparable to that in the sense that you similarly also can have covalent or non-covalent (metallic, ionic) interactions. Accordingly, DORI should be able to capture the differences between covalent and metallic/ionic bonding. In a metal bond like in Pt the bond (in blue) is spread all over the molecules, in covalent system like benzene it is strongly localized between the atoms with a constant intensity that is not present in an ionic specie like MgO.

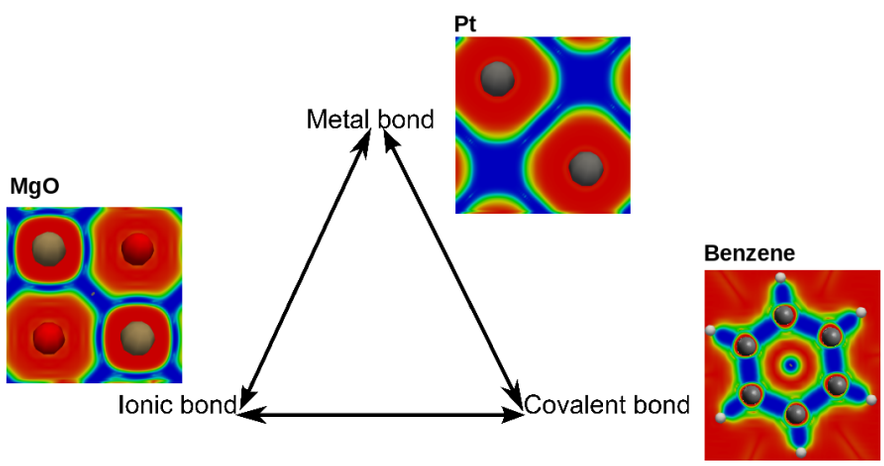

Figure 96*. DORI representation of different types of bonds.*

According to Figure 97 the strain is not affecting in a significative way the bond character and all the studied 3D strains show the same covalent character as expected for a material like Cu_2O. The bond is strongly localized and not spread all over the molecules indicating a pure covalent character (blue area within O and Cu).

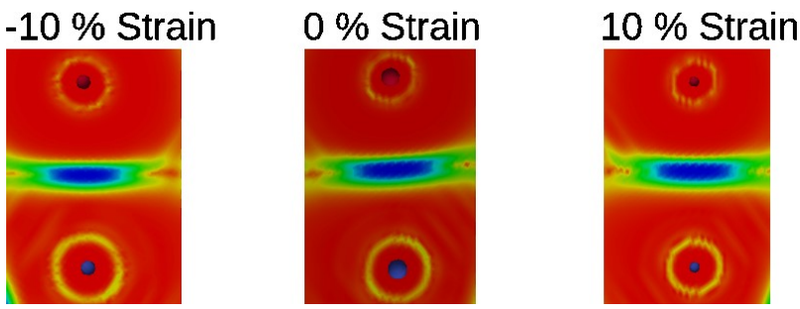

***Figure 97**: DORI plots for different 3D strains. The focus is on the O-Cu-O bond. The values go from blue (bond) to red (absence of bond).*

Vice versa, a Cu-Cu weak electrostatic interaction was found between the tetrahedrally coordinated coppers (with a net attractive interaction of about -0.26 eV per formula unit (-0.0434 eV per Cu-Cu contact)[340,341]. We can see how with compression (-10% strain) this interaction became stronger and localized and this can be an explanation for the decrease of BG with compression. It's possible that this weak Cu-Cu interaction we have noticed with DORI can be attractive d^{10}-d^{10} interaction responsible also for the band gap width suggested by literature[244,245,340,342]. Indeed, an increase in this interaction will lead to a decreased BG. Same situation but with a lower intensity was found for the cell expansion (+10% strain) were the bond is still more localized than the unstrained one but less respect to the compressed system. This explain the different slope found for the two sides of the bell-shaped curve in Figure 94.

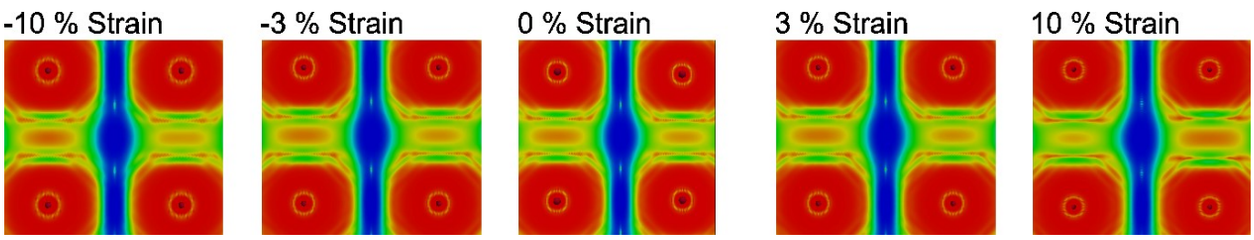

***Figure 98.** DORI plot for different 3D strain. The focus is on the Cu-Cu bond.*

According to these results the BG of a Cu_2O photoelectrode can be easily modified in both the direction applying some strain to the lattice. This strain can be induced in the material simply because of the lattice-lattice interactions between metallic underlayer and semiconductor. According to our measurements the BG can be reduced to a maximum value of 42% with the reduction of the lattice constants of 10% or increased to a maximum of 13% applying a negative strain of 3%.

2.2.3.2 DOS Evaluation

To give a more quantitative explanation of this behavior we analyzed the DOS structure of 3D strained and unstrained systems. For the readers' sake, are reported only the borderline case (-10% and +10%) compared to the unstrained one. The DOS were split and only the contributes of Cu *3d* (main component of VB) and Cu *4s* and O *2p* (main components of CB) were taken in account.

We can see with positive and negative strain that the orbitals responsible of BG are largely affected by the strain. The changes are indeed induced on both the strain directions giving the Gaussian-like curve showed in Figure 94.

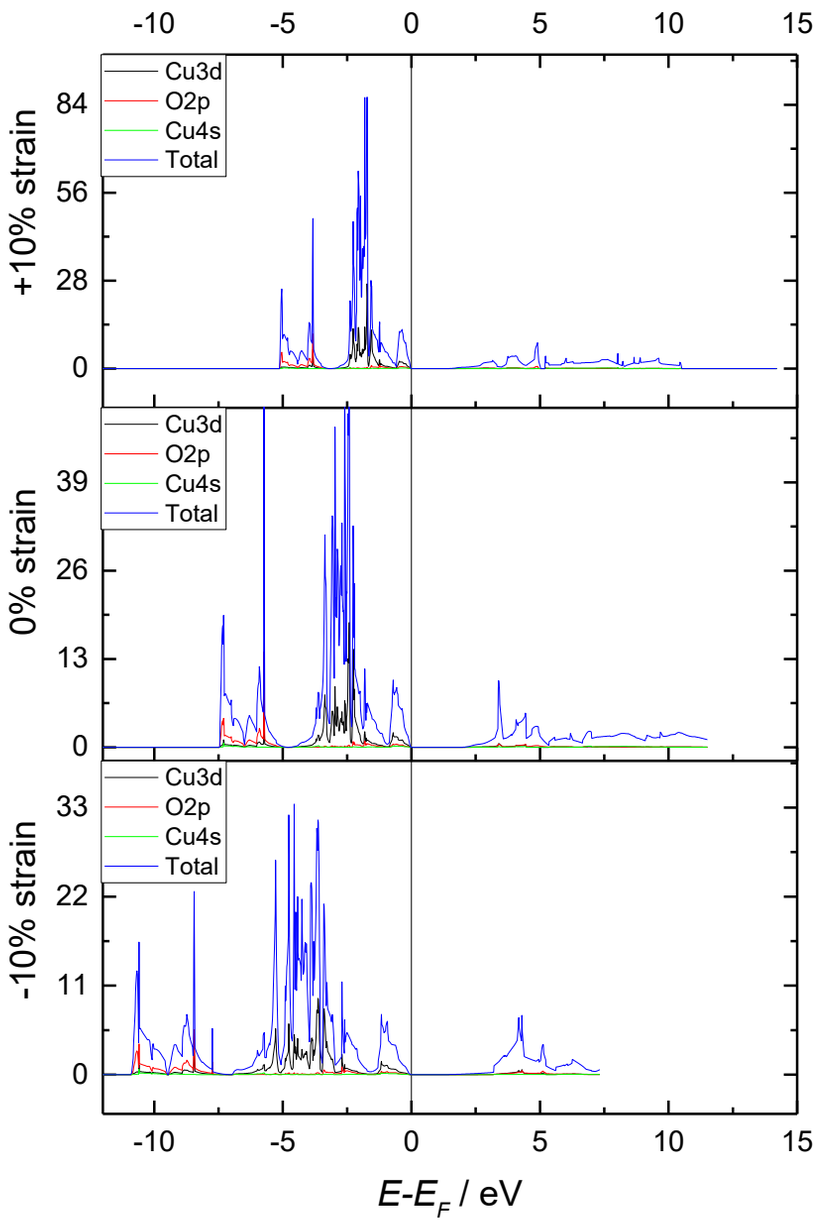

***Figure 99**: DOS comparison of +10% strain (upper boxes), -10% strain (lower boxes) and unstrained cell for the 3D systems. For all the systems are reported the total DOS (blue) and the major component of VB (Cu3d in black) and CB (O2p in red and Cu4s in green). All the DOS were normalized according to the Fermi energy level.*

A confirmation comes from the evaluation of VB and CB edges. We can see how "VB energy vs strain" slope is higher during cell compression (after the value of -3%) respect to the cell expansion. Opposite trend is found for the "CB energy vs strain" slope confirming how O *2p* orbitals are more affected from expansion than compression of the cell.

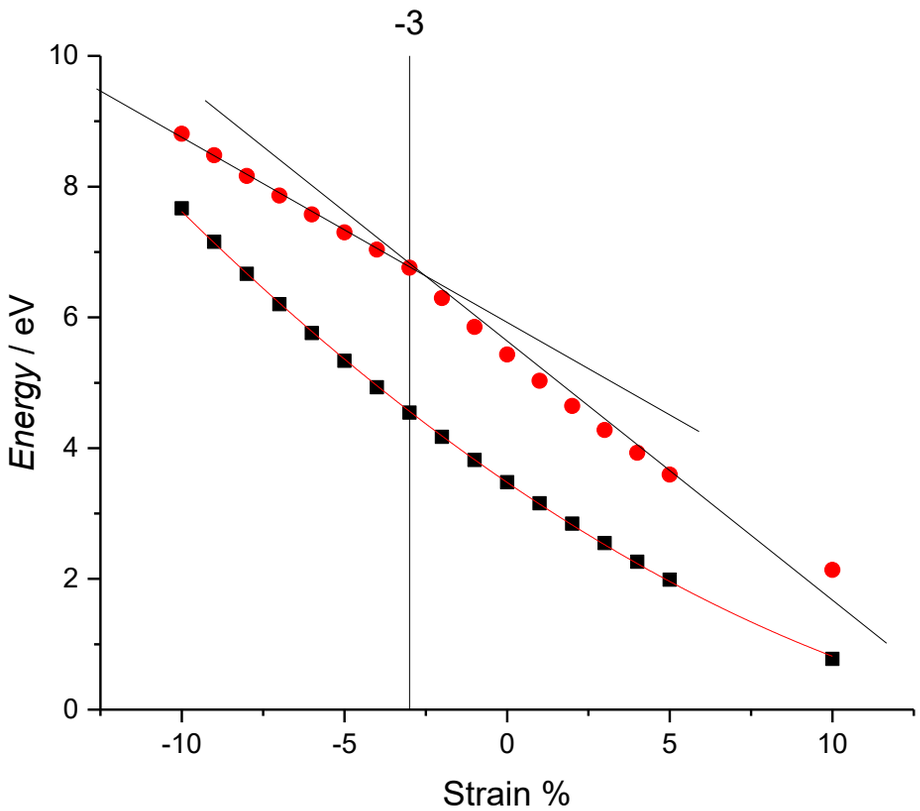

***Figure 100**: VB (black) and CB (red) positions respect to core level at different 3D strains.*

Interestingly we observe 3 very different contributions. The VB, as seen in the introduction, is determined mostly by *d-d* interactions and it is varied in equivalent way over the whole range of compressive and expansive strain considered here. This is opposed to the CB which is composed of two main contributions that affect the bands positions differently above and below the band gap maximum. Considering the *d-d* interactions to be mostly comprised of attractive electrostatic interactions[340] an expansion or contraction of the unit cell will affect the position of the orbital in an equivalent manner governed by the reduction of the attractive electrostatic interactions when increasing the unit cell or vice versa. This is opposed to the CB which consists of an overlap between O *sp* states and Cu *4s* and Cu *3d* states[343]. These interactions can be interpreted as the antibonding contribution to the σ-bond between the O *sp* hybrid orbitals and Cu *4s* or *3d* states. Accordingly, the CB is shifted due to a compression of a true chemical bond. This is reflected in the different contributions in the compressive and tensile strain regimes. Under compressive strain, the overlap between the orbitals contributing to the σ-bond is increased which in turn should in principle result into a strengthening of the chemical bond. Simultaneously, however, the repulsive electrostatic interactions increase, rendering the compression energetically less favourable. In our case this results in a shift of the CB to higher energies.

In the tensile strain regime on the other hand, the energetics are governed by the breaking of the σ-bond, i.e. an extension of the lattice results in a weakening of the chemical bond between Cu and O. This in turn results into a decrease of the splitting between bonding and antibonding states which stabilizes the σ*-antibonding states.

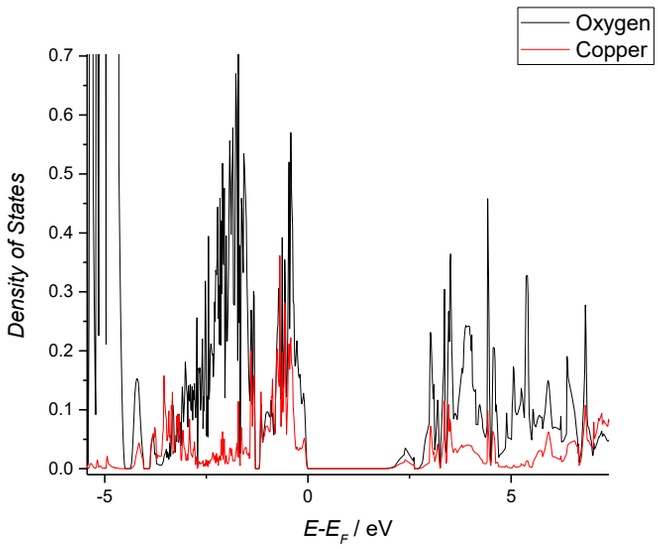

Figure 101. *DOS of oxygen (in black) and copper (in red) states.*

A theoretical strain was calculated for the different underlayer tested.

	M-M	Cu-Cu	Strain
Ag	2.93115	3.03768	-3.50695
Au	2.94000	3.03768	-3.21561
Pt	2.80664	3.03768	-7.6058
Pd	2.78598	3.03768	-8.28593
Ir	2.73912	3.03768	-9.82855
Os	2.69451	3.03768	-11.2971
Mo	2.82354	3.03768	-7.04946
Ru	2.65268	3.03768	-12.6741
Rh	2.70439	3.03768	-10.9719
W	2.74773	3.03768	-9.54511
Pb	3.55366	3.03768	16.98599
Sn white	3.07483	3.03768	1.222973
Sn gray	2.87787	3.03768	-5.26092
Ni	2.48618	3.03768	-18.1553
Co	2.48422	3.03768	-18.2198
Fe	2.45212	3.03768	-19.2766
Mn	2.47120	3.03768	-18.6484
Cr	2.55234	3.03768	-15.9773
Ti	2.86227	3.03768	-5.77447
Al	2.86349	3.03768	-5.73431
Cu	2.56537	3.03768	-15.5484

Table 17. *Strain on Cu_2O lattice with different metallic underlayers.*

Most of the materials will lead to a negative strain the Cu_2O lattice, sometimes quite high. The only with a positive strain will be Sn and Pb probably because of their larger dimension. Is also important to notice that these values are merely indicative and that the experimental one can largely differ according to the main exposed faces on the metal as well on the semiconductor. This parameter is strongly related to the synthetic parameters for the semiconductor as seen in the introduction.

2.2.4 Punctual Strain

The punctual strain induced by the presence of dopants of different size from the alkaline series gives is studied to evaluate the weight of dopant size and electronic effect in the BG of doped systems. In literature indeed[230,243,244,252], is usually studied the total effect induce by a dopant on the final properties (conductivity, BG etc..) of the doped material. For the first time here, we try to decouple the two effects using dopant with the closer electronic effect possible. Indeed by previous calculations[243] it was found that cation with radius larger than Cu, like Cd^{2+} and Hg^{2+} can still reduce the BG.

2.2.4.1 Bond Distances

Bond distances were evaluated with the doped system in a 1x1x1 supercell. Table 18 shows the variation of atomic distances inside the doped and undoped cells. All the distances increase with the size of the dopant but the one between the oxygen far from the dopant and the tetrahedrally coordinated coppers around it is quite stable. These distances were calculated on a volume relaxed cell. We can see that with the increase of dopant size we increase all the interatomic distances despite the O2-Cu that is poorly modified.

Dopant	M-O	M-Cu	O1-Cu1	Cu-Cu	O-O	O2-Cu	ionic radius (I)
Li	1.893	3.082	4.754	3.082	3.785	1.885	76
Na	2.196	3.174	5.126	3.174	4.392	1.874	102
K	2.459	3.235	5.431	3.235	4.917	1.876	138
Rb	2.574	3.294	5.596	3.294	5.148	1.905	152
Cs	2.668	3.328	5.718	3.328	5.336	1.922	167
Cu_2O	1.89	3.086	4.756	3.086	3.78	1.89	77

***Table 18**: Distances comparison with different alkaline dopants with relaxed volume cell.*

When a small supercell (1x1x1) is used a trend of BG is present but all the values of the BG are increased respect to the pure Cu_2O (in orange). Looking at the ionic size of the atoms starting from Li, all these dopants are indeed bigger than Cu. This seems to agree with literature who claims that bigger dopant size reduce d^{10}-d^{10} interactions increasing the band gap.

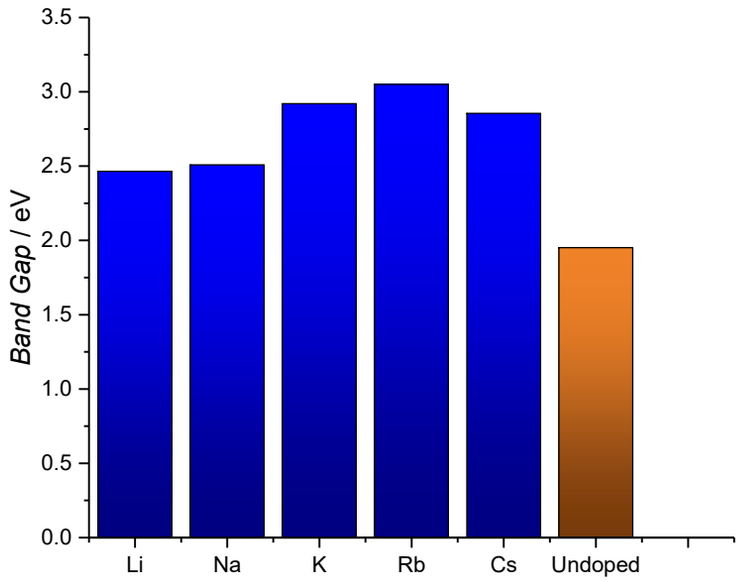

***Figure 102**: Computed BG (HSE06 level) of a 1x1x1 supercell of Cu_2O doped with different alkaline metals. The formal oxidation state for all the dopants was kept to +1 to simulate the one of Cu^+ in Cu_2O.*

In the plot of Figure 102 is impossible to divide the contribute of cell dimensions increase and the electronic effect due to the dopant. Indeed, despite the similar valence configurations these dopants have large differences in their inners level. Li interacts only with its *s*-orbitals and so the number of *d-d* interactions inside the material is reduced. Na and K have the additional contribute of Na *2p* and K *3p* empty orbitals while Rb and Cs are the only one in which, together with the *p* contribute, are present *d* orbitals. To evaluate the intensity of the electronic effect we relax all the volumes of the different doped structures until the minimum of energies were recorded.

To obtain the value of band gap for the relaxed volume showed in Figure 103, different cell volumes were tested until the minimum of energy was found.

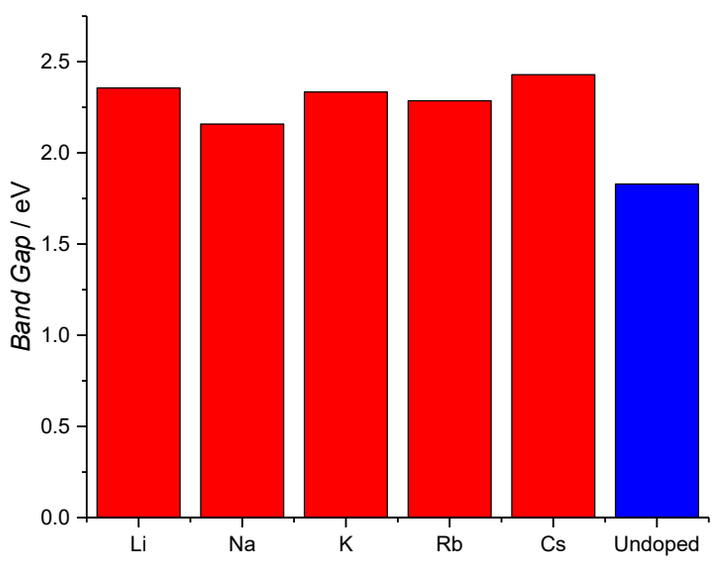

***Figure 103**: Computed BG (HSE06 level) of a 1x1x1 supercell of Cu_2O with different alkaline metal dopants and volume relaxed.*

BG calculated with relaxed cell volume shows a different behavior respect to Figure 102 because all the size effects were dismissed. The BG is always increased, and this can be related to a reduction of the *d-d* interactions number. Indeed, all the dopants miss the *d-d* interactions that in the end, for such a small cell, are reduced of 25%. This electronic effect increases all the BG with some fluctuation probably due to the presence of different empty orbitals in the dopants. Li indeed, has only s orbitals, Na and K have *p*-empty orbitals and Rb and Cs *d*-empty ones. In general, is not possible to obtain a clear trend.

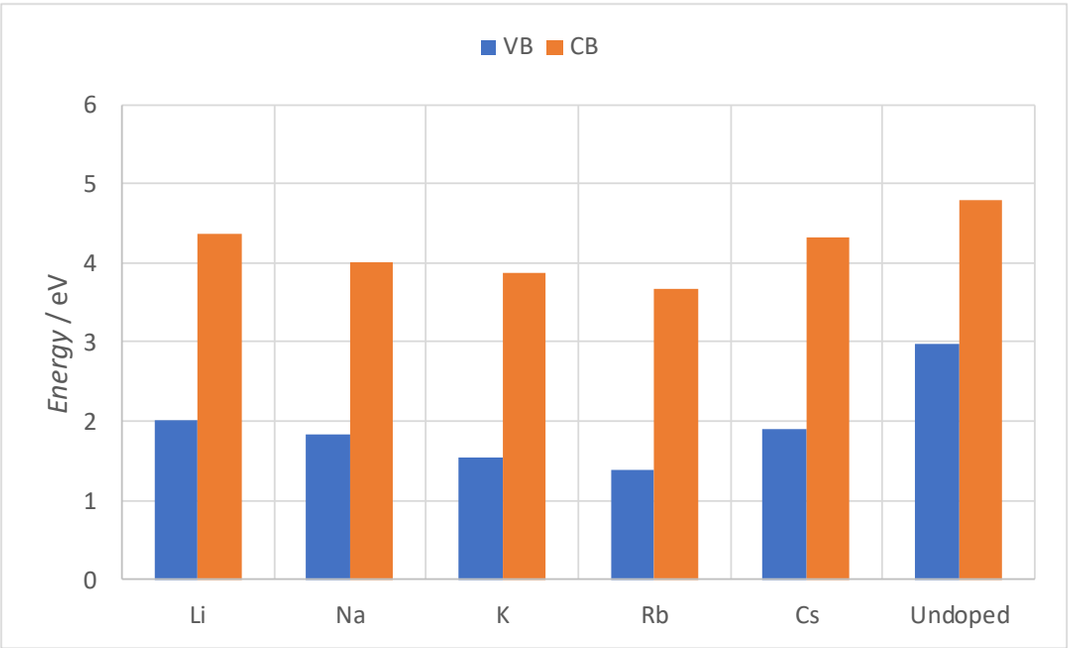

***Figure 104**: VB and CB energies from eigenvalue of doped Cu_2O (small supercell) with volume relaxed.*

From the energy value of VB and CB with the different dopants we can see how Li, Na, K and Rb have a VB lying at lower energies meaning that it is stabilized if compared to the one of pure Cu_2O. This probably occurs because of the ionic nature of the bond removes charge from the Cu making it more stable and so the Cu *3d*, major component of VB as confirmed by the charge recorded on the Cu atoms of the different structures.

With Cs VB energy starts to increase again due to the large compression present in the cell. Indeed, the large size of Cs can push the free electron pair of O destabilizing the whole structure. We can see this from the increased value of the O *2p* states in the VB of Figure 105.

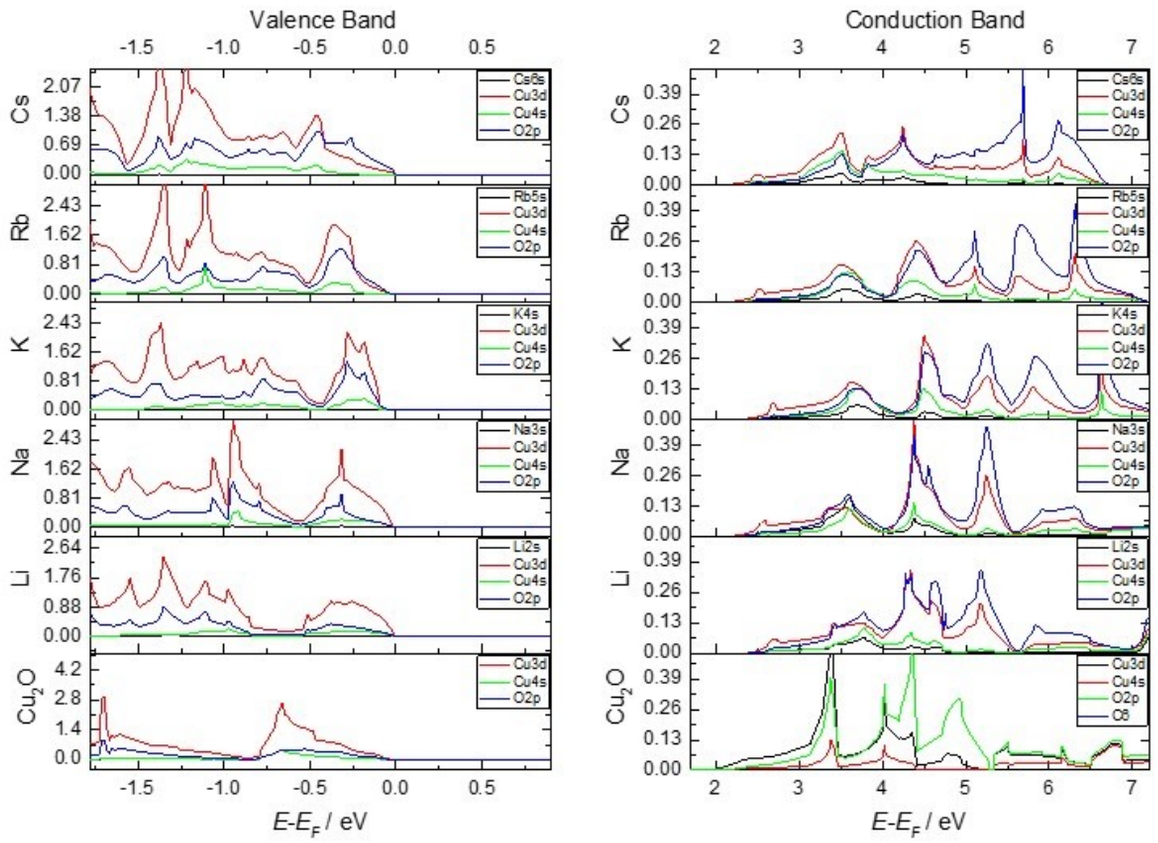

***Figure 105**: DOS evaluation of the doped system and pure Cu_2O split in the different orbital contributes.*

The results showed until now were obtained from a 1x1x1 supercell with 25% doping concentration. Nevertheless, if we move to a more realistic cell with 3% of cation doping, we can see how this large change in the BG completely disappears (Figure 106). This behavior is related to the impossibility of controlling band gap simply using the size of the dopant because this effect is diluted in the whole molecule. In general, an increase of the BG was noticed on the smaller cell because of the *s*-character of the dopant that, together with the size, destroy the d^{10}-d^{10} interactions between Cu in the lattice. We agree with previous authors on the important role on the BG of such internetwork and intranetwork interactions[225,242,243], but we have seen that once the cell is wide enough, with a reasonable low level of doping, the influence of size disappears.

Similar results were confirmed indirectly by other authors. J. Zhong Qian and co-authors showed an experimental reduction of the band gap using Au-doped Cu_2O of only 1.6% in spite of the good enhancement in absorption coefficient[269].

Similar results were obtained with the use of silver by V. R. Satsangi that declares a BG reduction of 0.09 eV with 3% Ag doping[266]. Indeed, seems that the whole contribute to BG modification in a real system is to be related to the electronic configuration of the dopant overlapping with the one of Cu_2O moreover than to his size (Figure 106).

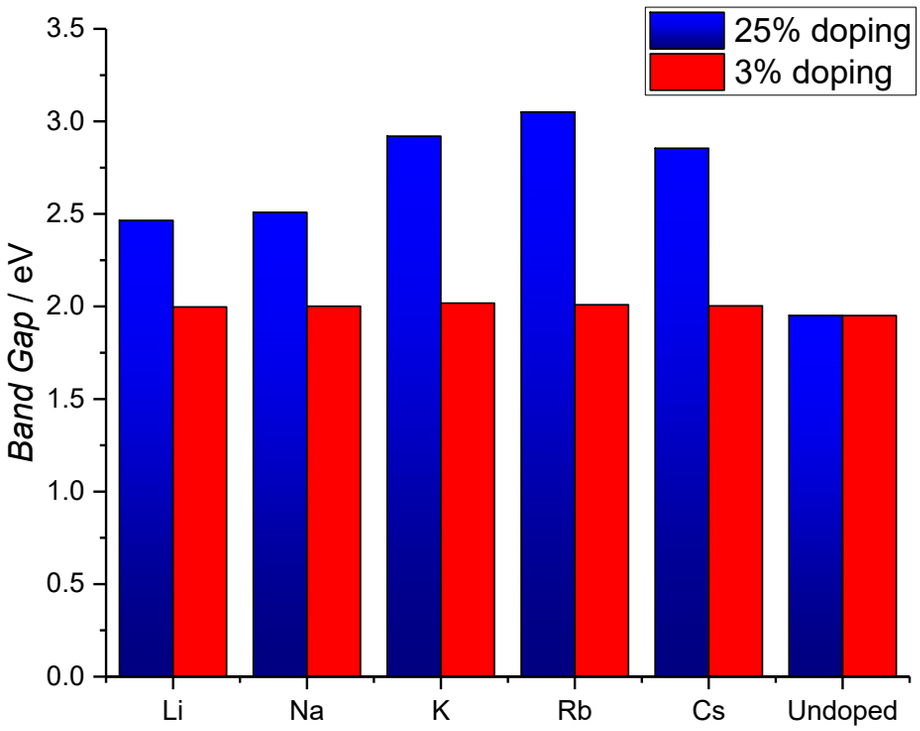

***Figure 106**: Computed BG (HSE06 level) of a 2x2x2 supercell of Cu_2O with different alkaline dopants. No real changes in the BG are introduced with this large matrix of dopant with same electronic structure and different size.*

Thus, we can see that geometrical effects from the dopant are irrelevant in a realistic situation of doping and that all the variation recorded in the BG are mostly related to electronic effect. Indeed, in the 2x2x2 supercell we can consider all the alkaline metals giving the same electronic effect coming from the interactions of *s* orbitals.

2.2.5 Vacancy Formation

According to literature the *p*-type character of Cu_2O is strictly related to the formation of copper vacancies in its lattice. The aim of this part of the work was to evaluate if the presence of a specific metallic underlayers can affect the formation of Cu or O vacancies inside the Cu_2O. The vacancy formation would be favored if a Cu (or O) atom prefers to stay surrounded by the metal once than stay in the Cu_2O lattice. In some way we can consider this as an evaluation of the mixing energy between Cu_2O and different bulk metallic underlayers.

For this evaluation were computed different structures with 4 and 32 atoms of the following metallic underlayer: Ti, Cr, Mn, Fe, Co, Ni, Mo, Ru, Rh, Pd, Ag, W, Os, Ir, Pt, Au, Sn and Pb. For all these metals was also calculated the final structure in which a metal atom leaves the lattice and is substituted by a copper one, $M_{31}Cu$ (low concentration) and M_3Cu (high concentration). In addition, the structure of Cu_4O_2 (1x1x1 supercell), $Cu_{32}O_{16}$ (2x2x2 supercell) and $Cu_{108}O_{54}$ (3x3x3 supercell) and the structures with one copper vacancy and one oxygen vacancy, were calculated.

Then several different situations were considered:

Cu vacancy formation.

- Cu substituting a metal atom in the metallic underlayer lattice in a low concentration (~3%) to simulate a real situation:

$$Cu_4O_2 + M_{32} \rightarrow Cu_3O_2 + M_{31}Cu + \frac{1}{4}M_{32}$$

- Cu substituting a metal atom in the metallic underlayer lattice in a very high concentration (25%). This test is a limit case to simulate the formation of more than one vacancy:

$$Cu_4O_2 + M_4 \rightarrow Cu_3O_2 + M_3Cu + \frac{1}{4}M_4$$

- The substitution of Cu inside the metal lattice occurs together with the doping of the Cu_2O with an ion from the metallic underlayer:

$$Cu_4O_2 + M_4 \rightarrow Cu_3O_2 + M_3Cu + \frac{1}{4}M_4$$

- The substitution of Cu inside the metal lattice occurs together with the doping of the Cu_2O with an ion from the metallic underlayer but in higher concentration:

$$Cu_4O_2 + M_4 \rightarrow MCu_3O_2 + M_3Cu$$

O vacancy formation.

- O entering in the metal atom lattice in a tetrahedral position in a low concentration (~3%) to simulate a real situation:

$$Cu_4O_2 + M_{32} \rightarrow Cu_4O + M_{32}O$$

For all the situations, the variation of the energy was studied with different Cu_2O cell dimensions (1x1x1 means starting from Cu_4O_2, 2x2x2 means starting from $Cu_{32}O_{16}$ and 3x3x3 means starting from a $Cu_{108}O_{54}$ supercell) to validate the goodness of the results.

2x2x2 supercell energies are in good agreement with the 3x3x3 ones meaning that such dimension of the system is reliable to model the real system and this is confirmed by the supercell used in literature for the same material[242,243].

Even if the method here used can be applied to any metallic underlayer, to keep this research as close as possible to the reality, only materials that can be easy prepared and used as underlayer were tested (e.g. a K layer will be non-sense even despite the obtainable results). An exception to this rule is Al, unstable at the deposition bath pH, but that can be interesting if different preparation methods of Cu_2O are taken in account. Then applying the equation illustrated in the previous part is possible to obtain the energies for the substitution reaction of the studied materials. In Figure 107 and Figure 108 are reported the obtained values for the largest (and more realistic) supercell.

2.2.5.1 Copper Vacancies

The presence of a metallic underlayer can reduce the energy for a vacancy formation. The computed value for a vacancy formation in the pure material is 0.37 eV similar to previous experiments[225,237].

According to literature[239,344] Cu_2O is a material that spontaneously generate Cu vacancy and this means that in spite this value is positive, it can be easily achieved once the entropy is added to the system. Using the equation introduced before, it was possible to define which underlayers are more prone to generate a vacancy inside the Cu_2O accepting a copper in their lattice as a replacement for one metal atom. As we can see some of the tested materials present negative energies and so the vacancy is largely favoured with these underlayers (Mo, Pd and Pt).

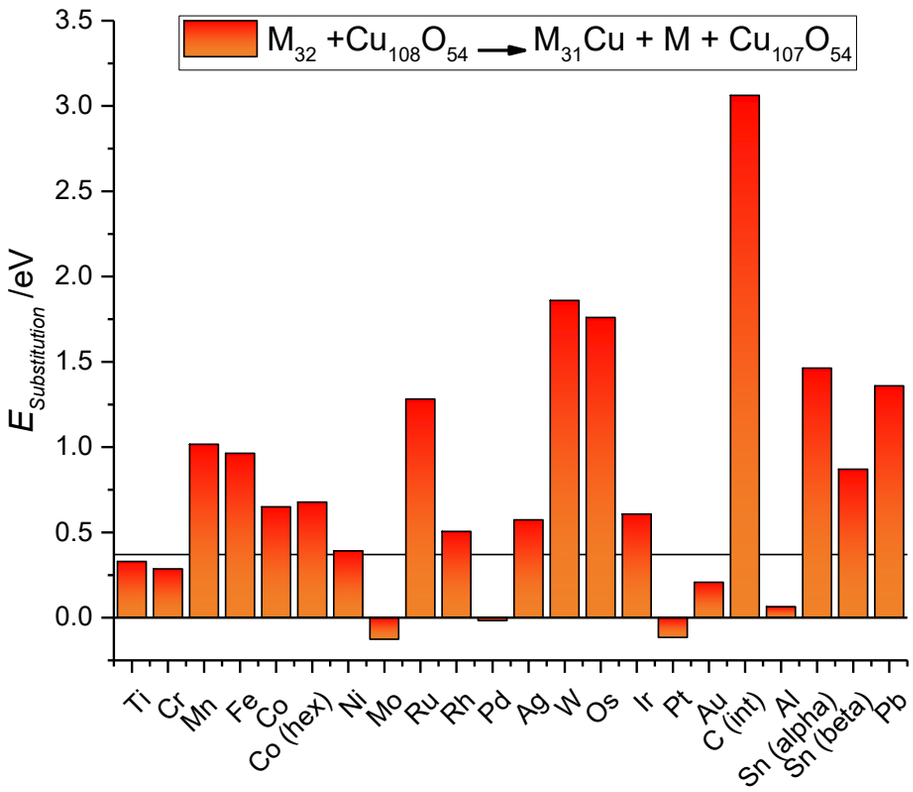

***Figure 107**: Substitution energies for the formation of a vacancy in a large 3x3x3 supercell of $Cu_{108}O_{54}$. The horizontal line at 0.37eVis the vacancy formation in pure Cu_2O.*

Moreover, also other material like Al, Au and Cr can lead to the formation of additional vacancies in the material in spite the positive energy of formation because DFT does consider entropy and the value are still lower respect to those of pure Cu_2O. The use of a specific underlayer thus can easily modify the behaviour of the material respect to vacancy formation increasing so the number of majority carriers and consequently the conductivity[229]. Vice versa, is very difficult to obtain a higher vacancies concentration with the use of material like C (Cu enter in an interstitial position) or Os, W and both the phases of Sn.

2.2.5.2 Oxygen Vacancies

Some of the materials tested seems more prone to generate oxygen vacancies. This should give a n-type character to the material but according to literature Cu_2O is a self-compensating material[234]. This means that, because the formation of Cu vacancies naturally occurs in the material, once a O vacancy is created the material compensates with the creation of the proper number of new Cu vacancies. Interesting is how Al and Mo are materials able to generate both oxygen and copper vacancies, while a noble material like Pt is able only to generate Cu vacancies having very high energy for the addition of an O to its lattice.

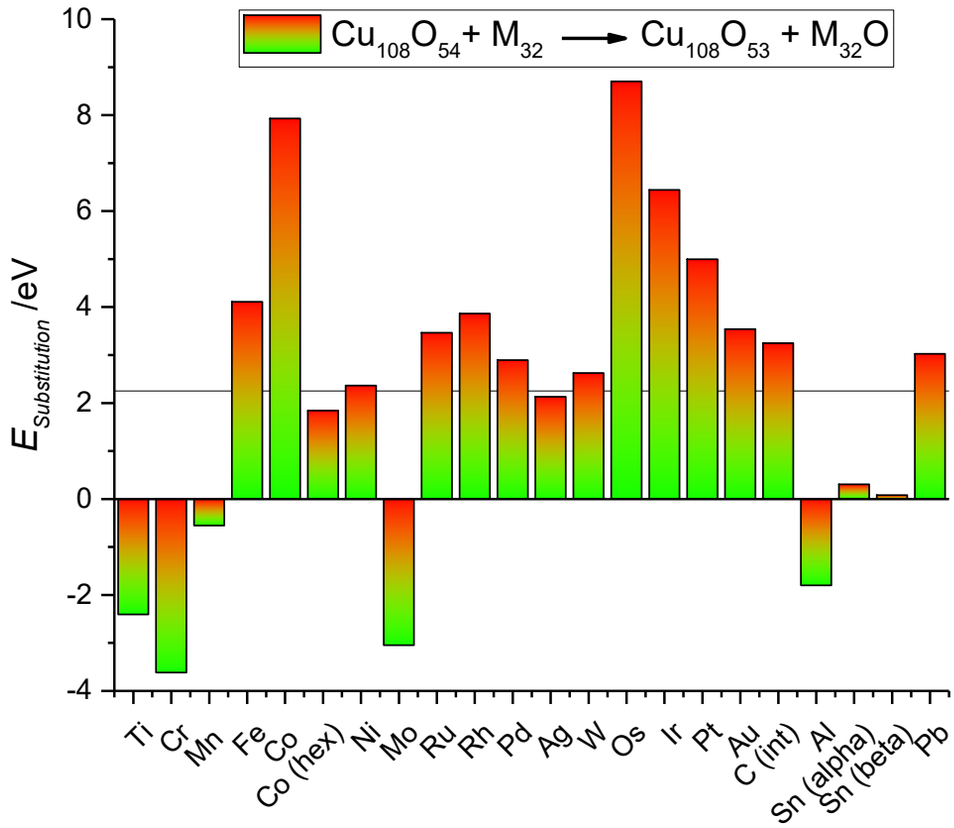

Figure 108. *Substitution energies for the formation of an oxygen vacancy in a large 3x3x3 supercell of $Cu_{108}O_{54}$. The horizontal line at 2.25eV is the oxygen vacancy formation in pure Cu_2O.*

We can see that usually the oxygen vacancy formation is much more energy demanding than the Cu one. Despite this some materials show very negative energy values, but these results are related in this case to the very easy formation of oxides.

2.2.5.3 High Concentration/Low Concentration in Underlayers

For the creation of copper vacancies, a comparison between low and high doping will give us an idea of the trend in Cu substitution inside the metal. The high concentration will model the formation of more than one vacancy in the Cu_2O with an enriched concentration of Cu inside the metal. We can see from Figure 109 that for some metallic underlayers (Fe, Ru, Cr), adding more copper is a more favourable reaction. These materials can thus take more copper atoms from the Cu_2O lattice with the creation of a larger number of vacancies. It was possible to study only this limit case to study the loading importance. This because if we want to introduce 2 Cu in a M_{32} cell, the relative positions of the Cu in the metal, together with the position of the copper vacancies in Cu_2O becomes important and this evaluation would be computationally too expensive due to the need of testing all potential sites. The increase of doping is indeed obtained by a reduction of the number of metallic atoms considered in the calculated structures.

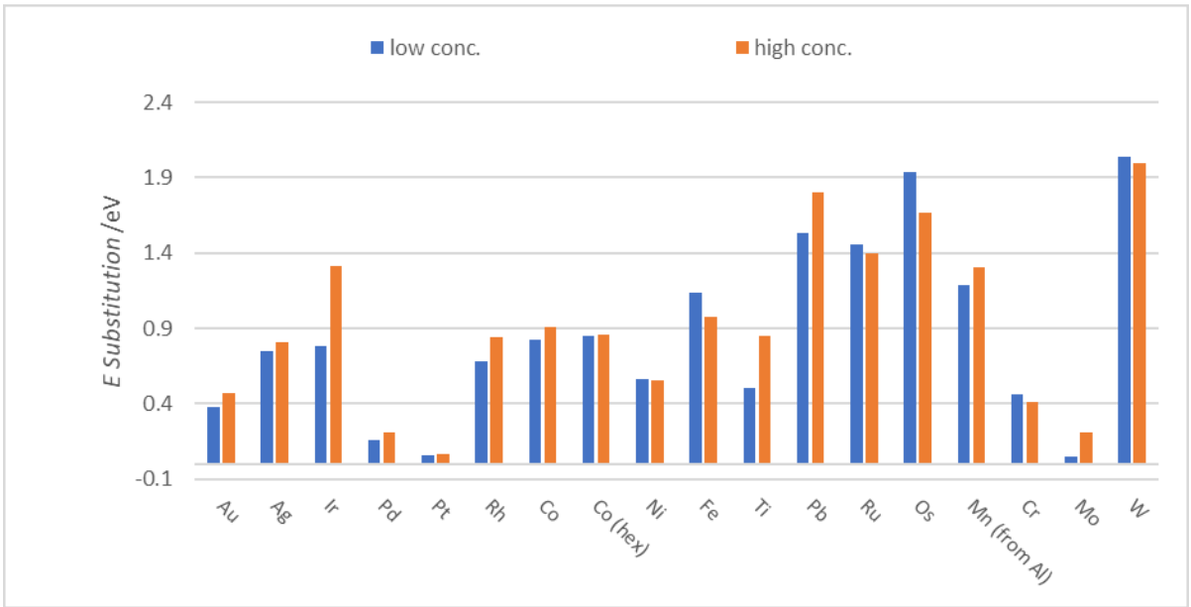

Figure 109. *Comparison between low vacancy concentration (in blue) and high vacancy concentration (in orange).*

The comparison of the results with high and low doping shows a more favorable energy for the formation of many vacancies in system like Fe, Ru, Os, Cr, W. On the contrary, Au, Ag, Ir, Rh Co, Al, Pb prefer to accept a limited number of copper atoms in their lattices.

2.2.5.4 Exchange Reaction

A comparison between the simple vacancy formation and the vacancy formation plus the simultaneous formation of a doped Cu_2O is here reported. The energy required for this reaction is, for most of the material studied, higher respect than the on for simple substitution of copper in the lattice material. Interesting results are obtained for Ti and Cr where the material enter so easily in the Cu_2O lattice (see doping paragraph) to move the energy of this reaction too.

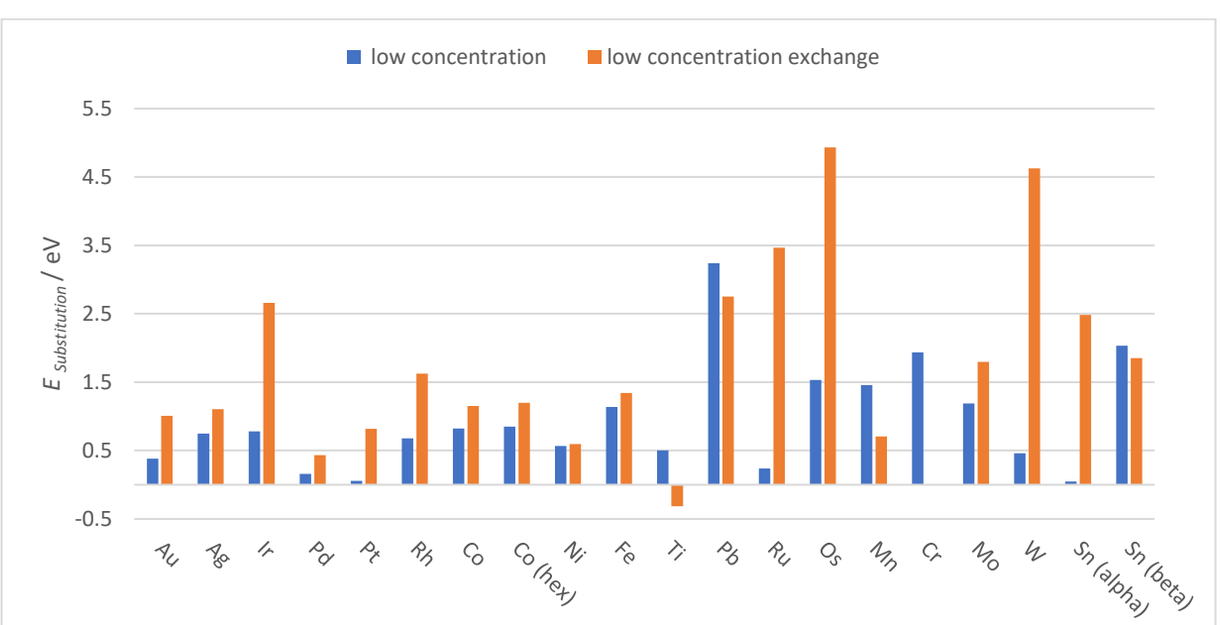

Figure 110*. Low doping comparison between simple substitution (Cu entering in the metal lattice) and the exchange one (Cu in the metal and metal doping the Cu_2O).*

This comparison allows us to understand which is the reaction occurring once the metallic underlayer and Cu_2O are in contact. Seems that Ti and Cr were the ones following this type of reaction, but as explained before, is still possible that such reaction occurs even for material like Pd, Pt or Ni where the exchange substitution energy is still quite low.

Similar results were also obtained increasing the level of doping. The same behavior for the cell let free to relax the volume was recorded despite for Pb, that can largely distort the Cu_2O cell due to its larger dimension.

2.2.6 Doping

The exchange reaction occurs with the doping of the material with a metal atom entering in the Cu_2O lattice in a copper position. The same transition metals were studied to see how the presence of a doping ion (with its electronic configuration and size) can affect the formation of the vacancies and modify the bang gap. The idea was to follow the possible mixing of the two phases once in contact with the formation of a doped semiconductor. Moreover, the results can be of interest giving useful information about the properties of doped-Cu_2O systems that can be obtained from different synthetic procedures. From literature[252] was found that there are two main parameters affecting the result of doping:

- The ion size: a bigger ion increases the Cu-Cu distance reducing the metallic character of Cu_2O and increasing the band gap.
- The electronic configuration of the atom.

Considering both parameters is not easy to predict immediately which can be an interesting doping ion because ions with bigger radius than Cu can still give a reduction of the BG if its electronic configuration for example generates an intermediate band like what happens with nitrogen. Semiconductor doping is one of the most used techniques to modifies properties like the band gap width. The insertion of a dopant can increase or decrease the band gap with a shift in the valence band or conduction band position. In the view of this work, the perfect candidate should be able to reduce the band gap, to increase the available part of the light for the reaction. All the materials used as underlayer were tested to show if the contact between the two different phases will be enough for doping the material. With these calculations is not possible to underline the depth of such type of doping, that remain a possibility, but all the results obtained are still fully valid for M-doped Cu_2O with different preparation routes.

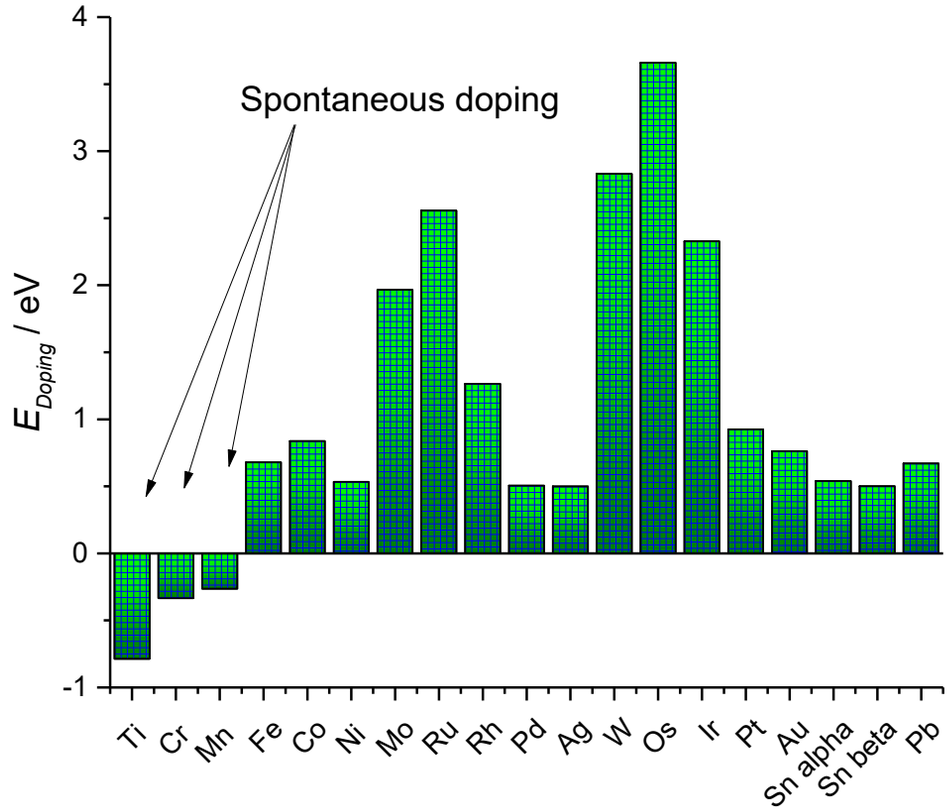

***Figure 111**. Doping energy calculated with PBE on a 2x2x2 supercell.*

The energy calculated in Figure 111 are related to the reaction:

$$Cu_{32}O_{16} + \frac{1}{32}M_{32} \rightarrow MCu_{31}O_{16} + \frac{1}{32}Cu_{32}$$

Material like Ti, Cr and Mn spontaneously will dope the Cu_2O but they are not the only materials that can be used. We must remember that these values are mean to be not fully real because of the approximations made with the DFT functional. The idea behind this plot is to have a trend of which material is easier, compared to the other, to be used as dopant. Moreover, these results don't take in account the entropy. Entropic contribute is around 0.3eV and, once subtracted to the obtained values, even material like Pd, Ag, Ni and Au can lead to spontaneous (or very low energy demanding) doping of the material. In literature[248] was also found that is possible to achieve doping until 1.5eV of required energy meaning that in the proper conditions most of the materials studied can be easily synthetized.

The obtained DOS for the doped system where here reported without any vacancy in comparison with the one of pure Cu_2O. For the sake of clarity all the DOS are zoomed in the area of high interest, the one with VB and CB edges.

Gold and Silver

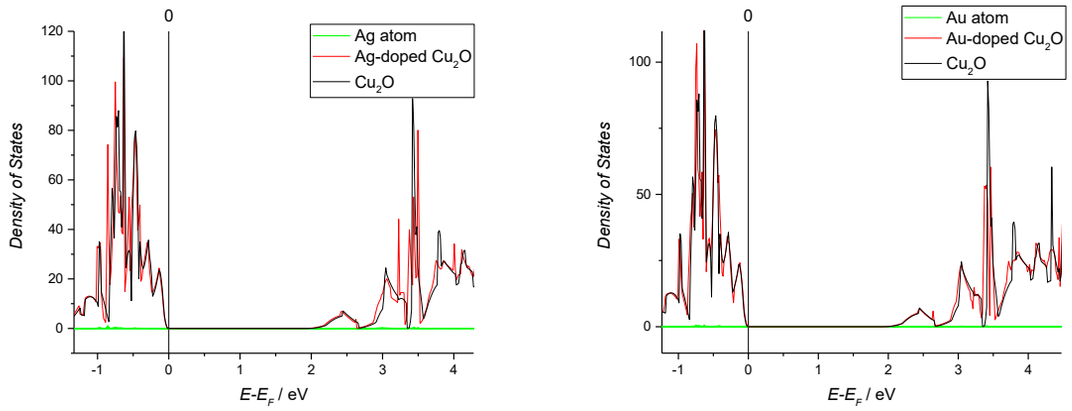

***Figure 112**. A) DOS of Au-doped Cu_2O (in red) compared to the pure Cu_2O (in black). B) DOS of Ag-doped Cu_2O (in red) compared to the pure Cu_2O (in black). The green line is the contribute of the dopant atom. DOS obtained from HSE06 calculation on a 2x2x2 supercell.*

The insertion of gold into the Cu_2O lattice (3% concentration) did not lead to any qualitative change in the density of state of the material. As is possible to see from the DOS of the simple gold atom its band lies far from the BG that keeps its initial value. Similar results can be obtained with silver as well. These two metals are indeed the closer, in terms of electronic structure, to the original Cu removed from the lattice being all part of the 10^{th} group. The recorded band gap in this case is the same of the undoped system.

Palladium and Platinum

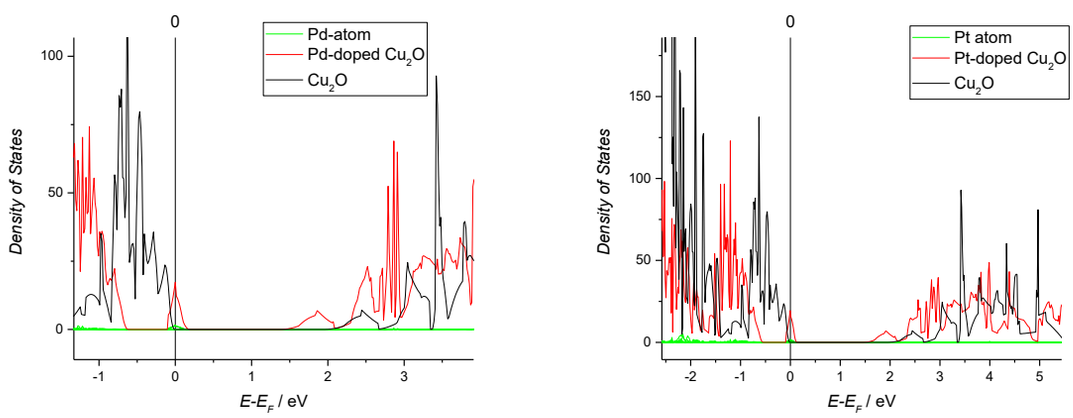

***Figure 113.** A) DOS of Pd-doped Cu_2O (in red) compared to the pure Cu_2O (in black). B) DOS of Pt-doped Cu_2O (in red) compared to the pure Cu_2O (in black). The green line is the contribute of the dopant atom. DOS obtained from HSE06 calculation on a 2x2x2 supercell.*

Palladium is one of the dopants with one of the most interesting results when no vacancies are considered in the material. The red line shows that the DOS of Pd-doped Cu_2O is far different from the pure one. In particular, the VB and the CB are shifted to lower energy of around 0.5eV but an interesting intermediate band (IB) is present. This intermediate band has all the requirements to be useful in a photoelectrochemical system.

The band, lying on the Fermi level is instead only partially filled, is localized and far both from the valence and the conduction bands. Such IB allows the material to absorb photon with energy much lower than the band gap, and with a double step, allows to bring them to the CB where the water reduction reaction can still occur because of the highly enough energy of the CB. A similar situation is achieved with Pt-doped Cu_2O where the IB have the same requirement fully satisfied.

Cobalt and Nickel

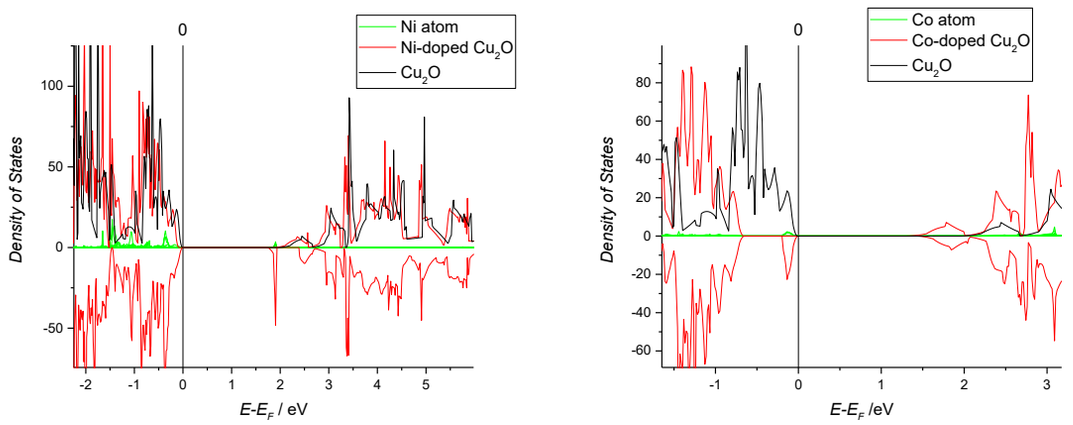

***Figure 114**. A) DOS of Co-doped Cu_2O (in red) compared to the pure Cu_2O (in black). B) DOS of Ni-doped Cu_2O (in red) compared to the pure Cu_2O (in black). The green line is the contribute of the dopant atom. DOS obtained from HSE06 calculation on a 2x2x2 supercell.*

With Co (triplet) a filled band is still present before the Fermi level. The band can still act as an electrons donor to the CB but being separated from the continuous part of the VB the intensity of the excited electron is probably reduced. Anyway, this band allows to reduce the band gap for at least some of the electrons that can reach the VB with an energy jump of less than 1.5eV.

The insertion of Ni (with the duplet configuration) induces some changes in the DOS. First of all, there is a spin polarization of the DOS that becomes split in the UP and DOWN contributes. While the UP is only slightly shifted to lower energy respect to the pure Cu_2O, the DOWN one has a quite different shape with a localized state before the CB at 1.9eV. Such a localized state could act as a trap state for electrons coming from the VB and we can see from the DOS of the Ni (green line) that this state is partially localized on the Ni itself.

Rhodium and Iridium

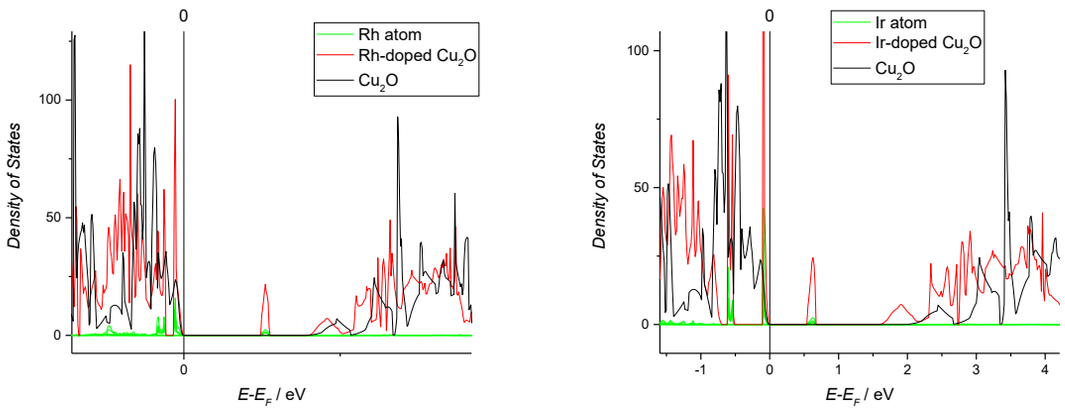

Figure 115. *A) DOS of Rh-doped Cu_2O (in red) compared to the pure Cu_2O (in black). B) DOS of Ir-doped Cu_2O (in red) compared to the pure Cu_2O (in black). The green line is the contribute of the dopant atom. DOS obtained from HSE06 calculation on a 2x2x2 supercell.*

Rhodium instead has a band fully empty (lies above the Fermi level). Electrons can jump from the VB to this band but, being empty, the only electrons able to jump to CB are only a minority of the ones previously excited from the VB. Is more probable that with this configuration the band could act as a recombination center.

With Ir-doped Cu_2O the situation becomes more complex. In the band gap are present two fully filled bands, strongly localized on the Ir atoms and an empty one still with a partial localization on the dopant. Is difficult to predict the behavior of the doped material in this situation. Such highly localized states moreover suggest us the need of introducing vacancies inside the material. As showed later the energy for the formation of additional vacancies is extremely favorable.

Iron and Manganese

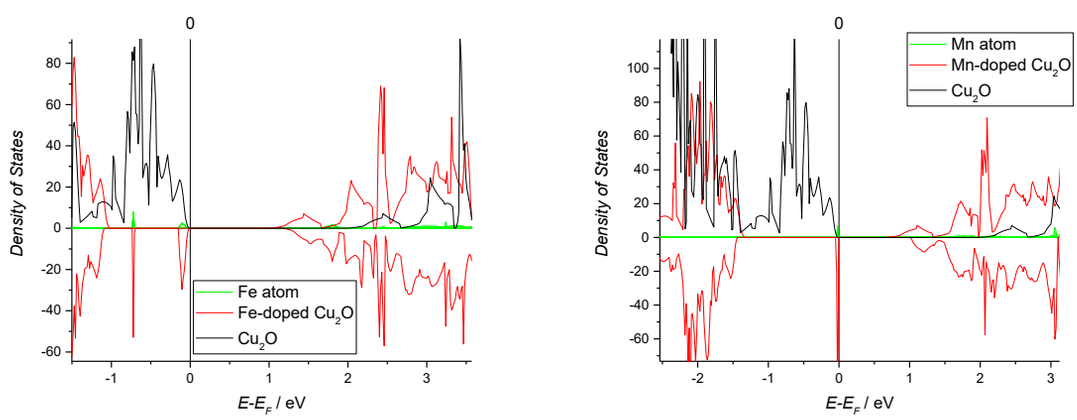

Figure 116. *A) DOS of Fe-doped Cu_2O (in red) compared to the pure Cu_2O (in black). DOS of Mn-doped Cu_2O (in red) compared to the pure Cu_2O (in black). The green line is the contribute of the dopant atom. DOS obtained from HSE06 calculation on a 2x2x2 supercell.*

Also, iron shows two fully occupied localized bands. Manganese doped Cu_2O instead has a simpler band structure with a single localized band, fully occupied, just before the Fermi level.

The distance between the continuous VB and the CB is close to the one of the undoped material but the excitation of electrons from the localized part of the VB will be much easier and will require less than half of the usual photon energy. Despite this a localized band can't guarantee a high electrons flux from VB to CB.

Ruthenium and Osmium

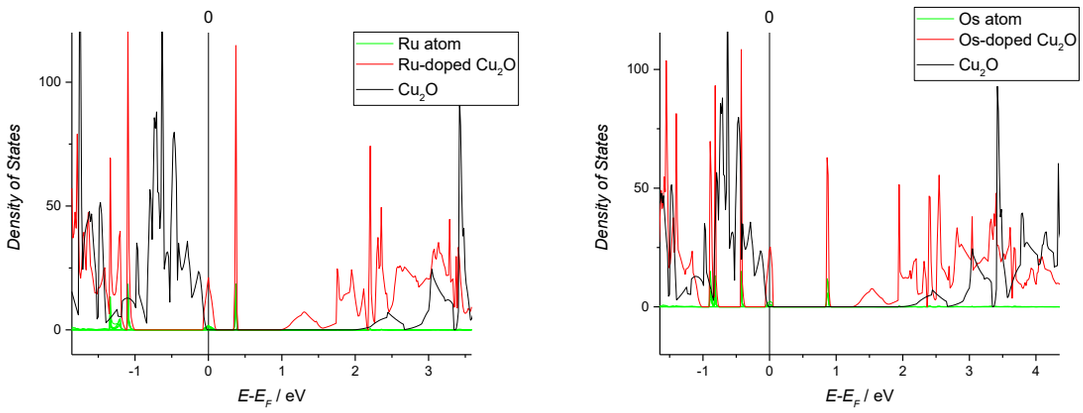

Figure 117. *A) DOS of Ru-doped Cu_2O (in red) compared to the pure Cu_2O (in black). B) DOS of Os-doped Cu_2O (in red) compared to the pure Cu_2O (in black). The green line is the contribute of the dopant atom. DOS obtained from HSE06 calculation on a 2x2x2 supercell.*

Ruthenium has the same intermediate band of Pt and Pd doped systems, but an additional empty band is present in the BG. This band could reduce any additional advantages induced by the IB acting as a recombination center.

Also, osmium-doped Cu_2O shows a particular behaviour with several localized states on the dopant atoms. Two of them are fully occupied, one is partially occupied, and one is empty. This wide presence of localized states suggests the necessity of introduce some vacancy to reduce the number of localized electrons. Indeed, osmium is one of the material with the most favourable energy for multiple vacancies formation as we will see later.

Molybdenum and Tungsten

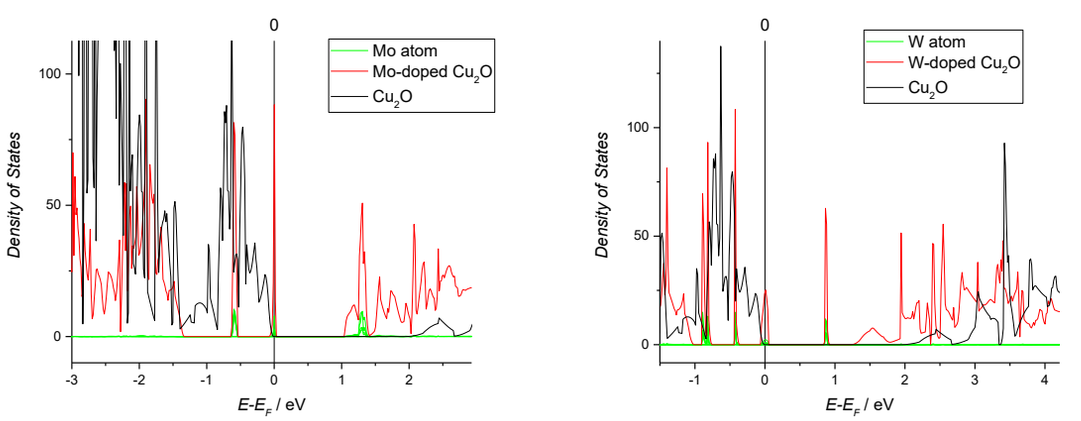

Figure 118. *A) DOS of Mo-doped Cu_2O (in red) compared to the pure Cu_2O (in black). B) DOS of W-doped Cu_2O (in red) compared to the pure Cu_2O (in black). The green line is the contribute of the dopant atom. DOS obtained from HSE06 calculation on a 2x2x2 supercell.*

Mo and W-doped Cu_2O show several localized states on the metal. This behaviour together with the extremely low energy for a vacancy formation suggest that this is not the most stable and final configuration for these materials.

Chromium and Titanium

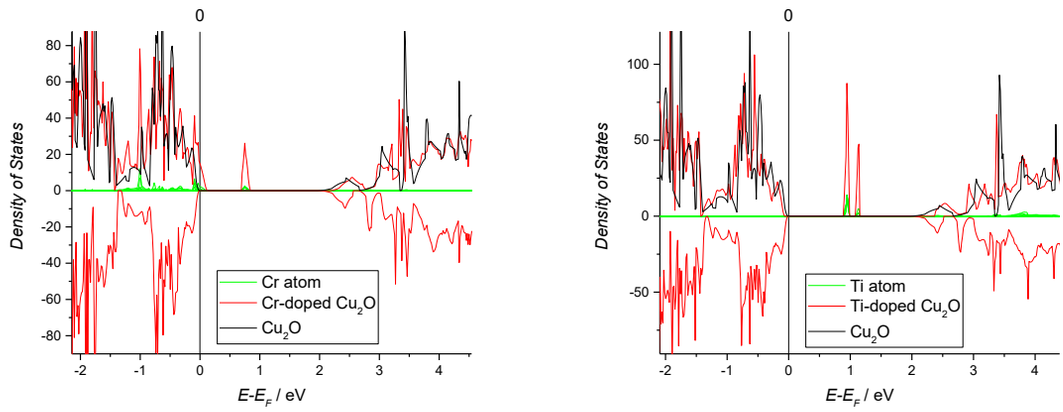

***Figure 119**. A) DOS of Ti-doped Cu_2O (in red) compared to the pure Cu_2O (in black). B) DOS of Cr-doped Cu_2O (in red) compared to the pure Cu_2O (in black). The green line is the contribute of the dopant atom. DOS obtained from HSE06 calculation on a 2x2x2 supercell.*

Chromium, as Pb and Sn, once used as dopant in Cu_2O makes the material showing a metallic behaviour with the VB crossing the Fermi level. It is the only *3d* transition element showing this behaviour that is probably due to the very large number of oxidation states possible on the dopant.

Tin and Lead

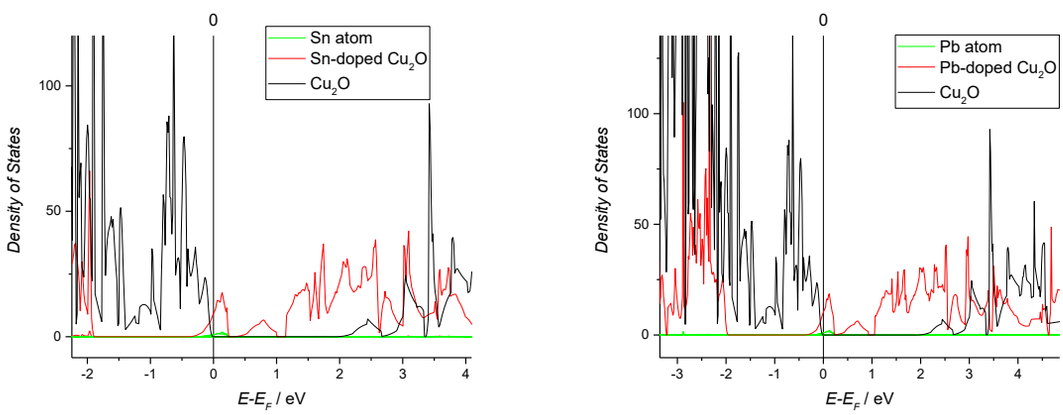

***Figure 120**. A) DOS of Sn-doped Cu_2O (in red) compared to the pure Cu_2O (in black). B) DOS of Pb-doped Cu_2O (in red) compared to the pure Cu_2O (in black). The green line is the contribute of the dopant atom. DOS obtained from HSE06 calculation on a 2x2x2 supercell.*

With tin, the doped material shows a metallic behavior with VB and CB not separated. The material then loses is semiconducting properties if no-vacancies are considered. Similar behaviour was found for lead whose electronic structure is indeed close to the one of tin.

If we consider this state as the final one, these materials will be of any use. From the computed energy of vacancy formation instead we have found that these systems can easily form vacancies respect to pure Cu_2O. The formation of vacancies was then studied.

2.2.7 Doped System with Vacancies

2.2.7.1 1st Vacancy

The so obtained systems are in good agreement with the results obtained by literature while in some cases are completely new. In addition, we want to shine light on the possibility of vacancy formation in presence of a dopant.

The formation of a single Cu vacancy in the pure Cu_2O lattice was computed using the equation:

$$Cu_{32}O_{16} \rightarrow Cu_{31}O_{16} + \frac{1}{32}Cu_{32}$$

The recorded value for the reliable 2x2x2 supercell was 0.37eV. While the energy for the formation of an oxygen vacancy is given by:

$$Cu_{32}O_{16} \rightarrow Cu_{32}O_{15} + \frac{1}{2}O_2$$

Giving the higher value of 2.25eV for the oxygen vacancy formation in pure Cu_2O.

These results are in good agreement with literature and confirm the easiness of Cu vacancy formation in Cu_2O respect to the oxygen one.

A first series of PBE level calculations for different positions of the vacancy in the lattice were computed. The results are reported below.

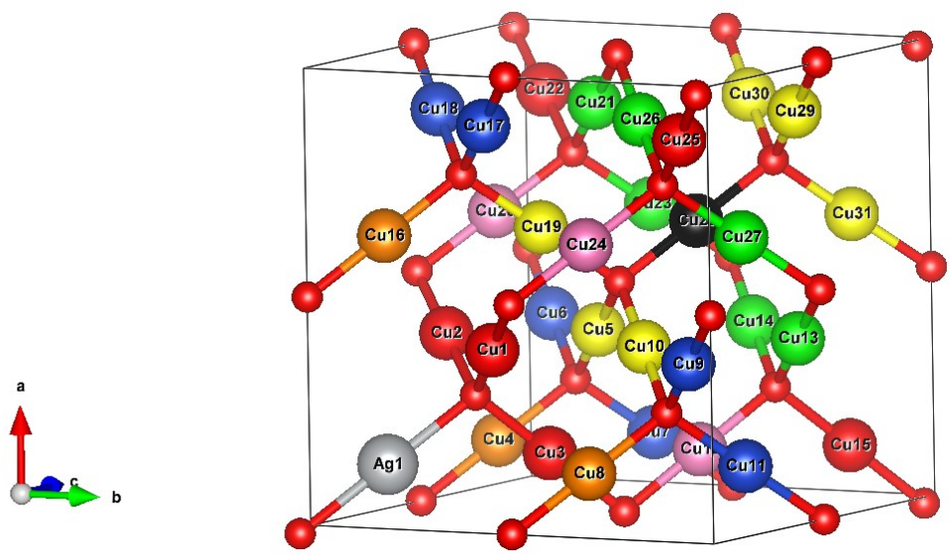

***Figure 121**. 2x2x2 Cu_2O supercell with a dopant (Ag). The different positions for a Cu vacancy are coloured in different colours. Cu atoms of the same colour are equivalent from the distance from the dopant and energy point of view.*

In a Cu_2O 2x2x2 supercell an Ag dopant was added. Then the relative distances between the dopant and all the different copper atoms in the structure were measured and reported in the following Table 20.

All the dopant-Cu couples with the same distance (and then energy) were considered equivalent (e.g. Cu_4, Cu_8 and Cu_{16} are equivalent) and computed just one time. In Figure 121 each position is marked with different colours.

Position #	Dopant-Copper Number	Distance (Å)
1	Ag-$Cu_{1,2,3,15,22,25}$	3.156
2	Ag-$Cu_{4,8,16}$	4.296
3	Ag-$Cu_{5,10,19,29,30,31}$	5.281
4	Ag-$Cu_{13,14,21,23,26,27}$	8.026
5	Ag-Cu_{28}	7.441
6	Ag-$Cu_{12,20,24}$	6.075
7	Ag-$Cu_{6,7,9,11,17,19}$	6.794

Table 19. *Different vacancy positions with respect to the dopant (e.g. Ag) with their distances. All the atoms positions with same energy and distance were grouped together.*

Once the energies for the different positions were calculated, considering the vacancy formation equation, the formation of the single vacancy on each doped system was computed.

$$MCu_{31}O_{16} \rightarrow MCu_{30}O_{16} + \frac{1}{32}Cu_{32}$$

The lower the $E_{formation}$ value, the higher is the probability of vacancy formation in that position. The lower value was then chosen for the evaluation of DOS using HSE level calculation. The converged structure with the lowest energy vacancy was used as starting structure.

For each dopant all the positions were calculated and the one with lower energy vacancy formation is reported in the next tables together with the position:

Dopant	Position #	$E_{formation}$
Ag	4	0.25544
Pt	1	0.164234
Au	1	0.149994
Pd	6	0.193825
Ir	1	-0.1333
Os	1	-0.65909
Mo	1	-0.68817
Ru	1	-0.71214
Rh	1	0.083207
W	1	-0.82491
Pb	7	-1.44389
Sn	7	-1.20469
Ni	2	0.256254
Co	1	-0.01712
Fe	1	-0.43099
Mn	1	-0.45248
Cr	2	-0.10388

Table 20. *First vacancy formation energy from the system $MCu_{29}O_{16}$ and its lattice position.*

Simply looking at the energies we can see how for all the considered systems the vacancy formation is less expensive in energy respect with the formation in the pure Cu_2O (compute value = 0.37eV). As a first result we can immediately notice how higher is the possible oxidation state in the metal, lower are the energies required for the vacancy formation. This is in agreement with literature[242,243,252] that suggest the formation of *n* vacancies if the dopant is M^{n+}. The energies of vacancy formation for Pb and Sn systems are extremely low, and this can be explained by the large dimension of the dopant ion that probably "push" out of the lattice one (or more) copper atom. Moreover, can be noticed how most of the vacancies lies in the first neighbour group of Cu atoms around the dopant (position 1) but there are some exceptions. This means that the position of the vacancy cannot be predicted and must be calculated every time checking all the possible positions.

Interesting the only two dopants of the *p*-group, Pb and Sn, are the only in which position 7 is preferred, probably because of the large dimension of the dopant if compared to transition metals. On the base of the easiness of vacancy formation with all the structures, DOS of some specific doped system with a vacancy in the most favourable position were computed to see if the presence of the vacancy can affect the BG as well as the p-type conductivity[243].

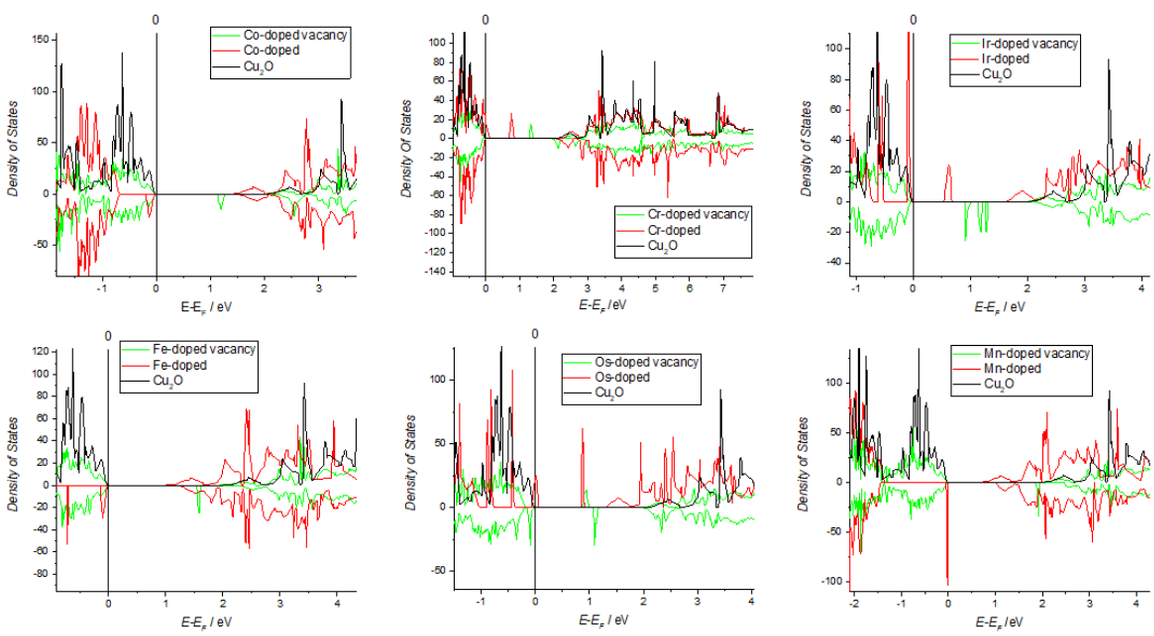

Figure 122. *DOS of A) Co-doped Cu_2O, B) Cr-doped Cu_2O, C) Ir-doped Cu_2O, D) Fe-doped Cu_2O, E) Os-doped Cu_2O, F) Mn-doped Cu_2O without (in red) and with a vacancy (in green) compared to the pure Cu_2O. DOS obtained from HSE06 calculation on a 2x2x2 supercell.*

With most of the material the high localized band disappeared with the formation of the vacancy or became empty. Moreover, the metallic behaviour of Cr-doped Cu_2O disappear and an empty band is formed within the BG. The metallic behaviour disappeared also for Sn and Pb-doped Cu_2O were no bands were recorded in the BG. These materials were the ones with the lowest energy vacancy formation, so this final state is largely favoured. Moreover, the BG is increased making these two materials interesting for the preparation of TCO that need wide BG to ensure the transparency of the layer.

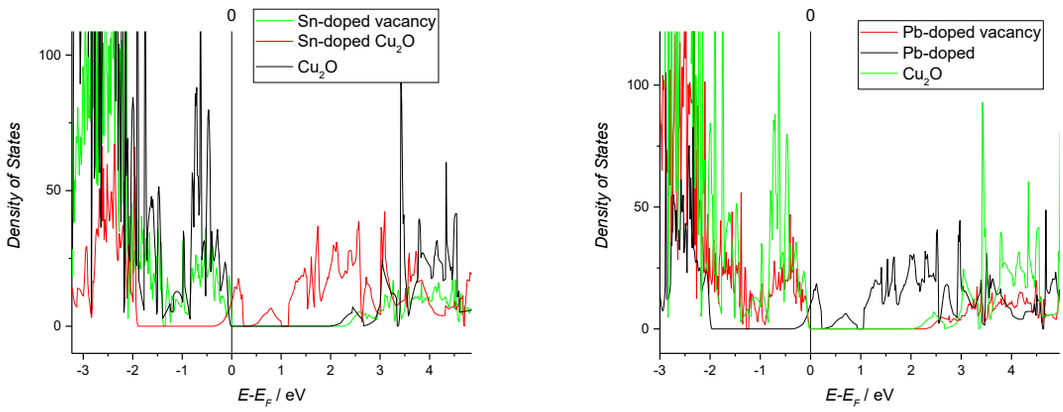

Figure 123. *DOS of Sn-doped Cu_2O and Pb-doped Cu_2O without (in red) and with a vacancy (in green) compared to the pure Cu_2O. DOS obtained from HSE06 calculation on a 2x2x2 supercell.*

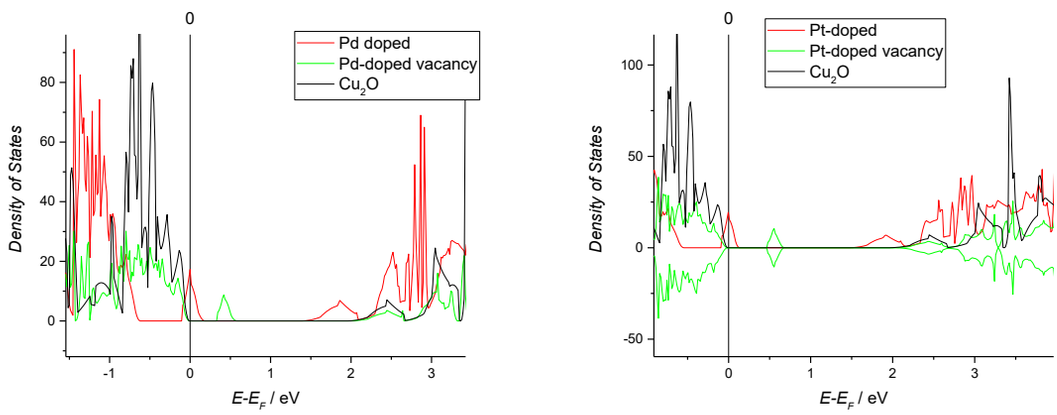

Figure 124. *DOS of Pd-doped Cu_2O and Pt-doped Cu_2O without (in red) and with a vacancy (in green) compared to the pure Cu_2O. DOS obtained from HSE06 calculation on a 2x2x2 supercell.*

Pt and Pd-doped Cu_2O with one vacancy lost the partially filled character of the IB that became empty. According to these results will be very important to have experimental results on this type of doped materials.

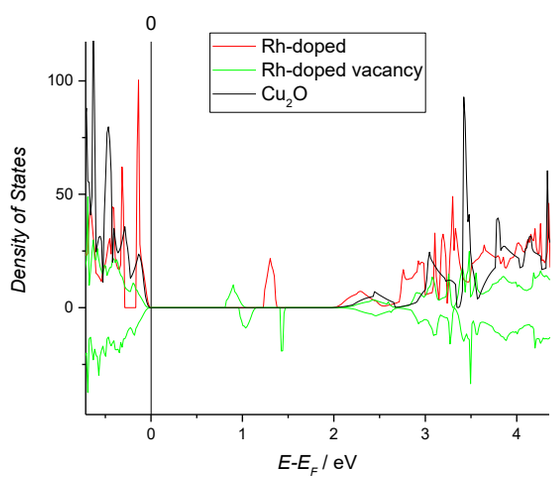

Figure 125. *DOS of Rh-doped Cu_2O without (in red) and with a vacancy (in green) compared to the pure Cu_2O. DOS obtained from HSE06 calculation on a 2x2x2 supercell.*

2.2.7.2 2nd Vacancy

Most of the computed vacancy formation energies have large negative value. The formation of the first vacancy is then sure and the formation of a second one is now studied. From literature the position of the 2 vacancy is suggested to be on the other Cu_2O network with respect to the first one[243]. According to the following figure and table, different positions were tested.

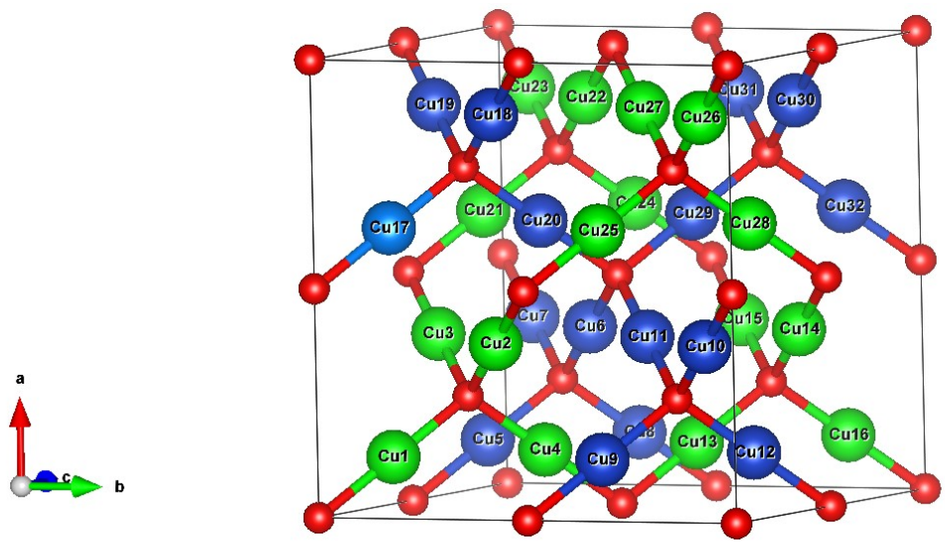

Figure 126. *VESTA representation of the Cu_2O lattice composed by two different networks (in green and blue).*

Considering the two interpenetrating network structures, we have now to imagine the dopant is in the Cu1 position, while the first vacancy in Cu2 position. According to literature the 2nd vacancy will be on the other network (the blue one in this case). Below are reported the different possible positions.

Position #	1st Vacancy – 2nd Vacancy	Distance (Å)
1	Cu_2-$Cu_{5,12,19,31}$	5.26142
2	Cu_2-$Cu_{6,10,18}$	4.29593
3	Cu_2-$Cu_{7,8}$	6.79246
4	Cu_2-$Cu_{9,11,17,20}$	3.03768
5	Cu_2-Cu_{29}	7.44077
6	Cu_2-$Cu_{30,32}$	8.03693

Table 21. *Different vacancy positions with respect to the first one (here chosen in Cu2 position) with their distances. All the atoms positions with same energy and distance were grouped together.*

Once the energies for the different positions were obtained, was possible to calculate the energy for the 2nd vacancy formation with the equation:

$$MCu_{30}O_{16} \rightarrow MCu_{29}O_{16} + \frac{1}{32}Cu_{32}$$

As we can see from the formation energy, the formation of a second vacancy for the selected dopant is far less favourable but still possible if we use as a threshold the value of pure Cu_2O. According to the results all the materials could in principle generate the second vacancy apart from Au and Ag were the formation energy exceed the one of the pure material.

Dopant	Position #	$E_{formation}$
Ag	2	0.45094938
Au	6	0.46530682
Ni	1	0.37183636
Mn	3	0.32211529
Fe	1	0.31151152
Co	1	0.31264318
Rh	1	0.25811918
Ir	1	0.20893439
Pt	1	0.35339577
Cr	4	0.19213459
Sn	2	0.197015
Pb	2	0.1614399
Pd	6	0.36736952
Ru	1	0.22429626
Os	1	0.17481105
Mo	1	-0.21051607
W	1	-0.11163543

***Table 22**. Second vacancy formation energy from the system $MCu_{30}O_{16}$ and its lattice position.*

2.2.7.3 3rd Vacancy

In order to follow the vacancies formation behaviour on different dopants, the formation of a 3rd vacancy was computed. Indeed, all the energies until the second vacancy are still lower to suggest the 3rd vacancy formation. All the remaining Cu in the lattice were considered and the following position were found. These positions are related to structures like those of Fe-doped system where the 1st vacancy and the 2nd one are both in position 1. For different combinations of previous vacancies all the copper positions were tested.

Position #	Cu atom
1	$Cu_{1,2}$
2	$Cu_{3,12,21,22,27}$
3	$Cu_{4,5}$
4	$Cu_{6,10,11,14,17,18,19,24,25}$
5	$Cu_{7,15}$
6	$Cu_{9,16}$
7	$Cu_{13,20,23}$
8	Cu_{26}
9	$Cu_{28,29}$

***Table 23**. 3rd vacancy position and energy equivalent copper in a 2x2x2 supercell with the dopant in position Cu1, the first vacancy in position Cu2 and the second one in position Cu5.*

Due to the extremely long computational time was not possible to compute reliable DOS of these structures. But for each dopant was computed the most favourable position as reported in the following table.

Some materials still have the possibility for the formation of a 4th copper vacancy due to the high negative formation energy, some instead probably stopped at the 2nd one like Pt ($E_{formation}$ =0.508eV).

Dopant	Position #	$E_{formation}$
Mn	13	0.40431611
Fe	7	0.3474608
Co	7	0.35101018
Rh	7	0.34882788
Ir	7	0.2219704
Pt	7	0.50855009
Cr	3	-0.18468642
Sn	5	0.36536908
Pb	5	0.2699108
Ru	7	0.32074681
Os	7	0.04281872
Mo	2	-0.60632949
W	2	-1.24454311

Table 24. *Third vacancy formation energy from the system $MCu_{29}O_{16}$ and its lattice position.*

From the plot we can see how the more vacancies are formed, the less easy is the formation due to increased instability in the lattice. Indeed, if we consider the value of 0.37eV recorded with the pure Cu_2O, material like Ag, Au, Pd and Ni will stop at the first vacancy. Material like Pt, Rh, Co, will stop at the 2nd while Ir and Fe at the 3rd. For the remaining material is our opinion non-sense to insert a 4th copper vacancy in a 32 copper atoms lattice due to the final instability of the whole structure. Results obtained for higher oxidation state materials are indeed consider unrealistic for such small cell. We therefore expect these materials to reconstruct and to not be stable in the considered structure.

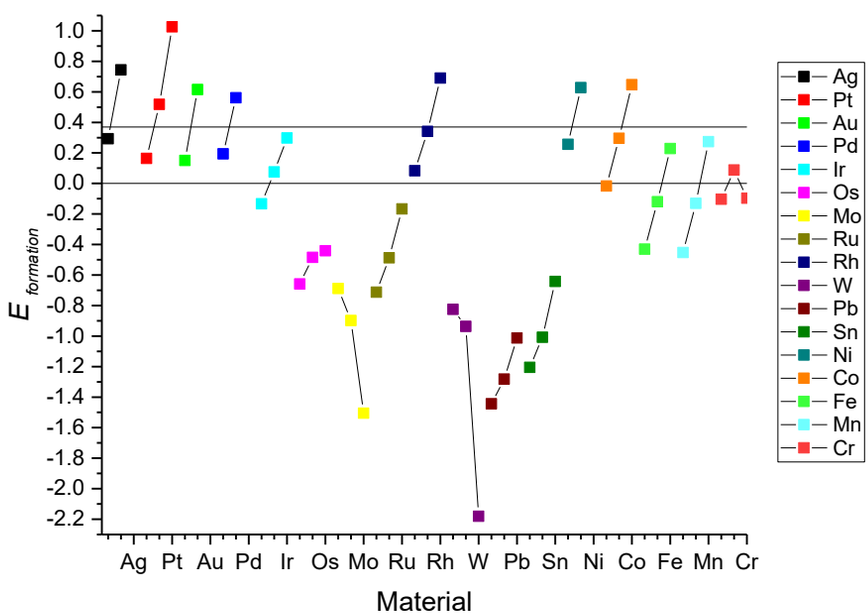

Figure 127*. Copper vacancy formation energies trend in different doped system. The horizontal line at 0.37eV is the value for the vacancy formation in pure Cu_2O.*

2.2.8 Conclusions

The strain effect on this semiconductor gives extremely interesting results. First of all, was noticed the possibility of largely tune the material BG with the appropriate induced strain in the lattice. The use of different underlayers with different lattice dimensions and structures can indeed modify the strain on the Cu_2O lattice with changes in the DOS probably due to the d^{10}-d^{10} interactions responsible of the band gap width. In particular, was noticed the possibility of reducing the band gap up to 42% with a 10% decrease in Cu_2O lattice and a smaller decrease if the lattice is increased up to 10%. This result is of large interest in the field of semiconductors for solar application because will allow to use a larger part of the solar spectrum for the electron-hole couple generation. Surprisingly, the unstrained structure is not at the top of the volcano-like plot of BG vs strain. The BG can indeed be increased if the strain is reduced up to 3%. This possibility can be of interest in the field of Transparent Conductive Oxide (TCO) with p-type behavior[249,345]. In these materials, indeed a wide BG ensure the transparency of the material still keeping its conductivity.

With this computational study was possible to shine light on different aspect able to modify the properties of Cu_2O. The contact with the underlayer and the semiconductor indeed can affect the material from 2 different points of view: an induced strain able, as we have seen, of tune the material band gap simply due to the contact of two different lattice structures, and an increased formation of vacancies due to the favourable mixing of Cu atoms inside some specific metals.

An increase in this vacancy will also improve the conductivity of the material. Eventually were studied different doping systems. The low influence of some material was noticed, but very interesting results with the formation of an intermediate band with Pd and Pt were found. Moreover, Pb and Sn-doped Cu_2O show increased band gap an interesting property to produce p-type TCO. With different doped systems was also evaluated the vacancies formation with the identification of the most favourable position for the vacancy and the energy required for its formation in a large matrix of dopant until the reliable formation of 3 vacancies.

The study of different dopants from the first group was performed to identify the influence of the doping ion size. We found that the ion size can affect the BG and the atomic distances, but only in highly doped cells (25% doping). This is mainly due to the decrease in number of d^{10}-d^{10} interactions and to the shift toward the BG of oxygen bands increasing the size of the dopant. Moving to a more realistic situation (3% doping) the effect of the simple ion size is deleted and the only thing that matter is the electronic structure.

An interesting development of this results will be the experimental tests of different materials as underlayer to identify the different strain on Cu_2O and the real influence on the BG. As seen before FTO, Au and Cu can indeed give very different results in the same working conditions. Is our opinion that this can be one of the affecting parameters in such different performances.

2.2.9 Potentiostatic Measurements

In an PEC-WS cell the potential is fixed where the system is able to obtain the highest photocurrent with the lower external potential applied. To see the material lifetime once biased at potential for strong hydrogen evolution reaction, potentiostatic measurement at 0.175 V vs RHE in Na_2HPO_4 0.5M +NaOH 0.5M (pH11) were performed. The electrochemical setup is the same used during the LSV measurements. A typical result on a Cu_2O@Cu@FTO electrode is here reported.

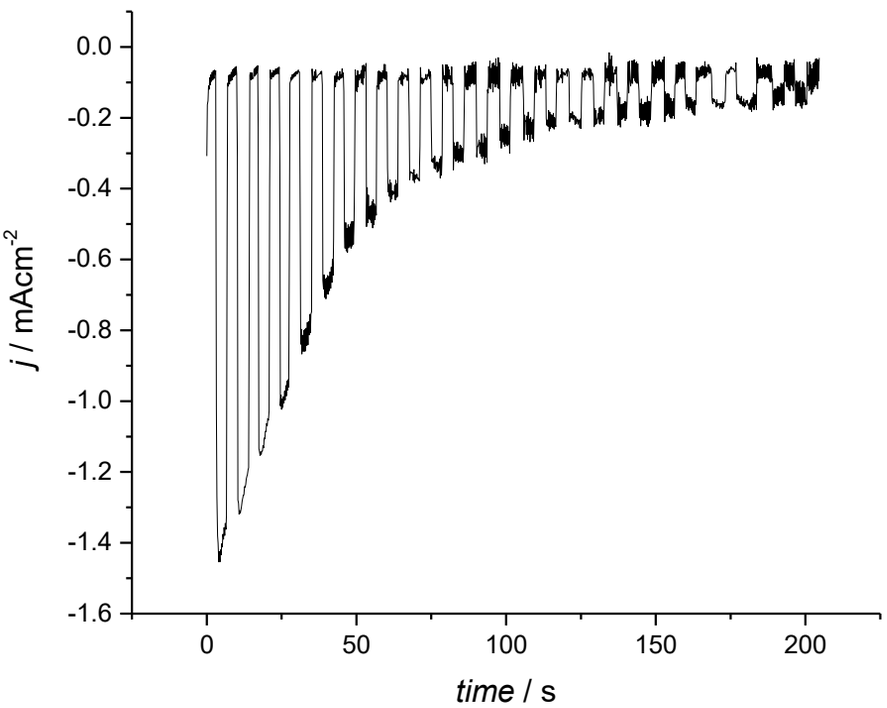

***Figure 128**. Potentiostatic measurement on a Cu_2O@Cu(-0.545)@FTO in Na_2HPO4 0.5M + NaOH 0.5M (pH 11) under pulsed irradiation of a green LED light.*

The electrode work under pulsed light to underline the differences between dark and light measurements. We can see how the deactivation time is extremely short and in less than 2 minutes the electrode has lost most of its activity. Similar results were obtained with Au underlayer. This instability is present only whenever the electrode is under working conditions, while if outside the solution an electrode can last for several weeks without any deactivation in the first photocurrent recorded.

The potentiostatic measurements indeed show the extremely low stability in time under working condition for this material. A strong deactivation occurs while hydrogen is produced making this material unsuitable for any industrial application if used as it is. No influence of the underlayer was recorded from this point of view.

2.3 XAS Evaluation of Photodegradation Processes

As seen from the potentiostatic measures Cu_2O is not stable under working conditions for hydrogen production. The *in-situ* evaluation of the involved processes was performed with the use of XAS.

2.3.1 Introduction

Thermodynamically Cu_2O can lost its photoactivity both because of electrons from the CB and from holes in the VB generated under irradiation. As seen in the introduction indeed, the redox potential for Cu_2O lies inside the band gap so both the processes of reduction to metallic copper (performed by electrons) and the oxidation to Cu(II) (performed by holes) can occur. The photoelectrochemical degradation of Cu_2O to metallic copper was previously seen in literature from different analysis of exhausted samples. XAS measurements were performed to evaluate which process occurs under working condition, its intensity and the potential stability window of the material.

Synchrotron light is mandatory for these experiments and during this work the analysis were performed at the LISA (Linea Italiana Spettroscopia Atomica) beamline at ESRF (European Synchrotron Radiation Facility) in Grenoble (France).

In particular, were used EXAFS and XANES to identify the final species and their amount under working conditions while FEXRAV during potentiodynamic measurements on the sample gives information on the potential stability window. The use of these techniques with *in-situ* and *operando* measurements allows to follow what happens on these electrodes under light-induced HER in the chosen electrolyte.

The following measurements were performed:

- EXAFS on a Cu_2O@Au@FTO electrode before and after the loss of 50% and 75% of its initial photoactivity.
- FEXRAV with CV from 0.52 to -0.307 V vs RHE. Rate: $0.5 mVs^{-1}$ in dark and in light.
- XANES of Cu_2O sample on Au left all the night in NaH_2PO_4 0.5M and NaOH 0.5. pH 11.1 electrolyte under UV LED.
- Difference spectra of Cu_2O@Au@FTO, Cu_2O@Cu(-0.545)@FTO and Cu_2O@FTO at fixed potential of 0.49 V vs RHE.

2.3.2 Experimental Setup

The electrodes were prepared according to the procedure described before with the only exception of the amount of Cu_2O that here was raised to 1C to have higher resolution from XAS. Indeed, here we were not interested in the value of photocurrent but in the evaluation and study of the photoelectrochemical processes affecting the material. Moreover, for the study of the stability window the Cu_2O@Au@FTO were preferred in order to reduce the error in Cu evaluation due to the presence of the underlayer.

Hard X-rays have indeed deep penetration in the matter and it might be difficult to distinguish the formation of metallic copper if a thick layer of Cu(0) is present. During all the *in-situ* and *operando* measurements a Pt counter electrode was used while the reference was an Ag/AgCl 3M in a $KClO_4$ 0.2M double bridge gelled with agar. The cell used for this experiment is the so-called "flat cell" reported in the next chapter.

Applied potential was supplied by a Chi633D galvanostat/potentiostat while the light source was a high intensity LED focused on the sample.

2.3.2.1 Agar-agar Double Bridges Preparation

In the XAS experiments the use of a commercial double bridge is impossible because of the need of modify the spectro-electrochemical cells according to the beamlines structure and the studied samples. For this reason, custom, double bridge were employed with good results.

A solution of $KClO_4$ 0.2M was prepared and heated at least at 60°C under stirring. While the solution is still warm, 3g of agar-agar powder were added to every 100 ml of $KClO_4$ electrolyte. The suspension is kept under stirring until a clear solution is obtained. Some Pasteur pipettes were bended with an oxygen-rich flame at the shape required for the experiment (usually an "L-shape" with a 90-degree angle just 2-3 cm before the end of the tip) according to the cell dimension and working electrode position. The solution of agar and electrolyte is then sucked into the pipette avoiding the formation of small bubbles inside the capillary before it starts gelling while cooling down. The formation of bubbles will interrupt the electrical contact and in this case the pipette must be throw away. Once all the pipettes are filled with the agar gel, a small amount of electrolyte is added on the top of the gel. The pipettes are stored in a beaker filled with the same electrolyte under dark. The presence of the solution is useful to avoid drying of the gel while the dark is necessary to avoid bacteria proliferation on this organic polysaccharide. Agar-agar double bridges must be stored in fridge and for a limited amount of time because moulds formation can occur.

The so-prepared double bridges are low-cost and show no differences respect to the use of a commercial double bridge as seen from preliminary measurements. They can be prepared with almost any electrolyte of interest and help in reducing the Cl^- contamination of the cell electrolyte when an Ag/AgCl or an SCE reference electrode is used.

2.3.2.2 XAS Parameters

The XAS experiments performed at the BM08 are characterized by the high beamline resolution ($\Delta E/E = 10^{-4}$), high photon flux (~ 1011 ph/s) and the small dimension of the spot on the sample. With this beamline is possible to obtain information in a wide energy range (5 – 90 KeV) with the possibility of observing heavy elements and be able to work with the K-edges of elements between Ca and Au, and with the L-edge of the elements from Sb. In the experiments performed in this chapter the monochromator was a Si(311) crystal with Pd mirrors. The cut-off energy was 18KeV. The detector was composed by 13 high purity Ge elements allowing the study of highly diluted samples. All the spectra were recorded at room temperature.

Spectra were recorded here at the Cu-K edge (E = 8979eV) and the calibration was done with a high purity copper foil (the same used as Cu standard). Standard spectra were recorded in transmission while the samples ones were recorded in fluorescence. For the standard measurements, a proper amount of sample (enough to give a unit jump in the absorption coefficient) was mixed to cellulose and pressed into a pellet. The signal extraction was performed by means of the ATHENA code.[346,347]

For the X-ray Absorption Near Edge Structure (XANES) analysis, the raw spectra where first background subtracted using a straight line, and the normalized to unit absorption at 800 eV above the edge energy, where the EXAFS oscillations are not visible anymore.

2.3.3 Photodegradation Process Evaluation

First of all, the spectra of the different standard samples of the Cu species possibly involved in the reaction was recorded. As explained before, the more the specie is reduced the more the spectrum is shifted on the right, to higher energies.

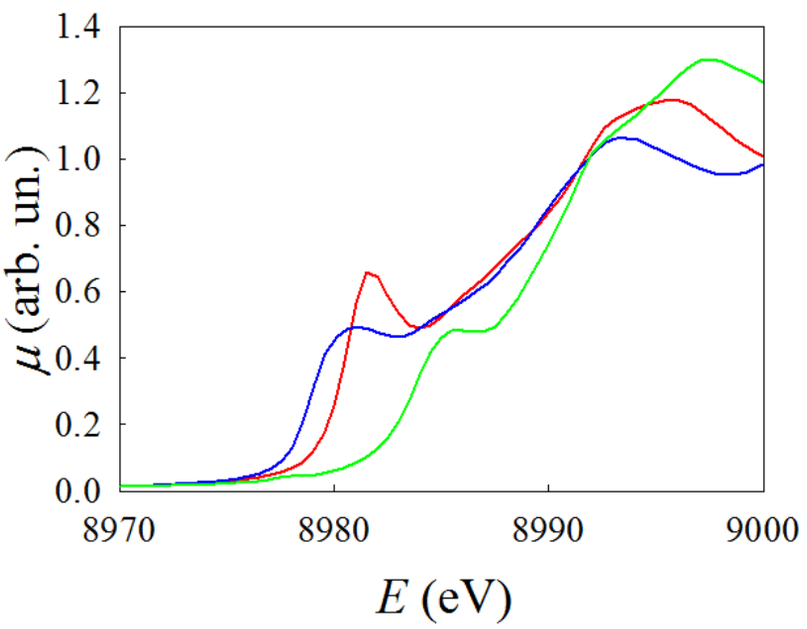

***Figure 129**. Comparison between the XANES spectra (at Cu-K edge) of metallic copper (blue line), Cu_2O (green line) and CuO (red line).*

To evaluate which of the two possible photodegradation processes occurs on the material, 3 *ex-situ* measurements were performed on the same Cu_2O@Au@FTO electrode. The first measurement, on the electrode as new, was used also as an additional proof of the presence of pure Cu_2O. No other additional oxidation states were found and the electrode, prepared a week before, and it was stated to be stable with time. The same electrode was then biased in the working electrolyte at 0.175 V vs RHE under light like in the potentiostatic measurement of Figure 128. The material was left under working conditions until the value of the photocurrent was half of the initial value on the new electrode.

The EXAFS spectra were recorded *ex-situ* after this treatment. Then the electrode was once again biased at 0.175 V vs RHE until the photocurrent reached 25% of the initial value and again an *ex-situ* EXAFS was recorded.

The three XAS measurements are below reported.

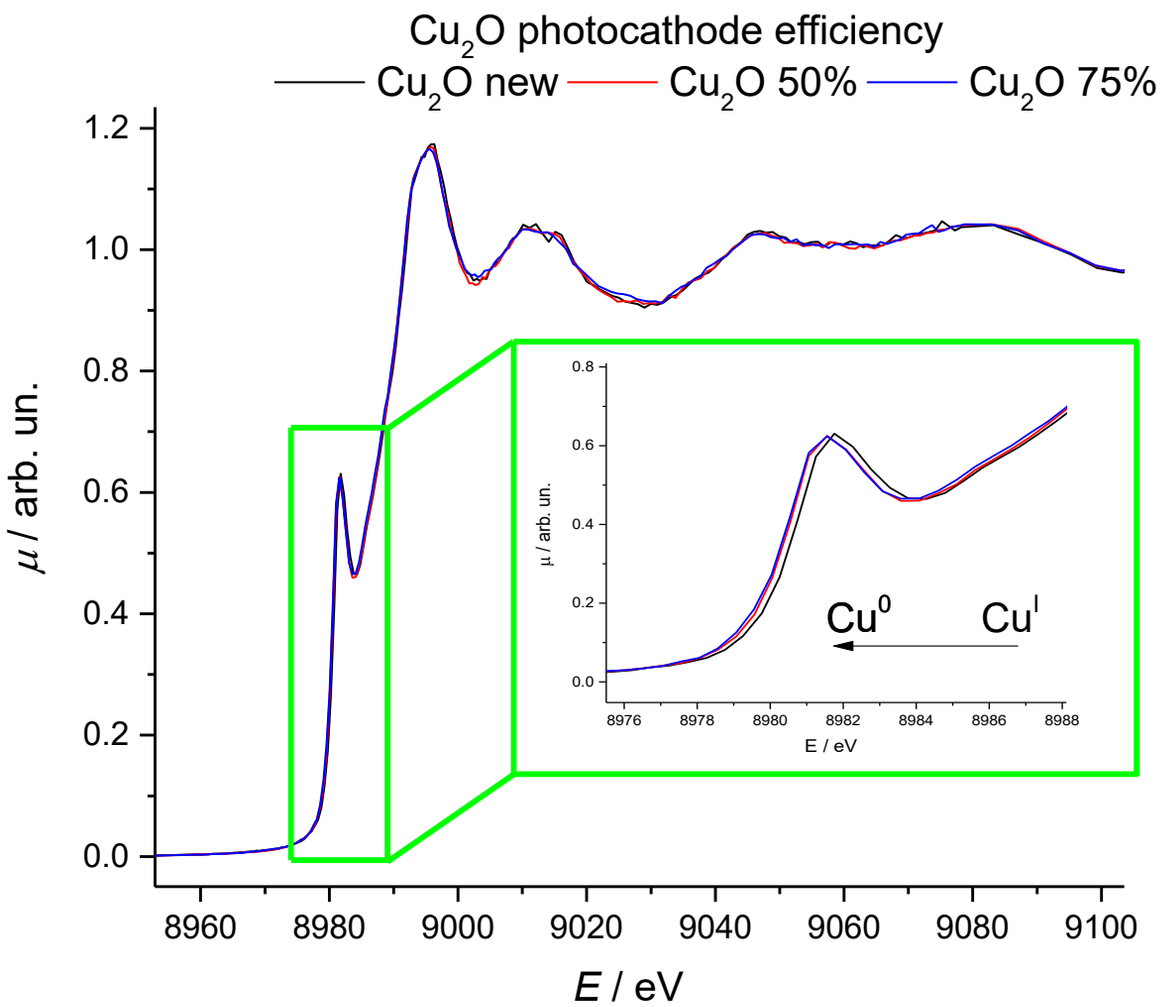

***Figure 130**. XANES spectra of Cu_2O@Au@FTO in ex-situ measurements. In black the electrode as new, in red the electrode that have lost half of its initial photocurrent and in blue the electrode with only 25% of the initial efficiency.*

The electrode as new, the black line, is 100% Cu_2O from the comparison within the different standard and their relative linear combinations. Once the electrode is used under HER condition under light, it lost its initial photocurrent because of photodegradation processes. The changes in the spectra in Figure 130 are small, but looking more in detail in the edge area and at the derivate of the edge we can see the shift in the energies. In particular, in Figure 131A the new sample spectrum is in red, while the spectra after the loss of 50% and 75% of the initial activity they are in green and blue respectively. In the derivative spectra (Figure 131B) the shift is more evident if are compared the electrode as new (in red) and the electrode with only 25% of the initial activity (in blue).

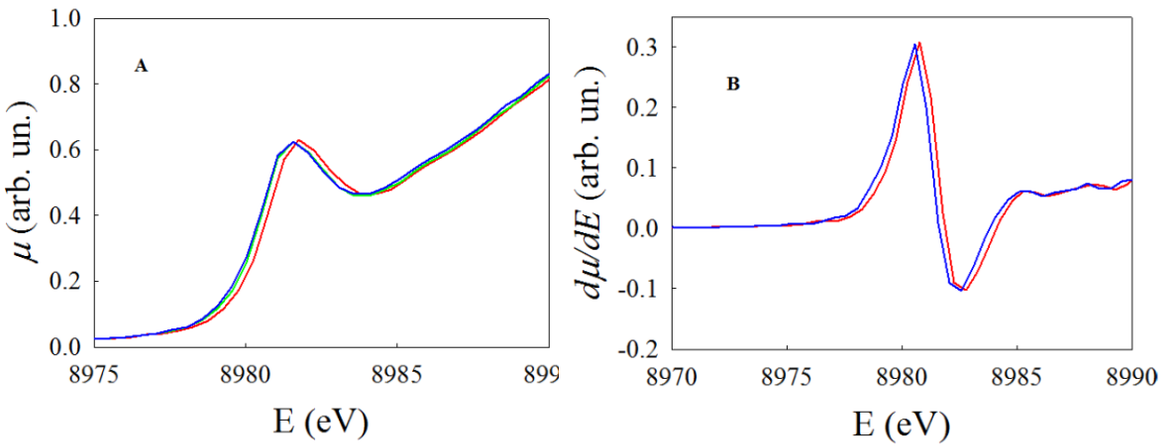

Figure 131. *(A) Detail of the absorption edge of Cu_2O@Au@FTO as new (red), after 50% loss of photocurrent (green) and after 75% loss (blue) in EXANES ex-situ measurements. (B) Derivative spectra of Cu_2O@Au@FTO as new (red) and after 75% loss of activity (blue).*

As we can see the more the electrode stays under photoelectrochemical working conditions for water reduction, the more photocurrents decrease together with a shift of the material spectrum to lower energies. This solid shift to lower energies indicates the formation of Cu(0) from the reduction of Cu_2O, indeed as we have seen before, metallic copper standard spectra is found at lower energy if compared to the Cu_2O one. In this way, we have confirmed that the loss of activity is to be addressed to the high energy electrons generated in the conduction band that instead of reducing water to hydrogen can also reduce the material itself to metallic copper. Of course, copper is not a light-active material and this lead to the loss in recorded photocurrents.

To see if any structural variation occurred on the reduced electrode a fit of the EXAFS was performed.

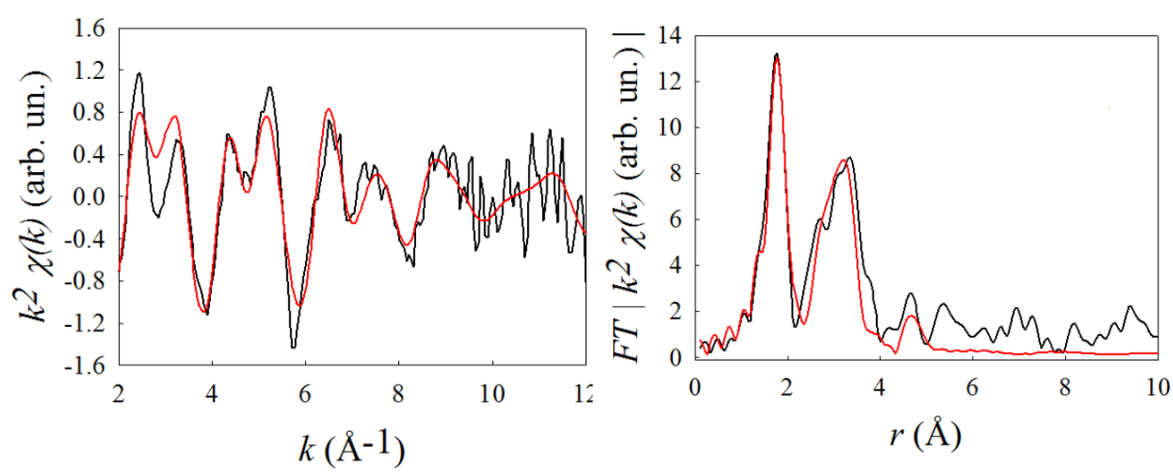

Figure 132. *EXAFS spectra (on the left) and FT (on the right) of Cu_2O@Au@FTO degraded until only 25% of the initial current is left. The black curve is the experimental data, the red one is the fit.*

The signals of the electrode as new (see. Cu_2O chapter) and the one after the photocatalytic activity are almost fully overlapping. These extremely small variations were due to the low amount of photogenerated copper during the measure. To quantify the amount of converted material was indeed not possible to use the EXAFS signal but was necessary to use the part of the spectra more sensible to the oxidation state, the XANES.

A linear fit combination in the region between -20 eV and 30 eV was then done considering metallic copper and the initial spectrum of the electrode. The best fit was obtained for a metallic Cu content of 7.6 (± 1.4) % in the electrode with 50% of the initial photocurrent (Figure 133A). For the further degraded electrode, the Cu content increase to 12 (±1.6)% (Figure 133B). In Figure 133 are reported the experimental data (in red), the obtained fit (in black) and the Cu and Cu_2O spectra evaluated on their content. As is possible to notice the only species present are Cu and Cu_2O without any product from holes oxidation.

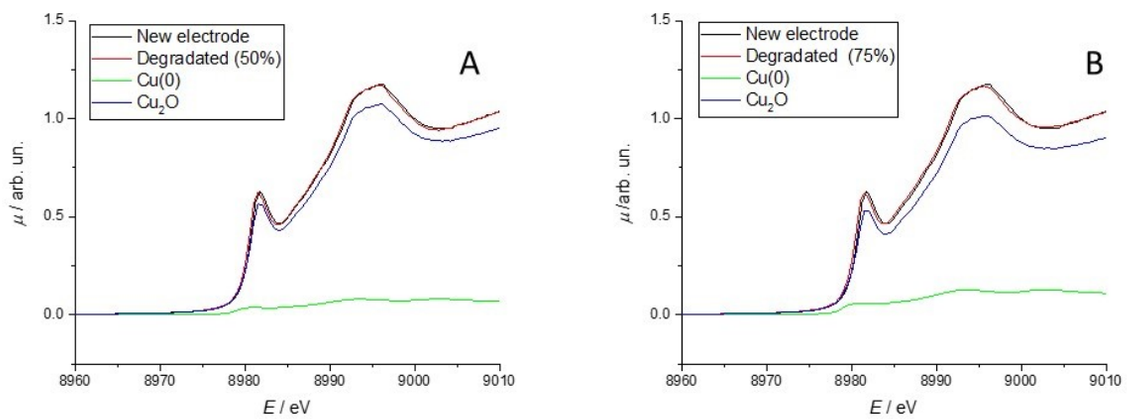

Figure 133. *(A) The red line is the spectrum of the electrode after 50% of photocurrent loss, the black line is the electrode as new. The blue and the green curve are respectively the ones of Cu_2O and Cu considering a Cu_2O content of 92.4% and Cu content of 7.6%. (B) Same line legend but for the electrode with only 25% of the initial photocurrent. Here the fit is agreement with the electrode spectrum when the Cu content is 12% and the Cu_2O one of the 88%.*

From these measurements we have seen that under working conditions, when both light and potential are applied, the electrode is photoelectrochemically degraded to Cu(0). Until now we don't know if the electrode degradation occurs because of the light, because of the potential or because of a combined effect. To de-couple the light effect from the potential one we performed a XANES spectra on a Cu_2O electrode left overnight in the electrolyte under UV irradiation.

The XANES spectrum shows no variation respect to the pristine electrode indicating no reaction occurring in absence of applied potential. The differences between recorded spectra (inset of Figure 134) are extremely low and related to instrumental errors or due to different areas of the sample under X-ray beam.

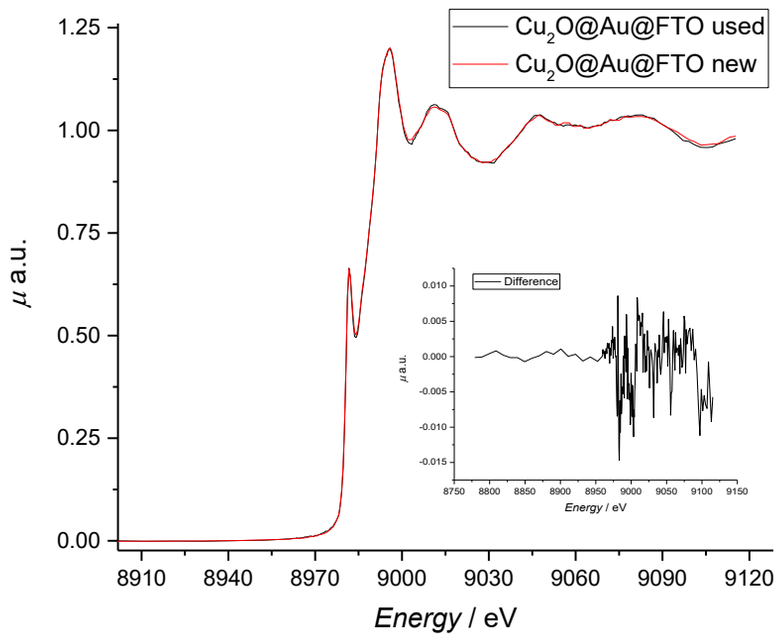

Figure 134. *XANES spectra of electrode as new (red line) and after 10 h of irradiation under 400 nm LED light in 0.5 M Na_2HPO_4 and 0.5 M NaOH, pH 11.1. The inset shows the negligible difference between the two spectra (used – new).*

2.3.4 FEXRAV Analysis

In this recently introduced technique, X-ray energy is kept constant[103] at a value at which the difference between the absorption coefficient of the selected atom at different oxidation states is at its maximum. While the energy is constant, the applied potential is swept in the range of interest. FEXRAV experiments were carried out in dark or under illumination by a 400nm light emitting diode (LED). The electrode potential was swept in the range given in figures captions, with a scan rate of 0.5 or 1 mV s^{-1}.

The use of FEXRAV was of extremely importance to be able to evaluate the stability windows of the material under working conditions. Is indeed not possible to decouple the hydrogen evolution reaction and the material photodegradation simply looking at the LSV in pulsed light conditions.

Considering a photocathode in a photoelectrochemical water splitting system, we might expect three reactions to occur in parallel:

1) The photoelectrochemical reduction of water to hydrogen:

$$H_2O + e^- \rightarrow \frac{1}{2}H_2 + OH^- \qquad E^0 = 0.00V$$

2) The same as 1) but driven solely by the applied potential (in this case the reaction can be observed in the dark as well as under illumination).

3) The reduction of the photocathode material:

$$Cu_2O + 2e^- + H_2O \rightarrow 2Cu + 2OH^- \qquad E^0 = -0.361V$$

The first one is the desired reaction, the last one is the main responsible of poor performance in time due to photodegradation. We have seen from previous measurements that this reaction occurs because of the combined effect of light and potential. We have seen that only light is not enough to transform the material. The aim of this measure is to see which potential is required to start the photodegradation and which is the potential window of stability.

Changes in the oxidation state during the photoelectrochemical reaction can be directly monitored (in real time) using FEXRAV[103,348] that can be thus conveniently adopted to decouple the overall photocurrent from parasitic processes occurring at the photoelectrode.

In FEXRAV, X-ray energy is fixed at a value where the difference between the absorption coefficient, μ, of two or more phases is at its maximum. The choice is made after recording spectra of standard materials. For Cu, Cu_2O and CuO, this is shown in Figure 135.

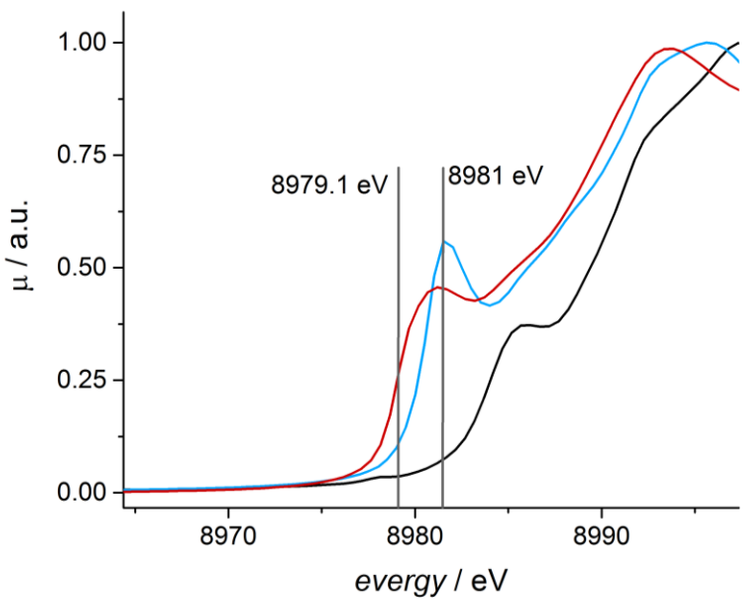

Figure 135. *XANES spectra of commercial CuO (black line), Cu_2O (blue line) and Cu (red line), used as standard materials. Spectra acquired in the transmission mode.*

In the present case, the energy of the incoming X-ray was alternatively fixed at 8979.1 eV giving the maximum contrast between the absorption coefficient (μ) of Cu_2O and Cu. In this way, the electrode potential can be swept at will and any variation of μ indicates a change of the oxidation state of copper.

In both cases, we can attain a quantitative comparison between:

1) The degree of reduction (by FEXRAV): considering the relative absorption coefficients of the pure phases at the selected X-ray energy, it is possible to estimate the composition of the photoelectrodes during the potential scans.

2)The overall integrated quantity of charge that, for the sake of an easier comparison, is here considered fully due to the electrode material reduction (in the dark scan).

Figure 137 shows the results of a FEXRAV experiment carried out in 0.5 M Na_2HPO_4 and 0.5 M NaOH (pH 11.1) on Cu_2O@Au@FTO at 8971.1 eV, both in the dark and under 400 nm illumination. During this FEXRAV experiment, the electrode potential was swept in the dark in the first cycle and under illumination in the second one. As in this experiment the energy of the impinging X-ray beam is fixed to that of inflection point of the pre-edge peak of metallic Cu (8979.1 eV), and as at this energy the absorption of Cu_2O is negligible, we can safely attribute any increase in μ to the reduction of the material (reaction 3). Figure 137 shows that, in the dark (A), FEXRAV indicates a stable composition until *ca.* -0.3 V, probably because of some difficulties in Cu grains formation at the beginning of the reaction and to the non-perfect synchronization between XAS and electrochemistry (a certain amount of material need to be present to be recognized by XAS). The material reduction continues until 0 V where also the electrochemical signal shows no further reduction. Indeed, in dark the only possible reaction is reaction 3 of material electrochemical degradation.

In the second cycle (in light, Figure 137B), the reduction starts at 0 V and eventually stabilizes. This occurs in parallel to a dramatic increase at 0 V of the recorded photocurrent. We can see from the variation of μ how in light the material reduction is far away higher (larger variation of μ), and moreover how the onset potential for the material reduction is shifter toward less negative potential. This confirm that light and potential must be applied together to start the degradation of the material and that a potential window until 0.05V can be considered safe for the material itself.

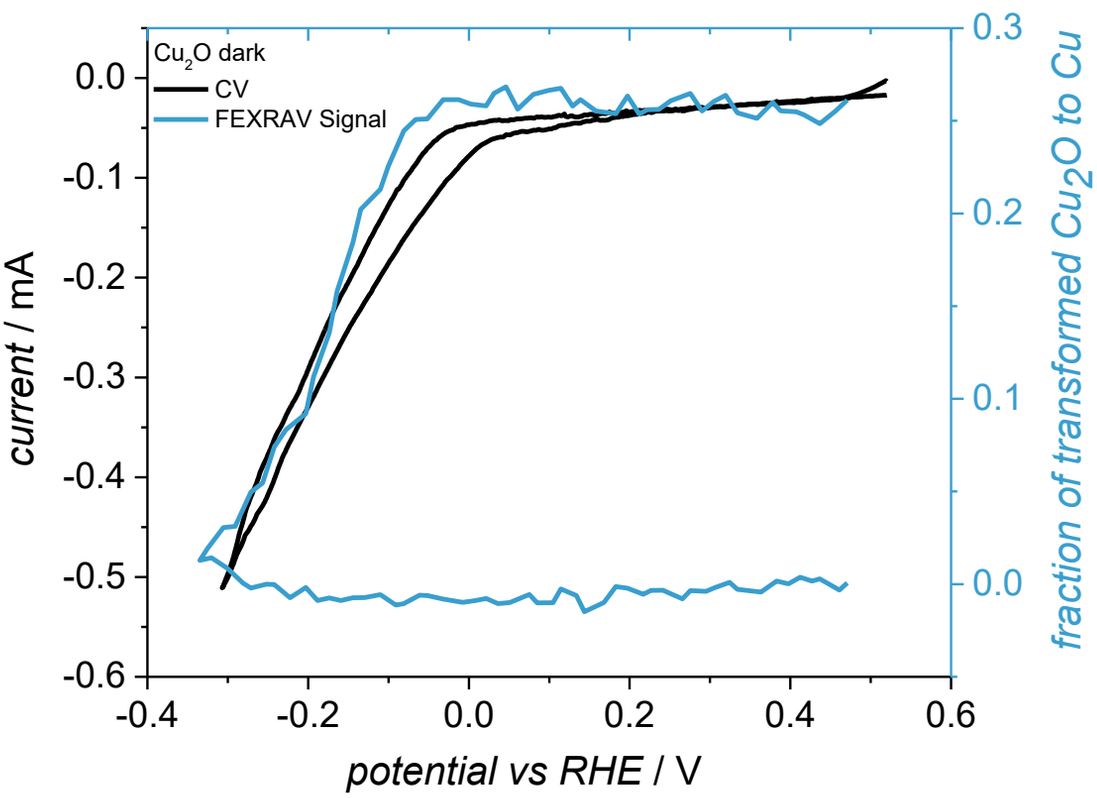

Figure 136. *Fraction of Cu_2O reduced to Cu and current intensity as a function of the applied potential during a FEXRAV experiment on Cu_2O@Au@FTO electrode in 0.5 M Na_2HPO_4 + 0.5 M NaOH, pH 11 in the dark.*

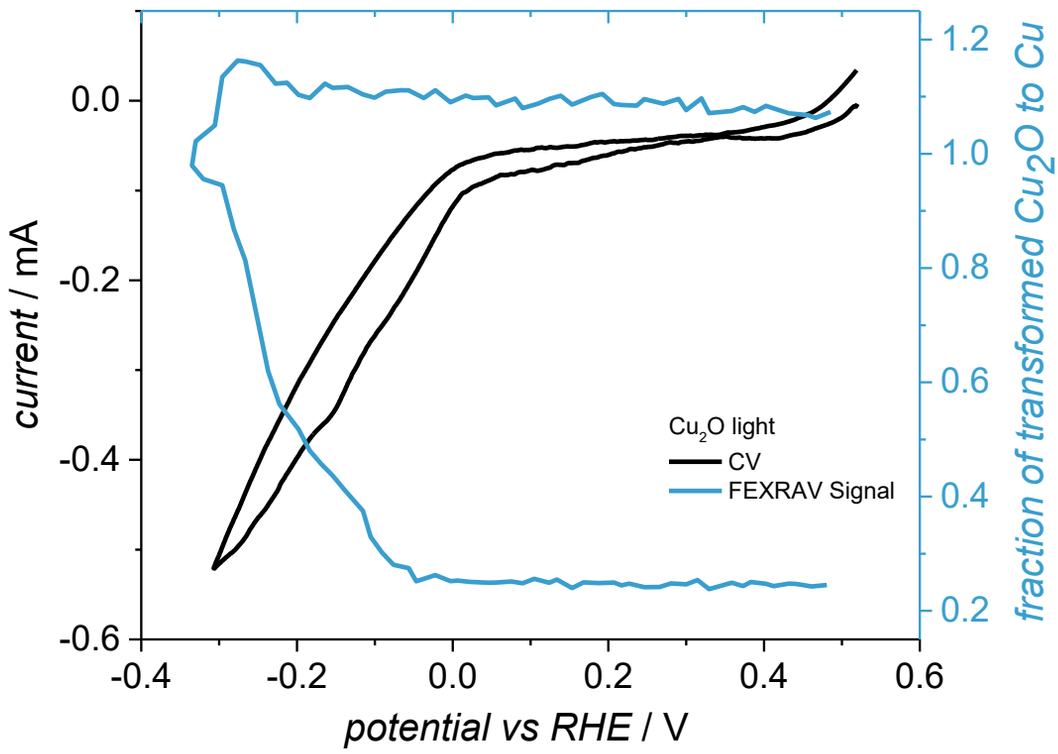

Figure 137. *Fraction of Cu_2O reduced to Cu and current intensity as a function of the applied potential during a FEXRAV experiment on Cu_2O@Au@FTO electrode in 0.5 M Na_2HPO_4 + 0.5 M NaOH, pH 11 under LED 400 nm illumination.*

From these results, it is evident that Cu_2O results to be active towards H_2 evolution, in parallel to a severe reduction to Cu. This observation serves as preliminary background for the study of Cu_xO and explains the need of a protecting layer for Cu_2O.

2.3.5 *Operando* Difference Light-dark ($\Delta\mu$) XANES Spectra

To further investigate the nature and origins of photogenerated holes, we recorded difference XANES spectra (light-dark). This was done at potentials at which a cathodic photocurrent is observed, yet the stability is guaranteed (see FEXRAV).

$\Delta\mu$ spectra (light-dark) were collected at the Cu-K edge by setting the monochromator at the desired energy and then waiting for 30 seconds for stabilization. The point in dark conditions was acquired and the light was subsequently switched on. After 30 seconds, the photocurrent was stable and the X-ray absorption under illumination was recorded. The light was then switched off and the whole sequence was repeated for each energy point. This system allows to record the spectra in dark and under illumination by nullifying any experimental artifact due to different monochromator conditions. The visible illumination source was in all cases a 5W 400 nm LED.

Difference spectra on Cu_2O@FTO electrodes were recorded applying a potential of 0.49 V vs. RHE and are shown in Figure 138A. The potential is “safe” from photodegradation effect but still enough to see photocurrents. The corresponding trace of the photocurrent recorded during the measurements is reported in Figure 138B. The difference spectrum (light-dark) shows a remarkable positive peak at *ca.* 1.5 eV below the pre-edge peak of the Cu_2O edge.

This sharp transition is a signature of linearly coordinated Cu(I) and it is due to the *1s→4pπ**dipole allowed transition.[20] In Cu_2O, the Cu *4p* states make a significant contribution to the bottom of the valence band,[21] whereas the top of the valence band is essentially made up by Cu $3d_z^2$ states. If we recall here that the band gap value is 2.2 eV, and that in the band structure of Cu_2O the partial covalence of the Cu-O bond mixes Cu $3d_z^2$ and O *2p* states, then the positive peak in the Δ*μ* spectrum can be attributed to an increase of the density of holes with $3d_z^2$ symmetry at the top of the valence band.

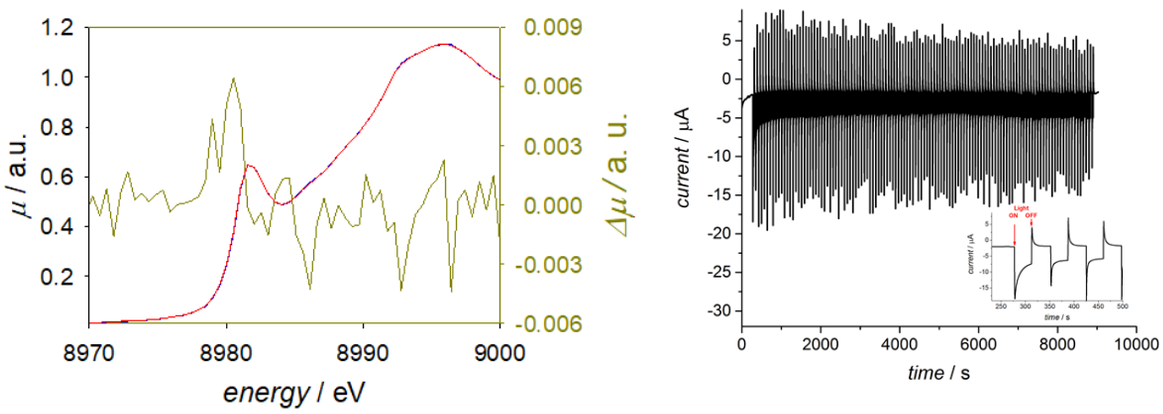

Figure 138. *(A) XANES spectrum of Cu_2O@FTO electrode at 0.49 V in Na_2HPO_4 0.5M + 0.5M NaOH at pH 11 in the dark (blue line) and in presence (red line) of 400 nm illumination. The difference spectrum (Δμ light-dark) is shown by the green line. (B) Photocurrent generated by Cu_2O upon chopped irradiation (LED 400 nm) and applied potential 0.49 V vs RHE in electrolyte of pH 11. Inset: zoom at initial time of experiment. By red arrows the time of light ON and OFF is indicated.*

2.3.6 Conclusions

According to these results we can conclude that Cu_2O is a material stable under light in absence of applied potential. The electrode can also be stored in light without any loss of activity for several weeks. With the *ex-situ* measurements was possible to identify the main actor in the photodegradation of Cu_2O, the high energy electron in the CB generated after irradiation. This electron instead of reducing water to hydrogen, reduce the material itself to metallic copper, probably at the solid-liquid interface. The amount of metallic copper generated was recorded by a linear fit combination of the new electrode and metallic Cu. This small amount is enough to largely reduce the Cu_2O photoactivity probably because of the formation of a non-transparent layer on the surface that prevent the inner Cu_2O to be reached by the light once Cu is formed. The stability windows for this material was also evaluated both in dark and in light conditions by the mean of FEXRAV. This technique gives important information about the intensity of the two parallel processes occurring on Cu_2O but it was difficult to evaluate the relative intensity and moreover is not so easy to have access to XAS beam-time. For this reason, in a later chapter a novel method for the evaluation of the relative intensity of the photodegradation process will be presented.

2.4 Structure and Stability of Copper(II) Lactate Complex

2.4.1 Introduction

Energy dispersive X-ray absorption spectroscopy (EDXAS) were applied aiming at solving the problem of structure and stability of Cu(II): lactate complex in alkaline solution, used as precursor for the electrodeposition of Cu_2O[349]. The application of multiple scattering calculation to the simulation of the X-ray absorption near edge structure (XANES) part of the spectrum allowed an accurate resolution of the structure: the Cu(II) cation is surrounded by four lactate ions in a distorted tetrahedral environment, the lactate anions acting as a monodentate ligands. This results in an atomic arrangement where Cu is surrounded by 4 oxygens located at a quite short distance (ca. 1.87 Å) and four oxygens located quite far apart (ca. 3.1-3.2 Å). The complex was finally found to be stable in a wide range of applied potentials.

To explain the different microstructures found at different temperatures for electrodeposited Cu_2O layers, De Jongh et al.[350] proposed a complex reaction mechanism for the reduction, involving hole transfer from the lactate to the growing layer at high temperatures and an electron transfer from surface defects of the growing layer to the lactate solution at lower T. In order to better understand the mechanisms of Cu_2O electrodeposition, the structure and stability of the Cu(II) lactate complex in aqueous solution have to be investigated. Based on solid state structural determinations, lactate ions (L) are thought to form a complex with copper with 1:2 (Cu:L) stoichiometry[351], but no direct information is presently available. In addition, Cu(II) alkaline solutions with L excess can display complicate electrochemical behaviour showing different peaks in cyclic voltammograms as seen before. This chapter is aimed at addressing the structure and electrochemical stability of Cu(II) lactate complexes in alkaline solution. In this respect, X-Ray Absorption Spectroscopy (XAS) plays a key role, especially to characterized electrocatalytic nanoparticles as already demonstrated by some of us[101,123,352,353]. The ability of XAS to solve structural problems in solution was demonstrated since the early days of synchrotron light science[354]. While the EXAFS part has been widely used to gain information on the structure of complexes in solution, the state of the art is quite different for what concerns the XANES. Indeed, in the study of aqueous complexes, only a small number of ab-initio XANES calculations can be found in literature, while qualitative interpretations of XANES spectra[355–358] is still employed. This is at least partially due to the complicate nature of the systems. Moreover, only complexes characterized by high symmetry have been examined. However, XANES contains the finer details of the structure, and it is capable, in principle, to retrieve the whole 3D structure around the photoabsorber[359]. The infrequency of structural determination based on XANES is mainly due to the difficult theoretical treatment required.

We wanted also to investigate the stability of the CuL complex versus the electroxidative process. For this, we studied the Cu(II) complex in alkaline solution by Linear Sweep Voltammetry (LSV), starting from anodic potentials and reaching the potential for Cu_2O deposition (at about -0.4 V vs. Ag/AgCl). In this respect, Energy Dispersive XAS (EDXAS) is the technique of choice: as a matter of fact, in the energy dispersive mode, a XAS spectrum can be acquired in milliseconds or less. The main drawbacks are a quite limited signal to noise ratio, and a loss in resolution.

In this work we show, however, that fine and reliable details on the structure of the Cu(II) lactate complex in solution can be obtained also starting form EDXAS data. Moreover, thanks to the favourable time resolution of EDXAS, we were able to obtain some insights into the electrochemical behaviour of the compound.

2.4.1.1 Spectro-electrochemical Cell for *Operando* X-ray Absorption Measurements

In order to perform *operando* XAS measurements a spectroelectrochemical cell was designed and built by means of a 3D printer[360]. Figure 139A schematically shows the main components of the electrochemical device. This consists of two parts: a polycarbonate disc (1) and a Teflon® hollow cylinder (21 mm diameter, 6 mm thickness, and 7 mm cavity, 2). The working electrode (3) is a screen printed carbon electrode (DropSens® DRP-P-C11XX) loaded with gold nanoparticles, because gold is an effective substrate for Cu_2O deposition[57,58,306,361]. The electrode is held between the main body of the polycarbonate cell and the Teflon® plate that also includes a hole for the X-rays beam through the use of an O-ring (4). The cell can contain 2 mL electrolyte solution and can host a Pt wire counter electrode and Ag/AgCl reference electrode. The Pt counter electrode was shaped to form a hook just above the DropSens® working electrode. The reference electrode is separated from the solution by a salt bridge made of a glass pipette filled with a gelled solution of 0.2 M aqueous $KClO_4$. The solution under study was prepared as previously described in the first chapter.

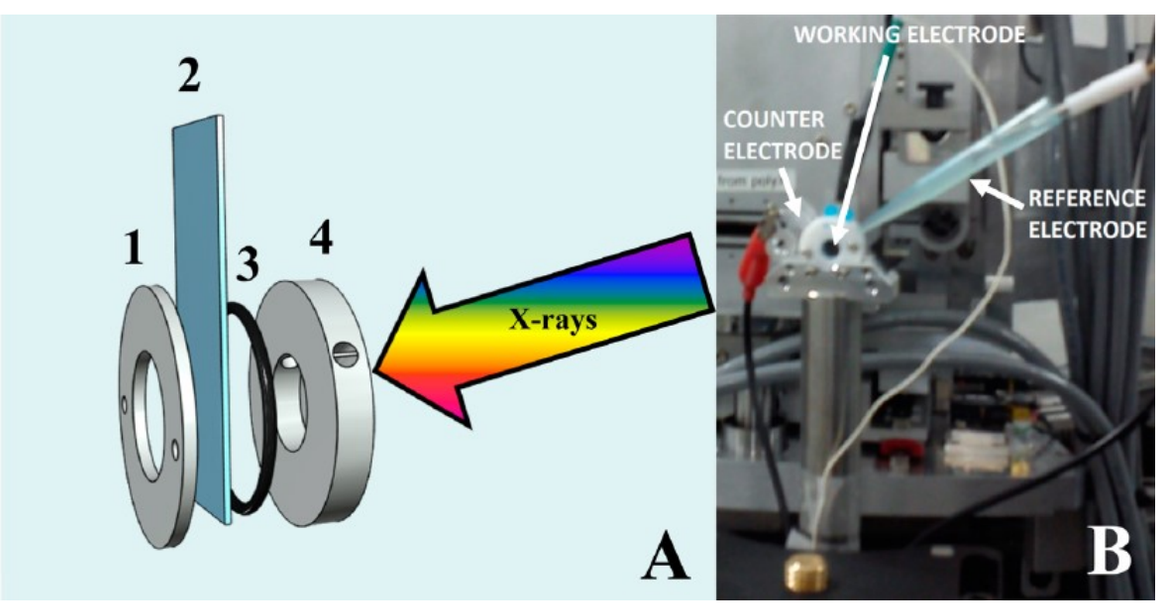

***Figure 139**. Illustration of the 3D printed spectro-electrochemical cell. (A): schematic representation of the two sides (1,4), the working electrode (2) and the O-ring (3). (B): image of the cell with the three electrodes set up, mounted in the beamline hutch.*

2.4.2 XAS Experiments

X-ray Absorption measurements were performed in the transmission mode at the ID24 beamline[362] at the European Synchrotron Radiation Facility, ESRF, Grenoble (the ring energy is 6.0 GeV, with a ring current ranging from 150 to 200 mA). Figure 139B provides an image of the electrochemical cell with the three-electrodes set up mounted in the experimental hutch. The X-ray source consists of two undulators whose gaps were adjusted to tune constant counts of the first harmonic for energies around the Cu K-edge spectra. The horizontal beam focusing was achieved by means of a curved polychromator (Si 111) crystal in Bragg geometry while the vertical beam focusing was obtained with a bent Si mirror at a glancing angle of 2.5 mrad with respect to the direct beam. The beam size at the sample was focused at 8 µm FWHM horizontally and defocused at 80 µm FWHM vertically to decrease the photon density for preserving the samples with respect to beam damage. The curved geometry allows the polychromator to pass a broad band of energy through the sample and to diverge towards a linear photodiode array detector (FreLonCCD camera[363]), where the beam position can be correlated to the energy. X-ray Absorption data were collected in *operando* in order to investigate both the structure of Cu(II) lactate complex in the starting solution and the pertinent stability. The integration time chosen for the Cu(II) lactate solution single spectrum was 500 ms. The stability of the solution was investigated by recording a sequence of spectra while LSV was performed on the CuL solution. In this case we acquired 320 spectra with an integration time of 500 ms for a total time equal to 160 s. These values were chosen for a good compromise in order to avoid saturation and to obtain an adequate signal-to-noise ratio. The LSV measurements, from 1.2 to -0.4 V vs Ag/AgCl at 0.01 V/s, were triggered by the spectra acquisition system through the trigger option of the potentiostat (CH Instrument 630D). All measurements were carried out at room temperature.

2.4.2.1 XAS Data Analysis

Two kinds of measurements were performed in the work described in this paper: recording of a single XAS spectrum, to gain information about the local structure of the Cu(II) lactate complex in aqueous solution, and acquisition of a sequence of spectra during a LSV, from 1.2 to -0.4 V vs Ag/AgCl, to investigate the electrochemical oxidation stability of the Cu lactate deposition bath.

The analysis of a single spectrum is based on three main steps: (i) preliminary processing and data extraction, (ii) EXAFS fitting and (iii) XANES theory calculation. The investigation of the sequence of XAS spectra is constituted of: (i) preliminary processing and data extraction, and (ii) automatic XANES fitting by linear combinations of spectra of model compounds. For both measurements, the first step was carried out by means of PyMCA[364] and PRESTOPRONTO[365] codes. It starts from the evaluation of a pre-edge function and a post-edge baseline function that were the applied to the raw signal. The former is associated to additional excitations of the photo-absorber or to possible excitation of any other element present ($\mu_n x$) and was modeled with a straight line calculated by interpolating the pre-edge data and then extrapolated to the after-edge XAS signal.

The latter can be described as the absorption profile that can be observed if the photo-absorber were isolated (usually defined as $\mu_0(E)$) and was obtained with a 2nd order spline using the first inflection point of μ(E) as E_0.

Thanks to these preliminary analyses it was possible to normalize XAS spectra and perform EXAFS extraction. For the sequence of spectra acquired during the LSV, the data extraction was carried out by observing the first spectrum and applying the same parameters to all the spectra of the series. EXAFS fitting on the extracted signals was carried out by means of the EXCURVE code[366]. The calculation of the atomic scattering parameters (phases and amplitudes) employed the muffin-tin approximation, in the framework of the Hedin-Lundquist and Von Bart approximations for the exchange and ground state potentials[366], respectively. This includes the effects of losses due to the electron inelastic scattering. The fittings were made using a full multiple scattering calculation within the assumed clusters. As goodness of fit (GOF) we used the F-factor:

$$F = 100 \sum_{i}^{N} \frac{\left[\chi_{i,exp} - \chi_{i,calc}\right]^2}{\sigma_i}$$

The fittings were made in the k space, using a k2 weighting scheme.

XANES calculations by means of EXCURVE software are based on full multiple scattering (FMS) approach to generate theoretical signals[367]. The simulation is obtained through the use of the exact calculation of the scattering path operator. In order to validate the XANES calculation procedure applied in this work, a calculation was performed to simulate the XANES spectrum recorded on a 0.1 M solution of $CuSO_4 \cdot 6H_2O$ standard. We think that the Cu(II) hydrated ion is a very good test system for our XANES fitting approach. In fact, because of the high exchange rate of water molecules it is not simple to obtain good theoretical simulations[368,369]. Very good simulations are obtained by means of the distorted octahedral and the square pyramidal arrangements whereas large discrepancies arise if the trigonal bipyramidal arrangement is employed (Figure 140).

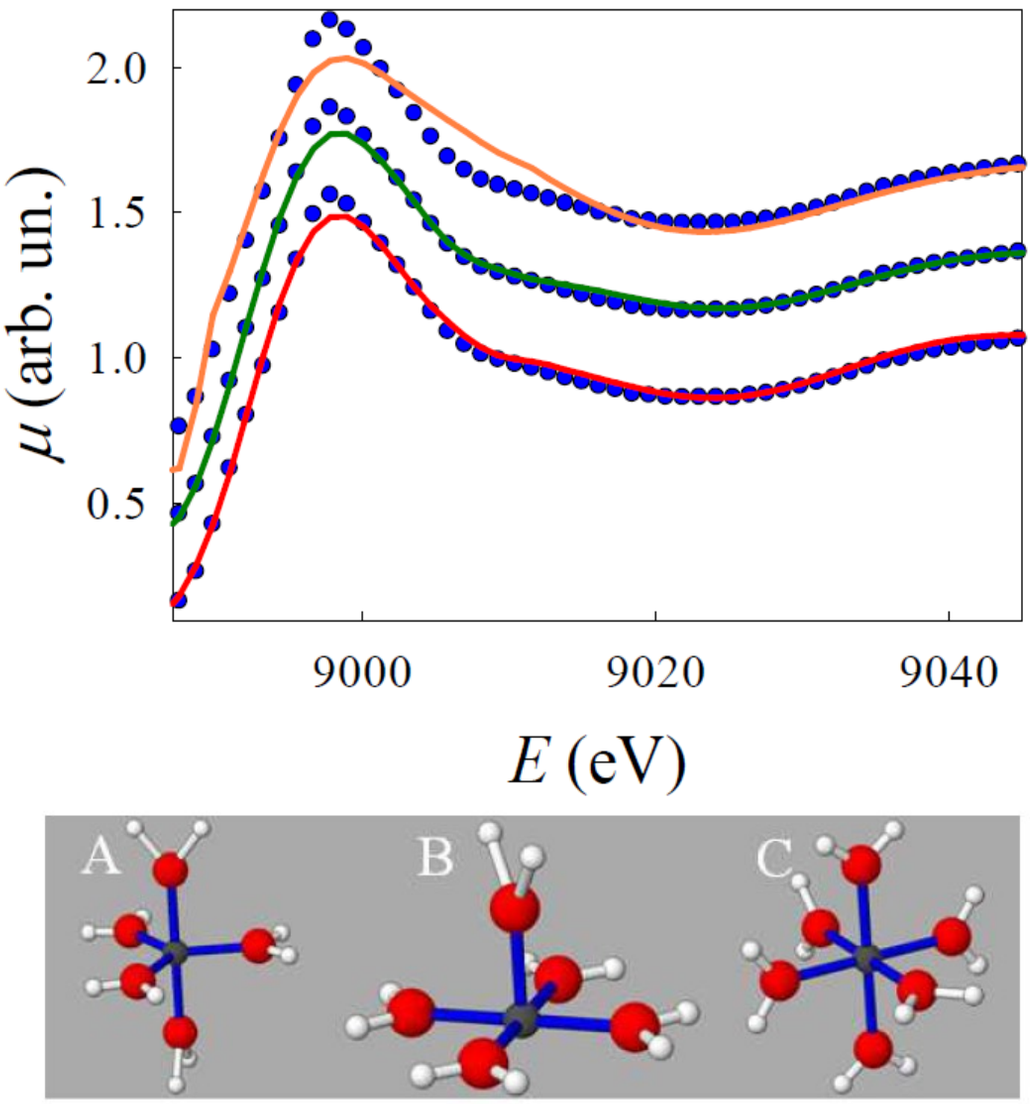

Figure 140. *K edge XANES simulations of Cu(II) aquaion. The blue spots represent the experimental signal while the colored lines are the theoretical calculations based on a trigonal bipyramidal local arrangement (orange line, A), on a square pyramidal local arrangement (green line, B) and on a distorted octahedral local arrangement (red line, C).*

These results, which also show that the XANES signal is very sensitive to local geometry, are in good agreement with recent literature[370], where the distorted octahedral and square pyramidal geometries have been identified with the most probable local structures for the Cu(II) hydrated ion. The best fitting parameters that have been obtained are illustrated in Table 25 and Table 26. The results are in quite good agreement with those found in literature[355,371–375]. It should be noted that adding a skewness parameter (β) for some of the coordination shells was important for improving the GOF. This is reasonable in the light of the high fluxionality claimed by several authors for hydrated Cu(II)[372,376,377]. We finally note that the agreement between experiment and calculations shown here is by far better than any other found in the current literature. As for the stability investigation, the variations along a sequence of XAS spectra were evaluated by means of a XANES linear combination performed automatically with the software LinComb[365].

Simulation 1. Distorted Octahedral Arrangement			
Atom	x(Å)	y(Å)	z(Å)
O	1.396	1.396	0.000
O	-1.396	1.396	0.000
O	-1.396	-1.396	0.000
O	1.396	-1.396	0.000
O	0.000	0.000	2.092
O	0.000	0.000	-2.092
H	0.541	0.541	2.952
H	-0.541	-0.541	2.952
H	-0.541	0.541	-2.952
H	0.541	-0.541	-2.952
H	1.264	2.345	0.000
H	-2.345	1.264	0.000
H	-1.264	-2.345	0.000
H	2.345	-1.264	0.000
H	2.345	1.264	0.000
H	-1.264	2.345	0.000
H	-2.345	-1.264	0.000
H	1.264	-2.345	0.000

Simulation 2. Square Pyramidal Arrangement			
Atom	x(Å)	y(Å)	z(Å)
O	-1.347	1.347	0.000
O	1.347	-1.347	0.000
O	1.347	1.347	0.000
O	-1.347	-1.347	0.000
O	0.000	.0000	1.898
H	-1.264	2.345	0.000
H	1.264	-2.345	0.000
H	1.264	2.345	0.000
H	-1.264	-2.345	0.000
H	-2.345	1.264	0.000
H	2.345	-1.264	0.000
H	2.345	1.264	0.000
H	-2.345	1.264	0.000
H	0.765	0.000	2.952
H	-0.765	0.000	2.952

Simulation 3. Triginal Bipyramidal Arrangement			
Atom	x(Å)	y(Å)	z(Å)
O	1.910	0	0
O	-0.956	1.654	0
O	-0.956	-1.654	0
O	0	0	1.967
O	0	0	-1.967
H	-0.603	2.573	0
H	-1.927	-1.808	0
H	2.529	-0.765	0
H	2.529	0.765	0
H	-1.927	1.808	0
H	-0.603	-2.573	0
H	0.541	0.541	2.952
H	-0.541	0.541	2.952
H	-0.541	0.541	-2.952
H	0.541	-0.541	-2.952

***Table 25**. Coordinates referred to the three different geometries employed in the simulation of the spectrum of Cu(II) aquaion.*

Simulation 1. Distorted Octahedral Arrangement					
Shell	**Coordination Number**	**Type of atom**	**Distance from Cu(II) (Å)**	**σ^2 (Å^2)**	**β(Å^3)**
1	4	**O**	1.97(2)*	4(2) x 10^{-3}*	--
2	2	**O**	2.09(3)*	7(7) x 10^{-3}*	-1.1(3)*
3	8	**H**	2.664	5.0 x 10^{-3}	--
4	4	**H**	3.050	5.0 x 10^{-3}	--
Goodness of Fit *F*: 2.8 %					
Simulation 2. Square Pyramidal Arrangement					
Shell	**Coordination Number**	**Type of atom**	**Distance from Cu(II) (Å)**	**σ^2 (Å^2)**	**β(Å^3)**
1	4	**O**	1.90(3) *	3(4) x 10^{-3}*	-0.4(2)
2	1	**O**	1.90(8)*	1(1) x 10^{-2}*	-2(1)
3	8	**H**	2.664	5.0 x 10^{-3}	--
4	2	**H**	3.050	5.0 x 10^{-3}	--
Goodness of Fit *F*: 2.8 %					
Simulation 3. Trigonal Bipyramidal Arrangement					
Shell	**Coordination Number**	**Type of atom**	**Distance from Cu(II) (Å)**	**σ^2 (Å^2)**	**β(Å^3)**
1	3	**O**	1.91(5)*	1(1) x 10^{-2}*	--
2	2	**O**	1.97(6)*	1(2) x 10^{-2}*	--
3	6	**H**	2.642	5.0 x 10^{-3}	--
4	4	**H**	3.050	5.0 x 10^{-3}	--
Goodness of Fit *F*: 13.9 %					
* Fitted values					

***Table 26**. XANES Calculation parameters of the simulations obtained for the three different geometries. For each shell is reported the coordination number, the type of atom, the distance from the photo-absorber, the thermal disorder (σ2) and the skewness (ß) when different from zero.*

This is based on the comparison of the experimental spectrum with the spectra of reference compounds. The experimental spectra μ_{exp} of a data set are fitted by a theoretical curve μ_{th} calculated as a linear combination of normalized reference compound spectra:

$$\mu_{exp} = \sum_j \alpha_i \mu_{th}$$

The two reference compounds are the copper(II) lactate complex in the starting solution and standard Cu_2O. The time evolution of the parameters α_i allowed us to evaluate the percentage of copper(II) lactate while performing the LSV measurements.

2.4.3 Results and Discussion

Figure 141 shows Cu-K edge EXAFS signal of the starting solution of copper(II) lactate (A) and the corresponding Fourier Transform (FT) (B). Oscillations above the noise level are well apparent in the spectrum up to k = 8 $Å^{-1}$. This allows obtaining reasonable quantitative parameters for the first coordination shells, within ca. 4 Å. Copper lactate is known to yield a square planar complex CuL_2 in the solid state, with lactate acting as a bidentate ligand[351]. This structure is assumed for the complex in solution as well. For what concerns the data here presented, the presence of a clear beating in the EXAFS between 5 and 6 $Å^{-1}$ clearly indicates that a single frequency cannot account for the experimental signal. Therefore, the cluster employed for the initial fit is composed of two shells of oxygen atoms: the first shell is made up of four oxygens situated at ca. 1.9 Å, that are provided by the carboxylate and hydroxyl groups of lactates in a bidentate arrangement, and the second shell is composed by two oxygens situated at ca. 3 Å, provided by the carboxylate group. This large distance implies that these two oxygen atoms are not directly bonded to the central Cu(II). The values obtained from the best fitting procedure are shown in Table 27, and the fit is reported in Figure 141 and Figure 141B as a full line. In the subsequent step of data analysis, represented by the XANES simulation, the models tested for the aqueous complex were constructed based on the previous results.

Therefore, the XANES simulation has been started by assuming a square planar coordination around Cu(II) and two lactate molecules acting as bidentate ligands (model 0, Figure 142B). The results are shown in Figure 142A, showing the Cu-K edge XANES calculations for the solution of copper(II) lactate: although the overall shape of the XANES manifold is quite satisfactorily interpreted, there are however large discrepancies in the finer structure, leading to the conclusion that a different structural model is required. Therefore, we constructed three different models for the coordination geometry of copper in the lactate solution: i) model 1 (Figure 142C) comprises two lactate ions acting as bidentate ligands and is characterized by a distorted tetrahedral geometry; ii) model 2 (Figure 142D) is made up by two lactate ions acting as bidentate ligands in a square planar arrangement with two additional water molecules in apical position to yield an overall distorted octahedral geometry, and iii) model 3 (Figure 142E) is composed of four lactate ions acting as monodentate ligands to yield a coordination number of 4 in an geometrical arrangement characterized by point symmetry S4.

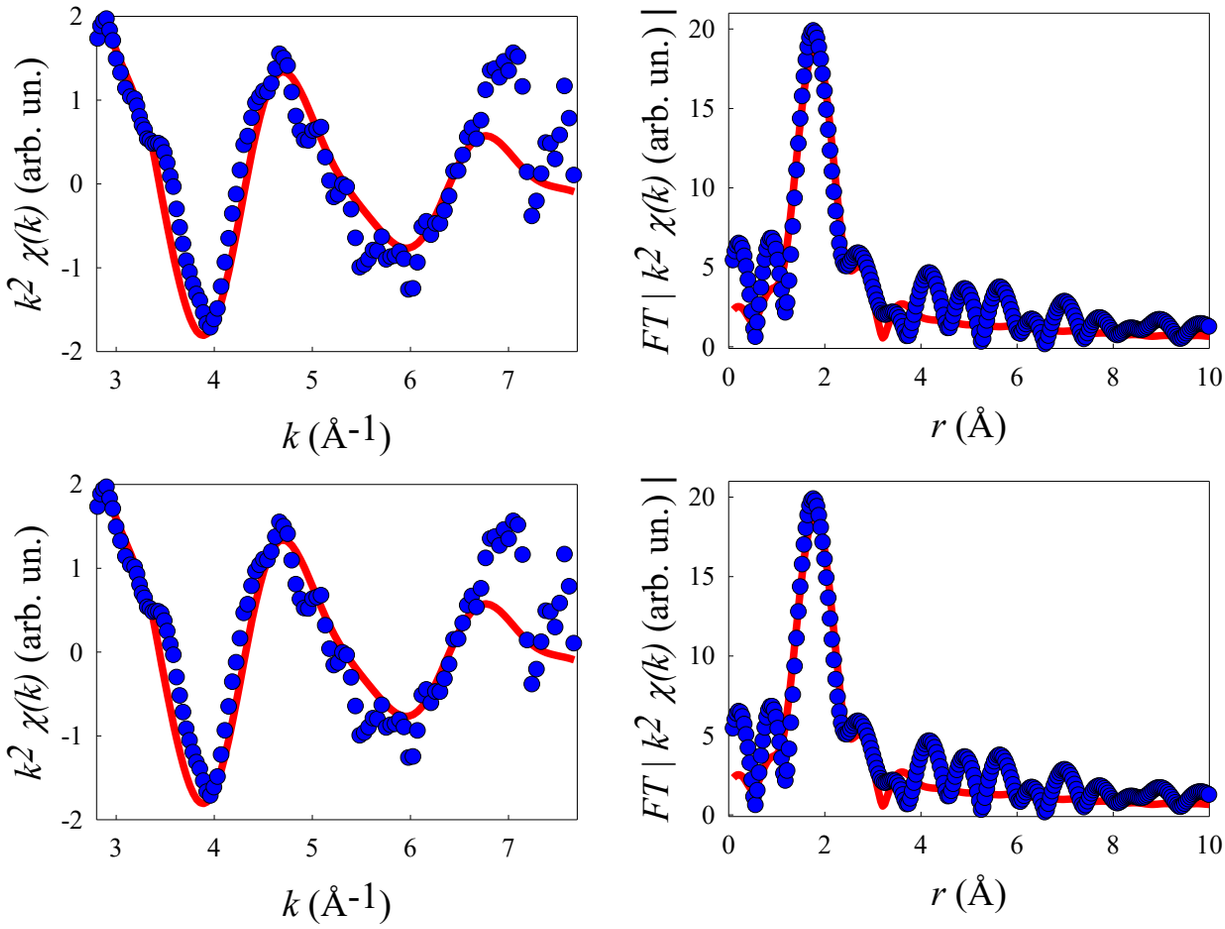

***Figure 141**. Cu-K edge EXAFS signal (A) and the corresponding FT (B) of the starting solution of Copper(II) lactate. The experimental signal is represented by the blue spots, whereas the fit according to the models described in the text is represented by the red line. A and B refer to the 4+2 model, while C and D to the 4+4 model.*

Shell	*N*	Atom	*r* (Å)	σ^2 (Å^2)
1	4	**O**	1.87(2)	10(2) x 10^{-3}
2	2	**O**	3.33(7)	0(1) x 10^{-2}
Goodness of Fit *F*= 23.9 %				
Shell	***N***	**Atom**	***r* (Å)**	**σ^2 (Å^2)**
1	4	**O**	1.87(2)	10(2) x 10^{-3}
2	4	**O**	3.35(6)	8(9) x 10^{-3}
Goodness of Fit *F*= 23.1 %				

***Table 27**. EXAFS fitting parameters for spectra shown in Figure 141. r: Distances, σ2: Distance variances. Coordination numbers N have been kept constant to 4+2 and 4+4 as described in text.*

These models can be tested against the experimental data by fitting the XANES. The first attempt concerns the model 1, where we removed the requirement of a strict square planar geometry. In this case the XANES simulation (orange line) leads to better but still unsatisfactory results.

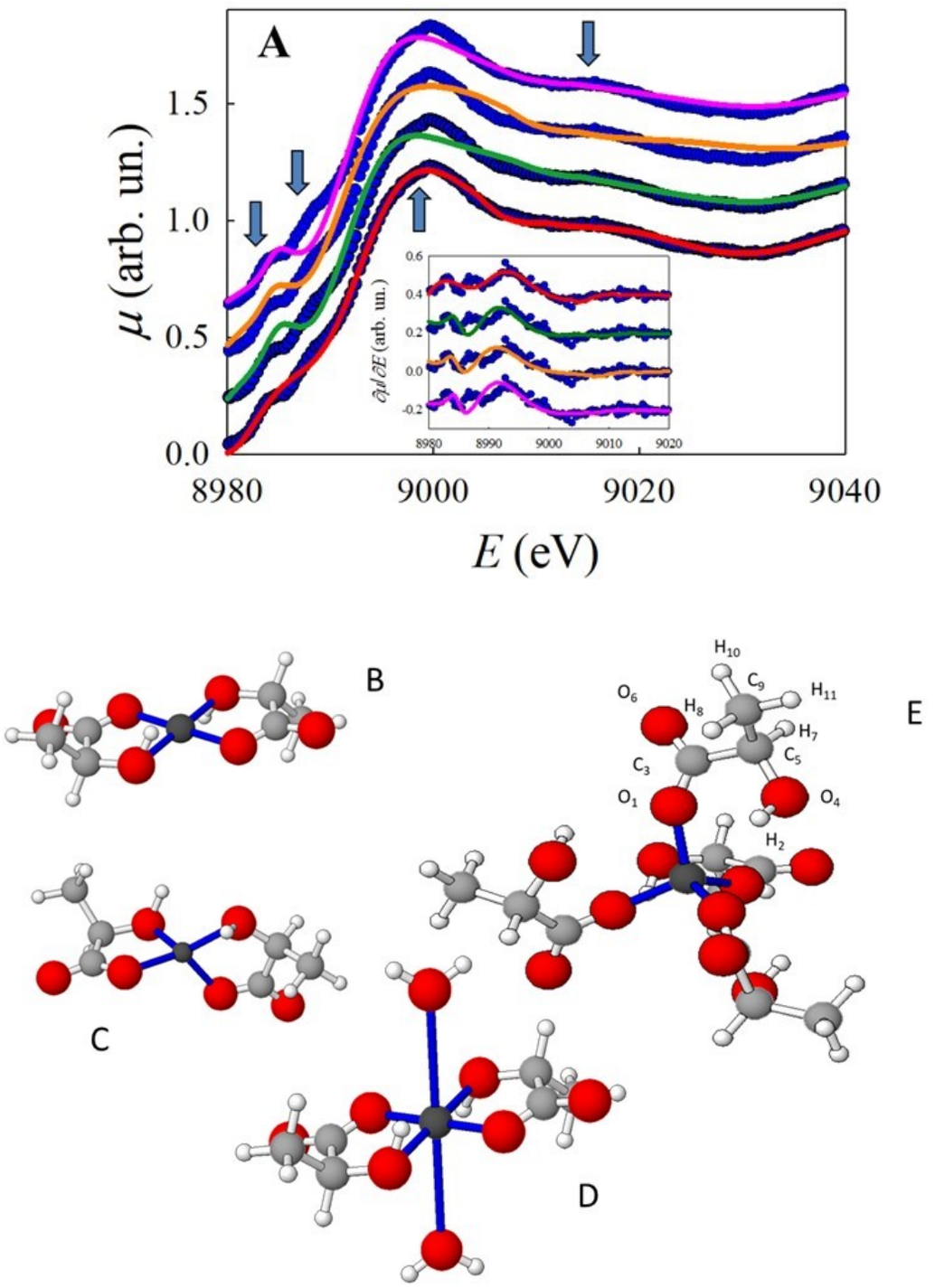

***Figure 142**. (A): Cu-K edge XANES simulations of Copper(II) lactate starting solution. The blue spots represent the experimental signal while the colored lines are the theoretical calculations according to the models shown in B (pink line, model 0), C (orange line, model 1), D (green line, model 2) and E (red line, model 3). The arrows mark the energy regions where the largest differences between the different models are found. An insight illustrating the derivative of both the experimental and the calculated spectra is included to better visualize the most important discrepancies between the models.*

This led us to consider a model in which two ligands act as bidentate ions in a square planar coordination and two oxygen atoms (water molecules) are added in the apical positions to yield an overall distorted octahedral geometry (model 2), thus removing the requirement of having two oxygen atoms in the second coordination shell. This model gives a little improvement in the XANES simulation, indicated as a green line in Figure 142, when compared to that obtained for model 1, but the results are still far from an optimal theoretical simulation. The blue arrows indicate the energy regions where major discrepancies between theoretical and experimental signal are observed. These discrepancies can even be better evidenced looking at the corresponding derivatives shown in the insight of Figure 142A. Thus, we remove the constraint imposing the lactate anions acting as bidentate ligands. Considering that even though lactate anion is 15 times more concentrated than copper sulphate, steric hindrance limits the maximum number of ligands around Cu in a single complex, and assuming the presence of four lactate anions acting as monodentate ligands (model 3), we obtain that the agreement between experimental signal and theoretical simulation (red line) is largely improved and all the relevant spectral features of the XANES manifold are correctly simulated. We then propose model 3 for the structure of copper(II) lactate in alkaline solution. Therefore, the structure of copper(II) lactate in alkaline solution is different from that assumed by copper(II) lactate in the solid state[351]. The best fit results obtained by XANES calculation are shown in Table 28. For each atom of the cluster used to calculate the XANES theoretical spectrum, the distance from the photo-absorber and the corresponding Debye-Waller factors are illustrated. The distance of the nearest oxygen atoms and the Debye-Waller factors were fitted treating the lactate anions as a rigid unit. In addition, all the Debye-Waller factors have been treated as equal.

Atom Number	Type of atom	Distance from Cu(II) (Å)	σ^2 (Å^2)
1	**O**	1.855(4)*	6(2) x 10^{-3}*
2	**H**	2.977	6(2) x 10^{-3}*
3	**C**	3.000	6(2) x 10^{-3}*
4	**O**	3.234	6(2) x 10^{-3}*
5	**C**	3.720	6(2) x 10^{-3}*
6	**O**	3.919	6(2) x 10^{-3}*
7	**H**	4.351	6(2) x 10^{-3}*
8	**H**	4.704	6(2) x 10^{-3}*
9	**C**	4.871	6(2) x 10^{-3}*
10	**H**	5.492	6(2) x 10^{-3}*
11	**H**	5.583	6(2) x 10^{-3}*
Goodness of Fit *F*: 1.3 %			* Fitted values

Table 28*. XANES calculation parameters employed to simulate the experimental signal shown in Figure 142A according to the model illustrated in Figure 142E. The fitted parameters are marked by *.*

This procedure is somewhat arbitrary but has been used to keep the number of fitted parameters to a minimum value to avoid correlations. The fitting results are illustrated in Table 28 and all the nearest distances between carbon and oxygen atoms, in each lactate, obtained by the theoretical calculation were checked by a comparison with literature. No significant differences are detected as illustrated in Table 30. Finally, coordinates of all the atoms comprised in the cluster of model 3 are displayed in Table 29.The fitting according to the structural model is good, as supported by the GOF (goodness of fit) F that is ca. 1.3 %. We note that the parameters obtained are in perfect agreement to the values obtained by EXAFS fitting for the same oxygen atoms (see Table 27).

Coordinates of all atoms in Model D			
Atom	x(Å)	y(Å)	z(Å)
O_1	-1.071	1.071	1.071
O_1	1.071	-1.071	1.071
O_1	1.071	1.071	-1.071
O_1	-1.071	-1.071	-1.071
H_2	0.750	2.795	0.698
H_2	-0.750	-2.795	0.698
H_2	-2.795	0.750	-0.698
H_2	2.795	-0.750	-0.698
C_3	-1.238	1.762	2.088
C_3	1.238	-1.762	2.088
C_3	1.762	1.238	-2.088
C_3	-1.762	-1.238	-2.088
O_4	0.951	2.627	1.629
O_4	-0.951	-2.627	1.629
O_4	-2.627	0.951	-1.629

Coordinates of all atoms in Model D			
Atom	x(Å)	y(Å)	z(Å)
O_4	2.627	-0.951	-1.629
C_5	-0.177	2.751	2.498
C_5	0.177	-2.751	2.498
C_5	2.751	0.177	-2.498
C_5	-2.751	-0.177	-2.498
O_6	-2.249	1.640	2.758
O_6	2.249	-1.640	2.758
O_6	1.640	2.249	-2.758
O_6	-1.640	-2.248	-2.758
H_7	0.131	2.548	3.524
H_7	-0.131	-2.548	3.524
H_7	-2.548	0.131	-3.524
H_7	2.548	-0.131	-3.524
H_8	-1.047	4.373	1.380
H_8	1.047	-4.373	1.380

Coordinates of all atoms in Model D			
Atom	x(Å)	y(Å)	z(Å)
H_8	4.373	1.047	-1.380
H_8	-4.373	-1.047	-1.380
C_9	-0.739	4.171	2.406
C_9	0.739	-4.171	2.406
C_9	4.171	0.739	-2.406
C_9	-4.171	-0.739	-2.406
H_{10}	-1.599	4.265	3.069
H_{10}	1.599	-4.265	3.069
H_{10}	4.265	1.599	-3.069
H_{10}	-4.265	-1.599	-3.069
H_{11}	0.028	4.885	2.703
H_{11}	-0.028	-4.885	2.703
H_{11}	-4.885	0.028	-2.703
H_{11}	4.885	-0.028	-2.703

***Table 29**. Coordinates referred to the cluster indicated in Figure 139 E.*

LACTATE INTERATOMIC DISTANCES		
Atoms	**Distance in the model (Å)**	**Literature values(Å)**
O_1—C_3	1.241	1.219
C_3—C_5	1.507	1.507
C_3—O_6	1.219	1.219
O_4—C_5	1.429	1.429
C_6—C_7	1.507	1.507
C_5—C_9	1.530	1.530

***Table 30.** Nearest distances between carbon and oxygen atoms in each lactate molecule present in Model E (Figure 142E): a comparison between fitted and literature values.*

It is also worth noting that the EXAFS can be fitted with a structural model made up by a first and second coordination shell of oxygen, both containing 4 atoms, with a slight improvement in the fit quality (see Figure 141C, D) and with a more reasonable value for the Debye-Waller factor of the second shell (see Table 27). This, agrees with the results of the XANES fitting, and it is due to the quite poor accuracy of EXAFS in the determination of the coordination numbers.

An important remark concerns the inclusion of hydrogen atoms in the simulation of XANES. In XAS spectroscopy hydrogen atoms are intrinsically not well defined because of their small scattering factor. Figure 143 shows a comparison of XANES calculations for CuL_4 complex in presence (red lines) and in absence (green lines) of hydrogen atoms in the cluster. The inclusion of hydrogen atoms determines a substantial variation in the simulated XANES spectrum, in particular in the energy regions indicated by the arrows.

Looking at the difference signals between the theoretical spectrum and the experimental one, we note that the calculation carried out including hydrogen atoms leads to a better fitting. This has the obvious meaning that multiple scattering paths involving hydrogen atoms cannot be neglected at least up to 40 eV above the absorption edge.

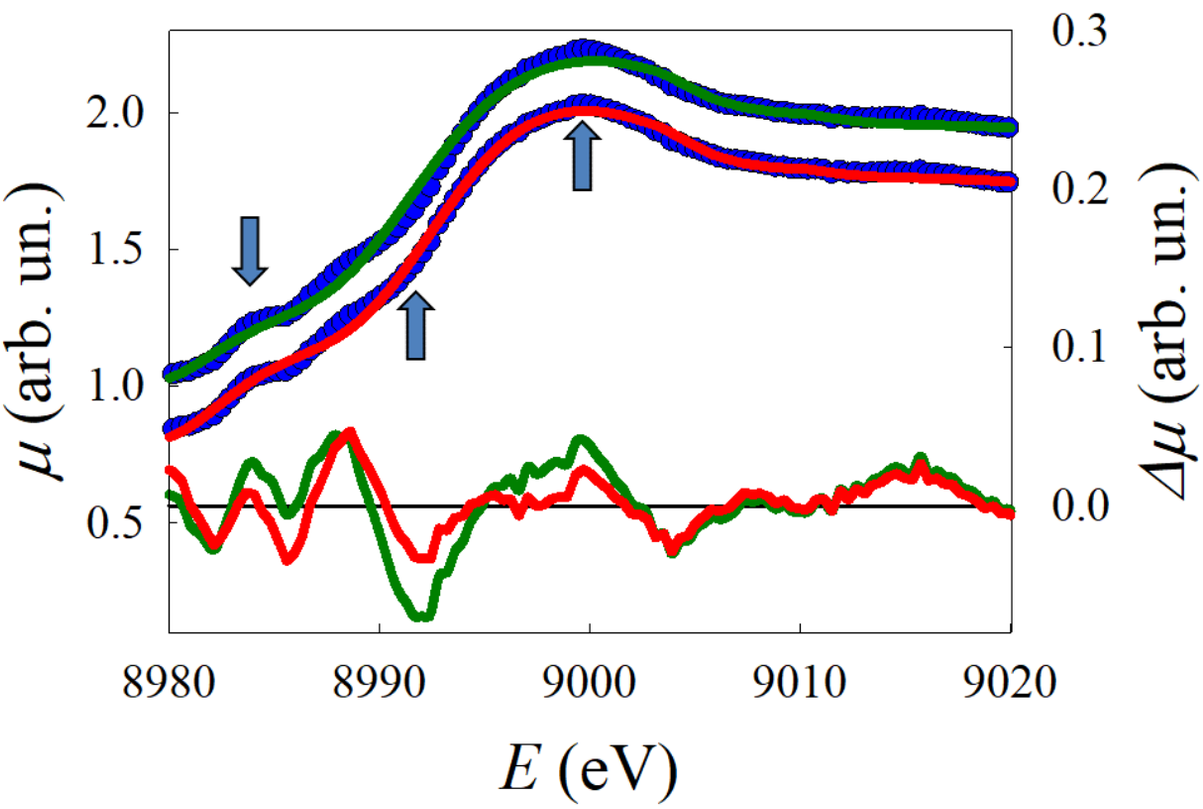

Figure 143. *Comparison of the simulations of Copper(II) lactate XANES according to the model shown in Figure 142E with (red line) and without (green line) the hydrogen atoms. The experimental signal is represented by the blue spots and the experimental calculated differences are illustrated in the bottom of the figure for the two cases. The arrows mark the energy regions where the largest differences between the models with and without hydrogens are found.*

The electrochemical stability of the lactate solution was investigated by LSV measurements from 1.2 to -0.4 V (vs. Ag/AgCl at 0.01 $V \cdot s^{-1}$), while acquiring the XAS spectra with a time resolution of 500 ms. The total time for one LSV measurement was 160 seconds. Figure 144A shows some spectra of the sequence separated by time intervals of ca. 25 s. A spectral weight increase of the pre-peak indicated by the arrows is clearly detected. A comparison with the standard spectra presented in Figure 144B shows that in this energy region Cu_2O has a sizeable pre-edge structure.

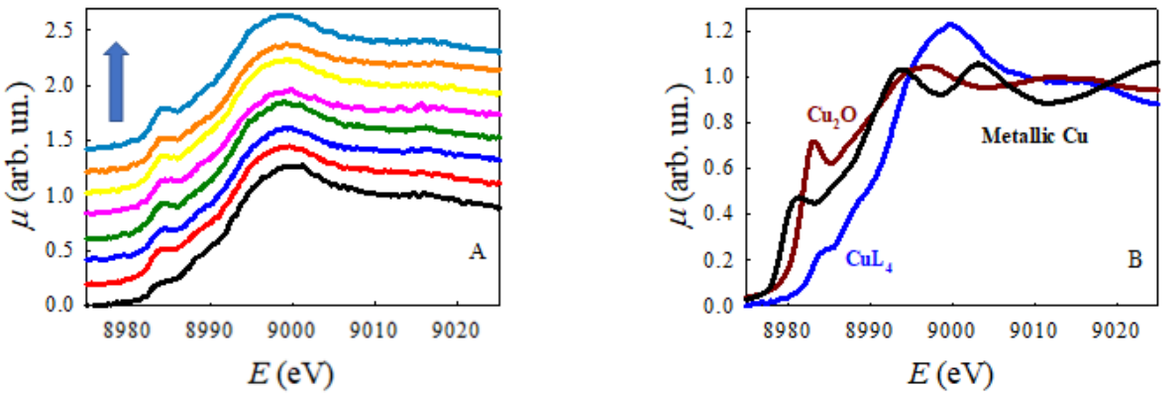

***Figure 144**. (A): seven spectra selected from the sequence recorded on the copper(II) lactate solution during the application of the LSV and separated by a time interval of ca. 25 s. (B) Cu-K edge XANES spectra of the standards of Copper(II) lactate (blue line), Cu_2O (brown line) and metallic Cu (black line).*

Therefore, the increase of the pre-edge is attributed to a partial reduction of Cu(II) to Cu(I). At a given time, the XANES spectrum can be simulated with linear combinations of standard XANES. In particular, we used Cu_2O as a standard for Cu(I). The fitting range selected was 8950 – 9030 eV. The results obtained from the fitting procedure by means of LinComb software are reported in Figure 146. This shows the time evolution of the coefficients related to the two standards used for the linear combination. At time zero the amount of copper(II) lactate is equal to 100 % and no Cu(I) is present. A little amount of Cu(I) (10 %) appears at potential ca. 1.1 V, increasing up to ca. 20 % at 1 V. Then it remains almost constant during the rest of the linear sweep. The automatic linear combination fitting procedure was checked by manually fitting four spectra at four potential values along the LSV, finding excellent agreement (Figure 145).

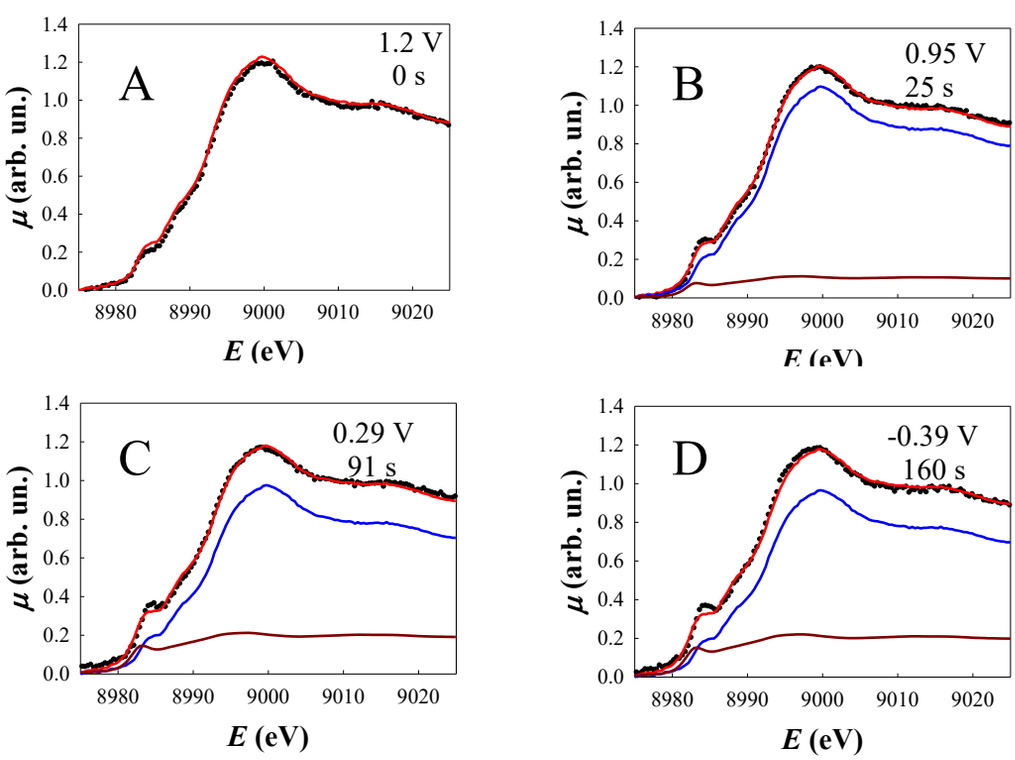

***Figure 145**. Manual linear combination fit of four XANES spectra selected among the entire data set acquired during the LSV program at 1.2 V (A), 0.95 V (B), 0.29 V (C) and -0.39 V (D). The Black spots represent the experimental signal and the red line the theory, the blue line is Copper(II) lactate contribution and the brown line Cu2O contribution.*

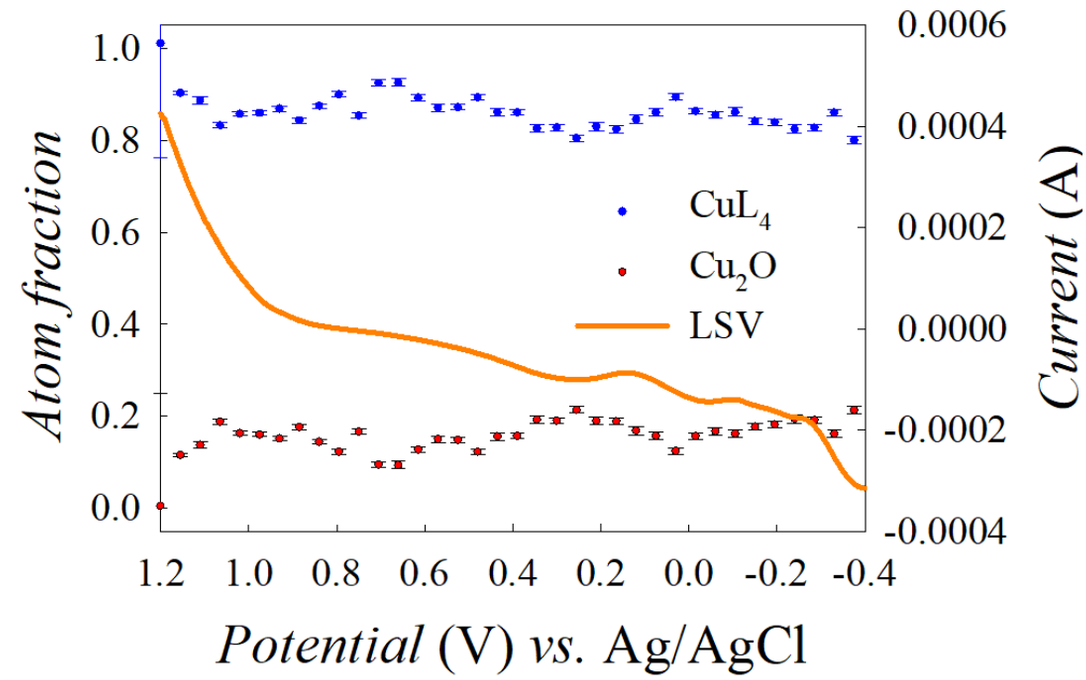

***Figure 146**. Results of the automatic linear combination fitting of the XANES spectra of the sequence recorded during the application of the LSV. The blue dots represent the percentage of Copper(II) lactate, the red dots represent the percentage of Cu_2O and the orange line is the current recorded during the LSV. To reduce the scattering of the results, only a spectrum every five was selected.*

The initial formation of Cu(I) is quite surprising as the current flowing is anodic up to applied potential of ca. 0.4 V. Radiolysis phenomena generated by the X-ray beam are irrelevant as demonstrated by preliminary tests in absence of the applied potential, showing that the spectral shape remains the same along the whole sequence. The rationale we propose for this complex behaviour is as follows. At the beginning of the LSV, the potential is sufficiently anodic to oxidise water to oxygen, at the working electrode, and this accounts for the anodic current. The counter electrode acts therefore as a cathode, thus reducing an amount of Cu(II) in solution to Cu(0). The presence of Cu(0) onto counter electrode and of $Cu(II)L_4$ in the solution can then produce Cu_2O as described by Bijani[309] for similar complex, thus explaining the XANES spectra of Figure 144. The amount of Cu(I) remains then constant during the rest of the LSV because no reaction involving Cu species occurs both at cathode and anode, due to the smaller applied potentials. An alternative explanation involves possible formation of radicals, due to the presence of lactate anions as already observed by Rubinstein et al.[378]. These radicals are generated upon oxidation of the lactate ion and can act as strong reducing agents on CuO, thus producing Cu_2O. However, this scenario seems to be less probable. In fact, the anodic stability of lactate–based ionic liquid at room temperature was demonstrated up to 1.0-1.3 V vs. SCE in dependence on cations[379]. In conclusion, CuL_4 complex remains largely stable in a wide range of applied potentials.

2.4.4 Conclusions

In this work, we used EDXAS to determine the structure and electrochemical properties of copper lactate complex in alkaline solution. For what concerns the structure, our approach consists in: i) first fitting the EXAFS in order to obtain reasonable coordination numbers; ii) formulate structural models accounting for the coordination numbers obtained; and finally, iii) testing the structural models against a fit of the XANES.

We found that the best fit is obtained by a model where four lactate ions act as monodentate ligands, 1:4 (Cu:L), in a distorted tetrahedral geometry. This is in contrast with structural determination of the complex in the solid state[351], according to which the stoichiometry is 1:2, but is quite reasonable considering the large excess (15:1, L:Cu) of lactate in the solution.

Concerning the electrochemical properties of the solution, the sequence of spectra recorded while applying the Linear Sweep Voltammetry from 1.2 to -0.4 V (vs Ag/AgCl) showed that the modest production of Cu_2O is due to the co-presence of metallic Cu, on the counter electrode, and $Cu(II)L_4$ in the solution. In any case we can confirm the electrochemical stability of the Cu lactate complex in the potential range scanned, 80% still present at the end of the LSV.

2.5 SECM Evaluation of Photodegradation Processes

2.5.1 Introduction:

As stated before, an ideal semiconductor should possess the following characteristics: i) be abundant, low-cost, and non-toxic, ii) have narrow band gap iii) have the correct bands position iv) be stable in aqueous environment. Most frequently, the choice is based on a compromise between stability and efficient transformation of sunlight into hydrogen, the latter depending on the range of frequencies that the semiconductor can absorb. For example, titanium dioxide has a large stability in time but its wide band gap (around 3 eV) makes it absorb only UV light[30,380,381]. On the other side, Cu(I) and Cu(II) oxides can absorb part of the visible spectrum but present instability due to photodegradation processes[57,58,157,161,382]. Indeed, in parallel to water splitting, self-reduction processes are possible with the reaction $Cu_2O + 2e^- + 2H^+ \rightarrow Cu + H_2O$ that lead to a loss of photoefficiency of the material due to the formation of a thin film of metallic copper on the surface[353]. No evidence on Cu_2O oxidation were achieved with the use of XAS, meaning that there is no self-oxidation of the material induced by free holes generated in the material, but this process can still occur on other photoactive materials. Being able of quantify the intensity of undesired degradation processes will allow to choose wisely the best candidates for long-term and efficient PEC-WS system.

Cu_2O, one of the most studied material for photocathodes, is just an example of unstable semiconductor used for PEC-WS system with a photodegradation process occurring under light. As previously reported[383] is largely common that the redox potential of the material lies inside the band gap making photodegradation probable from a thermodynamic point of view.

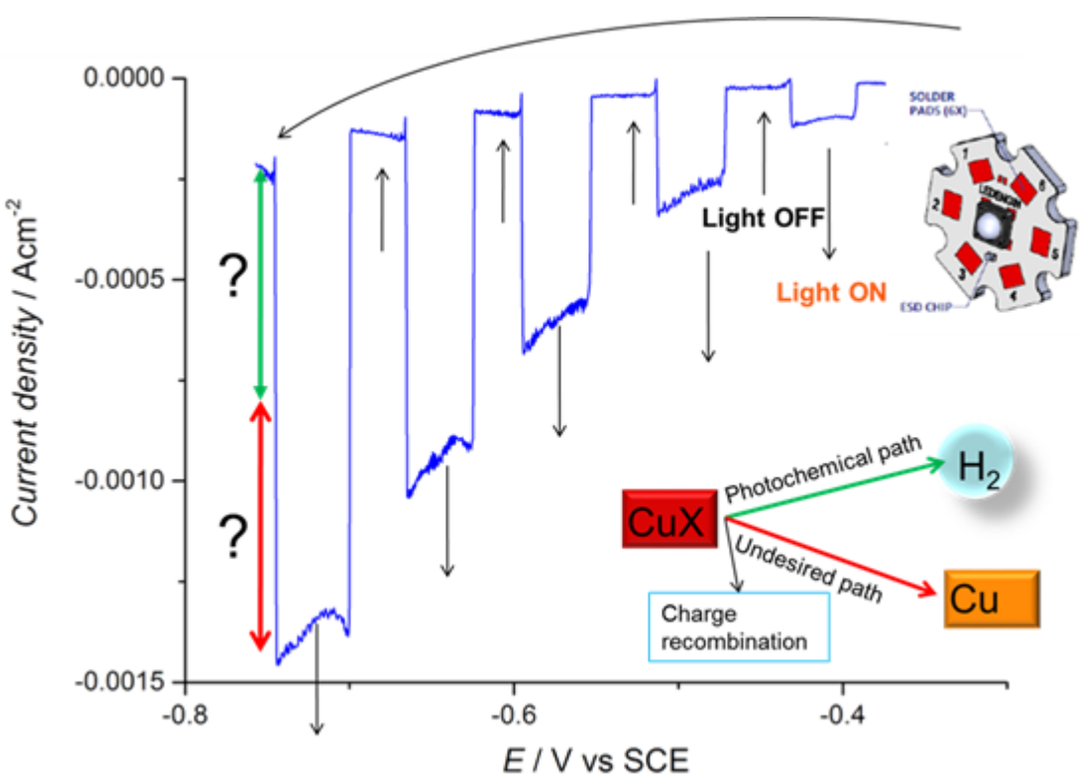

Figure 147. *Desired and undesired processes occurring at a photocathode. From the simple evaluation of LSV is not possible to identify the intensity of the two contributes underlined in green and red.*

This means that looking at the Cu_2O LSV presented before for the evaluation of the electrodes performances is impossible to distinguish from the value of photocathodic currents the intensity of hydrogen evolution and material photodegradation (reduction to Cu(0)). Indeed, a high reduction current in light can be mostly be due to material transformation. The ratio between the total photocurrent and the photocurrent related to hydrogen (or oxygen) production is defined as photocurrent efficiency:

$$Photocurrent\ Efficiency = \eta_{cat} = \frac{I_{related\ to\ H_2\ production}}{I_{total\ under\ light}}$$

In the present work, is proposed a novel method based on the combined use of the scanning electrochemical microscopy (SECM) and cavity micro-electrodes (C-MEs) for the rapid screening of semiconductors photoactivity and for the determination of the relevant photocurrent efficiencies. The method here described can be applied easily to all the materials of interest thanks to the use of a cavity microelectrodes.

The most adopted methods for evaluating η include gas chromatography and volume liquid displacement[384–387]. These techniques have two big disadvantages, the complexity in procedure and instrumentation with GC and the low precision (error near to 13%) for volume displacement. Moreover, the second method used without GC give no evidence on the nature of the gas evolved[57]. Using a thermal conductivity detector (TCD) in GC the response in hydrogen detection is linear between 10^{-9} to 10^{-3} g (argon or nitrogen flux) while using SECM we can follow amount of produced hydrogen in the order of 10^{-14}g or even lower. The time required for the measure is also far shorter with the possibility to obtain information about photocurrent efficiencies in a wide range of applied potentials (using a single electrode) in few seconds (respect to at least 20 minutes necessary to achieve enough gas for GC measurements). The novel method here introduced seems interesting for the study of unstable materials that cannot show the same efficiency during a long scale time. The results can be compared with IPCE measurements for further analysis at different wavelengths[388].

Equally is important to have a method for the fast screening of different semiconducting materials avoiding the influence of the supporting material (i.e. FTO or ITO) that is usually able to give some, usually small, photocurrents or introduce some larger resistance in electrons flow or even gives not reproducible result due to the inhomogeneity of the F@SnO layer. Moreover, FTO is a n-type TCO and the coupling with Cu_2O will generate a p-n heterojunction.

Advantages of C-ME are well established[125,127] while its combined use with SECM was previously introduced in the case of high conductivity powders for OER[126]. The use of Au cavity micro-electrode filled with the studied material is equivalent to preparing custom microdisk tips, avoiding time consuming techniques for the preparation of large number of electrodes. Here is presented how the same method can be easily used in the determination of side reactions occurring in PEC-WS semiconductor materials and in their characterization under external potential and illumination.

Measurements with pulsed illumination will show the light-driven H_2 production on different materials and the differences between tip current and the one recorded at the substrate will give the percentage of photodegradation.

2.5.2 Materials and Methods:

Different materials were tested for the method validation:

Cu_XO photocathode: a mixed copper oxide material was prepared by calcination of copper iodide in air atmosphere at 400°C for 1 hour [389]. Subsequently, the obtained black powder was grinded in a mortar to obtain a thinner powder without agglomerates, easy to load in the cavity. This material was studied in 0.5M disodium hydrogen phosphate + 0.5M potassium dihydrogen phosphate buffer electrolyte (pH 7) in potential windows that usually goes from 0.7 to 0.2 V vs RHE.

TiO_2 photoanode: hydrogenated self-doped titanium dioxide is obtained by commercial TiO_2 anatase (99.7% purity, 15 nm average particle size, Alfa Aesar) reduced at 500°C for 1 h in flowing hydrogen (50 $mLmin^{-1}$) inside a U-shape Pyrex reactor. The result was a blue–grey powder (14 nm average particle size) that is stable for several weeks. This material was studied in 0.1M NaOH between 1 and 1.5 V vs RHE[126] for oxygen evolution reaction (OER).

NiO photocathode: nanoparticles were prepared by grinding a stoichiometric amount of $Ni(OAc)_2{\cdot}4H_2O$ with NaOH and the appropriate amount of Tween-80 in an agate mortar at room temperature for about half an hour. Then the product was washed with distilled water and ethanol, centrifuged, and dried at 80°C for 12 h.

The so-prepared light-green powder was sintered at 800°C for 2 h. The material optical and chemical properties were studied with UV-vis spectroscopy and X-ray powder diffraction. Optical properties of photocatalysts were studied using UV-Vis diffuse reflectance spectroscopy recorded using UV-3600 spectrophotometer (Shimadzu) equipped with an integrating sphere. Samples were ground with $BaSO_4$ (1:50 wt. ratio). Diffuse reflectance spectra of this material, transformed to Kubelka-Munk function, is shown in Figure 148. NiO absorbs UV light, however the rise in absorbance starting form 500 toward IR was also observed. This continuous band is reflected as a black color of material. Band gap from Tauc plot was 3.49 eV. The chemical composition of the material was investigated on the X-ray powder diffractometer (MiniFlex 600, Rigaku) operated at a voltage of 40 kV and by using energy dispersive X-ray spectroscopy (EDX-720, Shimadzu spectrometer) operating at 5 kV voltage.

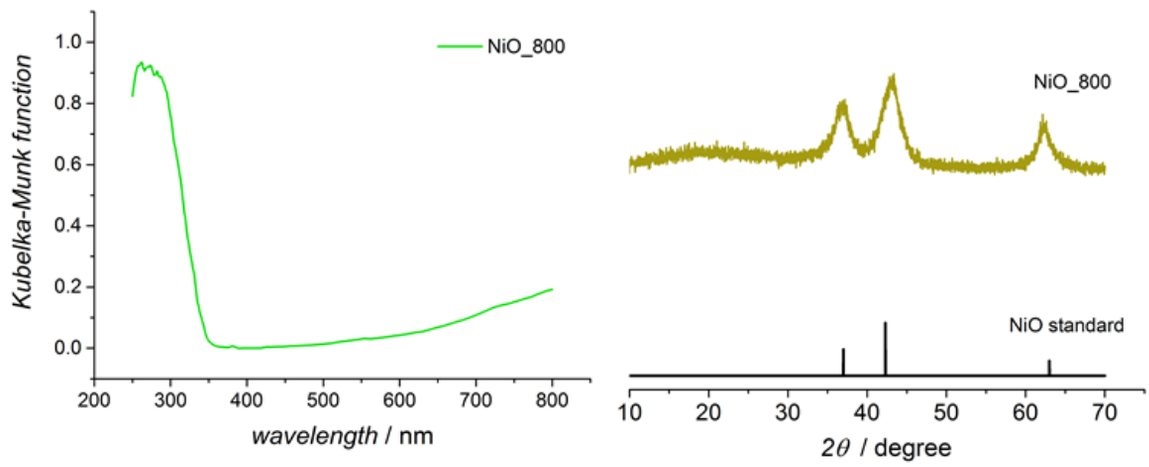

Figure 148. *UV-Vis diffuse reflectance spectrum converted in Kubelka-Munk function (on the left) and XRD diffractogram of NiO powder.*

As shown in Figure 148 the diffraction peaks of NiO appear at 37, 43 and 62 degrees and can be indexed as (111), (200), (220) crystal planes, respectively. Obtained patterns are typical for face-centered cubic crystalline structure of nickel oxide. Black color of the material may result from the presence of metallic nickel.

CuI photocathode: Copper iodide was synthesized according to the following procedure; 100 mL of 0.01 M Na_2SO_3 were added to 60 mL of 0.05 M $CuSO_4$ while stirring. Then, 300 mL of 0.01 M KI were added dropwise to the resultant green suspension. The obtained white precipitate was separated by centrifugation, washed 3 times with water and ethanol, and dried in air at about 80°C for 8 hours. This material was studied in the same experimental condition of Cu_XO being its precursor.

2.5.3 Tips Preparation:

C-ME tips were prepared starting from 25µm radius gold wire (Goodfellow, 99.99% purity) and glass capillary (O.D/I.D 1.5/0.75mm #27-37-1, Frederick Haer & Co, Bowdoinham, ME) previously cleaned with acetone in ultrasound bath. Once dried the gold wire is embedded in the capillary glass tube using a hot metal coil (through which a high current is flowing, to heat it) under vacuum. In this way, air in the capillary and adsorbed impurities on the metal were eliminated. The temperature of the coil is raised, and the capillary is moved slowly inside it in order to melt the glass and seal it around the wire.

First, the closed side of the capillary is kept in correspondence with the center of the coil (i.e. the hottest part) then it is moved downward, at around 1mm every 5 minutes. Using a microscope, the capillary is checked, to verify that a good sealing was obtained, without bubbles between the glass and the metal. The Au disk is first exposed and then polished using emery papers (400−800−1000−2400−4000 mesh) and alumina powders suspension in water (mean particle size 0.3 and 0.05 µm). The surface then is sharped until the desired RG (ratio between tip and gold radius) value is reached (here between 4 and 6). Silver epoxy glue was used to connect a copper wire to the gold one in order to have the electric contact. The so prepared electrode is left to dry in oven at 60°C overnight.

The cavity preparation procedure consists in four different steps starting from the gold tip previously prepared;

2.5.3.1 Determination of the Real Tip Radius.

This preliminary procedure is done to evaluate the tip parameters for the cavity digging. A very slow ($2mVs^{-1}$) cyclic voltammetry of the tip is performed in a 1mM $Ru(NH_4)_6Cl_2$, 0.1M $KClO_4$ bath. The potential sweeps from 0 to -0.4 V vs SCE. The real tip radius is obtained from the steady state current, I_{ss}, of the sigmoidal shaped CV using equation:

$$I_{ss} = 4nFC_bDr$$

where n is the number of exchanged electron, F is the Faraday constant, C_b is the bulk concentration of the redox mediator, D its diffusion constant and r is the tip radius. The I_{ss} current is obtained from the plateau at cathodic potential using the baseline created using the first points. Considering the extremely small current is important to avoid noise sources and work under a Faraday cage.

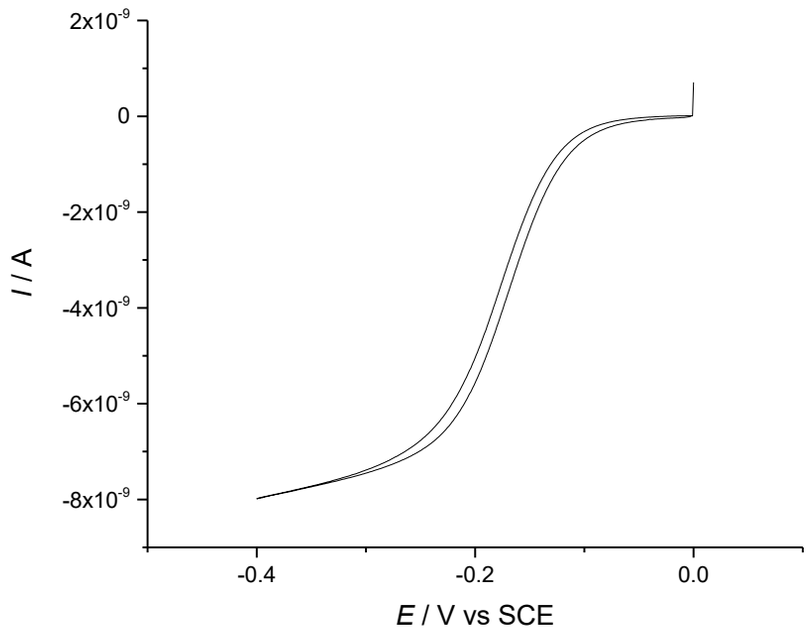

Figure 149. *Cyclic voltammetry in 1mM $Ru(NH_4)_6Cl_2$, 0.1M $KCLO_4$ bath. The potential sweeps from 0 to -0.4 V vs SCE at 2mVs^{-1}. The counter electrode is a platinum foil.*

2.5.3.2 Cavity Formation

The cavity is then dig in a Cl^- (0.5M HCl, 0.5M H_2SO_4) bath using square wave voltammetry techniques with pulsed current densities of 1.5 and -7.5 mAcm^{-2}. Anodic time (1000s) were chosen to be ten times of cathodic ones (100s). The anodic part of the square wave voltammetry is used to oxidize gold to gold ions in solution, while the shorter cathodic part is used to produce small amount of hydrogen able to clean the cavity from the gold ions trapped inside because of the small dimensions. This procedure was tested by a previous Ph.D. student giving good results in terms of calculated depth and depth obtained from optical microscope evaluation.

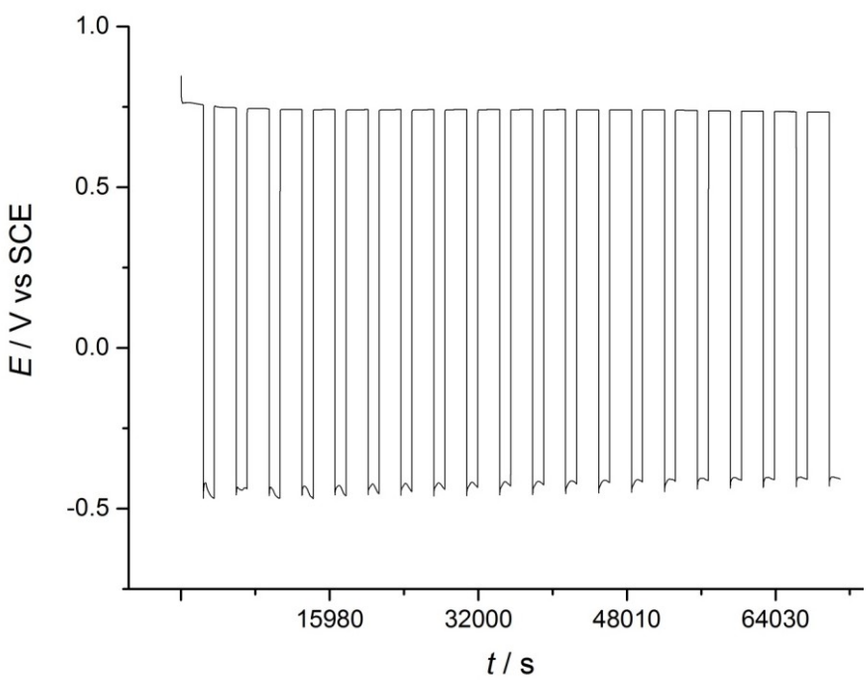

Figure 150. *Pulsed chronoamperometry performed in the Cl^- bath with 0.5M HCl and 0.5M H_2SO_4.*

The number of total steps is related to the desired cavity depth. Different depths were tested, 20.4 µm, 39.9 µm and 47.8 µm.

2.5.3.3 Surface Homogenization

Fast ($1Vs^{-1}$) cyclic voltammetry (500 cycles) in the same Cl^- bath between gold reduction and oxidation peaks were performed to have surface reconstruction and obtain a final homogeneous surface. Cycling between gold oxidation and reduction reaction indeed, allows to reconstruct the surface leading to a more uniform bottom of the cavity.

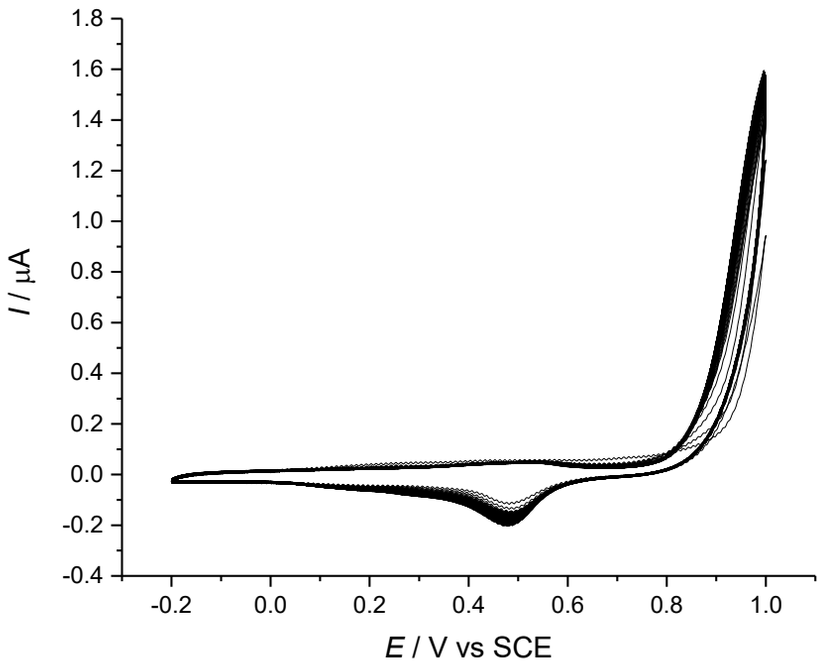

Figure 151. *Surface homogenization CV between Au oxidation and reduction peaks. Scan rate $500mVs^{-1}$ in 0.5M HCl, 0.5M H_2SO_4. 500 cycles were performed.*

2.5.3.4 Depth Evaluation

Eventually, the cavity depth is evaluated performing a slow cyclic voltammetry ($2mVs^{-1}$) in the 1mM $Ru(NH_4)_6Cl_2$ bath. A different equation is used for the depth evaluation:

$$I_{ss} = \frac{4\pi nFC_bDr^2}{4L + \pi r}$$

where *L* is the cavity depth while other parameters remain unchanged.

Then the cavity was washed with distilled water and dried in a hoven for some hours at the temperature of 60°C. Once cooled down, the cavity is filled with the material of interest simply using it as a pestle. The degree of filling is checked at the optical microscope and the external edge of the cavity was cleaned with laboratory paper to avoid interference during the measurements from material present outside the cavity.

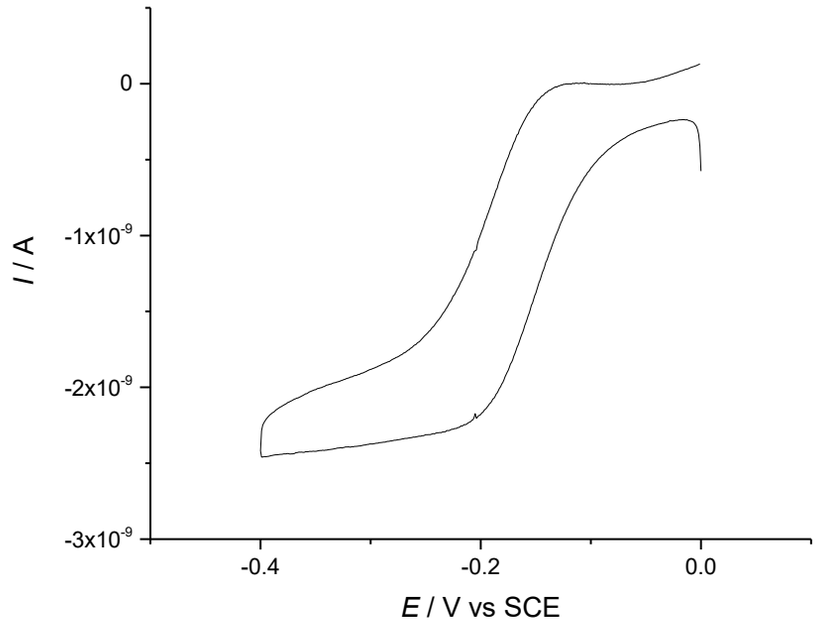

***Figure 152**. Cyclic voltammetry in 1mM $Ru(NH_4)_6Cl_2$, 0.1M $KCLO_4$ bath. The potential sweeps from 0 to -0.4 V vs SCE at 2mVs^{-1}. The counter electrode is a platinum foil.*

The cavity can be used several times previous emptying the exhausted material. The required procedure is very simple and consists in the sonication in ultrasound bath with water or acid solution of the tip. To avoid cracking in the sealed glass over the gold microwire is mandatory to do not dip the whole electrode but only the edge of the tip with the creation of a convex meniscus on the solution surface. The procedure is repeated until a microscope evaluation shows a powder-free cavity.

The following photos show a cavity from the bottom view once filled and on the side view. We can see that is possible to notice the gold wire embedded in the glass capillary from which the cavity itself is created.

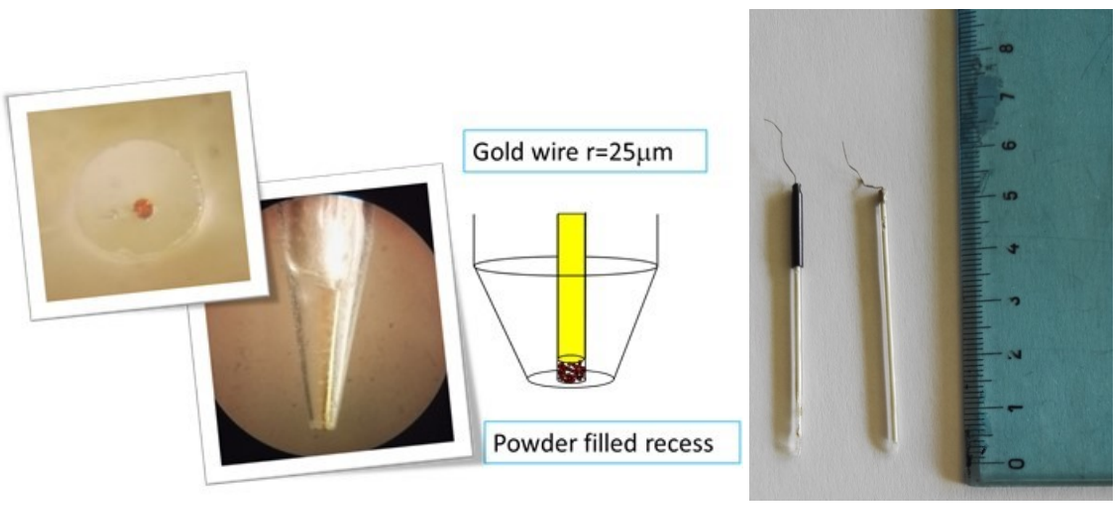

***Figure 153.** A) Optical microscope photos of a cavity. View from the bottom and on the side. B) Schematic view of the cavity structure; c) photos of two different cavities and their size.*

2.5.4 System Setup

The experimental setup is composed by the gold cavity microelectrode (tip) while a large Pt disk (A=0.125cm^2) is used as substrate in order to achieve 100% collection efficiency of species produced at the tip. The cavity microelectrode filled with the desired material was positioned above the substrate at a distance in the order of less than one tip radius (usually 10μm). Is also possible to control the position in the 3 dimensions of the tip microdisk respect to the metallic substrate using a stepped motor. The tip and substrate potentials are independently controlled using a bipotentiostat in a 4-electrodes cell configuration. SECM is used in Tip-generation/Substrate-Collection (TG/SC) mode, which give us the possibility to discriminate Hydrogen Evolution Reaction (HER) or Oxygen Evolution Reaction (OER) from photodegradation side reactions at the photocathode or photoanode respectively.

In a conventional TG/SC configuration, the substrate is used to collect the tip reaction products acting as a probe. Usually the substrate area is much larger than the tip one, so that the collection efficiency (C.E.=i_S/i_T where i_S is substrate current and i_T is the tip one) is 1[36].

To evaluate photoactivity, 3.5W reflected light of high intensity LED was used. The LED is positioned at 5 cm above the electrolyte level in a controlled position.

Each semiconductor was studied in its typical environment using different solutions in 5mL Teflon® SECM cell. For all the measurements, the reference electrode is Ag/AgCl 3M in double bridge while the counter is a high surface area wire of Pt. All potentials here reported are referred to RHE.

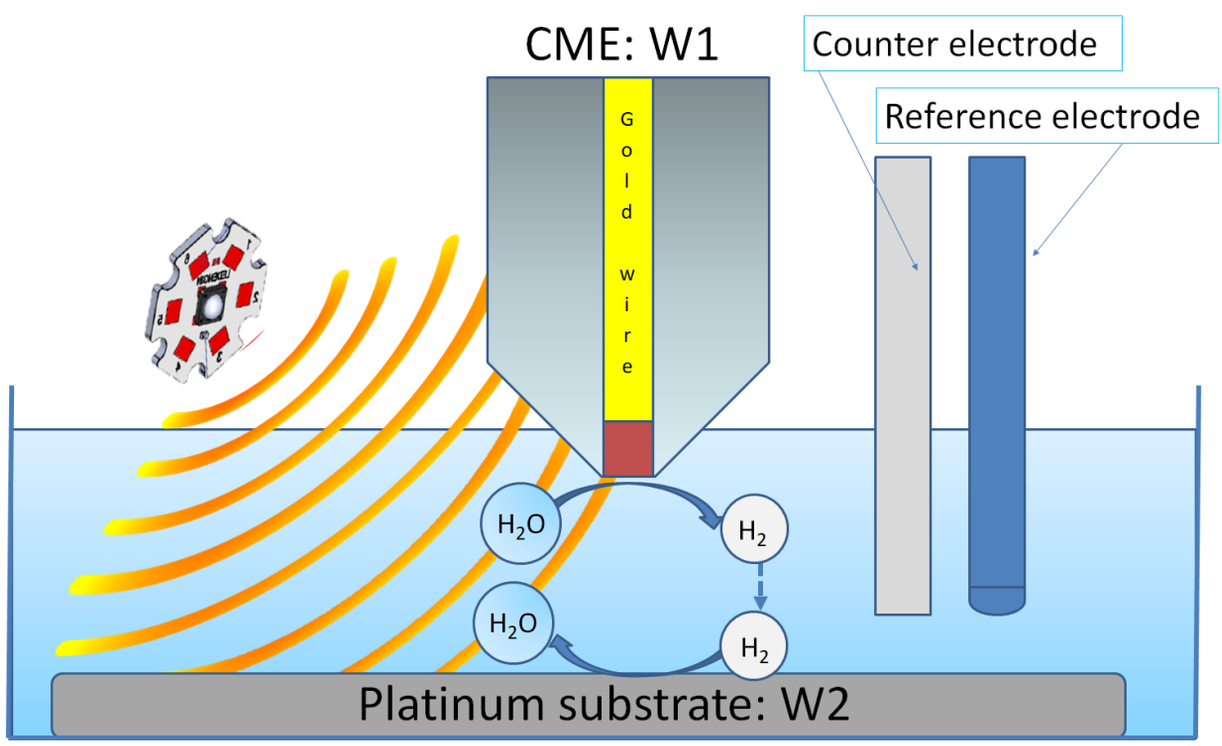

Figure 154. *Cell configuration for the evaluation of semiconductors activities and photodegradation process. The represented process is the one for a photocathodic material able under light of reducing water to hydrogen, while the substrate performs the opposite reaction consuming the so-produced hydrogen.*

2.5.5 SECM Measurements Results:

2.5.5.1 The Approach

The procedure for the evaluation of tip photocurrent and substrate hydrogen (or oxygen) consumption always starts with the approaching curves for the tip. This means to move, with the stepped motor, the tip 10 µm closer to the surface of the substrate to be sure that the hydrogen produced at the tip during light can be collected and oxidized by the substrate. To complete this task is possible to use some redox mediator couples like Ferrocene, but this could contaminate the cavity. For this reason, was used a redox couple always present in a de-aerated system, the O_2/H_2O couple. The distance was evaluated measuring the current related to reduction of the O_2/H_2O couple with an approach curve as explained in the introduction. The system is indeed biased at a potential for oxygen reduction.

Until the tip is quite far from the Pt substrate, currents are constant and far from zero, but closer we get, less is the amount of oxygen that can reach the electrode. For this reason, as the electrode get closer to the surface of the platinum, the current start to deeply decrease until zero (the point where tip and substrate touch themselves).

Is always better to avoid their contact to avoid contamination of the platinum. This type of approach is called negative approach because the current decrease with the distance. Then the tip is raised of the desired height (10 µm) and once obtained the correct positioning of the two working electrodes the solution was bubbled with N_2 for at least 30 minutes in order to avoid the influence of the ORR (Oxygen Reduction Reaction). Moreover, the cell was covered with Parafilm® to keep inert atmosphere into the cell.

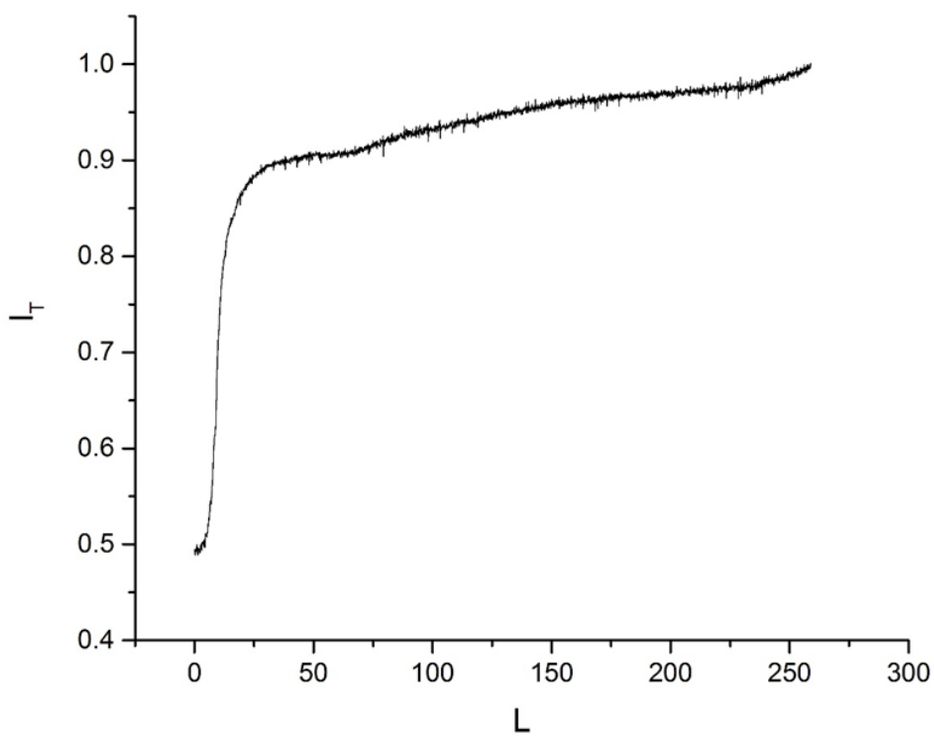

Figure 155. *Negative approach example. While the tip approach to the substrate the current deeply goes to zero. A change in the slope means that the substrate is reached.*

2.5.5.2 SECM Measurements:

Before starting the main experiment, bubbling is moved above the liquid level to avoid oxygen entrance and at the same time noises from bubbles close to the tip. Then the material was investigated in the interested windows of potential under pulsed illumination performing Linear Sweep Voltammetry (LSV) at $10mVs^{-1}$ with a CHi bipotentiostat (model CH920). The tip potential is controlled in order to allow a photoelectrochemical process to occur. The reaction product can thus diffuse within the gap between the two electrodes and be consumed at the large substrate, whose potential is fixed to a value far enough from the equilibrium potential of the considered redox couple, thus guaranteeing mass transport controlled kinetics. The difference between tip "in-light" current (hydrogen evolution + material photodegradation) and substrate current (re-oxidation of the hydrogen produce at the tip), gives the amount of photocurrent related to the material photodegradation. Of course, from the difference is also possible to obtain information on the intensity of HER on different photocathodic materials (Cu_XO, CuI and NiO) or the intensity of OER (Oxygen Evolution Reaction) on the TiO_2 photoanode.

2.5.6 Results

To confirm the effectiveness of the proposed setup, we considered a model system composed by platinum tip ($1.96x10^{-5}cm^2$) and a platinum substrate ($0.125cm^2$) in 0.5M sulphuric acid. The tip-to-substrate distance is 10 µm, as determined after the recording of negative feedback approach curves using the dissolved O_2 as redox active species. The tip potential is varied from 0.9 to -0.05 V vs the reversible hydrogen electrode (RHE). As notable in Figure 156 (red line), the current raises below 0 V. Under these conditions, we assume that only the reduction of water to H_2 occurs. The potential of substrate electrode is kept constant at a potential that guarantees mass transport controlled H_2 oxidation. The substrate current is recorded in parallel to the tip one and is reported in red in Figure 156. It is evident that the ratio between the two currents at any potential is 1. All the tip produced hydrogen is then recorded and oxidized at the platinum substrate meaning that no side reactions are occurring.

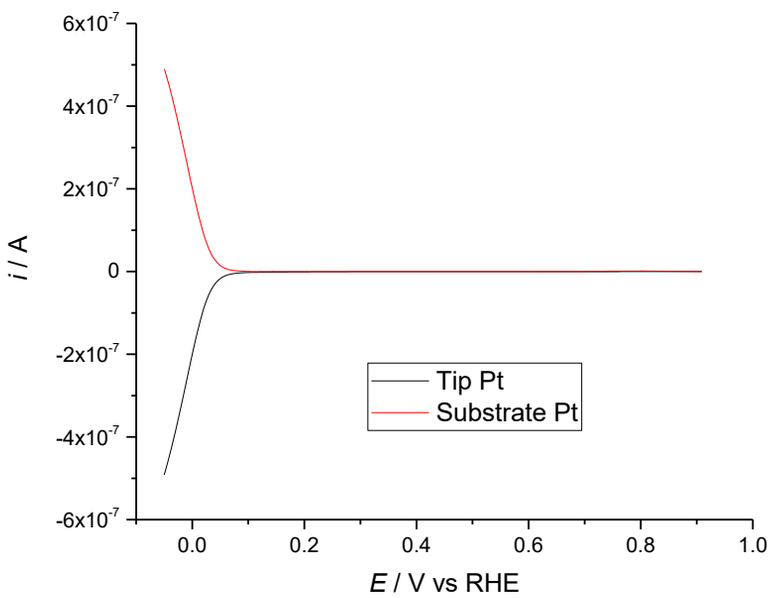

Figure 156. *Model system based on Pt tip vs Pt substrate in H_2SO_4 0.5M. Here tip reduction current and substrate hydrogen oxidation current are the same due to the absence of side reactions respect to HER on the tip.*

The experiment was repeated in 0.5 M phosphate buffer solution at pH 7 that will be also adopted for semiconductor measurements and the same results were obtained. Eventually, using a cavity-microelectrode tip filled with Pt/Vulcan XC-72 (28.6% w/w) once again, the results show that substrate and tip current intensities are equal. In this way, the absence of any influences from pH or the use of a cavity instead of a microdisk were confirmed.

A similar setup can thus be applied to reactions with unknown current efficiencies, including photo-driven ones. In photoelectrochemistry, one of the most debated and discussed aspects is the stability of the photoelectrodes. Indeed, many of them show non-negligible photocorrosion phenomena (photoinduced self-oxidation -reduction). In these cases, the method here described can provide useful information to distinguish between concurrent reactions since:

$$I_{tip}=I_{t,c}+I_{f,a}+I_{f,b}+I_{f,c}+...$$

where I_{tip} is the tip current intensity, $I_{t,c}$ the tip capacitive current, $I_{f,a,b,c}$ faradaic currents of different electrochemical reactions:

a) $X+ne^- \rightarrow A$ i.e. $Cu_2O + 2e^- + 2H^+ \rightarrow Cu + H_2O$

b) $Y+n'e^- \rightarrow B$ i.e. $2H^+ + 2e^- \rightarrow H_2$

c) $Z+n''e^- \rightarrow C$

and so on.

On the other side, the substrate current, I_{sub}, can be related to one or more of the products generated by reaction at the tip. For example,

$$I_{sub}=I_{s,c}+I_{f,sub}+I_{f,a}$$

where $I_{s,}$ is the substrate capacitive current, $I_{s,sub}$ the faradaic current relevant to any process occurring at the substrate independently on the presence of the tip, $I_{f,a}$ the current due to the reaction consuming the product of reaction "A":

a) $A \rightarrow X' + n'''e^-$ i.e. $H_2 \rightarrow 2H^+ + 2e^-$

On Cu_XO electrodes quantitative analysis were performed to obtain information about the relationship between cavity depth and signal intensity while for the other materials the efficiency in HER or OER was evaluated. To avoid the contribution of oxygen reduction and current related to photoemission (see Appendix) from substrate, background subtraction of each substrate and tip currents was performed.

Sweep potentials in the range of chemical stability for the selected material was applied to WE1 while led light was pulsed with a frequency of circa 0.25Hz to see differences between dark and light currents generated by the material. On photocathodes, we saw an increase in cathodic current (WE1) under light, due to hydrogen evolution but also to possible side reactions. At the same time, the platinum substrate working at a selected fixed potential consumes the produced specie (H_2) performing hydrogen oxidation. There are no reactions at both the working electrodes in the dark, because the semiconductor is inactive without light and platinum has no hydrogen to consume.

The working potential for platinum was indeed accurately chosen to have a clean surface, without reducible oxides and in a potential region were only capacitive currents were recorded.

2.5.6.1 Cu_XO

The first semiconductor studied is a mixed copper oxide, Cu_XO, a material with a proper band gap for HER, with relative low-cost and high abundancy still subdued to some small photoreduction process. Figure 157 shows photocurrents of the C-ME tip filled with copper based material (WE1=black line) together with the substrate current (WE2=red line). The magnitude of the photodegradation processes was confirmed by the difference in intensity between the tip current (made by the sum of water reduction, material photodegradation and charges recombination) and substrate one (related only to the consumption of hydrogen produced by copper oxide under light). From the tip-to-substrate current ratio, almost 60% of observed photocurrent is related to hydrogen evolution while the residual is rather due to other by-processes (photodegradation process and charge recombination). In order to further confirm this conclusion, we extended the investigated potential window to force the semiconductor towards the electrochemical reduction of Cu_2O. This is represented in Figure 158, where the electrochemical reduction of the material onset is clearly evident for E<0.2 V (RHE). When tip currents undergo to a dramatic increase, the substrate current remains constant meaning that this increase in current is not related H_2 formation but to material transformation. A further extension of the potential window, as in Figure 159, leads to reach electrochemical water reduction potentials, where the increase in tip currents is followed by substrate ones at E < 0V because of electrochemical HER occurs.

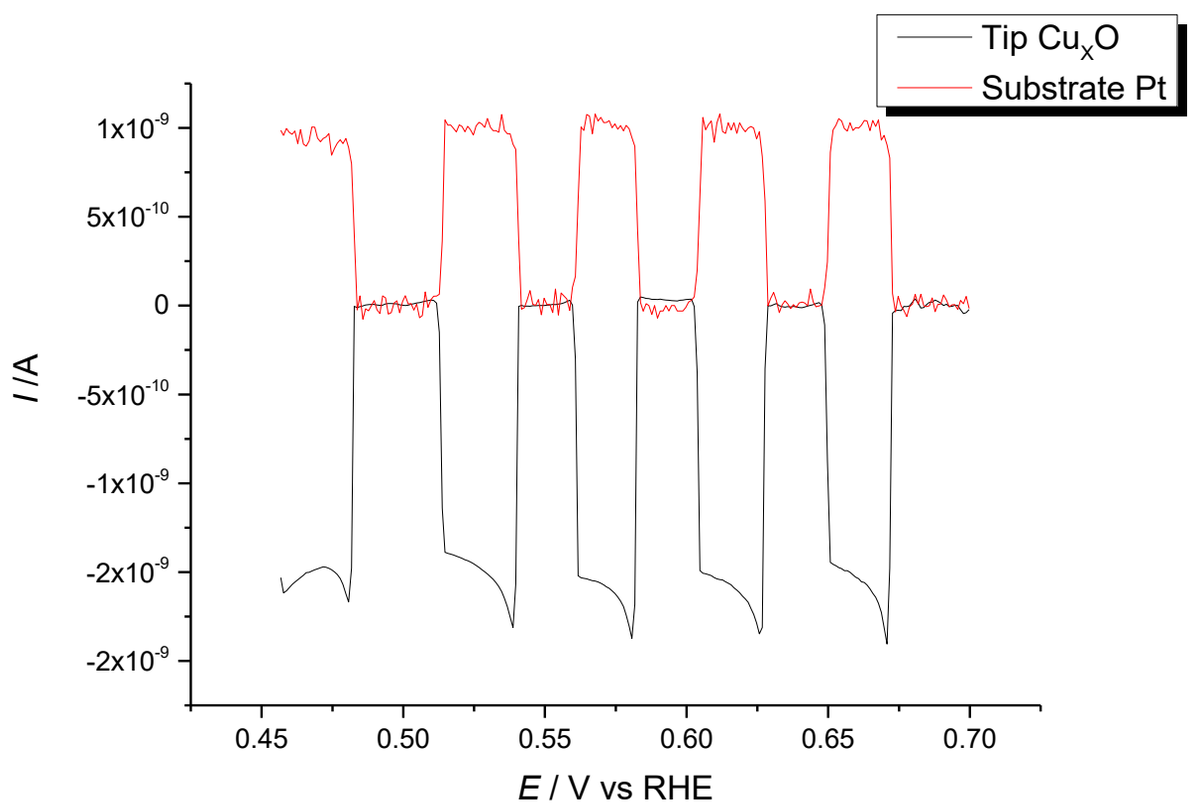

***Figure 157**. Linear sweep voltammetry at 10mVs^{-1} in pH 7 buffered solution under pulse illumination. WE1= cavity filled with Cu_XO, WE2= Pt substrate. Counter: Pt wire, reference: Ag/AgCl 3M.*

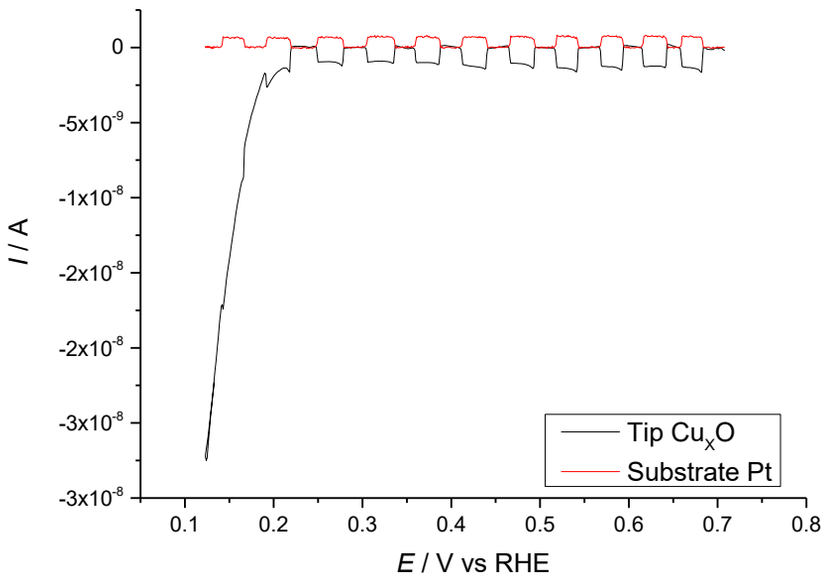

Figure 158. *Linear sweep voltammetry at 10mVs^{-1} in pH 7 buffered solution under pulse illumination. WE1= cavity filled with Cu_xO, WE2= Pt substrate. Counter: Pt wire, reference: Ag/AgCl 3M.*

From Figure 158 and Figure 159 is extremely clear how the substrate (red line) is able to recognize only the produced hydrogen. Indeed, the strong reduction recorded at the tip starting from 0.2V gives no changes on the substrate if the light is off. This means that in the potential region from 0.2V to 0.1 V vs RHE the material reduction is much higher than the produced hydrogen, even if the light is off because in this case is pure electrochemical reduction. When the potential is negative enough to have HER on Cu_2O (Figure 159 from 0V vs RHE) because of the pure electrochemical reaction also the substrate began to record some oxidation current, but only after 0V vs RHE as expected.

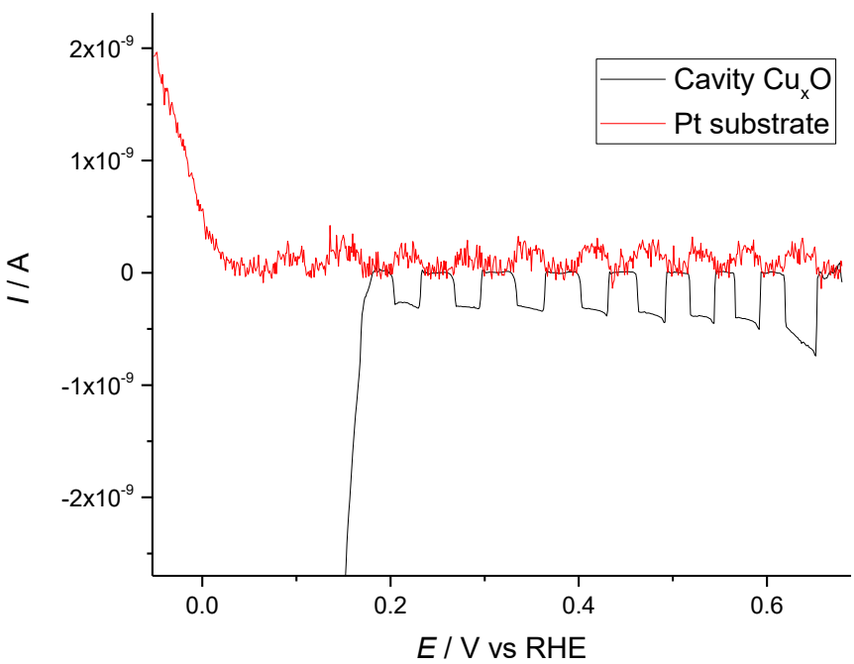

Figure 159. *Linear sweep voltammetry at 10mVs^{-1} in pH 7 buffered solution under pulse illumination. WE1= cavity filled with Cu_xO, WE2= Pt substrate. Counter: Pt wire, reference: Ag/AgCl 3M.*

2.5.6.2 CuI

The second material tested is CuI, the precursor material for Cu_XO, a semiconductor with p-type character but a higher BG (3eV) used for the preparation of photocathodes.

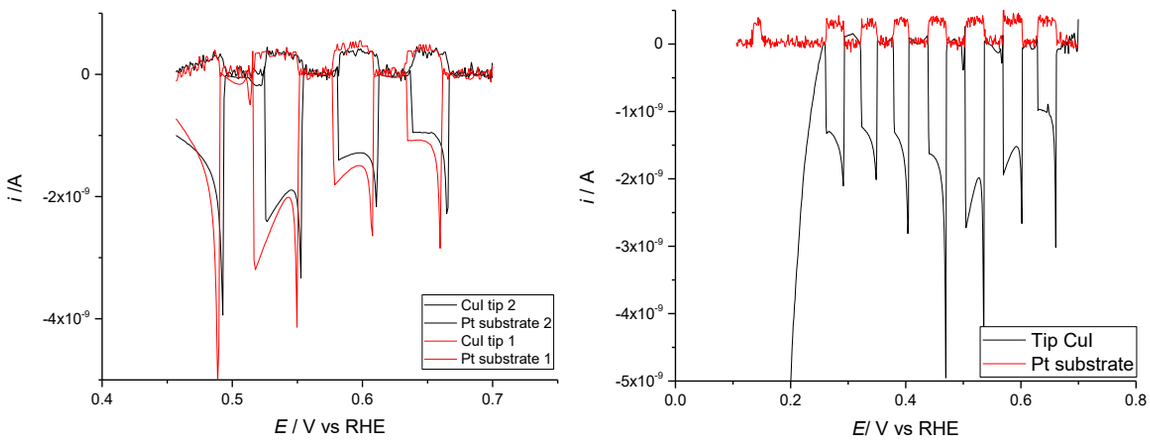

Figure 160. *Two different experiments of CuI in buffer electrolyte pH 7. Tip potential is scanned between 0.7 and 0.45 V vs RHE while substrate potential is held at 0.785 V vs RHE to oxidize the produced hydrogen during light pulsation at the frequency of 0.25Hz.*

Is possible to see how in the case of such material, in particular CuI, the photodegradation contributes is higher and the material is able to produce only very small amount of hydrogen. The recorded tip photocurrents are indeed quite high, but only a very small percentage of those is related to hydrogen production as we can see from the small substrate currents (in comparison with the tip ones). In spite of this the reproducibility among measurements is quite good.

2.5.6.3 NiO

NiO is still a p-tye material that can be used for the preparation of photocathodes and for this reason was tested for HER conditions. From Figure 161 is possible to see that it has a particular behaviour with the efficiency changing according to the applied potential. Indeed, seems that incresing the applied potential can only improve the material degradation while the higher efficiencies are reached at less negative energies.

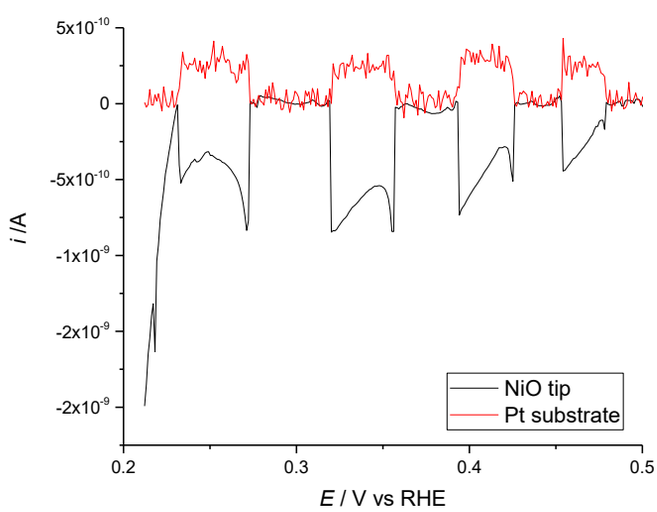

Figure 161*. Linear sweep voltammetry at 10mVs^{-1} in pH 7 buffered solution under pulse illumination. WE1= cavity filled with NiO, WE2= Pt substrate. Counter: Pt wire, reference: Ag/AgCl 3M.*

2.5.6.4 TiO_2

We can see the opposite situation with TiO_2, a well-know photoanode for its longterm stability. Tip currents of water oxidation (in blue) in light and substrate current of oxygen reduction (in orange) have indeed more or less the same intensities. This material then shows near 100% efficiency in oxygen production with all the holes generated under light only able to oxidize water. This means that there are no side reactions occurring at the material while performing oxigen evolution reaction (oxigen reduction on platinum substrate). Of course the main disadvantage of this material is that it need UV light to be excited.

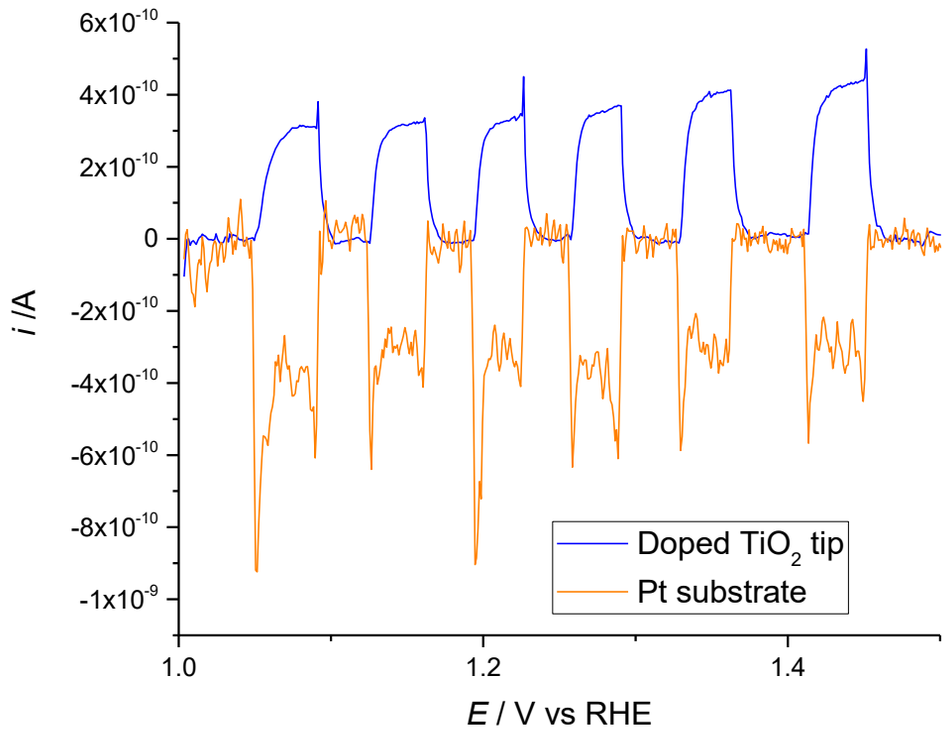

***Figure 162**. Exeriment with doped TiO_2 inside the cavity in NaOH 0.1M in the potential range between 1 and 1.5V vs RHE. Tip current of oxygen production (blue line) and substrate current of oxygen reduction (orange line).*

2.5.7 Cavity Depth Influence

During this work, several cavities of different depths were prepared as described in previous sections. Most of them were used with Cu_xO and from the obtained data was possible to obtain a correlation between cavity depths and tip currents. The following table shows the value of cavity depth and tip radius. While the tip radius is almost constant (variation depends on the sealing of the glass tube around the gold wire), the cavity was varied up to almost to 150%, from 20 to 47.8 μm.

	Cavity 3	**Cavity 5**	**Cavity 7**	**Cavity 8**
Radius (μm)	27,5	26	25,3	24,6
Depth (μm)	47,8	20,4	39,9	40,1

***Table 31**. Radius and depth of the different cavities used. Not all the cavities prepared were considered good enough for these experiments.*

In Figure 163, even if the proportion is not completely linear, is clear how increasing cavity depth we increase the tips current. This confirms that almost all the material inside the cavity can be reached by the light and work.

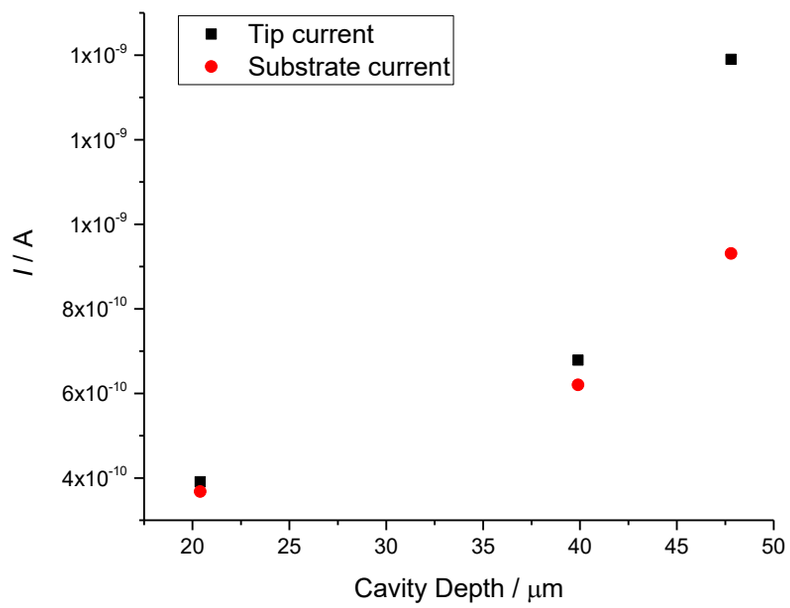

Figure 163. *Relationship between tips currents and substrate currents with cavity depths of Cu_xO powder in buffered electrolyte pH 7.*

From this point of view is better to work with deeper cavity to be able to have higher current less affected by noises and interferences. Anyway, this is not the only parameter to evaluate while choosing the cavity depth.

The next table shows the value of recorded efficiencies and tip and substrate currents recorded with cavity 3, 5 and 7. We can immediately notice that the value of interest, the material efficiency, is slightly lower if a longer cavity is used. This can be related to the impossibility of some produced hydrogen to exit from the inner part of the cavity to be recorded at the substrate reducing the performances. The values of the currents were obtained from Figure 164 that clearly shows how with smaller cavities, the recorded values are lower, but at the same time the efficiencies are higher.

	I_{Sub} (A)	I_{Tip} (A)	Sub/Tip	% Sub/Tip	Depth (μm)	i_{tip}/Depth
Cavity 3	$9.31x10^{-10}$	$1.29x10^{-09}$	0.722	72.2	47.8	$2.70x10^{-11}$
Cavity 7	$6.03x10^{-10}$	$6.92x10^{-10}$	0.871	87.1	39.9	$1.73x10^{-11}$
Cavity 5	$4.12x10^{-10}$	$4.49x10^{-10}$	0.918	91.8	20.4	$2.20x10^{-11}$

Table 32*. Tip and substrate currents under light vs cavity depth.*

On the base of these results we suggest the use of a cavity as short as possible, still able to maintain the material without giving lost in photoefficiency because of trapped hydrogen (or oxygen). A balance between these two parameters have to be evaluated during cavities creation.

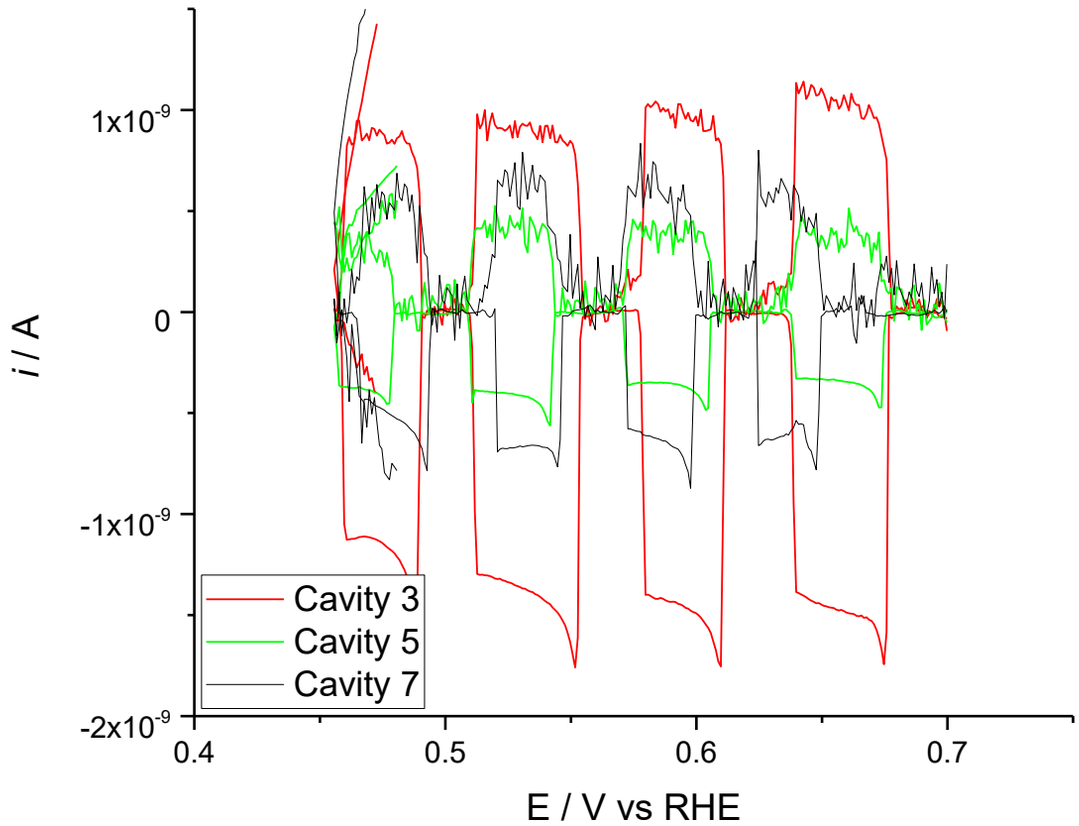

***Figure 164**. Different experiments with 3 different cavities containing Cu_XO in buffer electrolyte. Tip potential is usually scanned between 0.7 and 0.4 V vs RHE while substrate potential is held at 0.785 V vs RHE to oxidize the produced hydrogen during light pulsation at the frequency of 0.25Hz.*

2.5.8 Conclusions

By using this novel method, the rapid distinction in photoactivity of various semiconductors, easily loaded inside the cavity, is possible. Moreover, this method gives an idea of hydrogen evolution efficiency and oxygen evolution efficiency on photocathode and photoanode, respectively. This allows the discrimination of the desired reaction from any undesired side reaction that can occurs at the semiconductor. Thanks to this method is then possible to have an idea of the real efficiency of different materials as reported in the following table without any substrate contributes because the surface area of the current collector is negligible if compared to the powder one. The use of the cavity also ensures to quickly find a way to study the material avoiding the research of the best conductive support (inert in working window) and the presence of powder detachment from the surface during the analysis.

It was only possible to define an interval of photoefficiency percentage probably because of the small currents and the errors that can be obtained during the data elaboration.

Material	**Cu_XO**	**NiO**	**CuI**	**TiO_2**
% of photoefficiency	68-92%	28-53%	12-35%	75-100%

***Table 33**. Materials efficiencies recorded during different experiments.*

Despite this seems that among the photocathodic materials studied for testing this method, Cu_XO was the more stable while CuI, the less one.

2.6 XAS Cells Preparation

2.6.1 Introduction

In this brief section is presented the preparation and the characterization of two types of innovative cells for the combined use of electrochemistry and XAS developed in our laboratory[360]. The aim of this work is to show how three-dimensional printing can be a strategy for the creation of electrochemical cells for *in-situ* and *operando* experiments by means of synchrotron radiation. As a case study, the description of two cells which have been employed in experiments on photoanodes for photoelectrochemical water splitting are presented.

The main advantages of these electrochemical devices are associated with their compactness and with the precision of the three-dimensional printing systems which allows details to be obtained that would otherwise be difficult. Thanks to these systems it was possible to combine synchrotron-based methods with complementary techniques in order to study the mechanism of the photoelectrocatalytic process. The main limitation of the X-ray probe lies here in the attenuation coefficient of the other materials present. The presence of the hematite and FTO on the back-side of the electrocatalytic film prevents us from irradiating the system with X-rays from the back-side, and in addition forbids the use of transmission geometry. Consequently, XAS investigation should take place at the other side of the IrO_x film, which is in direct contact with the electrolytic solution, and in fluorescence mode. With respect to the water attenuation coefficient at the Ir L_{III}-edge, the solution layer cannot be thicker than 1 mm. A photo-spectroelectrochemical cell for hosting such a photoanode should also allow a three-electrode assembly where the working electrode (at which the process of interest takes place) is combined with a counter electrode (a Pt foil) and a reference (usually Ag/AgCl). It is important to point out that in these small-sized electrochemical cells small channels and holes are present that are difficult to obtain manually or with conventional tools. These channels and holes should guarantee the electrical contact between the electrodes via the electrolyte. Another requirement for these devices is the resistance against X-rays in order to avoid the formation of holes in the material and the subsequent loss of content.

The employment of a 3D printer based on the use of photopolymers represents the easiest and fastest way to produce efficient photo-spectroelectrochemical devices characterized by details that would be difficult to obtain using standard subtractive manufacturing technologies. The first example of the use of 3D printing of a cell for spectroscopy dates back to a few years ago (Symes et al.[390]) but, to the best of our knowledge, 3D printing has not yet been employed for building photoelectrochemical devices for *in-situ* and *operando* experiments with synchrotron radiation.

2.6.2 Spectroelectrochemical Cells

The photo-spectroelectrochemical devices described in this work are entirely made of a 3D printed photopolymer resin.

2.6.2.1 Cell Type A

As shown in the scheme presented in Figure 165A, the device is composed of two parts. Side 1 in Figure 165A is the cell main body, while side 2 is a rectangular cover. The two parts are assembled by means of screws and bolts, inserting an O-ring ensuring tightness against electrolyte leakage. The frontal circular window is used for illumination by both UV–Vis and X-rays.

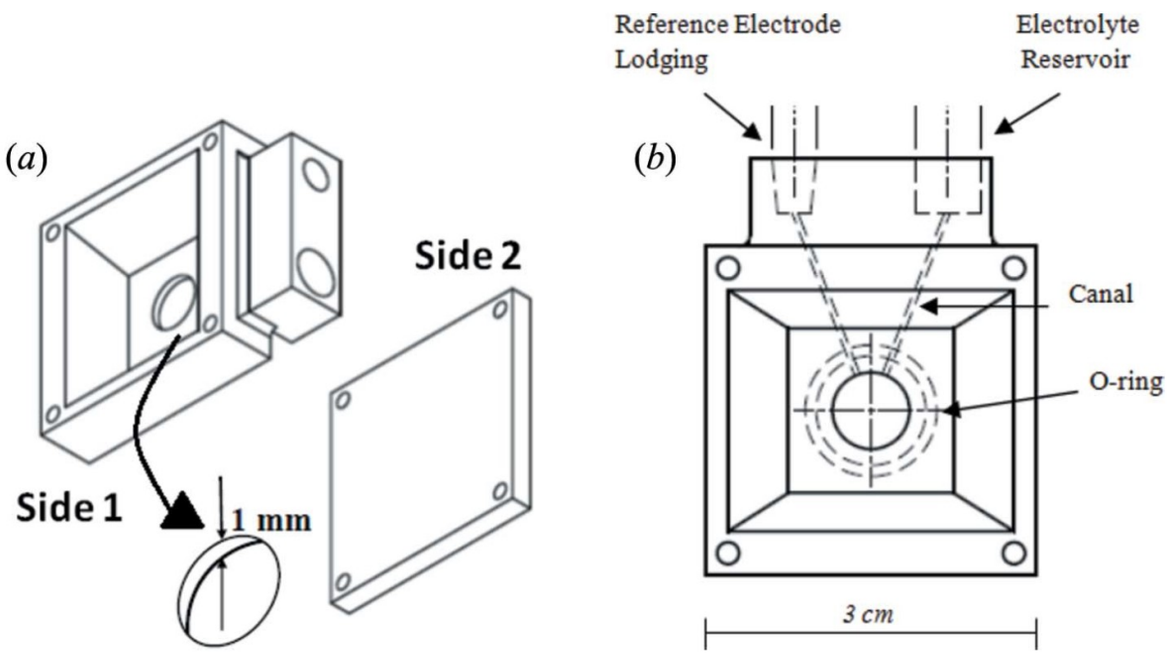

Figure 165. *Design of cell type A: rectangular plate and cover with hole (a) and schematic representation of the canals connecting the reference and counter electrodes holders to the inner part of the cell (b).*

The internal cell volume is then filled with the electrolyte as explained below. In this case, the thickness of the frame defined by the two arrows in Figure 165A is limited to 1 mm, due to the absorption of water at the energy of the Ir L_{III}-edge (the absorption length for water at 11200 eV is 2.5 mm).

The rectangular shape is ideal for adding an upper external part that in turn allows a stable lodging of the reference electrode. The lodging constitutes a rectangular block with two cylindrical holes, of which one is used for housing the reference electrode and the other for filling the cell, once assembled, with the electrolyte by means of a syringe, and also works as an electrolyte reservoir. Both holes are connected to the inner part of the cell by means of small canals, whose diameter is 500 µm (Figure 165B): this diameter is in turn dictated by the thickness of the 1 mm frame as detailed above. The counter electrode consists of a Mylar® square film, half of which is covered with a Pt/C+Nafion® mixture. The latter is deposited by dropcasting over the Mylar® while kept on a laboratory hot plate. The electrical contact is ensured by Ag epoxy (EPOTEK® H20E) and a Cu wire.

The electrode is glued onto the frontal face of the cell using melted Parafilm®. The counter electrode thus also works as a closure of the whole internal cell volume.

The electrochemical device with and without the three electrodes assembly is shown in Figure 166 The stable architecture achieved by means of this design allows the best conditions for performing photo-electrochemical measurements to be obtained. In this case the working electrode is the photoanode made of two parts, namely the electrocatalytic domain, IrO_x, which is subjected to the XAS investigation, and a semiconductor part Fe_2O_3, which is illuminated by an UV–Vis diode. The cell contains the electrolyte solution with a controlled thickness and presents a frontal window allowing illumination by X-ray photons. This electrochemical cell was employed to investigate electrodeposited IrO_x overlayers. Hematite/IrO_x photoanodes were prepared as described by Marelli et al. (2014)[391]. In the present case, the deposition of IrO_x required 800 s.

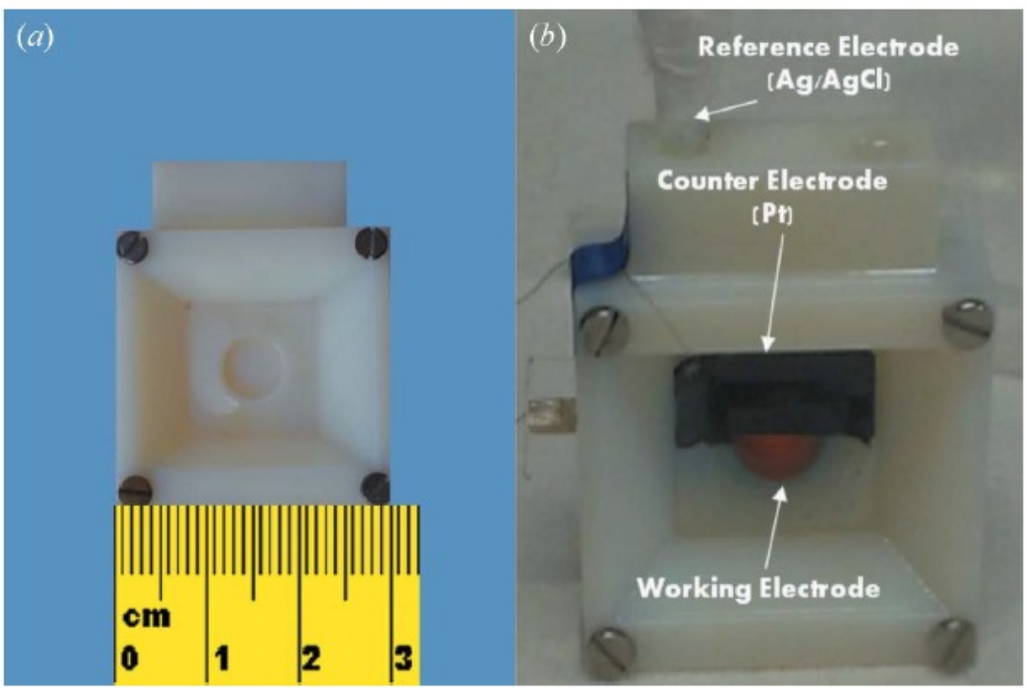

Figure 166. *Image of the assembled photo-spectroelectrochemical cell of type A without (a) and with (b) the three-electrode setup.*

2.6.2.2 Cell Type B

The scheme of cell B, that is clearly a modification of cell A, is illustrated in Figure 167A (front side) and Figure 167B (back side). There are two main differences of this cell if compared with cell A. The first lies in the presence of an additional electrolyte reservoir (Figure 167D) in the main body of the device. This part is open at the upper side and is electrically connected to the photoanode by the electrolyte. The design of this feature is aimed at: (i) obtaining room devoted to the lodging of the counter electrode in direct electrical contact with the photoanode; and (ii) having a larger static reservoir for the electrolyte to cope with possible radiation damage (local heating, radical formation, etc.) induced by the X-ray beam.

The second important characteristic of this electrochemical cell is represented by the circular hole generated in the rectangular cover. This feature provides a window on the working electrode and is accomplished to perform UV–Vis illumination at the back-side of the hematite, thus avoiding absorption in the visible region by the IrO_x layer.

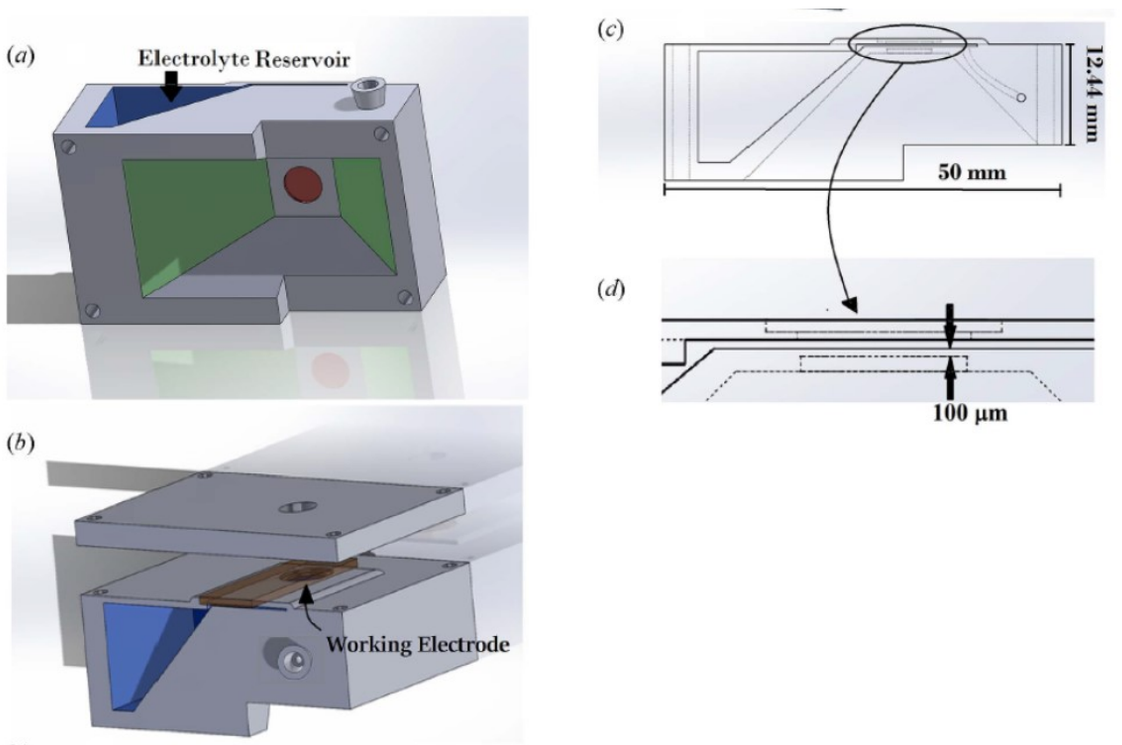

Figure 167. *Scheme of the photo-spectroelectrochemical cell of type B showing the electrolyte reservoir (a), the rectangular cover with circular hole (b), the curved canal connecting the reference electrode to the inner part of the cell (c) and the working electrode lodging (d).*

The main body of the device and the rectangular cover are held together by means of screws and bolts, and an O-ring is inserted to ensure tightness against solution leakage.

The rectangular-shaped electrolyte chamber presents an upper slot, ideal for the insertion of the Pt counter electrode. The lodging for the reference electrode is achieved by a hole generated in the upper part. This is connected to the electrolyte chamber by means of a curved canal with a diameter equal to 500 mm as one can see in the cross section illustrated in Figure 167C. In addition, this second cell has a 100 mm-thick window for X-ray illumination that is directly printed on the front side, ensuring a proper sealing against the back pressure of the electrolyte solution. The realization of such details would not be possible (or very difficult to realize) with the traditional and manual instrumentation. Figure 168 shows a photograph of the electrochemical device with the three-electrode assembly mounted in the experimental hutch of the LISA beamline (BM08) at ESRF, where all the experimental results described in this paper were obtained: UV–Vis illumination is carried out on the left-hand side by means of a solar simulator lamp whereas the X-ray illumination takes place on the other side of the cell.

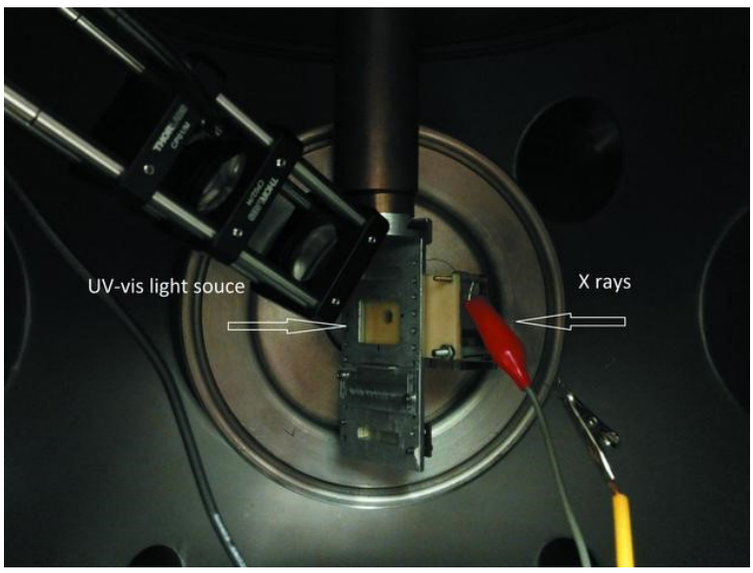

Figure 168. *Photograph of the assembled photo-spectroelectrochemical cell of type B, mounted in the experimental hutch. UV–Vis illumination is carried out on the left-hand side by means of a solar simulator lamp whereas the X-ray illumination takes place on the other side of the cell.*

Cell type B was used to study photoelectrodeposited IrO_x overlayers. In this case, the hematite photoanode was prepared according to the procedure reported by Malara et al. (2015)[392]. IrO_x is then photoelectrodeposited by a 0.45 mM $IrCl_3$ solution at pH = 13, after immersing FTO@-Fe_2O_3 in the solution together with a saturated calomel electrode and platinum sheet as reference and counter electrodes, respectively. The deposition lasted 15 min and was carried out at +0.6 V relative to the saturated calomel electrode (SCE) while the photoelectrode was kept under illumination using a LED (λ= 400 nm, LED ENGINE LZ1-00UA00) as a light source.

2.6.3 Cell Fabrication

The photo-spectroelectrochemical devices are manufactured using a photopolymer-based printer (Objet 30 Pro, Objet- Stratasys). This technology was selected among different 3D printing solutions available on the market because of its ability to print very small parts with high resolution and using a material that is resistant to chemicals. The printer uses photopolymeric resins that are laid down on the printing bed in a liquid form and polymerized using a UV lamp. The device is printed at a layer resolution of 28 µm, that is the height of each deployed layer, while the in-plane printing error is about 1 µm per 1 mm. This is well appropriate to the diameter of the channels for the reference electrode and for the electrolyte reservoir (500 µm, as mentioned above).

The printer can deploy one material at a time, in combination with a support material that can be removed using a water jet machine and a sodium hydroxide solution. The presence of the support material in all the inner cavities was considered during the device design. All the inner channels have been designed with the minimum level of curved parts, in order to facilitate the cleaning process. The devices are printed using the VeroWhite material, an opaque rigid photopolymeric polyacrylic resin characterized by an adequate stiffness and resistance to chemicals. An adequate resistance to temperatures and mechanical stresses forced by the experimental conditions characterizes this material.

The resin has a softening temperature of 52–54°C (measured with ASTM standard DMA) and has a heat deflection temperature of about 45–50°C (measured with ASTM standard D-648-06 and D-648-07). Since the experimental procedure is carried out in contact with a liquid, water absorption represents another important feature for consideration; actually, the prototyped object always has a little porosity because of the layering process that builds it. The water absorption parameter ranges from 1.1% to 1.5% within 24 h. Since each experimental test lasts for less than 8 h, the devices can be considered as waterproof for this application.

The printer can realize an entire set in about 2 h. After printing, the device components are cleaned first using a water jet machine, paying attention to not damaging the thin walls. After that, the parts are immersed in a solution of water (90%) and sodium hydroxide (10%) to facilitate the removal of the support material. A thin wire has been used to ensure a good cleaning of the inner channels.

2.6.4 XAS Results

The capabilities of the photo-spectroelectrochemical cells described are illustrated in this section.

Before discussing the X-ray absorption results, it is important to show that the 3D-printed electrochemical devices actually work. A comparison between a cyclic voltammetry obtained by means of a 3D-printed XAS cell and one obtained by means of a standard electrochemical cell is illustrated in Figure 169. These electrochemical measurements were performed between −0.2 and 0.4 V versus Ag/AgCl (KCl 1 M) at 20 mV s^{-1} in ferrocene methanol 1 mM in $KClO_4$ 0.1 M. The working electrode was a Pt foil. The signals clearly show that the cell response is very similar in the two cases, thus probing the conformity between the electrochemical behaviors.

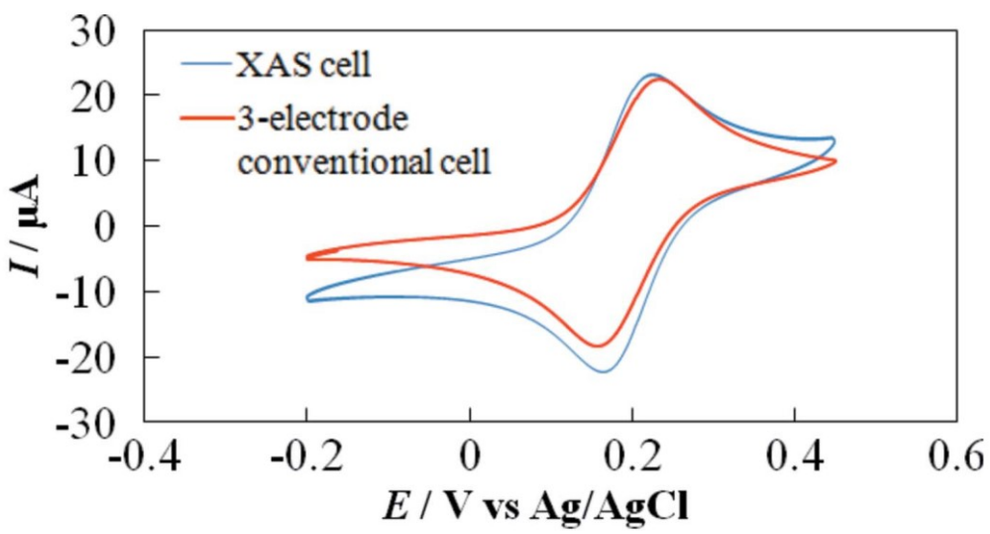

Figure 169. *Comparison between a cyclic voltammetry obtained by means of a 3D printed XAS cell (blue line) and one obtained by means of a standard electrochemical cell (red line). These were performed between −0.2 and 0.4 V versus Ag/AgCl (KCl 1 M) at 20 mV s^{-1} in ferrocene methanol 1 mM in $KClO_4$ 0.1 M. Working electrode: Pt foil.*

Figure 170 illustrates XAS results obtained *in-situ* and *operando* by means of the 3D-printed electrochemical devices previously described. Two different types of sample have been considered: electrodes onto which the IrO_x film was electrodeposited (Figure 170A, B and C) and electrodes onto which the IrO_x film was photodeposited (Figure 170D).

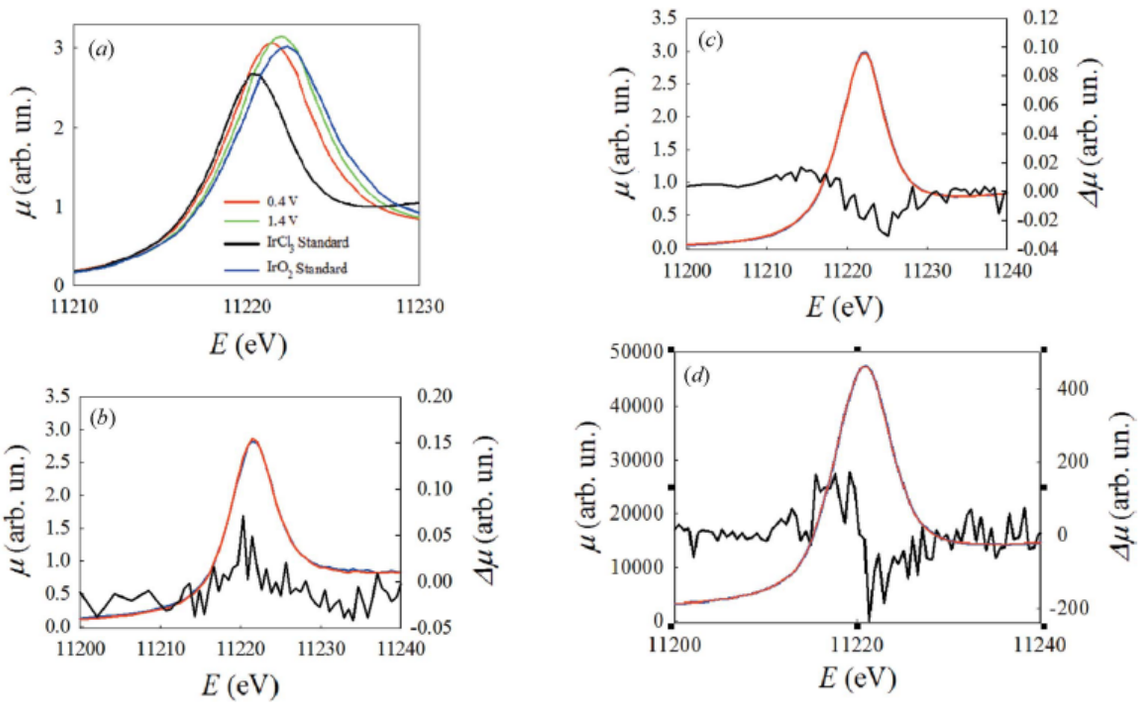

Figure 170. *XAS results obtained with in-situ and operando by means of the 3D-printed electrochemical devices. Two different types of sample have been considered: electrodes onto which the IrO_x film was electrodeposited (a, b, c) and electrodes onto which the IrO_x film was photo-electrodeposited (d). (a) Ir L_{III} XANES spectra acquired in-situ at two different potential values: 0.4 V (red line) and 1.4 V (green line) versus RHE. The spectra of $IrCl_3$ (black line) and IrO_2 (blue line) standard materials are plotted as references for Ir(III) and Ir(IV), respectively. (b, c) Ir L_{III} normalized XANES spectra acquired at a constant potential value equal to 0.4 V (b) and to 0.8 V (c) under UV–Vis light conditions (red line) and dark conditions (blue line), and the respective differences (black lines) obtained from the subtraction of the spectrum under dark conditions from that acquired under UV–Vis light conditions. (d) Response of the photoanode to the illumination by UV–Vis light when the IrO_x layer is prepared by photo-electrodeposition, recorded at a potential of 1.56 V relative to RHE. The signal is different between the XANES spectrum recorded in the presence and that recorded in the absence of the UV–Vis illumination (light − dark).*

Figure 170A shows Ir L_{III} XANES spectra obtained at two different potential values: 0.4 and 1.4 V relative to the reversible hydrogen electrode (RHE) (in the latter case oxygen evolution takes place) by means of the A type cell. The spectra of $IrCl_3$ and IrO_2 standard materials are added as better references for Ir(III) and Ir(IV), respectively. Transitions from the Ir *2p* levels to continuum states and to *5d* localized states give rise to steps and peaks (white lines). The energy position of the peak maximum is directly associated with the Ir oxidation state: a shift to a larger potential value corresponds to an oxidation process.

When the applied potential is 0.4 V the peak maximum is situated between that of $IrCl_3$ and IrO_2, thus indicating that the mean oxidation state is between (III) and (IV). Under oxygen evolution conditions, when the potential is equal to 1.4 V, the peak maximum is shifted towards larger energy values.

This suggests that the oxidation state of the photo-absorber is very close to Ir(IV). This corresponds, considering the ohmic drops in the α-Fe_2O_3 layer, to what has been previously described by some of us [348,393]by using a much larger volume cell.

In Figure 170B and C the response of the IrO_x layer to the illumination of α-Fe_2O_3 by UV–Vis light is shown for two different applied potentials: 0.4 V (Figure 170B) and 0.8 V (Figure 170C). The normalized XANES spectra acquired in UV–Vis light (red line) and dark conditions (blue line) are illustrated. Their differences (represented by the black lines), resulting from the subtraction of the spectrum acquired in light conditions from that observed in dark conditions, are different in the two cases but very small. However, considering that the signal is recorded *in-situ* by means of a photo-spectroelectrochemical device, these differences can be considered as significant. For an applied potential equal to 0.4 V the difference is positive; for an applied potential equal to 0.8 V the difference is negative.

As a further example, Figure 170D shows the response of the photoanode to the illumination by UV–Vis light when the electrodic layer is prepared via photo-electrochemical deposition. In this case, measurements were performed by means of the electrochemical cell of type B. The red line and the blue line are the XANES spectra acquired in the presence and absence of UV–Vis light illumination, respectively. The difference between them is indicated by the black line. Its trend clearly accounts for a peak shift towards lower energy values under UV–Vis illumination.

A detailed explanation of the mechanism and the kinetics of the photo-electrochemical processes involved in the results reported above is well beyond the aim of this paper and it will be the object of future work. These results, however, show that the experimental setup provides a key tool for monitoring the UV–Vis light driven variations in the hole density of iridium *5d* states under different applied potentials. What can be noted here is that the IrO_x overlayers prepared by different methods (by electrochemical or photoelectrochemical deposition) respond differently to UV–Vis illumination.

2.6.5 Conclusions

In the current work we designed and built multi-purpose photo-spectroelectrochemical devices for *in-situ* and *operando* X-ray absorption spectroscopy by means of a 3D printer. Thanks to these systems it was possible to combine synchrotron-based methods with complementary techniques. In particular we created two innovative types of photo-spectroelectrochemical cell for investigating photoelectrochemical water splitting providing a key link between spectroscopy and electrochemistry and photochemistry.

The main characteristics of these electrochemical devices are summarized below:

(i) The devices are compact and small enough to allow an easy and fast experimental setup in the beamline hutch.

(ii) Thanks to the precision of the 3D printing system, it is possible to achieve detail that otherwise would be difficult to obtain. For example, it is possible to control the thickness of the electrolytic solution avoiding problems associated with X-ray attenuation coefficient by water. Furthermore, we can obtain small and curved canals for the counter and reference electrodes ensuring electric contact between the different parts of the cell.

(iii) The cell geometry is easily adaptable for other experiments, for example for studying different materials or for performing RIXS or XRD. In particular, the experiments described here were performed at the Ir L_{III}-edge (11215 eV). However, the design of cell B allows softer X-rays to be used thanks to the fact that the X-ray window is printed and can in principle be made thinner to cope with the smaller penetration depth at low energies, still ensuring a proper stiffness for sustaining the back pressure of the electrolyte.

Experiments carried out by means of these photo-spectroelectrochemical devices allowed measurements at different potential values to be performed, including those where oxygen evolution is expected to occur. Furthermore, thanks to specific details mentioned above, it was possible to study the different responses of the catalyst under UV–Vis light and dark conditions. Results obtained led to a better understanding of the mechanism and the kinetics associated with the photoelectrocatalytic process of water splitting.

As a final remark, we note that the small volume parts of the photo-spectroelectrochemical devices described here can hardly be fabricated without the 3D printing technology. It is quite straightforward to expect that this technology will be of increasing importance in the creation of environmental chambers for *in-situ* and *operando* synchrotron radiation experiments.

2.7 Protective Layers for Cu_2O

2.7.1 Introduction

The long-term instability of Cu_2O under working conditions moves our research through the development of a protective layer for this semiconductor. There are some requirements that the protective layer should fulfil:

- Be stable and ensure the stability of the Cu_2O layer.
- Don't' stop the HER reaction under light of Cu_2O.
- If applied as an overlayer must be as transparent and homogeneous as possible.
- Should be prepared from low-cost materials with simple and low-cost techniques.
- Possibly should be non-toxic.

Different heterojunctions were proposed in literature also with good results. Beside this, most of them use expensive techniques like ALD[134,394] or need the use of Pt catalysts to regenerate the activity of protected-Cu_2O[57]. For this reason, our first choice goes to FeOOH, a cheap and abundant n-type semiconductor usually found as corrosion product of steel cathodes in industrial plants[171]. The easier way for the preparation of FeOOH homogeneous layer is the electrochemical one. Different synthesis were present in literature starting from different deposition baths[395–397] with the purpose of having an OER catalyst[169,170,172] or photoanode[398,399]. In this work we followed the synthesis proposed by Martinez et al.[400].

To have a better knowledge of the material, XAS study on the two main phases of iron oxyhydroxide (goethite and lepidocrocite) were performed. In this study, the behavior of the material until HER was observed by the combined use of XAS and electrochemical methods.

Moreover, the role of a Cu-oxide based protective underlayer was studied as well. The material is composed by a junction between CuO and Cu_2O but differently from literature, where CuO is the light activated part of the electrode[163,401], or a protective passive layer[310] or the precursor[402], here CuO is in the inner part of the material. Also, this core-shell material was studied under working conditions with the combined use of XAS and electrochemical methods.

Eventually both the materials are extremely cheap, easily produced by electrochemical and electrochemical + thermal methods starting from environmental-friendly reagents. The use of XAS allows us to define their stability together with their activity once combined with Cu_2O.

2.7.2 XAS on FeOOH

Iron oxyhydroxide was found to be the main corrosion product of steel cathode in the chlorate process[403]. The occurrence of goethite and lepidocrocite depends on plant conditions and electrodes used[404–406]. Water reduction on corroded iron surfaces is the desired cathodic reaction. The main goal of this section is to study the stability of the oxide phases and the nature of electrocatalytic species involved in the reaction together with the reversibility properties of both the materials.

The complete electrochemical behaviour was studied for α-FeOOH and γ-FeOOH electrodeposited on Fluorine Tin doped Oxide (FTO), Ti or on powder from wet-synthesis.

The materials were studied under cathodic polarization until strong hydrogen evolution by the mean of *in-situ*, *ex-situ* and *operando* electrochemical methods with X-ray Absorption Spectroscopy (XAS). Information about the oxidation state of the species involved in the potential windows between 0.9 and -0.8V vs RHE shows the formation of an iron (II) phase attributable to reduced green rust on both the FeOOH phases while the hydrogen evolution reaction occurs. This result is in contrast with the supposed formation of $Fe(OH)_2$ hypothesized by previous authors[176,407] and clarify more recent result[177] thanks to the use of XAS. Despite the reduced phase is common to both the iron oxyhydroxide species, once re-oxidized the electrodes were found to show an interesting memory effect leading to the original phase. This behaviour was observed only during electrochemical oxidation in solution, while under atmospheric oxidation the reduced green rust is re-oxidized to a mixture of goethite and lepidocrocite. Eventually the thermodynamic stability of α-FeOOH was observed by means of Fixed Energy X-Rays Absorption Spectroscopy (FEXRAV) showing its conversion to the gamma-phase in basic environment. Information obtained from this work will help clarifying the complex chemistry of iron ions under different conditions.

Both corrosion products were prepared by electrochemical method and tested in a well-established cell from their open circuit potential (OCP) until strong hydrogen evolution reaction (HER). A proof of the electrochemical specie involved during hydrogen evolution was so given while the reversibility of the system was studied too. In addition, the electrochromic properties of such materials together with the self-conversion of α-FeOOH in γ-FeOOH were observed.

2.7.3 FeOOH Preparation

Goethite and lepidocrocite were prepared using electrochemical deposition and wet synthesis. Two different substrates, FTO and Ti foil were used in the electrochemical deposition, while the bulk samples were drop casted on screen printed carbon electrodes.

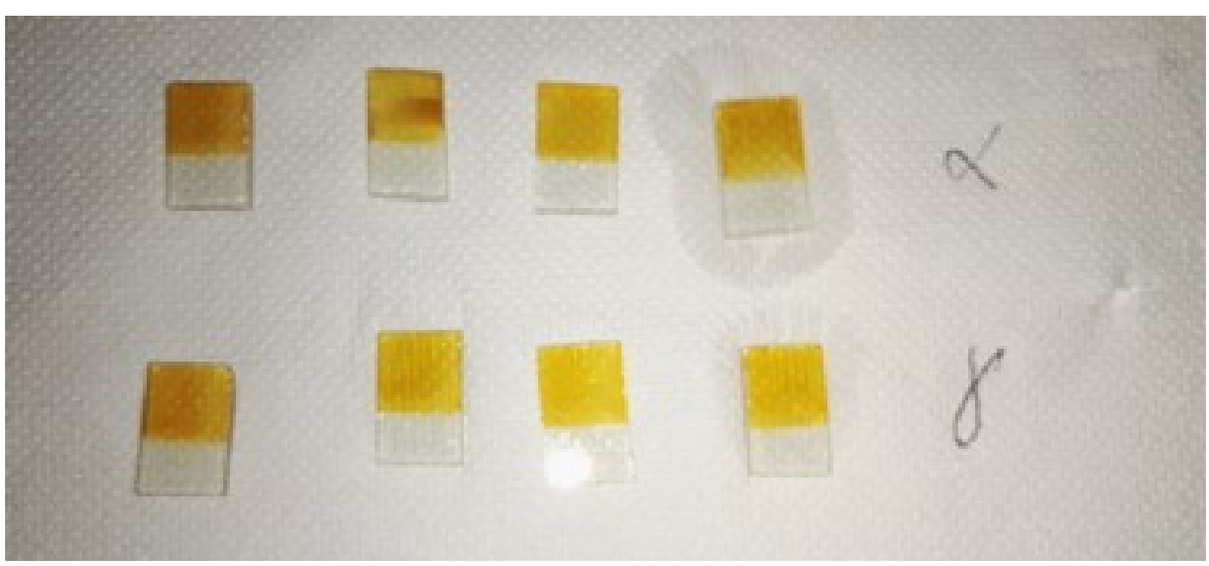

Figure 171. *Photo of some electrodeposited samples of goethite and lepidocrocite.*

2.7.3.1 Electrodeposited Samples

The FTO was previously washed in an ultrasound bath for 30 minutes in acetone, 30 minutes in ethanol and 30 minutes with water. This long procedure allows to remove any trace of skin grease and dust that can affect the deposition. The electrodes were then dried under N_2 flux before being used otherwise they were kept in distilled water to avoid any type of contamination. Ti electrodes (2x1cm) were instead treated in boiling oxalic acid solution (3g in 100 mL of water) for 40 minutes. A platinum foil (2x1 cm) was used as counter electrode and the reference was a Saturated Calomel Electrode (SCE) in a double bridge filled with KNO_3 0.5M to avoid Cl^- interferences. All potentials in this paper are referred to the Reversible Hydrogen Electrode (RHE). A reflux condenser was allowed to keep the electrolyte concentration stable during the deposition. The electrode's area was controlled using a Teflon® tape and it was $1cm^2$ for all the electrodes.

FeOOH electrode were prepared on FTO (Fluorine Tin doped Oxide) glass (Sigma-Aldrich 8 Ω 1x1.6cm) by potentiostatic deposition in 0,01M $Fe(NH_4)_2(SO_4)_2$ x $6H_2O$ (Sigma Aldrich® 99%) + 0,04M CH_3COOK (Baker analyzed Reagent ® 99.0%) at 90°C in N_2-satured solution under stirring.

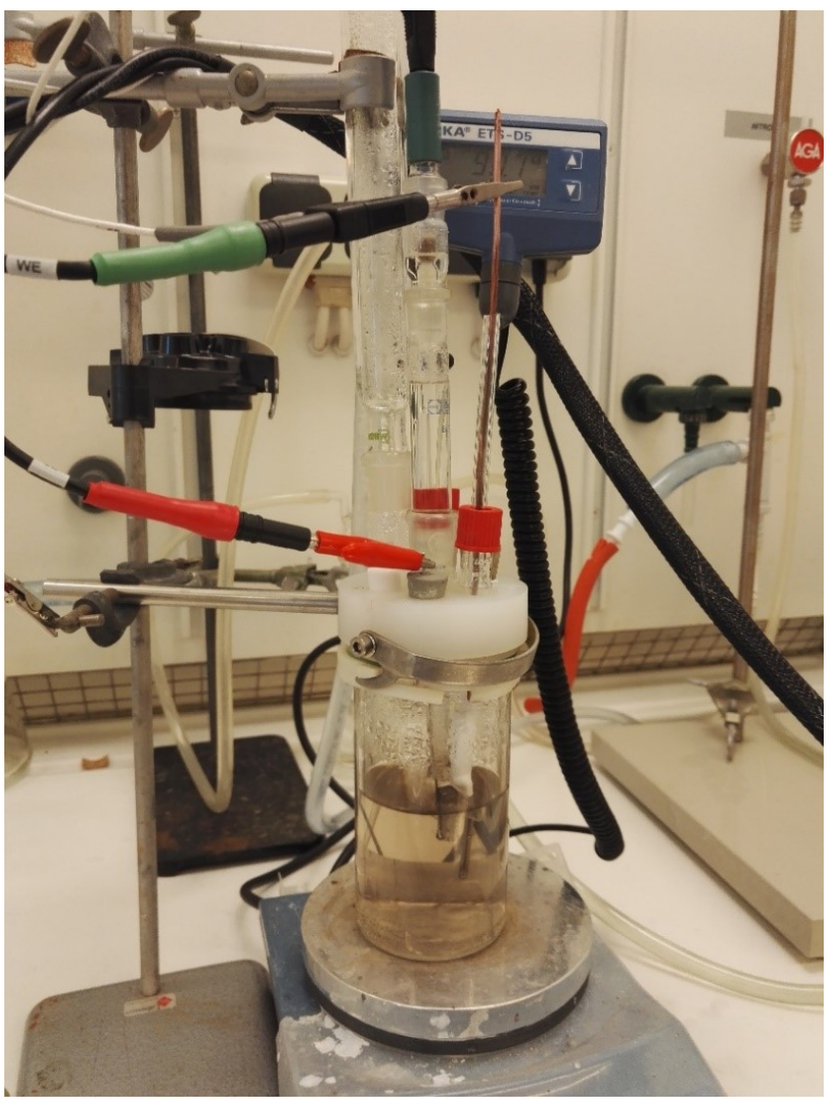

Figure 172. *Experimental setup for the deposition of FeOOH.*

The linear sweep voltammetry of the so composed bath is reported in Figure 173 in comparison with the same material deposited on polished Ti foil (Alfa Aesar® 99% metal basis).

The LSV, recorded at a low scan rate ($1mVs^{-1}$) allows the identification of the different potential regions for the deposition of the iron oxides of interest. Indeed, is possible to notice on the LSV a shoulder and two distinct peaks. The shoulder is related to the formation of Fe_3O_4, while, moving in anodic direction, the two peaks are for alpha and gamma FeOOH respectively. The deposition potentials were chosen in accordance to L. Martinez et al. paper[408]. The deposition was performed at +0.45 V vs RHE for the alpha phase and +1.60 V vs RHE for the gamma one. The selected values should ensure high purity of the two materials. Indeed, according to literature, it is possible to obtain pure goethite working in the potential range between 0.39 and 0.47 V vs RHE while pure lepidocrocite is obtained for values higher than 1.2 V vs RHE. The short range, especially for the alpha phase is due to the large overlap of deposition peaks that would lead to the formation of mixture of the different oxides. Using a Ti substrate the characteristic peaks are more evident, but even on FTO is clearly possible to identify each specific region. Interesting, the Fe_3O_4 peak is absent on FTO were a stronger induction potential is needed to start any deposition.

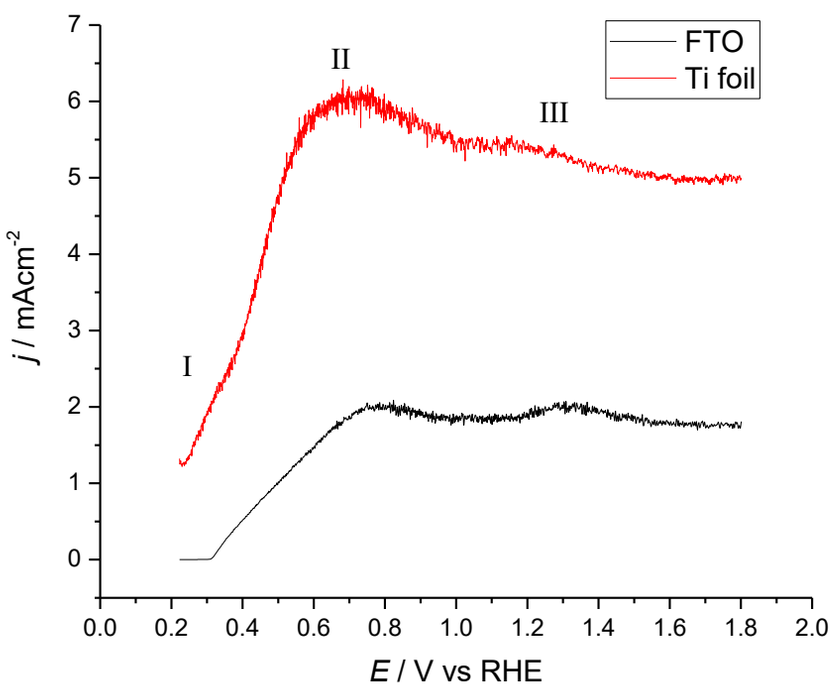

Figure 173. *Linear Sweep Voltammetry (LSV) of two different substrates in 0,01M $Fe(NH_4)_2(SO_4)_2$ x $6H_2O$ + 0,04M CH_3COOK at 90°C in N_2-satured solution under stirring at $1mVs^{-1}$. The counter was a platinum foil while the reference was a SCE electrode (E_0=+0.248 mV vs NHE). The working electrode was a titanium foil (in red) or a FTO (in black). Peak "I" refers to Fe_3O_4, peak "II" refers to α-FeOOH and peak "III" refers to γ-FeOOH.*

Deposition on FTO was kept ongoing until 0.11C of charge had passed to have a loading of $0.1mgcm^{-2}$ on the electrode. The use of a such thin layer is important to ensure a significant electrochemical signal while reducing the possibility of XAS self-absorption.

Goethite and lepidocrocite were also deposited on polished and annealed titanium foil (Alfa Aesar® 99% metal basis) using similar potential.

A Teflon® tape ensure that the deposited surface was 1cm^2 each side. The loading on this type of electrode is 2Ccm^{-1} in order to have almost the same amount of material for any face of the Ti foil.

The so prepared electrodes were rinsed with 18.2MΩ MilliQ water to remove any trace of deposition solution and were stored for the XAS analysis.

The potential for electrodeposited electrode is in accordance with the recorded linear sweep voltammetry LSVs (Figure 173) and in the L. Martinez et al. paper[400]. The deposition potentials at pH 6 are:

- α-FeOOH on Ti: 0.46 V vs RHE
- γ-FeOOH on Ti: 1.60 V vs RHE
- α+γ-FeOOH on Ti: 0.59 V vs RHE
- α-FeOOH on FTO: 0.45 V vs RHE
- γ-FeOOH on FTO: 1.60 V vs RHE
- α+γ-FeOOH on FTO: 0.65 V vs RHE

α+γ electrodes were prepared to follow the self-conversion of gamma-phase in the alpha one as will be explained at the end of the chapter. The purity of the phases was confirmed with XRD on samples with 4C of material on FTO measured with a gracing angle of 4deg. The results are reported below. Each phase is reported together with the FTO substrate that even in presence of the FeOOH shows peaks of high intensity.

FTO Substrate

The bare and clean FTO was firstly measured alone. The peaks position is basically coincident with those of tin oxide[409].

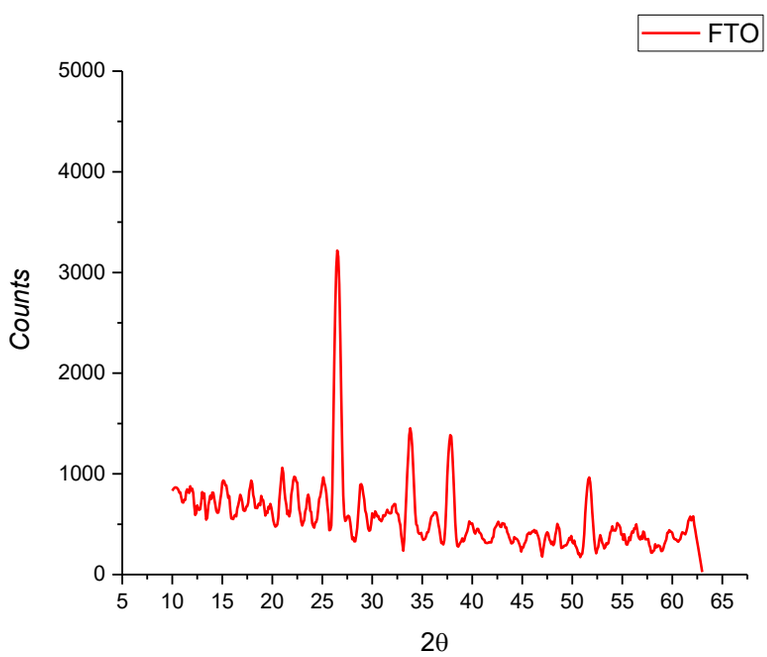

Figure 174. XRD analysis of the bare FTO at 4 degrees. 2theta recorded from 10 to 63 degrees.

Alpha FeOOH on FTO

Alpha-FeOOH (in red) shows different peaks together with those of FTO (in black). Unfortunately this measurement was extremely noisy but still the main peaks for goethite (the black vertical lines) coincide with the electrodeposited material[410].

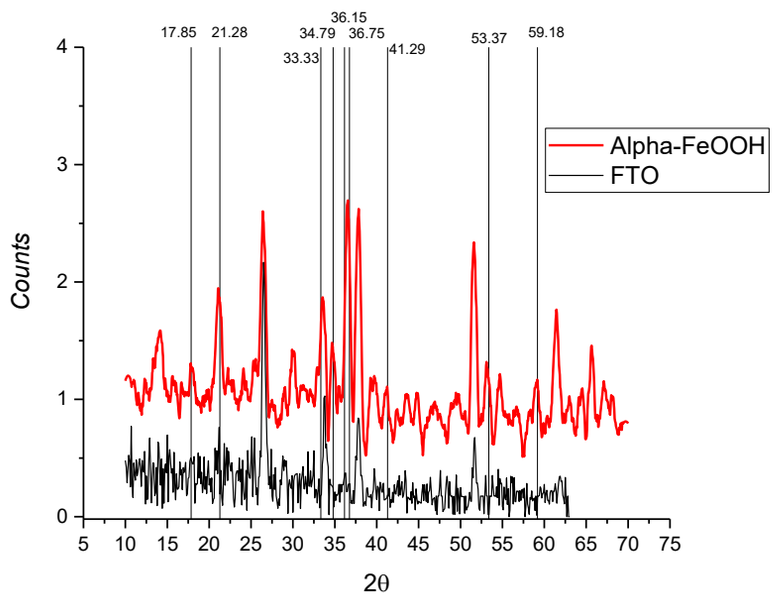

Figure 175.*Comparison between the alpha-FeOOH (red) and the FTO substrate (black). The vertical line are the main peaks for the alpha phase from the PDF file.*

Gamma FeOOH on FTO

The main peaks for gamma-FeOOH are reported by the vertical black lines. The only one presents for the gamma and totally absent in the FTO substrate is the one at 29.95 degrees. This phase seems to be very structured showing a single peak. Despite this, once removed from the electrode the whole specific peaks were found confirming the purity of the phase[411].

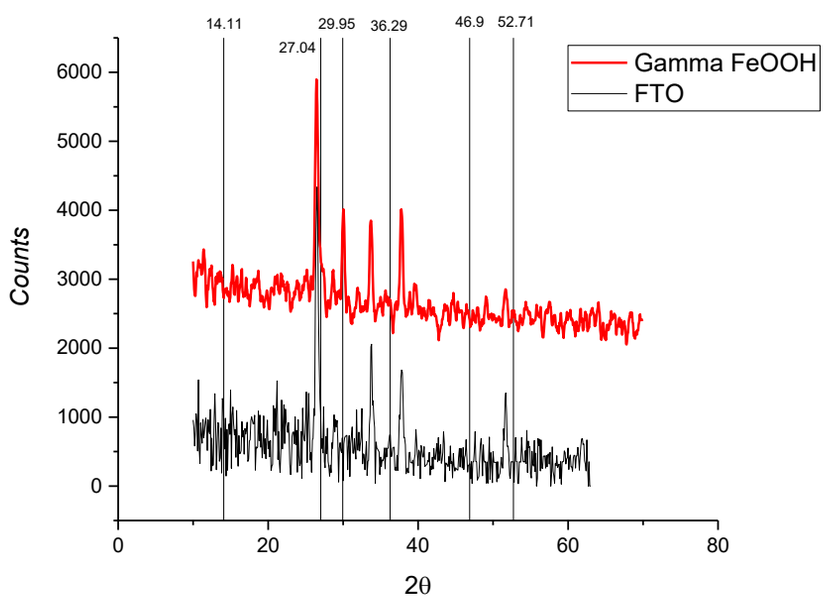

Figure 176. *XRD analysis of the gamma FeOOH (red) and the bare FTO substrate (black). The main lines for lepidocrocite from PDF file are also reported.*

2.7.3.2 Bulk Materials

Goethite and lepidocrocite powders were synthetized follow the following recipe[412]:

Goethite: 0.495 g $FeCl_2 \cdot 4H_2O$ were dissolved in 50ml of Milli-Q water previously purged with N_2. Then 5.5 ml of 1M $NaHCO_3$ was added and the solution was left for 24h under air flow. The filtered precipitate was rinsed with 18.2MΩ Milli-Q water and dried in oven for 48 hours at 65 °C.

Lepidocrocite: 2 g $FeCl_2 \cdot 4H_2O$ were dissolved in air condition in 100 ml Milli-Q water under stirring. NaOH was added until pH was between 6.7-6.9. The precipitate was filtered, rinsed with Milli-Q water, and dried in oven for 48 hours in 65°C.

The so prepared powders were suspended in EtOH and deposited by drop casting on screen-printed carbon electrode (DropSens® DRP-P-C11XX). The amount of material was 0.1mgcm^{-1} on each electrode. Once the electrode was dried 1/70 w/w of Tokuiama® membrane was added to ensure material adhesion (1.2 µL of 0.003% w/w).

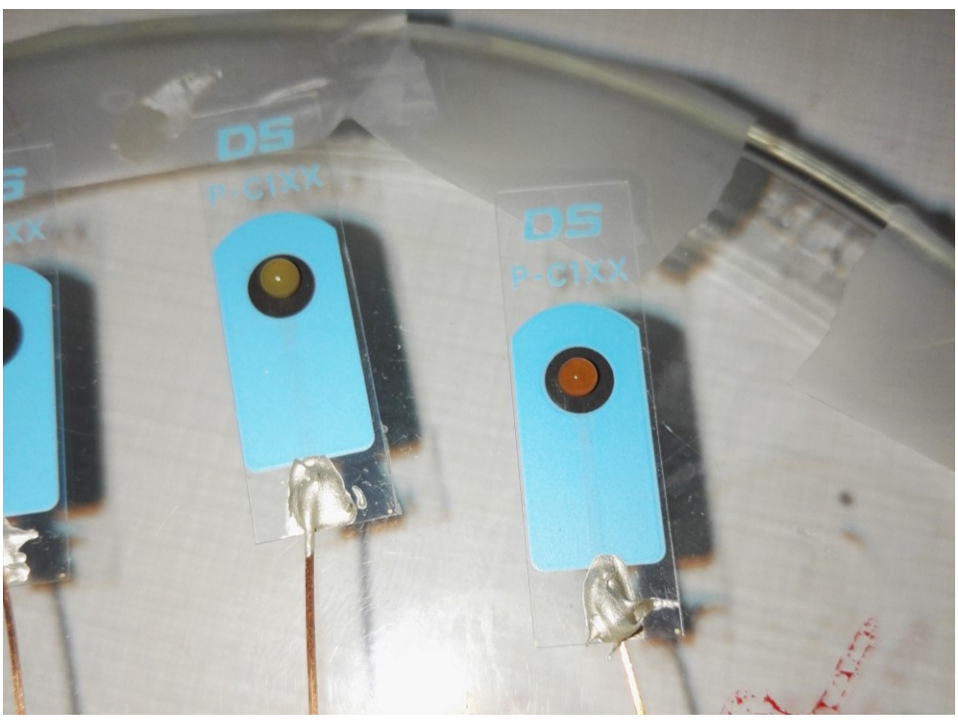

Figure 177. *Photo of the two FeOOH powders suspension just after the deposition on the screen-printed electrodes. A clearly different colour was found as well as for the electrodeposited ones.*

2.7.4 Experimental Setup

All electrochemical work was done with a CHi 630d potentiostat in a single compartment three electrodes cell. The counter electrode was platinum foil (1x2cm) faced to the FTO working one (1cm^2). The reference used was an SCE (saturated calomel electrode, E = + 0.248 V vs. NHE) electrode. A double junction was used to avoid chlorides leaking into the electrolyte. The electrolyte for material testing was 0.200 M Na_2SO_4(aq) (Sigma Aaldrich ReagentPlus) with pH 11 set with NaOH (Sigma Aaldrich ReagentPlus). The choice of this basic pH was done in order to simulate the basic environment presents during strong hydrogen evolution on industrial plants electrodes.

2.7.4.1 Photo-spectroelectrochemical Cells

The homemade “flat-cell” used in these experiments has a very simple design. Despite this, was able to guarantee reliable results and was very easy to manipulate. The backbone of the cell is made of inert plastic material. The width of the gum was enough to accommodate the FTO glass with just a very thin film of solution in front of the electrode. Reducing the thickness of this solution is very important because allows to have the highest number of photons reaching the sample avoiding electrolyte absorption. This is a very important parameter to consider in particular when light elements are studied.

Cell’s walls were made of inert plastic apart from a small window of Mylar® in front of the working electrode. Mylar® was chosen for its very high transparency to UV light and low absorption of photon. Transparency in all other parts of cell are unnecessary because not interested by the “eye” of X-ray.

The electrode disposition was also studied to be optimal from the electrochemical point of view. Working and counter electrodes were as close as possible while the reference electrode (Ag/AgCl 3M in double bridge) record the potential exactly in the middle of current lines between platinum counter and working electrode thanks to an “L-shaped” micropipette. To avoid loss of solution from double bridge it was sealed with Parafilm® while the cell was filled. The whole cell is kept together by epoxy glue dried in hoven at 70°C. All experiments were performed at room temperature.

A schematic view of the cell structure is reported in Figure 178 together with a photo taken inside the beamline during the experiment.

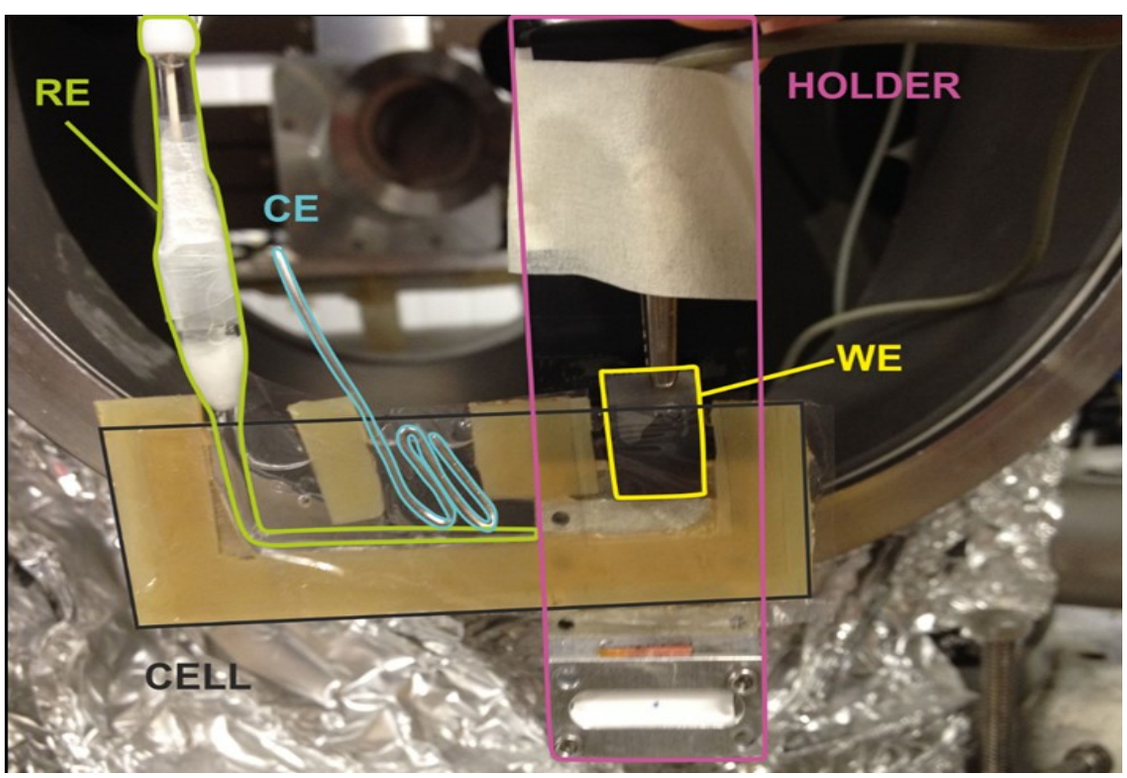

Figure 178. *Schematic view of the cell used for the X-rays Absorption Spectroscopy characterization experiments and a photo taken just before a XAS experiment starts.*

2.7.5 XAS Measurements

XAS measurements were performed in the fluorescence mode at the LISA (Linea Italiana Spettroscopia Atomica) beamline 08, ESRF (European Synchrotron Radiation Facility) at the Fe K-edge (7112 eV). A Si(311) double crystal monochromator was used; the harmonic rejection was realized by Pd mirrors with a cut-off energy of 20 keV, and a High Purity Germanium fluorescence detector array (13 elements) was used. The energy calibration was performed by measuring the absorption spectrum of metallic iron foil at the Fe K-edge (Fe-K: 7112 eV). The energy stability of the monochromator was checked by measuring the absorption spectrum of a Fe foil several times during the experiment. All data were obtained at room temperature. Spectra of standard samples Fe_2O_3, Fe_3O_4 and FeO, were acquired in the transmission mode while the spectra of $Fe(OH)_2$ was digitalized from literature[413]. For these measurements, a proper amount of sample (enough to give a unit jump in the absorption coefficient) was mixed to cellulose and pressed to pellet. The signal extraction was performed by means of the ATHENA code. The EXAFS (Extended X-ray Absorption Fine Structure) data analysis was performed by using the Excurve code, using a k2 weighing scheme and full multiple scattering calculations.

The goodness of fit (GOF) is given by the F-factor parameter:

$$F = 100 \sum_{i}^{N} \frac{\left[\chi_{i,exp} - \chi_{i,calc}\right]^2}{\sigma_i}$$

For the X-ray Absorption Near Edge Structure (XANES) analysis, the raw spectra where first background subtracted using a straight line, and the normalized to unit absorption at 800 eV above the edge energy, where the EXAFS oscillations are not visible anymore. XANES calculations were performed by means of EXCURVE software; the theoretical signals were generated through a Full Multiple Scattering (FMS) approach. For the fitting of the pre-edge peaks the background was simulated through a second-grade polynomial function, and then subtracted to the experimental signal. The resulting curve was modelled by Gaussian functions.

In the recently introduced technique of FEXRAV, X-ray energy is kept constant at a value at which the difference between the absorption coefficient of the selected atom at different oxidation states is at its maximum. While the energy is constant, the applied potential is swept in the range of interest. FEXRAV experiments were carried out in dark to avoid any possible influence of light on this semiconductor material. The electrode potential was swept in the range given in figures captions, with a scan rate of 0.5 or 1 mV s^{-1}.

2.7.5.1 Samples Characterization

Preliminary characterizations of so obtained materials were performed in Na_2SO_4 0.2 M (pH 11 with 0,1M NaOH) by means of slow cyclic voltammetry (5mVs^{-1}) from 0.9 to 0.1V vs RHE show a pristine reduction shoulder for the gamma phase with respect to alpha one as reported in literature[404]. The use of pH 11 electrolyte ensures to mimic the operation conditions found at the industrial plants of chlorate production under hydrogen evolution.

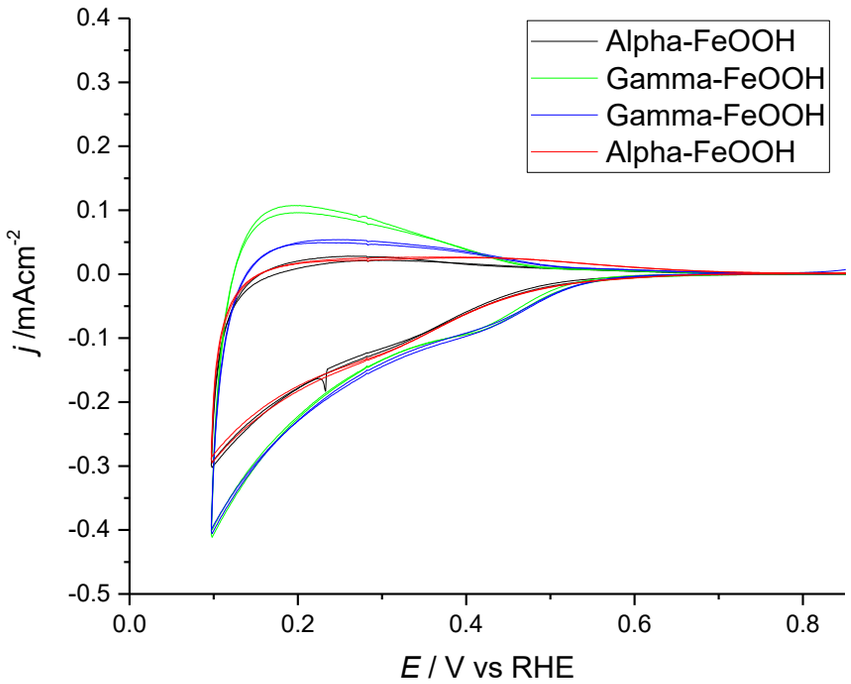

Figure 179. *Comparison of cyclic Voltammetries between two alpha-FeOOH electrodes (black and red) and two gamma-FeOOH (green and blue) in Na_2SO_4 0.2M + NaOH, pH 11. Scan rate 5mVs^{-1}.*

As preliminary information, we performed complete spectra of materials on different supporting materials in order to select the most reliable one in terms of deposit homogeneity, structure, and stability. EXAFS (Extended X-rays Absorption Fine Structure) spectra of α-FeOOH on FTO, γ-FeOOH on FTO, α-FeOOH on Ti and α-FeOOH powder on carbon screen printed electrode (DS) were recorded. The selected amount of material was 0.11 C (0.1mgcm^{-2}) for electrodes on FTO, 0.2C (2 working faces) on Ti substrates and 0.1mgcm^{-2} for the powders. Tokuyama membrane was added (1.2µl of 0.003% w/w) for powder electrodes. The amount of material must be in this range to avoid detector overflow and at the same time have enough resolution.

XANES measurements performed on the different substrates also showed a reliability on the spectra of the differently prepared electrodes. In particular, the spectra for the powder and for electrodeposited material were the same as well as no differences were recorded between Ti and FTO.

Basing on this comparison all further measurements were performed on FTO substrates that show better homogeneity of the layer, poor hydrogen evolution properties and quite high conductivity. Titanium foil electrodeposited electrodes were indeed discharged because of their inhomogeneity and an HER activity higher than the one of FeOOH (as showed by previous experiments) that leads to FeOOH detachment under hydrogen evolution conditions. Screen printed electrodes were abandoned because of their high resistivity and to avoid any interference from the ionic membrane.

Figure 180 shows the complete similarity of the spectra obtained for alpha-FeOOH deposited on Ti, a substrate well known in literature for this material, and on FTO: this proves the goodness of the synthesis performed on such different type of electrodes. Moreover, no differences were recorded between a dried electrode and an electrode inside in Na_2SO_4 0.2 M (pH 11 with 0,1M NaOH) electrolyte at the Open Circuit Potential (OCP). This ensure no contributes on the spectra due to the presence of the electrolyte. Meanwhile a small difference between the two phases was found in the XANES spectra recorded in in Na_2SO_4 0.2 M (pH 11 with 0,1M NaOH) showing the excellent sensibility of this techniques (black and light blue lines).

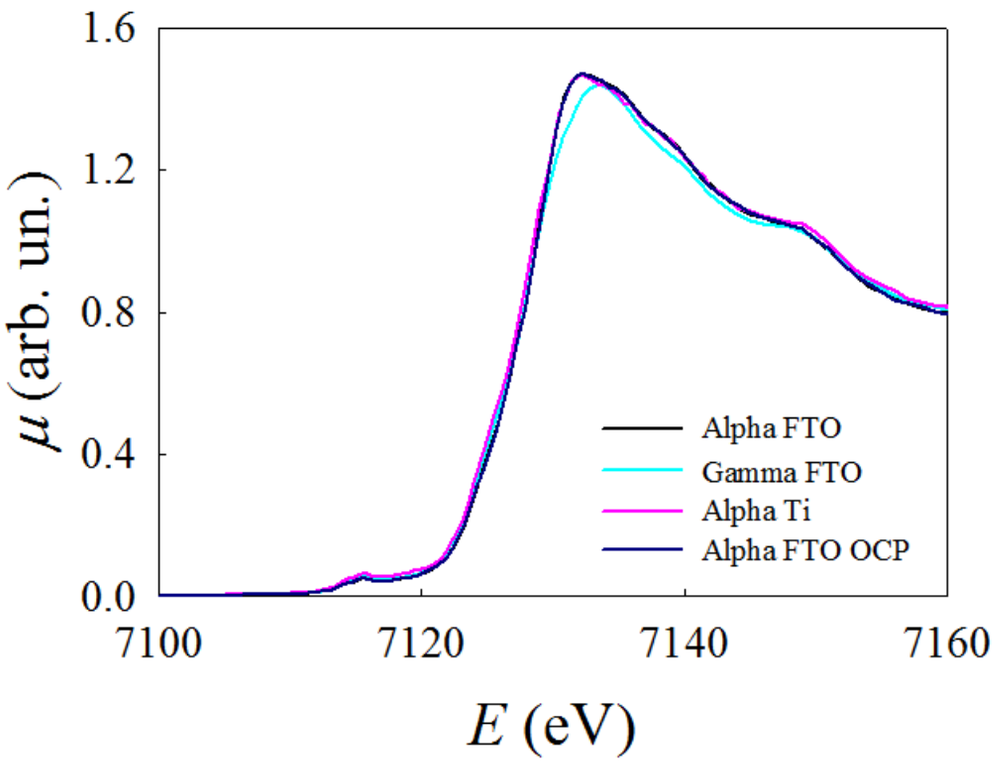

***Figure 180**. Ex-situ XANES of alpha and gamma FeOOH on different substrates, and in-situ XANES of alpha FeOOH on FTO in Na_2SO_4 0.2M + NaOH pH11 (red lines) during OCP measurements.*

Electrodes of α- FeOOH (goethite) and γ-FeOOH (lepidocrocite) were studied through *in-situ* and *operando* XAS spectroscopy at the Fe-K edge, in order to get information on their behaviour and on the species formed under various applied potentials. As a preliminary test, the XANES spectra of the two phases were acquired to confirm the oxidation states and highlight any differences between alpha and gamma phases. As expected, the two phases show some differences in the XANES region; as seen in Figure 181, the alpha phase gives rise to a more intense and broad White Line. However, the most effective way to distinguish the two phases is through the comparison of their FTs but this aspect will be considered later.

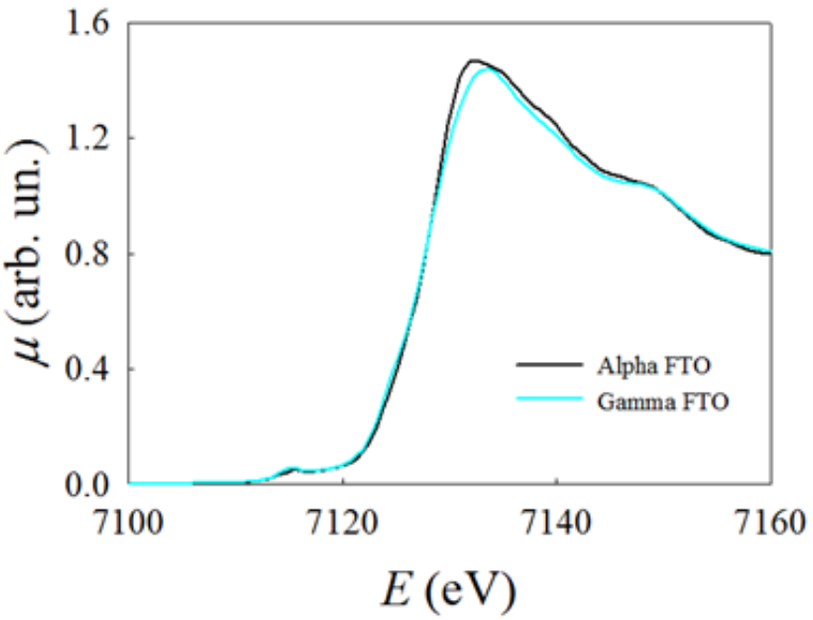

***Figure 181**. Comparison of the XANES spectra of alpha and gamma-FeOOH on FTO.*

2.7.6 FEXRAV Analysis

FEXRAV (Fixed-Energy X-ray Absorption Voltammetry)[100] was performed on both the electrodes; this technique consists on recording the absorption coefficient (μ) while sweeping the applied potential, at a properly selected energy as to give the maximum contrast of the absorption coefficient between two oxidation states. In this case, the recording of μ was combined with a cyclic voltammetry; the potential was scanned from 0.9 to -0.8 V vs. RHE and then back to 0.9 V (two cycles). The chosen energy was 7125 eV, so an increase in the absorption coefficient accounts for the reduction from Fe(III) to Fe(II) (Figure 182).

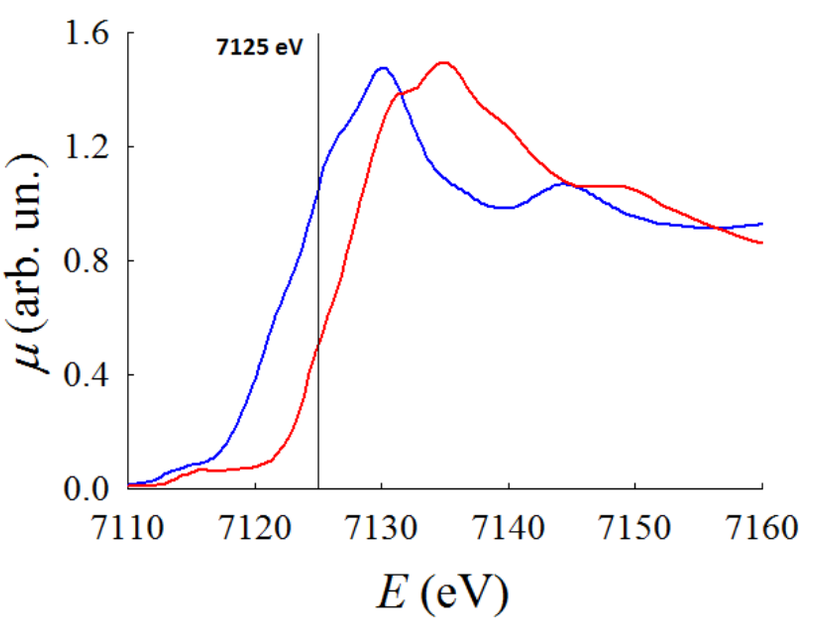

***Figure 182.** Reference spectra of FeO (blue line) and Fe_2O_3 (red line). The vertical line is set at 7125 eV, where the absorption coefficients of FeO and Fe_2O_3 show a high contrast.*

When the electrode is in the cell, preliminary linear sweep voltammetry in Na_2SO_4 0.2M+ NaOH 0.1M (pH 11) of α-FeOOH on FTO was performed. Two cathodic peaks were identified at different potential: +0.3 and -0.55V vs RHE. The potential of -0.7 V was considered for studying the material under strong HER condition.

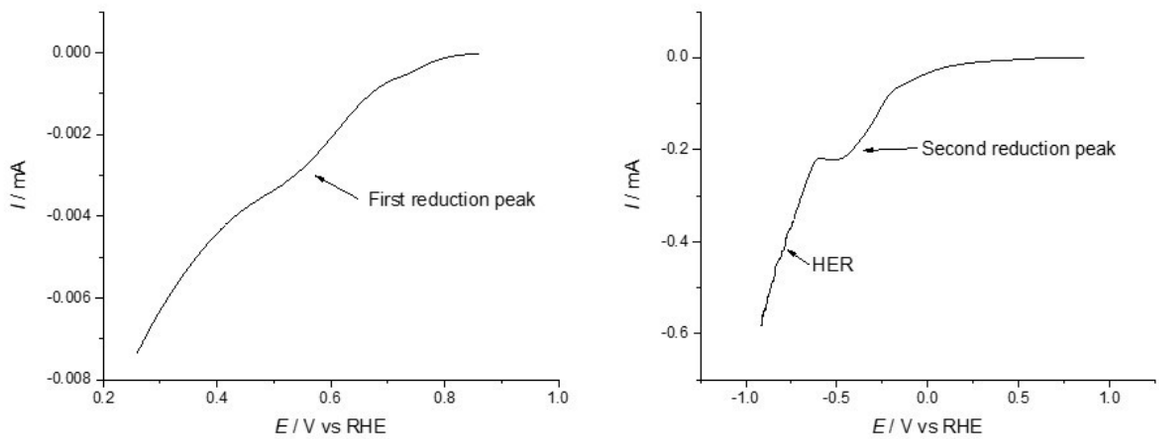

***Figure 183**. LSV at 1mVs^{-1} on alpha-FeOOH in Na_2SO_4 0.2M+ NaOH 0.1M (pH 11). Specific attention was devoted to the evaluation of reduction peaks in the potential window of interest.*

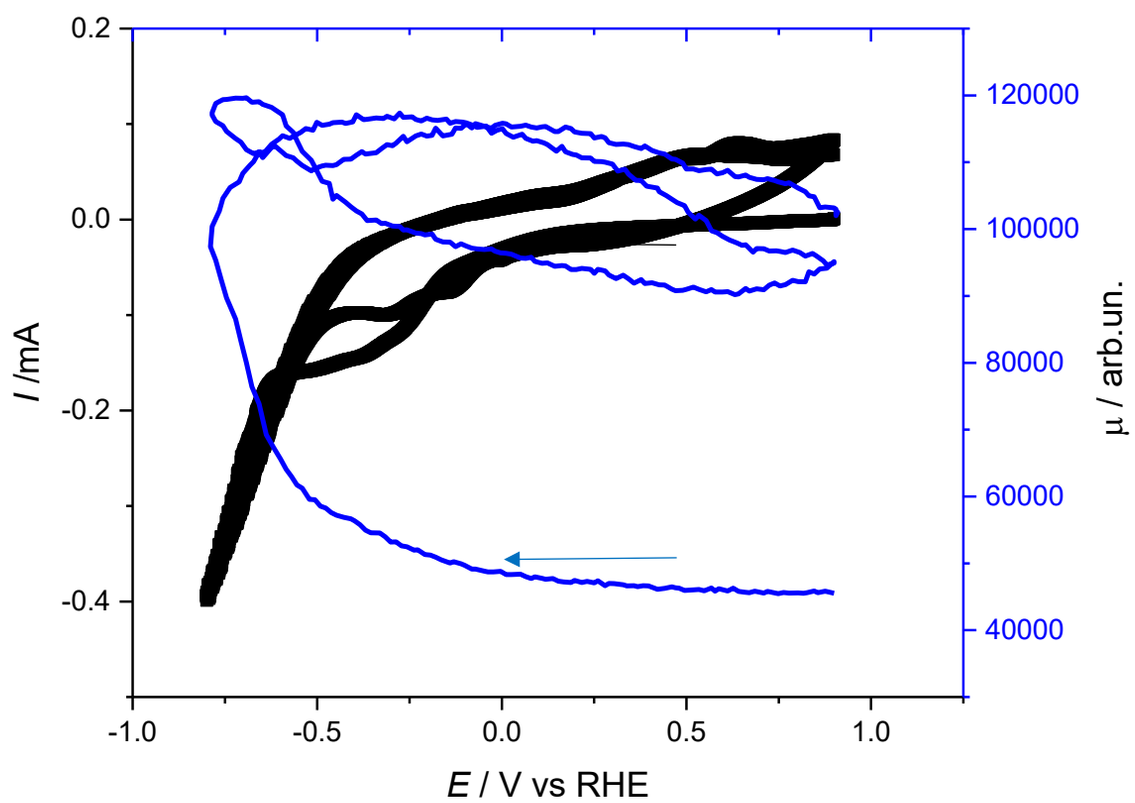

***Figure 184.** FEXRAV experiment on α- FeOOH (blue line) during a cyclic voltammetry (black line). The potential was scanned from 0.9 V to -0.8 V vs RHE with a rate of 1mVs^{-1}, and the absorption coefficient was recorded at 7125 eV.*

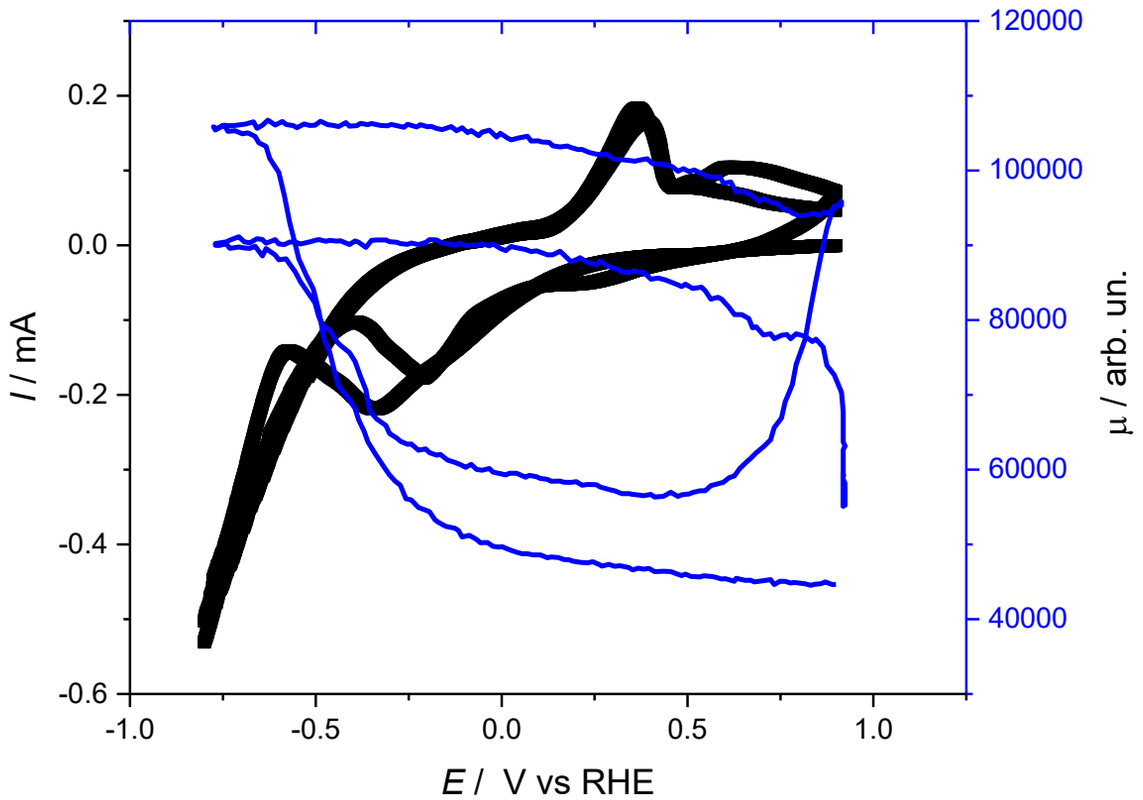

***Figure 185**. FEXRAV experiment on γ- FeOOH (blue line) during a cyclic voltammetry (black line). The potential was scanned from 0.9 V to -0.8 V vs RHE with a rate of 1mVs^{-1}, and the absorption coefficient was recorded at 7125 eV.*

During the first half-cycle, the two FEXRAV signals are similar and they show an increase in the absorption coefficient, thus indicating a reduction from Fe(III) to Fe(II). From the second half of the cycle the trend of the FEXRAV signal becomes markedly different depending on the type of the electrode. In the curve corresponding to the goethite (Figure 184) there is only a slight decrease of the absorption coefficient, thus demonstrating that at the end of the cycles the electrode is substantially not re-oxidized. The reversibility of α- FeOOH is therefore scarce, at least in the scale of times considered in this experiment. Moreover, in the potential window studied is present just a small oxidation peak at 0.7V that is probably not enough to revert the reaction.

Vice versa, in the curve corresponding to the lepidocrocite (Figure 185) the initial increase of μ is almost fully compensate by a decrease at the beginning of the second cycle; γ-FeOOH shows therefore almost a total reversibility, and the fraction of iron which is reduced is essentially completely re-oxidized after the second cycle. In particular, a second oxidation peak is clearly evident during the CV for this phase. This could be related to a different transition specie between Fe(II) and Fe(III) that can be easily re-oxidized to the initial FeOOH. Eventually, it was found that the final product of the electrochemical re-oxidation is 100% lepidocrocite. As expected, the gamma phase is slightly more prone to the reduction with respect to the alpha one[407]. Despite this, the final potential for the subsequent analysis was chosen in a way that ensure the total reduction of both the FeOOH phases.

Note that there is no bubble gas evolution in the cell and any disturbance of the optical path by bubbles can be ruled out. Another sign that the variation is not to be related to a loss of material is the same intensity of HER current recorded for both the cycles.

Afterwards, we recorded in *operando* spectra of α- FeOOH (pink line in Figure 186) and γ-FeOOH (red line in Figure 187) at different potentials according to the peaks revealed by the cyclic voltammetry. To identify the species present at each potential of interest, we performed a series of potentiostatic measurements at the peak-selected potentials. The potential was kept constant for all the measurements and the acquisition of the XANES spectra was started only when the current reached a stable value. The initial polarization time was at least 15 minutes to ensure a complete transformation of the starting material.

2.7.7 Alpha-FeOOH Electrode

The first potential studied was the one related the first cathodic shoulder, 0.3V. Here the XAS signal was not so different from the initial one meaning that no electron transfer, (change in oxidation states) was recorded. This small current could be related to the removal of majority carrier inside the valence band as it is well known for other semiconducting materials like TiO_2. This result is in good agreement with the absence of any variation in the absorption coefficient (μ) during the FEXRAV until -0.1V.

The second potential studied was -0.55V vs RHE. Here much higher currents were recorded and indeed a Faradic reaction occurs. A large shift in spectra position to lower energies and a change of shape was recorded. The potential of -0.7V was tested too to identify any possible variation of oxidation states hidden by the hydrogen evolution signal. The two resulting spectra, identified by the green and dark green curves, are nearly identical; this indicates that under HER condition the electrode is not further reduced.

The XANES experiment carried out at 0.7V just after having kept the electrode at -0.7V vs RHE indeed showed an oxidation state between 2 and 3. This oxide with an intermediate oxidation state between Fe(II) and Fe(III) seems to be the most probable material that can occurs at that potential. Despite this it seems that in the studied range of potential no successive oxidation to FeOOH occurs and that the material lies in this oxidation state even if biased at very cathodic potential during the second cycle of the CV.

The spectra recorded starting from the α-FeOOH and γ-FeOOH electrodes at different potentials are shown in Figure 186a and Figure 187, respectively.

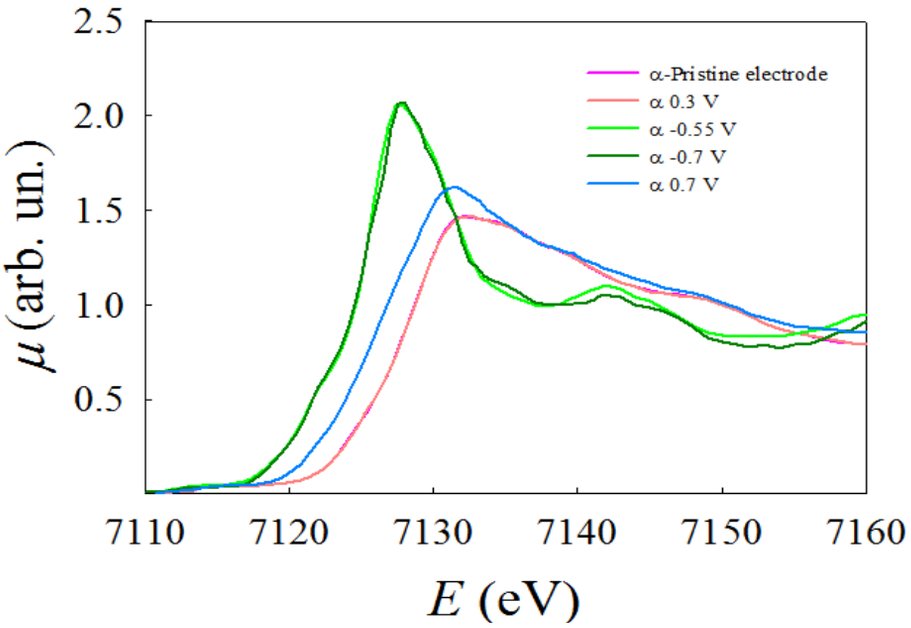

Figure 186. *XANES spectra at different applied potentials for α-FeOOH (goethite)*

2.7.8 Gamma-FeOOH Electrode

The same procedure was followed for the gamma electrodes as well. The study of each peak was performed with potentiostatic measurements at the following potentials: -0.4 V (second reduction peak), -0.65 (HER), 0.41 (first oxidation peak), 0.76 (second oxidation peak) and 0.32 V (first reduction peak). The values of the reduction peaks are close to the one of the alpha electrode, and the main differences between the electrochemical behaviour of goethite and lepidocrocite is the presence of a second oxidation peak in the latter material that lead to a complete reversibility of the material in the selected potential window as showed by the FEXRAV measurements.

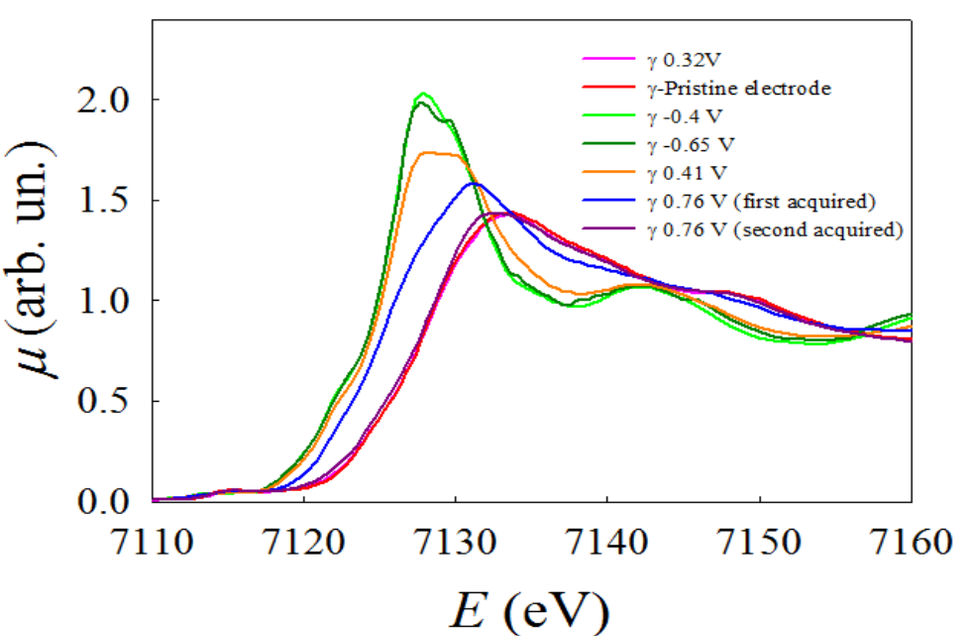

Figure 187*. XANES spectra at different applied potentials for γ-FeOOH (lepidocrocite)*

As stated for the goethite, the first reduction peak is not involved with any electron transfer reaction, while is starting from the peak at -0.4V that a reduction on the material is recorded. Also on this material no change between the spectra obtained at -0.4 and -0.65V (where hydrogen evolution is fast) occurs (Figure 187). From the two materials' CV we can note that gamma FeOOH acts as expected with a pristine reduction. It seems to have high catalytic activity for HER and a larger reversibility as showed by the bigger oxidation peak during FEXRAV measurement.

Moreover, after reduction, the spectra of alpha and gamma electrodes show impressive similarity, pointing towards the fact that the structure of the reduced material is the same independently on the starting phase. For the sake of simplicity, therefore, the four spectra will be considered as being the same, representative of the reduced phase.

The spectrum of the reduced phase is shifted towards lower energies with respect to the spectrum of FeOOH, and it lies in the range of energies typical of Fe(II). The considerable intensity of the White Line and the edge position excludes the presence of metallic iron. The spectrum was compared to various spectra available in literature; its profile is similar to that of $Fe(OH)_2$ [414] and green rust[415], but in our case the intensity of the White Line is far higher. A possible explanation of this anomalous intensity is the presence of Fe(II) in a high spin state; in fact, it is known in literature that the magnitude of the White Line increases after a Fe(II) low spin → high spin transition. When this transition occurs the distance between the iron and the atoms in the first coordination shell increases, leading to a lower overlap between the *4s* and *4p* orbitals of iron. As a result, the number of accessible empty *4p* states increases along with the intensity of the White Line, which is due to the *1s-4p* transition[416,417].

Precise information about the valence, the coordination geometry and the spin state of iron can be obtained by the so-called pre-edge peaks. These peaks result from the formally dipole forbidden *1s-3d* transition and their positions, their intensity and shape are sensitive to the structural and electronic properties of iron.

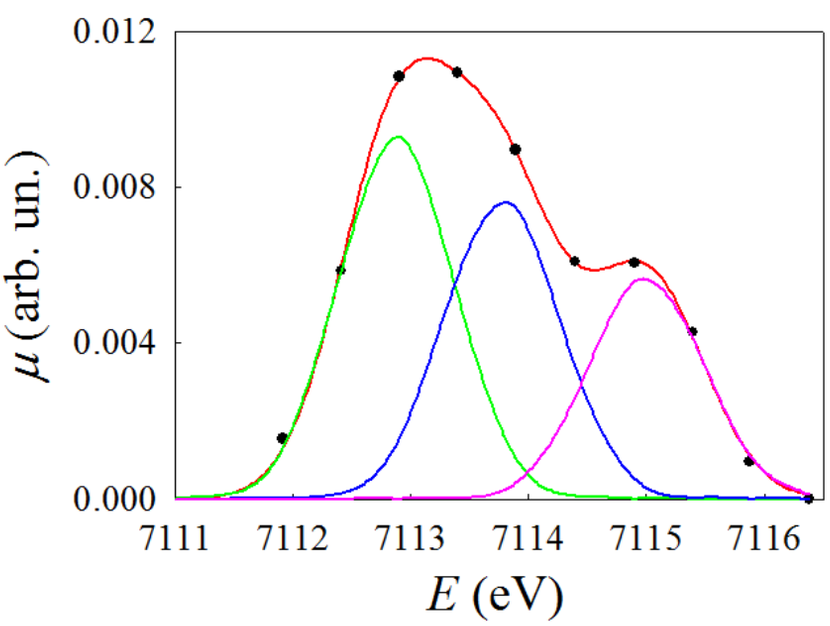

***Figure 188**. Fe-K edge pre-peak for γ- FeOOH at -0.4 V: the black dots represent the experimental signal, while the red curve is the fit. The green, blue and pink curves are the Gaussian functions used for the fitting.*

The region of the pre-edge peaks was isolated and the background, simulated with a quadratic polynomial, was subtracted to the experimental signal. This procedure was repeated for the four spectra, and in all cases the peak has the profile shown in Figure 188.

The shape shows a characteristic splitting which is consistent with the presence of high spin iron (II) in an octahedral environment [418]. According to Tanabe and Sugano[419] the electronic configuration of octahedrally coordinated Fe(II) in a high spin configuration is expected to give three multiplets. Therefore, three Gaussian functions were used to fit the signal, obtaining a good agreement with the experimental. The values of the intensity (calculated as total integrated area) and of the centroid (intensity-weighted mean of the energy positions) are listed in Table 1 for the four spectra.

Spectrum	Centroid	Intensity
α-FeOOH at -0.55 V	7113.34 eV	0.0310
α-FeOOH at -0.7 V	7113.34 eV	0.0258
γ-FeOOH at -0.4 V	7113.71 eV	0.0274
γ-FeOOH at -0.65 V	7113.75 eV	0.0338

***Table 34**. Values of centroids and intensities for the four extracted pre-edge peaks*

According to Winkle et. Al. [420], the centroid is located at 7113.7 eV in minerals where the iron oxidation state is (II). This value coincides with that of reduced γ- FeOOH, while the values resulting from the reduced α- FeOOH are shifted of 0.4 eV towards lower energy. The cause of this shift has not yet been identified; at any rate, it can be safely stated that in all cases the iron is substantially present as Fe(II). The low intensity of the pre-edge peak is consistent with the non-distorted octahedral coordination, where an inversion centre is present. In this case 3d-4p mixing is strictly forbidden and the 1s-3d transition has therefore a very weak intensity.

The centroid energy position, the low intensity, and the peculiar profile of the pre-edge peak are therefore in accordance with the presence of high spin iron (II) in an almost undistorted octahedral coordination. This is also in agreement with the shape and the intensity of the White Line.

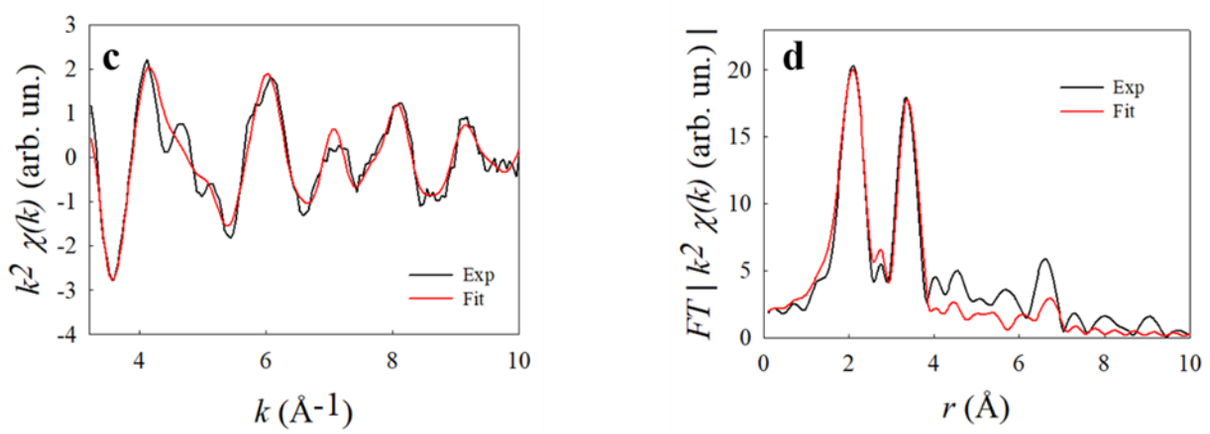

***Figure 189**. Fe K-edge EXAFS signal (a) and the corresponding Fourier Transform (B) of the spectrum of the reduced phase. The black line represents the experimental curve, while the red line is the fitting with the reduced-green rust model.*

Shell	N	Atom	R(Å) XANES	R(Å) EXAFS	σ^2 (Å^2) XANES	σ^2 (Å^2) EXAFS	R (Å) crys.
1	6	O	2.20(3)*	2.15(1)*	0.010(7)	0.008(1)	2.031
2	6	Fe	3.189	3.28(1)*	0.010(7)	0.007(1)	3.189
3	6	O	3.747	3.747	0.010(7)	0.06(7)	3.747
4	12	O	4.894ì	4.894	0.010(7)	0.03(2)	4.894
5	6	Fe	5.524	5.524	0.010(7)	0.02(3)	5.524
6	6	Fe	Not fitted	6.379	Not fitted	0.004(3)	6.379
7	12	O	Not fitted	6.703	Not fitted	0.004(3)	6.703

Table 35. *Parameters obtained after EXAFS and XANES refinement. Only the values marked with * were fitted.*

A combined fit of the XANES and the EXAFS region was performed in the attempt of identifying the structure of the reduced phase. While the EXAFS region gives specific information about the local distances, the XANES calculation is more sensible to the structural details, and it can help discriminating between very similar structures. Initially, the model used for the simulation was $Fe(OH)_2$, since it satisfies all the conditions imposed by the pre-edge peak analysis; however, the goodness of fit of the EXAFS and especially of the XANES region was unsatisfactory (Figure 190).

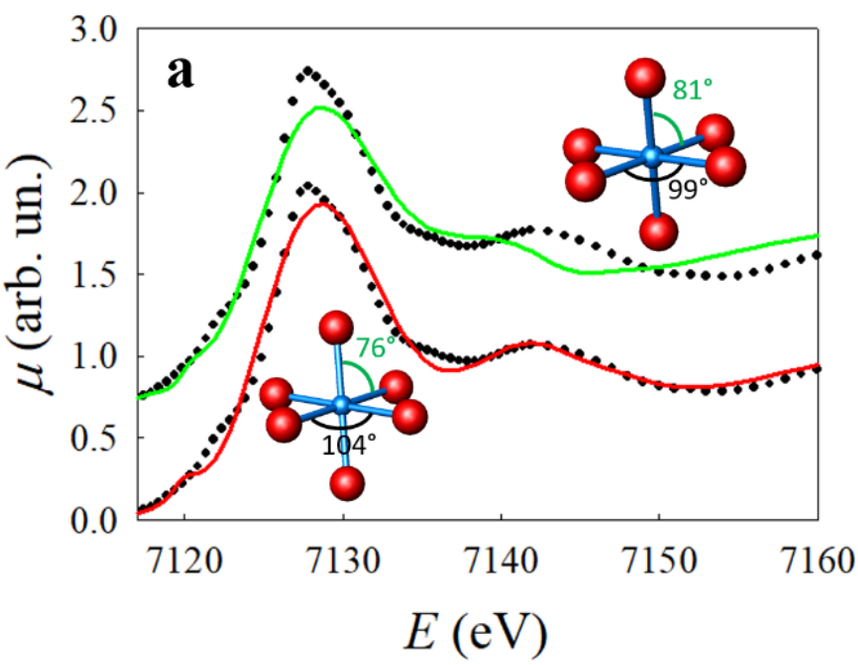

Figure 190. *Fe-K edge XANES simulation of γ-FeOOH. The black dots represent the experimental signal, while the coloured lines are the simulation with a) reduced green rust b) $Fe(OH)_2$.*

The focus was therefore shifted on the green rust, which is made by brucite-like layers with alternatively Fe(II) and Fe(III), and sulphate anions to compensate the positive charges. Since in our case the oxidation state of iron is (II), the structure used for the fit represents a reduced green rust, where both Fe(III) and the sulphate anions are not present. Both the XANES and the EXAFS region are well fitted by this model, and their goodness of fit F respectively 0.55% and 8.97%; the parameters obtained after refinement are resumed in Table 35.

The distance between Fe and the first shell of oxygens is higher with respect to the crystallographic one: this is consistent with the presence of high spin iron (II). The surprising fact is that the model used for the fit is very similar to $Fe(OH)_2$, since the connectivity of the atoms is exactly the same, and the distances are not so different in the two cases. What strongly affects the goodness of fit are the different angles formed by the oxygen and the iron atoms in the two structures. The angle formed by two equatorial oxygens is 104.5° in the reduced green rust and 99° in $Fe(OH)_2$, while the angle formed by an axial and an equatorial oxygen is respectively 75.5° and 81°. The reduced green rust structure shows a higher discrepancy from the standard value of 90° and XANES, being determined by three and four body correlation functions is very sensitive to changes in the bond angles. This explain the large differences seen in the two fits of Figure 190.

It should be noted that *in-situ* Mossbauer analysis on lepidocrocite showed that after the reduction the resulting signal was not fully coincident with that expected for $Fe(OH)_2$ [176]. In addition, the results are in agreement with Monnier et al.[178] showing an Fe(II) specie preferential formation with higher pH and the complete absence of magnetite signal.

After the reduction α- FeOOH and γ-FeOOH were electrochemically re-oxidized to test their behaviour and their reversibility. The cyclic voltammetry of γ-FeOOH shows two oxidation peaks, one at 0.41 V and one at 0.76 V vs RHE; the corresponding spectra are shown by the orange and the blue line in Figure 186b (two spectra were acquired subsequently at 0.76 V, and for now we consider the first one). The spectrum at 0.41 V has a White Line with a peculiar split shape, and it can be efficiently simulated with a linear combination fit (Figure 191) of the spectra at -0.4 V (55%) and 0.76 V (45%). The edge energy position is very close to that typical of Fe(II): therefore, only a small quantity of Fe(III) is formed.

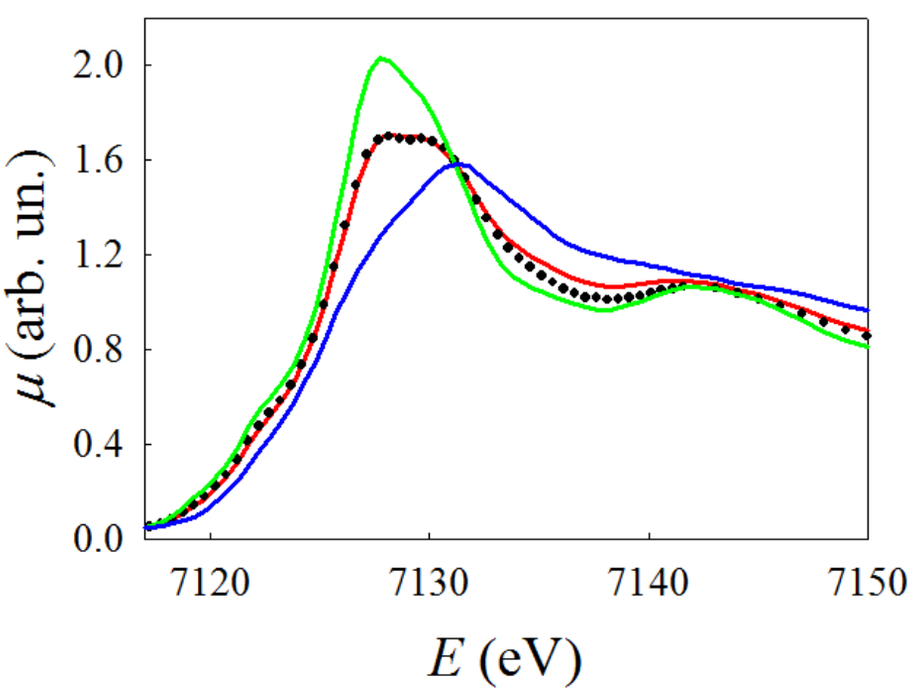

***Figure 191**. Linear combination fit of the spectrum at 0.41 V. The black dots represent the experimental curve, while the red line is the fit obtained with 55% of the spectrum at -0.4 V (green line) and the spectrum at 0.76 V (blue line).*

The spectrum acquired at 0.76 V, shown by the blue line in Figure 186b, is the result of the re-oxidation of γ-FeOOH electrode, while the one acquired at 0.7 V (shown by the light blue line in Figure 186a) is the result of the re-oxidation of α- FeOOH electrode.

Since the product of reduction is the same independently of the starting phase, the process of re-oxidation is expected to proceed in a similar way in the two cases. However, the two spectra at 0.7 V and at 0.76 V show a neat difference which is apparent in the EXAFS spectra as well; Figure 192 compares the corresponding Fourier transform with those of pristine γ-FeOOH and α-FeOOH.

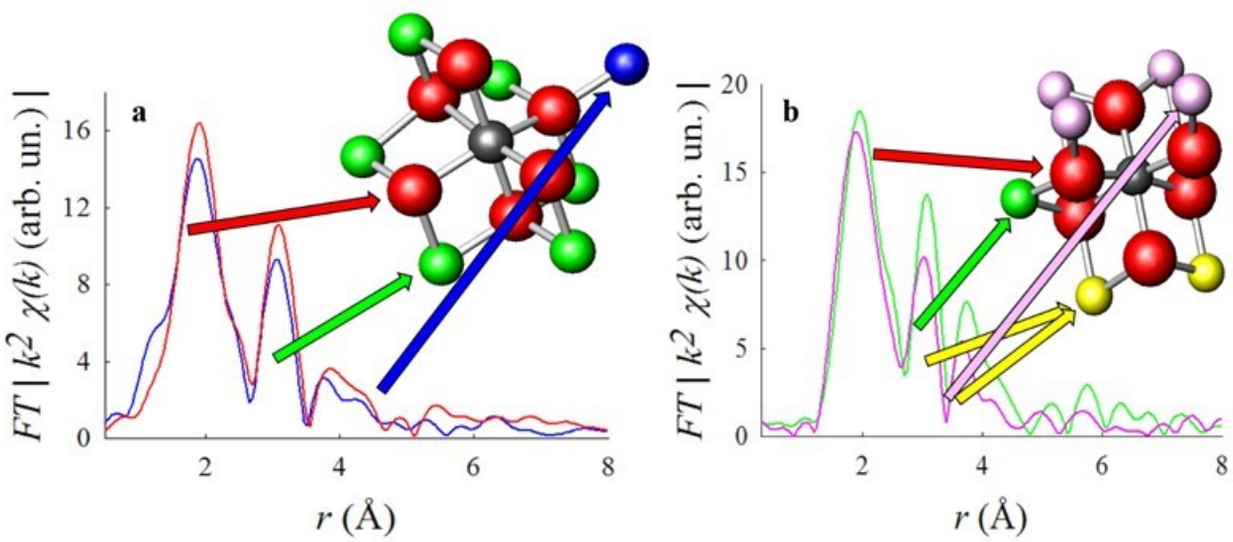

Figure 192*. Fourier transforms calculated from the corresponding EXAFS signals. a) Comparison between the FT of pristine α- FeOOH (green line) and α- FeOOH at 0.7 V (pink line) b) comparison between the FT of pristine γ-FeOOH (red line) and γ-FeOOH at 0.76 V (blue line). Clusters of goethite (a) and of lepidocrocite(b) are shown to help identifying the atoms which contribute to the peaks: the central iron is grey, oxygens are red, and all the others are iron atoms at various distances from the central one.*

Goethite and lepidocrocite show some structural differences that influence their radial distribution function. Three main peaks can be identified in the region up to 5 Å; the atoms that contribute to every peak are schematized in Figure 192, where the atom identified as “central iron” is coloured in black. The intensity of the third peak represents the main difference between the two FTs, and it can be used as a fingerprint to distinguish the two phases. Lepidocrocite has a layered structure, so all the iron atoms belonging to other layers with respect to the central iron are too distant to give a significant signal. The third peak is therefore due to only two iron atoms (blue in Figure 192b), which lie in the same plane of the central iron at a distance of 3.87 Å; as a result, this peak in γ-FeOOH is very weak.

In goethite, the third peak has two contributions: one from two iron atoms (yellow in Figure 192a) that lie in the same layer as the central atom (these atoms contribute partially also to the second peak), and one from four iron atoms that serve as a connection between two consecutive layers (pink in Figure 192a). As a result, the third peak is much more intense in goethite than in lepidocrocite. The edge position of the spectra acquired at 0.7 V (α- FeOOH) and 0.76 V (γ-FeOOH) shows that the valence state of iron is intermediate between (II) and (III); however, their FT signals, shown in Figure 192 a and b, are similar to those of FeOOH, thus indicating that the structure is substantially coincident with that of the oxidized electrode.

In particular, the Fourier transform of the spectrum recorded at 0.7 V shows the intensity of the third peak typical of the alpha phase. On the contrary, the Fourier transform of the spectrum acquired at 0.76 V presents a weak intensity of the third peak, perfectly comparable to that of γ-FeOOH. As a result, it can be stated that even if the reduced phase is the same independently of the nature of the starting electrode, a different behaviour arises during the electrochemically driven re-oxidation; the electrode presents therefore a "memory effect", since it is able to preserve a memory of the initial crystal structure.

This hypothesis is also confirmed by a second acquisition in time of the spectrum at 0.76 V; (violet curve in Figure 186b). The profile and the position in energy are very different from the previous acquisition, thus indicating that the process of oxidation is slow. The spectrum is almost identical to γ-FeOOH, and this confirms the presence of a "memory effect" of the electrode. The slight shift towards lower energies, however, indicates that the oxidation process is not complete. The results for the reoxidation process are also different from those of Monnier et al. who suggest the conversion of the reduced specie to an oxidation degree intermediate between magnetite and maghemite. This is probably due a pH effect and to the fact that the reduced phase in fully composed by iron (II) specie.

2.7.9 Additional Properties

In addition, two other interesting properties of this material were evaluated, the self-conversion of lepidocrocite in goethite in basic conditions and the air oxidation of reduced green rust.

To follow the first reaction, which is well-known in literature[421], the use of FEXRAV was very helpful. Indeed, fixing the energy at the point of maximum difference between the pristine α and γ-FeOOH electrodes spectra, we followed the transformation of γ-FeOOH in α-FeOOH in basic conditions (1M NaOH) without any applied current using the variation of the absorption coefficient. The electrode was deposited on FTO at a potential in which there is the deposition of both the FeOOH phases with a prevalence of γ-FeOOH. The presence of α-FeOOH is necessary to let the reaction starts and increase the kinetics[421]. An increase in the value of the absorption coefficient signal means a transformation of the material to α-FeOOH. The transformation continues in time (Figure 193) but was not observed until the end of the process for time reason. The advantages of FEXRAV is that allows to follow the reaction directly while it occurs in *operando* condition explaining the increase in the OCP value with time.

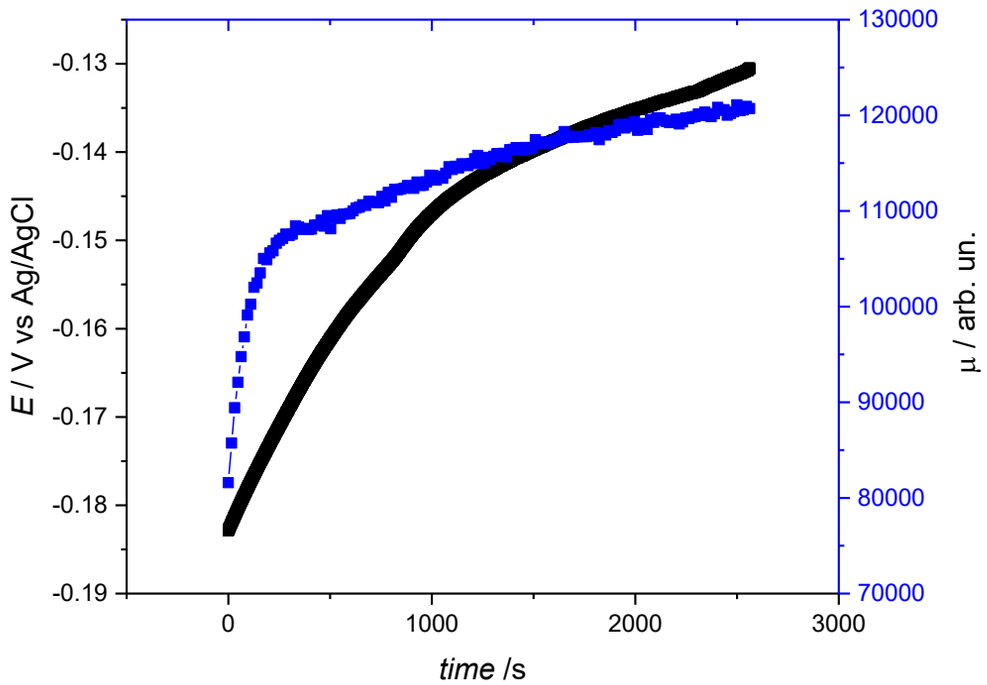

Figure 193. *FEXRAV (in blue) and OCP measurement (in black) during the conversion of lepidocrocite in goethite in basic condition (NaOH 1M). An increase of absorption coefficient is related to the shift from the pristine phase to goethite.*

From previous measurements it was found that goethite (as well as lepidocrocite) shows a memory effect once re-oxidized from green rust under electrochemical conditions. We also want to prove if a similar behaviour occurs for spontaneous re-oxidation of the material in air. It was noticed that the electrode biased at HER potential (-0.7V) in the reduced green rust phase is transparent while at OCP condition the colour of gamma and alpha phases is almost reddish or orange. This electrochromic behaviour is reversible and if the electrode is left in air condition at room temperature after few hours it turned to the initial colour. To investigate the complete reversibility in air of a transparent reduced green rust, the XANES spectra of new and in- air re-oxidized electrode was compared. A goethite sample was biased at -0.7V until complete conversion. The electrode became transparent and was then left in air until reddish colour was observed again. *Ex-situ* XANES spectra were acquired and the result shows the formation of something very similar to the pristine material. Moreover, a linear combination of the spectra of the pristine α and γ-FeOOH electrodes demonstrates the formation of almost 41% of alpha and 59% of gamma (Figure 195). This behaviour is in contrast with the one proposed by Encina et al.[422] who claims the full conversion of $Fe(OH)_2$ in goethite under air flow. It has to benoticed anyway that the starting phase is here indeed different and probably almost equally prone to produce both the phases in the considered conditions.

This shows how in contact with air the reversibility of the reduced green rust to FeOOH can occurs passing probably trought another route that deletes the memory effect. The formation of both goethite and lepidocrocite shows that passing trought this routes, that we hypothize to be δ-FeOOH, the electrode rearrange and is able to produce both phases.

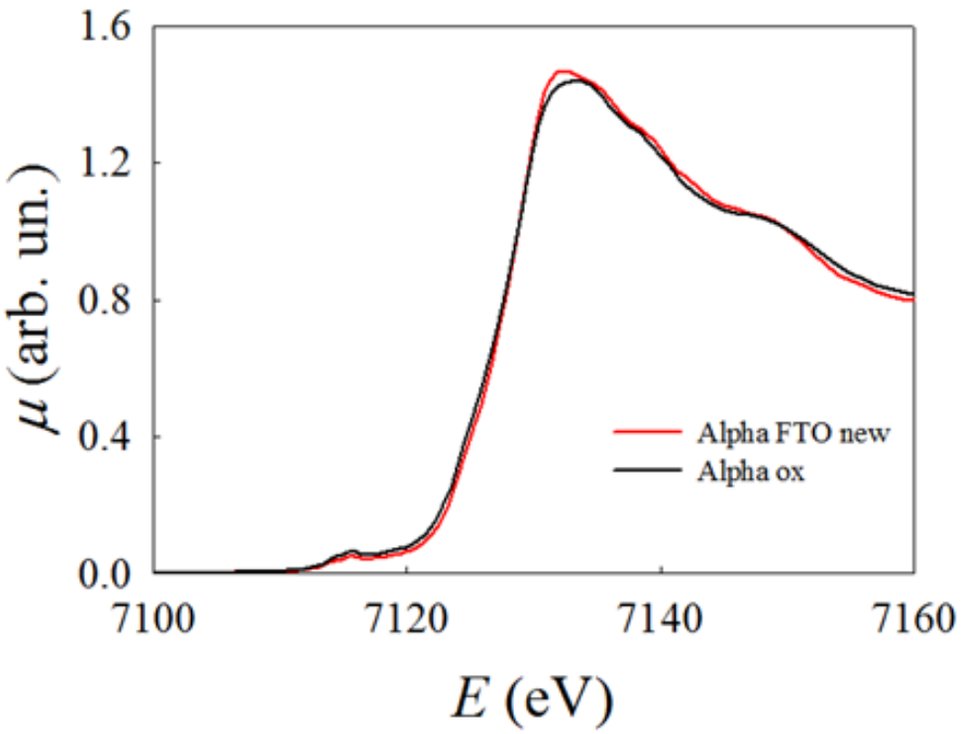

Figure 194. *XANES spectra of a goethite electrode (in red) and the same electrode after being reduced to green rust and then reoxidized in air (in black).*

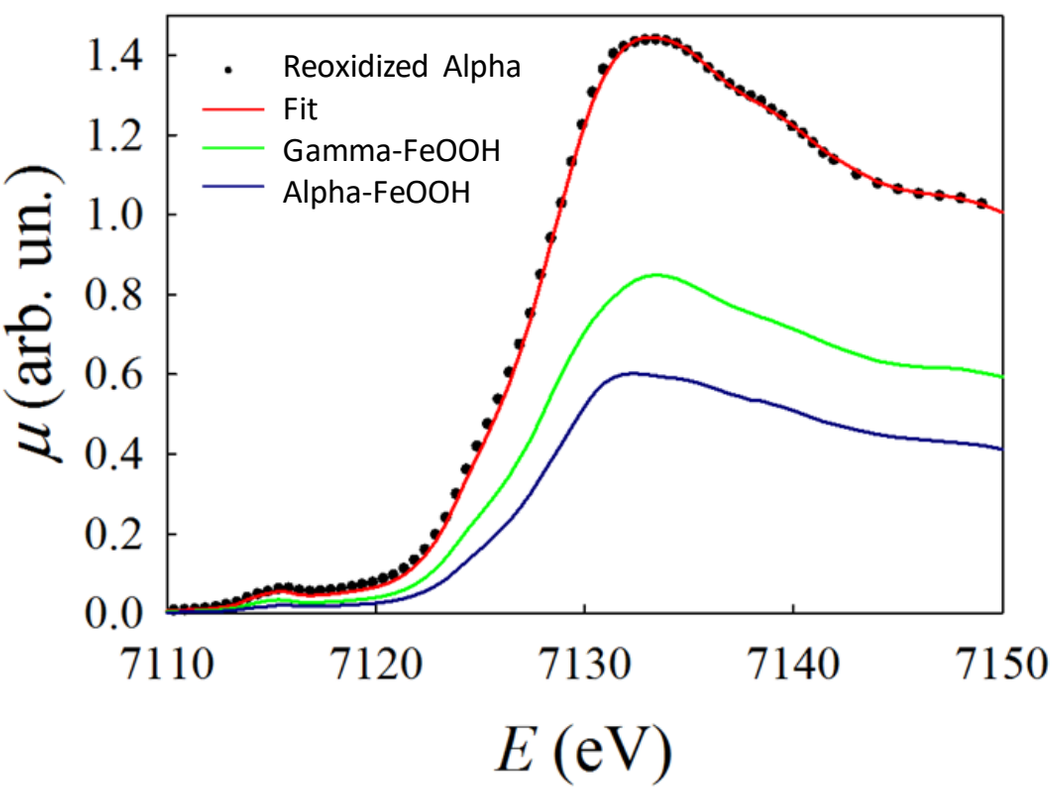

Figure 195. *XANES fit of the species present on the electrode after air oxidation. The fit shows a combination of alpha (41%) and gamma (59%) FeOOH.*

2.7.10 Conclusions

With these experiments, we obtained chemical and structural information about the behaviour of FeOOH under cathodic conditions. Interesting results were obtained on its reversibility for both goethite and lepidocrocite and a first proof of the formation of reduced green rust under HER conditions is given by the mean of XAS. In particular, the different behaviours and stability of the studied phases were achieved. It was found that independently from the starting phase the final reduction product under HER is reduced green rust. An interesting memory effect was recorded for both the phases once electrochemically oxidized, while if the oxidation occurs in air the formation of both the phases is achieved probably because a different route is taken during the slow re-oxidation process. This is probably due to a kinetic effect for the electrochemical reaction that prefer the formation of the initial phase, while once oxidized in air there is enough energy to move towards both the phases. To the best of our knowledge the electrochromic behaviour of FeOOH was firstly showed in this paper with a transition from transparency at cathodic potential (while reduced green rust is present) to a yellow-orange colour at OCP condition.

These results can be of interest in the development of chlorate process cathodes of higher stability and better selectivity for the hydrogen evolution reaction as well on the study of iron corrosion products.

Moreover, it was our interest to evaluate the stability of this compound in the pH and potential window used for Cu_2O electrode to see if it can be used for its protection.

2.7.11 FeOOH@Cu_2O

Previous experiments with XAS, denote that Cu_2O photodegradation product was a thin layer of metallic copper that reduces the photoactivity. This instability is related to the redox potential of the material lying between the valence and the conduction band energies. This implies that the photocurrents recorded in conventional chopped light experiments are composed by the sum of two contributes, water splitting and photodegradation.

To avoid that, it was proposed to cover Cu_2O with a protective layer that should avoid the semiconductor/electrolyte contact maintaining the photo-electrosplitting activity of the material. Here we propose the use of FeOOH as protective layer. FeOOH should work with the redox cascade principle. In this way electrons from the CB of the material instead of reducing the material itself are quickly injected to the FeOOH in contact with the solution where the HER occurs.

Once pure FeOOH behaviour was studied, we tried to use it as protective overlayer for Cu_2O under HER condition. A few nanometres transparent protective overlayer was then electrodeposited onto the surface of previously prepared Cu_2O@Cu@FTO samples. Both the FeOOH phases were electrodeposited from the same deposition bath until the theoretical amount on the Cu_2O electrode was 80nm.

This amount was considered in our opinion a good balance between transparency and the required amount to have a good signal-to-noise ratio with the XAS measurements.

The so prepared electrodes where then tested in the $NaHPO_4$ 0.5M + NaOH 0.5M (pH11) electrolyte under pulsed light condition in deaerated solution. To evaluate the enhanced stability potentiostatic measurements at 0.175 V vs RHE were performed. Preliminary result shows enhanced life time for the FeOOH protected electrodes with respect to unprotected one:

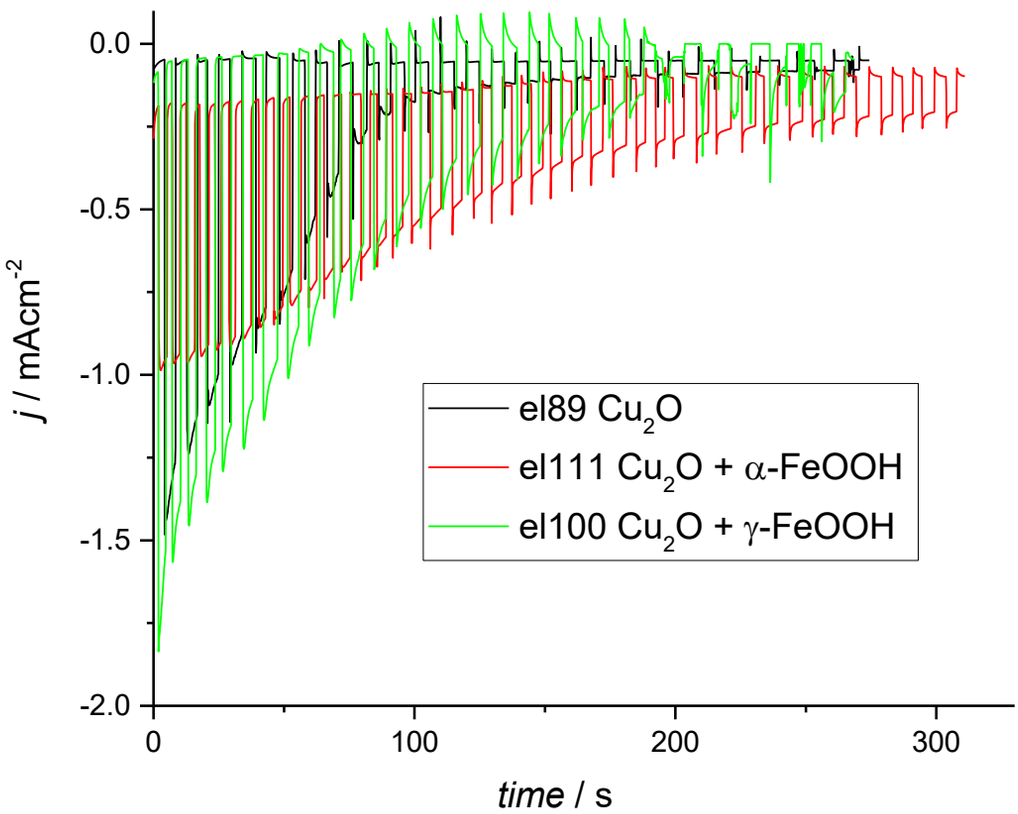

***Figure 196**. Comparison between unprotected (black) and FeOOH protected (with alpha in red and with gamma in green) Cu_2O during potentiostatic measurements at -0.723 V vs SCE.*

The extended life time of the electrodes are still not suitable for an industrial use but some improvements both in the obtained photocurrent and in the electrodes life-times were achieved mainly with the lepidocrocite overlayer.

2.7.12 XAS Study of FeOOH-protected Cu_2O

The stability of all the iron oxyhydroxides under UV light was previously determined[423]. Our first interest was then to evaluate if the material is stable in the working electrolyte under light and applied potential. For XAS measurements the studied electrodes were so composed: FTO + Au (200um by Physical Vapor Deposition - PVD) + Cu_2O (0.5C deposited at -0.4 V vs SCE deposited from a 0.2M $CuSO_4$, 0.5M K_2HPO_4 + 3M lactic acid at pH 12 with 2M KOH) + 0.037C of FeOOH (80nm) deposited at the potential previously seen.

The use of the gold underlayer was necessary to have a better resolution on the possible formation of metallic copper from Cu_2O. The electrodes were first studied at the Fe-K edge, then at the Cu-K edge to observe any change occurring under 400nm high intensity LED light illumination of either the protective layer and/or of copper oxide respectively.

2.7.12.1 Fe-K Edge

Considering the Fe K-edge, the electrodes were first tested with FEXRAV to see if in the considered potential window the protective layer is subdued to electrochemical reduction or photocorrosion. As we can see from the following plots, where alpha and gamma FeOOH on Cu_2O are compared, the material is stable in the dark (Figure 197) and under light (Figure 198). Gamma-FeOOH probably have a small reduction under light at the end of the cycle.

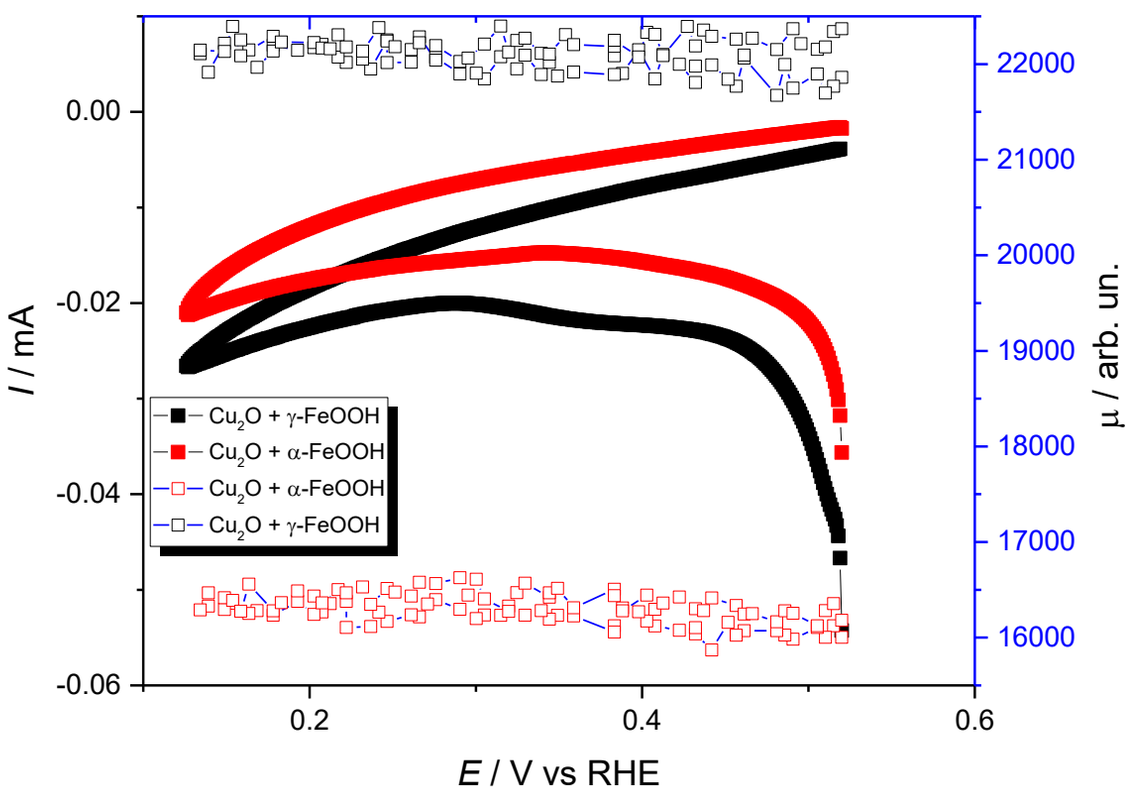

Figure 197. *FEXRAV measurements of alpha (red) and gamma (black) FeOOH at the Fe-K edge during CV in Na_2SO_4 0.2M+ NaOH 0.1M (pH 11). Scan rate 1mVs^{-1} in dark.*

The electrode is composed by different layers (Au, Cu_2O and FeOOH) and with electrochemistry only, we don't know if the recorded cathodic currents under light are related to the reduction of water, of Cu_2O or the reduction of FeOOH to reduced species.

Working at the Fe K-edge allows us to be able to see the oxidation states changes only on the iron. Indeed, the other atoms excitation energies are far from the iron one and we can be pretty sure that any variation in the absorption coefficient μ is related to Fe oxidation changes. In particular an increase in the absorption coefficient will be related to a material reduction. With these measurements, we wanted to confirm one of the requirement for a protective overlayer, its stability. Indeed, the stability of the FeOOH on the junction is confirmed under applied potential and light because just small reductions are recorded.

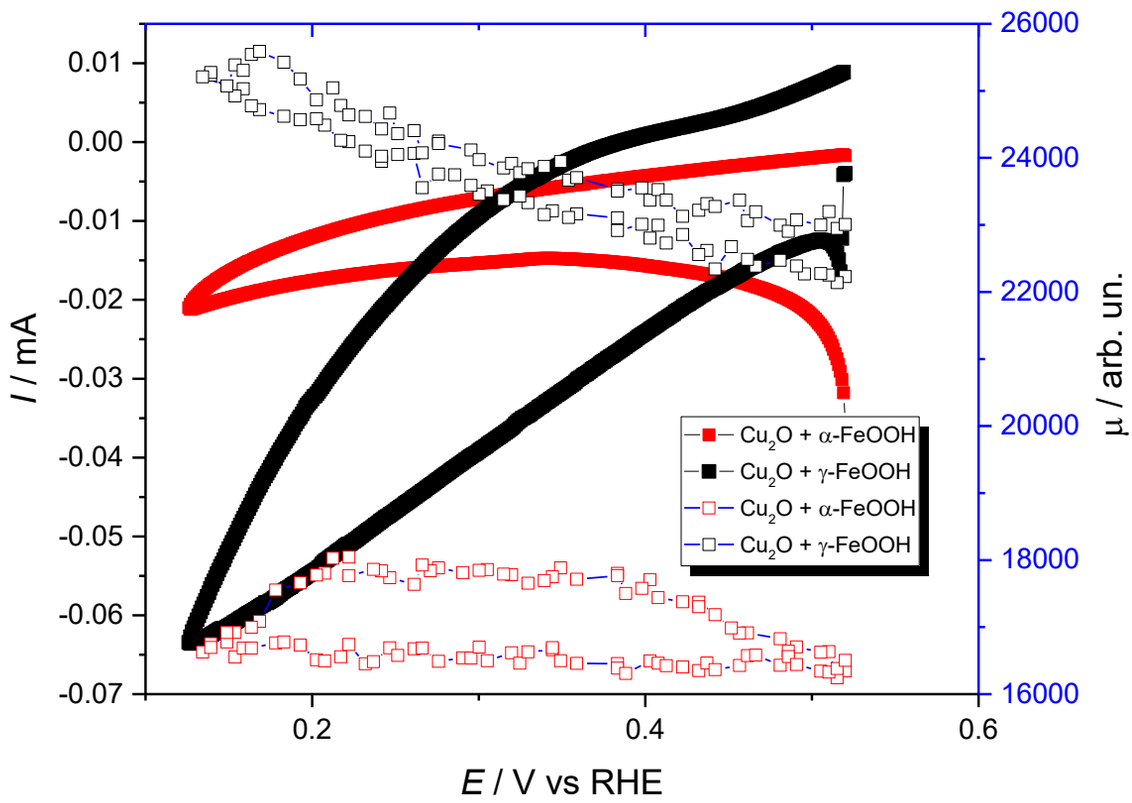

Figure 198. *FEXRAV measurements of alpha (red) and gamma (black) FeOOH at the Fe-K edge during CV in Na_2SO_4 0.2M+ NaOH 0.1M (pH 11). Scan rate 1mVs^{-1} in light.*

Unfortunately seems that the light-activity of the Cu_2O disappear when it coupled with the alpha-FeOOH (red line) because no sensible difference is recorded between dark and light spectra. This is probably related to an electrochemical coupling of Cu_2O and FeOOH were the excited electrons of Cu_2O move to FeOOH promoting some reduction of the layer recorded by the FEXRAV in light. The gamma one is instead able to generate the photocurrent whit just a small reduction on the FeOOH layer. In dark, no reduction of the material was recorded at these potentials (just a small 2%) as seen on the material studied alone. Similar electrodes were studied using difference spectra measurements (XAS spectra in the light minus the one in the dark) to see if there are reversible differences under light and dark.

2.7.12.2 Cu-K Edge

Moving to the Cu-K edge, we were able to follow the variation of the oxidation state of the copper (I) oxide under working conditions in presence of the FeOOH protective overlayer. Initially, a complete spectrum of the Cu_2O electrode covered with α-FeOOH was recorded and no differences with the pure Cu_2O were recorded meaning that structure and lattice distances of this semiconductor are not affected by the presence of the overlayer.

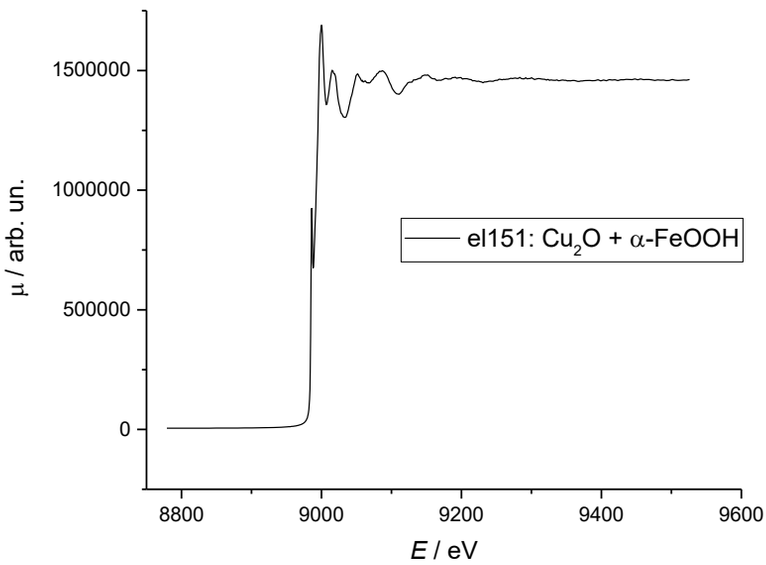

Figure 199. *XANES spectra of Cu_2O covered with 80nm of a-FeOOH. Cu-K edge.*

On the same electrode, we performed a constant energy experiment (8979.0 eV) while alternating dark and light. At this energy, as previously seen, an increase in the absorption coefficient is proof of the Cu_2O reduction to metallic copper. The applied potential was 0.56V, a "stable condition" for the electrode.

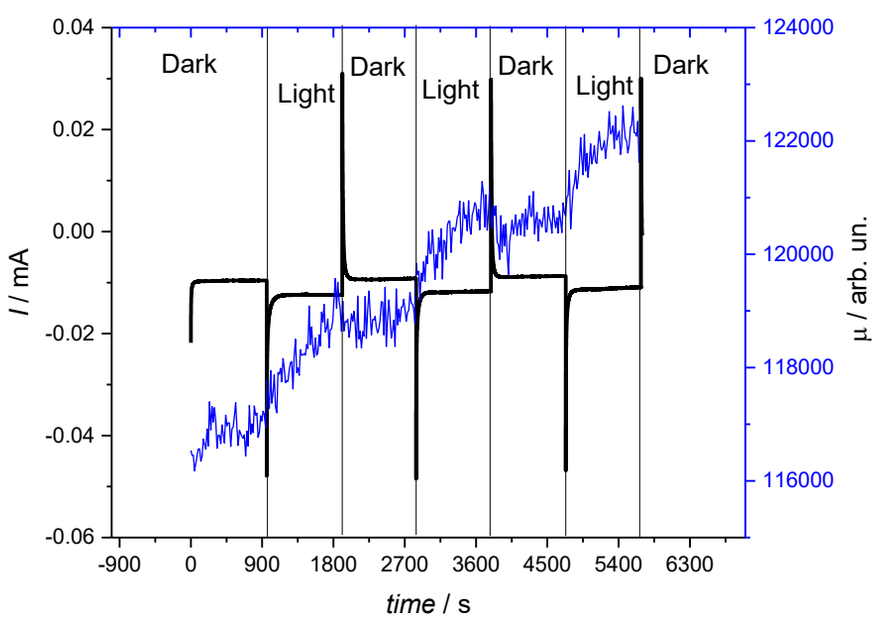

Figure 200. *Constant energy XAS performed at 0.56V under pulsed light. Under light a reduction is recorded as pointed by the increase of absorption coefficient. Both the current (black line) and the absorption coefficient (blue line) are shown.*

A reduction, or at least a difference between light and dark structure, was recorded for steps of 900s. Meanwhile, small photocurrent was recorded at the working electrode under light step. We can consider this a preliminary information of the undesired reaction occurring even on a protected electrode.

FEXRAV was then performed (first cycle in dark and second under light) of alpha-FeOOH protected electrode and unprotected Cu_2O. All experimental conditions were the same.

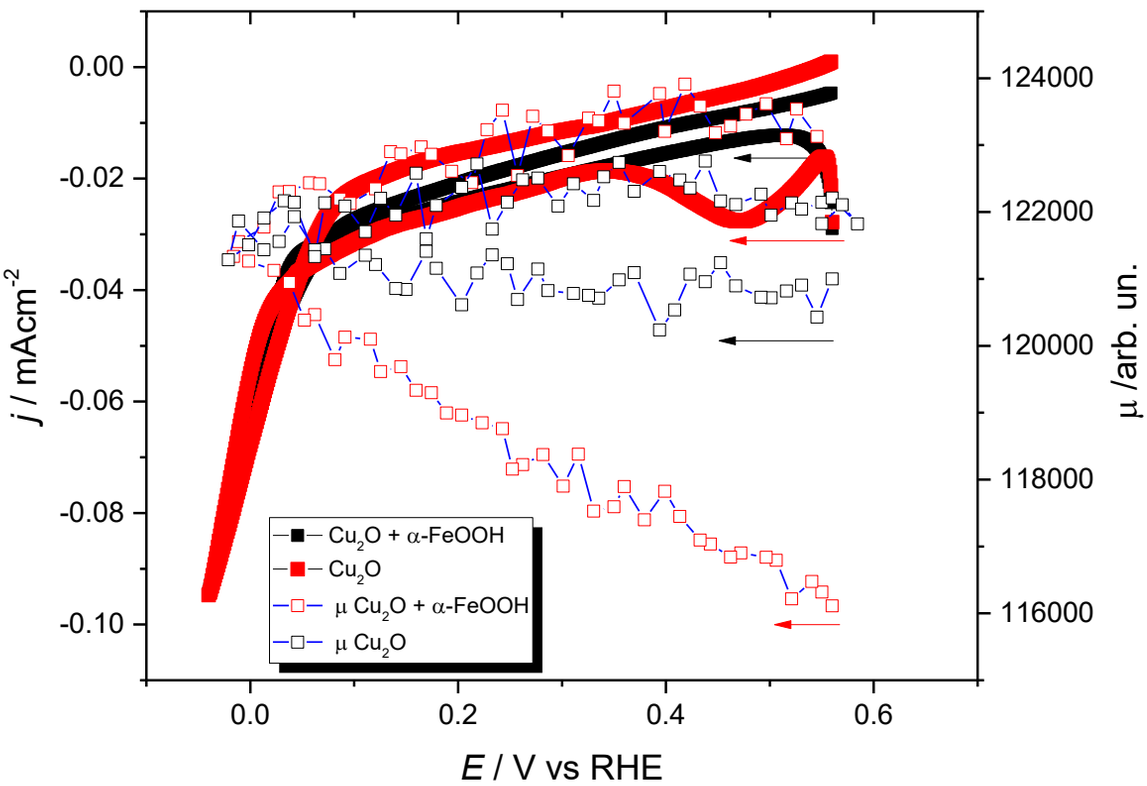

Figure 201. *FEXRAV spectra and CV of alpha-FeOOH protected (black) Cu_2O and unprotected one (red) in dark Measurements performed at 8979 eV.*

In these conditions, from the absorption coefficient trend, we can see that in dark (Figure 201) the protected electrode is safe from reduction to metallic copper also at the more negative potentials while the unprotected is subdued to photodegradation process just from 0.56 V vs RHE. Indeed, the percentage of reduced Cu_2O in dark is 1% on the protected electrode and 5% on the unprotected one. Same result was not achieved in Figure 202 where the same electrode under light is subdued to a strong reduction comparable to those in absence of a protective layer. Both the electrodes at the end of the cycle have indeed a 12% of the initial Cu_2O transformed in Cu. A possible explanation for this behaviour is an incomplete coverage of the surface due to the small amount of material used or because the layer was not homogeneous enough. It was not possible indeed to verify if the overlayer deposit all over the Cu_2O surface or only in some specific areas.

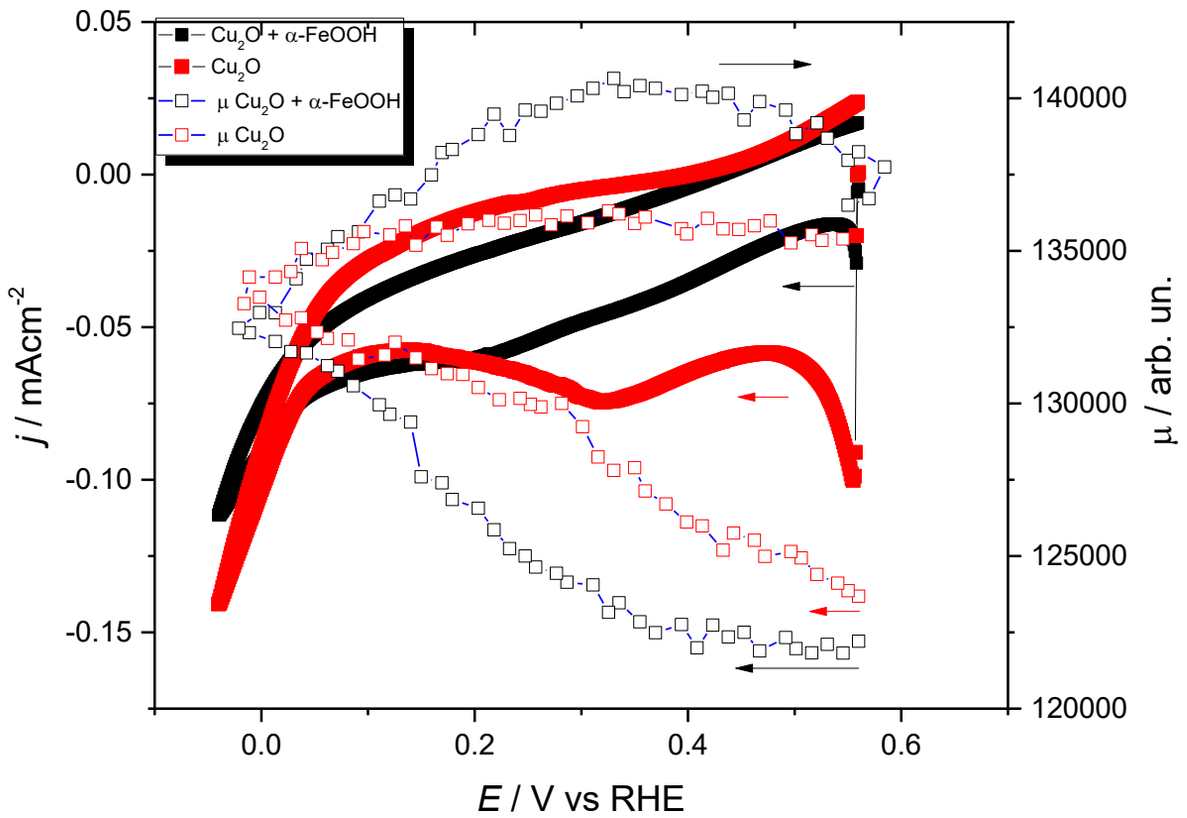

Figure 202. *FEXRAV spectra and CV of alpha-FeOOH protected (black) Cu_2O and unprotected one (red) in light. Measurements performed at 8979 eV.*

2.7.12.3 Difference Spectra

Difference spectra were also recorded. In these experiments, the system collects 2 points for each energy value. During the two data acquisitions, the position of the monochromator is unvaried, this exclude any instrumental contribution to the final result. The first point is recorded in the dark, the second in light with a quiet time in the middle to let the system stabilize. Thanks to this expedient it is possible to calculate the difference of the two recorded spectra and observe any reversible change induced by the light in the material. These measurements were performed on Cu_2O + α-FeOOH at the Cu-K edge close to the OCP value. The difference spectrum (light-dark) shows a remarkable positive peak at ca. 1.5 eV below the pre-edge peak of the Cu_2O edge. This sharp transition is a signature of linearly coordinated Cu(I) and it is due to the *1s*→*4pπ**dipole allowed transitions.

The Cu *4p* states make a significant contribution to the bottom of the valence band. The top of the valence band is essentially made up by Cu $3dz^2$ states. If we recall here that the band gap value is 2.2 eV, and that in the band structure of Cu_2O the partial covalence of the CuO bond mixes Cu $3dz^2$ and O *2p* states, then the positive peak in the Δμ spectrum can be attributed to an increase of the density of holes with $3dz^2$ symmetry at the top of the valence band.

The following plots show the difference recorded on the Cu_2O + α-FeOOH electrode.

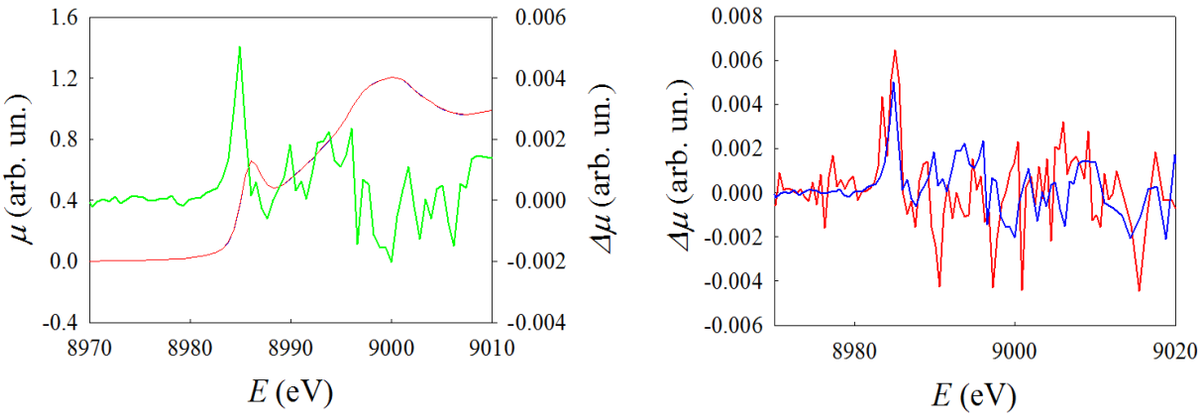

Figure 203. *A) Difference spectra between light and dark measurements performed on Cu_2O at -0.3V vs SCE. The green line is the difference between the two spectra. B) Comparison in difference spectra between FTO/Au/Cu_2O/α-FeOOH (red line) and FTO/Au/Cu_2O (blue line).*

The difference recorded is comparable with the one recorded in a previous experiment on the unprotected Cu_2O meaning that the excitation that occurs under light is to be assigned to the same transition even in the presence of the protective layer.

2.7.13 Cu_XO Core-shell System

In this section, a different approach was studied. According to the literature the main role of a protective layer is to quickly remove electrons from the CB in order to avoid the degradation of the material. Thus, is not necessary that the protective layer stays between the solution and the light-active semiconductor. HER occurs on Cu_2O together with the material reduction. The only electrons to be removed are those who undergoes to the material reduction. In this view, the protective layer can be placed inside the electrode between Cu_2O and the substrate. Here the protective layer act as electrons scavenger for those electrons which will undergoes to the photodegradation reaction while the external Cu_2O still can produce hydrogen from water reduction.

2.7.13.1 Material

Cu_XO photoelectrodes have been prepared as follow. Briefly, 100 µl of the suspension of freshly prepared nanocrystalline CuI in ethanol (3 $mg \cdot mL^{-1}$, 100 µL) were drop-casted on a FTO (Sigma Aldrich, surface resistivity ~7 Ω/sq) glass plate, previously washed with H_2SO_4, water and ethanol under ultrasounds. Subsequently, the electrodes were dried at room temperature and then annealed at 400 °C in air. The so-prepared material is similar to the one tested in the SECM section with good results in hydrogen evolution photoconversion. In this preliminary phase, the material is mainly done by CuO, while is only after some time of applied potential and light that the true active species (Cu_2O) is formed as shown in the FEXRAV section. In the end the material will be composed by a core-shell system where CuO is the electrons scavenger core and Cu_2O is the light activated shell.

2.7.13.2 FEXRAV

FEXRAV on a Cu_xO electrode was performed in dark (Figure 204A) or under illumination (Figure 204B and C) by fixing the energy at 8981 eV, that is the pre-edge peak energy for Cu_2O.

In this case, an increase in μ indicates that the material is reduced to Cu_2O (no metallic Cu was observed by XPS, see CuI paper).

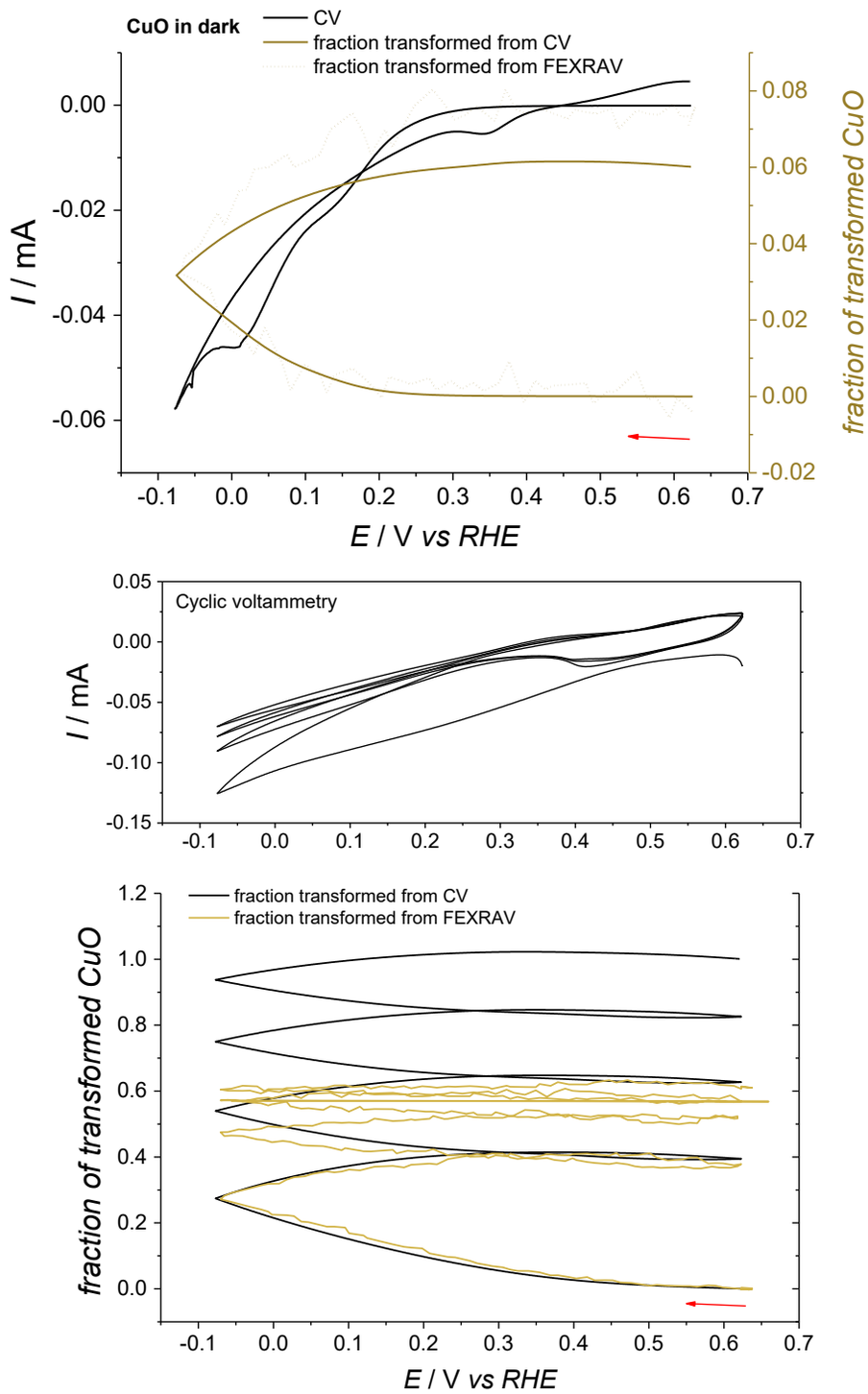

***Figure 204**. Fraction of reduced CuO and current intensity as a function of the applied potential during a FEXRAV experiment of a Cu_xO electrode at 8981 eV in the dark (A) and under LED 400 nm illumination (B). 0.1 M K_2HPO_4 + KH_2PO_4, pH = 7, was used as an electrolyte. Starting points are indicated by arrows.*

Quite interestingly, no activity towards H_2 evolution is observed in the dark: here the two traces (FEXRAV and quantity of charge) are almost perfectly overlapped. This means that any small change recorded by the electrochemistry is due to a change in the material composition. This change, by the way, is very small if we compare the scale of the axes of dark and light measurements. On the contrary, observing four consecutive cycles recorded under illumination Figure 204B and C, an interesting trend is easily recognizable: while the quantity of charge constantly increases, the FEXRAV signal tends to stabilize up to a constant value of about 60% reduced CuO.

This means that in light, during the first 2 cycles, the material is subdued to a photodegradation that lead to the formation of a reduced specie of copper oxide, mainly Cu_2O. This reduction at a certain point stops and the material starts to produce hydrogen. Indeed, the increasing quantity of charge parallel to an unchanging FEXRAV of the last two cycles means that the photocurrent efficiency for H_2 evolution is close or equal to 100%.

This indicates that a partial reduction of CuO to Cu_2O is at the bases (and thus needed) to obtain an active material towards H_2 production. This means that the active species toward light is not CuO but only the Cu_2O formed under irradiation and applied potential, while the role of CuO is to protect the whole material. The final reduced fraction indicates the formation of a Cu_2O shell (60% at.) that can thus be considered as the optimal final composition of Cu_xO particles for coupling activity and stability. After these considerations, the higher intrinsic stability of Cu_xO with respect of Cu_2O is evident: while the latter is easily reduced to Cu, the second is less prone to be further reduced after reaching a stable composition.

2.7.13.3 XANES

The behavior of Cu_xO is markedly different respect to that of pure Cu_2O. As earlier reported, this material is initially composed only of pure CuO[352], whereas we observed that about 60% of the initial CuO was reduced to Cu_2O after 8h at 0.3 V and under 400 nm illumination. This is likely at the bases of the improved stability observed for Cu_xO with respect to Cu_2O: while the former maintains about 30% of its initial activity after 5h, the latter becomes inactive after a few minutes. Under mere photochemical conditions, i.e. with the electrode immersed in the electrolyte (aqueous 0.1 M K_2HPO_4, pH=9.1) and illuminated for 10 hours using a 400 nm LED at OCP, impressive differences were detected: the Cu_XO XANES spectrum presents a marked shift towards higher energies of the pre-edge peak with respect to the pristine material, as shown in Figure 205.

This is a clear evidence of the formation of some Cu(III) species, as it is made evident by the vertical lines, showing the energies of the first maximum in the absorption coefficient for CuO and $KCuO_2$[424,425]. XANES changes were accompanied by relevant changes of UV-Vis spectrum (Figure 206). Very interestingly, the formation of copper(III) can be blocked by the addition of a sacrificial hole scavenger as methanol (30 % vol.), meaning that the observed modifications in the XAS spectra are indeed caused by photogenerated holes. These findings indicate that photogenerated holes are long living and, with no applied bias, that the oxidation of water to oxygen is not favored with respect to the oxidation of the material itself. It is worth noting that Cu(III) can be strongly stabilized when complexed by suitable ligands (e.g. oxamate or hydroxy-iminoamide or polyanionic chelating ligands)[426,427].

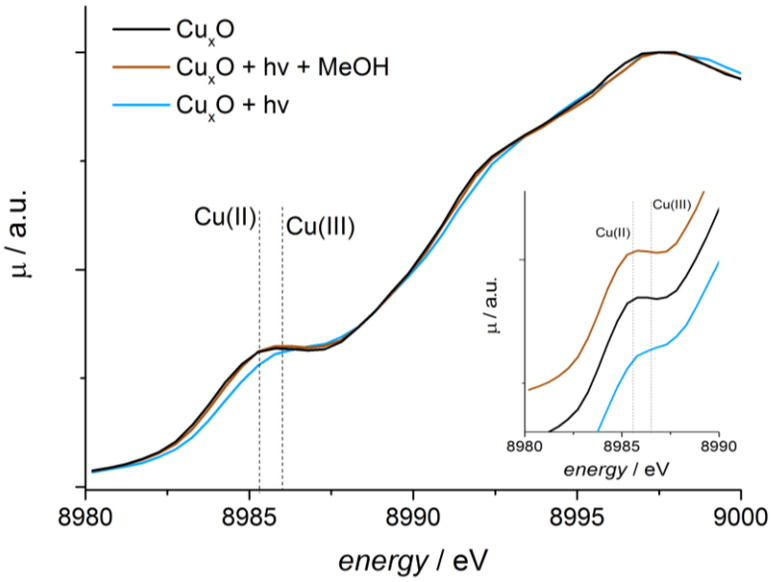

Figure 205. *XANES spectra of Cu_xO photoelectrodes: freshly prepared (black line), electrode irradiated in electrolyte for 10 h (blue line) and irradiated in electrolyte with addition of methanol (brown line). The inset shows the spectra on an enlarged energy scale. For better reference, the energies of the first maximum in the absorption coefficient of CuO and of a Cu(III) compound ($KCuO_2$, as taken from the literature[424,425]) are shown as vertical line.*

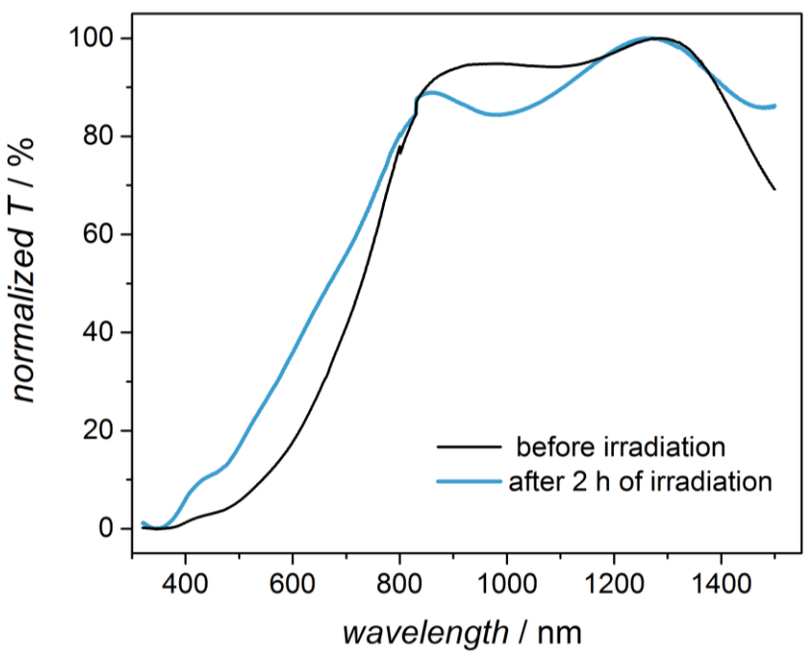

Figure 206. *UV-Vis absorption spectra of freshly prepared Cu_xO at FTO electrode (black line) and electrode irradiated for 2h using LED 400 nm (blue line).*

Moreover, no changes in the XANES with formation of Cu(III) were observed when the sample was irradiated in air. This confirms that the presence of an electrolyte is essential for the observed phenomenon to occur.

After these results, we can safely suggest the formation of Cu(III) centers according to the following reaction:

$$Cu(II)O + h^+ + OH^- \rightarrow Cu(III)O(OH)$$

This behavior recalls what occurs on TiO_2 illuminated in the presence of a hole scavenger, when a self-reduction of Ti centers occurs[428]. A similar experiment carried out on Cu_2O didn't lead to significant photo-induced modifications and the pure material under applied light is totally stable.

2.7.13.4 Difference Spectra

Difference spectra on Cu_xO (that is, in the presence of both CuO and Cu_2O) electrode were recorded while the photoelectrode was polarized at 0.7 V *vs.* RHE. Three spectra were subsequently recorded.

The XANES spectrum of CuO when immersed in the electrolyte (Figure 207) shows a sizeable increase in the spectral weight in this energy region when compared to the spectrum of standard CuO.

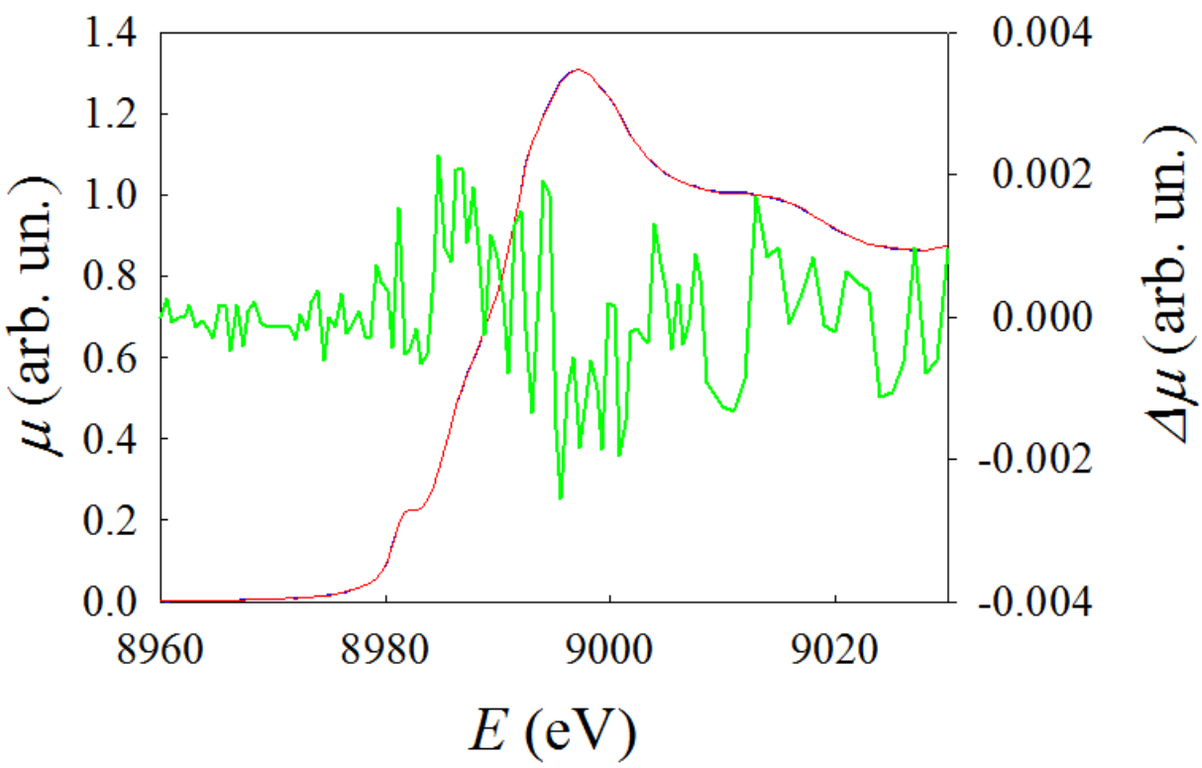

Figure 207. *Difference spectra XANES spectrum of Cu_xO@FTO electrode at 0.7 V in 30% methanol, 0.1 M K_2HPO_4 + KH_2PO_4, pH = 7 in the dark (blue line) and in presence (red line) of 400nm illumination. The difference spectrum (light-dark) is shown by the green line.*

Multiple scattering calculations show that this region of the Cu-K XANES is very sensitive to distortion of the coordination around Cu; in particular, the spectral weight increases when the coordination octahedron in CuO is made less distorted. This effect is similar to that found for $Ni(OH)_2$ at the Ni-K edge[425]. Thus, the distortion of the CuO_6 octahedron in CuO decreases after immersion in the electrolytic solution and is further decreased after illumination. This is likely due to a modification of the material's surface, that enriches in adsorbed –OH when immersed and further on during illumination.

The first spectrum (Figure 208) indicates that the material is almost fully made of CuO (with a small presence of Cu_xO).

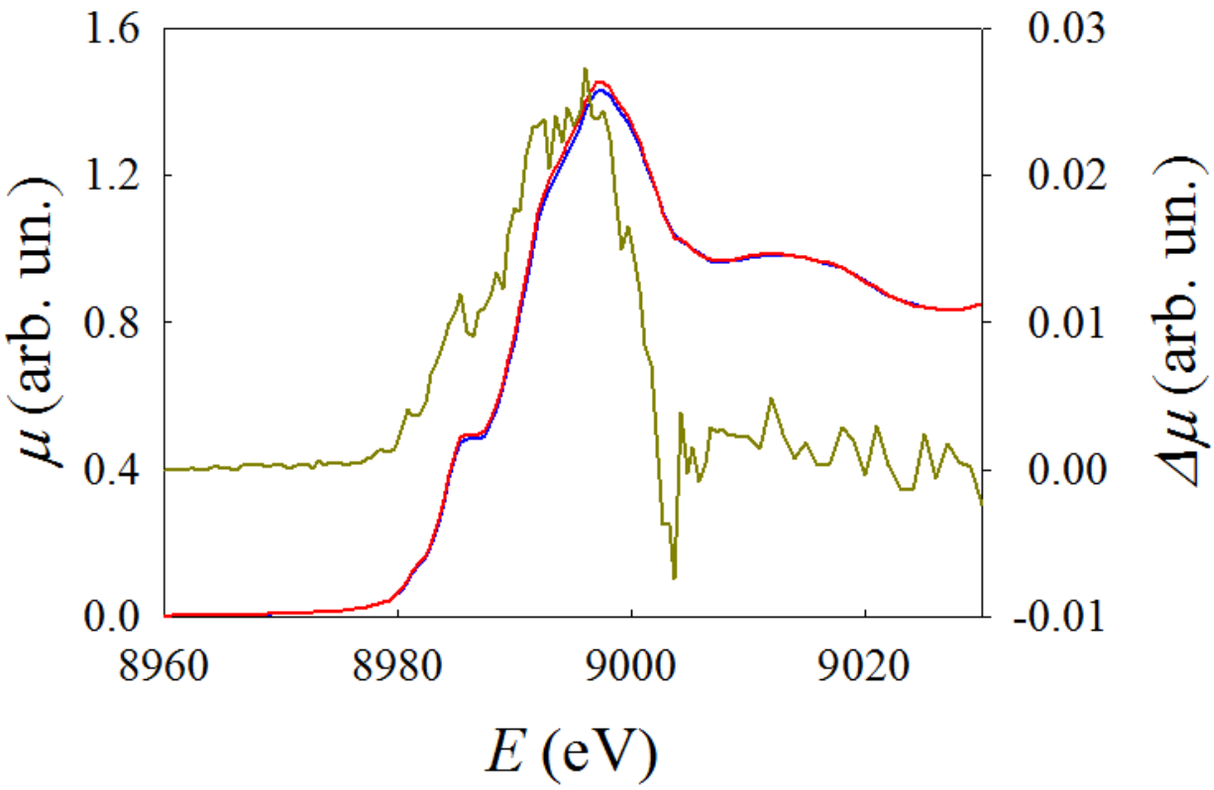

***Figure 208**. First XANES spectrum of Cu_xO@FTO electrode at 0.7 V in 0.1 M K_2HPO_4 + KH_2PO_4, pH = 7 in the dark (blue line) and in presence (red line) of 400nm illumination and their difference.*

In the intermediate spectra (Figure 209), Cu_xO (that is a CuO core – Cu_xO shell) is formed. In fact, fitting the spectra with a linear combination of CuO and Cu_2O standard spectra indicates the presence of Cu_2O. Here, the $\Delta\mu$ (light-dark) presents three significant features: a positive feature in the region between 8979 eV and 8985 eV, a positive one around 8990 eV and a negative peak in the region between 8995 eV and 9005 eV. These three effects appear on distinct sections of the Cu-K XANES spectrum and can be discussed separately as they have different origin.

The feature at the lowest energy is analogous in energy position to that previously discussed for the Cu_2O@Au@FTO material, when the fact that for the Cu_xO electrode both Cu_2O and CuO are present. We can then assign this contribution to the $\Delta\mu$ signal to photogenerated holes with $3d_z^2$ symmetry that are formed in both Cu_2O and CuO.

The second positive feature falls in the same range as observed for the first spectra but is one order of magnitude less intense. This is likely due to the almost complete covering of CuO by Cu_2O.

To attribute the origins of the third (negative) peak, one might want to consider the spectral differences between Cu_2O and CuO. The difference of the two leads to a negative feature that coincides with the observed one. This is turn indicates that, under illumination, a portion of Cu_2O forms reversibly.

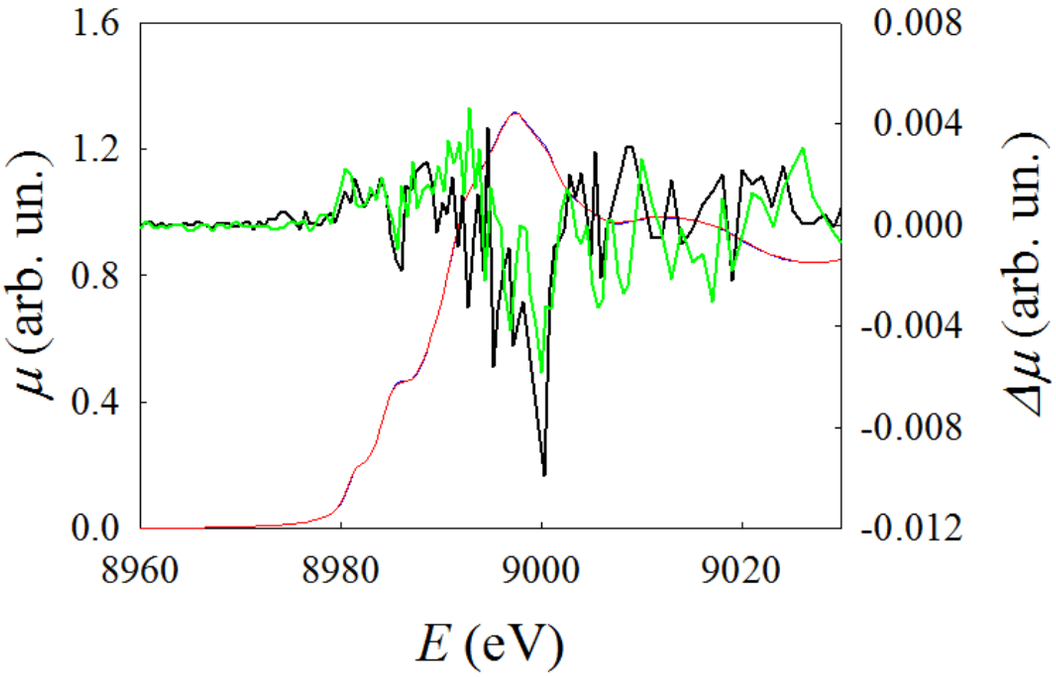

***Figure 209**. Second XANES spectrum of Cu_xO@FTO electrode at 0.7 V in 0.1 M K_2HPO_4 + KH_2PO_4, pH = 7 in the dark (blue line) and in presence (red line) of 400nm illumination and their difference.*

The third spectrum (Figure 210) is rather similar to the second one but with a further reduced intensity of the second peak, due to the further growth of the Cu_2O layer on top of CuO.

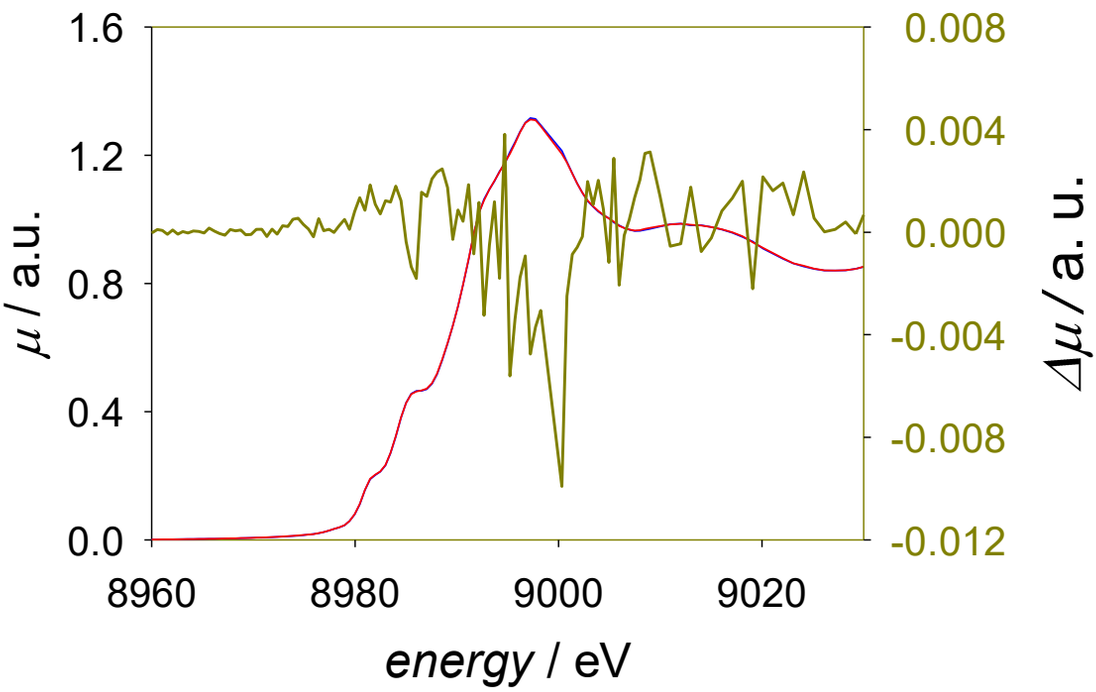

***Figure 210.** Third XANES spectrum of Cu_xO@FTO electrode at 0.7 V in 0.1 M K_2HPO_4 + KH_2PO_4, pH = 7 in the dark (blue line) and in presence (red line) of 400nm illumination and their difference.*

Finally, we note that the assignment of the positive peak in both the $\Delta\mu$ signals of Cu_2O and Cu_xO to photogenerated holes is confirmed by the fact that performing the same experiments in presence of a hole scavenger as CH_3OH gives zero difference.

2.7.14 Conclusions

Cu_XO is composed by a CuO core and an external shell of Cu_2O with the proportion determined *via* FEXRAV. Cu_2O is grown on CuO by cycling the potential under light, and eventually a stable and active material for HER is obtained. We were also able to assess that CuO is not an active species for HER, but also that the electrochemically generated Cu_2O (the true active material for HER) is protected from photo-degradation by the CuO core. Our explanation for this protective action lies in the relative bands position of CuO and Cu_2O. CuO has a smaller band gap (1.5eV) that lies inside the larger band gap of Cu_2O (Figure 211). FEXRAV supports this explanation, since the signal becomes constant in time, to indicate that the material transformation is stopped and that the only reaction occurring at the electrode is hydrogen evolution. These results agree with the high photoefficiency of the Cu_XO powder determined with SECM.

The relative positions of CB and VB for these semiconductors were also computed with the use of DFT and the HSE06 functional, the one able to give the best results in terms of BG values.

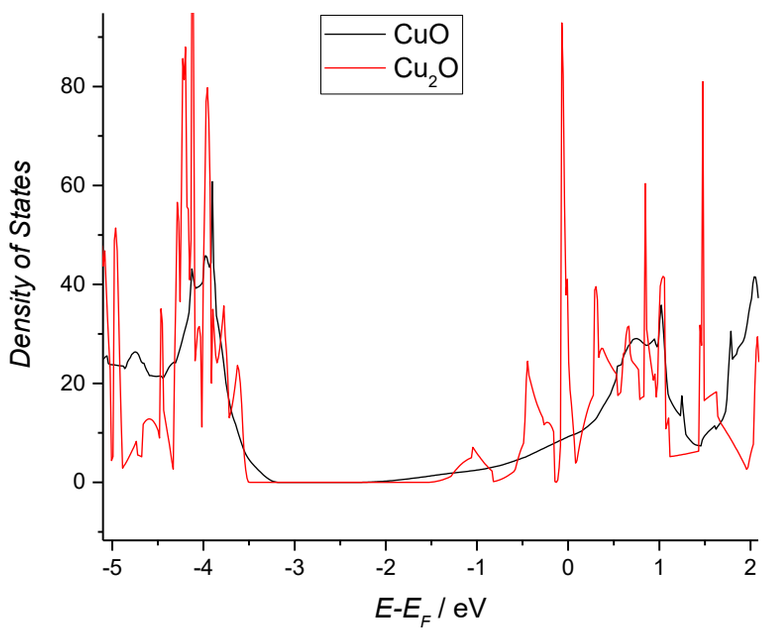

***Figure 211**. DOS of CuO (in black) and Cu_2O (in red) recorded for a 2x2x2 supercell with HSE06.*

The obtained band structure of the core-shell material is then represented in Figure 212 with the possible electrons paths due to the bands alignment.

In this view 3 different paths can be followed by the electrons in the CB of Cu_2O when it is irradiated and under applied potential:

(I) Water reduction.
(II) Cu_2O reduction.
(III) Flow to CuO CB.

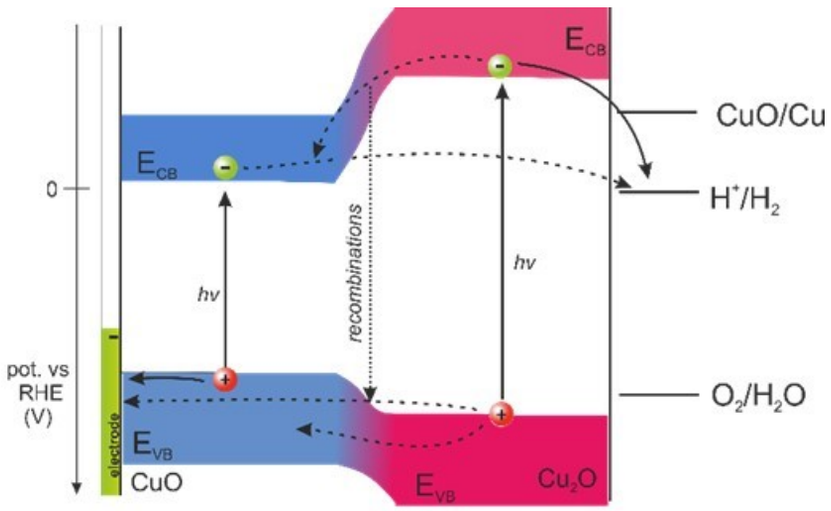

***Figure 212**. Bands position for the heterojunction between CuO and Cu_2O after once the stable final material is formed under applied potential and light.*

In pure Cu_2O the second reaction is the responsible for material photodegradation and strongly occurs while, according to the recorded stability, in presence of CuO is high probable that reaction (II) is suppressed by reaction (III) while the HER in light condition still occurs. So, when CuO is close to Cu_2O, the electrons prefer to undergo to CuO CB instead of perform material photodegradation. The new electrons in CuO CB did not continue the production of Cu_2O because material stability was recorded but probably are consumed by recombination with holes coming from the VB. In this way, the full stability of the electrode is achieved. The material indeed once the first reduction is performed and the optimal layer of Cu_2O is formed, is then able to work with stable photocurrent for very long period (Figure 213).

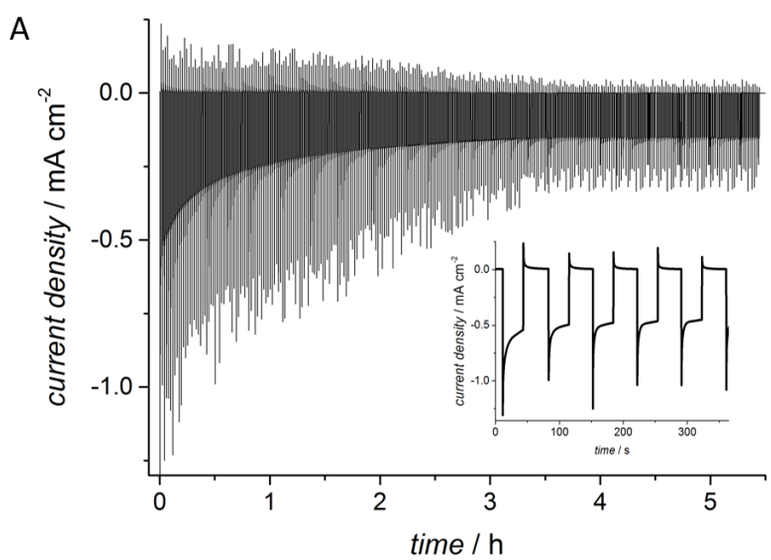

***Figure 213.** Stability test at 0.35 V vs. RHE in 0.1 M K_2HPO_4 + KH_2PO_4 (pH = 7) under chopped illumination with LED λ= 400 nm;*

With this composed material was then possible to fulfil the different requirements for a protective layer. It indeed left on the material an acceptable photoactivity leading to a high stability. Moreover, no expensive or toxic materials were used for its synthesis.

2.7.15 Dismissed Protective Overlayer: C-protected Cu_2O

A carbon-based protective overlayer was tested and then dismissed because of the poor protective activity and because of some synthetic obstacles if compared to the previous synthesis.

According to the literature the use of conductive overlayer on a semiconductor can remove the photodegradation phenomena due to the ability of the overlayer of quickly removing electrons from the material to inject them into the solution after excitation[429].

The protective layer must be thick enough to prevent the semiconductor being in contact with the electrolyte and at the same time be thin enough to not stop the semiconductor light-adsorption process. High conductibility is also required[136]. The use of a carbon, and in particular graphene, seems to be a promising choice looking at the ability of fulfil the requirements. Indeed this material have high mechanical strength, flexibility, high transparency (in some case up to 95%[430])and good electrical conductivity[431](in the order of 400 Scm^{-1}).

A 3$mgmL^{-1}$ glucose in water solution was prepared. The Cu_2O electrode was then dip inside for few minutes then left in air for drying. The dry electrode was calcinated at 500°C under N_2 flux for 4h with a T ramp of 10°$Cmin^{-1}$. The obtained samples were more yellowish than the pure Cu_2O one. Tested in the pH 11 electrolyte the electrode gives the following results.

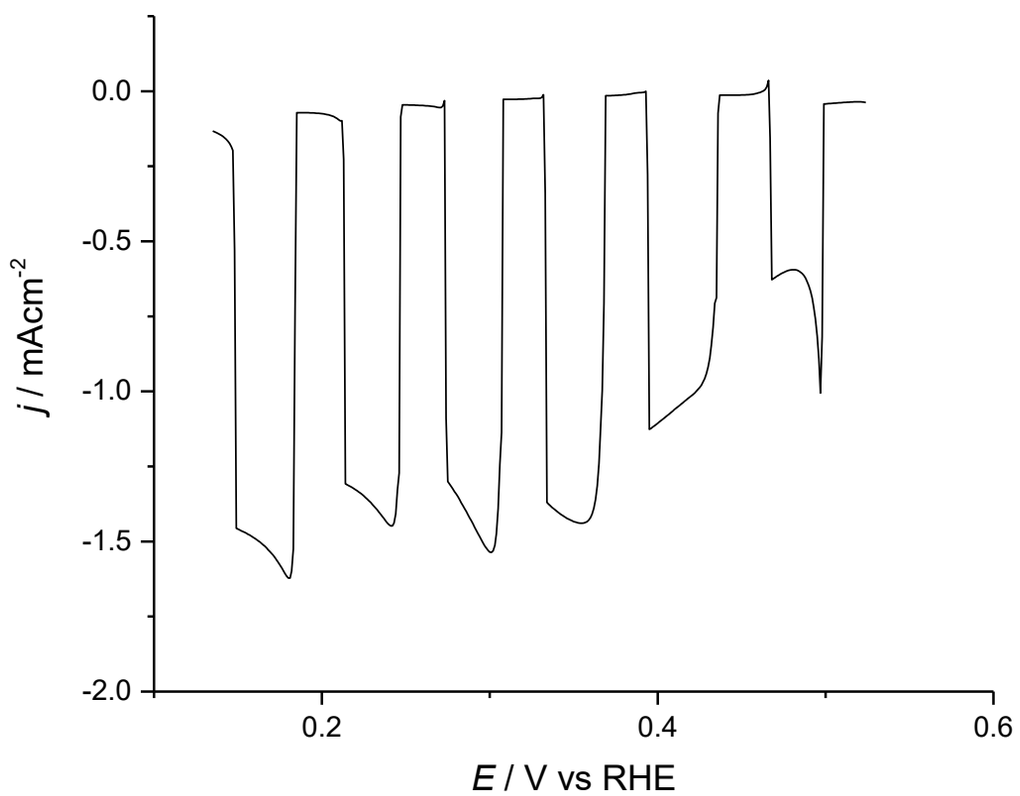

Figure 214. *LSV under pulsed light in Na_2HPO_4 0.5M + 0.5M NaOH at 10mVs^{-1} of a C-protected Cu_2O electrode.*

The obtained photocurrents are comparable with those obtained without the protective overlayer on Cu_2O, meaning that the layer did not affect the light-absorption properties.

The potentiostatic measurement at 0.175 V vs RHE shows instead a poor protective ability for this overlayer with a fast photocurrent decreases after few minutes.

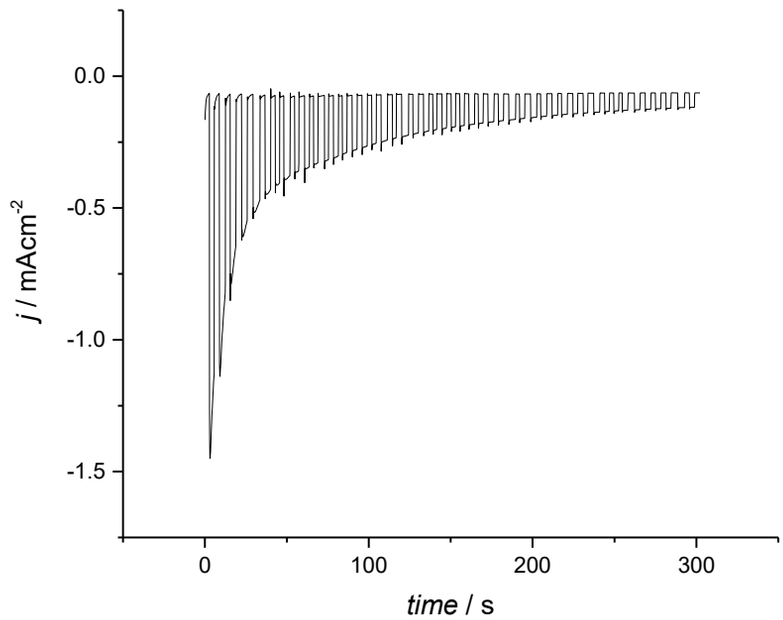

***Figure 215**. Potentiostatic measurement under pulsed light in Na_2HPO_4 0.5M + 0.5M NaOH at 0.175V vs RHE of a C-protected Cu_2O electrode.*

The electrochemical results on the stability obtained for this electrode are not so far from those with FeOOH but the low results combined with the use of an organic protective material stops us from further measurements. Moreover, the control of the overlayer cannot be done with the same accuracy and tunability that an electrochemical deposition can offer.

3. Appendices

3.1 Appendix 1: Becquerel Effect on Pt Electrodes

3.1.1 Introduction

The topic of this first appendix is unconnected with the main work discussed until now and aim in giving a brief discussion on the study performed on a complication involved in the SECM work. Meanwhile the setup for the evaluation of semiconductor efficiency was developed, a photo-induced effect was found and briefly studied to have a better knowledge of what was happening. We noticed that the electrochemical behaviour of the Pt substrate used for the hydrogen re-oxidation was influenced by the presence of the light.

Pulsing a UV led light while the platinum was biased in the pH 7 electrolyte, generates some currents on the electrode. This behaviour was previously noticed in literature and called Becquerel effect. It is mainly due to changes in potential of a metal electrode submerged in an electrolyte solution when is illuminated. The change in potential of course leads to the recorded changes in currents. To have a better knowledge of the photocurrent recorded during the experiment with semiconductor we wanted to shine light on this process and confirm its nature.

3.1.2 Photoemission Process and the Solvated Electron

The first study on photovoltaic phenomenon on metal-electrolyte interfaces started in 1839 when Becquerel observed changes in metal electrode potential under illumination. Three hypotheses were formulated in the years to explain the Becquerel effect:

I) The photocurrent is related to an increase of electrons energy due to the absorbed light. Thus, the probability of transferring an electron from the metal to ions or molecules increase meaning that the reaction rate increases[432,433].

II) Heyrovsky instead associates the photocurrent with light-mediated decomposition of surface charge transfer complex formed between the metal and the solvent (or solute). The bond between metal and solvent (or solute) is broken when the light quantum is absorbed and the released electrons are transferred to the electrode (giving anodic photocurrents) or to the absorbed molecules (cathodic photocurrents) with electrons leaving the electrode[434–436].

III) Barker instead considers the photoemission when electrons are emitted from the metal to the solution where they can exist in a delocalized states[437].

Considering the process III, the recorded photocurrent will be dependent from electrode potential and light quantum energy following the so-called 5/2-law.

$$I = A(\hbar\omega - \hbar_{\omega 0} - e\delta)^{5/2}$$

Where $\hbar$, the Plank constant, is 1.054571×10^{-34} J·s or 6.582119×10^{-16}eV·s, A is a proportionality coefficient, ω is the frequency, ω_0 is the threshold frequency (so that $\hbar\omega_0$ is the work function for the photoemission of one electron from a metal in the solution at δ=0), e is the absolute charge of the electron and δ is the electrode potential.

We can summarize the transformation which the photoemitted electrons undergoes[438]:

1. Thermalization due to inelastic scattering in the medium. For electrons with an energy of 1eV it will takes 10^{-13}s[439].
2. Solvation of the electrons in the solution in an estimated time of 10^{-11}-10^{-12}s [440].
3. The solvated electrons enter in chemical reaction or physicochemical transformation: diffusion, migration, or chemical reactions in the liquid with the electron-acceptor substances (scavengers) like H_3O^+, NO_3^-, O_2, N_2O or others or either on the electrode surface. The possibility of interaction of "dry" electrons is negligible.
4. Conversion of the products of the interaction of solvated electrons with scavengers.

Photoemission from the metal to the solution produces solvated electrons close to the interfaces. Many of these electrons return to the surface but some react with species in solution called scavengers to produce radical species that can undergoes to cathodic or anodic reactions at the electrode. The current related to these reactions give the recorded photocurrent.

The process is then based on the transfer of electrons through the interfacial boundary when the metal absorbs light quanta of the proper wavelength. Then the photoemitted electron is thermalized and solvated (in 10^{-11}s) in the electrolyte. The stable solvated electrons enter in chemical contact with the electron-acceptor species in solution (scavengers) like H_3O^+, NO_3^-, O_2, N_2O or others[441,442]. One of the most common scavenger is H^+ with H atom being the radical species produced after photoemission. For sake of clarity the possible reactions will be discussed considering the H^+ ions as scavenger.

1. $e_M^- + h\nu \rightarrow e_0^-$
2. $e_0^- \overset{k_0^a}{\rightarrow} e_M^-$
3. $e_0^- + H^+ \overset{k_0^S}{\rightarrow} H$
4. $H \overset{k_1^a}{\rightarrow} H^+ + e_M^-$
5. $H + H^+ + e_M^- \overset{k_1^c}{\rightarrow} H_2$

Reaction (1) is the photoemission process itself with the absorption of a photon of energy $h\nu$ and its termalization and solvation in the solution. Process (2) is the electron returning to the electrode without any reaction in solution. This ususally occurs quite slowly (100 cms^{-1}) allowing the electron to travel some distance through the solution[437]. With reaction (3) the solvated electron interacts with the scavenger creating the radical specie, while reactions (4) and (5) are respectively the anodic and cathodic reactions of the H atoms on the electrode.

The current resulting from the different processes can be expressed by:

$$i = I - I_e \pm I_A$$

Where I_e is the current related to the electron returning to the electrode, I_A is the current for the electrochemical reaction of [eA] (positive sign for reduction and minus for oxidations).

If the product [eA] is not discharged at the electrode, we have *i=I* where *i* is the current recorded during the experiment. If no-acceptor mets the solvated electrons, they quickly return to the electrode giving a net photocurrent equal to zero.

Vice versa, the product [eA] can enter in the electrode reactions undergoing oxidation or reduction. Consequently, the recorded current decreases in case of oxidation while increases for reduction (I_A).

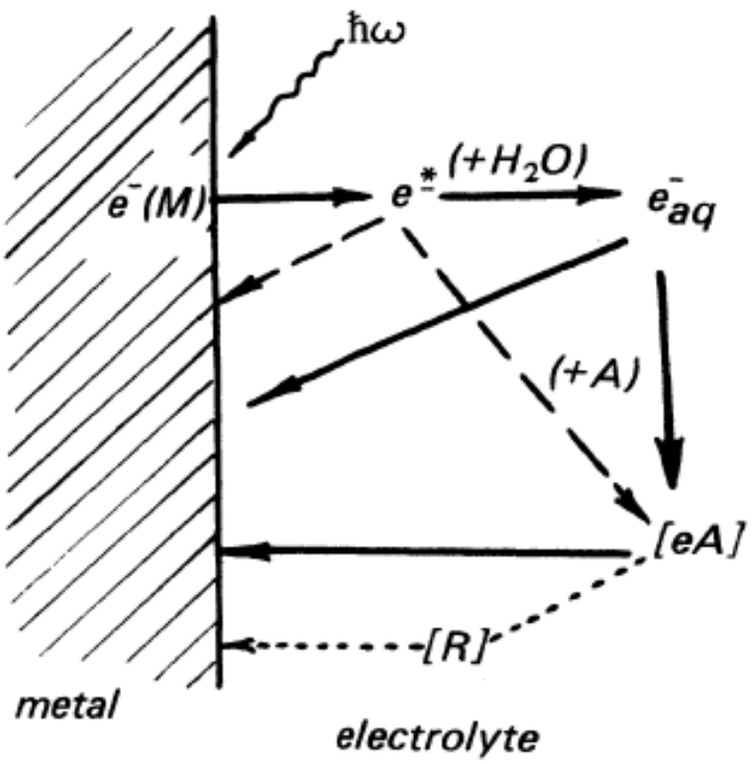

Figure 216. *Scheme for the transformation of solvated electrons in solution.*

This effect was recorded by different authors on Hg, Bi, Pb, Au[443] and in just few paper on Pt. The interaction light-matter is strongly related to ε (dielectric constant) that depends on frequency ω with 3 different characteristic frequency intervals:

- $\omega < \tau^{-1}$: the metal strongly reflects radiation. No reaction of interest occurs in this interval.
- $\tau^{-1} < \omega < \omega_e$: the absorption decreases while increasing frequency. The electromagnetic field is still not able to enter in the bulk of the material. Photoemission occurs only from a very narrow surface layer. This is called surface external photoeffect.
- $\omega > \omega_e$: metal transparency, no reflection, negligible absorption. Electrons emerge from bulk and the magnitude of photocurrent quickly increases.

$\tau = 10^{-12}$- 10^{-13}s is the relaxation time of excited states in the conduction band, between 3000-30000nm, ω_e is the plasma frequency of electron in metal, for Pt is $2{,}31 \times 10^{15}$Hz.

3° interval start at wavelength lower than 130nm, so we deal with surface external photoemission using the near UV source.

3.1.2.1 Affecting Parameter

- Photocurrent decreases while decreasing electrolyte concentration. Probably related with the increase of the electrode double layer. For low electrolyte concentration: $I = k\sqrt{Ca}$
- Threshold potential is independent from concentration.
- While in vacuum the photoemission depends on the material work function, in electrolyte-metal interfaces is the electrode potential that define the initial level of electron energy and Fermi level. The final level depends on the electrolyte, so photoemission threshold is independent from the metal.
- Photoemission is sensible to light polarization: no photocurrent for the absorption of waves polarized in the plane of incidence.

3.1.3 Results

The following results were recorded during SECM measurement were the Pt electrode acted as a substrate for the hydrogen oxidation. It's important to notice that the platinum surface was considered clean in these experiments thanks to several cyclic voltammetry in H_2SO_4 0.5M until all the characteristic peaks can be observed. Then to remove any oxide on the surface the electrode is swept only in the cathodic part of the CV with a final potential just before the formation of PtO_x. That was consider the best potential for hydrogen oxidation reaction because of the absence of any other faradic reaction.

The photoeffect was first noticed while measuring with SECM the hydrogen produced at a semiconductor-filled cavity. We notice the phenomenon because while the material tested was not active under light (WO_3) we saw some changes on the substrate electrode current together with light pulsation.

The electrode was then tested in a 3-electrodes configuration giving the same response with extremely small photocurrents (nanoamperes) recorded in light. To evaluate the nature of the phenomena different potentiostatic measurements were recorded at different potentials. A 100 seconds potentiostatic measurement was performed every 20 mV starting from 0.211 V vs RHE to 0.811 V vs RHE. Each potentiostatic measurement was composed of 60 second of quite time to allow the stabilization of the current and 20 second in dark plus 20 second in light in order to be able to record the photocurrent at each potential for enough time. The final results are reported in Figure 217. We can immediately notice how the recorded photocurrents change with the applied potential. So, to verify the five-seconds law the $I^{0.4}$ was plotted versus the applied potentials (Figure 218). The expected linear correlation between 0.8 and 0.4 V vs RHE was found. From the intercept with the X-axes was possible to define the threshold potential for the material in the selected electrolyte that is around 1.1 V vs RHE. The value of the threshold potential is obviously related to the wavelength of the light sources. The negative slope of the linear part in the region of sufficiently positive potentials implies that electrons flows from the metal to the solution.

At less positive potentials the dependence dramatically deviates from the five-seconds law probably because of solution reaction starts or because the surface of the Pt starts to change due to adsorbed H. Indeed, looking at the CV of the Pt substrate in the same electrolyte (Figure 219) we can see that 0.4 V vs RHE is exactly the potential at which H adsorption on Pt starts. This is expected because this phenomenon is a surface phenomenon strongly related to nature of the interfaces but also because of the depletion of the H^+ scavenger close to the electrode. This behaviour was previously studied on Pt electrode with different scavengers (NO_3^- and NO_2)[444] but also noticed with different materials like gold[443] or mercury[445].

Photocurrent on platinum could be anodic if the material is illuminated with UV light in the region of oxygen evolution[446], while they are cathodic in alkaline and neutral solutions[447]. The sign of the photocurrent is moreover related to the scavenger species reactivity with the electrode.

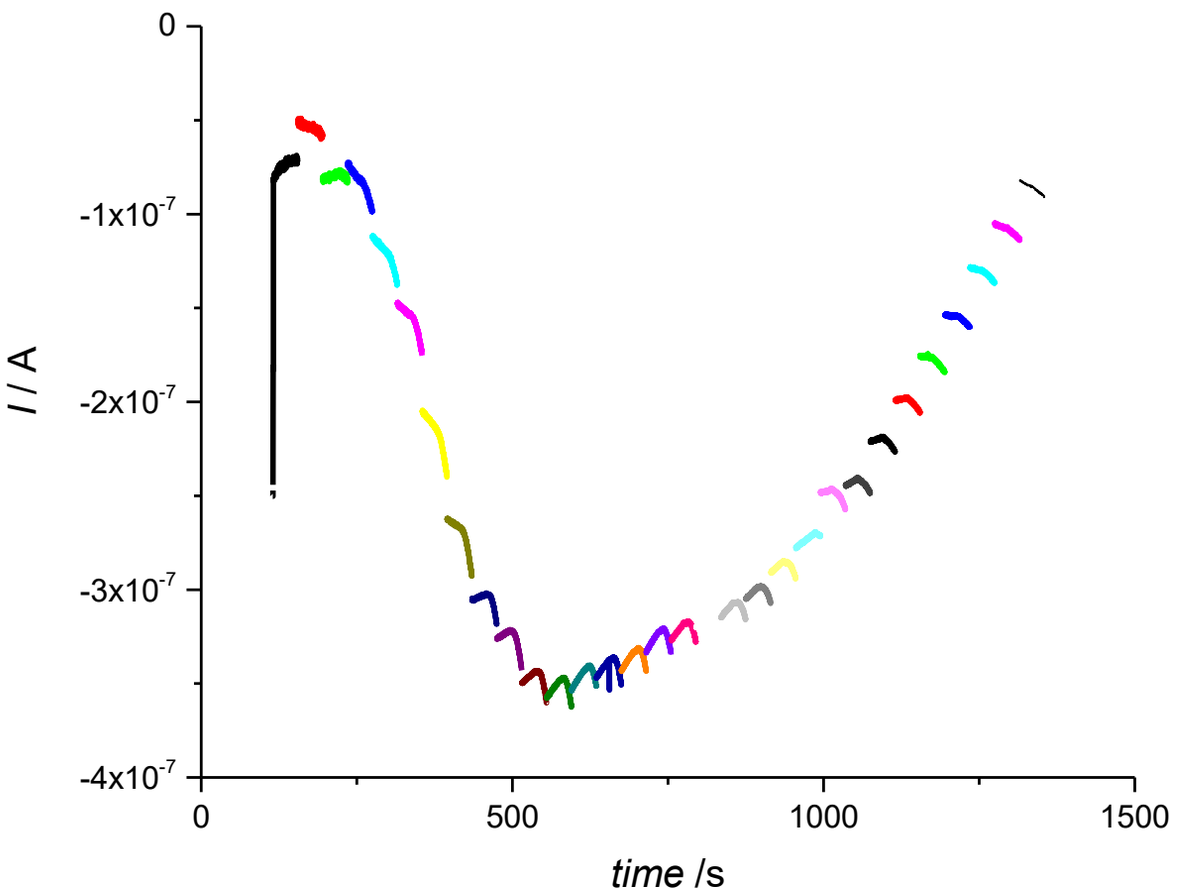

***Figure 217**. Photocurrents recorded at different potentials under green LED light. Each colour is a potentiostatic measurement kept for 20 second in dark and 20 seconds in light. Each step is 20mv far from the previous and between each of them there are 60 seconds of quite time (here not showed) to stabilize the current.*

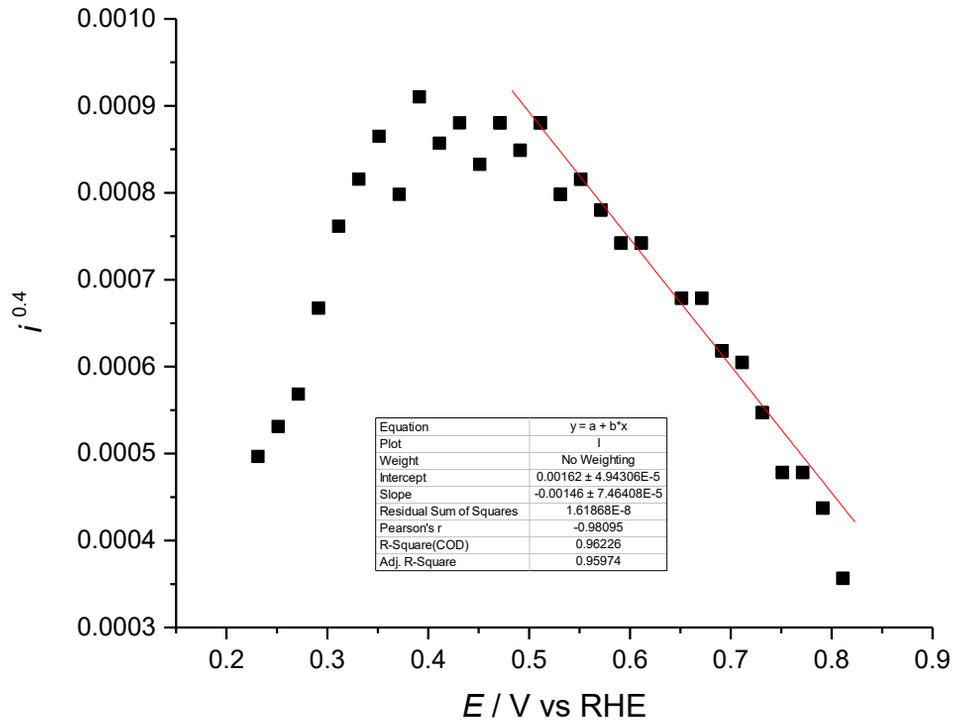

***Figure 218**. Voltammetric dependence of photocurrent (in arbitrary units) for Pt electrode in pH 6.8 buffer electrolyte. The red line is the fit for the linear part of the curve.*

The shape, photocurrent trend inversion and threshold potential are in accordance with Ansone et al. [447]whose experiment was the closer in terms of material and wavelength respect to ours.

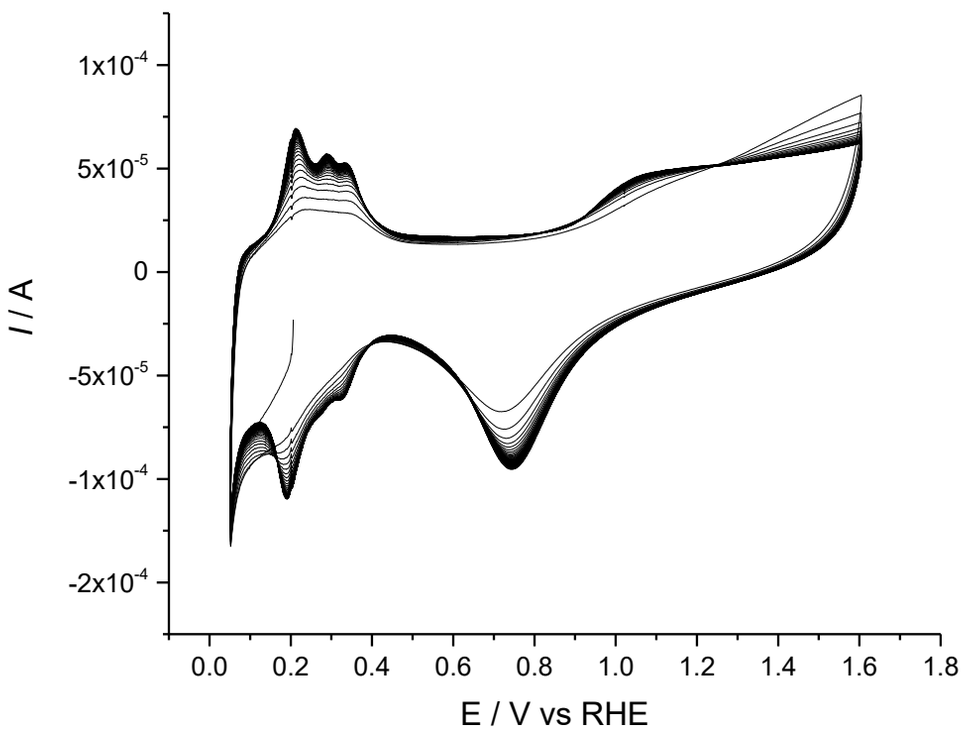

***Figure 219.** Pt cyclic voltammetry in pH 6.8 buffer electrolyte at $1Vs^{-1}$.*

With different experiments we confirmed that the effect is independent from:

- Exposition time: longer or shorter step provide on Pt the same photocurrent once a plateau is reached.
- The used platinum: as confirmation of the cleanliness of the Pt surface, the experiments were carried on with different Pt foils giving the same response.
- Light distance: moving the lamp further or closer affects only the intensity of the phenomenon because of the number of electrons excited outside the material.
- Cotton in the double bridge: any interference from organic material in the double bridge was discarded.

Despite this it is strongly affected by the presence of scavenger and pH (H_3O^+ is one of the available scavenger) and light wavelength (and so energy). We can see how changing the wavelength from 400nm (near UV) to 520nm (green light) the effect is far less pronounced, and the direction of the photocurrent is inverted.

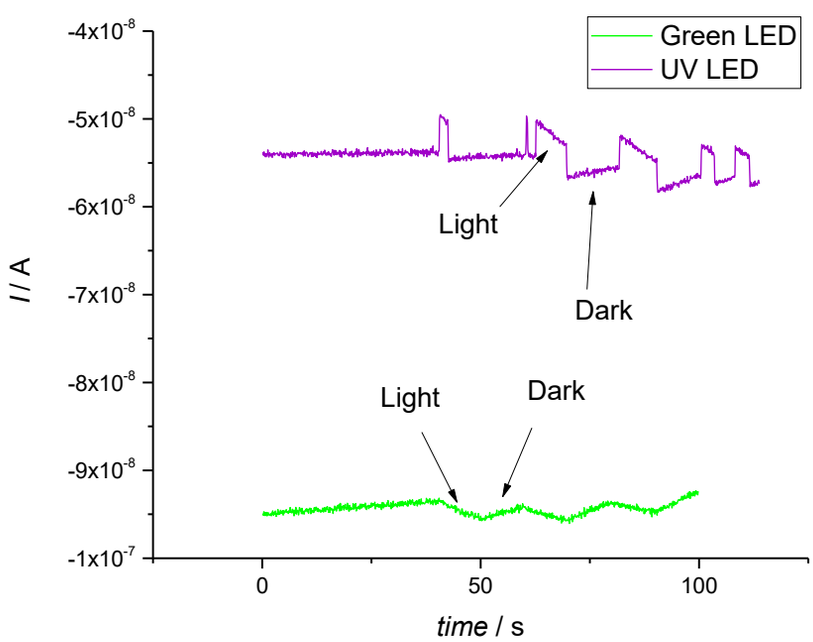

***Figure 220**. Comparison between photoeffect obtained with two different wavelengths LED with potentiostatic measurements at 0.78 V vs RHE in H_2SO_4 0.5M. The green one has λ=520nm, the UV one λ=400nm.*

The photoeffect intensity and photocurrent is also related to the number of scavengers able to react with the solvated electrons coming from the metal. In Figure 221 are reported 3 measurements with different amount of scavengers. In a deaerated solution (black line) there are at least 2 scavenger that can react with the solvated electron, O_2 and the proton. Indeed, the photocurrent recorded for the oxidation (a cathodic photocurrent is recorded) of the formed radical species on the electrode is quite high. Purging the solution with N_2, the O_2 is stripped away and the amount of scavengers is reduced as well as the photocurrents (red line).

In the last measurement tetrabutylammonium (TBA) cation is added to the solution. From literature, it is known to be able to reduce the speed of these processes[447].

Indeed, photocurrents are still lower even if not so much probably because TBA is less active in acid environment (measure in H_2SO_4 0.5M) and also because at this pH H^+ is the main scavenger present.

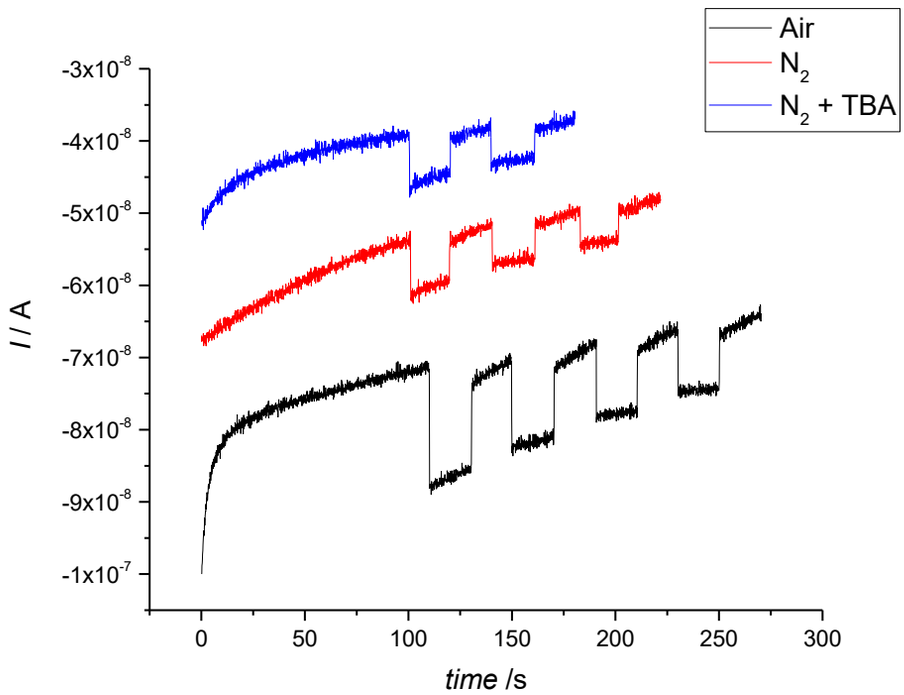

***Figure 221**. Comparison between potentiostatic measurements under pulsed light on a Pt electrode with the presence of different scavenger. Electrolyte H_2SO_4 0.5M at the potential of 0.78 V vs RHE.*

When the concentration of H^+ is reduced because of the neutral environment (pH 6.8) the effect of TBA on the phenomenon is much more evident with an almost complete suppression of the photoeffect.

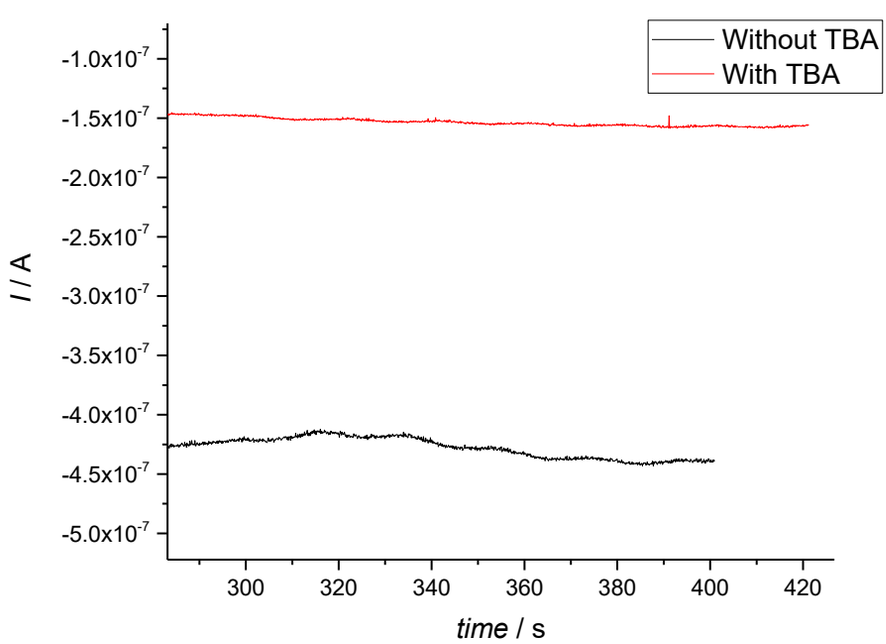

***Figure 222.** Comparison between potentiostatic measurements under pulsed light on a Pt electrode with (red) and without (black) the presence of TBA in buffered electrolyte pH 6.8 at the potential of 0.78 V vs RHE.*

Interesting the phenomenon was noticed for the first time on a glassy carbon (GC) electrode. Again, on this electrode when the light is on the [eA] species is oxidized at the electrode giving a cathodic photocurrent. In particular, on GC the effect seems to be stronger (almost one order of magnitude) at the potential of 0.21 V vs RHE in H_2SO_4 0.5M.

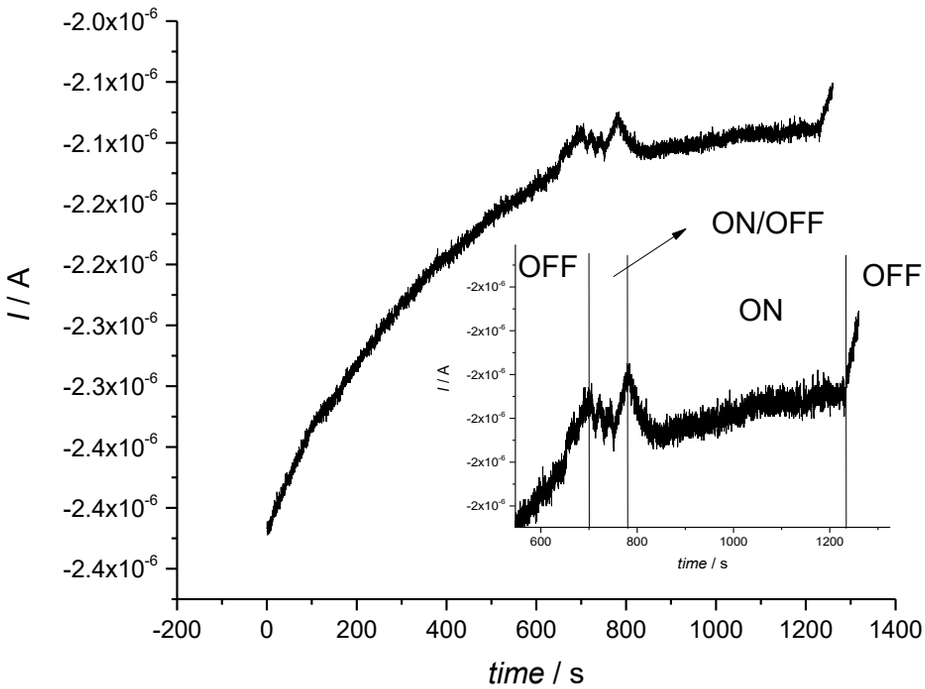

Figure 223. *Pulsed potentiostatic measurement at 0.21 V vs RHE (hydrogen oxidation potential on GC) on a glassy carbon electrode in H_2SO_4 0.5M. The light ON and OFF is reported on the figure. The inset is a magnification of the time between 600 and 1200 seconds.*

Once evaluated the nature of the process and the affecting parameters we wanted to evaluate if this process could be an obstacle in the evaluation of hydrogen oxidation currents on Pt in the SECM measurements with the semiconductor-filled cavity. Indeed, the order of magnitude for the photoeffect current was similar to those of the oxidized hydrogen raising some question about the possibility of differentiating the two phenomena. For this reason, an additional experiment was performed. In the SECM cell a 4-electrodes setup was prepared. The working 1 was a Pt tip while the working 2 is the Pt foil for the study of the photoeffect. Then 2 different types of measurements were performed:

- Pulsed potentiostatic measurement in dark with the Pt tip producing H_2. The H_2 produced in a limited amount of time is detected by the Pt substrate. H_2 here is produced electrochemically on the Pt tip but this measurement should be the reference for a measurement without photoeffect (red line in Figure 224).
- Pulsed potentiostatic measurement with both production of H_2 from the Pt tip and photoeffect due to the pulsed light over the Pt substrate (blue line in Figure 224).

From these experiments, we can easily see how in presence of photoeffect hydrogen oxidation current can be easily evaluated simply by removing the background and adding a proper baseline that consider only the influence of the H_2. The light effect indeed seems only to bend the current direction but left intact the intensity of the photocurrent gap if a green LED is used.

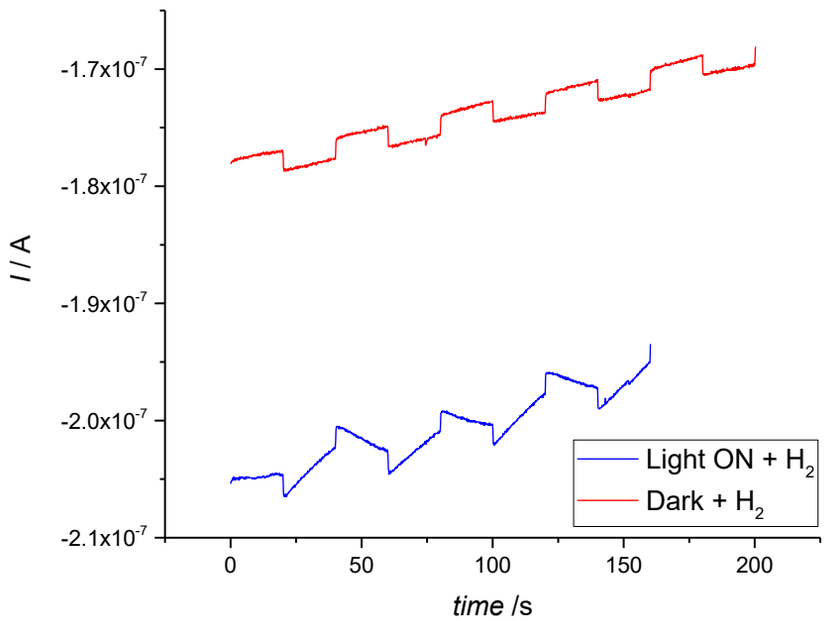

Figure 224. *Comparison between 2 potentiostatic measurements of a Pt electrode at 0.781V vs RHE in buffer electrolyte (pH 6.8). Red line: measurement in dark with hydrogen produced by Pt tip with pulsed frequency (pulse between 0.13 and 0.08 vs RHE). Blue line: measurement with a pulsed light and pulsed H_2 production from the tip.*

3.2 Appendix 2: Absorption of Halides on Ag with XAS

3.2.1 Introduction

Organic halides, like haloacetic acid, are common pollutants in the environment due to different processes like, water chlorination, atmospheric degradation of freezing molecules, degradation of pesticides and herbicides[448] and as derived pollutants from waste treatments. In addition, organohalides are still actually used in several industrial processes as solvents or building blocks for high-value chemicals. Their treatment is becoming an important task due to their high toxicity, stability and potential carcinogenity.

Different techniques were suggested to be applied for their treatment like biodegradation, ultrasound or microwave assisted photolysis, Fe(0)-mediated reduction processes[449], thermal degradation or chemical oxidation. Unfortunately, these techniques have low dehalogenation efficiency with the possible formation of derived pollutants or unsatisfactory practical and economical applicability. If compared to other methods, electrochemical treatments are extremely selective, need mild reaction conditions (low temperature and pression), avoid formation of secondary toxic products and can be easily scaled according to the dimension of the waste flow.

The electrochemical method for the carbon-halide bond breaking includes both electrooxidation and electroreduction processes. Oxidation processes are more studied and used because lead to the full degradation of the pollutants. Despite this, sometimes undesired reactions occur with the formation of halogenated compounds with a higher toxicity than the original compound. Cathodic processes are from this point of view safer without the production of any by-products and the potential recycling of the waste with the creation of high value products[450].

In this view, was demonstrated the high efficiency and high electrocatalytic activity of silver towards dehalogenation of organic halides[451–457]. However, the reasons behind the exceptional activity of Ag are still not completely clear. More recent study evidenced the role of the adsorption of the organic halide molecules on silver adopting the benzylchloride as model substrate[458]. A fine study on Ag chemical surrounding in term of nature of the adsorption of reactants and products during the reaction can in principle shine light on the reaction mechanism. In the present study the adsorption of bromide anions on silver nanoparticles (3-5 nm diameter from Nanocomposix) is studied by X-Ray Absorption Spectroscopy (XAS) in the fluorescence mode at the Br-K edge.

3.2.1.1 The Cell

The cell used for this experiment was a first prototype of those described during the thesis. It is composed by two identical circular side with a 7mm hole inside. On one side a Mylar® film was applied in order to create an internal chamber of small volume (almost 2-3mL of electrolyte, $KClO_4$ 0.1M plus the selected halide). The 2 counterparts were sealed on a carbon screen-printed electrode. The use of an O-ring helps avoiding electrolyte leaking. The counter electrode was a Pt wire inserted in the upper part of the cell while the references was an Ag/AgCl 3M in a small double bridge.

The working electrode was a DropSens® DRP-P-C11XX loaded with 20 µL of 5nm silver nanoparticles. All the measurements were taken in fluorescence mode as show by Figure 226.

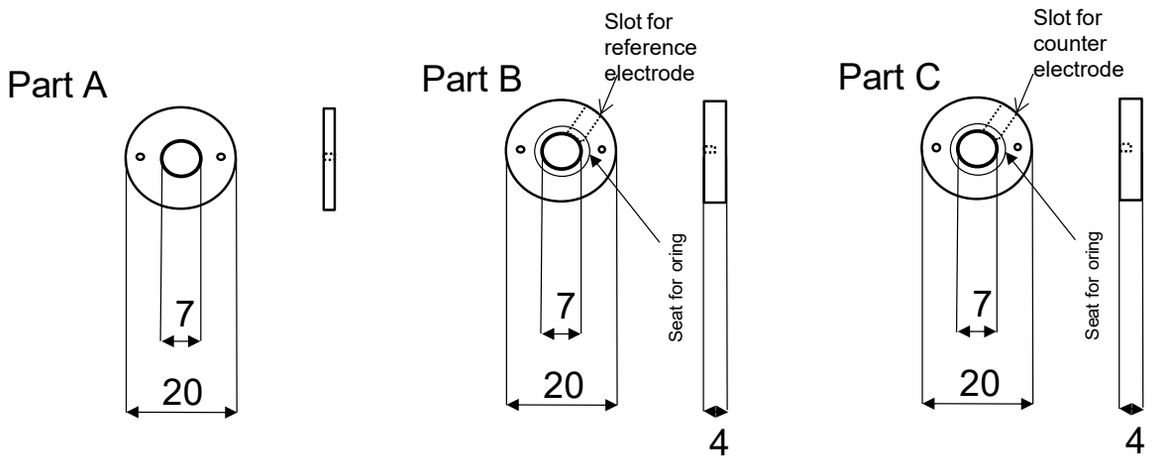

Figure 225. *Scheme of the homemade cell used for these experiments.*

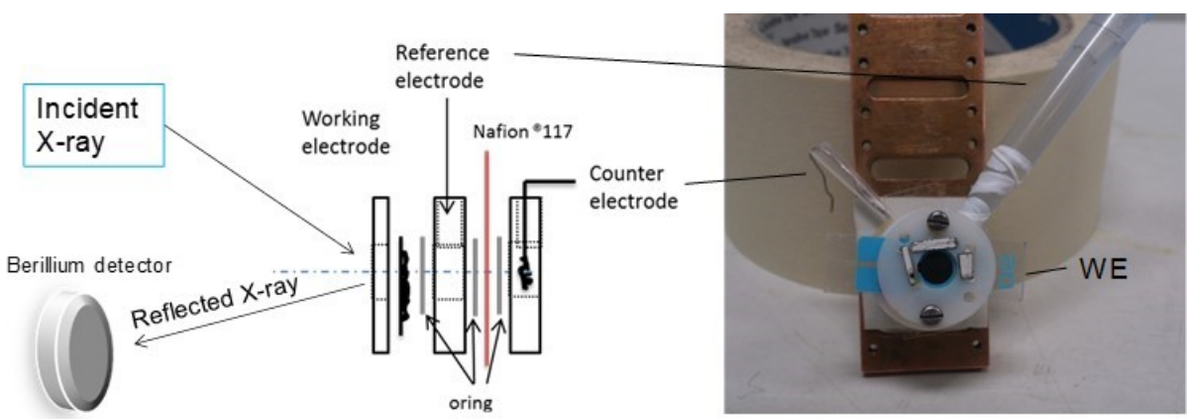

Figure 226. *Working scheme of the cell for this experiment. All the measurements were taken in fluorescence mode.*

3.2.2 Electrochemical Results

The adsorption/desorption ability of silver towards different halides and the respective positions of absorption-desorption peaks was previously studied in our group by Rossella Monaco using a Ag microelectrode with a fresh surface totally oxide-free.

In Figure 227 is possible to notice the effect of the different affinities for the selected halides with the silver surface of the microdisk during 80mVs^{-1} fast cyclic voltammetries. In particular, we can notice how the sequence for absorption with potential is Cl^-<Br^-<I^-. The effect of Cl^- seem to be the smaller one due to the small variation of current (at -0.35V vs SCE) respect to the background. A more marked effect due to the adsorption/desorption phenomena of the halides is present with Br- and I-. In particular for the I^- was noticed a reduction of the capacitive current in the region of the more positive potentials. The recorded results are in good agreement with those previously reported by Ardizzone et al.[459] using mono and polycrystalline silver. The desorption peaks are obviously the cathodic ones while the adsorption ones are the anodic.

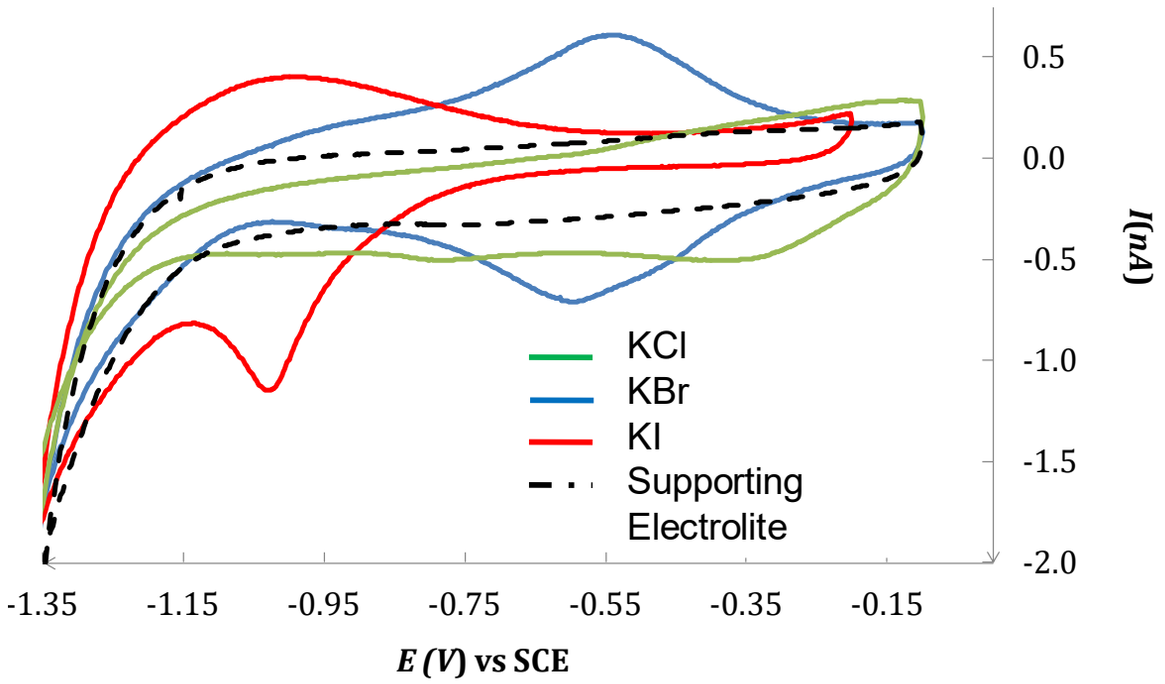

Figure 227. *Cyclic voltammetries at 80 mVs^{-1} of a silver microelectrode in different salt solution; KCl 5x10^{-4}M (green), KBr 5x10^{-4} M (blue) and KI 5x10^{-4} M (red) in $KClO_4$ 0.1M*

3.2.3 XAS Results

To evaluate the right energy for the FEXRAV we use two different standards. KBr was use as standard for free bromine in solution, while AgBr was used as standard for the adsorbed halide on silver. The full spectra are here reported together with the energy (13480eV) chosen for the FEXRAV analysis. The reaction of interest is indeed:

$$Ag + RBr \rightarrow Ag - Br_{ads} + R^{+}$$

Considering the XANES spectra recorded in Figure 228, an increase in the adsorption coefficient during FEXRAV is related to the reaction going towards the adsorbed halide condition because at 13480eV the spectra of AgBr is higher than the one of KBr.

Following the adsorption/desorption reactions with FEXRAV we were able to see an increase in the adsorption coefficient in correspondence of the adsorption peak, meaning that the adsorption of the Br- on silver, giving an AgBr-like specie is real. A decrease in μ was instead recorded after the desorption peak confirming again the detachment of the halide from the metal. Note that the potential window in Figure 229 is not enough to reach the AgBr formation potential. The increase in FEXRAV signal is then related only to the absorption phenomenon showing the paramount ability of FEXRAV in following even adsorption processes.

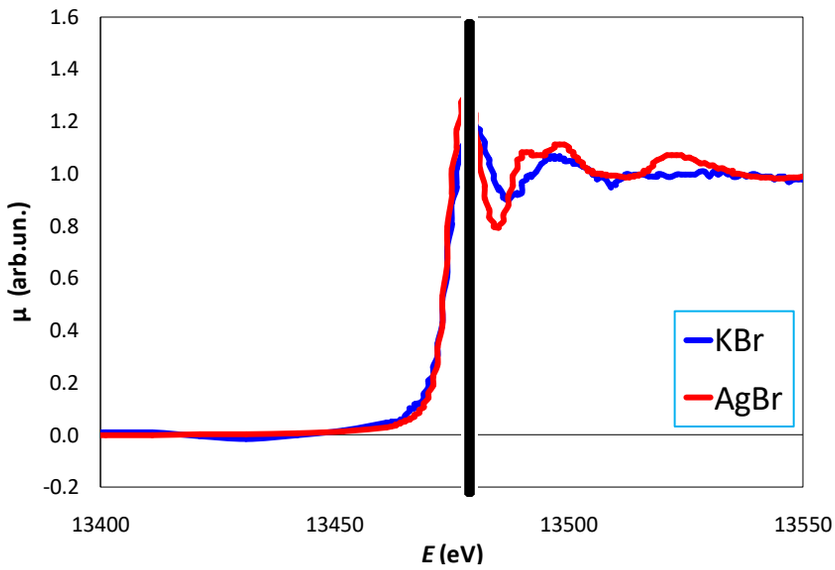

Figure 228. *XANES spectra of the standard for reagent and product of the reaction of interest. In blue the KBr standard, in red the AgBr one.*

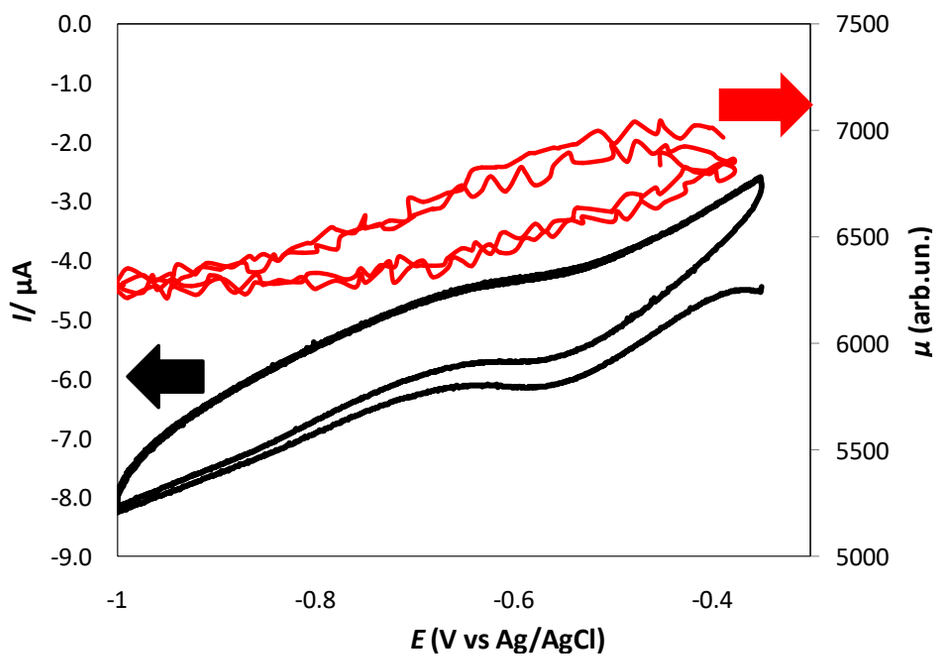

Figure 229. *FEXRAV (in red) and CV (in black) of silver nanoparticles on DropSens® electrode In $KClO_4$ 0.1M + 150μL at 1mVs^{-1}.*

3.2.4 Conclusions

With these experiments we were able to confirm the reaction path followed by organohalides reduction on silver electrodes. It consists on a preliminary adsorption step of the halides on Ag, as showed by the FEXRAV with the next broking of the R-X bond during the dehalogenation. In particular, using simple salts like KBr we were able to confirm that is the halide side of the R-Br to adsorb on the silver and not the organic one. Moreover, FEXRAV was validated as a useful technique to follow adsorption/desorption processes.The data for this section come from a series of experiment performed at BEAMLINE 08, LISA (Linea Italiana Spettroscopia Atomica), in Grenoble (FR).

3.3 Appendix 3: Study of Cu UPD on Au with EDXAS

This experiment was a brief test to evaluate the performance of the EDXAS beamline (ID24 at ESRF) with a well-known and established process occurring extremely fast and in a controlled way. Underpotential deposition of copper on gold was the chosen process, studied first in a classical electrochemical cell and then in the small cell presented in Appendix 2 under EDXAS. Involving a single layer of material, the process is extremely fast and a large variation in the signal can be achieved in few seconds.

3.3.1 Introduction

The cost of platinum electrocatalysts is one of the main limiting factor to the large-scale development of low temperature fuel cell for example in wide application like automotive[460]. One way to reduce the Pt cost is reduce the loading on the electrode by removing the unused platinum inside the particles. The idea is to create a particle with only the external shell made of platinum[461,462]. Several researches were devoted to this aim and actually the best to prepare these core-shell catalysts is to use the galvanic displacement from a Cu UPD[463–465]. The reaction spontaneously will lead to the replacement of Cu with Pt thanks to the oxidation of Cu(0) to Cu^{2+} and the reduction of a Pt^{2+} solution to Pt(0). One of the used core particles for this reaction is gold on which Cu UPD is a well-documented process[466].

3.3.2 Electrochemical Results

The first step was to define the UPD deposition and stripping potentials. In a 3-electrodes electrochemical cell a solution of H_2SO_4 0.5M and $CuSO_4$ 2mM was prepared. The working electrode was a gold wire as well as the counter, while the reference electrode was an SCE immersed in a double bridge filled with H_2SO_4 0.5M. The cyclic voltammetry was performed between gold oxidation peak to massive Cu deposition on the Au. From Figure 230 we can notice the different peaks recorded on a massive electrode. UPD deposition peaks in particular were recorded at 0.15 and 0.1 V vs SCE while the UPD stripping one is at 0.2 V vs SCE. These results are in good agreement with the value reported inliterature[467,468].

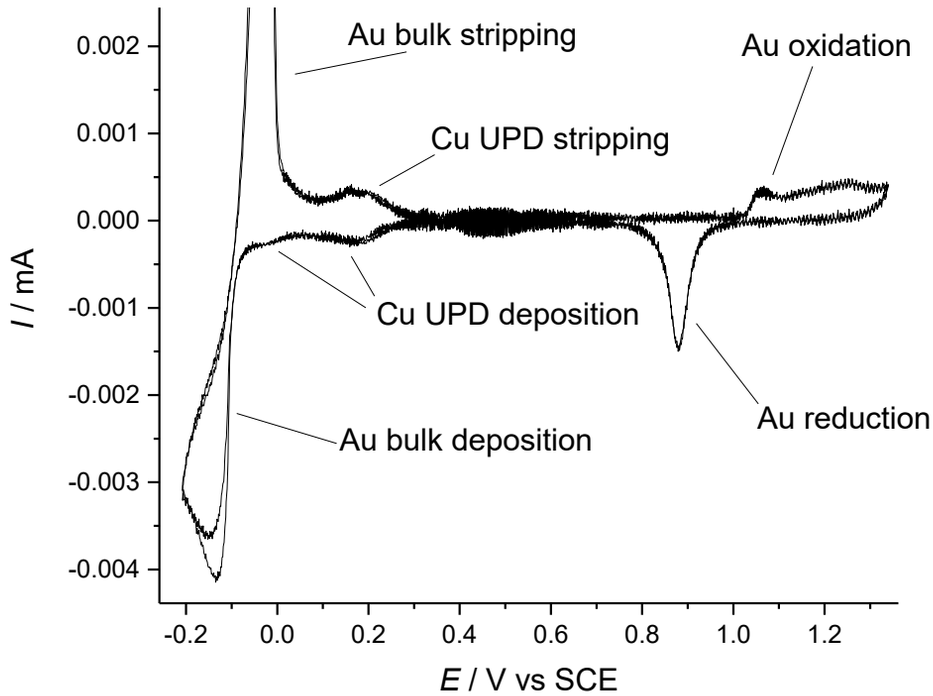

***Figure 230**. Zoomed cyclic voltammetry of a gold electrode in H_2SO_4 0.5M + $CuSO_4$ 2mM at 2mVs^{-1}. In the figure are marked the Cu bulk and UPD deposition and stripping peaks.*

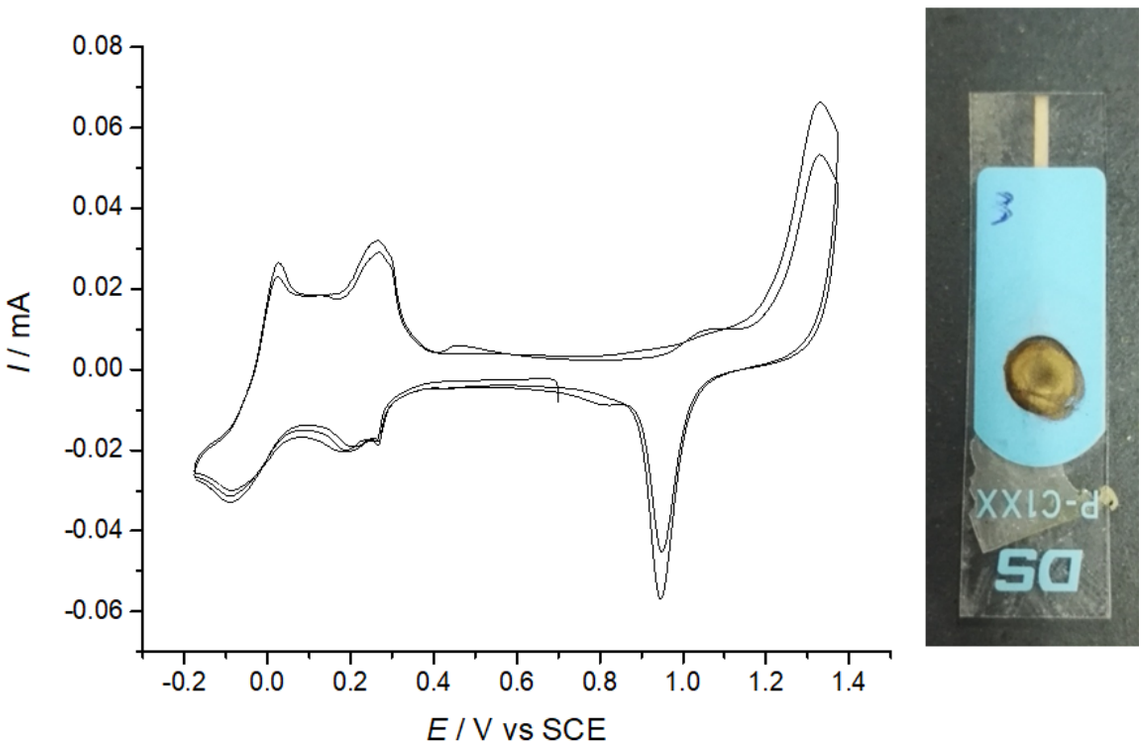

***Figure 231.** Cyclic voltammetry of Au nanoparticles on screen printed carbon electrode in H_2SO_4 0.5M + $CuSO_4$ 2mM at 2mVs^{-1}. Loading 610 µL.*

The same measurement performed on the carbon screen printed electrode cover with 610µL of Au nanoparticles in PVA shows the same peaks position and definition if compared to the bulk electrode and to electrochemical results found in literature with NP. The nanoparticles electrode will be used during EDXAS experiment because nanoparticles will ensure a high surface to volume ratio. UPD is a surface phenomenon and XAS use hard X-rays, so highly penetrating in the matter. If a bulk electrode will be used the final signal will be mostly composed by the signal of the bulk material without having a chance to follow a surface-limited phenomenon. The use of highly dispersed nanoparticles with high surface area will increase the ratio between the surface signal and the bulk one with the possibility to follow the reaction.

3.3.3 XAS Results

A carbon screen printed electrode cover with Au nanoparticles was the loaded with a monolayer of metallic copper working at the UPD potential until the current for the reaction is approached to zero. The Au + Cu electrode was then tested in the XAS cell presented in Appendix 2 in H_2SO_4 0.5M to follow the dissolution of the monolayer to Cu^{2+}. Considering the extremely small amount of copper on the electrode the process is expected to be extremely fast.

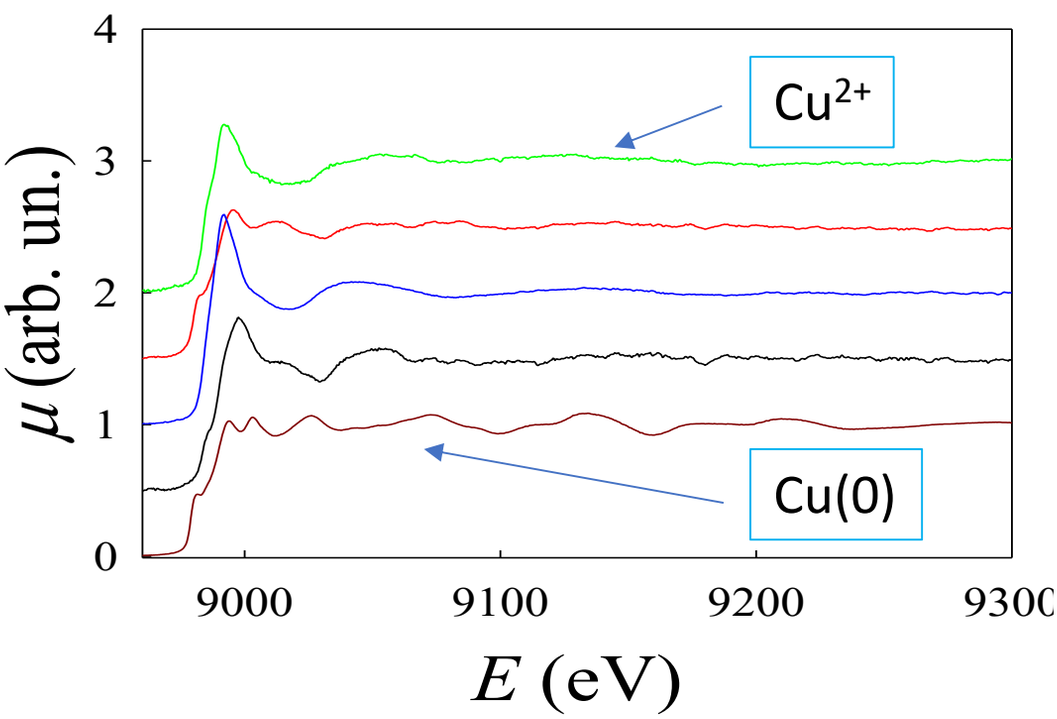

***Figure 232**. XANES spectra in time of Cu(0) stripping from gold nanoparticles in PVA on DropSens® electrode.*

Figure 232 and Figure 233 show the XANES variations with time once the potential for the Cu(0) dissolution is applied. In Figure 232 we can clearly see a shift from the initial signal (in brown) that is the spectrum of metallic copper, to the spectrum of Cu^{2+} in the last measurement (in green). The advantage of EDXAS is the possibility of taking a large number of complete spectra in few milliseconds with an adequate resolution. This allows to follow fast reactions that with normal XAS will end before obtaining a single point in the spectrum. We can see how the change between spectra in time is higher in the ones reported in Figure 233A respect to those of B and C, just because in the first second most of the Cu(0) is dissolved.

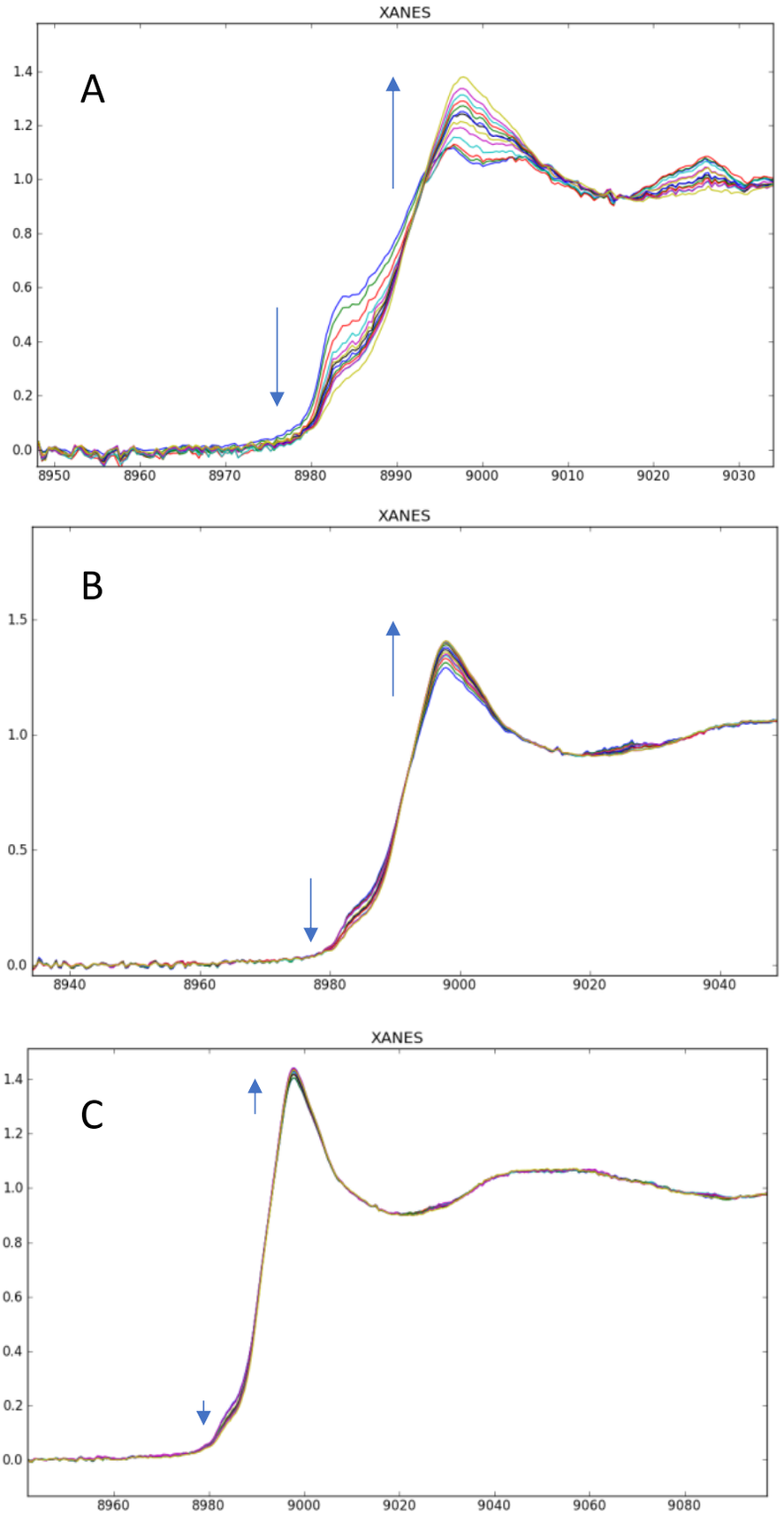

***Figure 233**. Evolution of XANES signal with time from figure A to C we can see the formation of Cu^{2+} ions.*

Calculating the converted fraction for each spectrum it was possible to obtain the plot in Figure 234 where we can see how in less than 5 seconds the amount of metallic copper is quickly reduced to almost zero, while it is found in solution as Cu^{2+}. Being the electrode prepared and stored in air, a small amount of native oxide, CuO, is present on the electrode in the first second of reaction.

Moreover, from this measurement we were able to evaluate the extremely high time resolution of this techniques that is able to acquire a complete spectrum in less than 30ms still maintaining a good resolution and ability to discriminate different species.

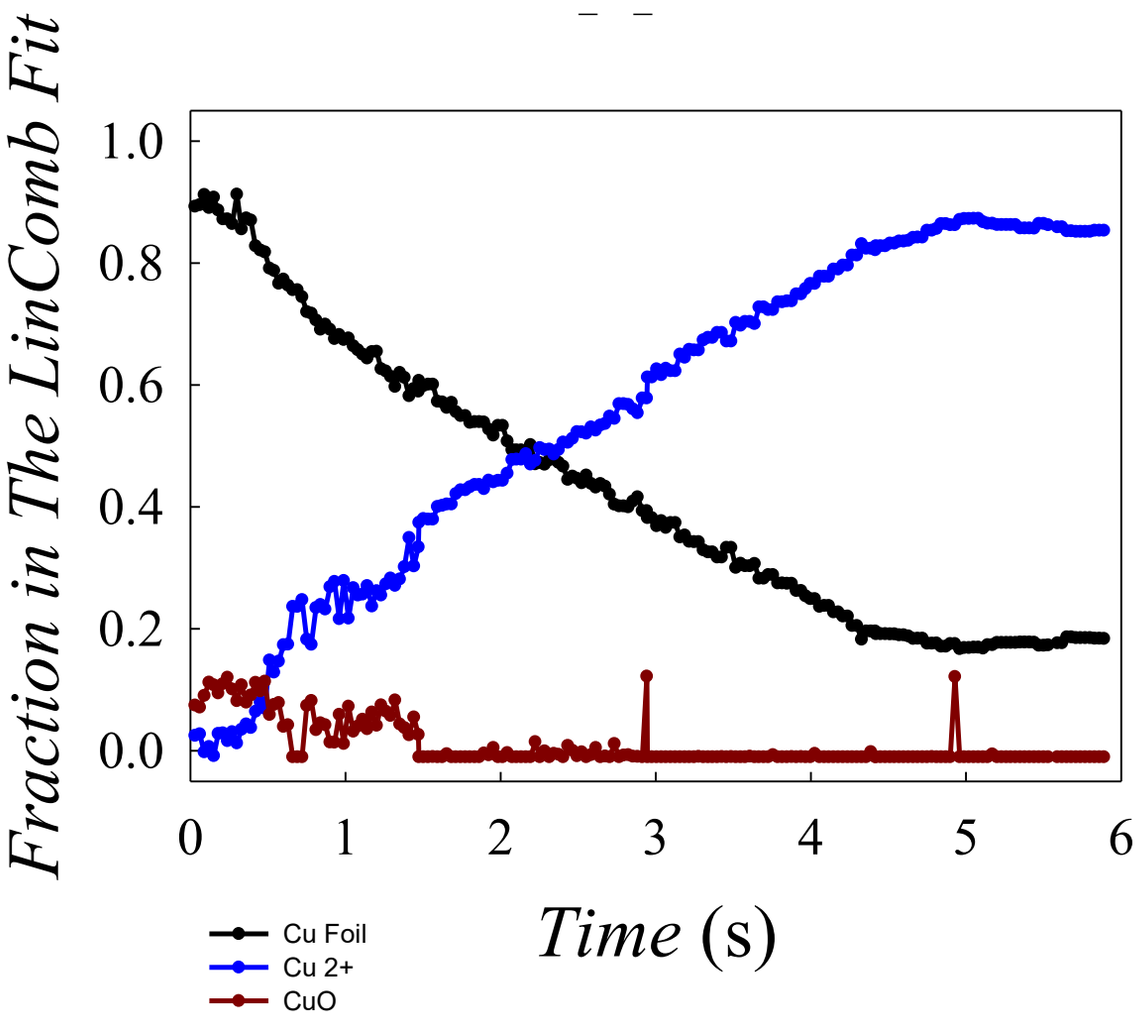

Figure 234. *Fraction of the converted material vs time. In blue the fraction of Cu^{2+} ions, in black the Cu(0) on the electrode and in brown the native CuO formed on the electrode.*

Paper 1: Reverse Type I Core - CuI /shell - Cu_xO: a Versatile Heterostructure for Photoelectrochemical Applications

Here we report the synthesis of a core - CuI / shell - Cu_xO nanostructure that depending on applied potentials works as photocathode or photoanode in neutral pH upon visible light irradiation. Under cathodic polarization, this material generates a stable photocurrent density of about 150 μA/cm^2 but functions as photoanode when anodic polarization is applied, showing a photocurrent density of 40 μA/cm^2. In this new core-shell structure, the relevant position of the band edge potentials is pH–tunable but does not follow the typical Nernstian dependence as shown by many semiconductor oxides, opening new directions in the nanoscale design of stable photoelectrodes for solar water splitting.

Introduction

Very recently, we found that a copper oxide composite prepared from copper iodide acts as a stable and efficient photocathode for hydrogen production in neutral and alkaline pH.[469] Annealing of copper iodide drop-casted on FTO (fluorine doped tin oxide) glass at 400°C led to an effective photoelectrode mainly composed of copper(II) oxide. Here we present a modification of the former approach that leads to a new material consisting of a core - CuI /shell - Cu_xO nanostructure (denoted as CuI/Cu_xO). A core-shell heterostructure prepared by thermal treatment of powder copper iodide in an air atmosphere is presented. Interestingly, this material can act both as photoanode and as photocathode: upon irradiation electrode generates anodic or cathodic photocurrents depending on the applied potential. The potential induced photocurrent switching effect was reported for semiconductors functionalized with metal complexes[470,471], organic modifiers[472] or in composites in which two semiconductors of different conductivity type are present.[473] Photocurrent switching phenomena can be easily observed in semiconducting composites in which two semiconductors of different conductivity type are present[473]. A recently reported composite represents a significant example: an anodic response was produced by α-Fe_2O_3 and the cathodic response by $CuFeO_2$.[474] However, to the authors' best knowledge, it has been never reported in literature that composite such as CuI/CuxO, that is based on two p-type semiconductors can generate both anodic and cathodic photocurrents

Copper iodide is a p-type semiconductor and its photocatalytic activity was evaluated towards carbon dioxide reduction,[475] degradation of organic pollutants,[476] inactivation of microorganisms,[476] dye sensitized solar cell[477] or as a hole-injection layer in OLEDs.[478] The low temperature *γ*-phase is a wide-bandgap semiconductor with bandgap energy close to 3.1 eV[479] and potential of conduction band edge at *ca.* –2.1 V *vs.* SHE (standard hydrogen electrode).[480] Copper oxide(II) is also a p-type semiconductor with a significantly different band structure: its band gap energy varies in the range from 0.7 to 1.6 eV and the valence band edge at about -0.5 eV *vs.* SHE.[481] These features, together with low cost and high abundance make copper oxide a good candidate as a material for photoelectrochemical water splitting,[83,481–483] as well as for photocatalysis and photovoltaics.[484,485]

In semiconducting metal oxides, the flat band potential (V_{FB}) varies linearly with pH with a slope of -0.059 V/pH at 25°C.[383,486] This dependence is based on the fact that H^+ and OH^- are potential determining ions for any oxide in aqueous solutions. Furthermore, also for some non-oxide materials such as FeS_2 and ZnS, the pH dependence was reported to be consistent with the Nernstian relation.[487,488] As suggested by the results shown in the present paper, the flat band potential of CuI/ Cu_xO varies with pH but does not strictly follow the Nernstian relation because of the CuI core, whose energy diagram is not influenced by pH changes. Moreover, the relative position of the bands for the two solids (CuI and CuO) can be tuned by modifying of electrolyte pH.

The presented a CuI/ Cu_xO material can be classified as a reverse type I core-shell heterostructure.[489] In this configuration, the core has a wider band gap than the shell, and the valence and conduction band edges of the shell are located within the band gap of the core. The lowest available exciton energy separation occurs for the charge carriers localized in the shell. Reverse type-I nanostructure is considered to be beneficial in the case of water splitting as demonstrated in literature for In_2O_3–In_2S_3 core–shell nanorods.[490] In a reverse type-I structure, electrons and holes can be preferentially transferred to the shell layer through cascaded energy levels. This may facilitate efficient charge transfer to the aqueous medium, thus enhancing the efficiency of water reduction to H_2. Moreover, in this paper we demonstrate that reverse type-I core–shell CuI/ Cu_xO is not only active for water splitting but can be used also in optoelectronic applications such as switches.

Preparation of Photocatalyst and Photocathode

Nanocrystalline copper iodide has been prepared as follow[469]: a 100 mL of 0.01 M Na_2SO_3 aqueous solution was added to 60 mL of 0.05 M $CuSO_4$ while stirring. A green suspension is obtained; subsequently, 300 mL of a 0.01 M KI solution were added dropwise. The resulting white precipitate is thus separated by centrifugation, washed with water and ethanol, and dried at 80°C for 8 h. The product is CuI, as demonstrated in the following. In order to partially oxidize CuI, the powder was annealed at 400°C in air atmosphere for 1 h. Calcination under a N_2 atmosphere leads to a significantly different product (white-yellowish instead of black) that is not further considered in this work. Finally, the product CuI/Cu_xO was ground in a mortar to obtain a fine powder. Photoelectrodes were prepared from a suspension of CuI/Cu_xO in ethanol (3 mg mL^{-1}) drop-casted on FTO (fluorine doped tin oxide, purchased by Aldrich); FTO was previously washed with diluted H_2SO_4, water, acetone, and ethanol in an ultrasounds bath. The electrode was dried in air at 80°C for 30 min.

Characterization of Materials

Different techniques were used for the characterization of the material:

- High resolution (HR) X-Ray Powder Diffraction (XRPD) measurements on CuI and CuI/Cu_xO samples were performed at room temperature at the ID22 beamline of the European Synchrotron Radiation Facility (ESRF). The polycrystalline samples were loaded in Kapton capillaries (1.0 mm diameter) and spun during measurements in order to improve powder randomization. Data were collected at λ = 0.35423(1) Å in the angular range $2° < 2\vartheta < 28°$ for a total counting time of ~0.5 hours/pattern.

The wavelength was selected using a double-crystal Si(111) monochromator. The diffracted intensities were detected through nine Si(111) analyzer crystals which spanned over 16° in 2ϑ. The instrumental resolution function was determined using Si standard. The XRPD patterns were analyzed via the Rietveld method as implemented in the GSAS software suite of programs[491] featuring the graphical interface EXPGUI.[492] The background was fitted using Chebyshev polynomials. Absorption correction was performed through the Lobanov empirical equation[493] implemented for the Debye-Scherrer geometry. Line profiles were fitted using a modified pseudo-Voigt function[494] accounting for asymmetry correction. Anomalous scattering coefficients f' and f'' for all the atoms were taken from the program *FPrime.*[491]

- UV-Vis diffuse reflectance spectra (DRS) were recorded using a UV-2600 spectrophotometer (*Shimadzu*) equipped with an integrating sphere (15 cm dia.). Barium sulphate was used to dilute the sample and as a reference material. Instrument setup: slit width – 1 nm, threshold 0.001. Powder samples were ground with standard - $BaSO_4$ (1:50 wt. ratio). Commercial samples used for DRS are: CuO (99+%, Acros), Cu_2O (POCH), $BaSO_4$ (dried, Sigma-Aldrich). CuI/Cu_xO was not ground with $BaSO_4$ but analyzed in transmittance mode without filters, from a thin film drop casted on the quartz glass plate (to avoid intense grinding that can influence the core/shell structure). After acquisition, DRS spectra were normalized to 100% and transformed to Kubelka-Munk function.[495]
- Photoluminescence spectra were collected at ambient temperature using FluoroLog-3 (Horiba) spectrofluorometer with R928 photomultiplier tube (Hamamatzu) and cut-off filter 420 nm. Incident light (150XBO - xenon short-arc lamp with monochromator) wavelength was λ= 400 nm. Material suspension (0.01 g dm^{-3} in 1M aqueous phosphate buffer solutions of pH = 7) was prepared by sonication of appropriate amounts of powder for 10 minutes.
- TEM (Transmission Electron Microscopy) and HRTEM (High-Resolution Transmission Electron Microscopy) micrographs were collected by a ZEISS LIBRA 200FE HRTEM. Elemental distribution maps were collected by STEM-EDS analysis (Scanning Transmission Electron Microscopy coupled with an Energy Dispersive X-ray Spectrometry Oxford INCA Energy TEM 200). The specimen was ground in an agate mortar and then dispersed in isopropanol in an ultrasonic bath, then a drop of the suspension was deposited on a holey-carbon supported Molybdenum TEM grid dried overnight and analyzed.
- Electrochemical impedance spectroscopy (EIS) measurements were performed in the following deaerated electrolytes (by means of N_2 bubbling): 1) 0.1 M K_2HPO_4 solution, pH = 9, 2) 0.1 M K_2HPO_4 + KH_2PO_4 solution, pH = 7, 3) 0.1 M K_2HPO_4 + KOH solution, pH = 10.5. Impedance spectra were recorded at a constant potential in the frequency range 10 kHz to 0.1 Hz and 5 mV amplitude using a 1260A Impedance/Gain-Phase Analyzer (*Solartron*). The potential was stepped by 100 mV with a waiting time of 200 s before the next spectrum was recorded. The equivalent circuit used to fit the impedance spectra contains the solution resistance, the polarization resistance and the constant phase element (CPE) associated to the space charge capacitance, C_{SC} (vide infra).

The impedance of the CPE, $Z_{CPE,}$ is given by

$$Z_{CPE} = \frac{1}{Q(j\omega)^{\alpha}} \quad (1)$$

where ω is the frequency and equals unity for an ideal capacitor. When α equals 1, the CPE simplifies to a capacitor, while when α is 0, the CPE represents a pure resistor, and when α equals −1, the CPE behaves as a pure inductor. The CPE is a flexible circuit element, but its physical meaning is still controversial.[496] Since in the present case α was close to 1, we assigned the numerical value of Q to the $C_{SC.}$

Photocatalytic Tests

A three-electrode cell equipped with a home-made light chopper was used in PEC measurements. CuI/Cu_xO on FTO was employed as the working electrode. A saturated calomel electrode (SCE) and a platinum plate were used as the reference and the counter electrodes, respectively. The scan rate for the linear sweep voltammetry was 10 mV s^{-1}. Experiment was controlled by an Autolab PGSTAT204. A solar simulator (Xe lamp coupled with an air mass 1.5 global AM 1.5G filter, purchased by LOT Oriel), UV lamp (HG 200L, 250W, Jelosil Srl) or LED illuminator (λ = 400 nm, LED ENGINE LZ1-00UA00) were used as light source. The following solutions were used as electrolytes: 0.1 M potassium hydrogen phthalate (pH 4), 0.1 M K_2HPO_4 + KH_2PO_4 (pH 7) or 0.1 M K_2HPO_4 (pH 9). Electrolyte was bubbled with nitrogen prior to each experiment.

Scanning electrochemical microscopy (SECM) experiments were carried out using a 920C CH Instrument SECM and a cylindrical cell where the sample is placed horizontally, with the active side facing a cavity-microelectrode tip[126] and using a AgCl/Ag (in 1M KCl) and a glassy carbon rod as the reference and the counter electrode, respectively. Tip generation- Substrate Collection SECM measurements were performed after reaching a 10 µm distance between the cavity-microelectrode and the substrate (platinum plate). The electrolyte (0.1 M K_2HPO_4 + KH_2PO_4 (pH 7)) was bubbled with nitrogen for 30 min before experiments to avoid the influence oxygen, while the cell was covered with Parafilm® and nitrogen sent to form a blanket over the solution/air interface to maintain an inert atmosphere inside. The substrate was polarized at a constant potential while a liner linear sweep function (scan rate 10 mV s^{-1}) was applied to the micro-cavity tip.

The latter was irradiated by a LED placed above the cell – LED illuminated he powder contained in the tip through the glass (with which the microelectrode is made) and after reflection from the underneath Pt plate.

Physico-Chemical Characterization

The chemical composition of the as-prepared material was investigated by using synchrotron XRPD, as shown in Figure 1, that reports patterns of CuI (precursor) and CuI/Cu_xO. The respective refinement results are reported in Table 1. The CuI sample is single phase and only contains highly crystalline Marshite (structure type - sphalerite[497]).

In the CuI/Cu_xO sample the Marshite phase is still observed (weight fraction 40%) beside a monoclinic Tenorite CuO phase.[498] The weight fraction of CuI and CuO is about 40% and 60%, respectively.

Oxygen and copper occupational factors (o.f.) in CuO were varied in preliminary refinements, bringing to oxygen full occupation and to copper almost full occupation (o.f.(Cu) = 0.96(1), see Table 1). For this reason, only The Cu o.f. was varied in the last refinement. The atomic mean square displacements (*U*) values of CuI phase are two-three times larger than the Cu_xO ones. It should be noted that the fits are very sensitive to the *U* values. Attempts to apply constrains, e.g. fixing all the *U* values equal, brought to much poorer fits ($R(F^2)$ = 0.131 instead of 0.036, see Table 1). The very large *U* values detected in the CuI phase could suggest that some static disorder is present in this phase.

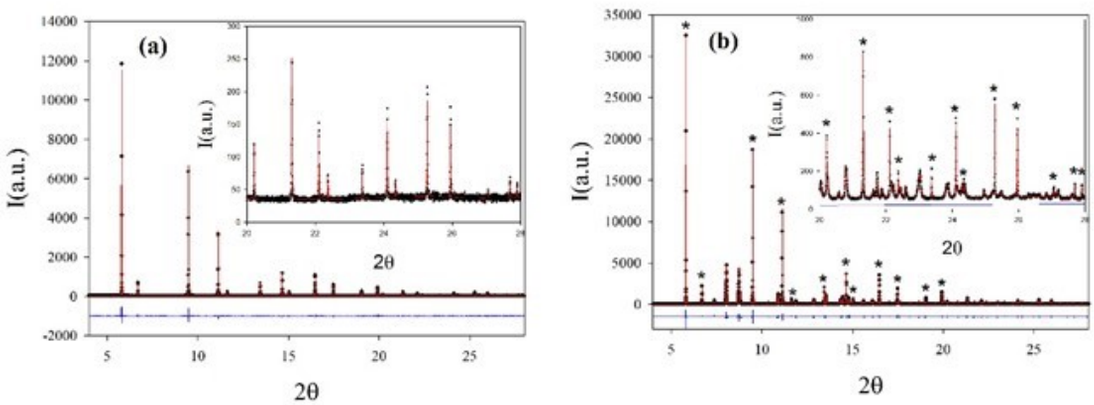

Figure 1. *XRPD patterns of CuI (a) and CuI/Cu_xO (b) samples. Experimental (black crosses) and calculated (red line) profiles are shown as well as background (green line) and residuals (blue line). The insets highlight the high range zone. In Figure b - peaks of CuI phase are labeled by asterisk to distinguish these two phases in this composite (peaks of CuO are not labeled).*

Sample Standard		CuI	CuI/ Cu_xO
CuI	Space group	*F*4-3*m*	*F*4-3*m*
	a/Å	6.05820(1)	6.05697 (1)
	U_{iso}(Cu)/ Å^2	0.0383	0.0356(4)
	U_{iso}(I)/ Å^2	0.0211(2)	0.0197(2)
	WF/%	100	39.7(1)
CuO	Space group	*Phase absent*	*C* 2/*c*
	a/Å	----------	4.68671(3)
	b/Å	----------	3.42749(3)
	c/Å	----------	5.13422(4)
	β/°	----------	99.43(1)°
	o.f.(Cu)	----------	0.96(1)
	y(O)	----------	0.418(1)
	U_{iso}(Cu)/ Å^2	----------	0.0060(2)
	U_{iso}(O)/ Å^2	----------	0.010(1)
	WF	----------	60.3(1)
	$R(F^2)$	0.0959	0.0356
	R_P	0.0493	0.0588

Table 1*. Structural parameters extracted from Rietveld refinement of synchrotron XRPD patterns for CuI (left) and CuI/Cu_xO analyzed. The oxygen y coordinate in Cu_xO is the only positional degree of freedom. o.f.(Cu) is the occupational factor of copper.*

TEM analysis shows shaped and well-defined grains of highly crystalline and poorly aggregated CuI (Figure S1). On the other hand, particles after the thermal treating (the CuI/Cu_xO) appear more aggregate (preserving anyway the original single crystal-core domains), smooth and more roundish (Figure 2 and S2, on the right side).

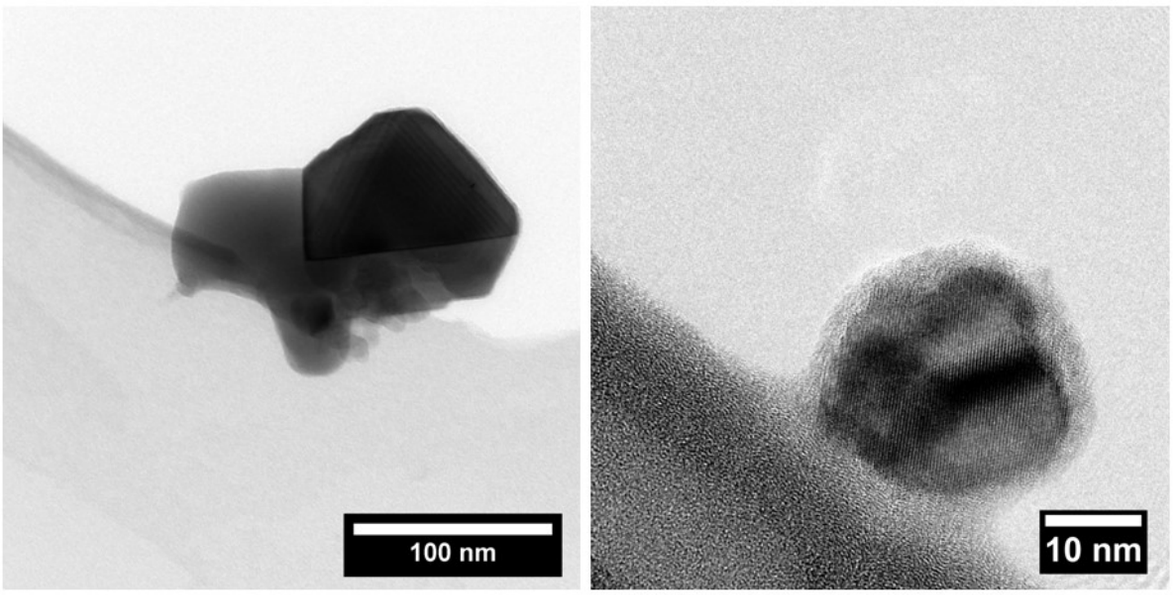

Figure 2. *TEM images of representative CuI/Cu_xO nanoparticles: medium-big aggregates on the left side and small grains on the right side.*

The estimated grain size distribution for both samples (Figure S2) highlights an increase from a median value of 23 nm (CuI) to 32 nm (the CuI/Cu_xO) due to the formation of the Cu_xO layer. The size distribution appears broader and shifted to higher values with the presence of a low amount of big conglomerate up to 120 nm. EDX-STEM maps (Figure 3) on the thermal treated CuI sample for elemental Cu, I and O confirms the presence of a thin oxide shell in the range of 8 to 12 nm thickness. These data are in agreement with the median value deviation estimated by size distribution.

Figure 3 suggests the possible presence of small, exposed CuI spots, as indicated by the white arrows.

Finally, EDX-STEM analysis on randomly selected grains, detected a minority fraction of big nanoparticles appears to be made of CuO only (Figure S3) or with a thinner CuO shell (Figure S4). We believe that the presence of these fractions does not significantly influence the photoelectrochemical behavior of our samples (see, for example, EIS results) but can explain the CuI:CuO 40:60 ratio determined by XRD, which otherwise is apparently not consistent with the reported results.

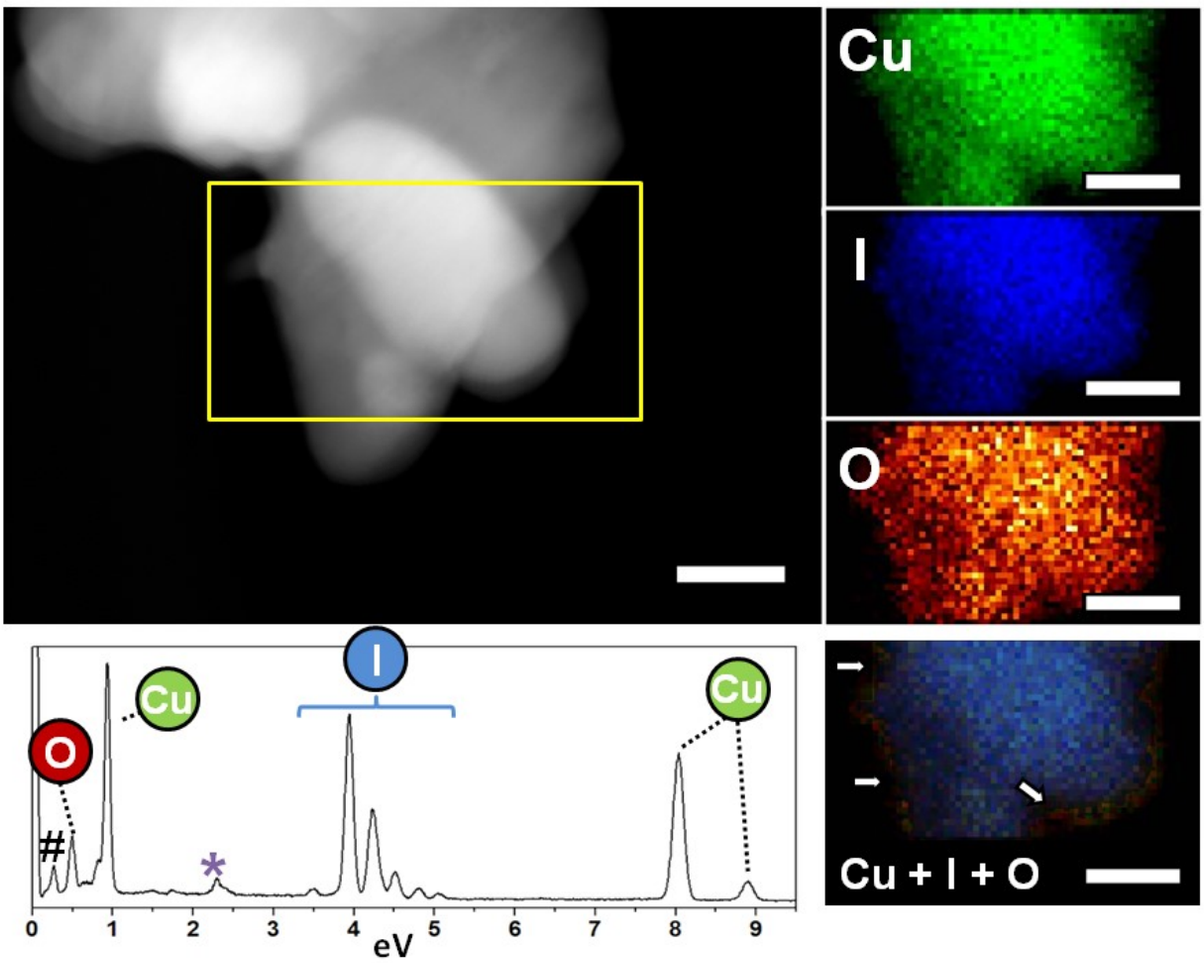

Figure 3. *EDX -STEM mapping of CuI/Cu$_x$O core-shell nanoparticles. Above, STEM micrograph and on the right side related selected area Cu, I and O EDX elemental Maps. Below: EDX spectra of selected area (on the spectra, peaks # and * are C and Mo signals, respectively, from supported holey carbon Molybdenum TEM grid) and composed elemental colour EDX map on the right side. White arrows indicate points of low thickness CuO, where CuI might be exposed to the solution. All scale bars are 50 nm.*

The band gap energy (E_{BG}) was determined by means of diffuse reflectance spectroscopy (DRS) measurements. Reflectance spectra of CuI/Cu$_x$O, CuI (as precursor) and commercially available Cu$_2$O and CuO were transformed to the Kubelka-Munk function (KM) and the results are shown in Figure 4. The Kubelka-Munk functions is given by equation 2:

$$KM = \frac{(1-R_\infty)^2}{2R_\infty} = \frac{\alpha}{S} \qquad (2)$$

where $R_\infty = \frac{R_{sample}}{R_{reference}}$, α and S are an absorption and a scattering coefficient, respectively.

The CuI/Cu$_x$O spectrum shows a broad absorption range, similar to that of copper(II) oxide, but with a clear shift of the absorption onset towards higher photon energy. Moreover, the KM profile of CuI/Cu$_x$O presents a combination of the spectral features of CuI and CuO alone, with CuI absorbing mainly in the UV region, while CuO absorption falling in the visible and near infrared range. From Figure 4a, it is evident that CuI/Cu$_x$O absorbs below 400 nm, where KM function of copper oxide approaches zero, while CuI shows a strong absorption.

This feature is well demonstrated especially for a sample obtained at a lower calcination temperature (see Figure S5), i.e. of a lower CuO:CuI ratio. In this case, the spectrum shows a strong absorption band below 400 nm that stems from CuI due to a thinner oxide external shell.

It is now interesting to determine the band gap of the core-shell material from Tauc plot.[499] The E_{BG} value of CuI/Cu_xO results to be 1.39 eV using the function $(E \cdot KM)^2$ vs E (for direct allowed transitions) where *E* is photon energy, as presented in Figure 4B.

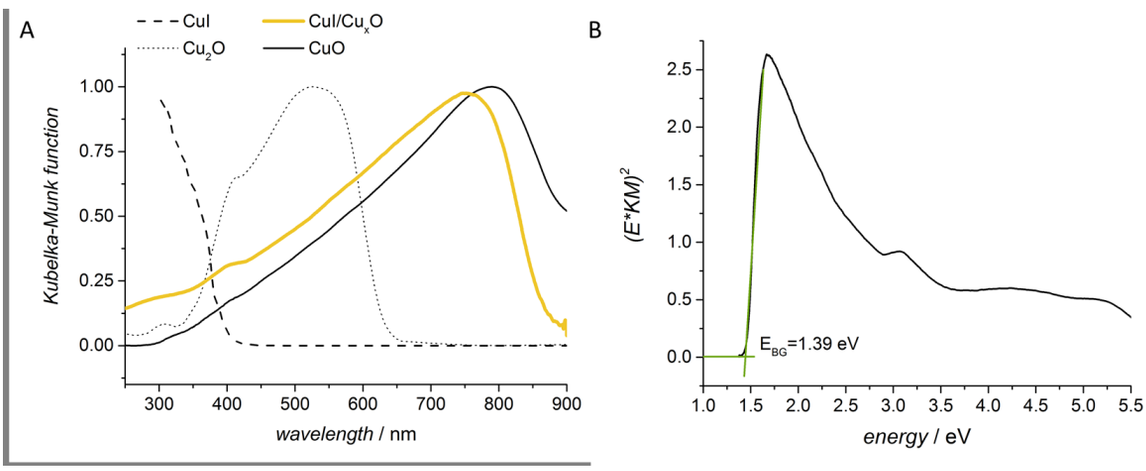

Figure 4. *Diffuse reflectance spectra of the CuI/Cu_xO, CuI (precursor) and commercial Cu_2O and CuO transformed to the Kubelka-Munk function (A). Estimation of band gap energy using a Tauc plot (B).*

Photoluminescence spectroscopy (Figure 5) was used to investigate the electronic properties and to evidence the presence of energy levels within the band gap corresponding to defect sites. In a typical photoluminescence experiment, CuI/Cu_xO was excited by photons with energy (3.1 eV, λ=400 nm) larger than the Cu_xO band gap energy (1.39 eV) but very close to that of CuI (3.05 eV). Photogenerated electrons recombine with holes with emission of photons, which can be observed as a strong luminescence band at about 460 nm, the so-called band-edge emission (transition from conduction to valence band).[469,500,501]

Moreover, the spectrum shows an additional shoulder at about 500 nm, that could be attributed to a defect-related emission. As suggested elsewhere, the green emission arises from the recombination of singly ionized oxygen vacancies with holes from the valence band.[500] The results show also weak emission bands in the red range related to either the recombination of electrons and holes at vacancies, surface defects or a conduction to valence band transition within copper oxide.[233,502] Such lower energetic emission is described also in the literature, for instance as a transition from the conduction band to an acceptor level located above the valence band or from the donor level located below the conduction band to the valence band.[500]

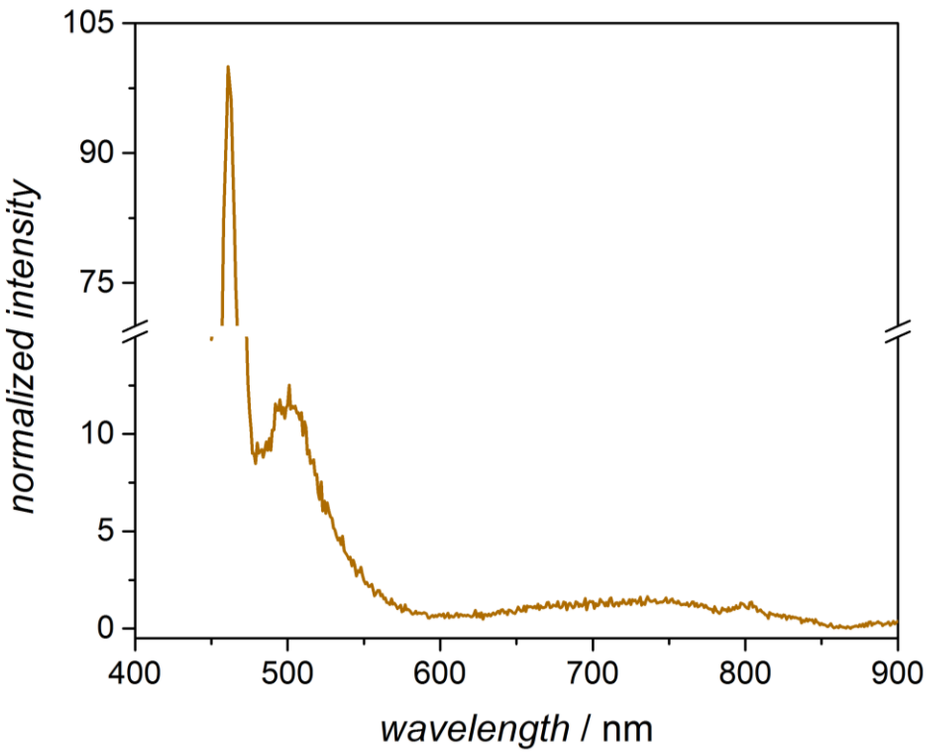

Figure 5. *Emission spectra of CuI/Cu_xO suspensions measured in phosphate buffer solution, pH 7. λ_{exc} = 400 nm, cut-off filter 420 nm.*

Mott–Schottky analysis (from EIS) was used for the estimation of valence band edge potential of CuI/Cu_xO, E_{FB}. To this end, the space charge capacitance (C_{sc}) of the CuI/Cu_xO/solution interface was measured in a selected range of frequencies (0.1 Hz to 10 kHz) and various applied potentials in the range 0.77 to 1.78 V vs RHE (reversible hydrogen electrode) at pH 10.5, pH 9 and pH 7. The results for pH 7 are shown in Figure 6 as a Mott-Schottky plot, where the linear portion is described by the equation:

$$1/C_{SC}^2 = 2/e\varepsilon\varepsilon_0 N\,(E - E_{FB} - kt/e) \qquad (3)$$

where ε is the dielectric constant of the sample, ε_0 is the vacuum permittivity, e is the elementary charge, N is the acceptors concentration (for a p-type semiconductor), E_{FB} is the flat band potential, k is the Boltzmann constant, T the temperature.[503] The Mott-Schottky plot of CuI/Cu_xO exhibits a negative slope, indicating that the core-shell composite has a p-type semiconducting character, the same type as in the case of neat CuI and CuO. The straight line extrapolation leads to 1.29 V vs RHE. Figure 6 presents also the equivalent circuit used to fit the impedance data. Flat band potential of CuI/ Cu_xO changes only slightly with pH and at pH 9 it is higher of about 100 mV in comparison with that in pH 7. The linear pH dependence of V_{VB} with slope of 0.059 V/pH has been found for metal oxide semiconductors and is associated with the protonation/deprotonation equilibrium of the electrode surface:[486] The voltage drop across the Helmholtz double layer is influenced by ionic charges on the surface of materials that depends on pH of electrolyte. For metal halides semiconductors, such as CuI, the pH dependence of E_{FB} appears more unclear than for metal oxides (see, e.g. brown line in Figure 7, relevant to literature data on CuO) due to the lack of OH groups on the surface.

An unresolved issue is thus the nature of potential determining ions. In case of non-oxide materials, such as halide ions (I^-) or chalcogenide ions (HS^-) are potential determining ions, giving rise to a non-Nernstian pH dependence of flat band potential. From Mott-Schottky analysis, it has been found that the flat band potential of copper iodide does not follow the Nernstian relation (green line in Figure 7). The non-Nernstian relation between flat band potential and pH can be rationalized on the basis of all the equilibria involving surface species (adsorption, ionic exchange equilibria).

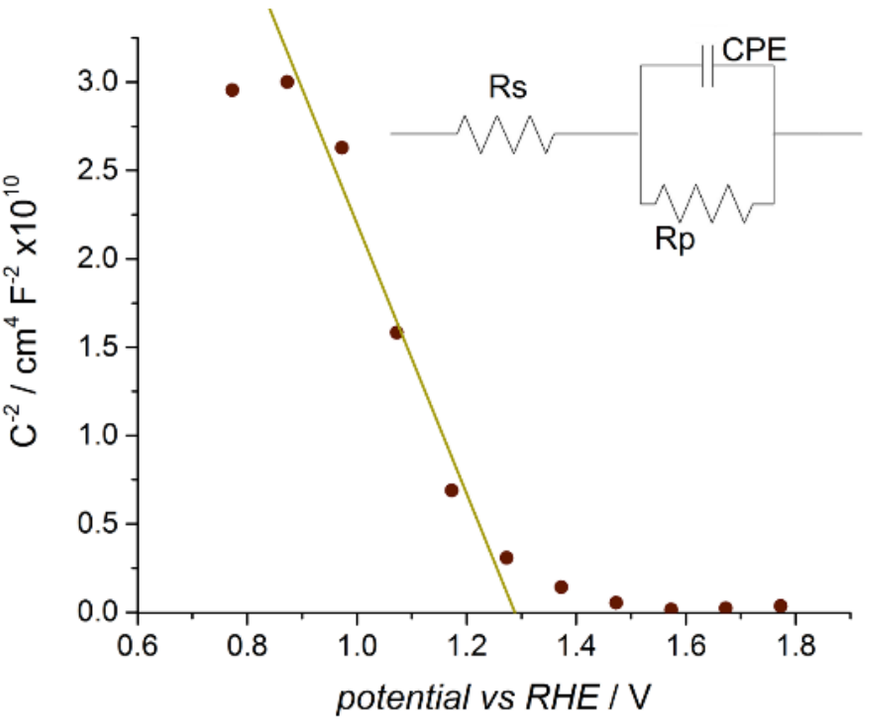

***Figure 6**. Mott-Schottky plot for CuI/Cu_xO at pH 7. E_{FB} calculated from linear fitting (green curve). The inset presents the equivalent circuit used to fit the impedance data, where R_S and R_P rare solution and polarization resistances, respectively, while CPE is a constant phase element.*

Such effect was described in literature also for other materials e.g. InP.[504,505] As shown in Figure 7, the CuI/Cu_xO flat-band potential vs. pH plot is linear but tends to deviate from the expected slope of -0.059 V/pH unit. In addition, its behavior lays in between that of pure CuO and CuI. As noticed, E_{FB} of CuI/Cu_xO depends on pH, although the dependence is not exactly Nernstian, probably also because of the partial exposure of CuI to the electrolyte, as evidenced earlier. In summary, these preliminary evidences suggest that the new material acquires mainly the superficial properties of the shell but is strongly influenced by the core nature. This is in line with the results from EDX-TEM (Figure 3) that show the thin nature of the shell layer (less than 10 nm) compared to a rather "bulky" core.

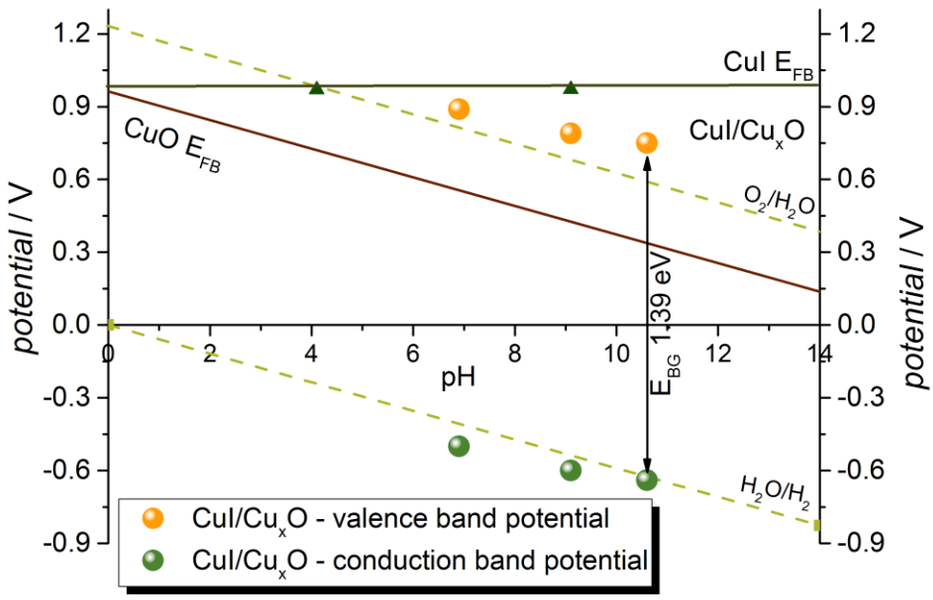

Figure 7. *pH dependence of flat-band potentials vs SHE (E_{FB}) for CuO (continuous line, data from literature [506]), CuI (triangles) and CuI/ Cu_xO (circles). Conduction band potential estimated from E_{FB} and band gap energy.*

Photoelectrochemical Activity

The peculiar structure of CuI/Cu_xO strongly affects its photoelectrochemical features. A typical voltammogram recorded upon chopped solar light irradiation (AM 1.5 G) for CuI/Cu_xO is presented in Figure 8. The current density changes sign by varying the applied potential and the crossover is at 0.68 V vs RHE. This potential approximately coincides with the triple point equilibrium between Cu^+, Cu_2O and some Cu(II) species, as is apparent from Pourbaix diagrams.[507] Note that quite understandably, the cathodic photocurrent is more pronounced and reaches 150 μA/cm^2 at 0.3 V, while the anodic one limits to 40 μA/cm^2 at 1.3 V. Notwithstanding the difference in magnitude (about 1:4), the observed anodic photocurrent is quite unexpected for a p-type material. We suggest that it could be due to: 1) its unique structure, and specifically to its inner core, which favors charge transport as will be discussed below; and/or 2) the nanosize of the material, for which concepts like band bending and space charge loose physical meaning.[508] Therefore, under appropriate applied potentials also anodic photocurrents can be recorded in a nanocrystalline p-type semiconductor being not hindered by a severe internal potential barrier. The photocurrent switching potential is independent from the light wavelength.[473] In the same conditions (pH, absence of oxygen) the photocurrent switching was observed for the same potential using various wavelengths of incident light (in the range 400-850 nm). Moreover, using ultraviolet as an incident light does not change the material behavior and current switching occurs at the same potential (Figure S6, in pH 9). However, the current density is lower than under full solar spectrum. It is worth noting that the dark currents at potentials lower that 0.68 V (Figure 8) can be attributed to a partial reduction from Cu(II) to Cu(I)[507] and that the presence/absence of oxygen does not influence the photocurrent density (Figure S7).

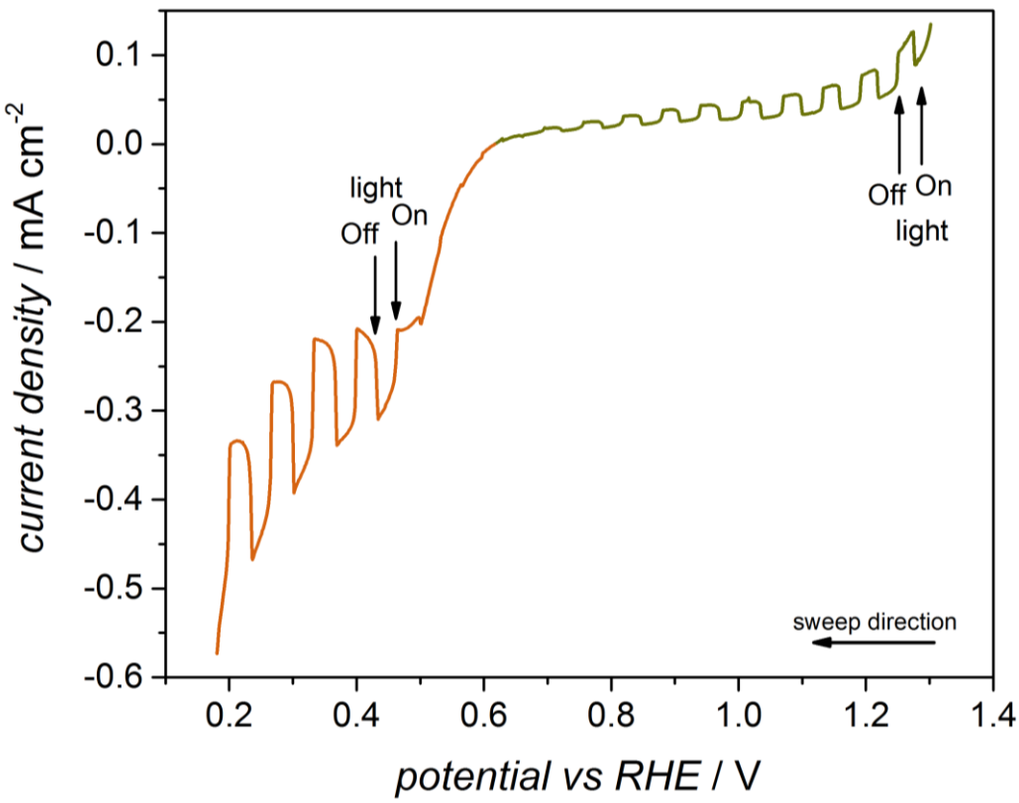

Figure 8. *Voltammogram recorded upon chopped light irradiation (solar simulator, with AM 1.5 global filter) for CuI/ Cu_xO in deoxygenated 0.1 M K_2HPO_4 + KH_2PO_4 (pH 7). Green line – anodic photocurrent, brown line – cathodic photocurrent.*

As evident from Figure 8, the photoelectrode performance does not compete with other systems proposed in the literature, where the photocurrent reached values in the mA scales. At the same time, it is hard to compare the facile preparation and the single-element nature of the present composite with multicomponent, multilayered photoelectrodes (see for example, the "limit" case of the 5-component photocathode FTO/Au/Cu_2O/Al:ZnO/TiO_2/RuO_x[509]). We believe that suitable nanostructuring/engineering and the addition of over-/under-layer would lead to a significant increase of photocurrents. In fact, charge recombination may lead to a significant decrease of photocurrent density but can be partially blocked by addition of suitable overlayers.[510]

In addition, photocorrosion/degradation reactions represent an additional reason for low photocurrent densities. As indicated above, low potential dark currents (Figure 8) are likely related to CuO reduction. To further investigate this aspect, we added spectroscopic investigations. The unbiased electrode was irradiated in phosphate solution at pH 7 for several hours using LED λ = 400 nm; during irradiation, the changes of UV-Vis spectrum were observed by DRS. Light-induced processes led to the increase of the band between 200 nm and 400 nm (Figure 9), similar to that of CuI. This can be related with progressive photodissolution or photoleaching of outer Cu_xO shell thus partially exposing the core CuI.

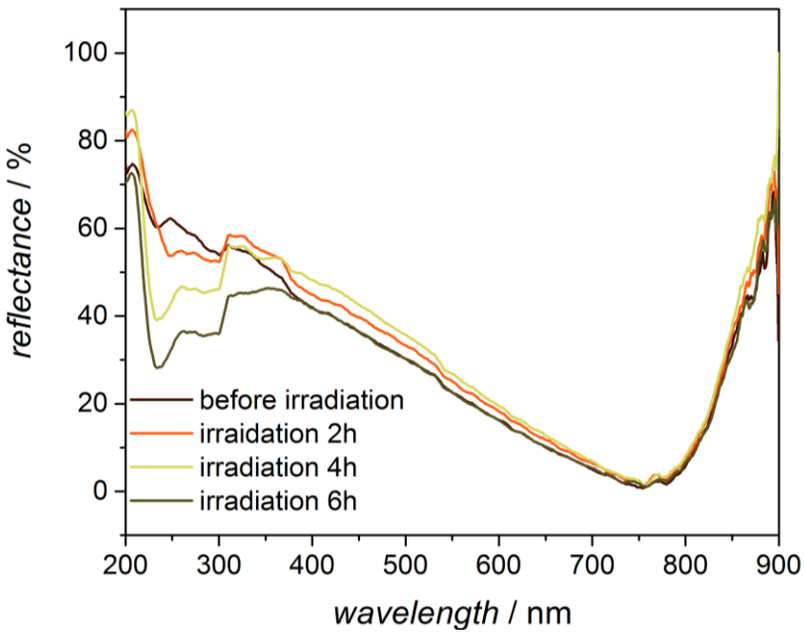

Figure 9. *Reflectance spectra up to 6 h irradiation of CuI/ Cu_xO electrode in 0.1 M K_2HPO_4 + KH_2PO_4 (pH 7).*

The activity of CuI/Cu_xO core-shell structure depends on pH as shown in Figure 10. As for the previously reported Cu_xO,[469] the semiconductor is particularly active in neutral pH. In acidic solution, the cathodic photocurrent density is comparable to pH 7, while the anodic one is significantly lower. The lowest photocurrent was observed in alkaline solution.

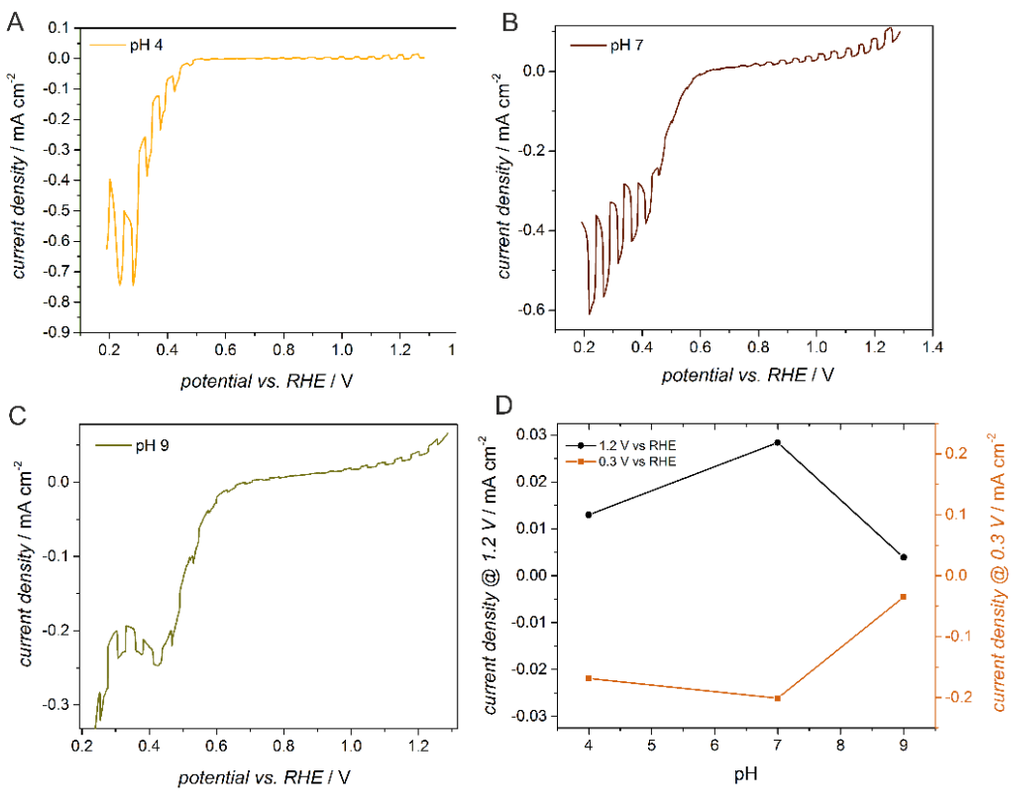

Figure 10. *Voltammograms recorded upon chopped light irradiation (LED λ = 400 nm) for CuI/ Cu_xO in electrolytes of various pH: 4 (A), 7 (B), 9 (C) - sweep direction: from higher to lower potentials. (D): current density as a function of pH.*

The influence of pH on the photoelectrochemical performance can be explained based on different aspects, that will be further discussed in the discussion section.

According to the Poubarix diagram, materials are less stable in pH $\leq$ 4 and the highest stability is observed at neural pH.[507]

Moreover, Figure S8 demonstrates the influence of annealing temperature on the materials photoactivity (to be compared with DRS spectra obtained by various annealing temperatures (Figure S5). It is evident that photocurrent densities reach the highest values for the sample calcined at 400°C, followed by the one treated at 500°C.

The incident photon to current efficiency (IPCE) was determined at pH = 7 and at 0.3 V vs. RHE (cathodic photocurrent) and at 1.0 V vs. RHE (anodic photocurrent). As shown in Figure 11 A, IPCE varies from 2% to more than 8% and cathodic photocurrents are generally characterized by the highest IPCE values. Moreover, IPCE measured at 0.3 V vs. RHE in the 400 nm – 600 nm range, are almost equal and reach the lowest values at 700 nm. At all wavelengths, the IPCE measured at 1.0 V vs. RHE is lower than at 0.3 V vs. RHE. Obviously, cathodic photocurrents are generated by a different mechanism than anodic ones, thus the changes of IPCE are not related each other. The quite high IPCE over this broad wavelength range indicates a broad-band visible light absorption and efficient carrier transport in the material and at the material/electrolyte interface. Both cathodic and anodic photocurrents are generated in the whole wavelength range (Figure 11 B) and the wavelength does not affect the potential at which photocurrent switching occurs (see above).

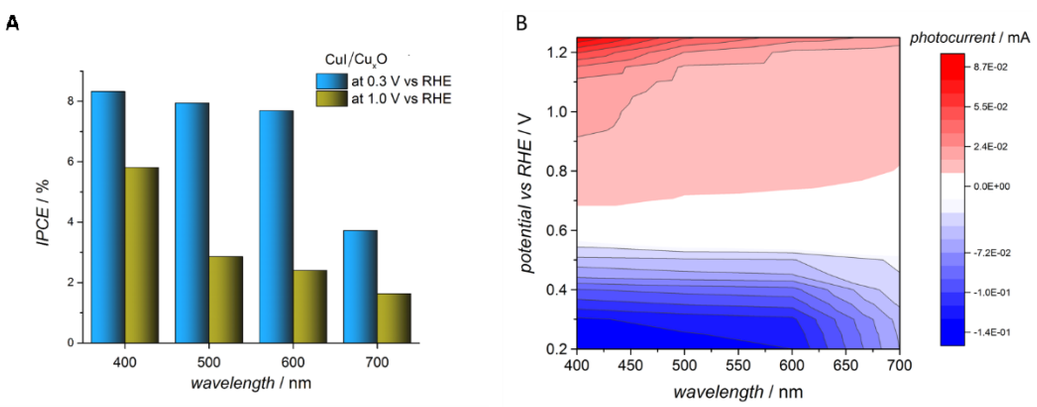

Figure 11. *Influence of incident light wavelength on the activity of CuI/ Cu_xO. A - IPCE measured for selected wavelength at 0.3 vs. RHE and 1.0 V vs RHE, B - dependence of current density on wavelength and applied potential. All data were obtained in phosphate solution at pH = 7, using solar simulator equipped with band pass filters.*

Photocurrent efficiency towards H_2 production was determined using a novel method implemented on the scanning electrochemical microscope (SECM). Here, SECM is used in the tip generation-substrate collection mode, and uses a cavity microelectrode filled with photocatalyst powder (microcavity tip) facing a large metallic electrode (substrate). In the present set up, the products of the reduction reaction at the powder in the microcavity tip diffuse within the gap between the two electrodes and can be collected and reoxidized at the metallic substrate with 100% collection efficiency.

The potentials of the tip and substrate electrodes are controlled by a bipotentiostat. The large substrate was polarized at a value higher enough than the equilibrium potential of the H_2/H_2O redox couple to guarantee mass-transfer diffusion control. In the present case, a microcavity tip filled with CuI/Cu_xO was placed 10 μm above a platinum plate. The latter was polarized at 0.77 V *vs*. RHE while a linear sweep potential in the range 0.45 V to 0.60 V *vs*. RHE was applied at the tip. Upon irradiation with chopped light cathodic photocurrent generated at the material was observed. At the same time, a current related to H_2 oxidation at the Pt electrode appeared, as shown in Figure 12. Thanks to this configuration, the ratio between the photocurrent generated by the material placed in the cavity (denoted as *t* in Figure 12) and the current measured on the Pt substrate (denoted as *s*), directly gives the photocurrent efficiency for hydrogen produced at the tip, whose average value is 82%. The residual current is attributed to the parallel reaction, namely reduction of oxygen.

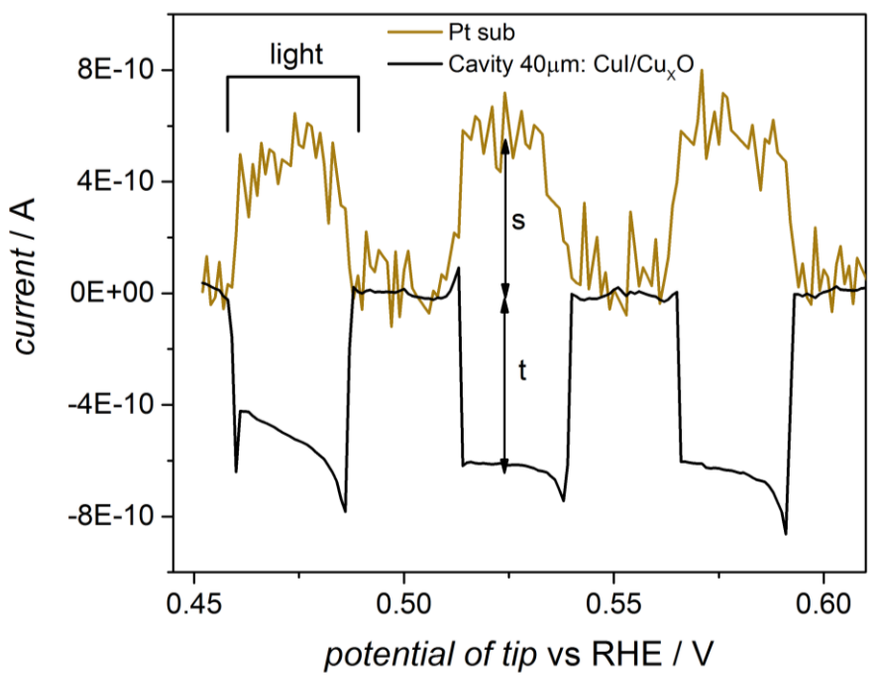

***Figure 12**. SECM detection of hydrogen production at the CuI/Cu_xO placed in microcavity tip upon chopped light (λ = 400 nm). Linear sweep potential at tip electrode and chronoamperometric measurement at Pt substrate electrode.*

Discussion

The core-shell CuI/Cu_xO prepared by thermal treatment of nanocrystalline copper iodide powder shows two interesting properties: a potential-induced reductive-oxidative photocurrent switching effect and a pH-tunable relation between the band edges of the core (pH independent) and the shell (pH dependent, being H^+ a potential determining ion), that will be better discussed further on. The core-shell nature of the material was confirmed by XRPD, HRTEM and EDX TEM mapping. Since that core's band gap straddles that of the shell, CuI/Cu_xO can be classified as a reverse type I core-shell heterostructure (see Figure 13).

As demonstrated in the present work, the flat band potential of CuI/Cu_xO varies with pH but deviates from the Nernstian relation (0.059 V per pH unit).

Therefore, the electronic properties of the resulting core-shell material are pH-tunable, as also evident from the voltamperometric characterization.

As mentioned in Introduction copper iodide and copper oxide are both p-type semiconductors and, in principle, only cathodic photocurrents should be observed. However, upon positive polarization, anodic photocurrents were generated. Figure 13 presents a schematic energy diagram of the composite material and shows simplified pathway of charges transition. The main simplification is the absence of any schematization for the band bending induced by the current collector potential, which obviously greatly influences the material's behavior. Our best explanation considers that, when the photoelectrode is illuminated and polarized at lower potentials (Figure 13 A), the electrons from conduction band of semiconductor reduce water to hydrogen, while photogenerated holes are collected by the conducting support (FTO) and a cathodic current is observed. Three various cases can be considered: i) visible light only: results in the excitation of CuO while CuI remains inactive. Still, at least from a thermodynamic point of view, photogenerated electrons from the conduction band of CuO are able to reduce water; ii) visible + UV light (AM 1.5G): leads to excitation of both, CuI and CuO and the observed photocurrent origins from both semiconductors; iii) under only UV light also cathodic photocurrent is generated. Under opposite conditions, as shown in Figure 13 B, the electrode is polarized at potentials higher (more positive) than the valence band potential of CuI/ Cu_xO (see the Mott-Schottky analysis) and electrons are collected by the conducting support while photogenerated holes can oxidize water (since V_{VB} is more positive than the $E^0_{H2O/O2}$). Photogenerated holes from the CuI valence band can be transferred to CuO due to their higher potential The applied potential (bias) is a driving force for photogenerated charge carriers' migration. For this reason, low potentials (Fig. 13 A) holes preferentially migrate towards the current collector and do not oxidize water, while the opposite occurs under positive potential (Fig.13 B), where electrons are driven preferentially towards the current collector. The proposed mechanism is in agreement with several literature examples.[511,512]

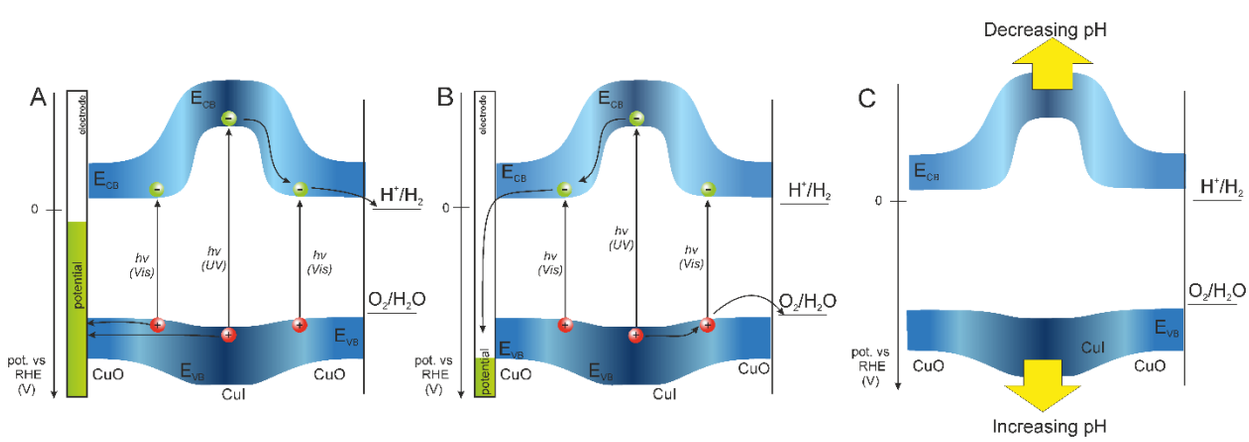

Figure 13. *Schematic energy diagrams of photocatalytic water splitting at core-shell CuI/ Cu_xO electrodes at pH 7: (A) photocathodic behavior, (B) photoanodic behavior, (C) dependence on pH (non-considering any non-Nernstian behavior). The green bar on the left of A and B indicates the applied potential. Potential-induced bands bending is not shown in order to simplify the scheme.*

Figure 13C tentatively explains the pH dependence of the recorded photocurrents and thus the pH tunable features of the material. In fact, one might want to consider the relative shift of band edges with pH. Even considering a partial exposure of CuI at the electrolyte, the material is characterized by a shell with pH-dependent band edges and a core with pH-independent ones.

This leads to a pH tuning effect that has important consequences on the observed photocurrents and that could be adopted as materials design strategy in other combination of materials and in other types of applications.

About the here presented material, in acidic electrolyte the CuI valence band energy could reach higher values that the CuO one, thus inverting the beneficial hole cascade effect and decreasing photocurrents, as observed for the results showed at pH4. In neutral environments the CuI bands straddle those of CuO and the materials behave as schematized in Figure 13 A and B. On the other extreme, i.e. at high pHs, we have to consider the non-nernstian behavior of the core-shell material (see Figure 7) whose conduction band edge potential reaches the H_2O/H_2 couple equilibrium potential. Even in the presence of an applied potential, this could explain the lower cathodic activity observed in alkaline media.

Moreover, as suggested elsewhere, the differences in pH may be reflected in various mechanism of charge transfer at the electrode/electrolyte interface and on the various nature of the surface sites active.[513]

As stated before, the character of photocurrent generated by CuI/Cu_xO depends on the photoelectrode potential: for potentials higher than 0.68 V vs RHE anodic photocurrents are observed, while for potentials lower than 0.58 V vs. RHE the electrode generates cathodic photocurrents (see Figure 11B). This potential induced photocurrent switching effect allows using CuI/Cu_xO in various applications, e.g. as a data selector in logic gates.[471] In this type of device, the system accepts information encoded in light and returns it as a current, depending on the applied potential. The current answer (return signal) can be positive or negative (the signal could be directed into various channels (p- or n-channel) as shown in Figure 14A). As shown in Figure 14B, a third answer is possible in the absence of light or for 0.58 V < E < 0.68 V the answer is “zero”.

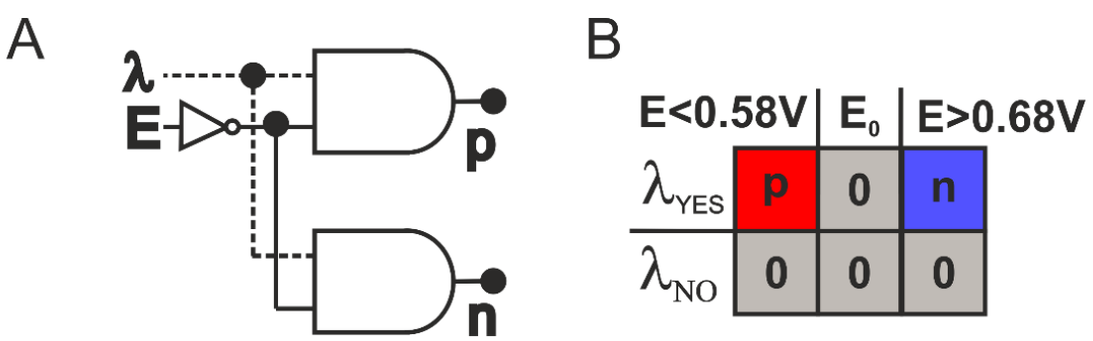

Figure 14. *Hypothetical logic gate based on CuI/Cu_xO – gate scheme (A) and corresponding table (B) where E values are vs. RHE and $0.58<E_0<0.68$ V. λ- light, E – applied potential.*

Conclusions

In the present paper, a facile method to prepare reverse type I core/shell CuI/Cu_xO material by a thermal treatment of nanocrystalline copper iodide is reported. The synthetized material can act as photocathode (under more negative potential) or photoanode (under more positive potential) for photoelectrocatalytic water splitting. Upon ultraviolet as well as visible light irradiation, CuI/Cu_xO reduces or oxidizes water, depending on working conditions as observed by generated anodic or cathodic photocurrent. Besides the photocurrent switching, the photoelectrode shows also ability to change the mutual relation between band edges (at least flat band potential) of the core (CuI) and the shell (CuO) upon pH change, following a non-Nernstian behaviour. CuI/Cu_xO is very promising not only for photoelectrochemical water splitting but also due to its unique properties for optoelectronic gates or solar cell. We believe that this material's design could be successfully extended towards other combination of materials and for different applications.

Supporting Info

1. TEM Images

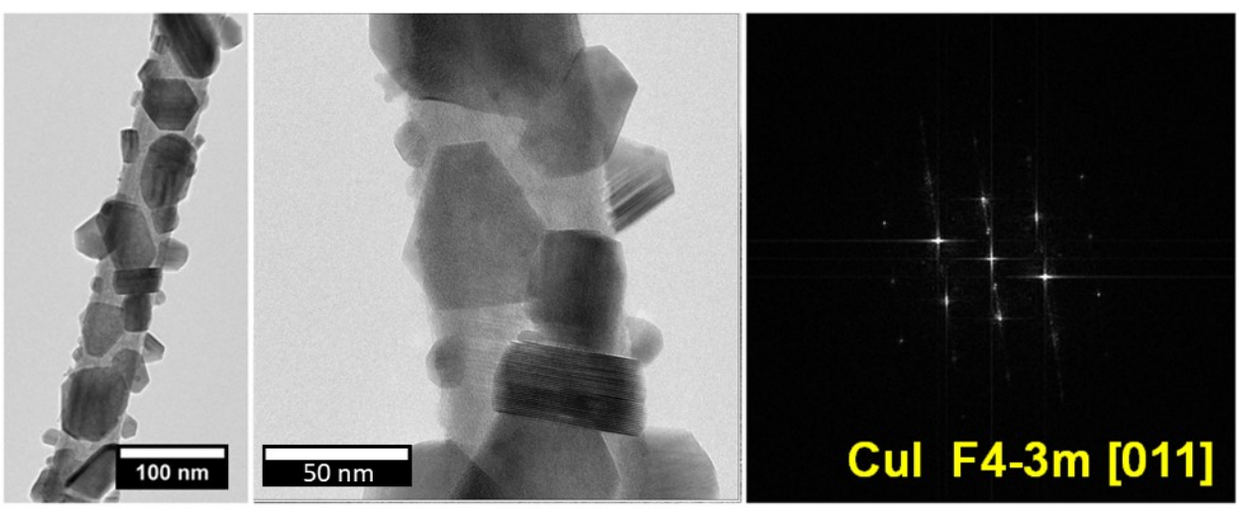

Figure S1. *TEM images and HRTEM details of CuI nanoparticles. On the right side, the FFT (Fast Fourier Transform) image calculated from the selected area (see the related square area on the middle HRTEM micrograph) show the high CuI crystallinity.*

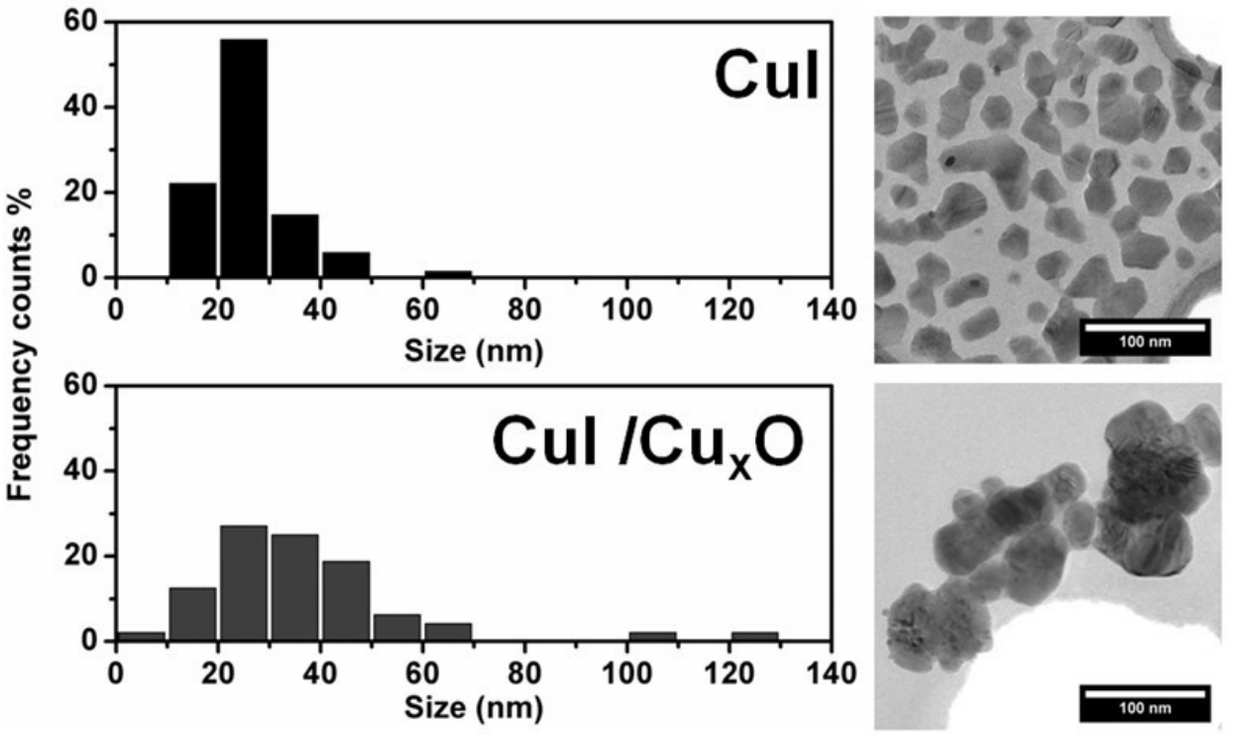

Figure S2. *Particle size distribution for samples CuI and CuI/Cu_xO and related representative TEM micrographs on the right side.*

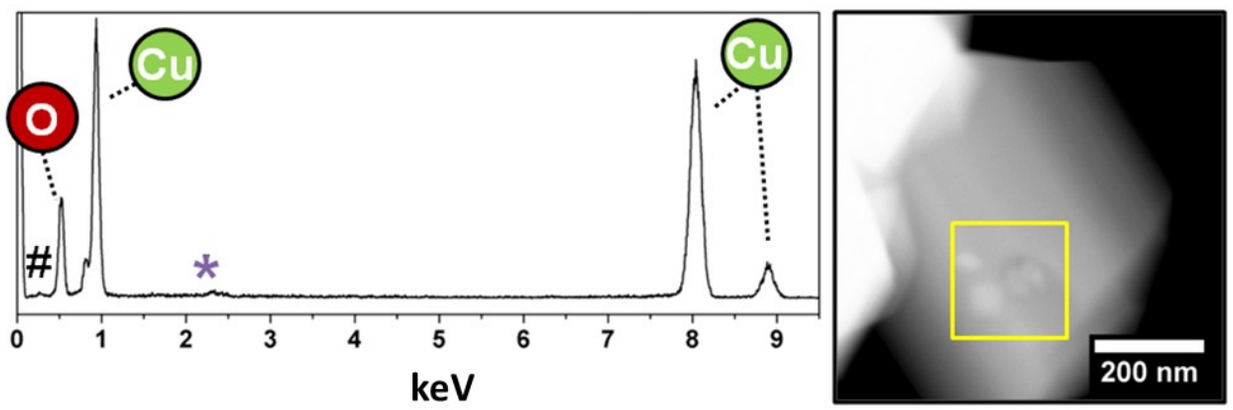

Figure S3*. EDX spectra of selected area (on the spectra, peaks # and * are C and Mo signals, respectively, from supported holey carbon Molybdenum TEM grid) of a big particle of CuO, related STEM micrograph on the right side.*

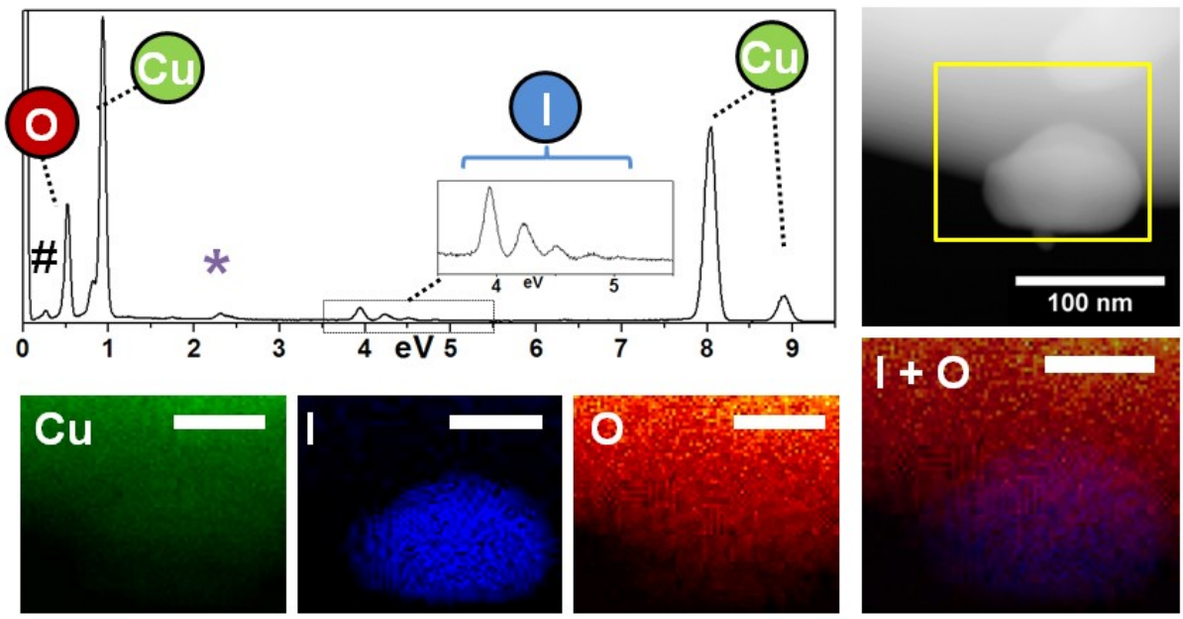

Figure S4. *EDX -STEM mapping of CuI/Cu$_x$O core-shell nanoparticles. Above, EDX spectra of selected area (on the spectra, peaks # and * are C and Mo signals, respectively, from supported holey carbon Molybdenum TEM grid) and, on the right side, related STEM micrograph. Below: Cu, I and O EDX elemental Maps and composed I+O elemental colour EDX map on the right side. All scale bars are 50 nm if not specified.*

2. The influence of Annealing Temperature on the UV-Vis Spectrum

The influence of annealing temperature on the UV-Vis spectrum has been studied by Diffuse Reflectance Spectroscopy by UV-2600 Shimadzu spectrophotometer equipped with integrating sphere. Two materials were studied: CuI/Cu$_x$O obtained at 200°C and 400°C

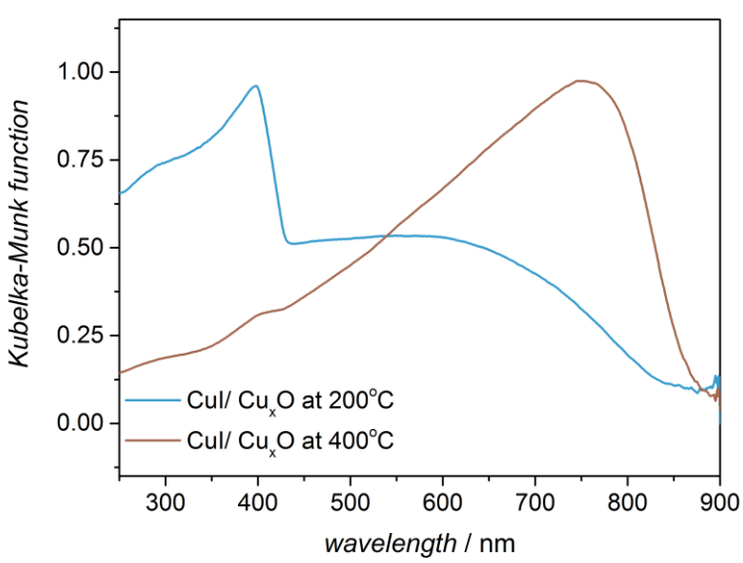

Figure S5. *Diffuse reflectance spectra of the CuI/Cu$_x$O obtained at 200°C and 400°C transformed to the Kubelka-Munk function.*

3. The influence of Light Wavelength

Figure S6 shows the photocurrent registered under UV irradiation in electrolyte of pH 9.

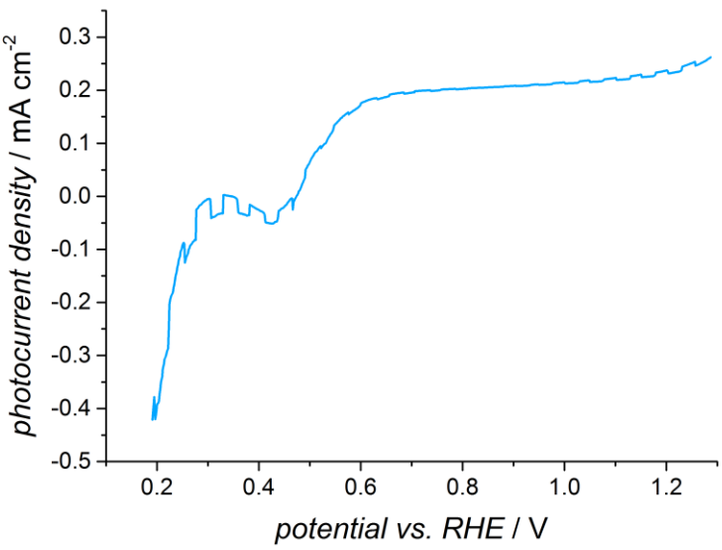

Figure S6. *Voltammograms recorded upon chopped light irradiation (UV) for CuI/ Cu_xO in electrolytes of pH 9.*

4. The Influence of Oxygen

The influence of oxygen on the photocurrent generation was investigated using chronoamperometric technique at 1 V vs RHE in 0.1 M K_2HPO_4 + KH_2PO_4 (pH = 7) under chopped illumination with solar simulator. Results shown in figure S4 proved almost equal photocurrent density obtained in electrolyte saturated with nitrogen an in the presence of oxygen (under air atmosphere).

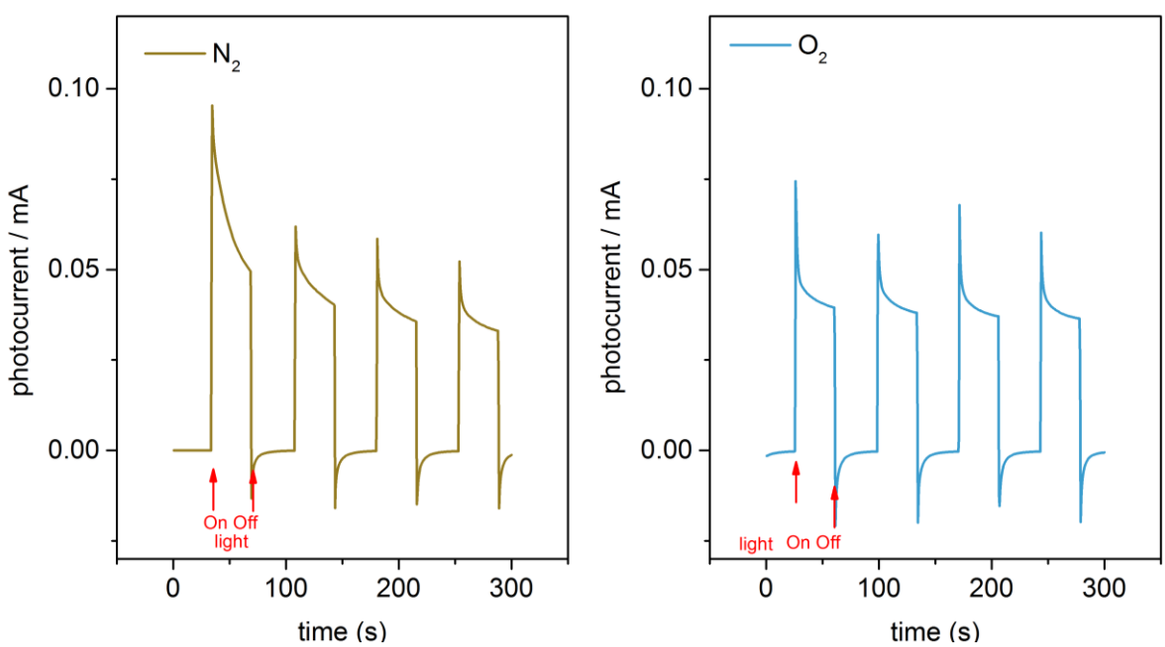

Figure S7. *Chronoamperometric measurement at 1 V vs RHE in 0.1 M K_2HPO_4 + KH_2PO_4 (pH = 7) under chopped illumination with solar simulator. Left– test in electrolyte saturated with nitrogen; right - test in the presence of oxygen (air atmosphere). SCE – reference electrode, Pt plate – counter electrode.*

5. The influence of Annealing Temperature on the Activity.

Prepared copper iodide was annealed at 500°C 400°C, 200°C or 50°C in air atmosphere for 1 h. Photoelectrodes were prepared from a suspension of as prepared materials in ethanol (3 mg mL^{-1}) drop-casted on FTO glass. Voltammograms of prepared photoelectrodes recorded under chopped light.

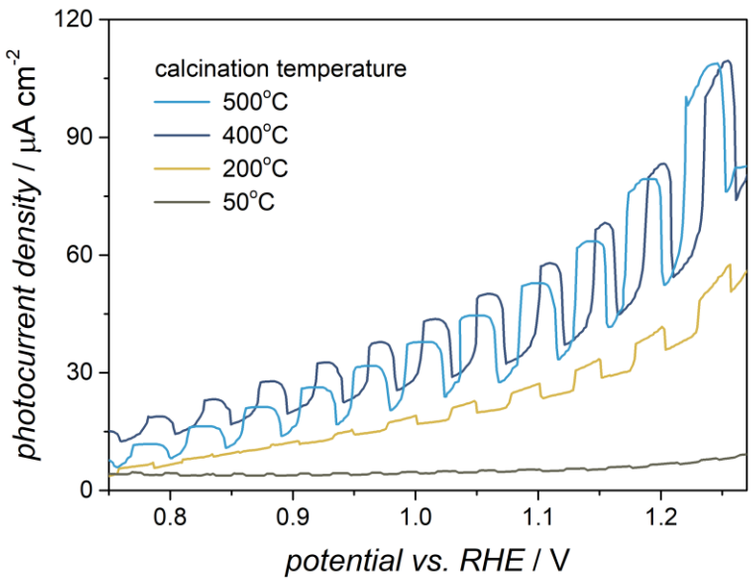

Figure S8. *Voltammograms recorded upon chopped light irradiation (LED 400 nm) for CuI calcinated in various temperatures (50°C, 200°C, 400°C, 500°C) in deoxygenated 0.1 M K_2HPO_4 + KH_2PO_4 (pH 7).*

List of Figures

List of Acronyms (in order of appearance)

IEA = International Energy Agency

OECD = Organization for Economic Co-operation and Development

PV = Photovoltaic

LED = Light Emitting Diode

ESD = Energy Storage Devices

SMES = Superconductive Magnetic Energy Storage

DOE = U.S Department Of Energy

FC = Fuel Cell

VRE = Variable Renewable Energies

FCEV= Fuel Cell Electric Vehicles

STCH= Solar ThermoChemical Hydrogen

PEC = PhotoElectroChemical

PEC-WS = PhotoElectroChemical Water Splitting

MOF = Metal Oxide Framework

STH = Solar To Hydrogen

VB = Valence Band

CB = Conduction Band

Eg = Band Gap (in eV)

HER = Hydrogen Evolution Reaction

OER = Oxygen Evolution Reaction

D = Donor

A= Acceptor

NP = Nanoparticles

PV-NP = Photovoltaic Nanoparticles

UV = Ultraviolet

BG = Band Gap

NHE = Normal hydrogen Electrode

XRD = X-ray Diffraction

XAS = X-ray Absorption Spectroscopy

XAFS = X-ray Absorption Fine Structure

EXAFS = Extended X-ray Absorption Fine Structure

XANES = X-ray Absorption Near Edge Structure

FEXRAV = Fixed Energy X-ray Absorption Voltammetry

EDXAS = Energy Dispersive X-ray Absorption Spectroscopy

Linac = Linear Accelerator

SECM = Scanning ElectroChemical Microscopy

TG/SC = Tip Generation / Substrate Collection

SG/TC = Substrate Generation / Tip Collection

UME = Ultra Micro Electrode

C-ME = Cavity Micro Electrode

SCJL = Semiconductor-liquid Junction

CNT = Carbon Nanotubes

PVD = Physical Vapour Deposition

CVD = Chemical Vapour Deposition

ALD = Atomic Layer Deposition

RGO = Reduced Graphene Oxide

ECF= Electrochemically Chlorine Free

DSA = Dimensionally Stable Anode

OCP = Open Circuit Potential

DFT = Density Functional Theory

LDA = Local Density Approximation

GGA = Generalized Gradient Approximation

PBE = Perdew-Burke-Ernzerhof

HSE = Heyd-Scuseria-Ernzerhof

DOS = Density Of States

CPU = Central Processing Units

RAM = Random Access Memory

C3SE = Chalmers Centre for Computational Science and Engineering

TMs = Transition Metals

TCO = Transparent Conductive Oxide

ITO = Indium Tin Oxide

FTO = Fluorine Tin doped Oxide

AFM = Atomic Force Microscopy

IBSC = Intermediate Band Solar Cell

IB = Intermediate Band

SEM = Scanning Electron Microscopy

SS = Solar Simulator

EIS = Electrochemical Impedance Spectroscopy

SCE = Saturated Calomel Electrode

RHE = Reversible Hydrogen Electrode

EDX = Energy Dispersive X-ray

UPD = Under Potential Deposition

CV = Cyclic Voltammetry

LSV = Linear Sweep Voltammetry

ESRF = European Synchrotron Radiation Facility

MM = Molecular Mass

BM = Beamline

GOF = Goodness of Fit

TCD = Thermal Conductivity Detector

GC = Gas Chromatography

IPCE = Incident Photon to Current efficiency

ORR = Oxygen Reduction Reaction

WE = Working Electrode

ASTM = American Society for Testing and Materials

TBA = Tetrabutylammonium

GC = Glassy Carbon

PVA = Polyvinyl Alcohol

DS = DropSens®

OLED = Organic Light Emitting Diode

XRPD = X-ray Powder Diffraction

TEM = Transmission Electron Microscopy

HRTEM = High Resolution Transmission Electron Microscopy

DRS = Diffuse Reflectance Spectrum

STEM = Scanning Transmission Electron Microscopy

KM = Kubelka-Munk

Units of Measurement

Units	Name
Toe	Ton of oil equivalent
Wh	Watt-hour
g	Gram
L	Liter
m	Meter
gge	Gasoline gallon equivalent
V	Volt
eV	Elettronvolt
psi	Pound per square inch
atm	Atmosphere
Pa	Pascal
S	Siemens
Hz	Hertz
A	Ampere
C	Coulomb
F	Farad
K	Kelvin
Ω	Ohm
Å	Armstrong
W	Watt
s	Second
J	Joule
mol	Mole
A.M	Air mass

References

(1) International Energy Agency (IEA). *Key World Energy Trends Excerpt from: World Energy Balances*; 2016.

(2) U.S. Department of Energy (DOE). *Annual Energy Outlook 2015 with projection to 2040*; 2015; Vol. 1.

(3) EIA. *Annual Energy Outlook 2017 with projections to 2050*; 2017.

(4) International Energy Agency (IEA). *Next Generation Wind and Solar Power: from Cost to Value*; 2016.

(5) International Energy Agency (IEA). *Next Generation Wind and Solar Power*; 2016.

(6) International Energy Agency (IEA). *Technology Roadmap: Solar Photovoltaic Energy*; 2014.

(7) Yang, Z.; Zhang, J.; Kintner-Meyer, M. C. W.; Lu, X.; Choi, D.; Lemmon, J. P.; Liu, J. *Chem. Rev.* **2011**, *111* (5), 3577–3613.

(8) Liu, J.; Zhang, J. G.; Yang, Z.; Lemmon, J. P.; Imhoff, C.; Graff, G. L.; Li, L.; Hu, J.; Wang, C.; Xiao, J.; Xia, G.; Viswanathan, V. V.; Baskaran, S.; Sprenkle, V.; Li, X.; Shao, Y.; Schwenzer, B. *Adv. Funct. Mater.* **2013**, *23* (8), 929–946.

(9) Christen, T.; W.Carlen, M. *J. Power Sources* **2000**, *91* (2), 210–216.

(10) Barnhart, C. J.; Benson, S. M. *Energy Environ. Sci.* **2013**, *6* (4), 1083.

(11) Schon, T. B. *Chem. Soc. Rev.* **2016**, *45*, 22.

(12) International Energy Agency (IEA). *Status of Power System Transformation: System integration and local grids*; 2017.

(13) International Energy Agency (IEA). *Technology Roadmap: Hydrogen and Fuel Cells*; 2015.

(14) U.S. DRIVE Patnership. *U. S. Drive* **2013**, No. June, 98.

(15) International Energy Agency (IEA). *World Energy Outlook 2016*; 2016.

(16) International Energy Agency (IEA). *Hydrogen Production & Distribution*; 2007.

(17) U.S. Department of Energy (DOE). *Multi-Year Research, Development, and Demonstration Plan: Fuel Cells*; 2016; Vol. 2015.

(18) U.S. Department of Energy (DOE). *Multi-Year Research, Development, and Demonstration Plan: Hydrogen Storage*; 2015.

(19) Melaina, M.; Penev, M. *Natl. Renew. Energy Lab.* **2013**, No. September, 1–46.

(20) Ruth, M.; Joseck, F. *Hydrogen Threshold Cost Calculation*; 2011.

(21) Deutsch, T. G.; Contact, P.; Turner, J. A.; Young, J. L.; Döscher, H.; Wang, H.; Peterson, D. *High Efficiency Tandem Absorbers for Economical Solar Hydrogen Production*; 2015.

(22) U.S. Department of Energy (DOE). *Multi-Year Research, Development, and Demonstration Plan: Market Transformation*; 2015.

(23) International Energy Agency (IEA). *The power of transformation: Wind, Sun and the Economics of Flexible Power System*; 2014.

(24) Honda, K.; Fujishima, A. *Nature* **1972**, *238*, 37.

(25) Bicelli, L. P.; Scrosati, B. *Semiconductor material*.

(26) Beranek, R. *Adv. Phys. Chem.* **2011**, 20.

(27) Beranek, R. *Adv. Phys. Chem.* **2011**, *2011*.

(28) Graetzel, M.; Regan, B. O. *Nature* **1991**, *353*, 737.

(29) Lewis, N. S. *Nature* **2001**, *314*, 589.

(30) Jiménez Reinosa, J.; Leret, P.; Álvarez-Docio, C. M.; Del Campo, A.; Fernández, J. F. *Bol. la Soc. Esp. Ceram. y Vidr.* **2016**, *55* (2), 55–62.

(31) Kisch, H. *Angew. Rev.* **2013**, *52*, 812–847.

(32) Chen, S.; Wang, L. W. *Chem. Mater.* **2012**, *24*, 3659.

(33) James, B. D.; Baum, G. N.; Perez, J.; Baum, K. N. *Technoeconomic Analysis of Photoelectrochemical (PEC) Hydrogen Production*; 2009; Vol. 22201.

(34) Nandy, S.; Banerjee, A.; Fortunato, E.; Martins, R. *Rev. Adv. Sci. Eng.* **2013**, *2* (4), 273–304.

(35) Elliott, R. *Phys. Rev.* **1961**, *124*, 340.

(36) Bard, A. J.; Fan, F.-R. F.; Kwak, J.; Lev, O. *Anal. Chem.* **1989**, *61* (2), 132–138.

(37) Mittal, R.; Chaplot, S. L.; Mishra, S. K.; Bose, P. P. *Phys. Rev. B* **2007**, *75*, 174303.

(38) Werner, A.; Hocheimer, H. D. *Phys. Rev. B* **1982**, *25*, 5929.

(39) Timm, H.; Janek, J. *Solid State Ion.* **2005**, *176*, 1131.

(40) Tertian, L.; Hokim, D.; Riviere, J. P. *J. Phys.* **1978**, *39*, 1135.

(41) Ito, T.; Masumi, T. *J. Phys. Soc. Japan* **1997**, *66*, 2185.

(42) Baumeister, P. W. *Phys. Rev. B* **1961**, *121*, 359.

(43) Ito, T.; Yamaguchi, H.; Okabe, K.; Masumi, T. *J. Mater. Sci.* **1998**, *33*, 3555.

(44) Li, Y.; Zhang, X.; Chen, H.; Li, Y. *Catal. Commun.* **2015**, *66*, 1–5.

(45) Musa, A. O.; Akomolafe, T.; Carter, M. J. *Sol. Energ. Mat. Sol. Cell* **1998**, *51*, 305.

(46) Hsu, Y. K.; Yu, C. H.; Chen, Y. C.; Lin, Y. G. *J. Power Sources* **2013**, *242*, 541–547.

(47) Luo, J.; Steier, L.; Son, M.; Schreier, M.; Mayer, M. T.; Gra, M. **2016**.

(48) Wan, L.; Wang, Z.; Yang, Z.; Luo, W.; Li, Z.; Zou, Z. *J. Cryst. Growth* **2010**, *312* (21), 3085–3090.

(49) Stareck. Decorating Metals, 1937.

(50) Ng, S. Y.; Ngan, A. H. W. *Electrochim. Acta* **2011**, *56* (22), 7686–7695.

(51) Hu, F.; Chan, K. C.; Yue, T. M.; Surya, C. *Thin Solid Films* **2014**, *550*, 17–21.

(52) de Jongh, P. E.; Vanmaekelbergh, D.; Kelly, J. J. *Chem. Mater.* **1999**, *11* (12), 3512–3517.

(53) Mao, Y.; He, J.; Sun, X.; Li, W.; Lu, X.; Gan, J.; Liu, Z.; Gong, L.; Chen, J.; Liu, P.; Tong, Y. *Electrochim. Acta* **2012**, *62*, 1–7.

(54) Zhao, W.; Fu, W.; Yang, H.; Tian, C.; Ge, R.; Wang, C.; Liu, Z.; Zhang, Y.; Li, M.; Li, Y. *Appl. Surf. Sci.* **2010**, *256* (7), 2269–2275.

(55) Daltin, A. L.; Bohr, F.; Chopart, J. P. *Electrochim. Acta* **2009**, *54* (24), 5813–5817.

(56) Golden, T. D.; Shumsky, M. G.; Zhou, Y.; VanderWerf, R. A.; Van Leeuwen, R. A.; Switzer, J. A. *Chem. Mater.* **1996**, *8* (10), 2499–2504.

(57) Paracchino, A.; Laporte, V.; Sivula, K.; Grätzel, M.; Thimsen, E. *Nat. Mater.* **2011**, *10* (6), 456–461.

(58) Paracchino, A. *J. Phys. Chem. C* **2012**, *116*, 7341–7350.

(59) Lin, C.; Lai, Y.; Mersch, D.; Reisner, E. *Chem. Sci.* **2012**, *3* (3), 3482–3487.

(60) Nian, J. N.; Hu, C. C.; Teng, H. *Int. J. Hydrogen Energy* **2008**, *33* (12), 2897–2903.

(61) Mahalingam, T.; Chitra, J. S. P.; Chu, J. P.; Sebastian, P. J. *Mater. Lett.* **2004**, *58* (11), 1802–1807.

(62) Wu, G.; Zhai, W.; Sun, F.; Chen, W.; Pan, Z.; Li, W. *Mater. Res. Bull.* **2012**, *47* (12), 4026–4030.

(63) Yang, H.; Ouyang, J.; Tang, A.; Xiao, Y.; Li, X.; Dong, X.; Yu, Y. *Mater. Res. Bull.* **2006**, *41* (7), 1310–1318.

(64) Qiu, H.; Lu, L.; Huang, X.; Qu, Y. *Electrochim. Acta* **2010**, *56* (1), 291–296.

(65) Song, H. C.; Cho, Y. S.; Huh, Y. D. *Mater. Lett.* **2008**, *62* (10–11), 1734–1736.

(66) Huang, L.; Peng, F.; Yu, H.; Wang, H. *Mater. Res. Bull.* **2008**, *43* (11), 3047–3053.

(67) Ma, L. L.; Li, J. L.; Sun, H. Z.; Qiu, M. Q.; Wang, J. B.; Chen, J. Y.; Yu, Y. *Mater. Res. Bull.* **2010**, *45* (8), 961–968.

(68) Zhu, J.; Wang, Y.; Wang, X.; Yang, X.; Lu, L. *Powder Technol.* **2008**, *181* (3), 249–254.

(69) Huang, X. W.; Liu, Z. J.; Zheng, Y. F. *Chinese Chem. Lett.* **2011**, *22* (7), 879–882.

(70) Bai, Y.; Yang, T.; Gu, Q.; Cheng, G.; Zheng, R. *Powder Technol.* **2012**, *227*, 35–42.

(71) Shin, H. S.; Song, J. Y.; Yu, J. *Mater. Lett.* **2009**, *63* (3–4), 397–399.

(72) Dodoo-Arhin, D.; Leoni, M.; Scardi, P.; Garnier, E.; Mittiga, A. *Mater. Chem. Phys.* **2010**, *122* (2–3), 602–608.

(73) Grez, P.; Herrera, F.; Riveros, G.; Henríquez, R.; Ramírez, A.; Muñoz, E.; Dalchiele, E. A.; Celedón, C.; Schrebler, R. *Mater. Lett.* **2013**, *92*, 413–416.

(74) Wang, Y. Q.; Liang, W. S.; Satti, A.; Nikitin, K. *J. Cryst. Growth* **2010**, *312* (9), 1605–1609.

(75) Zhang, H.; Cui, Z. *Mater. Res. Bull.* **2008**, *43* (6), 1583–1589.

(76) Zhu, J.; Bi, H.; Wang, Y.; Wang, X.; Yang, X.; Lu, L. *Mater. Lett.* **2008**, *62*, 2081–2083.

(77) Zhang, X.; Cui, Z. *Mater. Sci. Eng. B Solid-State Mater. Adv. Technol.* **2009**, *162* (2), 82–86.

(78) Liang, Z. H.; Zhu, Y. J. *Mater. Lett.* **2005**, *59* (19–20), 2423–2425.

(79) Kuo, C. H.; Huang, M. H. *Nano Today* **2010**, *5* (2), 106–116.

(80) Luo, Y.; Tu, Y.; Ren, Q.; Dai, X.; Xing, L.; Li, J. *J. Solid State Chem.* **2009**, *182* (1), 182–186.

(81) Wang, H.; He, S.; Yu, S.; Shi, T.; Jiang, S. *Powder Technol.* **2009**, *193* (2), 182–186.

(82) Sui, Y.; Zhang, Y.; Fu, W.; Yang, H.; Zhao, Q.; Sun, P.; Ma, D.; Yuan, M.; Li, Y.; Zou, G. *J. Cryst. Growth* **2009**, *311* (8), 2285–2290.

(83) Lim, Y.-F.; Chua, C. S.; Lee, C. J. J.; Chi, D. *Phys. Chem. Chem. Phys.* **2014**, *16* (47), 25928–25934.

(84) Wei, M.; Huo, J. *Mater. Chem. Phys.* **2010**, *121* (1–2), 291–294.

(85) Wei, M.; Lun, N.; Ma, X.; Wen, S. *Mater. Lett.* **2007**, *61* (11–12), 2147–2150.

(86) Qu, Y.; Li, X.; Chen, G.; Zhang, H.; Chen, Y. *Mater. Lett.* **2008**, *62* (6–7), 886–888.

(87) Susman, M. D.; Feldman, Y.; Vaskevich, A.; Rubinstein, I. *ACS Sustain. Chem. Eng.* **2014**, *8* (1), 162–174.

(88) Balamurugan, B.; Mehta, B. R. *Thin Solid Films* **2001**, *396* (1–2), 90–96.

(89) Al-Kuhaili, M. F. *Vacuum* **2008**, *82* (6), 623–629.

(90) Barreca, D.; Comini, E.; Gasparotto, A.; Maccato, C.; Sada, C.; Sberveglieri, G.; Tondello, E. *Sensors Actuators, B Chem.* **2009**, *141* (1), 270–275.

(91) Wang, S.; Zhang, X.; Pan, L.; Zhao, F.; Zou, J.; Zhang, T.; Wang, L. *Appl. Catal. B Environ.* **2015**, *164*, 234–240.

(92) Ma, D.; Liu, H.; Yang, H.; Fu, W.; Zhang, Y.; Yuan, M.; Sun, P.; Zhou, X. *Mater. Chem. Phys.* **2009**, *116* (2–3), 458–463.

(93) Valodkar, M.; Pal, A.; Thakore, S. *J. Alloys Compd.* **2011**, *509* (2), 523–528.

(94) Togashi, T.; Hitaka, H.; Ohara, S.; Naka, T.; Takami, S.; Adschiri, T. *Mater. Lett.* **2010**, *64* (9), 1049–1051.

(95) Neskovska, R.; Ristova, M.; Velevska, J.; Ristov, M. *Thin Solid Films* **2007**, *515* (11), 4717–4721.

(96) Itoh, T.; Maki, K. *Vacuum* **2007**, *81* (9), 1068–1076.

(97) Konigsberger, D. C.; Prins, R. *Xray Absorption: Principles, Applications, Techniques of EXAFS, SEXAFS, and XANES, in Chemical Analysis*; Sons, J. W. &, Ed.; 1988.

(98) Newville, M. *Fundamentals of XAS*; Chicago University, Ed.; Chicago, 2004.

(99) Gaur, A.; Shrivastava, B. D.; Nigam, H. L. *Proc. Indian Natl. Sci. Acad.* **2013**, *79*, 921–966.

(100) Minguzzi, A.; Lugaresi, O.; Locatelli, C.; Rondinini, S.; D'Acapito, F.; Achilli, E.; Ghigna, P. *Anal. Chem.* **2013**, *85* (15), 7009.

(101) Rondinini, S.; Minguzzi, A.; Achilli, E.; Locatelli, C.; Agostini, G.; Pascarelli, S.; Spinolo, G.; Vertova, A.; Ghigna, P. *Electrochim. Acta* **2016**, *212*, 247–253.

(102) Rondinini, S. *J. Electroanal. Chem. 766*, 71–77.

(103) Minguzzi, A.; Lugaresi, O.; Locatelli, C.; Rondinini, S.; D'Acapito, F.; Achilli, E.; Ghigna, P. *Anal. Chem.* **2013**, *85* (15), 7009–7013.

(104) Pascarelli, S.; Aquilanti, G.; Dubrovinsky, L.; Guilera, G.; Mathon, O.; Muñoz, M.; Newton, M. A.; Pasquale, M.; Trapananti, A. *AIP Conf. Proc.* **2007**, *882*, 608–612.

(105) Wittstock, G.; Schumann, W. *Anal. Chem.* **1997**, *69*, 5059.

(106) Bard, A. J.; Faulkner, L. R. *Electrochemical methods: Foundamentals and Applications*; John Wiley & Sons, Ed.

(107) Bard, A. J.; Mirkin, V. *Scanning Electrochemical Microscopy Second Edition*.

(108) Minguzzi, A.; Alpuche-Aviles, M. A.; Rodríguez López, J.; Rondinini, S.; Bard, A. J. *Anal. Chem.* **2008**, *80*, 4055.

(109) Fernández, J. L.; Walsh, D. A.; Bard, A. J. *J. Am. Chem. Soc.* **2005**, *127*, 357.

(110) Lugaresi, O.; Perales-Rondon, J. V.; Minguzzi, A.; Solla-Gullon, J.; Rondinini, S.; Feliu, J. M.; Sanchez-Sanchez, C. M. *Appl. Catal. B Environ.* **2015**, *163*, 554–563.

(111) Rodríguez-López, J.; Minguzzi, A.; Bard, A. J. *J. Phys. Chem. C* **2010**, *114*, 18645.

(112) Lhenry, S. *Phys. Chem. Chem. Phys.* **2017**, *19*, 4627–4635.

(113) Bertoncello, P. *Energy Environ. Sci.* **2010**, *3*, 1620–1633.

(114) Walsh, D. A. *Chem. Soc. Rev.* **2010**, *39*, 4185–4194.

(115) Leonard, K. C.; Bard, A. J. *J. Am. Chem. Soc.* **2013**, *135* (42), 15890–15896.

(116) Wain, A. *Electrochim. Acta* **2013**, *92*, 383–391.

(117) Lee, J.; Ye, H.; Pan, S.; Bard, A. J. *Anal. Chem.* **2008**, *80*, 7445.

(118) Kylberg, W.; Wain, A. J.; Castro, F. A. *J. Phys. Chem. C* **2012**, *116*, 17384–17392.

(119) Minguzzi, A.; Alpuche-Aviles, M. A.; López, J. R.; Rondinini, S.; Bard, A. J. *Anal. Chem.* **2008**, *80* (11), 4055–4064.

(120) Cachet-Vivier, C.; Keddam, M.; Vivier, V.; Yu, L. T. *J. Electroanal.Chem* **2013**, *20*, 688.

(121) Li, C. M.; Hu, W. *J.Electroanal. Chem* **2012**, *12*, 688.

(122) Sun, P.; Mirkin, M. V. *Anal. Chem.* **2007**, *79*, 5809–5816.

(123) Minguzzi, A.; Locatelli, C.; Cappelletti, G.; Scavini, M.; Vertova, A.; Ghigna, P.; Rondinini, S. *J. Phys. Chem. A* **2012**, *116*, 6497–6504.

(124) Minguzzi, A.; Locatelli, C.; Cappelletti, G.; Bianchi, C. L.; Vertova, A.; Ardizzone, S.;

Rondinini, S. *J. Mater. Chem.* **2012**, *22*, 8896–8902.

(125) Locatelli, C.; Minguzzi, A.; Vertova, A.; Cava, P.; Rondinini, S. *Anal. Chem.* **2011**, *83* (7), 2819–2823.

(126) Morandi, S.; Minguzzi, A. *Electrochem. commun.* **2015**, *59*, 100–103.

(127) Minguzzi, A.; Locatelli, C.; Lugaresi, O.; Vertova, A.; Rondinini, S. *Electrochim. Acta* **2013**, *114*, 637–642.

(128) Sivula, K. *J. Phys. Chem. Lett.* **2013**, *4*, 1624–1633.

(129) Walter, M. G.; Warren, E. L.; McKone, J. R.; Boettcher, S. W.; Mi, Q.; Santori, E. A.; Lewis, N. S. *Chem. Rev.* **2010**, *110*, 6446–6473.

(130) Zhang, Z.; Yates, J. T. *Chem. Rev.* **2012**, *112*, 5520–5551.

(131) Tang, S. J.; Moniz, S. J. A.; Shevlin, S. A.; Martin, D. J.; Guo, Z.-X.; Tang, J. *Energy Environ. Sci.* **2015**, *8*, 731–759.

(132) Marschall, R. *Adv. Funct. Mater.* **2014**, *24*, 2421–2440.

(133) Minguez-Bacho, I.; Courté, M.; Fan, H. J.; Fichou, D. *Nanotechnology* **2015**, *26* (18), 185401.

(134) Martínez-García, A.; Vendra, V. K.; Sunkara, S.; Haldankar, P.; Jasinski, J.; Sunkara, M. K. *J. Mater. Chem. A* **2013**, *1* (48), 15235.

(135) Dubale, A. A.; Su, W.-N.; Tamirat, A. G.; Pan, C.-J.; Aragaw, B. A.; Chen, H.-M.; Chen, C.-H.; Hwang, B.-J. *J. Mater. Chem. A* **2014**, *2* (43), 18383–18397.

(136) Zhang, Z.; Dua, R.; Zhang, L.; Zhu, H.; Zhang, H.; Wang, P. *ACS Nano* **2013**, *7* (2), 1709–1717.

(137) Wang, H.; Zhang, L.; Chen, Z.; Hu, J.; Li, S.; Wang, Z.; Liu, J.; Wang, X. *Chem. Soc. Rev.* **2014**, *43*, 5234–5244.

(138) Cowan, J.; Durrant, J. R. *Chem. Soc. Rev.* **2013**, *42*, 2281–2293.

(139) Bak, T.; Nowotny, J.; Rekas, M.; Sorrell, C. C. *Int. J. Hydrog. Energy* **2002**, *27*, 991–1022.

(140) Tsui, L. K.; Zangari, G. *Electrochim. Acta* **2014**, *128*, 341–348.

(141) Tsui, L.; Wu, L.; Swami, N.; Zangari, G. *ECS Electrochem. Lett.* **2012**, *1* (2), D15–D19.

(142) Yasomanee, J. P.; Bandara, J. *Sol. Energy Mater. Sol. Cells* **2008**, *92* (3), 348–352.

(143) Su, X.; Zhao, J.; Li, Y.; Zhu, Y.; Ma, X.; Sun, F.; Wang, Z. *Colloids Surfaces A Physicochem. Eng. Asp.* **2009**, *349* (1–3), 151–155.

(144) Huang, L.; Peng, F.; Wang, H.; Yu, H.; Li, Z. *Catal. Commun.* **2009**, *10* (14), 1839–1843.

(145) Hu, C. C.; Nian, J. N.; Teng, H. *Sol. Energy Mater. Sol. Cells* **2008**, *92* (9), 1071–1076.

(146) Bansal, A.; Lewis, N. S. *J. Phys. Chem. B* **1998**, *102*, 4058–4060.

(147) Bansal, A.; Li, X.; Lauermann, I.; Lewis, N. S.; Yi, S. I.; Weinberg, W. H. *J. Am. Chem. Soc.* **1996**, *118*, 7225–7226.

(148) Hu, S.; Lewis, N. S.; Ager, J. W.; Yang, J.; McKone, J. R.; Strandwitz, N. C. *J. Phys. Chem. C*

2015, *119* (43), 24201–24228.

(149) Fernando, C. A. N.; De Silva, l. A. A.; Takahashi, K. *Semicond. Sci. Technol.* **2001**, *16*, 433–439.

(150) Jeong, H. W.; Jeon, T. H.; Jang, J. S.; Choi, W.; Park, J. H. *Phys. Chem. C* **2013**, *117*, 9104–9112.

(151) Abdi, F.; Van de Krol, R. *Phys. Chem. C* **2016**, *116*, 9398–9404.

(152) Seabold, J. A.; Choi, K. S. *J. Am. Chem. Soc.* **2012**, *134* (2186–2192).

(153) Choi, S. K.; Choi, W.; Park, H. *Phys. Chem. Chem. Phys.* **2013**, *15*, 6499–6507.

(154) Chatchai, P.; Kishioka, S.; Murakami, Y.; Nosaka, A. Y.; Nosaka, Y. *Electrochim. Acta* **2010**, *55*, 592–596.

(155) Tilley, S. D.; Schreier, M.; Azevedo, J.; Stefik, M.; Grätzel, M. *Adv. Funct. Mater.* **2014**, *24* (JANUARY), 303–311.

(156) Morales-Guio, C. G.; Liardet, L.; Mayer, M. T.; Tilley, S. D.; Graetzel, M.; Xu, H. *Angew. Chemie Int. Ed.* **2014**.

(157) Morales-Guio, C. G.; Tilley, S. D.; Vrubel, H.; Grätzel, M.; Hu, X. *Nat. Commun.* **2014**, *5*, 3059.

(158) Siripala, W.; Ivanovskaya, A.; Jaramillo, T. F.; Baeck, S.; McFarland, E. W. *Sol. Energ. Mat. Sol. Cell* **2003**, *77*, 229.

(159) Lin, C.; Lai, Y.; Mersch, D.; Reisner, E. *Chem. Sci.* **2012**, *3*, 3482–3487.

(160) Martinez-Garcia, A.; Vendra, V. K.; Sunkara, S.; Haldankar, P.; Sunkara, J.; Jasinski, M. K. *J. Mater. Chem. A* **2013**, *1*, 15235.

(161) Zhang, Z.; Wang, P. *J. Mater. Chem.* **2012**, *22*, 2456–2464.

(162) Dubale, A. A.; Pan, C.; Tamirat, G. *J. Mater. Chem. A Mater. energy Sustain.* **2015**, *3*, 12482–12499.

(163) Yurderi, M.; Bulut, A.; Ertas, I. E.; Zahmakiran, M.; Kaya, M. *Appl. Catal. B Environ.* **2015**, *165*, 169–175.

(164) An, X.; Li, K.; Tang, J. *ChemSusChem* **2014**, *7*, 1086–1093.

(165) Tran, P. D.; Batabyal, S. K.; Pramana, S. S.; Barber, J.; Wong, L. H.; Loo, S. C. J. *Nanoscale* **2012**, *4*, 3875–3878.

(166) Misawa, T.; Hashimoto, K.; Shimodaira, S. *Corros. Sci.* **1974**, *14* (2), 131–149.

(167) Jolivet, J.; Chaneac, C.; Trone, E. *ChemComm* **2004**, 481–487.

(168) Legodi, M. A.; de Waal, D. *Dye. Pigment.* **2006**, *74* (1), 161–168.

(169) Trotochaud, L.; Young, S. L.; Ranney, J. K.; Boettcher, S. W. *J. Am. Chem. Soc.* **2014**, *136* (18), 6744–6753.

(170) Chemelewski, W. D.; Lee, H. C.; Lin, J. F.; Bard, A. J.; Mullins, C. B. *J. Am. Chem. Soc.* **2014**, *136*, 2843–2850.

(171) Chen, H.; Lyu, M.; Liu, G.; Wang, L. *Chem. - A Eur. J.* **2016**, *22* (14), 4802–4808.

(172) Chemelewski, W. D.; Rosenstock, J. R.; Mullins, C. B. *J. Mater. Chem. A* **2014**, *2* (36), 14957.

(173) Wang, B.; Wu, H.; Yu, L.; Xu, R.; Lim, T. T.; Lou, X. W. *Adv. Mater.* **2012**, *24* (8), 1111–1116.

(174) Simonsson, G.; Lindbergh, D. *J. Electrochem. Soc.* **1990**, *137* (10), 3094.

(175) Vela, M. E.; Vilche, J. R.; Arvia, A. J. *Electrochim. Acta* **1986**, *31* (12), 1633–1641.

(176) Stratmann, M.; Hoffmann, K. *Corros. Sci.* **1989**, *29* (11), 1329–1352.

(177) Antony, H.; Legrand, L.; Maréchal, L.; Perrin, S.; Dillmann, P.; Chaussé, A. *Electrochim. Acta* **2005**, *51* (4), 745–753.

(178) Monnier, J.; Réguer, S.; Foy, E.; Testemale, D.; Mirambet, F.; Saheb, M.; Dillmann, P.; Guillot, I. *Corros. Sci.* **2014**, *78*, 293–303.

(179) Gualtieri, A.; Venturelli, P. *Am. Mineral.* **1999**, *84*, 895–904.

(180) R. W. G. Wyckoff. *Cryst. Struct.* **1963**, *1*, 290–295.

(181) Schrödinger, E. *Ann. Phys.* **1926**, *384* (6), 489–527.

(182) Fedak, W. a.; Prentis, J. J. *Am. J. Phys.* **2009**, *77* (2), 128.

(183) J. J. Sakurai. *Modern Quantum Mechanics 1st ed.*; Wesley, A., Ed.; Massachusett, 1994.

(184) Schwabl, F. *Quantum Mechanics (QM I)*; 2007.

(185) Born, M.; Oppenheimer, R. *Ann. Phys.* **1927**, *389* (20), 457–484.

(186) Szabo, A.; Ostlund, N. S. *Introduction to Advanced Electronic Structure Theory*. 1996, p 480.

(187) Groß, A. *Theoretical surface science: A microscopic perspective*; Springer, 2009.

(188) Hartree, D. R. *Math. Proc. Cambridge Philos. Soc.* **1928**, *24* (1), 89–110.

(189) Fock, V. *Zeitschrift fur Phys.* **1930**, *61* (1–2), 126–148.

(190) Fock, V. *Z. Phys* **1930**, *62*, 795–805.

(191) Slater, J. C. *Phys. Rev.* **1930**, *35*, 210–211.

(192) Hartree, D. R. *Proc. Camb. Soc.* **1928**, *24*, 111–132.

(193) Pople, J. A. *Rev. Mod. Phys* **1999**, *71*, 1267–1274.

(194) Cramer, C. J.; Truhlar, D. G. *Phys. Chem. Phys.* **2009**, *11*, 10757–10816.

(195) Schwerdtfeger, P. *ChemPhysChem* **2011**, *12* (17), 3143–3155.

(196) Jensen, F. *Introduction To Computational Chemistry*; Wiley, Ed.; 1999.

(197) Hohenberg, P.; Kohn, W. *Phys. Rev. B* **1964**, *136*, B864–B871.

(198) Kohn, W. **1999**, *71* (5), 1253–1266.

(199) Koch, W.; Holthausen, M. C. *Chemist's Guide to Density Functional Theory 2nd ed*; Wiley-VCH, Ed.; Weinheim, 2001.

(200) Pople, J. A. **1999**, *71* (5), 1267–1274.

(201) Kohn, W. *Rev. Mod. Phys.* **1999**, *71*, 1253–1266.

(202) Kohn, W.; Sham, L. J. *Phys. Rev. A* **1965**, *140*, A1133–A1138.

(203) Cremer, D. *Mol. Phys.* **2001**, *99*, 1899–1940.

(204) Polo, V.; Kraka, E.; Cremer, D. *Mol. Phys.* **2002**, *100*, 1771–1790.

(205) Perdew, J. P.; Schmidt, K.; VanDoren, V.; VanAlsenoy, C.; Geerlings, P. *Density Functional Theory and Its Application to Materials*; Press, A., Ed.; Melville, New York, 2001; Vol. 577.

(206) Ceperley, D. M.; Alder, B. J. *Phys. Rev. Lett.* **1980**, *45*, 566–569.

(207) Capelle, K.; J., B. *Phys. Rev.* **2006**, *36*, 1318.

(208) Kohn, W.; Becke, A. D.; Parr, R. G. *J. Phys. Chem.* **1996**, *100*, 12974–12980.

(209) Becke, A. D. *Phys. Rev. A* **1988**, *38*, 3098–3100.

(210) Colle, R.; Salvetti, O. *Theor. Chim. Acta* **1975**, *37*, 329–334.

(211) Perdew, J. P.; Zunger, A. *Phys. Rev. B* **1981**, *12*, 5048–5079.

(212) Perdew, J. P.; Burke, K.; Ernzerhof, M. *Phys. Rev. Lett* **1996**, *77*, 3865–3868.

(213) Lee, C.; Yang, W.; Parr, R. G. *Phys. Rev. B* **1988**, *37*, 785–789.

(214) Handy, N. C. *Theor. Chem. Acc.* **2009**, *123*, 165–169.

(215) Becke, A. D. *J. Chem. Phys.* **1993**, *98*, 1372.

(216) Pajer, J.; Marsman, M.; Kresse, G. *J. Chem. Phys.* **2007**, *127*, 24103.

(217) Heyd, J.; Scuseria, G. E.; Ernzerhof, M. *J. Chem. Phys.* **2003**, *118* (18), 8207.

(218) Perdew, J. P.; Zunger, A. *Phys. Rev. B* **1981**, *12*, 5048–5079.

(219) Cohen, A. J.; Mori-Sanchez, P.; Yang, W. *Science (80-.).* **2008**, *321*, 792–794.

(220) Mori-Sanchéz, P.; Cohen, A. J.; Yang, W. *J. Chem. Phys.* **2006**, *125*, 201–202.

(221) Mori-Sanchéz, P.; Cohen, A. J.; Yang, W. *Phys. Rev. Lett.* **2008**, *100*, 146401.

(222) Xiao, H.; Tahir-Kheli, J.; Goddard, W. A. *Phys. Chem. Lett.* **2011**, *2*, 212–217.

(223) Cramer, C. J.; Truhlar, D. G. **2009**, 10757–10816.

(224) Anisimov, V. I.; Zaanen, J.; Andersen, O. K. *Phys.Rev. B* **1991**, *44*, 943–954.

(225) Nolan, M. *Thin Solid Films* **2008**, *516* (22), 8130–8135.

(226) Min, L.; Ying, Z. J.; Yue, Z.; Tian-Min, W. *Chin.Phys. B* **2012**, *21* (8), 087301–1.

(227) Martínez-Ruiz, A.; Moren, M. G.; Takeuchi, N. *Solid State Sci.* **2003**, *5* (2), 291–295.

(228) Kleinman, L.; Mednick, K. *Phys.Rev. B* **1980**, *21*, 1549.

(229) Lloyd, M. A.; Siah, S. C.; Brandt, R. E.; Serdy, J.; Johnston, S. W.; Lee, Y. S.; Buonassisi, T. *Conf. Rec. IEEE Photovolt. Spec. Conf.* **2016**, *2016–Octob*, 3443–3445.

(230) Jiang, Y.; Yuan, H.; Chen, H. *Phys. Chem. Chem. Phys.* **2014**, *17* (1), 630–637.

(231) Mahalingam, T.; Chitra, J. S. P.; Chu, J. P. **2005**, *88*, 209–216.

(232) Liang, R.; Chang, Y.; Wu, P.; Lin, P. *Thin Solid Films* **2010**, *518* (24), 7191–7195.

(233) Jin, C.; Baek, K.; Park, S.; Kim, H. W.; Lee, W. I.; Lee, C. *Solid State Commun.* **2010**, *150* (37–38), 1812–1817.

(234) Tsur, Y.; Riess, I. **1999**, *60* (11), 8138–8146.

(235) Han, X.; Han, K.; Tao, M. *Electrochem. Solid-State Lett.* **2009**, *12* (4), H89–H91.

(236) Scanlon, D. O.; Watson, G. W. *Phys. Chem. Lett.* **2010**, *1*, 2582–2585.

(237) Scanlon, D. O.; Morgan, B. J.; Watson, G. W.; Walsh, A. *Phys. Rev. Lett.* **2009**, *103* (9), 1–4.

(238) Biccari, F.; Malerba, C.; Mittiga, A. *Sol. Energy Mater. Sol. Cells* **2010**, *94* (11), 1947–1952.

(239) Biccari, F. **2009**, No. 688774, 1–28.

(240) Aggarwal, S.; Topfer, J.; Tsai, T.; Dieckmann, R. *Solid State Ion.* **1997**, *101–103* (1), 321–331.

(241) Porat, O.; Reiss, I. *Solid State Ion.* **1995**, *81* (1–2), 29–41.

(242) Nolan, M.; Elliott, S. D. *Thin Solid Films* **2008**, *516* (7), 1468–1472.

(243) Nolan, M.; Elliott, S. D. **2008**, No. 5, 5522–5531.

(244) Buljan, A.; Llunell, M.; Ruiz, E.; Alemany, P. *Chem. Mater.* **2001**, *13* (2), 338–344.

(245) Filippetti, A.; Fiorentini, V. *Phys. Rev. B - Condens. Matter Mater. Phys.* **2005**, *72* (3), 1–8.

(246) Soon, A.; Wallman, J.; Delley, B.; Stampfl, C. *Curr. Appl. Phys.* **2013**, *13* (8), 1707–1712.

(247) Nolan, M.; Elliott, S. D. *Phys. Chem. Chem. Phys.* **2006**, *8* (45), 5350–5358.

(248) Palacios, P.; Sánchez, K.; Wahnón, P.; Conesa, J. C. *J. Sol. Energy Eng.* **2007**, *129* (3), 314.

(249) Kudo, A.; Yanagi, H.; Hosono, H.; Kawazoe, H. *Appl. Phys. Lett.* **1998**, *73*, 220.

(250) Tabuchi, N.; Matsumura, H. *Jpn. J. Appl. Phys* **2002**, *41*, 5060.

(251) Akimoto, K.; Ishizuka, S.; Yanagita, M.; Nawa, Y.; Paul, G. K.; Sakurai, T. *Sol. Energy* **2006**, *80*, 715–722.

(252) Caballero-Briones, F.; Palacios-Padrós, A.; Calzadilla, O.; Moreira, I. D. P. R.; Sanz, F. *J. Phys. Chem. C* **2012**, *116* (25), 13524–13535.

(253) Elfadill, N. G.; Hashim, M. R.; Chahrour, K. M.; Mohammed, S. A. *J. Electroanal. Chem.* **2016**, *767*, 7–12.

(254) Minami, T.; Nishi, Y.; Miyata, T. *Appl. Phys. Lett.* **2014**, *105* (21), 1–6.

(255) Elfadill, N. G.; Hashim, M. R.; Chahrour, K. M.; Mohammed, S. A. *Semicond. Sci. Technol.* **2016**, *31* (6), 65001.

(256) Zhao, Z.; He, X.; Yi, J.; Ma, C.; Cao, Y.; Qiu, J. *RSC Adv.* **2013**, *3*, 84–90.

(257) Zou, M.; Liu, H.; Feng, L.; Thomas, T.; Yang, M. *Solid State Sci.* **2017**, *65*, 22–28.

(258) Ping, Z.; Yurong, Z.; Qingbo, Y.; Fengzhen, L. *J. Semicond.* **2014**, *35* (10), 103001.

(259) Siah, S. C.; Lee, Y. S.; Brandt, R.; Buonassisi, T. *Conf. Rec. IEEE Photovolt. Spec. Conf.* **2012**, 2605–2607.

(260) Ye, F.; Su, X. Q.; Cai, X. M.; Zheng, Z. H.; Liang, G. X.; Zhang, D. P.; Luo, J. T.; Fan, P. *Thin Solid Films* **2016**, *603*, 395–399.

(261) Zhang, L.; Jing, D.; Guo, L.; Yao, X. *ACS Sustain. Chem. Eng.* **2014**, *2* (6), 1446–1452.

(262) Cai, X. M.; Su, X. Q.; Ye, F.; Zhang, D. P.; Luo, J. T.; Fan, P.; Zheng, Z. H.; Liang, G. X.; Roy, V. A. L.; Xiao, J. J. *J. Alloys Compd.* **2017**, *697*, 5–10.

(263) Hu, F.; Zou, Y.; Wang, L.; Wen, Y.; Xiong, Y. *Int. J. Hydrogen Energy* **2016**, *41* (34), 15172–15180.

(264) Heng, B.; Xiao, T.; Tao, W.; Hu, X.; Chen, X.; Wang, B.; Sun, D.; Tang, Y. *Cryst. Growth Des.* **2012**, *12* (8), 3998–4005.

(265) Ishizuka, S.; Kato, S.; Okamoto, Y.; Akimoto, K. *Appl. Phys. Lett.* **2002**, *80*, 950.

(266) Upadhyay, S.; Sharma, D.; Singh, N.; Satsangi, V. R.; Shrivastav, R.; Waghmare, U. V.; Dass, S. *J. Mater. Sci.* **2014**, *49* (2), 868–876.

(267) Upadhyay, S.; Sharma, D.; Satsangi, V. R.; Shrivastav, R.; Waghmare, U. V.; Dass, S. *Mater. Chem. Phys.* **2015**, *160* (APRIL), 32–39.

(268) Joseph, D. P.; David, T. P.; Raja, S. P.; Venkateswaran, C. *Mater. Charact.* **2008**, *59* (8), 1137–1139.

(269) Jiang, Z.-Q.; Yao, G.; An, X.-Y.; Fu, Y.-J.; Cao, L.-H.; Wu, W.-D.; Wang, X.-M. *Chinese Phys. B* **2014**, *23* (5), 57104.

(270) Resende, J.; Jiménez, C.; Nguyen, N. D.; Deschanvres, J.-L. *Phys. Status Solidi* **2016**, *7* (9), 1–7.

(271) Kardarian, K.; Nunes, D.; Maria Sberna, P.; Ginsburg, A.; Keller, D. A.; Vaz Pinto, J.; Deuermeier, J.; Anderson, A. Y.; Zaban, A.; Martins, R.; Fortunato, E. *Sol. Energy Mater. Sol. Cells* **2016**, *147*, 27–36.

(272) Brochen, S.; Bergerot, L.; Favre, W.; Resende, J.; Jiménez, C.; Deschanvres, J.-L.; Consonni, V. *J. Phys. Chem. C* **2016**, *120* (31), 17261–17267.

(273) Bergerot, L.; Jiménez, C.; Chaix-Pluchery, O.; Rapenne, L.; Deschanvres, J.-L. *Phys. Status Solidi* **2015**, *212* (8), 1735–1741.

(274) Pan, L.; Zhu, H.; Fan, C.; Wang, W.; Zhang, Y.; Xiao, J. Q. *J. Appl. Phys.* **2005**, *97* (10), 1–4.

(275) Wei, M.; Braddon, N.; Zhi, D.; Midgley, P. A.; Chen, S. K. *Appl. Phys. Lett.* **2005**, *86*, 72514.

(276) Kikuchi, N.; Tonooka, K. *Thin Solid Films* **2005**, *486* (1–2), 33–37.

(277) Zhang, J.; Tse, K.; Wong, M.; Zhang, Y.; Zhu, J. *Front. Phys.* **2016**, *11* (6).

(278) Lin, Y. M.; Jiang, Z. Y.; Zhang, R. Q.; Zhu, C. Y.; Hu, X. Y.; Zhu, X. D.; Zhang, H. Y. *J. Catal.* **2014**, *309*, 115–120.

(279) Yoshihumi, M.; Manickavachagam, K. *J. Phys. Chem. C* **2009**, *113*, 16144–16150.

(280) Huang, H. W.; Liu, K.; Chen, K.; Zhang, Y. L.; Zhang, Y. H.; Wang, S. C. *J. Phys. Chem. C* **2014**, *118*, 14379–14387.

(281) Luque, A.; Martí, A. *Phys. Rev. Lett.* **1997**, *78* (26), 5014–5017.

(282) Luque, A.; Martí, A.; Antolín, E.; Tablero, C. *Phys. B Condens. Matter* **2006**, *382* (1–2), 320–327.

(283) Palacios, P.; Sánchez, K.; Conesa, J. C.; Fernández, J. J.; Wahnón, P. *Thin Solid Films* **2007**, *515* (15 SPEC. ISS.), 6280–6284.

(284) Palacios, P.; Aguilera, I.; Sánchez, K.; Conesa, J. C.; Wahnón, P. *Phys. Rev. Lett.* **2008**, *101* (4), 2–5.

(285) L??pez, N.; Reichertz, L. A.; Yu, K. M.; Campman, K.; Walukiewicz, W. *Phys. Rev. Lett.* **2011**, *106* (2), 1–4.

(286) Luque, A.; Martí, A.; Cuadra, L. *IEEE Trans. Electron Devices* **2001**, *48* (9), 2118–2124.

(287) Okada, Y.; Ekins-Daukes, N. J.; Kita, T.; Tamaki, R.; Yoshida, M.; Pusch, A.; Hess, O.; Phillips, C. C.; Farrell, D. J.; Yoshida, K.; Ahsan, N.; Shoji, Y.; Sogabe, T.; Guillemoles, J.-F. *Cit. Appl. Phys. Rev. Appl. Phys. Lett* **2015**, *2* (90), 21302–233510.

(288) Luque, A.; Martí, A.; Stanley, C.; López, N.; Cuadra, L.; Zhou, D.; Pearson, J. L.; McKee, A. *J. Appl. Phys.* **2004**, *96* (1), 903–909.

(289) Malerba, C.; Azanza Ricardo, C. L.; Dincau, M.; Biccari, F.; Scardi, P.; Mittiga, A. *Sol. Energy Mater. Sol. Cells* **2012**, *105* (October), 192–195.

(290) LAI, G.; WU, Y.; LIN, L.; QU, Y.; LAI, F. *Surf. Rev. Lett.* **2014**, *21* (4), 1450052.

(291) Luque, A.; Martí, A. *Prog. Photovoltaics Res. Appl.* **2001**, *9* (2), 73–86.

(292) Palacios, P.; Sánchez, K.; Conesa, J. C.; Wahnón, P. *Phys. Status Solidi Appl. Mater. Sci.* **2006**, *203* (6), 1395–1401.

(293) Luque, A.; Martí, A.; Stanley, C. *Nat. Photonics* **2012**, *6* (3), 146–152.

(294) Aguilera, I.; Palacios, P.; Wahnón, P. *Phys. Rev. B - Condens. Matter Mater. Phys.* **2011**, *84* (11), 1–6.

(295) Norwich, N. Y. *Handbook of physical vapor deposition (PVD) processing*; 2010.

(296) Mahalingam, T.; Chitra, J. S. .; Rajendran, S.; Jayachandran, M.; Chockalingam, M. J. *J. Cryst. Growth* **2000**, *216* (1–4), 304–310.

(297) Daltin, A. L.; Addad, A.; Chopart, J. P. *J. Cryst. Growth* **2005**, *282* (3–4), 414–420.

(298) Wang, L.; Tao, M. *Electrochem. Solid-State Lett.* **2007**, *10*, H248–H250.

(299) Yoon, S.; Kim, M.; Kim, I.-S.; Lim, J.-H.; Yoo, B. *J. Mater. Chem. A* **2014**, *2* (30), 11621.

(300) Wang, L. C.; de Tacconi, N. R.; Chenthamarakshan, C. R.; Rajeshwar, K.; Tao, M. *Thin Solid Films* **2007**, *515* (5), 3090–3095.

(301) Liu, G.; Wang, L.; Xue, D. *Mater. Lett.* **2010**, *64* (22), 2475–2478.

(302) Tang, Y.; Chen, Z.; Jia, Z.; Zhang, L.; Li, J. *Mater. Lett.* **2005**, *59*, 434–438.

(303) Septina, W.; Ikeda, S.; Khan, M. A.; Hirai, T.; Harada, T.; Matsumura, M.; Peter, L. M. *Electrochim. Acta* **2011**, *56* (13), 4882–4888.

(304) Wijesundera, R. P.; Hidaka, M.; Koga, K.; Sakai, M.; Siripala, W. *Thin Solid Films* **2006**, *500* (1–2), 241–246.

(305) Mathew, X.; Mathews, N. R.; Sebastian, P. J. *Sol. Energy Mater. Sol. Cells* **2001**, *70* (3), 277–286.

(306) Yang, Y.; Li, Y.; Pritzker, M. *Electrochim. Acta* **2016**, *213*, 225–235.

(307) Zhang, Z.; Wang, P. *J. Mater. Chem.* **2012**, *22* (6), 2456–2464.

(308) Heng, B.; Xiao, T.; Hu, X.; Yuan, M.; Tao, W.; Huang, W.; Tang, Y. *Thermochim. Acta* **2011**, *524* (1–2), 135–139.

(309) Bijani, S.; Schrebler, R.; Dalchiele, E. A.; Gabas, M.; Martinez, L.; Ramos-Barrado, J. R. *J. Phys. Chem. C* **2011**, *115*, 21373–21382.

(310) Huang, L.; Peng, F.; Yu, H.; Wang, H. *Solid State Sci.* **2009**, *11*, 129–138.

(311) Kakuta, S.; Abe, T. *Solid State Sci.* **2009**, *11*, 1465–1469.

(312) Long, J.; Dong, J.; Wang, X.; Ding, Z.; Zhang, Z.; Wu, L.; Li, Z.; Fu, X. *J. Colloid Interface Sci.* **2009**, *333* (2), 791–799.

(313) Zhang, X.; Song, J.; Jiao, J.; Mei, X. *Solid State Sci.* **2010**, *12*, 1215–1219.

(314) Singh, D. P.; Singh, J. A. I.; Mishra, P. R.; Tiwari, R. S.; Srivastava, O. N. **2008**, *31* (3), 319–325.

(315) Zhou, Y.; Switzer, J. A. *Scr. Mater.* **1998**, *38* (11), 1731–1738.

(316) Paracchino, A.; Brauer, J. C.; Moser, J.-E.; Thimsen, E.; Graetzel, M. **2012**.

(317) Elmezayyen, A.; Guan, S.; Reicha, F. M.; El-Scherbiny, I.; Zheng, J.; Xu, C. *J. Phys. D Appl. Phys.* **2015**, *48*, 175502.

(318) Matula, R. A. *J. Phys. Chem.* **1979**, *8* (4), 1147–1298.

(319) Bockris, J. O. M.; Reddy, A. K. N.; Gamboa-Aldeco, M. *Modern Electrochemistry*; 2000.

(320) Siegenthaler, H.; Juttner, K. *J. Electroanal. Chem.* **1984**, *163*, 327–343.

(321) Vilche, J. R.; Juttner, K. *Electrochim. Acta* **1987**, *32* (11), 1567–1572.

(322) Brisard, G. M.; Zenati, E.; Gasteiger, H. A.; Markovie, N. M.; Ross, P. N. **1996**, No. 16, 2221–2230.

(323) Bewick, A.; Jovicevic, J.; Thomas, B. *Faraday Symp. Chem. Soc.* **1984**, *19*, 1–207.

(324) Bates, R. G.; Acree, S. F. *J. Res. Natl. Bur. Stand. (1934).* **1945**, *34* (4), 373.

(325) Delloyd's Lab Tech resources reagents and Solutions. *AnalChem Resour.* 4–8.

(326) Buck, R. P.; Rondinini, S.; Covington, A. K.; Baucke, F. G. K.; Brett, C. M. A.; Camões, M. F.;

Milton, M. J. T.; Mussini, T.; Naumann, R.; Pratt, K. W.; Spitzer, P.; Wilson, G. S. *Pure Appl. Chem* **2002**, *74* (11), 2169–2200.

(327) Kuo, C. H.; Hua, T.-E.; Huang, M. H. *J. Am. Chem. Soc.* **2009**, *131*, 17871–17878.

(328) Berger, R. F.; Fennie, C. J.; Neaton, J. B. *Phys. Rev. Lett.* **2011**, *107*, 146804.

(329) Huang, P.-R.; He, Y.; Cao, C.; Lu, Z.-H. *Sci. Rep.* **2015**, *4* (1), 7131.

(330) Kresse, G.; Hafner, J. *Phys. Rev. B* **1993**, *47*, 558.

(331) Kresse, G.; Furthmaller, J. *Comput. Mater. Sci.* **1996**, *6*, 15.

(332) Kresse, G.; Furthmaller, J. *Phys. Rev. B* **1996**, *54* (11), 169.

(333) Kresse, G.; Hafner, J. *J. Phys. Condens. Matt.* **1994**, *6*, 8245.

(334) Perdew, J. P.; Wang, Y. *Phys. Rev. B* **1992**, *45* (23), 13244–13249.

(335) Slater, J. C. *Phys. Rev.* **1951**, *81* (3), 358–390.

(336) Bloechel, P. *Phys. Rev. B* **1994**, *50*, 17953–17979.

(337) Krukau, A. V.; Vydrov, O. A.; Izmayloy, A. F.; Scuseria, G. E. *J. Chem. Phys.* **2006**, *125*, 224106.

(338) Hafner, S. S.; Nagel, S. *Phys. Chem. Miner.* **1983**, *9*, 19–22.

(339) De Silva, P.; Corminboeuf, C. *J. Chem. Theory Comput.* **2014**, *10* (9), 3745–3756.

(340) Carvajal, M. A.; Alvarez, S.; Novoa, J. J. *Chem. - A Eur. J.* **2004**, *10* (9), 2117–2132.

(341) Buljan, A.; Alemany, P.; Ruiz, E. *J. Phys. Chem. B* **1999**, *103* (38), 8060–8066.

(342) Ruiz, E.; Alvarez, S.; Alemany, P.; Evarestov, R. a. *Phys. Rev. B* **1997**, *56* (12), 7189–7196.

(343) Elschenbroich, C.; Salzer, A. 1992, p 496.

(344) Mittiga, A.; Biccari, F.; Malerba, C. *Thin Solid Films* **2009**, *517* (7), 2469–2472.

(345) Buljan, A.; Llunell, M.; Ruiz, E.; Alemany, P. *Chem. Mater.* **2001**, *13*, 338.

(346) Ravel, B.; Newville, M. *J. Synchrotron Radiat.* **2005**, *12* (4), 537–541.

(347) Newville, M. *J. Synchrotron Radiat.* **2001**, *8*, 322–324.

(348) Minguzzi, A.; Lugaresi, O.; Achilli, E.; Locatelli, C.; Vertova, A.; Ghigna, P.; Rondinini, S. *Chem. Sci.* **2014**, *5* (9), 3591–3597.

(349) Achilli, E.; Vertova, A.; Visibile, A.; Locatelli, C.; Minguzzi, A.; Rondinini, S.; Ghigna, P. *Inorg. Chem.* **2017**, *56* (12), 6982–6989.

(350) De Jongh, P. E.; Vanmaekelbergh, D.; Kelly, J. J. *Chem. Mater.* **1999**, *11*, 3512–3517.

(351) Prout, C. K.; Armstrong, R. A.; Carruthers, J. R.; Forrest, J. G.; Murray-Rust, P.; Rossotti, F. J. C. *J. Chem. Soc. A* **1968**, 2791–2813.

(352) Baran, T.; Wojtyła, S.; Lenardi, C.; Vertova, A.; Ghigna, P.; Achilli, E.; Fracchia, M.; Rondinini, S.; Minguzzi, A. *ACS Appl. Mater. Interfaces* **2016**, *8*, 21250–21260.

(353) Baran, T.; Fracchia, M.; Visibile, A.; Achilli, E.; Vertova, A.; Rondinini, S.; Ghigna, P.; Minguzzi, A. *Publ.*

(354) Garcia, J.; Benfatto, M.; Natoli, C. R.; Bianconi, A.; Fontaine, A.; Tolentino, H. *J. Chem. Phys.* **1989**, *132*, 295–302.

(355) Frank, P.; Benfatto, M.; Quayyam, M.; Hedman, B.; Hodgson, K. O. *J. Chem. Phys.* **2015**, *142*, 84310.

(356) Benfatto, M.; Solera, J. A.; Chaboy, J.; Proietti, M. G.; Garcìa, J. *Phys. Rev.* **1996**, *56*, 2447–2452.

(357) Frenkel, A. I.; Korshin, G. V.; Ankudonov, A. L. *Environ. Sci. Technol.* **2000**, *34*, 2138–2142.

(358) Brugger, J.; Etschmann, B.; Liu, W.; Testemale, D.; Hazemann, J. L.; Emerich, H.; Van Beek, W.; Proux, O. *Geochim. Cosmochim. Acta* **2007**, *71*, 4920–4941.

(359) Benfatto, M.; Natoli, C. R. *Phys. Rev.* **1986**, *34*, 5774–5781.

(360) Achilli, E.; Minguzzi, A.; Visibile, A.; Locatelli, C.; Vertova, A.; Naldoni, A.; Rondinini, S.; Auricchio, F.; Marconi, S.; Fracchia, M.; Ghigna, P. *J. Synchrotron Rad.* **2016**, *23*, 622–628.

(361) Zhao, W.; Fu, W.; Yang, H.; Tian, C.; Li, M.; Li, Y.; Zhang, L.; Sui, Y.; Zhou, X.; Chen, H.; Zou, G. *Nat. Mater.* **2011**, *10*, 456–461.

(362) Pascarelli, S.; Mathon, O.; Munoz, M.; Mairs, T.; Susini, J. *J. Synchrotron Rad.* **2006**, *13*, 351–358.

(363) Labiche, J. C.; Mathon, O.; Pascarelli, S.; Newton, M. A.; Ferre, G. G. C.; Vaughan, G.; Homs, A.; Carreiras, D. F. *Rev. Sci. Instrum.* **2007**, *78*, 091301 27.

(364) Solé, V. A.; Papillon, E.; Cotte, M.; Walter, P.; Susini, J. *Spectrochim. Acta B* **2007**, *62*, 63–68.

(365) Figueroa, S. J. A.; Prestipino, C. *J. Phys. Conf. Ser.* **2016**, *712*, 12012.

(366) Binsted, N.; Hasnain, S. S. *J. Synch. Rad.* **1996**, *3*, 185–196.

(367) Fujikawa, T. *J. Phys. Soc. Jpn.* **1993**, *62*, 2155–2165.

(368) La Penna, G.; Minicozzi, V.; Morante, S.; Rossi, G. C.; Stellato, F. *J. Chem. Phys.* **2015**, *143*, 124508.

(369) Chaboy, J.; Muñoz-Páez, A.; Merkling, P. J.; Marcosa, E. S. *J. Chem. Phys.* **2006**, *124*, 64509.

(370) Manceau, A.; Matynia, A. *Geochim. Cosmochim. Acta.* **2010**, *74*, 2556–2580.

(371) Blumberger, J. *J. Am. Chem. Soc.* **2008**, *130*, 16065–16068.

(372) Blumberger, J.; Bernasconi, L.; Tavernelli, I.; Vuilleumier, R.; Sprik, M. *J. Am. Chem. Soc.* **2004**, *126*, 3928–3938.

(373) Liu, X.; Lu, X.; Meijer, E. J.; Wang, R. *Phys. Chem. Chem. Phys.* **2010**, *12*, 10801–10804.

(374) Amira, S.; Spangberg, D.; Hermansson, K. *Phys. Chem. Chem. Phys.* **2005**, *7*, 2874–2880.

(375) Liu, X.; Cheng, J.; Sprik, M. *J. Phys. Chem. B* **2015**, *119*, 1152–1163.

(376) Pasquarello, A.; Petri, I.; Salmon, P. S.; Parisel, O.; Car, R.; Tóth, E.; Powell, D. H.; Fischer, H. E.; Helm, L.; Merbach, A. E. *Science (80-.).* **2001**, *291*, 856–859.

(377) Curtiss, L. A.; Halley, J. W.; Wang, X. R. *Phys. Rev. Lett.* **1992**, *69*, 2435–2438.

(378) Rubinstein, I.; Bard, A. J. *J. Am. Chem. Soc.* **1981**, *103*, 512.

(379) Meenatchi, B.; Renuga, V.; Manikandan, A. *J Inorg. Organomet. Polym.* **2016**, *26*, 423.

(380) Li, Z.; Luo, W.; Zhang, M.; Feng, J.; Zou, Z. *Energy Environ. Sci.* **2013**, *6*, 347.

(381) Minguzzi, A.; Snchez-Snchez, C. M.; Gallo, A.; Montiel, V.; Rondinini, S. *ChemElectroChem* **2014**, *1*, 1415–1421.

(382) Han, J.; Zong, X.; Zhou, X.; Li, C. *RSC Adv.* **2015**, *5*, 10790–10794.

(383) Xu, Y.; Schoonen, M. A. A. *Am. Mineral.* **2000**, *85*, 543–556.

(384) Castelo, G.; Biagini, E.; Munari, S. *J. Chromatogr.* **1965**, *0*, 447–451.

(385) Su, Y. H.; Huang, S. H.; Kung, P. Y.; Shen, T. W.; Wang, W. L. *ACS Sustain. Chem. Eng.* **2015**, *3* (9), 1965–1973.

(386) Uchiyama, S.; Matsuura, H.; Yamawaki, Y. *Electrochim. Acta* **2013**, *88*, 251–255.

(387) Dubale, A. A.; Tamirat, A. G.; Chen, H.-M.; Berhe, T. A.; Pan, C.-J.; Su, W.-N.; Hwang, B.-J. *J. Mater. Chem. A* **2016**, *4* (6), 2205–2216.

(388) Chen, Z.; Dinh, H. N.; Miller, E. **2013**, 87–97.

(389) Baran, T.; Visibile, A.; Wojtyła, S.; Scavini, M.; Malara, F.; Naldoni, A.; Minguzzi, A. *Publ.*

(390) Symes, M. D.; Kitson, P. J.; Yan, J.; Richmond, C. J.; Cooper, G. J. T.; Bowman, R. W.; Vilbrandt, T.; Cronin, L. *Nat. Chem* **2012**, *4*, 349–354.

(391) Marelli, M.; Naldoni, A.; Minguzzi, A.; Allieta, M.; Virgili, T.; Scavia, G.; Recchia, S.; Psaro, R.; Dal Santo, V. *Appl. Mater. Interfaces* **2014**, *6*, 11997–12004.

(392) Malara, F.; Minguzzi, A.; Marelli, M.; Morandi, S.; Psaro, R.; Dal Santo, V.; Naldoni, A. *ACS Catal.* **2015**, *5*, 5292–5300.

(393) Minguzzi, A.; Locatelli, C.; Lugaresi, O.; Achilli, E.; Cappelletti, G.; Scavini, M.; Coduri, M.; Masala, P.; Sacchi, B.; Vertova, A.; Ghigna, P.; Rondinini, S. *ACS Catal.* **2015**, *5*, 5104–5115.

(394) Dai, P.; Li, W.; Xie, J.; He, Y.; Thorne, J.; McMahon, G.; Zhan, J.; Wang, D. *Angew. Chemie - Int. Ed.* **2014**, *53* (49), 13493–13497.

(395) Antony, H.; Legrand, L.; Maréchal, L.; Perrin, S.; Dillmann, P.; Chaussé, A. *Electrochim. Acta* **2005**, *51*, 745.

(396) Kwon, S.-K.; Suzuki, S.; Saito, M.; Waseda, Y. *Corros. Sci.* **2005**, *47*, 2543.

(397) Jagminas, A.; Mažeika, K.; Juška, E.; Reklaitis, J.; Baltrūnas, D. *Appl. Surf. Sci.* **2010**, *256*, 3993.

(398) Wang, T. H.; Chen, Y. N.; Chiang, C. C.; Hsieh, Y. K.; Li, P. C.; Wang, C. F. *ChemElectroChem* **2016**, *3* (6), 966–975.

(399) Zou, S.; Burke, M. S.; Kast, M. G.; Fan, J.; Danilovic, N.; Boettcher, S. W. *Chem. Mater.* **2015**, *27* (23), 8011–8020.

(400) Martinez, L.; Leinen, D.; Martín, F.; Gabas, M.; Ramos-Barrado, J. R.; Quagliata, E.; Dalchiele, E. A. *J. Electrochem. Soc.* **2007**, *154* (3), D126.

(401) Han, J.; Zong, X.; Zhou, X.; Li, C. *RSC Adv.* **2015**, *5* (14), 10790–10794.

(402) Ajmal, M.; Maqsood, A. *Mater. Lett.* **2008**, *62* (14), 2081–2084.

(403) Wulff, J.; Cornell, A. *J. Appl. Electrochem.* **2007**, *37* (1), 181–186.

(404) Hedenstedt, K.; Simic, N.; Wildlock, M.; Ahlberg, E. *J. Electroanal. Chem.* **2016**, *783*, 1–7.

(405) Hedenstedt, K.; Gomes, A. S. O.; Busch, M.; Ahlberg, E. *Electrocatalysis* **2016**, *7* (4), 326–335.

(406) Hedenstedt, K.; Simic, N.; Wildlock, M.; Ahlberg, E. *J. Appl. Electrochem.* **2017**, *47* (9), 991–1008.

(407) Stratmann, M.; Bohnenkamp, K.; Engell, H. J. *Corros. Sci.* **1983**, *23*, 969.

(408) Martinez, L.; Leinen, D.; Martín, F.; Gabas, M.; Ramos-Barrado, J. R.; Quagliata, E.; Dalchiele, E. A. *J. Electrochem. Soc.* **2007**, *154* (3), D126.

(409) Gutierrez, J. A.; Baez, R.; Sebastian, P. J.; Vazquez, A. *Solid State Chem.* **2003**, *174*, 241–248.

(410) Kaur, N.; Singh, B.; Kennedy, B. J.; Graefe, M. *Geochim. Cosmochim. Acta* **2009**, *73*, 582.

(411) Christensen, H.; Christensen, A. *Acta Chem. Scand., Ser. A* **1978**, *32*, 87.

(412) Cornell, U.; Schwertmann, R. M. *Iron Oxides In The Laboratory*; 1991.

(413) Réguer, S. *Corros. Sci.* **2015**, *100*, 589–598.

(414) Monnier, J. *Corros. Sci.* **2014**, *78*, 293–303.

(415) Suzuki, S. *Corros. Sci.* **2008**, *50*, 1761–1765.

(416) Roux, C. *Inorg. Chem.* **1996**, *35*, 3.

(417) Brioius. *J. Am. Chem. Soc.* **1995**, *117*, 1019–1026.

(418) E., W. T.; Kennepohl, P. *J. Am. Chem. Soc.* **1997**, *119*, 6297–6314.

(419) Y., T.; Sugano, S. *J. Phys. Soc. Jpn.* **1954**, *9*, 753–766.

(420) Wilke, M. *Am. Mineral.* **2001**, *86*, 714–730.

(421) Schwertmann, U.; Taylor, R. M. *Clays Clay Mater.* **1972**, *20*, 151–158.

(422) Encina, E. R.; Distaso, M.; Taylor, R. N. K.; Peukert, W. *Cryst. Growth Des.* **2015**, *15*, 194–203.

(423) Morris, R. V.; Lauer, H. V. *J. Geophys. Res. Solid Earth* **1981**, *86* (B11), 10893–10899.

(424) Deng, Y.; Handoko, A. D.; Du, Y.; Xi, S.; Yeo, B. S. *ACS Catal.* **2016**, *6* (4), 2473.

(425) Alp, E. E.; Shenoy, G. K.; Hinks, D. G.; II, D. W. C.; Soderholm, L.; Schuttler, H.-B.; Guo, J.; Ellis, D. E.; Montano, P. A.; Ramanathan, M. *Phys. Rev. B* **1987**, *35* (13), 7199.

(426) Cervera, B.; Sanz, J. L.; Ibáñez, M. J.; Vila, G.; LLoret, F.; Julve, M.; Ruiz, R.; Ottenwaelder, X.; Aukauloo, A.; Poussereau, S.; Journaux, Y.; Muñoz, M. C. J. *Chem. Soc., Dalt. Trans.* **1998**, *5*, 781.

(427) Hanss, J.; Beckmann, A.; Krüger, H.-J. *J. Inorg. Chem.* **1999**, *1*, 163.

(428) Henderson, M. A.; Epling, W. S.; Peden, C. H. F.; Perkins, C. L. *J. Phys. Chem. B* **2003**, *107* (2), 534.

(429) F. Han, H. Li, J. Yang, X.Cai, L. F. *Phys. E* **2016**, *77*, 122–126.

(430) Woltornist, S. J.; Oyer, A. J.; Carrillo, J. M.; Dobrynin, A. V.; Adamson, D. H. *ACS Nano* **2013**, *7* (8), 7062–7066.

(431) Kaplas, T.; Kuzhir, P. *Nanoscale Res. Lett.* **2016**, *11*, 54.

(432) Berg, H. *Nature* **1961**, *191*, 1270.

(433) Berg, H.; Schweiss, H. *Electrochim. Acta* **1964**, *9*, 425.

(434) Heyrovsky, M.; Norrish, R. G. W. *Nature* **1963**, *200*, 880.

(435) M. Heyrovsky. *Nature* **1965**, *206*, 1356.

(436) Veselovsky, V. I. *Zh. Fiz. Khim.* **1946**, *20*, 1493.

(437) Barker, G. C.; Gardner, A. W.; Sammon, D. C. *J. Electrochem. Soc.* **1966**, *113*, 1182.

(438) Rotenberg, Z. A.; Gurevich, Y. Y. *J. Electroanal.Chem* **1975**, *66*, 165–182.

(439) Pikaev, A. K. *Nauka* **1969**, *5*.

(440) Bronskill, H. J.; Wolff, R. K.; Hunt, J. w. *J. Chem. Phys.* **1970**, *53*, 4201.

(441) Brodskii, A. M.; Gurevich, Y. Y.; Pleskov, Y. V.; Rotemberg, Z. *Modern Photolectrochemistry: The Photoemission Phenomena*; 1974.

(442) Benderskii, V. A.; Brodskii, A. M. *Photoelectron Emisssion from Metals into Electrolyte Solutions*; 1977.

(443) Gamayunova, I. M.; Churikov, A. V. *Russ. J. Electrochem.* **1999**, *35* (9), 1000–1006.

(444) Yakushev, V. V.; Skunddin, A. M. *Elektrokhimya (translated)* **1984**, *20* (1), 99–104.

(445) Presland, G. A.; Whitehouse, D. R. *J. Electroanal. Chem.* **1986**, *208*, 219–242.

(446) Bowden, F. P. *Trans. Faraday Soc.* **1931**, *27*, 505.

(447) Ansone, I. K.; Rotemberg, Z. A.; Slaidin, G. Y.; Pleskov, Y. V. *Elektrokhimya (translated)* **1976**, *12*, 1552.

(448) Hanson, M. L.; Solomon, K. R. *Environ. Pollut.* **2004**, *13* (10), 371–383.

(449) Zhang, L.; Arnold, W. A.; Hozalski, R. M. *Environ. Sci. Technol.* **2004**, *38*, 6881–6889.

(450) Rondinini, S.; Minguzzi, A.; Vertova, A. In *Encyclopedia of Applied Electrochemistry*.

(451) Xu, Y. H.; Ma, H.; Liu, Q.; Gong, J. X.; Zhang, J.; Xu, C. F. *CIESC* **2008**, *59*, 43–46.

(452) Xu, Y. H.; Zhang, H.; Chu, C. P.; Ma, C. A. *Electroanal. Chem.* **2012**, *664*, 39–45.

(453) Lugaresi, O.; Encontre, H.; Locatelli, C.; Rondinini, S.; Comninellis, C.; Minguzzi, A.; Vertova, A. *Electrochem. Comm.* **2014**, *44*, 63–65.

(454) Lugaresi, O.; Minguzzi, A.; Locatelli, C.; Vertova, A.; Rondinini, S.; Amatore, C. *Electrocatalysis* **2013**, *4*, 353–357.

(455) Minguzzi, A.; Lugaresi, O.; Aricci, G.; Rondinini, S.; Vertova, A. *Electrochem. Comm.* **2012**, *22*, 25–28.

(456) Huang, Y.-F.; Wu, D.-Y.; Wang, A.; Ren, B.; Rondinini, S.; Tian, Z.-Q.; Amatore, C. *J. Am. Chem. Soc.* **2010**, *132* (48), 17199–17210.

(457) Rondinini, S.; Vertova, A. In *Electrochemistry for the Environment*; 2010; pp 279–306.

(458) Klymenko, O. V.; Buriez, O.; Labbé, E.; Zhan, D.-P.; Rondinini, S.; Tian, Z.-Q.; Svir, I.; Amatore, C. *ChemElectroChem2* **2014**, *1*, 227.

(459) Ardizzone, S.; Cappelletti, G.; Mussini, P. R.; Rondinini, S.; Doubova, L. M. *Electroanal. Chem.* **2002**, *532*, 285–293.

(460) Vielstich, W.; Lamm, A.; Gasteiger, G. A. *Handbook of Fuel Cells: Fundamentals, Technology, Applications*; New York, 2003.

(461) Knupp, S.; Vukmirovic, M.; Haldar, P.; Herron, J.; Mavrikakis, M.; Adzic, R. R. *Electrocatalysis* **2010**, *1*, 213.

(462) Oviedo, O. A.; Inada, E. P. M.; Mariscal, M. . . *Phys. Chem. Chem. Phys.* **2008**, *10*, 3561.

(463) Wang, J. X.; Inada, H.; Wu, L.; Zhu, Y.; Choi, Y.; Liu, P.; Zhou, W.; Adzic, R. R. *J. Am. Chem. Soc.* **2009**, *131*, 17298.

(464) Zhang, J.; Lima, F. H. B.; Shao, M. H.; Sasaki, K.; Wang, J. X.; Hanson, J.; Adzic, R. R. *J. Phys. Chem. B* **2005**, *109*, 22701.

(465) Shao, M.; Sasaki, K.; Marinkovic, N. S.; Zhang, L.; Adzic, R. R. *Electrochem. Comm.* **2007**, *9*, 2848.

(466) Brankovic, S. R.; Wang, J. X.; Adzic, R. R. *Surf. Sci.* **2001**, *474*, L173.

(467) Price, S. W. T.; Speed, J. D.; Kannan, P.; Russel, A. E. *J. Am. Chem. Soc.* **2011**, *133*, 19448–19458.

(468) Rouya, E.; Cattarin, S.; Reed, M. L.; Kelly, R. G.; Zangari, G. *J. Electrochem. Soc.* **2012**, *159* (4), K97–K102.

(469) Baran, T.; Wojtyła, S.; Lenardi, C.; Vertova, A.; Ghigna, P.; Achilli, E.; Fracchia, M.; Rondinini, S.; Minguzzi, A. *ACS Appl. Mater. Interfaces* **2016**, *8* (33), 21250–21260.

(470) Oszajca, M.; McCall, K.; Robertson, N.; Szaciłowski, K. *J. Phys. Chem. C* **2011**, *115*, 12187–12195.

(471) Wojtyła, S.; Baran, T. *J. Inorg. Organomet. Polym. Mater.* **2017**, *27* (2), 436–445.

(472) Gawęda, S.; Stochel, G.; Szaciłowski, K. *J. Phys. Chem. C* **2008**, *112* (48), 19131–19141.

(473) Szaciłowski, K. In *Infochemistry: Information Processing at the Nanoscale*; John Wiley & Sons, Ltd, 2012; pp 165–197.

(474) Bourée, W. S.; Prévot, M. S.; Jeanbourquin, X. A.; Guijarro, N.; Johnson, M.; Formal, F. L.; Sivula, K. *Adv. Mater.* **2016**, *28*, 9308–9312.

(475) Baran, T.; Wojtyła, S.; Dibenedetto, A.; Aresta, M.; Macyk, W. *ChemSusChem* **2016**, *9* (20), 2933–2938.

(476) Wojtyła, S.; Macyk, W.; Baran, T. *Photochem. Photobiol. Sci.* **2017**.

(477) Zainun, A. R.; Mamat, M. H.; Noor, U. M.; Mohammad Rusop, M. *Adv. Mater. Res.* **2013**, *667*, 447–451.

(478) Stakhira, P.; Cherpak, V.; Volynyuk, D.; Ivastchyshyn, F.; Hotra, Z.; Tataryn, V.; Luka, G. *Thin Solid Films* **2010**, *518* (23), 7016–7018.

(479) Perera, V. P. S.; Tennakone, K. *Sol. Energy Mater. Sol. Cells* **2003**, *79* (2), 249–255.

(480) Buchalska, M.; Kuncewicz, J.; Świętek, E.; Łabuz, P.; Baran, T.; Stochel, G.; Macyk, W. *Coord. Chem. Rev.* **2013**, *257* (3–4), 767–775.

(481) Chiang, C. Y.; Shin, Y.; Aroh, K.; Ehrman, S. *Int. J. Hydrogen Energy* **2012**, *37* (10), 8232–8239.

(482) Guo, X.; Diao, P.; Xu, D.; Huang, S.; Yang, Y.; Jin, T.; Wu, Q.; Xiang, M.; Zhang, M. *Int. J. Hydrogen Energy* **2014**, *39* (15), 7686–7696.

(483) Jang, Y. J.; Jang, J.-W.; Choi, S. H.; Kim, J. Y.; Kim, J. H.; Youn, D. H.; Kim, W. Y.; Han, S.; Sung Lee, J. *Nanoscale* **2015**, *7* (17), 7624–7631.

(484) Zhang, L.; Wang, H. *ACS Nano* **2011**, *5* (4), 3257–3267.

(485) Zhang, L.; Jing, H.; Boisvert, G.; He, J. Z.; Wang, H. *ACS Nano* **2012**, *6* (4), 3514–3527.

(486) Bolts, J. M.; Wrighton, M. S. *J. Phys. Chem.* **1976**, *80* (24), 2641–2645.

(487) Fan, F. R.; Leempoel, P.; Bard, A. J. *J. Electrochem. Soc. 130*, 1866–1874.

(488) Chen, G.; Zen, J. M.; Fan, F. R. F.; Bard, A. J. *J. Phys. Chem.* **1991**, *95* (9), 3682–3687.

(489) Reiss, P.; Protière, M.; Li, L. *Small* **2009**, *5* (2), 154–168.

(490) Yang, X.; Xu, J.; Wong, T.; Yang, Q.; Lee, C.-S. *Phys. Chem. Chem. Phys.* **2013**, *15* (30), 12688–12693.

(491) Larson, A.; Von Dreele, R. *General Structure Analysis System (GSAS), Los Alamos National Laboratory Report LAUR 86-748*; 2004.

(492) Toby, B. H. *J. Appl. Crystallogr.* **2001**, *34* (2), 210–213.

(493) Lobanov, N.; Alte da Veiga, L. In *6th European Powder Diffraction Conference*; 1998; pp 12–16.

(494) Thompson, P.; Cox, D. E.; Hastings, J. B. *J. Appl. Crystallogr.* **1987**, *20* (2), 79–83.

(495) Tandon, S. P.; Gupta, J. P. *Phys. status solidi* **1970**, *38* (1), 363–367.

(496) Orazem, M. E.; Tribollet, B.; Vivier, V.; Marcelin, S.; Pébère, N.; Bunge, A. L.; White, E. A.; Riemer, D. P.; Frateur, I.; Musiani, M. *ECS Trans.* **2013**, *45* (13), 15–35.

(497) Cooper, M. A.; Hawthorne, F. C. *Can. Mineral.* **1997**, *35* (3), 785–786.

(498) Åsbrink, S.; Norrby, L. J. *Acta Crystallogr. Sect. B* **1970**, *26* (1), 8–15.

(499) Tauc, J. *Mater. Res. Bull.* **1968**, *3* (1), 37–46.

(500) Bhaumik, A.; Shearin, A. M.; Patel, R.; Ghosh, K. **2014**, *16* (22), 11054–11066.

(501) Al-Amri, S. *Curr. Nanosci.* **2015**, *11* (2), 191–197.

(502) Zhao, X.; Wang, P.; Yan, Z.; Ren, N. *Opt. Mater. (Amst).* **2015**, *42*, 544–547.

(503) Gelderman, K.; Lee, L.; Donne, S. W. *J. Chem. Educ.* **2007**, *84* (4), 685.

(504) Minella, M.; Maurino, V.; Minero, C.; Pelizzetti, E. *J. Nanosci. Nanotechnol.* **2015**, *15* (5), 3348–3358.

(505) Gonçalves, A.-M.; Mathieu, C.; Herlem, M.; Etcheberry, A. *Electrochim. Acta* **2010**, *55* (24), 7413–7418.

(506) Nakaoka, K.; Ueyama, J.; Ogura, K. *J. Electrochem. Soc.* **2004**, *151* (10), C661–C665.

(507) Pourbaix, M. *Atlas of electrochemical equilibria in aqueous solutions*; National Association of Corrosion Engineers: Houston, 1974.

(508) Bard, A. J.; Stratmann, M.; Licht, S. In *Encyclopedia of Electrochemistry*; Bard, A. J., Stratmann, M., Licht, S., Eds.; Wiley-VCH Verlag GmbH & Co. KGaA, 2002; Vol. 6.

(509) Bornoz, P.; Abdi, F. F.; Tilley, S. D.; Dam, B.; Van de Krol, R.; Graetzel, M.; Sivula, K. *J. Phys. Chem. C* **2014**, *118* (30), 16959–16966.

(510) Steier, L.; Herraiz-Cardona, I.; Gimenez, S.; Fabregat-Santiago, F.; Bisquert, J.; Tilley, S. D.; Grätzel, M. *Adv. Funct. Mater.* **2014**, *24* (48), 7681–7688.

(511) Zhan, X.; Wang, Q.; Wang, F.; Wang, Y.; Wang, Z.; Cao, J.; Safdar, M.; He, J. *ACS Appl. Mater. Interfaces* **2014**, *6* (4), 2878–2883.

(512) Cheng, Z.; Wang, Z.; Shifa, T. A.; Wang, F.; Zhan, X.; Xu, K.; Liu, Q.; He, J. *Appl. Phys. Lett.* **2015**, *107* (22), 223902.

(513) Salvador, P. *J. Electrochem. Soc.* **1981**, *128* (9), 1895–1900.

Acknowledgments

UNIVERSITÀ DEGLI STUDI DI MILANO

UNIVERSITY OF GOTHENBURG

CHALMERS
UNIVERSITY OF TECHNOLOGY

Consiglio Nazionale delle Ricerche

C3SE Chalmers Centre for Computational Science and Engineering

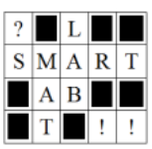

MINISTERO DELL' ISTRUZIONE, DELL'UNIVERSITÀ E DELLA RICERCA